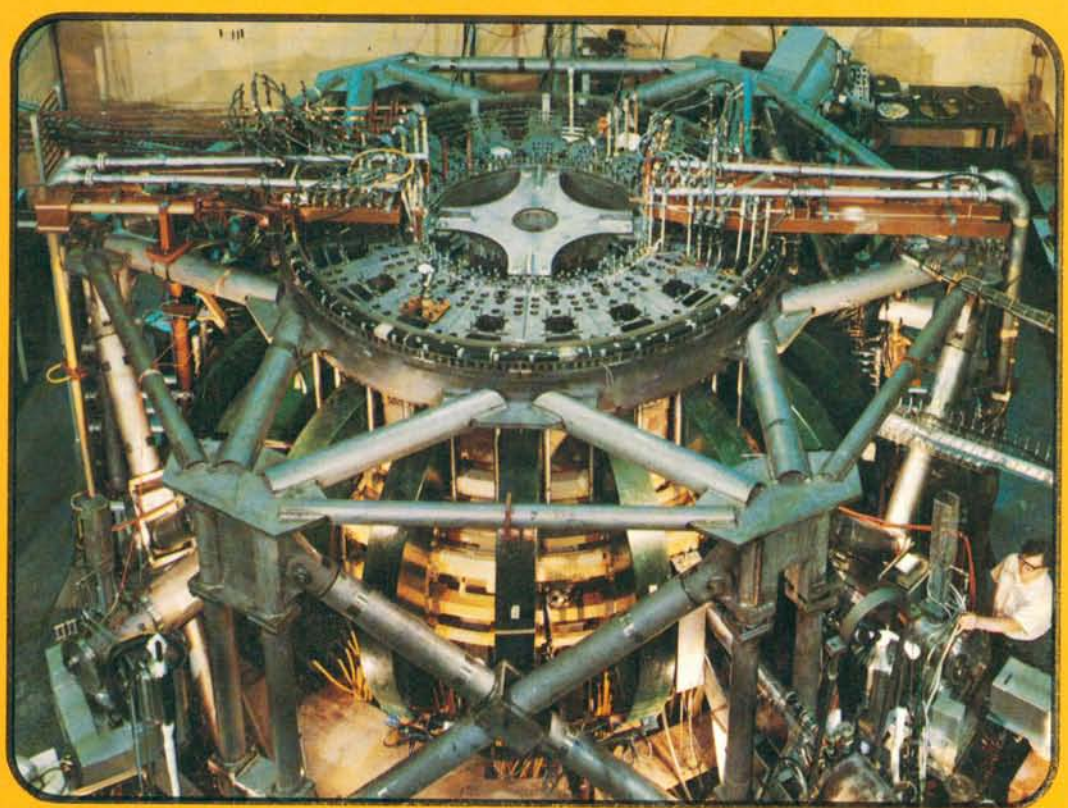
PLASMA PHYSICS AND CONTROLLED NUCLEAR FUSION RESEARCH 1978

VOL. III

Seventh Conference Proceedings, Innsbruck, 23-30 August 1978

NUCLEAR FUSION, SUPPLEMENT 1979



INTERNATIONAL ATOMIC ENERGY AGENCY, VIENNA, 1979

PLASMA PHYSICS
AND CONTROLLED
NUCLEAR FUSION RESEARCH
1978
VOL. III

The following States are Members of the International Atomic Energy Agency:

AFGHANISTAN
ALBANIA
ALGERIA
ARGENTINA
AUSTRALIA
AUSTRIA
BANGLADESH
BELGIUM
BOLIVIA
BRAZIL
BULGARIA
BURMA
BYELORUSSIAN SOVIET SOCIALIST REPUBLIC
CANADA
CHILE
COLOMBIA
COSTA RICA
CUBA
CYPRUS
CZECHOSLOVAKIA
DEMOCRATIC KAMPUCHEA
DEMOCRATIC PEOPLE'S REPUBLIC OF KOREA
DENMARK
DOMINICAN REPUBLIC
ECUADOR
EGYPT
EL SALVADOR
ETHIOPIA
FINLAND
FRANCE
GABON
GERMAN DEMOCRATIC REPUBLIC
GERMANY, FEDERAL REPUBLIC OF
GHANA
GREECE
GUATEMALA
HAITI
HOLY SEE
HUNGARY
ICELAND
INDIA
INDONESIA
IRAN
IRAQ
IRELAND
ISRAEL
ITALY
IVORY COAST
JAMAICA
JAPAN
JORDAN
KENYA
KOREA, REPUBLIC OF
KUWAIT
LEBANON
LIBERIA
LIBYAN ARAB JAMAHIRIYA
LIECHTENSTEIN
LUXEMBOURG
MADAGASCAR
MALAYSIA
MALI
MAURITIUS
MEXICO
MONACO
MONGOLIA
MOROCCO
NETHERLANDS
NEW ZEALAND
NICARAGUA
NIGER
NIGERIA
NORWAY
PAKISTAN
PANAMA
PARAGUAY
PERU
PHILIPPINES
POLAND
PORTUGAL
QATAR
ROMANIA
SAUDI ARABIA
SENEGAL
SIERRA LEONE
SINGAPORE
SOUTH AFRICA
SPAIN
SRI LANKA
SUDAN
SWEDEN
SWITZERLAND
SYRIAN ARAB REPUBLIC
THAILAND
TUNISIA
TURKEY
UGANDA
UKRAINIAN SOVIET SOCIALIST REPUBLIC
UNION OF SOVIET SOCIALIST REPUBLICS
UNITED ARAB EMIRATES
UNITED KINGDOM OF GREAT BRITAIN AND NORTHERN IRELAND
UNITED REPUBLIC OF CAMEROON
UNITED REPUBLIC OF TANZANIA
UNITED STATES OF AMERICA
URUGUAY
VENEZUELA
VIET NAM
YUGOSLAVIA
ZAIRE
ZAMBIA

The Agency's Statute was approved on 23 October 1956 by the Conference on the Statute of the IAEA held at United Nations Headquarters, New York; it entered into force on 29 July 1957. The Headquarters of the Agency are situated in Vienna. Its principal objective is "to accelerate and enlarge the contribution of atomic energy to peace, health and prosperity throughout the world".

© IAEA, 1979

Permission to reproduce or translate the information contained in this publication may be obtained by writing to the International Atomic Energy Agency, Kärntner Ring 11, P.O. Box 590, A-1011 Vienna, Austria.

Printed by the IAEA in Austria
July 1979

NUCLEAR FUSION SUPPLEMENT 1979

PLASMA PHYSICS AND CONTROLLED NUCLEAR FUSION RESEARCH 1978

PROCEEDINGS OF THE
SEVENTH INTERNATIONAL CONFERENCE ON PLASMA PHYSICS
AND CONTROLLED NUCLEAR FUSION RESEARCH
HELD BY THE
INTERNATIONAL ATOMIC ENERGY AGENCY
AT INNSBRUCK, 23 – 30 AUGUST 1978

In three volumes

VOL.III

INTERNATIONAL ATOMIC ENERGY AGENCY
VIENNA, 1979

PLASMA PHYSICS AND CONTROLLED NUCLEAR FUSION RESEARCH 1978
IAEA, VIENNA, 1979
STI/PUB/495
ISBN 92–0–130279–7

FOREWORD

Impressive progress towards the demonstration of the scientific feasibility of controlled fusion and the design and construction of a controlled thermonuclear power reactor was reported at the Seventh IAEA Conference on Plasma Physics and Controlled Nuclear Fusion Research. The three volumes of these Proceedings contain the contributed papers, summaries and discussions on the magnetic confinement approaches to fusion, inertial confinement fusion and fusion reactor engineering. These Conferences are now being held every two years to keep pace with the rapid progress being made, the previous one being held in Berchtesgaden, Federal Republic of Germany, in 1976.

The Seventh Conference was held by the IAEA in Innsbruck, Austria, from 23 to 30 August 1978. More than 500 participants and 38 observers from 32 countries and three international organizations attended. A total of 150 papers were presented at the technical sessions. The first session, on tokamak experiments, was called the Artsimovich Memorial Session to commemorate the contributions of Lev Andreevich Artsimovich to fusion research and to international co-operation in scientific endeavours.

The Proceedings are published in English as a supplement to the IAEA journal "Nuclear Fusion".

The Agency promotes close international collaboration among plasma and fusion physicists of all countries by regularly organizing conferences on controlled nuclear fusion and by holding seminars, workshops and specialists' meetings on selected topics. The activities will, it is hoped, contribute to the rapid use of this new source of energy to meet the world's future energy requirements.

EDITORIAL NOTE

The papers and discussions have been edited by the editorial staff of the International Atomic Energy Agency to the extent considered necessary for the reader's assistance. The views expressed and the general style adopted remain, however, the responsibility of the named authors or participants. In addition, the views are not necessarily those of the governments of the nominating Member States or of the nominating organizations.

Where papers have been incorporated into these Proceedings without resetting by the Agency, this has been done with the knowledge of the authors and their government authorities, and their cooperation is gratefully acknowledged. The Proceedings have been printed by composition typing and photo-offset lithography. Within the limitations imposed by this method, every effort has been made to maintain a high editorial standard, in particular to achieve, wherever practicable, consistency of units and symbols and conformity to the standards recommended by competent international bodies.

The use in these Proceedings of particular designations of countries or territories does not imply any judgement by the publisher, the IAEA, as to the legal status of such countries or territories, of their authorities and institutions or of the delimitation of their boundaries.

The mention of specific companies or of their products or brand names does not imply any endorsement or recommendation on the part of the IAEA.

Authors are themselves responsible for obtaining the necessary permission to reproduce copyright material from other sources.

CONTENTS OF VOLUME III

INERTIAL CONFINEMENT I (Session B)

The KMSF laser fusion programme (IAEA-CN-37/B-2) 3
R.L. Berger, P.M. Campbell, G. Charatis, J.G. Downward, T.M. Henderson, R.R. Johnson, T.A. Leonard, F.J. Mayer, D. Mitrovich, N.K., Moncur, G.R. Montry, D.L. Musinski, R.L. Nolen, L.V. Powers, S.B. Segall, L.D. Siebert, R.J. Simms, D.C. Slater, D.E. Solomon, C.E. Thomas

Inertial confinement fusion at NRL (IAEA-CN-37/B-3) 17
S.E. Bodner, J.P. Boris, G. Cooperstein, S.A. Goldstein, D. Mosher, B.H. Ripin, R. Decoste, J.H. Gardner, R. Lee, R.H. Lehmberg, E.A. McLean, J.H. Orens, J.A. Stamper, S.J. Stephanakis, F. Young, C.M. Armstrong, A. Drobot, M.J. Fritts, P.J. Moffa, W.F. Oliphant, P. Ottinger, F. Sandel, A. Sternleib
Discussion 28

Explosive-pusher-type laser compression experiments with neon-filled microballoons (IAEA-CN-37/B-4) 29
T. Bristow, J. Delettrez, A. Entenberg, Y. Gazit, A. Hauer, L. Goldman, E. Lazarus, C. Lee, S. Letzring, M. Lubin, R. McCrory, T. Mukaiyama, B. Nicholson, B. Perry, J. Rizzo, S. Skupsky, J. Soures, D. Steel, E. Thorsos, B. Yaakobi

INERTIAL CONFINEMENT II (Session D)

Recent progress in inertial confinement fusion research at the Los Alamos Scientific Laboratory (IAEA-CN-37/D-1) 41
R.B. Perkins
Discussion 52

Saturation of stimulated Brillouin backscatter in CO_2 laser-plasma interaction (IAEA-CN-37/D-2) 53
A.A. Offenberger, A. Ng, L. Pitt, D. Salzmann
Discussion 63

Work on laser interaction and implosion at Centre d'études de Limeil (IAEA-CN-37/D-3) 65
A. Bekiarian, E. Buresi, A. Coudeville, R. Dautray, F. Delobeau, P. Guillaneux, C. Patou, J.M. Reisse, B. Sitt, J.M. Vedel, J.P. Watteau
Discussion 72
Experimental studies of interaction and transport processes in laser fusion (IAEA-CN-37/D-4) 75
F. Amiranoff, R. Benattar, R. Fabbro, E. Fabre, C. Garban, C. Popovics, A. Poquerusse, R. Sigel, C. Stenz, J. Virmont, M. Weinfeld
Discussion 85
Dynamics of laser-produced implosion of gas-filled microballoon targets (IAEA-CN-37/D-5) 87
R.G. Evans, M.H. Key, D.J. Nicholas, F. O'Neill, A. Raven, P.T. Rumsby, I.N. Ross, W.T. Toner, P.R. Williams, M.S. White, C.L.S. Lewis, J.G. Lunney, A. Moore, J.M. Ward, T.A. Hall, J. Murdoch, J.D. Kilkenny, T. Goldsack, J.D. Hares

INERTIAL CONFINEMENT III (Session M)

Research on electron-beam inertial-confinement thermonuclear fusion (IAEA-CN-37/M-1) 105
L.E. Aranchuk, Yu.I., Arkhangel'skij, M.V. Babykin, K.A. Bajgarin, E.I. Baranchikov, A.V. Bartov, A.S. Chernenko, B.A. Demidov, S.D. Fanchenko, A.V. Gordeev, Yu.G. Kalinin, Yu.V. Koba, V.D. Korolev, D.N. Lin, V.I. Mizhiritskij, S.L. Nedoseev, A.M. Pasechnikov, V.S. Pen'kina, L.I. Rudakov, V.A. Skoryupin, V.P. Smirnov, E.Z. Tarumov
Discussion 121
Developments in Sandia Laboratories particle beam fusion programme (IAEA-CN-37/M-3) 125
G. Yonas, The Sandia Laboratories Particle Beam Fusion Group
Discussion 132
Inertial confinement fusion research at Osaka: New developments in laser energy drivers, laser and REB fusion research (IAEA-CN-37/M-4) 135
H. Azechi, H. Fujita, K. Imasaki, Y. Izawa, Y. Kato, Y. Kawamura, M. Matoba, K. Mima, S. Miyamoto, Y. Mizumoto, T. Mochizuki, S. Nakai, K. Nishihara, H. Nishimura, T. Norimatsu, T. Sasaki, H. Takabe, J.J. Thomson, K. Yoshida, T. Yamanaka, C. Yamanaka
Discussion 154

INERTIAL CONFINEMENT IV (Session V)

Laser fusion implications of resonance absorption and associated electrostatic field pressure (IAEA-CN-37/V-1-1) 157
T.P. Donaldson, J.E. Balmer, P. Wägli, P. Lädrach

Fast ions in laser-produced plasma (IAEA-CN-37/V-1-2) 167
N.E. Andreev, A.S. Shikanov, V.T. Tikhonchuk, Yu.A. Zakharenkov, N.N. Zorev
Discussion on papers V-1-1 and V-1-2 179

Non-linear theory of collective processes in laser-pellet interaction and soliton generation (IAEA-CN-37/V-2-1) 181
H.H. Chen, C. Grebogi, C.-S. Liu, V.K. Tripathi

Wave absorption and superreflectivity of laser plasmas due to electromagnetic structure resonances (IAEA-CN-37/V-2-2) 187
K. Sauer, N.E. Andreev, K. Baumgärtel

Theory of cavitons in laser-irradiated plasmas (IAEA-CN-37/V-2-3) 201
K.H. Spatschek, M.Y. Yu, P.K. Shukla
Discussion on papers V-2-1 to V-2-3 209

The United States programme in heavy ion beam fusion (IAEA-CN-37/V-3) 211
T.F. Godlove, D.F. Sutter
Discussion 222

Nuclear fusion by cylindrical ion implosion (IAEA-CN-37/V-4) 225
M. Gryziński, J. Appelt, J. Baranowski, M. Bielik, E. Górski, A. Horodeński, L. Jakubowski, A. Jerzykiewicz, J. Kurzyna, J. Langner, B. Lipiński, K. Melzacki, Z. Nawrocki, J. Nowikowski, M. Sadowski, E. Skłądnik-Sadowska, J. Stanisławski, K. Sudlitz

Calculations of inertial confinement fusion gains using a collective model for reheat, bremsstrahlung and fuel depletion for highly efficient electrodynamic laser compressions (IAEA-CN-37/V-5) 237
H. Hora, R. Castillo, R.G. Clark, E.L. Kane, V.F. Lawrence, R.D.C. Miller, M.F. Nicholson-Florence, M.M. Novak, P.S. Ray, J.R. Shepanski, A.I. Tsivinsky
Discussion 245

FUNDAMENTAL PROCESSES AND NEW TRENDS (Session X)

Low-aspect-ratio limit of the toroidal reactor: the Spheromak (IAEA-CN-37/X-1) 249
M.N. Bussac, H.P. Furth, M. Okabayashi, M.N. Rosenbluth, A.M.M. Todd
Discussion 264
Boundary layer analysis of cold-blanket systems (IAEA-CN-37/X-3) 265
B. Lehnert, B. Bonnevier, J.R. Drake, A. Kuthy, D. Ohlsson, E. Tennfors, B. Wilner
Discussion 275
Computer simulation of heat transport on a $2\frac{1}{2}$-D model and investigations of large-scale plasma simulations on the CHI computer (IAEA-CN-37/X-4-1) 277
J.M. Dawson, T. Kamimura, H. Naitou, R.W. Huff, C.C. Wu
Turbulent convective transport in a plasma (IAEA-CN-37/X-4-2) 285
A.S. Bakaj
Discussion on papers X-4-1 and X-4-2 309
Experiments on plasma confinement by relativistic-electron-beam ring (IAEA-CN-37/X-5) 311
A. Mohri, K. Narihara, T. Tsuzuki, Y. Kubota, Y. Tomita, K. Ikuta, M. Masuzaki
Discussion 320

TECHNOLOGY AND REACTOR CONCEPTS I (Session I)

A reversed-field-pinch reactor with superconducting windings (IAEA-CN-37/I-1) 323
R. Hancox, C.R. Walters
Discussion 331
Systems studies and conceptual reactor designs of alternative fusion concepts at LASL (IAEA-CN-37/I-2) 333
R.A. Krakowski, R.L. Hagenson, R.L. Miller, R.W. Moses
Discussion 341
The Elmo Bumpy Torus (EBT) reactor (IAEA-CN-37/I-3) 343
N.A. Uckan, D.B. Batchelor, E.S. Bettis, R.A. Dandl, C.L. Hedrick, E.F. Jaeger, D.G. McAlees, D.B. Nelson, L.W. Owen, R.T. Santoro, D.A. Spong, T. Uckan, H.L. Watts, H.T. Yeh, L.M. Lidsky, J.S. Herring, R.E. Potok
Discussion 356

Impact of technology and maintainability on economic aspects of tokamak power plants (IAEA-CN-37/I-4) 357
M.A. Abdou, C.C. Baker, J. Brooks, R. Clemmer, C. Dennis, D. Ehst, K. Evans, S. Harkness, R. Kustom, V. Maroni, D. Smith, H. Stevens, L. Turner, G.M. Fuller, H.S. Zahn
Discussion 367
Neutral-beam injector research and development work in the USA (IAEA-CN-37/I-5) 369
R.V. Pyle, W.R. Baker, K.H. Berkner, C.F. Burrell, C.F. Chan, W.S. Cooper, K.W. Ehlers, W.G. Graham, D.B. Hopkins, W.B. Kunkel, D.J. Massoletti, K.A. Milnes, H.M. Owren, J.A. Paterson, L. Ruby, R.R. Smith, J.W. Stearns, W.F. Steele, D.P. Yee, O.A. Anderson, W.L. Barr, D.H. Birdsall, D.R. Branum, K.R. DeVore, T.J. Duffy, G.W. Hamilton, E.B. Hooper, Jr., R.W. Moir, T.J. Orzechowski, L.C. Pittenger, P. Poulsen, T.L. Rossow, M.E. Smith, M. Grossman, C. Lam, R. Larson, R. McKenzie-Wilson, K. Prelec, Th. Sluyters, G.C. Barber, W.R. Becraft, C.W. Blue. W.K. Dagenhart, R.C. Davis, C.A. Foster, W.L. Gardner, H.H. Haselton, J. Kim, C.M. Loring, M.M. Menon, S.L. Milora, S. Ponte, P.M. Ryan, D.E. Schechter, S.W. Schwenterly, W.L. Stirling, C.C. Tsai, J.H. Whealton, R.E. Wright

TECHNOLOGY AND REACTOR CONCEPTS II (Session R)

Concept of tokamak-type reactor with high-temperature blanket (IAEA-CN-37/R-1) 379
N.N. Vasil'ev, V.E. Lukash, A.V. Nedospasov, L.B. Nefedkina, V.G. Petrov, M.Z. Tokor, B.N. Kolbasov, D.K. Kurbatov, V.V. Orlov, V.I. Pistunovich, G.E. Shatalov
Discussion 386
Tokamak TNS studies (IAEA-CN-37/R-2) 389
P.H. Sager, Jr., M. Roberts
Discussion 398
Tandem mirror reactors (IAEA-CN-37/R-3) 401
B.G. Logan, W.L. Barr, D.J. Bender, G.A. Carlson, W.L. Dexter, J.N. Doggett, R.S. Devoto, J.F. Fink, T.K. Fowler, G.W. Hamilton, D. Lappa, J.D. Lee, W.D. Neef, Jr., A.A. Mirin, R.W. Moir, M.A. Peterson, M.E. Rensink
Discussion 410

Fuel production characteristics of fusion hybrid reactors (IAEA-CN-37/R-4) 413
R.P. Rose, T.C. Varljen, F.L. Ribe, N.J. McCormick, G.C. Vlases, G.L. Woodruff, V.L. Teofilo, B.R. Leonard, Jr., D.T. Aase, R.T. Perry, S.C. Shulte, S.C. Burnett, K.R. Schultz, R.H. Brogli, D.W. Kearney
Discussion 419
Acceleration of macroparticles by laser light (IAEA-CN-37/R-5-1) 421
M.D.J. Burgess, H. Motz, I.J. Spalding, A.C. Walker
Application of bundle divertors to experimental tokamaks and reactors and some consequences of collisionless exhaust flow to divertor targets (IAEA-CN-37/R-5-2) 431
P.J. Harbour, M.F.A. Harrison, A.D. Sanderson, P.E. Stott
Discussion on papers R-5-1 and R-5-2 443

SUMMARY SESSION

Summary on magnetic-confinement experiments 447
C.M. Braams
Summary on magnetic-confinement theory 459
D.D. Ryutov
Summary on inertial-confinement fusion 469
K. Nishikawa
Summary on reactor systems 479
R.W. Conn

Chairmen of Sessions and Secretariat of the Conference 487
List of Participants 489
Author Index 535

Session B

INERTIAL CONFINEMENT I

Chairman

C. YAMANAKA
Japan

THE KMSF LASER FUSION PROGRAMME*

R.L. BERGER, P.M. CAMPBELL, G. CHARATIS,
J.G. DOWNWARD, T.M. HENDERSON, R.R. JOHNSON,
T.A. LEONARD, F.J. MAYER, D. MITROVICH,
N.K. MONCUR, G.R. MONTRY, D.L. MUSINSKI,
R.L. NOLEN, L.V. POWERS, S.B. SEGALL,
L.D. SIEBERT, R.J. SIMMS, D.C. SLATER,
D.E. SOLOMON, C.E. THOMAS
KMS Fusion Inc.,
Ann Arbor, Michigan,
United States of America

Abstract

THE KMSF LASER FUSION PROGRAMME.

Laser-driven implosion experiments have been performed at both 1.06 μm and 0.53 μm. The fractional absorption was greater at 0.53 μm although with the laser power available at 0.53 μm it was not possible to observe effects of a high-temperature corona. Other experiments were performed using cryogenic targets at 1.06 μm. It was found that the neutron yield and peak fuel densities were greater when the fuel formed a liquid or solid layer on the inside of the spherical glass-shell targets.

INTRODUCTION

The KMSF program has been engaged in the development of laser fusion physics by studying, experimentally and theoretically, the irradiation and implosion of spherical-shell, fuel-filled targets. Experiments have been done to quantify the conditions of the imploded target core, to measure the amount of laser energy absorbed, to examine the partitioning of this energy into its various components, and to examine the transport of the absorbed energy. Theoretical investigations have been directed toward achieving an understanding of the physical mechanisms relevant to these experiments.

The implosion process has been investigated by measuring the nuclear reaction products and the time-integrated x-ray emission from the compressed targets. Typical neutron yields of a few times 10^7 at 0.4 TW and fuel ion temperatures of 2.2 keV from the implosion of 60-μm-diameter [(10 atm) (1 MPa)] targets are consistent with peak compressed fuel densities of $\sim$ 1 to 2 g/cm^3. In implosion experiments with cryogenic fuel layers, x-ray pinhole photographs showed that the fuel was compressed to densities as high as 7 g/cm^3, but densities of $\sim$ 0.5 g/cm^3 were more frequently observed. In all of these cases, the relatively high densities achieved at modest absorbed energies are believed to be due to the symmetric target illumination afforded by the ellipsoidal mirror system.

* Work supported by US Dept. of Energy under Contract ES-77-C-02-4149.

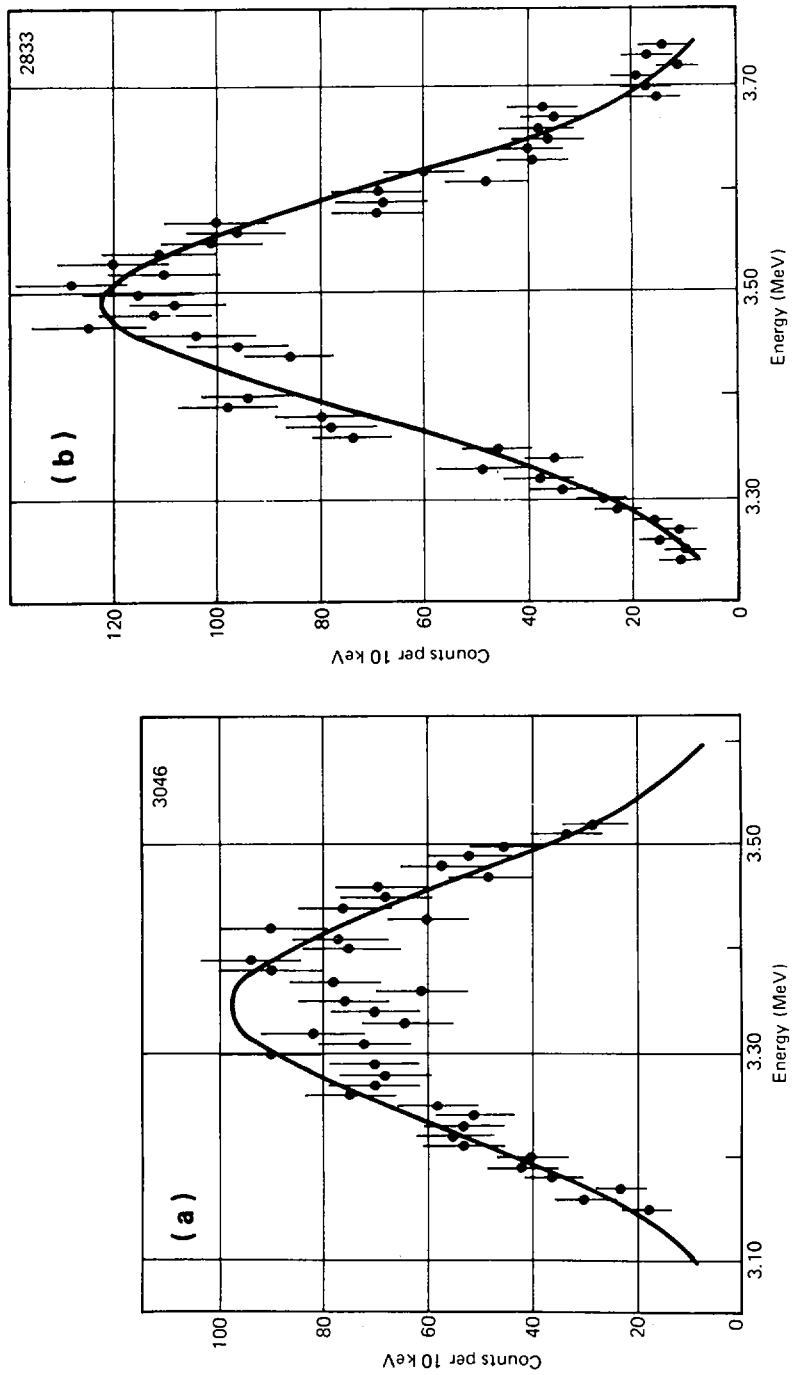


FIG. 1. (a) Alpha-particle energy spectrum for cryogenic liquid-layer target shot 3046. The fitted gaussian (solid line) has mean energy of 3.33 ± 0.07 MeV and FWHM of 265 ± 20 keV, corresponding to a fuel ion temperature of 2.2 ± 0.4 keV. (b) Alpha-particle energy spectrum for gaseous target shot 2833. The fitted gaussian (solid curve) has an FWHM of 250 ± 20 keV, corresponding to a fuel ion temperature of 2.0 ± 0.3 keV. The mean energy is 3.49 ± 0.07 MeV.

The production and dynamics of fast ions may have important implications for laser fusion. Fast ions constitute a small fraction ($\sim$ 8%) of the mass of the target, but carry off a sizeable amount ($\sim$ 40%) of the absorbed laser energy. The fast-ion spectra were used for determining the corona temperature in the experiments described here.

Spherical-target implosion experiments were performed using 0.532-μm laser light obtained by frequency-doubling the Nd:glass laser output. These experiments indicate that relative absorption of laser light increases at the shorter wavelength.

Targets typically absorb 20% to 30% of the 1.06-um laser light in the ellipsoidal mirror illumination geometry. Although the relative contributions of various absorption mechanisms have not been established, resonance absorption is believed to account for a significant fraction of the total absorbed energy at the higher laser powers [1-3].

IMPLOSION OF CRYOGENIC TARGETS

The most important experimental observations in laser fusion studies are those relating to the target implosion and fusion reaction processes. The experiments are performed with an ellipsoidal-mirror illumination system [4] which produces nearly uniform illumination at near-normal incidence [5] on DT-filled glass microshell targets. Measurements of neutron yield, alpha-particle energy spectra, and x-ray pinhole camera images together with numerical simulations are used to form a picture of the laser-driven implosion process [6].

The energy spectrum of alpha particles from the DT fusion reaction provides an upper limit to the fuel ion temperature at peak compression [7]. The energy lost by the alpha particles as they traverse the compressed fuel and shell can provide a measure of $\int \rho dr$. The magnetic spectrograph used to measure the alpha-particle spectra is described in Reference [8].

The time-integrated x-ray emission from the target is imaged using two pinhole cameras [9,10]. Each camera has an array of four 5-μm pinholes, which are covered with beryllium-foil filters of various thicknesses. The inner region of intense x-ray emission occurs when the imploding tamper material is stopped by the back pressure of the compressed DT gas. If the compressed core is larger than the resolution of the pinhole camera, the inner feature will appear as a ring from which the volume compression can be estimated. In some instances, the inner feature of the image appears as a solid core (a central peak on the microdensitometer tracer) rather than a ring. Computer simulations described in Reference [10] show that this could result if the compressed-core radius were less than the camera resolution. The peak could also be produced by mixing of the glass into the fuel. Thus reliable compression measurements cannot be obtained from these centrally peaked x-ray photographs.

Compression symmetry is affected by illumination uniformity, fluctuations in the laser beams, and irregularities in target surface and wall thickness. Compression symmetry is improved when the laser-light focal points are displaced slightly to improve the uniformity of illumination at the target surface and when the laser intensity fluctuations are reduced by the plasma spatial filter.

DT-gas-filled glass microshell targets of diameters between 55 μm and 80 μm were irradiated with approximately 0.5 TW of 1.06-μm laser light. On the gas targets, the best shots produced $\sim 7 \times 10^7$ neutrons, fuel ion

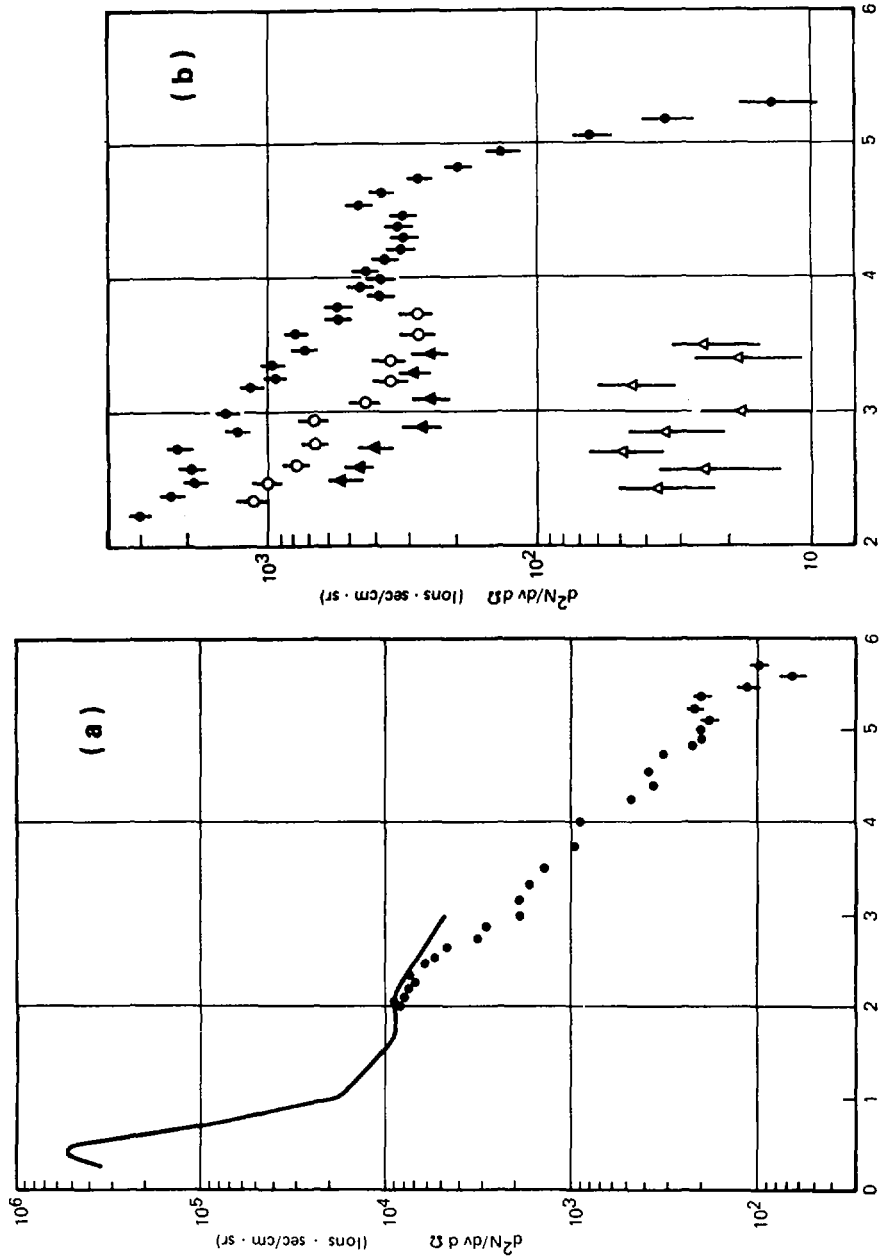


FIG.2. (a) Composite ion-velocity spectrum combining charge-collector (curve) and magnetic-spectrograph (points) data. (b) Selected fast-ion velocity spectra from a standard glass target obtained with a Thomson parabola analyser. Solid circles: O^{8+} plus C^{6+}; open circles: C^{5+}; solid triangles: O^{7+}; open triangles: Si^{13+}.

temperature $T_i \sim 2$ keV, compressions $\sim$ 1-to-2 x 10^3 and fuel densities $\sim$ 0.5 to 2 g/cm^3

Glass-shell targets, in which the fuel was condensed in a liquid layer on the inner surface, systematically produced higher DT-fuel densities. Targets giving the highest neutron yields had a nominal diameter of 60 μm and a wall thickness of 0.7 μm. The initial liquid density is assumed to be the triple point density of 220 mg/cm^3. The liquid layer was rarely uniform, displaying a typical asymmetry in thickness of two to one. This asymmetry persisted during compression, with the compressed region in x-ray pinhole photographs displaced from the target center an amount corresponding to the initial asymmetry. Compressions from 50 to 350 have been measured, corresponding to fuel densities from 0.8 g/cm^3 to 7 g/cm^3. Neutron yields were $\sim$ 2-to-7 x 10^7 and fuel ion temperatures $\sim$ 1 to 2 keV. Additional evidence of increased fuel densities for liquid-layer targets comes from alpha-particle energy spectra which are downshifted from 3.52 MeV by as much as 300 keV for liquid layer targets, but not more than 100 keV for gas-filled targets. This downshift is shown in Figure 1 with the experimental uncertainty being approximately 70 keV.

There have been additional experiments in which the fuel was condensed in a solid layer on the inner surface of the shell. The asymmetry in the fuel distribution was significantly reduced in comparison to the liquid-layer targets. The x-ray pinhole photographs showed a more symmetrical implosion, and as a result a more accurate measurement of the compressed fuel density was obtained. The neutron yields were comparable with those of the liquid-layer targets at equivalent laser power on target. The highest compression for a solid-layer target as inferred from the x-ray pinhole photograph was 370, corresponding to a maximum fuel density of 7 g/cm^3. The original target diameter was 88 μm which would result in a $\langle\rho R\rangle$ of approximately 5 mg/cm^2 in the fuel. This value for $\langle\rho R\rangle$ is consistent with the observed 10% downshift in the measured alpha spectrum.

FAST IONS AND TRANSPORT

Most of the laser light energy is absorbed near the critical density surface. Much of this energy ultimately appears as kinetic energy of the ions in the blowoff plasma. The study of the evolution of energy partitioning involves the interrelated questions of how the absorbed energy is transported to the remaining electrons, and how this energy is converted into ion kinetic energy.

Ion spectral measurements have been obtained with biased charge collectors, a magnetic spectrograph, and a Thomson parabola spectrograph [8]. The Thomson parabola measures the charge-to-mass ratio in addition to the ion velocity and so provides the most detailed information about the fast ions. The results of typical measurements are shown in Figure 2.

The velocity distribution of these ions shows the well-known two-component shape [11], consisting of a small number of fast ions with velocities in excess of 10^8 cm/sec followed by the majority of the ions whose velocities are a few times 10^7 cm/sec. If this two-component spectrum results from a two-temperature electron distribution, then by studying the ion spectrum in detail we may be able to draw inferences about the electrons and, therefore, about the absorption and transport processes at the target. A straightforward interpretation of the two-component ion distribution can be obtained from the isothermal rarefaction model [12,13]. Using this very simple model, a measurement of the scale velocity of the ion spectrum gives the electron temperature of the corona.

The fast ions, with a distribution characteristic of electron temperatures near 10 keV, presumably come from the hot corona, and represent material that has passed through the laser-light absorption region. The slow ions originate in the cooler ($\sim$ 1 keV) interior of the target wall. The sharp thermal gradient implied by this interpretation cannot be understood on the basis of classical transport coefficients, but it is consistent with the inhibited transport suggested in other experiments on planar targets [14] with a flux limiter $f \approx 6\ (Zm_e/2m_i)^{1/2} \approx 1/15$.

The reduced heat flow results in a high corona temperature. For an absorbed power of 10^{15} W/cm^2, the corona temperature becomes 10 keV, a value consistent with the temperature range inferred from the ion velocity spectra. We have compared the hot-electron temperature deduced from the continuum x-ray spectrum with that obtained from the fast-ion spectrum on a number of target shots. They are in rough agreement, but the x-rays indicate a somewhat higher temperature.

WAVELENGTH SCALING EXPERIMENTS

The two approaches currently underway for maximizing the absorption of laser light by a target are, first, varying the laser wavelength and bandwidth and, second, varying the target design. To investigate the first approach, neutron-producing implosion experiments were carried out at KMSF with laser wavelengths of 1.06 μm and 0.53 μm.

A differential calorimeter positioned in the annular gap between the ellipsoidal mirrors is used to measure the total absorbed energy. Total absorbed energy values are obtained by assuming a uniform plasma blow-off and extrapolating the energy measured in the acceptance angle of the detector to 4π solid angle. For the relatively uniform illumination pattern produced with the lens-ellipsoidal mirror focusing system, this is a good approximation.

Absorption data shown in Figure 3 were for 50 to 170-μm-diameter targets. Most target shots were taken using normal-incidence focusing, for which the focal positions of the two beams were coincident with the center of the target. For some of the data the focal position of each beam was displaced 5 to 20 μm relative to the center of the target in order to produce a more uniform illumination pattern on the surface of the target. No significant difference in absorption was noted in these cases compared with normal-incidence focusing.

Recent experiments at KMS Fusion on spherical targets have shown that the fractional absorption is wavelength dependent. Experiments were performed at power levels of about 0.1 TW with the optics shown schematically in Figure 4. The fractional absorption at 0.53 μm was greater than that observed under similar conditions with 1.06-μm radiation. Figure 5(a) shows the results of these experiments at 0.53 μm, some of which were conducted using the plasma spatial filter.

The plasma spatial filter is a beam-smoothing laser component consisting essentially of a planar target and lens interposed in the path of the laser beam at an early stage in the sequence of laser amplifiers. The plasma that forms on the target at the focus of the lens behaves as an active mirror, reflecting a portion of the beam back along the incident path to be amplified by subsequent amplifiers before being focused onto the fusion pellet.

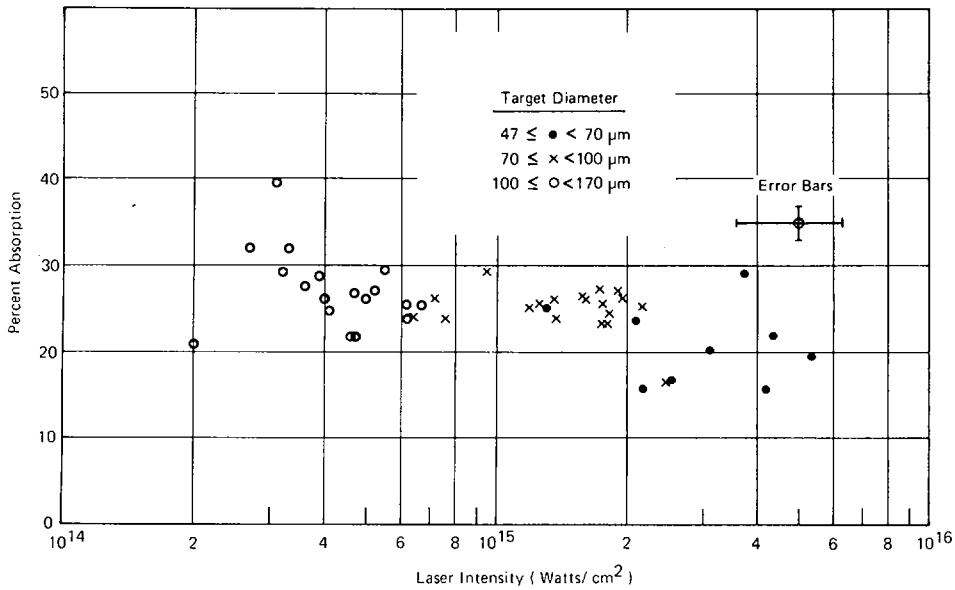


FIG.3. Percentage of incident laser energy absorbed by spherical glass-shell targets as a function of average laser intensity. All data were taken with the laser configuration employing the plasma spatial filter.

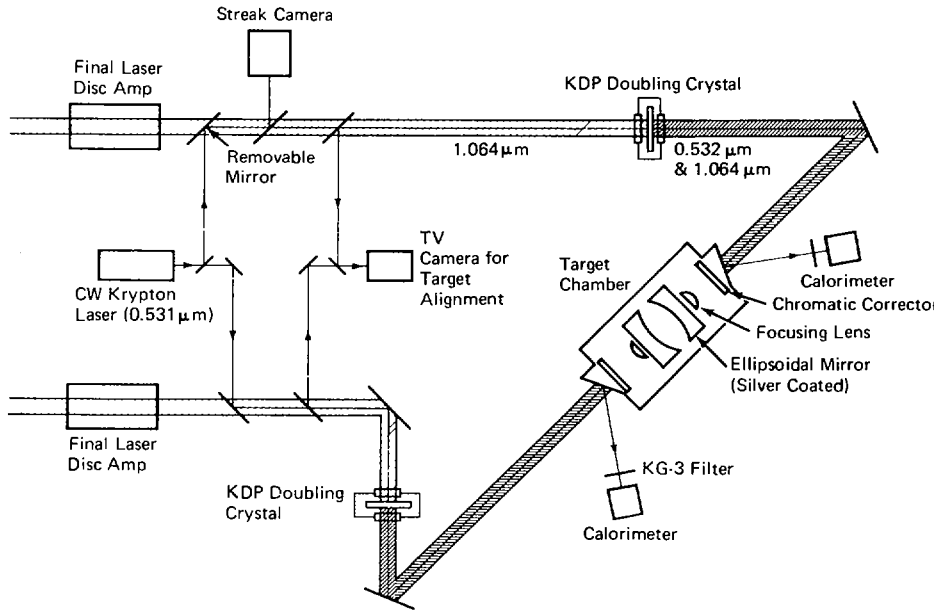


FIG.4. Optics used for the 0.53-μm target experiments.

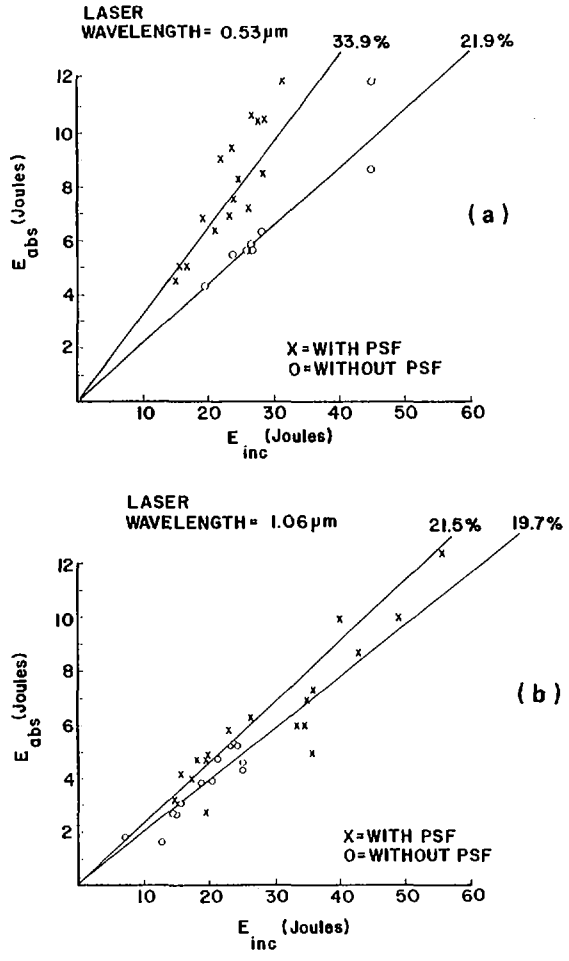


FIG.5. Absorption of laser energy at (a) 0.53 μm and (b) 1.06 μm, with and without the plasma spatial filter at 0.1 TW. The targets were nominal 85-μm-dia. glass shells of 1 μm wall thickness.

The result is a spatially more homogeneous laser beam with a bandwidth of approximately 40 Å as compared with the normal 4 Å bandwidth. The fractional absorption increased at 0.53 μm when the plasma filter was used. It is not clear whether the increase in the absorption was due to the decrease in the number of high-intensity fluctuations in the laser beam or to an increase in the bandwidth of the laser.

Laser power for the wavelength comparison shots was in the range 0.070 to 0.160 TW both at 1.06 μm and 0.53 μm. Corona electron temperatures determined from ion velocity spectra using an isothermal model of the plasma blowoff indicated electron temperatures in the range of 1 to 3 keV. The experiments indicate that the fractional absorption was 21.4 ± 3.9% at 1.06 μm with and 19.7 ± 3.1% without the plasma spatial filter, as shown in Figure 5(b).

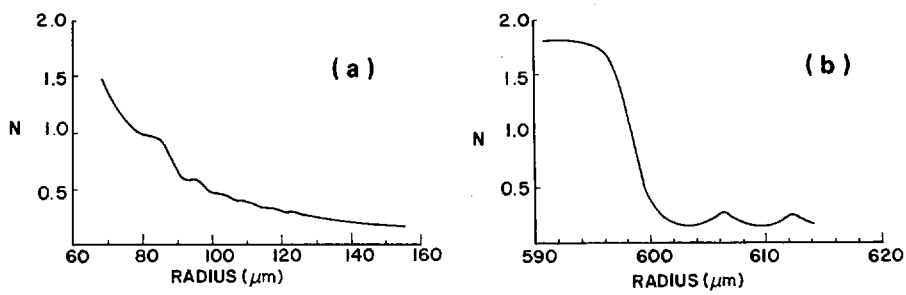


FIG.6. Examples of steady-state density profiles:(a) plateau for incident intensity $|E_c|^2/4\pi n_c T = 0.24$; *(b) D-front for incident intensity* $|E_c|^2/4\pi n_c T = 1.0$.

The experiments at 0.1 TW and 0.53 μm using the plasma spatial filter showed a fractional absorption of 33.9 ± 4.4%, whereas without the plasma spatial filter the fractional absorption was 22.3 ± 2.1%.

The highest neutron yield measured at 0.53 μm using the plasma spatial filter was 1.7×10^6 with 0.084 TW of laser power on target. The highest yield at 1.06 μm under similar conditions was 4.6×10^5 at 0.088 TW of laser power on target. The highest neutron yield at 0.53 μm without the plasma spatial filter was 7×10^6 at 0.08 TW compared with 2×10^5 at 0.08 TW at 1.06 μm. The difference in neutron yield is attributed primarily to the higher fractional absorption at 0.53 μm. Since the corona temperatures were 1 to 3 keV in both instances, it appears that the flux inhibition was not a serious factor in these experiments. The hot-corona temperature does not scale with wavelength for these experiments. Further results at higher laser power at 0.53 μm will be required in order to determine the scaling of the hot-corona temperature.

THEORY OF CRITICAL DENSITY PHENOMENA

Experiments at KMSF and elsewhere have shown that characteristics of the laser radiation, such as its bandwidth, can have important effects on absorption and profile modification. Moreover, certain observables such as the velocity of the critical surface are a measure of the thermal-electron temperature. We report some results on the influence on the hydrodynamics of the laser radiation pressure and, to a limited extent, of the localized electrostatic radiation due to resonance absorption.

For normal incidence and with no resonance absorption, the time evolution of the critical-density region was followed, starting from a one-dimensional, hydrodynamic equilibrium for an isothermal spherical plasma. The laser wave equation was solved exactly with a phenomenological damping rate. Since we were interested primarily in critical-surface phenomena, we replaced the pellet interior by a boundary condition on the flow and limited our interest to times short compared with an implosion time. Only those plasmas were studied for which there exist steady-state solutions of the coupled equations of mass conservation and momentum conservation and of the laser wave equation. We found, as anticipated, that the well-known density step profiles [15] are stable steady states. These profiles are characterized by subsonic fluid flow for radii less than the critical radius. However, it is well known [16] that, unless the heat flow is strongly flux-limited

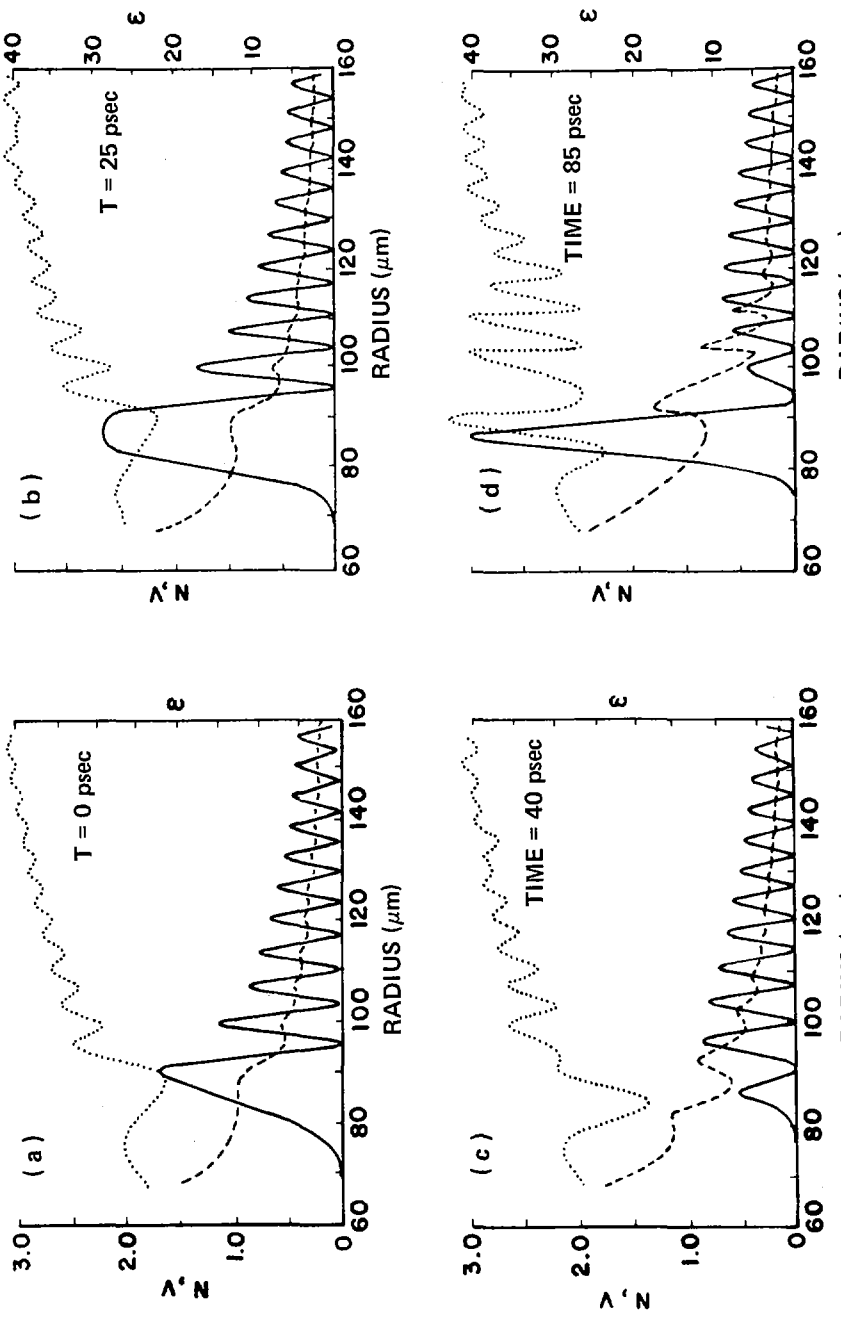


FIG. 7. Time history of unstable plateau for incident intensity $|E_c|^2/4\pi n_c T = 0.43$: *(a)* $t = 0$; *(b)* $t = 25$ *psec; (c)* $t = 40$ *psec; (d)* $t = 85$ *psec. The electric field intensity (solid curve) is normalized to the incident intensity. The scale on the right refers to the normalized electric field intensity* $\epsilon = |E|^2/4\pi n_c T$ *and those on the left to the density (dashed curve) and flow velocity (dotted curve).*

between the critical surface and the ablation surface, steady-state flow models require a sonic point interior to the critical radius. The only steady-state profiles with supersonic flow inside the critical radius are the plateau solutions of Mulser [17]. In Figure 6, we show an example of each type of profile for the same ratio of incident radiation pressure to plasma pressure at the critical surface. In this case, $|E|^2/4\pi n_c T_e = 0.25$. For higher intensities the density gradient outside the critical surface reverses and, for high enough intensities, i.e. $|E_i|^2/4\pi n_c T > 1$, no true steady state exists for supersonic flow interior to the critical radius. However, a quasi-stationary state exists for such intensities in the frame of a moving critical surface. In this moving frame, the flow velocity, which is supersonic in the laboratory frame, is subsonic so that an ordinary density step profile can result. This profile cannot be stationary very long because the expanding critical surface reduces the radiation pressure for a fixed incident radiation flux (Figure 7).

Fluid simulations in spherical geometry that include classical heat flow have observed this latter profile and not the plateau solution [18, 19]. That observation stimulated analysis that showed that plateaus were unstable, and prompted the suggestion made that they would evolve into quasi-stationary, supercritical density bumps [18].

Our simulations show that density plateaus indeed are unstable to the formation of bumps that propagate out from the critical surface roughly at the sound speed, provided a threshold radiation intensity is exceeded. The threshold intensity depends on the flow velocity, but typically $[E]^2/4\pi n_c T_e \geq 0.5$. Alternatively, plateaus exhibit a positive density gradient when the incident intensity exceeds a certain value, and it is for intensities above this value that plateaus are unstable. The bumps that form and propagate out from the critical surface remain subcritical, however, and new bumps are formed periodically. The critical surface remains fixed in space as it was at the outset of the simulation.

Experiments at KMSF have followed the time history of the critical surface by observing and time-resolving the harmonic emission at twice the laser frequency. The velocity of the critical surface, if set equal to the sound speed of thermals, as suggested by simulations, results in a temperature of about $T_e \sim 2$ to 3 keV. For such temperatures, the ratio of radiation pressure to plasma pressure at the critical surface is very small, i.e. $|E|^2/4\pi n_c T \approx 0.02$. Thus, ponderomotive force effects should be negligible and little profile modification due to ponderomotive forces should be present. If profile modification is observed, it could be indicative of rarefaction shocks due to two-temperature electron distributions or of non-classical heat flow.

Very little work has been done to find steady-state, self-consistent solutions of the hydrodynamic equations including ponderomotive forces when electrostatic resonant absorption fields are present. We have found solutions [20,21] in the parameter regime for which plateau solutions exist for normal incidence. For a fixed angle of incidence and for intensities such that the flow remains supersonic through the critical density region, we have found both the self-consistent profile and the amount of resonance absorption as a function of $I\lambda^2$. The model assumes an isothermal plasma and phenomenological damping of the electrostatic component. The amount of resonant absorption varies inversely with $I\lambda^2$ for this profile in a much stronger way than particle simulations show. We believe this results more from the fact that the particle simulations do not include supersonic flow or spherical geometry and less from the fact that our model is missing

essential physics. Work is in progress to try to reproduce the particle simulation results in the corresponding regime within a fluid formulation.

CONCLUSION

The studies reported here, especially the very significant work with cryogenic targets and green-light irradiation, open a promising avenue for further investigation. As higher laser power becomes available, it is expected that amplification and extension of these studies will lead to a more detailed practical and theoretical understanding of the laser fusion mechanism.

REFERENCES

[1] J.P. Friedberg, R.W. Mitchell, R.L. Morse, and L.I. Rudsinski, Phys. Rev. Lett. 28 795 (1972).

[2] K.G. Estabrook, E.J. Valeo, and W.L. Kruer, Phys. Fluids 18 1151 (1975).

[3] K.R. Manes, V.C. Rupert, J.M. Auerbach, P. Lee, and E. Swain, Phys. Rev. Lett. 39 281 (1977).

[4] C.E. Thomas, Appl. Opt. 13 1267 (1975).

[5] K.A. Brueckner, J.E. Howard, Appl. Opt. 14 1274 (1975).

[6] P.M. Campbell, P. Hammerling, R.R. Johnson, J.J. Kubis, F.J. Mayer, and D.C. Slater, Plasma Physics and Controlled Nuclear Fusion Research (Proc. Int. Conf. Berchtesgaden, 1976) IAEA, Vienna (1977) Vol. I, p. 227.

[7] V.W. Slivinsky, H.G. Ahlstrom, K.G. Tirsell, J. Larsen, S. Glaros, G. Zimmerman, and H. Shay, Phys. Rev. Lett. 35 1083 (1975); R.R. Goforth, F.J. Mayer, H. Brysk, and R.A. Cover, J. Appl. Phys. 47 2850 (1976).

[8] D.C. Slater and F.J. Mayer, Laser Interaction and Related Plasma Phenomena, Vol. 4B (H.J. Schwarz and H. Hora, eds) Plenum, NY (1977) p. 603.

[9] G. Charatis, J. Downward, R. Goforth, B. Guscott, T. Henderson, S. Hildum, R. Johnson, K. Moncur, T. Leonard, F. Mayer, S. Segall, L. Siebert, D. Solomon, and C. Thomas, Plasma Physics and Controlled Nuclear Fusion Research (Proc. Int. Conf. Tokyo, 1974) IAEA, Vienna (1975) Vol. II, p. 317.

[10] P.M. Campbell, G. Charatis, and G.R. Montry, Phys. Rev. lett. 34 74 (1975).

[11] C. Yamanaka, T. Yamanaka, T. Sasaki, K. Yoshida, M. Waki, H.B. Kang, Phys. Rev. A6 2335 (1972); A.W. Ehler, J. Appl. Phys. 46 2464 (1975); G. Charatis, J. Downward, R. Goforth, B. Guscott, T, Henderson, S. Hildum, R. Johnson, K. Moncur, T. Leonard, F. Mayer, S. Segall, L. Siebert, D. Solomon, and C. Thomas, Plasma Physics and Controlled Nuclear Fusion Research (Proc. Int. Conf. Tokyo, 1974) IAEA, Vienna (1975) Vol. II, p. 317.

[12] L.D. Landau, E.M. Lifshitz, Fluid Mechanics, Pergamon, London (1959) p. 359.

[13] K.A. Brueckner, in Laser-Induced Fusion and X-Ray Laser Studies (S.F. Jacobs, M.O. Scully, M. Sargent, and C.D. Cantrell, eds) Addison-Wesley, Reading, Mass. (1976).

[14] F. Young, R. Whitlock, R. Decoste, B. Ripin, D. Nagel, J. Stamper, J. McMahon, and S. Bodner, Appl. Phys. Lett. 30 45 (1977); B. Yaakobi and T. Bristow, Phys. Rev. Lett. 38 350 (1977); J. Pearlman and J. Anthes, Appl. Phys. Lett. 27 581 (1975); A.W. Ehler, D.V. Giovanielli, R.P. Godwin, G.H. McCall, R.L. Morse, and S.D. Rockwood, Los Alamos Scientific Laboratory Report La-5611-MS (1974).

[15] K. Lee, D.W. Forslund, J.M. Kindell, E.L. Lindman, Phys. Fluids 20 51 (1977).

[16] S.J. Gitomer, R.L. Morse, and B.S. Newberger, Phys. Fluids 20 234 (1977).
[17] P. Mulser and C. van Kessel, Phys. Rev. Lett. 38 902 (1977).
[18] J. Virmont, R. Pellat, and P. Mora, Phys. Fluids 21 567 (1978).
[19] K.A. Brueckner and R.S. Janda, Nucl. Fusion 17 451 (1977).
[20] L.V. Powers, G.R. Montry, and R.L. Berger, presented at the 8th Annual Conference on the Anomalous Absorption of Electromagnetic Waves, Tucson, AZ (1978) (Submitted to Nuclear Fusion).
[21] G.R. Montry and R.L. Berger, presented at the 8th Annual Conference on the Anomalous Absorption of Electromagnetic Waves, Tucson, AZ (1978)

INERTIAL CONFINEMENT FUSION AT NRL*

S.E. BODNER, J.P. BORIS, G. COOPERSTEIN,
S.A. GOLDSTEIN†, D. MOSHER, B.H. RIPIN, R. DECOSTE††,
J.H. GARDNER, R. LEE, R.H. LEHMBERG, E.A. McLEAN,
J.H. ORENS, J.A. STAMPER, S.J. STEPHANAKIS, F. YOUNG,
C.M. ARMSTRONG, A. DROBOT†, M.J. FRITTS,
P.J. MOFFA§, W.F. OLIPHANT, P. OTTINGER§§,
F. SANDEL§, A. STERNLEIB††
Naval Research Laboratory,
Washington D.C.,
United States of America

Abstract

INERTIAL CONFINEMENT FUSION AT NRL.

The NRL Inertial Confinement Fusion Program's emphasis has moved toward pellet concepts which use longer (~10 ns) lower intensity driver pulses than previously assumed. For laser drivers, this change was motivated by recent experiments at NRL with enhanced stimulated Brillouin backscatter. For ion drivers, the motivation is the possibility that substantial energy at 10-ns pulse lengths may soon be available. To accept these 10-ns pulses, it may be necessary to consider pellets of larger radius and thinner shell. The computational studies of Rayleigh-Taylor instability at NRL indicate the possibility of a dynamic stabilization of these thinner shells.

INTRODUCTION

The U.S. Naval Research Laboratory program in inertial confinement fusion is divided into four areas:

- Development of an experimental physics data base on laser-plasma coupling and hydrodynamic acceleration.
- Theoretical and computational studies of fundamental hydrodynamics, plasma physics, and charged particle beam propagation.
- Development of glass lasers and gas lasers.
- Generation, focusing, and transport of MeV light-ion beams.

* Supported by US Dept. of Energy.
† Science Applications, McClean, Virginia.
†† University of Maryland, College Park, Maryland.
§ JAYCOR, Inc., McClean, Virginia.
§§ NRC Research Associate at NRL.

The research emphasis in all of these areas has moved toward pellet concepts which use longer ($\geq$ 10 ns), lower intensity driver pulses than had been previously assumed. There are several motivations for this change in emphasis.

1. For laser coupling to targets, our recent measurements of enhanced stimulated Brillouin backscatter indicate that the highly structured laser pulses previously suggested for laser fusion may also encounter very large backscatter[1].

2. In recent experiments, using the Faraday rotation diagostic, we have measured megagauss magnetic fields at high laser intensities [2]. These fields may inhibit plasma energy transport and thereby reduce the net rocket efficiency. Several other laboratories have also found evidence for inhibited transport, due to magnetic field and/or the ion acoustic instability.

3. There are now several pellet concepts which use lower peak irradiance and longer pulse lengths, thereby avoiding large stimulated backscatter [3]. In one method for using lower irradiances, the pellet's shell mass is thinner and of larger radius. Computational studies at NRL of the Rayleigh-Taylor instability indicate the possibility of a dynamic stabilization of these thinner shells, so that the use of lower irradiance drivers may be feasible [4].

4. For light-ion coupling to targets, the natural voltage variation in the diodes can be used to bunch the ion beam during propagation in a plasma channel. With an order-of-magnitude power multiplication, 10-ns intense ion pulses may soon be available, to compete with lasers as a driver for these new pellet concepts.

BACKREFLECTION EXPERIMENTS

Until recently, one of the basic pellet concepts for laser fusion required a temporally shaped laser pulse with a long multi-nanosecond low-intensity pulse. In experiments at NRL the effect of this shaped pulse has been simulated by first forming a plasma blowoff with a prepulse, and then irradiating this preformed plasma with a short high-irradiance main pulse. The low-density plasma resulting from this prepulse will have many similarities to that produced by the long leading portion of the temporally shaped pulse. We found that the pre-formed plasma modifies most aspects of high-intensity laser-plasma coupling, including the generation of enhanced backscatter, significant increases in electron emission above 100 keV, and accentuation of self-generated magnetic fields.

In recently published experiments, we found that the backscatter increased with increasing prepulse, reaching 40% backscatter when the pre-formed plasma had a scale length of 100 μm [1]. This backscatter value is consistent with the theory of Phillion, Kruer and Rupert [5]. Extrapolation to a reactor-sized pellet with plasma scale lengths of 1000 μm or more suggest a possible backscatter value above 90% at laser intensities above 10^{15} Watts/cm^2. This extrapolation provides an additional basis for emphasizing those pellet designs which stay below 10^{14} Watts/cm^2, where backscatter should be less important.

We have also found that:

- Backreflection is nearly independent of the angle of incidence on the target, up to about 80 degrees, or nearly grazing incidence.
- Backreflected light nearly retraces the incident rays (within 5°).
- Backreflection is intensity-dependent, as in an instability.
- The backreflection rises as the prepulse to main pulse separation increases from zero to two nanoseconds.
- The backreflection is similar for gold and plastic targets, and for slab and pellet geometries.

THEORY OF OPTICAL RAY RETRACING

Optical ray retracing, in which the detailed transverse spatial structure of an incident beam is reproduced in its backscatter, is a well known experimental property of the Brillouin instability in high-power laser-plasma interactions [6]. This effect is explainable as a type of Bragg diffraction or volume hologram [7].

For simplicity, consider the incident pump radiation at the focusing lens to consist of two or more isolated beamlets, as a model of a non-ideal incident laser pulse. When these beams are focused in the plasma, their interference pattern produces an identical pattern in the gain coefficient. (The plasma is assumed to be operating in the strongly damped limit.) If this focal region is many wavelengths long, then the plasma behaves as an active volume hologram, i.e. a small plane wave noise field propagating through the region oppositely to any one of the pump beams will grow rapidly, while Bragg-diffracting into those directions opposite the other pump beams. Waves that do not propagate initially along any of these favored directions will not grow as rapidly.

In the limit of strong ion-acoustic damping, and negligible pump depletion, the steady-state backward wave amplitude satisfies

$$(\nabla^2 + k_1^2)\mathcal{E}_1 = 2ik_1\alpha[1 + \cos(\vec{K}\cdot\vec{r} + \varphi_o)]\mathcal{E}_1$$

Here $\vec{K} = \vec{k}_o' - \vec{k}_o$, where $\vec{k}_o'$ and $\vec{k}_o$ are the two wavenumbers of an incident pump beam, and α is the gain coefficient, assumed to vary slowly in a distance $\Lambda = 2\pi/K$. The focal region thus behaves as an active thick diffraction grating, with planes of maximum gain separated by Λ. Two diffraction-coupled noise waves will propagate through this structure with high gain and still have the same frequency beyond the periodic structure if they satisfy the Bragg condition, $\vec{k}_1 - \vec{k}_1' = \vec{K}$.

Quantitatively, one writes

$$\mathcal{E}_1(\vec{r}) = R\exp(i\vec{k}_1\cdot\vec{r}) + R'\exp(i\vec{k}_1'\cdot\vec{r} - i\varphi_o)$$

with $R = R(Z)$ and $R' = R'(Z)$ slowly varying. Then with paraxial ray conditions, one obtains

$$\frac{dR}{dZ} - \alpha R = \tfrac{1}{2}\alpha R' e^{i\varphi_o}$$

$$\frac{dR'}{dZ} - (\alpha + i\gamma)R' = \tfrac{1}{2}\alpha R\, e^{-i\varphi_o}$$

where $\gamma \equiv (k_1^2 - k_1'^2)/2k_1$ is a dephasing factor. If the angular detuning (γ/α) is small, and the gain (αL) is large, then one obtains the peak growth solution with a reversed phase shift:

$$\mathcal{E}_1(\vec{r}) \cong \tfrac{1}{2}\mathcal{E}_{1O} e^{\frac{3}{2}\alpha L/2} \left[\exp(-i\vec{k}_o\cdot\vec{r}) + \exp(-i\vec{k}_o'\cdot\vec{r} - i\varphi_o)\right]$$

and an angular resolution width for a uniform slab,

$$\theta_D = (8/\alpha L)^{\frac{1}{4}} \sqrt{\alpha/k_o} \simeq \sqrt{\alpha/k_o}$$

For a plasma with spatially varying gain, $\alpha(Z) = \alpha_o \exp(-Z/\ell)$, the angular resolution becomes

$$\theta_D \cong \sqrt{2.32/k_o\ell}$$

Since $\alpha_o\ell \gg 1$, this resolution is significantly better than for a uniform slab case.

SELF-GENERATED MAGNETIC FIELDS

In 1971, self-generated magnetic fields were proposed at NRL as an explanation of some magnetic probe data [8]. In 1974 their presence was confirmed by the Faraday rotation of a probing beam, with field strength in the megagauss range [9]. It was recognized that these fields play an important role in laser fusion through their inhibition of thermal transport. (For 10^6 gauss and a 10-keV electron temperature, the electron cyclotron frequency is about 10^3 times larger than the electron-ion collision frequency, resulting in a large inhibition in transport coefficients.)

However, although several laboratories undertook further Faraday rotation studies, there was no published confirmation for three years. This led to some doubt as to the magnitude and importance of these fields. Finally, in December 1977 we obtained reliable Faraday rotation results under a variety of conditions, e.g. probing beam timing, target material, irradiance, prepulse effects and pellet geometry [2].

These more recent results were quickly confirmed and extended at the Rutherford Laboratory[10], and have led to a new vitality in the experimental studies at various laboratories.

We found a large increase in the spatial extent of the fields (and possibly the magnitude) with the prepu lse. Figure 1 shows the transmission of a probe beam through polarizer-analysers when there was a laser prepulse containing 3% of the incident energy 2 ns before the main laser pulse. Near the axis of the main laser beam, the magnetic field is 1.5-2 megagauss, based on the rotation and interferometric data. Far from the axis, near

the edge of the laser beam, the field reduces to about 0.6 megagauss. These fields should be sufficient to strongly inhibit energy flow at the laser intensity of 2-7 x 10^{15} Watts/cm^2.

LIGHT ION GENERATION

It has been demonstrated[11] that proton beams can be efficiently extracted from low impedance (~ 1 Ω) relativistic electron beam generators operated in the pinched-beam mode. These light-ion beams offer several advantages for pellet fusion [12]. They can be ballistically focussed[13] for concentrating the beam down to pellet dimensions. The 10^{14}-W power required for pellet fusion can be generated from reasonable (~ 1 Ω) impedance generators (10 MA at 10 MV for protons). They have energy deposition characteristics well matched to efficient pellet designs. Additionally, the ion-beam energy is delivered to the target in a known fashion independent of any plasma-dynamic or electromagnetic effects. Finally, because of the natural voltage variation in diodes, the ion beam can be bunched during propagation in a plasma channel. An order-of-magnitude power multiplication may be achieved after propagation of 3-10 meters. Thus, present long-pulse diodes (~ 100 ns) may be used to generate short, intense ion pulses on target, significantly reducing the required generator power.

Before light ions can be seriously considered for fusion-reactor applications, a number of important technical capabilities must be demonstrated. These are the abilities to: (1) scale beam power to the 100 TW level; (2) focus the beam to pellet dimensions; and (3) propagate the beam over a few meters to demonstrate both standoff between accelerator and pellet and the ability to bunch. Here, new experimental and theoretical results will be presented which indicate that these achievements may be possible in a reactor scenario.

Proton- and deuteron-beam measurements have been made[14] using both flat and geometric-focussing geometries differing from previous solid anode geometries[11] in the following ways: (1) a thin-foil anode reflexing structure which extends beyond the cathode radius; (2) a controlled vacuum gap between foil anode and anode back-plate; and (3) the use of a small-diameter return path which provides on-axis electrical continuity between foil and anode back-plate. In this new flat pinch-reflex geometry, the maximum inferred proton current from carbon activation[11] averaged 0.32 ±0.1 MA corresponding to total proton yields of (1.3 ±0.4) x 10^{17} with ion pulse durations of 60-90 ns. These data indicate that nearly one half of the diode current can be routinely extracted as protons. This represents a nearly factor-of-two improvement in efficiency over that predicted by the Goldstein and Lee formula[15]. Thus, the efficiency originally predicted for 10^{14}-W generators has already been achieved on Gamble II at 0.5 TW. Recent numerical simulation results suggest that this improvement can be traced to the use of the thin-foil anode structures which allow for electron reflexing in the anode plane.

In the new spherical-section thin-anode-foil focussing geometries, ion focussing was tested using CD_2-coated anodes and targets. These data demonstrate a three-fold improvement in focussed-deuteron current density over that attainable with earlier designs [14]. Consistent with numerical simulation predictions, about 1/2 of the total deuteron number produced in the diode was observed to be focussed into a 1.9 cm^2 area, implying 70 kA/cm^2 at a location 12 cm from the anode. Additional improvements in focussing may require aspheric anode configurations in order to compensate for

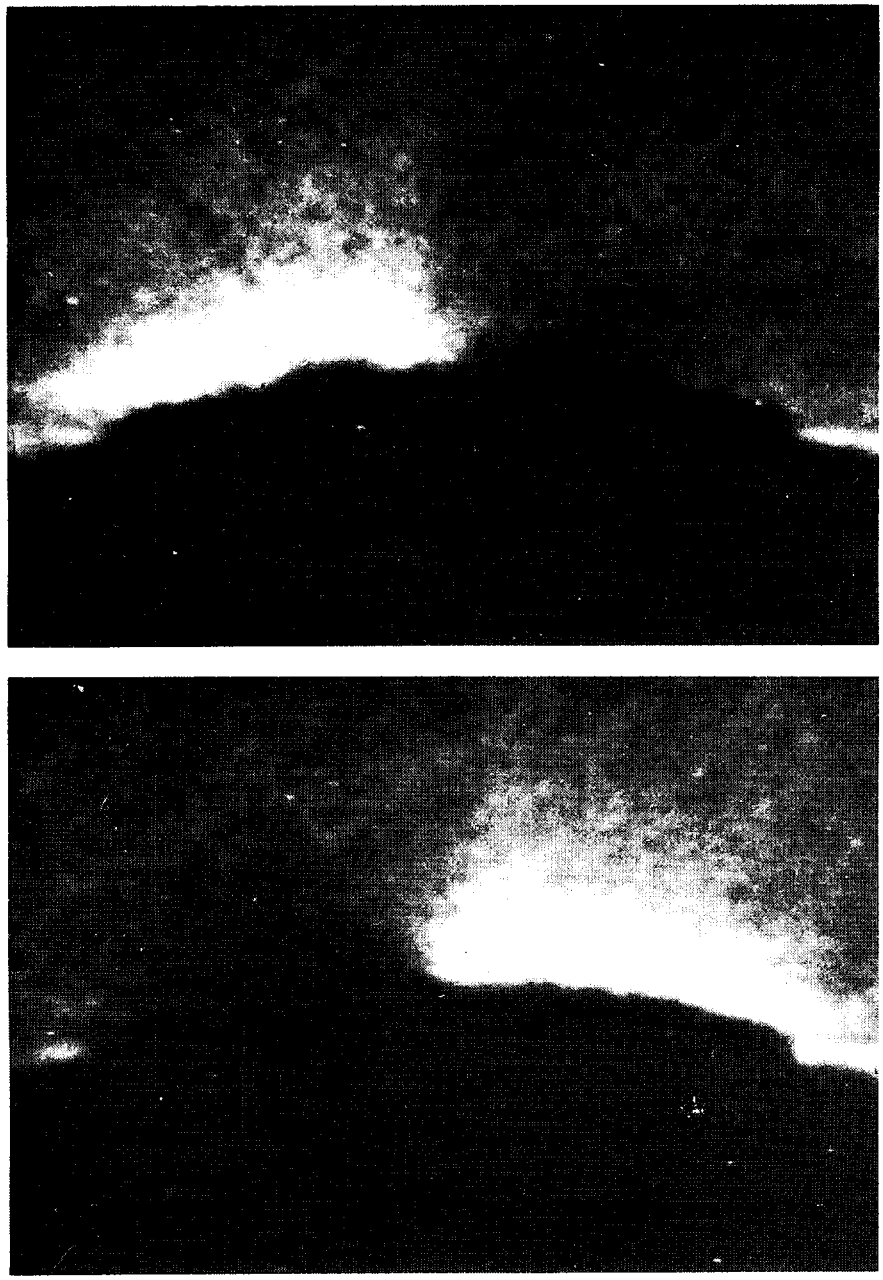


FIG. 1. Faraday rotation photographs for slab target. View is into 6329 Å probing beam, with main laser beam and prepulse incident from the right. Polarizer-analyser rotated to +82½°, -75°.

magnetic deflection in the diode. An upper limit of 4° beam divergence due to thermal, time-varying fields, or scattering effects can be associated with the deuteron-focussing results. As will be discussed below, this figure is sufficient to allow focussing over several-meter distances. The most recent measurements have determined the importance of current neutralization to good focussing. The observed large net currents are not fully understood at this time although their reduction to safe levels can be achieved by low-density gas or plasma fill in the drift chamber.

After geometric focussing, the intense ion beam can be propagated in Z-pinch plasma channels in a manner similar to that already achieved with pinched electron beams[16]. The low emittance of the ions allows transport of tightly focussed beams. In a reactor, return-current heating of the channel to 30-50 eV provides a high degree of current neutralization for fusion-level beams propagating in backgrounds of $\sim 10^{18}$ cm^{-3} densities [17]. The beam-channel system has been shown to be stable with respect to micro-instabilities for beam and background parameters of interest [18]. The current-carrying ($\sim 10^{5}$ A) plasma channel of small radius (~0.5 cm) is established a few microseconds before the short-focal-length geometrically focussed ion beam is introduced. The interface between the vacuum diode and the plasma channel consists of a thin foil placed at the focal point of the ion beam. The oscillatory motion of the ions in the azimuthal magnetic field is harmonic for a uniform current distribution. The radial displacement of the ions is easily computed from the channel current and focussing geometry and can be less than 0.5 cm. Self-consistent magnetic fields associated with channel hydrodynamics and magnetic diffusion enhance beam confinement [17]. Preliminary experiments, in which a 1-cm-diameter channel is created with an exploded wire, demonstrate 50% efficient transport of a focussed ion beam over 50 cm [19].

RAYLEIGH-TAYLOR INSTABILITY

Rayleigh-Taylor instability and the related but distinct asymmetry problems are fundamental concerns to the inertial confinement fusion community because of the severe energy penalties one must be willing to pay to design conservatively.

The theoretical treatment of Rayleigh-Taylor modes in the ablation layer is complicated so much by the convection, conduction and acceleration effects attendant in the ablation process itself that analytic treatments are at best approximate. Numerical treatments are complicated by the requirement to treat widely disparate time and space scales with nasty nonlinearities. Therefore little quantitative is known about the linear phase in laser pellet configurations and almost nothing qualitative about the nonlinear phases.

Our picture of the external (ablation layer) Rayleigh-Taylor instability was obtained using the sliding rezone Eulerian FAST2D [21, 4] code in an accelerating frame of reference. Our current calculations have been performed in slab geometry with a $K_{o}T^{5/2}$ thermal conduction law and ideal hydrodynamics. These calculations show that:

A. The initial linear growth for long wavelengths occurs qualitatively as predicted by the simplest linear theories.

B. There is a cutoff at short wavelengths which appears to force the growth rate γ toward zero.

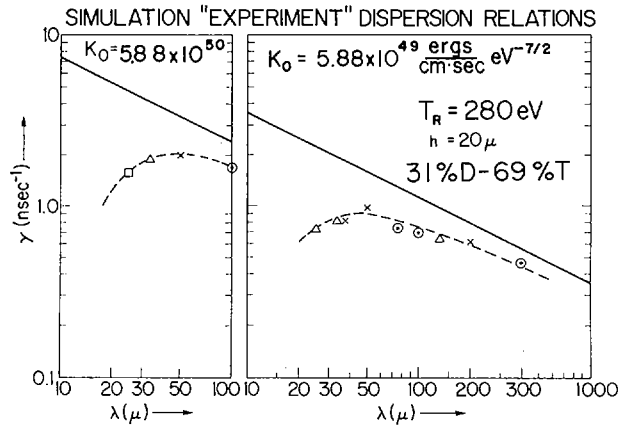


FIG.2. Dispersion relations depicting growth rate γ versus wavelength λ for the external (ablation layer) Rayleigh-Taylor instability as computed by the FAST2D computer code.

C. The nonlinear evolution observed is the formation of a droplet at the location classically occupied by a spike.

D. Rayleigh-Taylor modes with $\lambda \sim h$ (the shell thickness) do not immediately fracture the shell.

E. Dynamic stabilization by oscillating the ablation layer appears to stabilize a wide band of the Rayleigh-Taylor spectrum.

Figure 2 presents dispersion relations for the Rayleigh-Taylor instability of a D-T ice shell determined from a series of FAST2D calculations. Growth rate γ is shown as a function of wavelength λ for two cases. On the right the usual plasma thermal conduction for D-T is used. On the left it has been increased artificially by a factor of 10. For both cases the temperature at the critical region was forced to be 280 eV and the cold shell was initially 20 μm thick. The size of the plotting symbols indicates an estimate of the accuracy with which the growth rates could be determined from the numerical results.

In the standard case on the right, three separate calculations were performed with 1 μ x gridding. This was done to get information on both the long and the short wavelength ends of the spectrum. The cutoff at short wavelength is clearly indicated in the data but is difficult to follow down to zero growth because of the timestep limitations which result. At long wavelengths the runs also become very long because growth rates are low and the notion of a fixed growth rate is suspect. Nevertheless some evidence of accelerative stabilization can be argued from the deviations of γ below the $\sqrt{kg}$ limit shown as a solid diagonal line in the figures. This deviation is quite small, however, compared to what we would expect based on recent theoretical predictions which attempt to relate the Rayleigh-Taylor growth rate to the thickness and strength of the unstable region where pressure and density gradients are opposed [20,21]. A simple estimate of the growth rates is

$$\gamma^2 = \frac{\int_0^{\Delta} kL\xi^2 dx \, \frac{\nabla\rho_o \nabla P_o}{\rho_o^2}}{\int_0^{\Delta} \xi^2 dx}$$

where Δ is the width of the unstable region from the peak of ρ_o to the peak of P_o. L is a length of order Δ($L \equiv \Delta/2$ for the classical incompressible problem) which can absorb the geometric complications. The function $\xi(x)$ is the eigenfunction.

Growth rates estimated using this formula and realistic $\rho_o(x)$, $P_o(x)$ profiles predict that low power-law acceleration systems should be more stable in reaching a given implosion velocity than a high-power system because the thickness of the Rayleigh-Taylor unstable region goes to zero as the acceleration decreases. The numerical evidence for this accelerative stabilization is not all that clear-cut, as noted above. There are two possible explanations. The first is that the theory is wrong because the strong convection of fluid through the ablation layer is not properly accounted for. The second explanation, that simulation code calculations are wrong, can also be argued for the low power ablations under discussion.

Ablation layer analyses of varying sophistication performed on homogeneous, rather ideal situations such as treated in the simulations above [22,23,24] generally agree that 0.1 μ resolution or better is needed to resolve the details of the Rayleigh-Taylor unstable region for the low-temperature low-z ablations of interest. The time-dependent 2D and 1D piggy-back simulation models currently used to calculate the Rayleigh-Taylor growth do not resolve these scales effectively because the cost is prohibitive.

Dynamic stabilization of the Rayleigh-Taylor instability in the ablation layer has been demonstrated for the case where the laser intensity is varied periodically [21,4]. The combination of this phenomenon with accelerative stabilization and the natural cutoff at short wavelengths should permit successful implosion of shells with a dynamic aspect ratio of 20 or 30 to 1 [4]. We arecurrently investigating the dynamic stabilization of layered ablators where thin, higher-z layers temporarily interrupt the heat flow to produce the controlled oscillating accleration. To perform these calculations and to consider the occurrence of Rayleigh-Taylor instability at internal material interfaces, a version of the 2D SPLISH code[25] has been adapted for Rayleigh-Taylor calculations. A reconnectable Lagrangian grid of triangles is used to follow the Rayleigh-Taylor modes well into the "turbulent" regime as shown in Figure 3.

The calcuation, shown for two fluids of density ratio 2:1, is patterned on the situation of an ablator (below) accelerating a heavier pusher (above). The free surface above the pusher models the gas region at the center of filled microballoons. During implosion these interfaces are generally quite cold so the thermal conduction smoothing effects should be small. Convective stabilization is absent and the density changes in time will be small as well. Thus the classical Rayleigh-Taylor problem is a good starting place and the turbulent mixing theories[26] should be applicable here if anywhere.

Figure 3a shows the initial grid of triangles with a small sinusoidal perturbation of the interface at $t = 0$. The initial velocities (in the

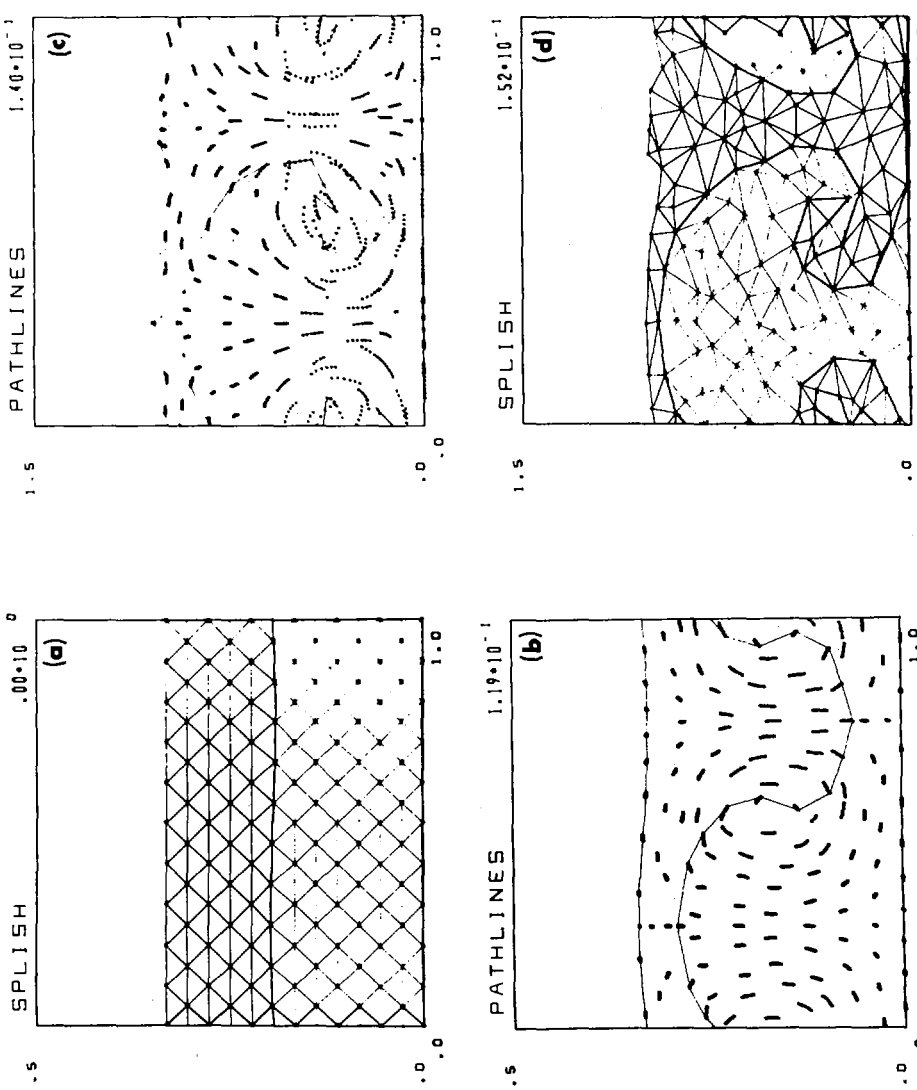


FIG. 3. Flow patterns, interface location and grid structure of the internal interface Rayleigh-Taylor instability as computed by the SPLISH computer code.

accelerating frame of reference) were all taken to be zero. Figure 3b shows the flow field as the instability enters its nonlinear phase. The vertex locations are plotted at successive timesteps to give streaks whose length is proportional to the local fluid velocity. Shear flow is established as the interface steepens, giving rise to vortices centered on the interface in a flow which has been likened to the onset of the Kelvin-Helmholtz instability [27]. In Figures 3c and 3d two fluids are beginning to mix in the Rayleigh-Taylor vortices and the rate of fall of the heavy material is no longer increasing.

REFERENCES

[1] RIPIN, B.H., et al., Phys. Rev. Lett. 39 10 (1977) 611.
[2] STAMPER, J.A., et al., Phys. Rev. Lett. 40 18 (1978) 1177.
[3] AFANASYEV, Yu. V., et al., JETP Lett. 21 (1975) 150;
NUCKOLLS, J., Topical Meeting on ICF, San Diego, Feb. 1978.
[4] BORIS, J.P., Comments on Plasma Physics and Controlled Fusion 3 1 (1977) 1.
[5] PHILLION, D.W., et al., Phys. Rev. Lett. 39 (1977) 1529.
[6] EIDMANN, K., SIGEL, R., "Laser Interaction and Related Plasma Phenomena," 3B, (SCHWARZ, H.J., HORA, H., eds), Plenum Press, NY (1974) 667; STAMPER, J.A., et al, ibid. 713.
[7] LEHMBERG, R.H., Phys. Rev. Lett. (to be published).
[8] STAMPER, J. A., et al., Phys. Rev. Lett. 26 (1971) 1012.
[9] STAMPER, J.A., RIPIN, B.H., Phys. Rev. Lett. 34 (1975) 138.
[10] RAVEN, A., et al., Rutherford Lab., Great Britain (unpublished).
[11] STEPHANAKIS, S.J., et al., Phys. Rev. Lett. 37 (1976) 1543.
[12] CLAUSER, M.J., Phys. Rev. Lett. 34 (1975) 570.
[13] COOPERSTEIN, G., et al., in Proceedings of the 1976 IEEE International Conf. on Plasma Sci., Austin, Texas, 1976.
[14] MOSHER, D., et al., in Proceedings of the 2nd International Conf. on Electron and Ion Beam Research and Technology, Cornell Univ., Ithaca, New York 1977; also NRL Memo Report 3658 (1977).
[15] GOLDSTEIN, S.A. and LEE, R., Phys. Rev. Lett. 35 (1975) 1079.
[16] MILLER, P.A., et al., Phys. Rev. Lett. 39 92 (1977).
[17] MOSHER, D., et al., IEEE Conf. Record Abstract, 1978 IEEE International Conf. on Plasma Sci., Monterey, CA 1978.
[18] OTTINGER, P.F., MOSHER, D., and GOLDSTEIN, S.A., NRL Memo Report 3784 (1978).
[19] SANDEL, F.L., et al., IEEE Conf. Record Abstracts, 1978 IEEE International Conf. on Plasma Sci., Monterey, CA, 1978.
[20] AFANAS'EV, Y.F., et al., JETP Lett. 23 11 (1976) 506.
[21] BORIS, J.P., Bull. Am. Phys. Soc. 22 4 (1977) 608, also Eastern Audio Association, Inc., Cassette Proceedings.
[22] BRUECKNER, K.A., JORNA, S., and JANDA, R., Phys. of Fluids 17 8 (1974) 1554.
[23] FELBER, F.S., Phys. Rev. Lett. 39 2 (1977) 84.
[24] ORENS, J.H., et al., Bull. Am. Phys. Soc. 22 9 (1977) 1180.
[25] FRITTS, M.J., and BORIS, J.P., Solution of transient problems in free surface hydrodynamics, accepted for publication in J. of Comp. Phys. An early version appears as NRL Memo Report 3446 (1977).
[26] BALEN'KII, S.Z., and FRADKIN, E.S., Proc. Lebedev Inst. 29 (1965) 197.
[27] CHANDRASEKHAR, S., "Hydrodynamic and hydromagnetic stability," Clarendon Press (1961) 428.

DISCUSSION

R.W. CONN: What is the diameter of the focus proton beam, both on geometric focusing and on transport through the channel, and how does this compare with what will be required for reactor-level targets?

S.E. BODNER: The beam remains at about 1 cm^2 after transport. Reactor-sized pellets will also be about 1 cm in radius. The remaining question is to demonstrate experimentally that the beam stays at about 2 cm^2 when the driver is scaled up to the megajoule level.

W. HEINZ: What would be the appearance of a plasma channel which focuses the beam over 10 m with a diameter of 1 cm^2?

S.E. BODNER: It has been created by a pre-formed plasma, produced perhaps by a laser beam, and the plasma is maintained by the return current. A background plasma is necessary for stable transport.

EXPLOSIVE-PUSHER-TYPE LASER COMPRESSION EXPERIMENTS WITH NEON-FILLED MICROBALLOONS

T. BRISTOW, J. DELETTREZ, A. ENTENBERG, Y. GAZIT,
A. HAUER, L. GOLDMAN, E. LAZARUS, C. LEE, S. LETZRING,
M. LUBIN, R. McCRORY, T. MUKAIYAMA, B. NICHOLSON, B. PERRY,
J. RIZZO, S. SKUPSKY, J. SOURES, D. STEEL, E. THORSOS, B. YAAKOBI
Laboratory for Laser Energetics,
University of Rochester,
Rochester, New York,
United States of America

Abstract

EXPLOSIVE-PUSHER-TYPE LASER COMPRESSION EXPERIMENTS WITH NEON-FILLED MICROBALLOONS.

Laser fusion targets filled with pure neon have been used to directly measure the peak density ρ and ρR product (density X radius) using spectrally and spatially-resolved neon X-ray line emission. In agreement with theoretical predictions for the explosive-pusher mode, we find peak densities in the range 0.25–0.5 $g \cdot cm^{-3}$ which are almost independent of laser power or fill pressure. In addition, (ρR) values increase from 2×10^{-4} to 6×10^{-4} $g \cdot cm^{-2}$ as the fill pressure increases from 2 atm to 56 atm. Using these methods for density measurement as well as other experimental signatures (such as X-ray pinhole imaging, X-ray streak photography and X-ray line emission from the tamper), the explosive-pusher mode of target dynamics for various fill pressures was systematically investigated. These results were used as critical normalization parameters for a one-dimensional hydrodynamic numerical code, LILAC. The new diagnostic methods not previously available result in a better understanding of the explosive-pusher mode. These and similar methods may become crucial in diagnosing future higher compression implosions.

The most important parameter in laser-induced fusion experiments, namely the product ρR of compressed core density and radius, has previously been inferred from dimensions of the region emitting x-rays or α-particles.[1,2] In this paper it is shown that spectral profiles of neon x-ray lines from neon-filled targets yield direct information on ρ and ρR. In addition we shall present the experimentally determined scaling dependence of ρR on fill pressure and as predicted by our computer code LILAC.

The experiments were performed on the DELTA four-beam laser system at a power on target of 0.15 TW in a 40-psec pulse. The targets were typically 65μm-diameter glass microballoons with a wall thickness of order 0.6μm. The targets were filled with pure neon at pressures ranging from 2 to 56 atm. See Table I.

TABLE I. COMPRESSION EXPERIMENTS

EXPERIMENTAL CONDITIONS	
Laser:	On-target power 0.15×10^{12} W Pulse width 40 ps Wavelength 1.06 μm Focusing 4 beams, f/2 optics
Target:	Glass microballoon Diameter 65 μm Wall thickness 0.6 μm Fill 2–56 atm neon
Principal diagnostic:	X-ray spectroscopy X-ray streak photography

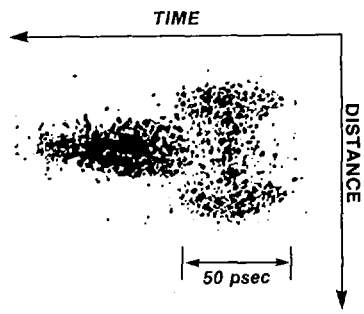


FIG.1. Time- and space-resolved X-ray emission of implosion from shot #17639.

The principal diagnostic was a thalium acid phthalate crystal x-ray spectrometer equipped with a slit of width 11μm, giving simultaneously spatially integrated spectra and spatially resolved spectra of resolution 13μm (at 10Å). In addition, an x-ray streak camera provided a time and space resolved image of the implosion. An example is shown in Figure 1. Spatial resolution is provided by an imaging slit at right angles to the temporally resolving slit. Note the narrowing of the emitting region as time increases, corresponding to the stagnation of the imploded fill.

Figure 2 shows part of the x-ray spectrum emitted from glass microballoons filled with neon at 2.0- and 8.6-atm pressure. The Ne^{+8} and Ne^{+9} x-ray lines are seen to be considerably broader than the sodium lines from the glass shell. Their width (FWHM as large as 20 eV) is much larger than the width (~1.5 eV) due to crystal imperfection and finite size of the source. As we go from 2.0- to 8.6-atm fill pressure the intensity of neon lines increases by varying amounts. For example, the intensity of the Lyman-α line remains nearly constant as the fill pressure increases.

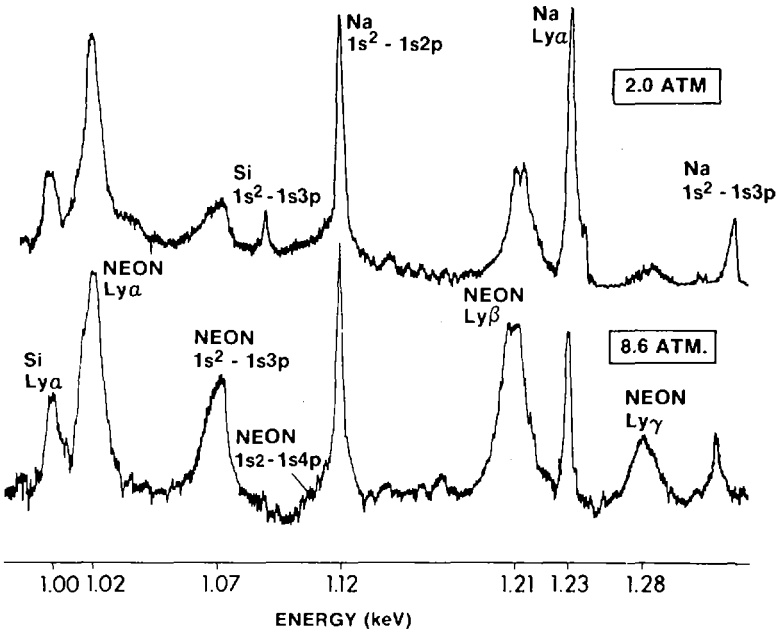


FIG. 2. Microdensitometer traces of the X-ray spectrum (in the same scale) at two different fill pressures. Sodium and silicon lines come from the glass shell. Note the wider lines of neon.

This is clear evidence of saturation due to the self-absorption (or opacity) of this line. As higher series members are progressively less self-absorbed, the Lyman-β line approaches the black-body limit for the 8.6-atm case. However, the Lyman-γ line remains optically thin: although it increases substantially with fill pressure it is still much below the black-body limit indicated by the other lines. In terms of the optical depth at line center (τ_0) we have then $\tau_0(Ly\alpha) >> 1$, $\tau_0(Ly\beta) \sim 1$, and $\tau_0(Ly\gamma) << 1$. The results below turn out to be entirely consistent with these results. Moving to higher series members, the broadening due to opacity decreases rapidly whereas Stark-broadening increases (other broadening mechanisms are negligible).[3] The spectrum therefore yields two kinds of complementary measurements: the Stark profile of the Lyman-γ line gives the density (hence the compression) and the opacity-broadened Lyman-α line gives the ρR product.

Figure 3 shows a comparison of the best-fit calculated Stark profile with the measured Lyman-γ line for the 8.6-atm case. Doppler and instrumental profiles were folded into the calculated profiles but they only have a small effect. The Stark profiles have been calculated by Hooper[4] and Tighe for the case of Ne^{+9} lines perturbed by a Ne^{+9} ion plasma*. The electron temperature T_e during the emission of neon lines needs only to be known approximately for these calculations. Using the measured intensity ratio $I(1s - 3p)/I(1s^2 - 1s3p)$, we estimate T_e to be ~ 300 eV.

* A full description of these profile calculations is being prepared for publication by C.F. Hooper.

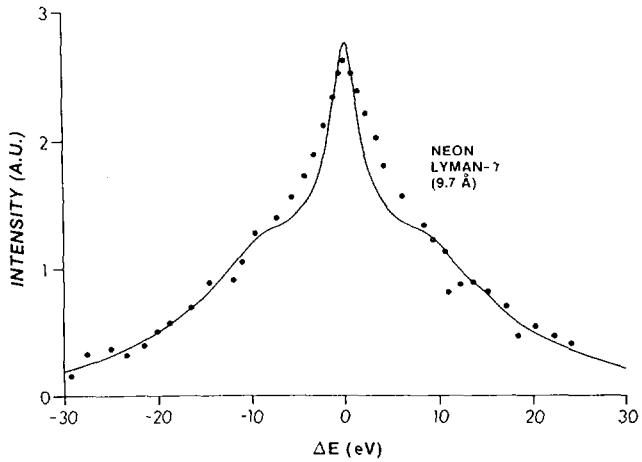


FIG. 3. Fitting a Stark profile (which includes Doppler and instrumental broadening) to the experimental profile of the Lyman-γ line of Ne^{+9} (at 9.7 Å). The profile corresponds to an electron density $N_e = 7 \times 10^{22}\ cm^{-3}$ and $T_e = T_i = 300\ eV$.

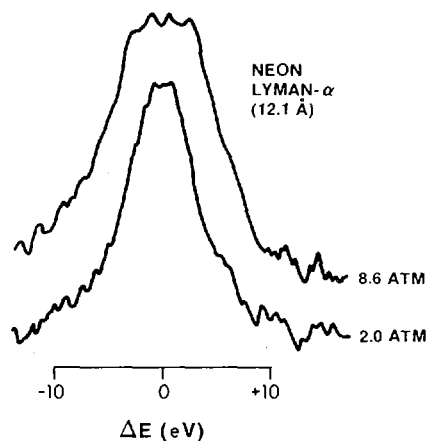


FIG. 4. Measured profiles of the Lyman-α line of Ne^{+9} (12.134 Å) at two different neon fill pressures of the target.

The intensity ratio between Lyα and Lyβ corresponds to a Planck distribution of about the same T_e. Figure 3 shows that the electron density for the 8.6-atm case is 7×10^{22} cm^{-3}, which corresponds to a mass density 0.26 g/cm^3. The uncertainty in N_e was found to be ±25% by varying the temperature and the assumed background level within their estimated error brackets. Assuming that the whole neon mass is uniformly compressed, we derive a diameter D = 19μm for the compressed neon core and a ρR value of 2.5×10^{-4} g/cm^2 (here R is the average chord length, $2D/\pi$). The compression ratio is 38. For the 2.0-atm case the final density is approximately the same and the compression ratio is ~ 150.

We next analyze the optically thick Lyman-α line profile which is shown in Figure 4 for the two pressure cases. Under the assumption of a homogeneous source, the line radiative transport equation can be solved and gives (in local thermodynamic equilibrium) $I_\nu = B_\nu^T[1-\exp(-\tau_o P_\nu/P_o)]$; where I_ν is the observed line profile at frequency ν; B_ν^T is Planck's function (blackbody limit) for a temperature T; P_ν is the intrinsic line profile; and τ_o the optical depth at line center (or at frequency at which P_o is evaluated). If $\tau_o \gg 1$, I_ν has a flat top of intensity B_ν^T and is wider than the source (i.e. Stark) width. This is what is indicated by Figure 4 where the measured Lyman-α profile is wider than the Stark width calculated for the density found from the Lyman-γ line. Fitting I_ν profiles to the observed profile for the 8.6-atm case we find $\tau_o/P_o^\nu = 2\times10^{16}$ sec^{-1}, using the Stark profile for $N_e = 7\times10^{22}$ cm^{-3}. The optical depth is related to ρR through $\rho R = (\tau_o/P_o)(\bar{m}Mc/\pi e^2 f)b^{-1}$ where M is the ion mass, f is the line oscillator strength, and b_{+9} is the fraction of all neon ions which are in the ground state of Ne^{+9}. Over a wide temperature range in which Ne^{+9} emission is significant b ~ 0.3, which gives $\rho R = 2.2\times10^{-4}$ g/cm^2. This value agrees well with that obtained above. The optical depth at the peak of the (electron-broadened) unshifted Stark component is ~ 100. For the 2-atm pressure case $\rho R \sim 1\times10^{-4}$ g/cm^2.

We can also fit Stark profiles to the Lyman-β line. Figure 5(a) shows the best fit for the 2-atm pressure case which yields the same density value as obtained from the Lyman-γ line: $N_e \sim 7\times10^{22}$ cm^{-3}. For the 8.6-atm case (Figure 5(b)) the same profile has the wrong width and shape. However, fitting a profile from a uniform source with the same density but an optical depth at line center $\tau_o = 0.5$ (or $\tau = 1.2$ at the peaks) we get good agreement with the experimental profile. To check consistency we calculate τ_o(Lyβ) using the ρR values obtained from the Lyman-α line. We get for the 2-atm case $\tau_o \sim 0.4$ and for the 8.6-atm case $\tau_o \sim 0.8$ (for the peaks of the profile $\tau \sim 2.5\tau_o$).

We next consider spatial profiles of neon lines. As an example, Figure 6 shows the spatial profile of the neon Lyman-β line for the 8.6-atm case. The diameter of the compressed neon core (after subtracting the continuum) is seen to agree very well with the value (19μm) inferred from the spectral profiles.

In addition to x-ray emission from the neon fill we also measured and analyzed silicon x-ray line emission from the glass shell. Such emission can come from the peripheral laser absorption region or from the center of the target. The latter radiation is emitted when the target reaches peak compression and the inner part of the glass shell stagnates against the compressed neon core. Spatially resolved silicon spectra are shown in Figure 7 for the hydrogen-like and helium-like resonance lines. As seen, the intensity ratio between Si^{+12} and Si^{+13} lines is very different in the core as compared with the ring. However, this does not indicate a core which is hotter than the ring: the intensity ratios of Si^{+13} and Si^{+12} lines are determined by two different atomic

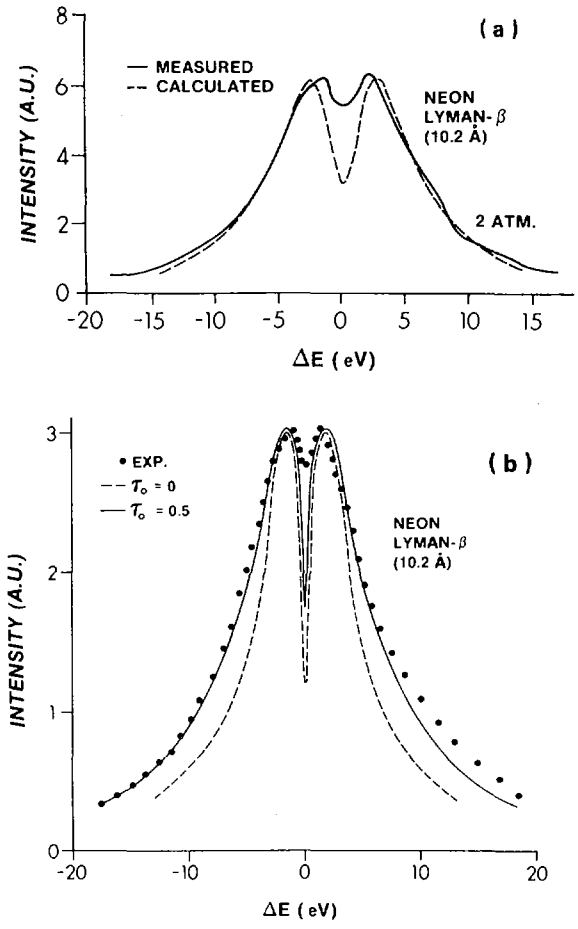


FIG.5. (a) Fitting of a Stark profile (which includes Doppler and instrumental broadening) to the measured profile of the Lyman-β line of Ne^{+9} (10.239 Å), at 2.0 atm neon fill pressure. The theoretical profile corresponds to $N_e = 7 \times 10^{22}$ cm^{-3}, $T_e = T_i = 300$ eV. (b) Same as (a) for a fill pressure of 8.6 atm neon. τ_0 is the assumed optical depth at the line center.

models in the two regions and in fact the core turns out to be cooler than the ring.

Most important, however, is that this data gives direct evidence for the presence of compressed and hot silicon in the core. We are presently unable to distinguish between the two cases of glass surrounding the compressed fill gas and actual glass-fill mixing. It is expected, however, that future experiments with brighter cores and improved instrumentation will allow resolution of this problem through studies of spatially resolved optically thin silicon x-ray lines.

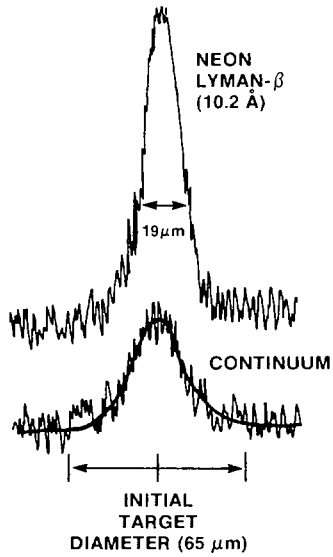


FIG. 6. Spatial profile of the Lyman-β line of Ne^{+9} (10.239 Å), and the nearby continuum. The 19-μm-long bar indicates the diameter of the compressed neon core if we assume homogeneous compression and use the density obtained from spectral profiles analysis.

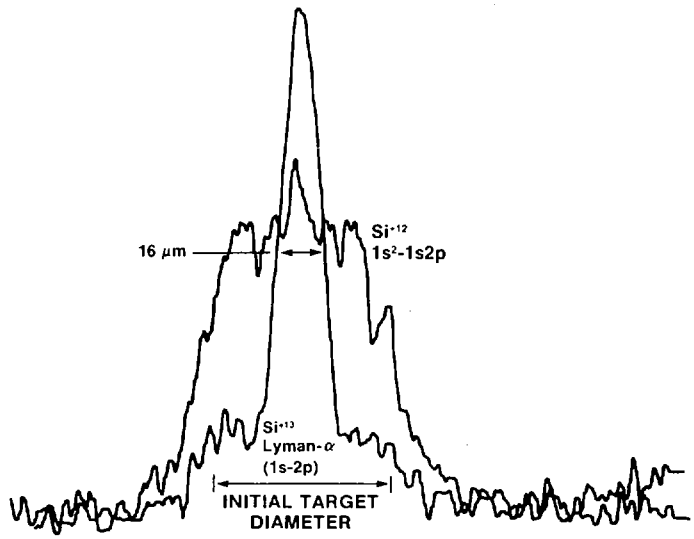


FIG. 7. Spatially resolved Si^{+13} (1s - 2p) and Si^{+12} ($1s^2$ - 1s2p) line emission from laser-imploded microballoon. Note the clear presence of silicon in the core.

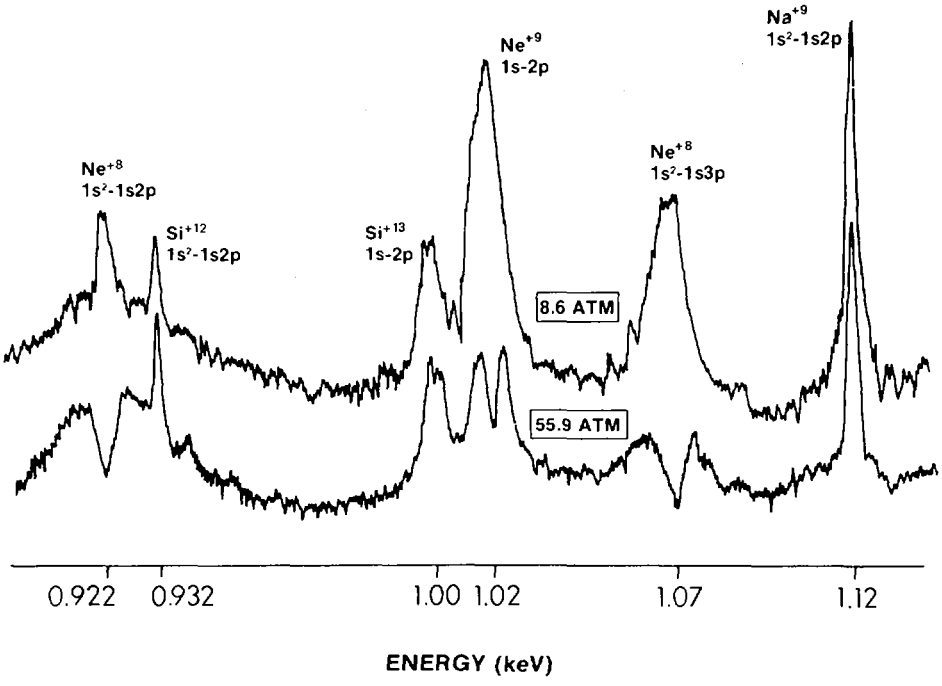


FIG. 8. Comparison between the spectrum obtained at two neon fill pressures: 8.6 and 55.9 atm. Note the self-reversal of neon lines.

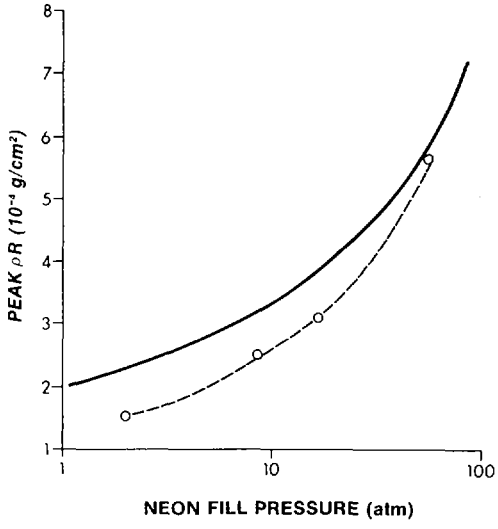


FIG. 9. Comparison of experimental and simulation results for peak neon ρR as a function of neon fill pressure. The circles are the experimental values. The curves are from simulations: solid curve, peak ρR; dotted curve, ρR at time of peak core X-ray emission.

Neon fill pressure was one of the most readily variable parameters in these experiments. Theory predicts that for higher pressures the peak density should be about the same, the temperature should drop and the ρR product increase. We have already found above that the neon temperature drops with increasing pressure. We have also found that in going from 2 atm to 8.6 atm fill pressure the Lyman-α line broadens, indicating a higher ρR value. We show now that for 55.9 atm fill pressure the ρR value is still higher.

Figure 8 shows the x-ray spectrum of neon and adjacent glass lines for 55.9 atm pressure compared with that for 8.6 atm. As can be seen, all the neon lines now appear with a prominent central dip: they are self-reversed. Self-reversal is the result of a temperature gradient; the relatively hot line-emitting neon plasma is surrounded by a cooler layer giving rise to the central dip. Since the far wings of the Lyman-α line for the 55.9 atm case seem to have about the same intensity and shape as for the 8.6 atm case, we approximate the 55.9 atm neon source as consisting of two distinct regions: a central uniform region where the line is broadened by self-absorption, having the same ρR as in the 8.6 atm case, surrounded by an annular region which only absorbs the line. We get fair agreement with the measured profile if we take the ρR in the outer layer to be equal to the ρR in the core. Alternatively, we can assume an optically thin central emission region and a peripheral absorbing region. Either model yields a $\tau_o \sim 260$. With this opacity and an upper estimate on the temperature, we estimate a lower bound on the ρR value from Figure 8 to be 5.5×10^{-4} g/cm^2. The results of ρR measurements as a function of fill pressure are summarized in Figure 9, where comparison is made between these measurements and the theoretical predictions based on our 1-D simulation code, LILAC.

Extensive implosion simulations were carried out with LILAC, which incorporates multigroup fast electron transport and multigroup radiation transport. Diagnostic replication capabilities include neon line profiles, x-ray pinhole photographs, and x-ray streak camera records. Replication of these measurements for a wide range of neon fill pressures has increased our confidence in the simulation model. It has been found that fast electron transport is essential for simulation of these exploding-pusher experiments. Also, the peak neon density obtained in these implosions is about a factor of two greater than that deduced directly from the neon line profiles; thus, it can be inferred that a peak neon density of about 0.5 g/cm^3 was obtained.

In conclusion, the following points emerged from these experiments:

1. Diagnostic methods were tested for measuring the density and the ρR product of laser-compressed targets. Spatially-resolved neon line emission is superior to methods based on non-spectral images which do not distinguish between fill gas and imploded glass shell emissions. However, spectral profiles of fill gas lines yield the most direct and unequivocal measurement of the compressed core density.
2. The inferred peak density in the present experiments was 0.5 g/cm^3 which is similar to the density achieved at much higher laser powers and similar targets, as expected from the explosive-pusher mode of implosion.
3. X-ray emission from a high-Z dopant proved to be a very useful probe for monitoring changes in target behavior when changing the experimental conditions.
4. Even though the density achieved in the explosive-pusher mode was found to be relatively independent of laser power or fill pressure, the ρR product did increase with the fill pressure.

5. Stark-broadened profiles of lines from a high-Z ion can only be obtained in the center of compressed targets. These profiles can form the basis for evaluating the theory for such profiles which is currently under development.
6. High fill pressure implosions showed indications of an approach to central heating which is essential for central thermonuclear ignition and burn propagation. X-ray line reversal provides a method for measuring such a mechanism.
7. Spatially and spectrally resolved silicon x-ray line emission may provide unique information on mixing between glass tamper and fill gas because of hydrodynamic instability at peak compression.

REFERENCES

[1] CAMPBELL, P.M., CHARATIS, G., MONTRY, G.R., Phys. Rev. Lett. **34** (1975) 74.
[2] CEGLIO, N.M., COLEMAN, L.W., Phys. Rev. Lett. **39** (1977) 20.
[3] GRIEM, H.R., Plasma Spectroscopy, McGraw-Hill, New York (1964);
GRIEM, H.R., Spectral Line Broadening, Academic Press, New York (1974).
[4] HOOPER, C.F., Jr., private communication;
TIGHE, R.J., dissertation, University of Florida (unpublished);
TIGHE, R.J., HOOPER, C.F., Phys. Rev. **A15** (1977) 1773.
[5] BOGOLYUBSKIJ, S.L., et al., Pis'ma Zh. Ehksp. Teor. Fiz. **24** (1976) 206 [JETP Lett. **24** (1976) 182].

Session D

INERTIAL CONFINEMENT II

Chairman

M.V. BABYKIN
USSR

RECENT PROGRESS IN INERTIAL CONFINEMENT FUSION RESEARCH AT THE LOS ALAMOS SCIENTIFIC LABORATORY*

R.B. PERKINS
Los Alamos Scientific Laboratory,
University of California,
Los Alamos, New Mexico,
United States of America

Abstract

RECENT PROGRESS IN INERTIAL CONFINEMENT FUSION RESEARCH AT THE LOS ALAMOS SCIENTIFIC LABORATORY.

Recent progress in the inertial confinement fusion programme at the Los Alamos Scientific Laboratory is reviewed. Helios, an eight-beam 10-kJ CO_2 laser, became operational in April 1978 and has produced output powers exceeding 21 TW. Antares, a 100-kJ CO_2 laser, is under construction and should permit breakeven experiments in 1983/84. Current and planned target experiments are discussed. Laser fusion power plants employing CO_2 lasers are being studied to identify areas requiring early attention.

1. OBJECTIVES

The Los Alamos Scientific Laboratory is pursuing an integrated research and development program in inertial confinement fusion based primarily on the use of CO_2 lasers. Our first major goal is scientific breakeven, a fusion yield equaling the incident laser energy. We plan to demonstrate breakeven during 1983/84 with the 100-kJ Antares CO_2 laser currently under construction. Success will confirm serious consideration of the CO_2 laser as the driver of choice for future inertial-fusion power plants.

Our program has three major thrusts: development of the high-power, short-pulse gas lasers needed for target experiments; target experimentation, requiring the development of sophisticated target designs, target fabrication methods, and diagnostics; and systems studies aimed at identifying potential designs for commercial reactors and other applications while simultaneously identifying problems that will have to be solved.

2. CO_2 LASER SYSTEMS

Our short-pulse CO_2 laser development is indicated in Fig. 1. The Single-Beam System, whose development began in 1970, has provided much information on the absorption of CO_2 light in materials. The Two-Beam

* Work performed under the auspices of the US Department of Energy.

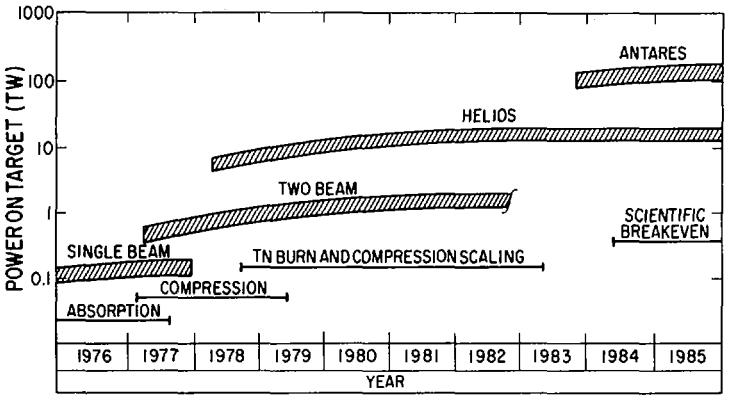


FIG.1. Los Alamos CO_2 gas laser systems.

System, which we designed as the prototype for the final amplifiers of the 10-kJ Eight-Beam System, Helios, has been used for compression experiments at powers up to one terawatt during the past year. The Helios system was brought to full power in April. Helios will generate the data we need on ablative compression of pellets to optimize the design of the breakeven target. The Antares laser system will provide the 100 to 200 TW of power believed to be required to reach breakeven.

3. HELIOS

Figure 2 shows Helios, in which four dual-beam modules provide eight laser beams for simultaneous target illumination in a central target chamber. Like all high-energy, short-pulse lasers, Helios employs an oscillator amplifier configuration. The master oscillator produces a smooth, gain-switched 100-ns pulse of about 100 mJ. This output pulse is directed to a three-stage Pockels cell shutter system capable of modifying the input to a 1-ns or shorter pulse with a contrast ratio in excess of one million. Commercially available double-discharge amplifiers amplify this master pulse to a level of about 1 J. The pulse is then split into four beams, further amplified and again split to provide eight synchronous beams for the final amplifiers.

The final amplifier stages are pumped by the now well-known electron-beam-controlled discharge technique [1]. To reduce input drive requirements for these amplifiers, a three-pass optical configuration has been developed, as shown in Fig. 3. Such a configuration reduces the drive requirements from about 100 J (for a single pass) to about 0.1 J for a triple-pass configuration. However, the small signal gain per pass in this system is about 1000, so that the introduction of such a folded path raises the possibility of optical parasitic oscillations. Such parasitics have limited the performance of this module to a gain-length product of about 5 (design value 8); it was determined that the main coupling was through the rear collimating mirror.

A program of gaseous, saturable absorber development was undertaken to decouple this mirror from the gain medium at low intensity levels. A gas mixture consisting of SF_6 and a combination of five Freons was chosen to ensure that the small signal gain in both the 9- and 10-μm bands was blocked, while permitting transmission of high-intensity pulses. Placing this saturable cell between the second and third passes raised the parasitic threshold and allowed the modules to reach full design value of 1250 J. Recently, in full system tests, approximately 10700 J were generated in a pulse shorter than 1 ns for a power output in excess of 21 TW.

The optical configuration for Helios is shown in Fig. 2. The output windows of the laser power amplifiers and the input windows to the target chamber are 40-cm-diam. polycrystalline NaCl windows developed at the Harshaw Corporation; they have a damage threshold of 6 J/cm^2 for 1-ns pulses, but are exposed in operation to only about 2 J/cm^2. The reflecting optics which transport the beam to the target are made by the Union Carbide Corporation with diamond-knife micromachining. The target is illuminated along the diagonals connecting the eight corners of an imaginary cube whose top half is rotated 45° to prevent the beams from directly facing each other.

4. ANTARES

Design and construction of Antares [2], which will operate at power levels of 100 to 200 TW, is well under way. This large CO_2 laser system, with which we intend to demonstrate scientific breakeven, consists of an oscillator-preamplifier subsystem, six segmented annular power amplifiers, beam tubes, and a target chamber. Figure 4 is a photograph of a scale model of the facility. The oscillator-preamplifier, housed in a basement under the main laser hall, incorporates a high-contrast-ratio electro-optical switchout and saturable absorbers between preamplifiers. The optical pulse is amplified to 100 kJ by six power-amplifier modules. The six high-energy beams are transported through evacuated beam tubes to a building containing the target chamber. The target building is shielded, as required by the anticipated thermonuclear yield. The power-amplifier modules (Fig. 5) are electron-beam-controlled annular discharge chambers of about 3200-liter pumped volume at 2.4 atm pressure of a CO_2:N_2 gas mixture. The optical design in the power amplifiers is a two-pass layout that requires 36-J input to extract 80% of the stored energy in 1 ns. Optics consist of single-point diamond-turned copper mirrors and of 46-cm-diam. NaCl windows. Control will be by computer, and all intercommunications of the control signals will be by means of fiber-optic links to avoid interference problems due to electrical noise.

A prototype of the power-amplifier module has recently completed successful testing, confirming the basic Antares design with regard to electrical and optical parameters. Operation at voltage exceeding 500 kV with the optical gain coefficient exceeding the design value gain length product of 6 was demonstrated. Measurement of the magnetic field effects confirmed the design calculations with regard to this effect. Taken together with the recent successful commissioning of Helios, we are confident of the Antares design. Procurement of the first of the six power-amplifier modules was begun this spring, with final tests on a single beam to be completed in October 1981. The remaining beams will be constructed in parallel for final facility completion in October 1983, according to our current funding assumptions.

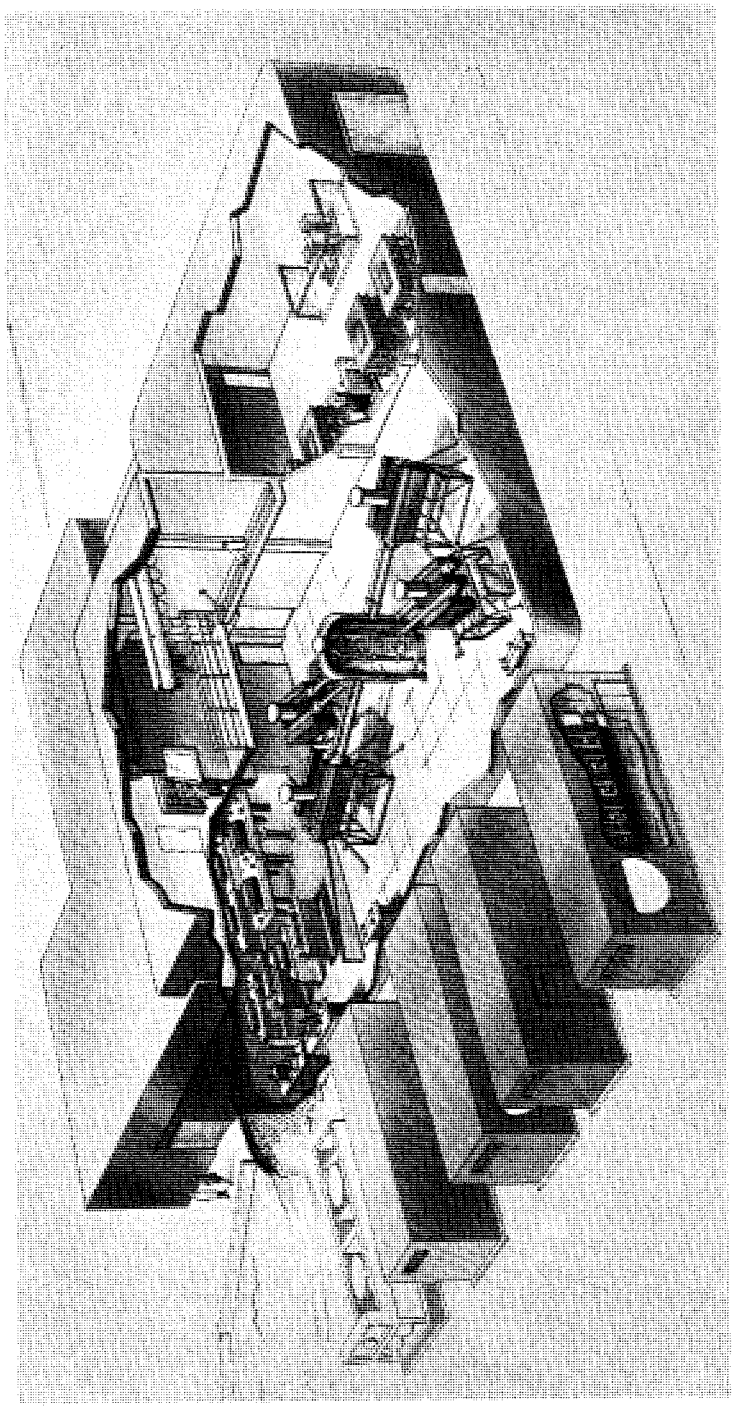


FIG.2. Helios, the 10-kJ CO_2 laser system.

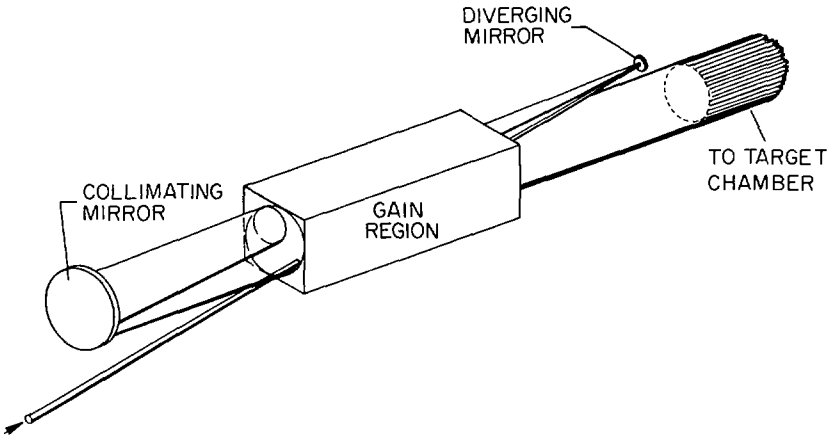


FIG.3. Optical layout of the triple-pass dual-beam module.

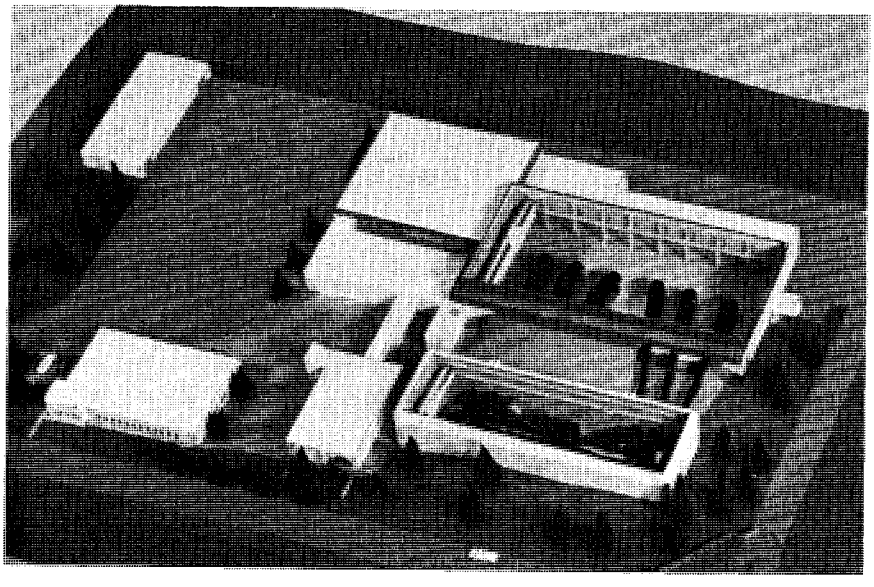


FIG.4. Scale model of the High-Energy Gas Laser Facility which houses the Antares laser.

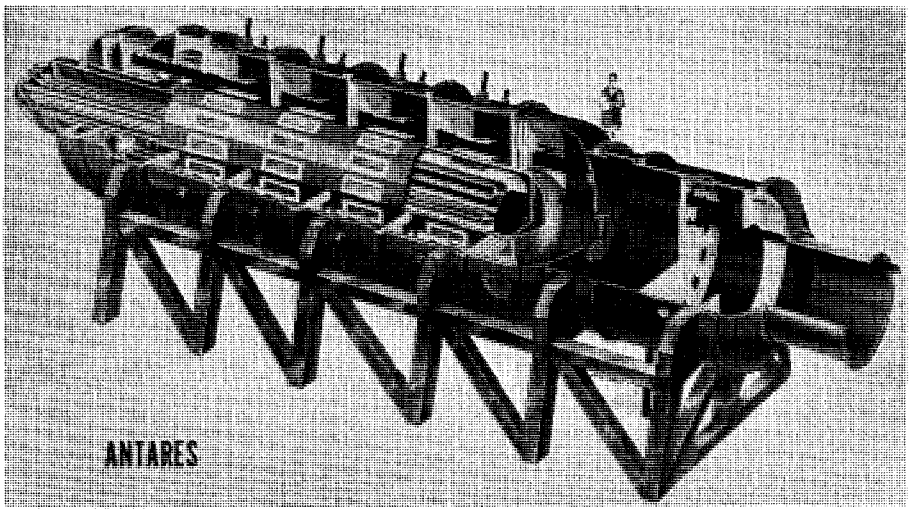


FIG.5. Antares power amplifier module.

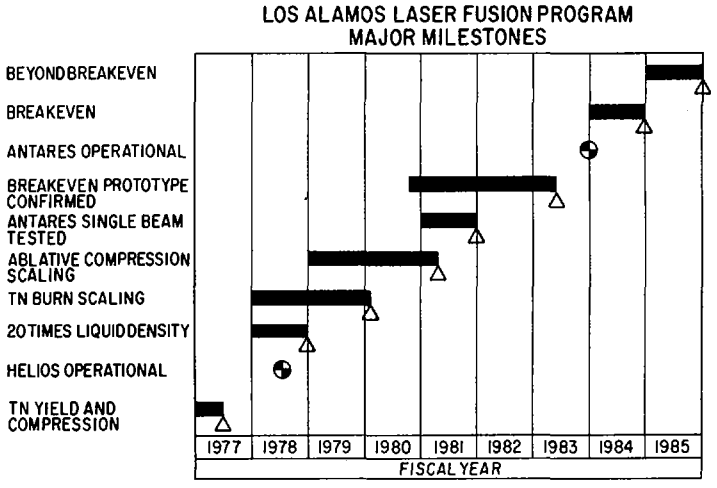


FIG.6. Major milestones of the Los Alamos Laser Fusion Program.

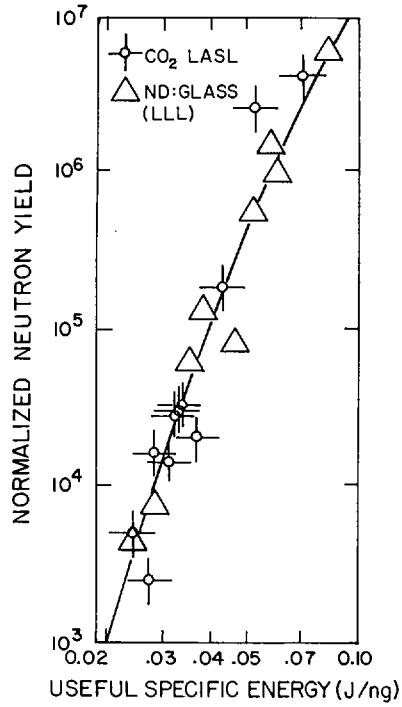


FIG.7. Neutron yields as a function of pellet driving energy.

5. EXPERIMENTS

In our second major area of activity, target experiments, we are beginning experiments in the 10-TW regime with Helios. Our plans for the next few years are determined by our major milestones, shown in Fig. 6. Six of these milestones involve target performance, which, in turn, are dependent on three milestones related to major laser facilities, because our target program, from its conception, has been restricted by laser-power limitations.

The first milestone, achievement of thermonuclear yield and compression with the Two-Beam System in 1977, verified our assumption that 10-μm CO_2 laser radiation is appropriate for inertial confinement fusion. Much of our theoretical and experimental program over the past several years sought to verify that 10-μm radiation is a satifactory energy source for pellet compression and heating [3]. This work was successful and provided convincing evidence that the radiation pressure (ponderomotive force) of the incident laser beam produces a plasma profile modification that enhances both energy absorption and its coupling to the core of the fuel pellet.

TABLE I

COMPRESSION MEASUREMENTS OF FUEL-FILLED GAS MICROSPHERES
(DT FILL WITH 10% Ne BY VOLUME)

SHOT #	Fill Pressure (atm)	Laser Power (TW)	Initial Diam. (μm)	Final Diam. (μm)	Ne Density Via Volume (10^{20} cm^{-3})	Ne Density Via Stark (10^{20} cm^{-3})	Volume Compression (Stark)
RR-11	8	0.32	189	68	4.2 ± 1.3	5.8	30
RR-21	8	0.45	185	56	7.1 ± 2.0	9.5	48
RR-26	7	0.82	181	50	8.1 ± 2.4	7.9	46

The fact that target performance is independent of laser wavelength is best illustrated by integral neutron-yield experiments on DT-filled glass microballoons imploded by the exploding-pusher mode. As shown in Fig. 7, similar yields are obtained from targets when driven by CO_2 and Nd:glass lasers under identical conditions. The solid line in the figure is the prediction of a simple analytic scaling model [4] which is consistent both with the experimental values and with more detailed calculations with the computer code LASNEX [5]. In this model, the useful specific energy is the net absorbed energy per unit mass that arrives before the minimum radius is reached. The neutron yield (normalized to a reference geometry and fuel fill by the model) appears to have the simple power dependence on the useful specific energy shown in Fig. 7. The wavelength independence over a significant range of yield is very striking.

Our confidence in the theoretical model is strengthened by a direct measurement of the density of the DT gas [6]. A spatially resolved spectrometer was used to measure the Stark broadening of x-ray lines emitted by neon gas which was added to the DT gas. The spatial resolution of the spectrometer allowed us to determine that the x-ray line emission was radiated from the imploded core and to compare the line-broadening with the density obtained from a volume measurement. Table I shows that the measurements are in good agreement, which is not usually the case for x-ray pinhole measurements, and that the density achieved in the DT gas is 0.2 times solid density. This result also agrees with the simple model and with LASNEX simulations.

Having achieved the second milestone, operation of the Helios laser at full power (Fig. 6), we are now completing the beam-transport and alignment systems and expect to begin target experiments in late summer. After shakedown experiments with exploding pusher targets, we will attempt to reach 20 times liquid (hydrogen) density with an ablatively driven target. LASNEX predicts that such densities can be achieved with relative ease. The experimental problem is to diagnose the density in the fuel because the expected neutron yields are very low and the targets are opaque to their self x-ray emission, due to the low temperature of the dense core.

A target design is shown in Fig. 8. In this design, a thick spherical layer of plastic is ablated by the approximately 1-ns-long laser pulse shown schematically in the Fig. 9 insert. The resulting impulse drives a series of shocks through the plastic into the nickel pusher, slowly accelerating the pusher toward the center and thereby compressing and heating the DT-gas

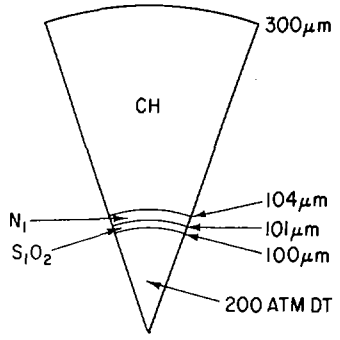


FIG.8. Radial profile of the 20 times liquid density target design.

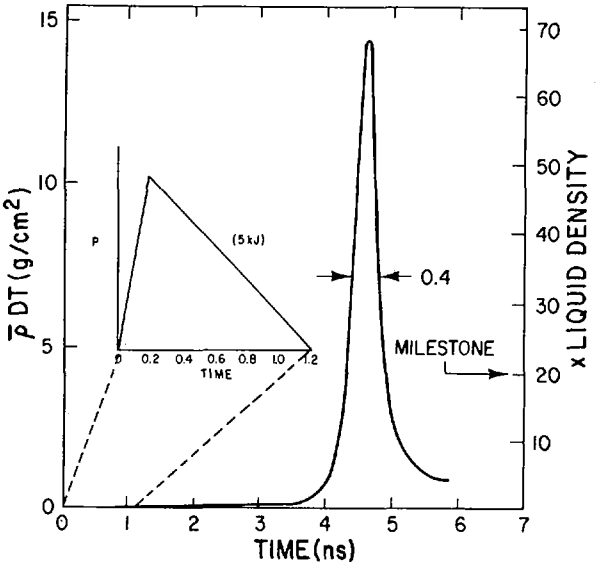


FIG.9. Calculated fuel-density time dependence of the 20 times liquid density target design.

fuel at the center. The thicknesses of the nickel and plastic layers are chosen to shield the fuel from all but the most energetic suprathermal electrons generated by the laser-plasma interaction, thus avoiding significant fuel preheat. The density of the fuel (Fig. 9) rises very slowly until the pusher approaches the center, a considerable length of time after termination of the laser pulse. One-dimensional calculations predict that the fuel density will rise to well above 20 times liquid density.

We expect to be able to infer the fuel density from the time interval between the moment the laser pulse impinges on the target and the time at which we observe neutron emission from the burning DT. We also hope to be able to measure directly the time history of the pusher position via x-ray backlighting of the pellet; this is, in principle, possible because the design has been tailored to avoid outward motion of the Ni-plastic interface.

Subsequent experiments will explore a number of target designs which should provide much higher fuel compressions. Cryogenic fuel layers appear advantageous and will be incorporated into several designs that will be explored on Helios. We will also study prototype targets on Helios for the breakeven experiments on Antares, not necessarily aiming for the highest yields or compressions we might achieve with 10 kJ, but rather attempting to confirm our computer design predictions and to optimize the target parameters so as to maximize the likelihood of success on Antares. The prototype target will be tested and optimized during final installation and checkout of Antares, between 1982 and 1983.

Upon completion of Antares, in October 1983, we expect to achieve breakeven within the following year.

6. SYSTEMS STUDIES

We turn now to the third component of our program: studies of potential systems for commercial energy production from inertial confinement fusion [7]. The path to scientific breakeven and commercial feasibility will be long and difficult but the payoff is so large that a vigorous effort is justified.

It is important to consider the major goals that must be addressed after achievement of scientific breakeven. We believe that the second major goal should be the attainment of net energy gain; that is, of a product of laser efficiency η and pellet gain Q equal to one ($\eta Q = 1$). The third goal would then be an ηQ high enough for a reactor system: an ηQ of 10 appears to be required for a pure fusion system, whereas an ηQ in excess of 2 seems sufficient for fission-fusion hybrid designs tailored for fissile fuel production.

For net energy gain, laser (or any other driver) efficiency is clearly an important parameter. The CO_2 laser offers relatively high efficiency. Helios has an electrical-energy to laser-energy efficiency of about 2%, compared to a current Nd:glass laser efficiency of about 0.1%. With multiple-pulse extraction schemes that have been proposed [8], efficiencies approaching 10% appear possible.

If we assume an efficiency of 10%, then to achieve an ηQ of 10 we must have a pellet gain of 100. Calculations indicate that such gains should be possible with a CO_2 laser energy of 1 MJ, and we are confident that CO_2 lasers can be scaled in size to such power levels.

Another important parameter is driver repetition rate capability. For commercial power application, a flowing gas laser is clearly the logical choice because it permits quick dissipation of the inevitable waste heat. We believe that the CO_2 laser offers the highest promise for commercialization. A laser selection based on wavelength criteria seems premature because no existing laser (or other driver) has yet achieved the

significant ablative (isentropic) compressions required for breakeven and higher pellet gains. Objections to a wavelength of 10-μm, based on excessive hot-electron production with attendant detrimental preheating of the target, disappear as one goes to high enough incident laser energies (and hence bigger pellets); we believe that pellet operation will become insensitive to preheating at target sizes well below those envisioned for achieving commercially useful pellet gains (Q = 100).

7. SUMMARY

I have outlined our recent progress at Los Alamos Scientific Laboratory and our plans for the future. We have demonstrated compression and fusion yield with CO_2 lasers. Our Helios CO_2 laser has operated at powers above 20 TW and will permit target experiments in the 10- to 20-TW range over the next four years, generating the information we need for the design and optimization of a breakeven target. Design of the Antares 100-kJ CO_2 laser is nearing completion, and all its facilities should be ready for operation in 1983. Achievement of breakeven in 1984 will set the stage for commercialization of inertial confinement fusion with CO_2 lasers. Systems studies continue to identify problem areas ahead, but we believe that the most difficult technical problem will be achievement of pellet breakeven. Thus, we seem to be on the threshold of very exciting times for inertial confinement fusion.

ACKNOWLEDGMENT

I wish to acknowledge the efforts of my colleagues at the Los Alamos Scientific Laboratory who have contributed the material for this paper and who have carried out the work described.

REFERENCES

[1] FENSTERMACHER, C. A., NUTTER, M. J. LELAND, W. T., and BOYER, K., "Electron-Beam-Controlled Electrical Discharge as a Method of Pumping Large Volumes of CO_2 Laser Media at High Pressure," Applied Physics Letters 20 (1972) 56.

[2] STRATTON, T. F., DURHAM, F. P., JANSEN, J., LELAND, W. T., REICHELT, W. T., and ZEIGNER, V. L., "The LASL 100-kJ CO_2 Laser For ICF Research: Antares," Inertial Confinement Fusion, Optical Society of America, 78CH1310-2QEA, (1977) TuC7-1.

[3] HENDERSON, D. B., "Shock Tube and Shock Wave Research," (Proc. 11th Int. Symposium on Shock Tubes and Waves), University of Washington Press, Seattle, Washington (1978) 542.

[4] GIOVANIELLI, D. V., and CRANFILL, C. W., "Simple Model for Exploding Pusher Targets," Los Alamos Scientific Laboratory, Los Alamos, New Mexico, LA-7218-MS (1978); OSBORN, R. K. and MAYER, F. J., Amer. Jour. Phys. 44 (1976) 149; STORM, E. K., et al, Phys. Rev. Lett. 40 (1978) 1570; PERKINS, R. B., "Recent Progress in Inertial Confinement Fusion Research at the Los Alamos Scientific Laboratory," U. S./IAEA Conf. on Inertial Conf. Fusion, San Francisco, California (1978), to be published.

[5] ZIMMERMAN, G. B., "Numerical Simulation of the High Density Approach to Laser-Fusion," Lawrence Livermore Laboratory Report UCRL - 74811 (1973).

[6] MITCHELL, K. B., VAN HULSTEYN, D. B., McCALL, G. H., LEE, P., and GRIEM, H. R., "Compression Measurements of Neon Filled Glass Microballoons Irradiated by CO_2 Laser Light," Los Alamos Scientific Laboratory Report, Los Alamos, New Mexico (1978), to be published.

[7] BOOTH, L. A., FREIWALD, D. A., FRANK, T. G., and FINCH, F. T., "Prospects of Generating Power with Laser-Driven Fusion," Proc. IEEE 64 (1976) 1460.

[8] PERKINS, R. B., "The Potentialities of CO_2 Lasers for Inertial Fusion," International Scientific Forum on An Acceptable Nuclear Energy Future of the World, University of Miami, Coral Gables, Florida (1977), to be published; CONN, R. W., et al, "Solase, A Laser Fusion Reactor Study," Nuclear Engineering Department, University of Wisconsin, Madison, Wisconsin, UWFDM-220 (1978); STARK, E.E., Jr., LELAND, W. T., and VOLKIN, H. C., "Nanosecond Pulse Amplification in CO_2 at Efficiencies Exceeding 20%," Topical Meeting on Inertial Confinement Fusion, Optical Society of America, 78CH1310-2QEA (1978) WC14-1.

DISCUSSION

P.C. THOMPSON: You show that the neutron output from exploding pusher targets scales as useful specific energy, independent of wavelength. For a given laser output, does useful specific energy depend on wavelength?

R.B. PERKINS: No, the useful specific energy is only a function of the rate of deposition of laser energy and of implosion time.

C. YAMANAKA: If one uses a long laser pulse in the CO_2 system, I should think that hot electrons might reduce the compression ratio. How do you propose to deal with the limitation imposed by the 10-μm-wave effect?

R.B. PERKINS: This will be handled by using sufficient material to stop the bulk of the hot electrons. In the 20-times-liquid-density design, most of the hot electrons will be stopped by the pellet materials before reaching the core, so very little pre-heat of the core is expected. As for longer pellets driven by larger lasers, the material in the pellet is sufficient to stop all the hot electrons.

P. AVIVI: How do you define efficiency?

R.B. PERKINS: We define it as the ratio of the optical energy delivered by the laser to the energy stored in the capacitor bank which pumps the laser.

SATURATION OF STIMULATED BRILLOUIN BACKSCATTER IN CO_2 LASER-PLASMA INTERACTION

A.A. OFFENBERGER, A. NG, L. PITT,
D. SALZMANN
Department of Electrical Engineering,
University of Alberta,
Edmonton,
Canada

Abstract

SATURATION OF STIMULATED BRILLOUIN BACKSCATTER IN CO_2 LASER-PLASMA INTERACTION.

Saturation of stimulated Brillouin scattering (SBS) has been observed in the interaction of long-pulse CO_2 laser radiation at intensities $\leqslant 10^{13}$ W · cm^{-2} with underdense hydrogen plasma. The high reflectivity observed (60%) is a direct consequence of the long plasma scale length (which results since the pulse length is large compared to the hydrodynamic response time) and the large instability growth rate associated with high-intensity, long-wavelength radiation. Significantly, the SBS is highly modulated with average long-time reflectivity approximately half the peak value. Spectral measurements show that, in fact, the Brillouin mode (weakly damped ion wave) has evolved to stimulated Compton scattering characteristic of large ion wave damping. Considerable ion heating occurs resulting in $T_i \sim T_e$, which would not be the case for collisional equilibration alone. Preliminary measurements also show a saturation in non-thermal X-rays generated in the underdense hydrogen plasma. Wavebreaking is postulated to be the principal saturation mechanism in the strong interaction of the laser radiation with underdense plasma.

1. INTRODUCTION

A problem of considerable interest and importance to the inertial confinement fusion concept is the role of stimulated backscatter in potentially reducing the coupling efficiency of laser energy to the target pellet. In particular, theoretical calculations suggest that intense laser radiation of frequency ω_0 interacting with ion wave fluctuations of frequency ω_s in the underdense coronal plasma surrounding the target may lead to strong backscatter of the laser radiation at a Stokes' frequency $(\omega_0 - \omega_s)$. An excellent summary of theory and simulation along with references to earlier calculations has been given by Forslund et al. [1]. In view of the large growth rates, even for relatively short scale length plasmas (characteristic of those generated by subnanosecond laser

pulse lengths, chiefly used to date) SBS[1] can be significant. For fusion grade targets and nanosecond pulse lengths, however, the underdense plasma scale length will be much greater. In this situation, unless mitigated by a rapid density reduction in the coronal plasma expansion, large backscatter is a likely result [2], [3], [4]. It is therefore of some importance to experimentally determine the nature and magnitude of backscatter from long scale length underdense plasma.

Earlier experiments with both 1 and 10 μm radiation have involved either short pulse, high intensity or long-pulse, moderate-intensity laser beams. As a consequence no direct evidence for saturation of SBS has been found. In particular, backscatter from gas rather than solid targets have yielded the clearest signatures of SBS: spectra, growth rates, etc., but the CO_2 laser intensities employed have not been high enough to show saturation (see [3], [5] and references therein for a survey of SBS studies). In addition, it has been shown that for long-pulse CO_2 laser radiation of focussed intensity $\sim 10^{12}$ watt/cm^2, high reflectivity leads to ion heating with Brillouin evolving to ion Compton scattering [3]. It would therefore seem likely that in most solid target experiments, since T_e is not much greater than T_i, stimulated Compton scattering should prevail. In such circumstances there is a very broad spectrum of interacting waves and, especially if the pump wave is not single-mode, it is more correct to describe the interaction and scattering in a random-phase rather than coherent wave process. Thus in our previous work using a multimode CO_2 laser with intensity $\leq 10^{12}$watt/cm^2, the level of backscatter was found to vary exponentially with incident power and the experimentally determined growth rate agreed with that calculated from random-phase theory.

In the present work, we wish to report on experimental observation of saturation in stimulated Brillouin backscatter from mm scale length underdense plasma.

2. EXPERIMENT

General details of the experimental arrangement have been given in earlier publications [3]. A schematic diagram of the set-up used for investigating backscatter is shown in Fig. 1. The incident CO_2 laser radiation was focussed by an off-axis paraboloid mirror with 10cm focal length onto a hydrogen gas target formed in a free jet expansion into vacuum. The initial gas density was set by triggering the laser at an appropriate time during the filling pressure pulse. Pressure equilibration in the gas cell was rapid compared to its risetime of 2 msec and gas flow out of the orifice into vacuum was negligible on this time scale.

In order to gain a higher focussed intensity for saturation studies, we modified the CO_2 laser optical cavity from a stable to an unstable resonator. Though the energy extracted was less, the substantially reduced beam divergence permitted better focussing (limited by focussing aberrations); the estimated mean focal spot intensity was slightly under 10^{13} watt/cm^2 for the 80-μm diameter focus and 35-nsec gain-switched output pulse of 15 J. As is evident in Fig. 2, several modes were beating in the optical cavity producing a modulated output. The laser power incident on the gas target was varied by using a propylene absorption cell.

---

[1] Stimulated Brillouin scattering.

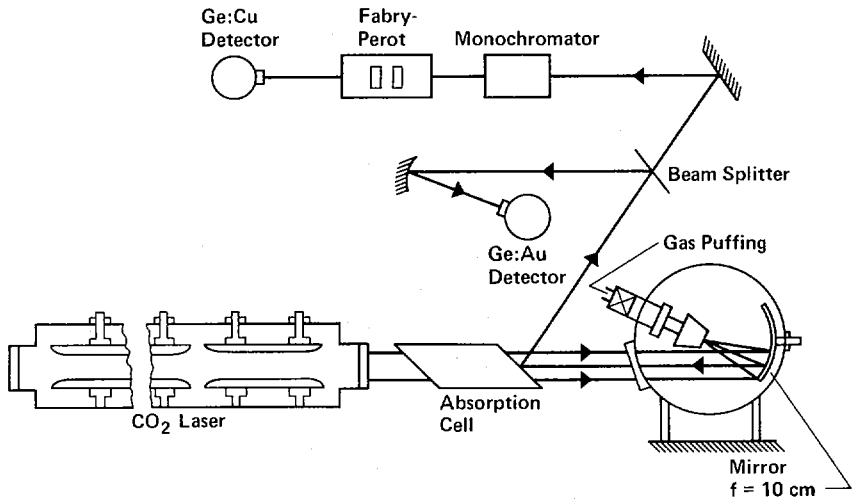


FIG.1. Schematic diagram of the experimental arrangement.

Principal measurements to be discussed here include infrared spectroscopy of the scattered laser radiation and foil-scintillator-photomultiplier determination of X-ray energy spectra. Backscattered radiation was collected by the input focussing mirror, coupled out by a beam splitter, spectrally analysed by a monochromator and Fabry-Perot interferometer in series, and detected by a Ge:Cu or Ge:Au infrared detector. System risetime of the detector, pre-amp oscilloscope was better than 2 nsec; wavelength resolution was 8 Å.

3. RESULTS AND DISCUSSION

3.1. SBS Pulse Shapes and Reflectance

Temporal characteristics of the backscatter at full laser intensity are to be seen in Fig. 2, where several different representative forms are presented. The depth of modulation varies substantially but, interestingly, the peak signal is nearly the same averaged over many shots. This demonstrates clearly the saturation in SBS even though growth begins from different noise levels. Also, over many shots it is difficult to infer much in the way of correlation between modulated CO_2 laser radiation and smaller modulations in the SBS signal. The more significant large modulations in backscatter occur at random times. The delay between incident and backscatter signals is real and is due to the finite time necessary for the laser beam to bleach successive cold gas layers and propagate from the gas-vacuum interface to the focus (typically 2.5 mm into the cell).

The average reflectivity, as determined by calibration using a NaCl window, was found to be $\sim$ 30% with peak modulated levels of $\sim$ 60%. Though individual sharp spikes of SBS, which may be present, would be integrated with our system bandwidth, nevertheless the waveforms shown in Fig. 2 indicate slower modulations which are easily followed by the 2-nsec response time. Thus no significant fraction of scattered energy is unaccounted for.

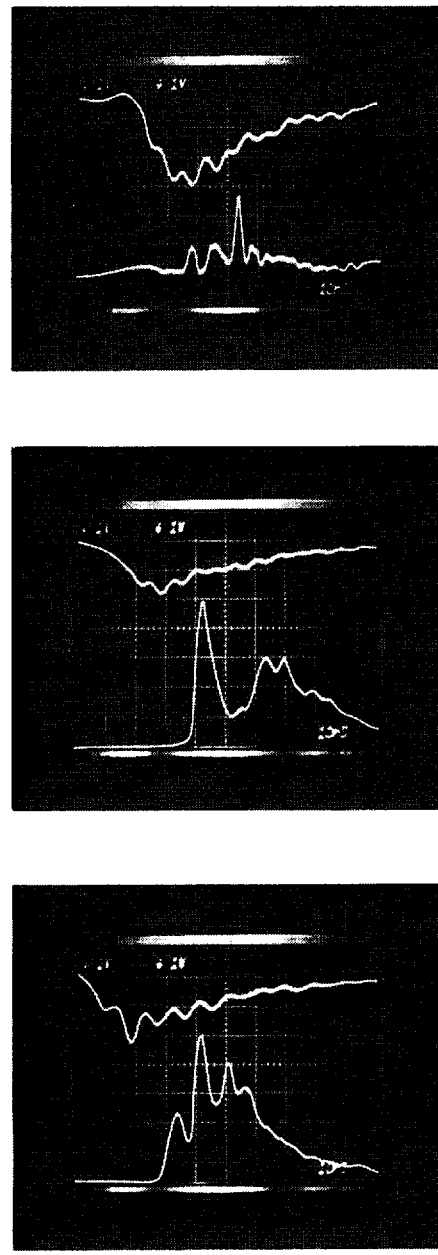


FIG.2. Lower trace: characteristic stimulated backscatter signals at full laser power showing strong modulation. Peak reflectivity is ~ 60%. Upper trace: CO_2 laser pulse shape.

3.2. SBS Spectrum

The spectrum of the backscattered radiation is shown in Fig. 3. This spectrum was obtained by integrating the modulated backscatter with a 7-nsec detection response time, thus providing single smooth pulses. It therefore represents a time-averaged characteristic. There is a clear redshift as found in our previous studies on gas target plasmas, identifiable as Brillouin scattering (or more correctly, ion Compton scattering, though we shall describe all such processes as Brillouin scattering). From the shift and width of the scattered radiation it can be inferred that ion Landau damping is strong. Indeed, we find $T_i \gtrsim T_e \gtrsim 100$ eV. Thus significant ion heating has occurred as a direct consequence of Brillouin scattering and the strong ion wave fluctuations induced with the large backscatter. We estimate peak density fluctuation levels $\delta n \sim n$.

In the absence of Compton heating, 2-D numerical simulations of the hydrodynamic equations predict $T_e \gtrsim 100$ eV and $T_i \gtrsim 50$ eV. With the long interaction time, however, the initial Brillouin mode evolves into ion Compton scattering as $T_i \rightarrow T_e$ and heavy-ion Landau damping sets in. A simple calculation balancing the energy flux deposited in ion waves with that transported away in free-streaming, assuming all ions are heated, confirms that there is more than adequate energy potentially imparted to the ions to account for a relatively modest 50 eV of additional heating.

These two features of the interaction, i.e. the ion heating resulting from strong SBS and the evolution of SBS to SCS[2] so that the heating is a bulk ion distribution effect rather than a high-energy tail effect, are important to the scattering process. The instability growth rate can, in fact, be higher for the Compton than the Brillouin regime. This, in turn, ensures that electron and ion temperatures will remain approximately equal. In addition, the broad spectrum of ion "waves" leads to a highly turbulent plasma which would favor wave-breaking over pump depletion as a saturation limit in the nonlinear interaction of plasma and electromagnetic waves.

3.3. SBS Saturation

The magnitude of backscattered power as a function of incident laser power is shown in Fig. 4. Saturation of the SBS signal is a significant departure from the pure exponential growth observed with lower laser intensity on the same gas target. In fact, saturation is even more dramatic since the delay between laser pulse and peak SBS signal is observed to decrease with increasing laser power. Since, in all cases, the laser pulse length and time delay for maximum SBS signal are much longer than the hydrodynamic response time, we can rule out strictly hydrodynamic expansion as responsible for the asymptotic backscatter behaviour. Numerical simulations of the interaction show axial density relaxation times of $\lesssim 5$ nsec and complete asymptotic states reached long before peak backscatter is observed.

On the other hand, the $I\lambda^2$ product of 10^{15} watt - $\mu m^2/cm^2$ is sufficiently large that, especially for times > 10 nsec, ponderomotive forces exceed thermal pressures for the plasma conditions. It should also be noted that the instability growth rate varies as $I\lambda^3$ in the Compton regime rather than as $I\lambda^2$ for the Brillouin. Since the plasma scale length $L \sim 1$ mm is substantial - estimated from numerical simulation

[2] Stimulated Compton scattering.

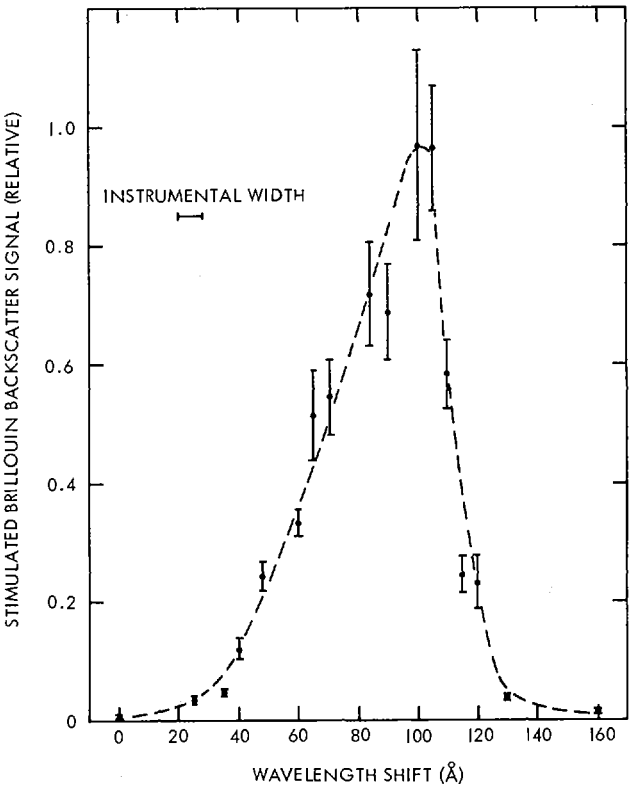


FIG.3. Spectrum of backscattered radiation showing the redshifted Brillouin-Compton component.

and streak photography - it is not surprising that growth of SBS to a limiting value is observed. The relevant question is: what saturating mechanism limits the backscatter level and is there any additional evidence for saturation of the turbulent electrostatic fields in the plasma? We shall present some evidence for the latter and briefly postpone discussion of the former.

3.4. X-ray Emission

Representative temporal waveforms of the X-ray emission from the underdense hydrogen plasma are shown in Fig. 5. Aluminum foil-scintillator-photomultiplier detectors were used for energy spectral measurements. As indicated in the photos, both single and multi-spike behaviour were observed, though multi-spikes were more typical of lower energy X-rays ($\sim$ keV). For intermediate foil thicknesses, characteristically the thermal bremsstrahlung X-ray emission would appear, on which the nonthermal component would break in and decay, after which a thermal spectrum would re-emerge. This is seen clearly in the waveforms of Fig. 5. The thermal and nonthermal spectra are plotted in Fig. 6. At a time of 20 nsec, just prior to non-

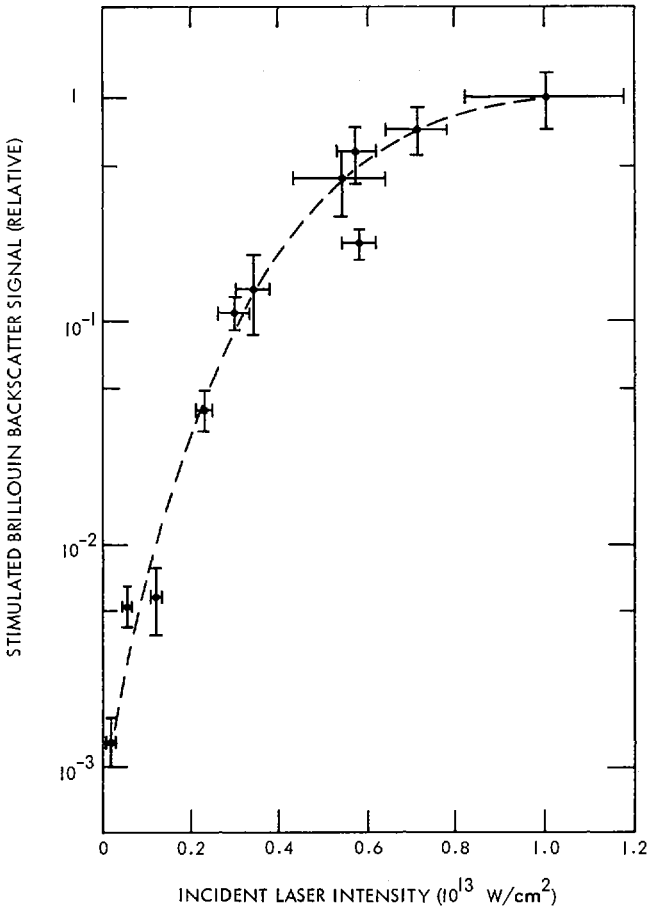
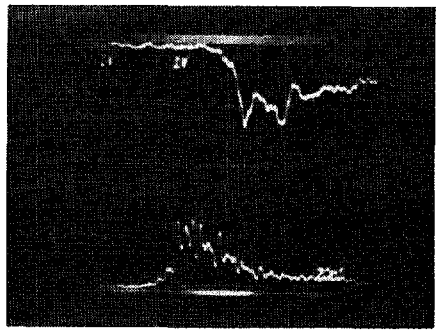


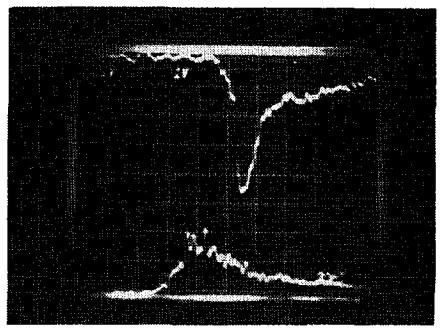
FIG.4. Stimulated Brillouin backscatter signal as a function of incident CO_2 laser intensity.

thermal emission arising, the derived temperature is $\sim$ 80 eV, and at a later time of 80 nsec, when the nonthermal X-rays are negligible, the calculated temperature is $\sim$ 50 eV. These values are reasonably close to those predicted from the 2-D code calculation. The equivalent "temperature" of the nonthermal spectrum is $\sim$ 1 keV. It should be noted that these X-rays arose entirely from the hydrogen plasma; a collimator translated axially confirmed that background secondary X-rays were negligible and therefore did not interfere with the bulk plasma measurements.

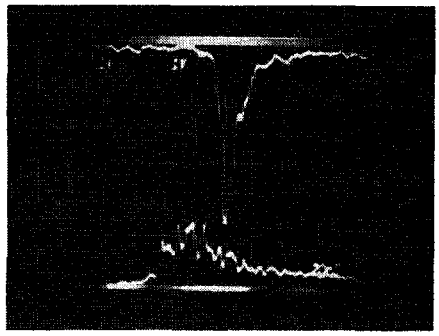
The magnitude of the nonthermal X-ray emission was determined as a function of incident laser power, and the results are shown in Fig. 7. The quantity plotted is actually thermal plus nonthermal signal for the 3-μm aluminum foil used, but the nonthermal level was approximately three times the thermal level. Importantly, this figure shows a saturation in



3 μm ALUMINUM FOIL



6 μm ALUMINUM FOIL



9 μm ALUMINUM FOIL

FIG.5. Upper trace: X-ray pulse shapes behind various aluminum foil thicknesses at full laser power. Lower trace: CO_2 laser pulse shape.

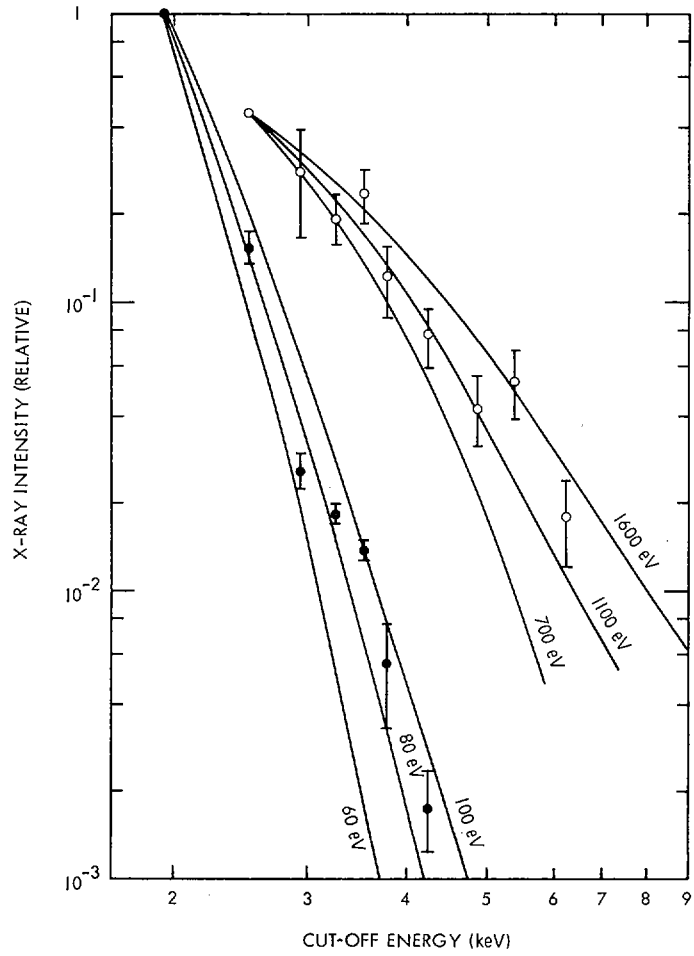


FIG. 6. X-ray energy spectra for thermal and nonthermal component in the hydrogen plasma emission.

nonthermal emission from the plasma which very accurately coincides with the plot of SBS versus incident laser power. This data should be considered as a preliminary result, for which additional work is required before any good quantitative inferences may be drawn. Nevertheless, it indicates a striking corroboration of the SBS saturation characteristic. For the underdense plasma in which these measurements were made ($n/n_c \lesssim 0.2$), ion turbulence is dominant and a strong correlation would be anticipated.

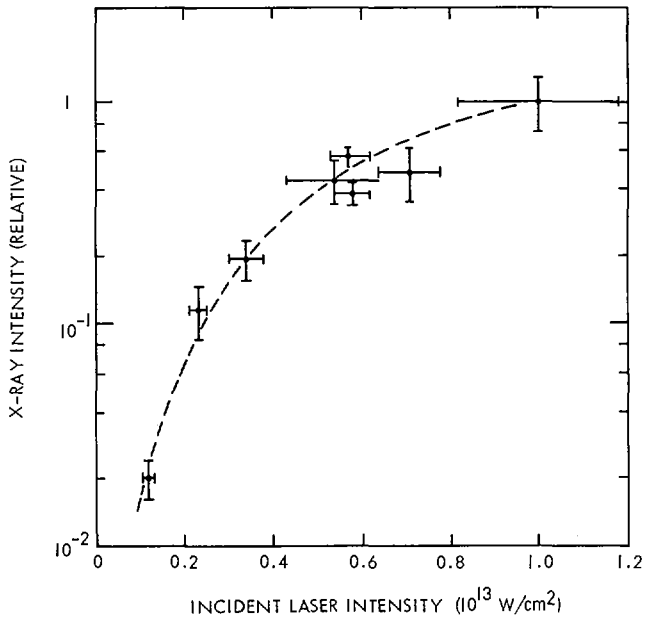


FIG.7. X-ray intensity behind 3-μm aluminum foil as a function of incident CO_2 laser power. The saturation in X-ray emission when overlaid on the SBS saturation curve agrees exactly.

4. DISCUSSION

Apart from hydrodynamic expansion, possible mechanisms for saturating the backscatter level include pump depletion, wave-breaking and filamentation. We have argued that, because of the relatively long pulse length and short hydro time scale, plasma expansion is not the limiting process. Two separate pieces of information suggest that pump depletion is not a likely candidate either. In the first place, for a coherent wave interaction the growth and decay should occur on much faster time scales than those observed. The temporal and spectral behaviour of the SBS signals is more indicative of a broad non-resonant process where more than a single wave mode is involved. Secondly, it is known from earlier work on the target that a very broad spectrum of ion turbulence is generated - both in geometry and wavenumber [3], [6]. It may be expected that longer time scales would result as a consequence of the growth and dissipation of many modes (all with different time scales). Indeed, stimulated Compton scattering is a broad spectral process with many individual scattering events occurring at different rates. In this situation, it appears more likely that wave-breaking associated with the highly turbulent fields ($\delta n \sim n$ and $\delta E \sim 3 \times 10^6$ V/cm) will dominate the saturation of SCS. Both the temporal and spectral character of the backscatter and the temporal X-ray behaviour support such an interpretation.

Filamentation may also play a role in the saturation mechanism, though in an energy balance it is probably not as important for long laser

pulses as for shorter ones. Certainly the threshold for instability is modest and the large ponderomotive forces would be very effective in leading to saturation in small filaments. Any hot spots in the incident laser beam would aggravate the problem. For our experimental situation, however, relaxation times should be faster than the several nanosecond times observed.

In conclusion, strong stimulated Brillouin-Compton scattering has been found to saturate when long scale length underdense hydrogen plasma is irradiated with focused CO_2 laser intensities $\leq 10^{13}$ watt/cm^2. Modulated reflectivities up to 60% were observed with significant ion heating resulting in SBS evolving to SCS. Nonthermal X-ray emission showed the same saturation behaviour as the backscatter. Temporal and spectral shapes of the SBS signal, along with calculated ion density fluctuations, support wave-breaking as the dominant saturation mechanism.

REFERENCES

[1] FORSLUND, D.W., KINDEL, J.M., LINDMAN, E.L., Phys. Fluids 18 (1975) 1002, 1017.
[2] PHILLION, D.W., KRUER, W.L., RUPERT, V.C., Phys. Rev. Lett. 39 (1977) 1529.
[3] OFFENBERGER, A.A., NG, A., CERVENAN, M.R., Can. J. Phys. 56 (1978) 381.
[4] RIPIN, B.H., et al., Phys. Rev. Lett. 39 (1977) 611.
[5] MASSEY, R., BERGGREN, K., PIETRYZK, A.Z., Phys. Rev. Lett. 36 (1976) 963.
[6] OFFENBERGER, A.A., NG, A., PITT, L., Phys. Rev. Lett. 40 (1978) 873.

DISCUSSION

P.K. KAW: When you say that maximum backscatter is 60%, do you know that the rest of the energy is absorbed or is it simply scattered in other directions?

A.A. OFFENBERGER: Our measurements indicate that very little energy is scattered or refracted in other directions. With the long-pulse laser beam used here, most of the laser energy is absorbed in the plasma.

S.W.A. WITKOWSKI: It is a familiar fact that reflectivity and scattering depend not only on intensity but also on the geometry of the experiment. I suppose that your measurements were made with the target as sharply in focus as possible. Have you also obtained data on backscattering with the target very much out of focus, and compared such data with those quoted in your paper?

A.A. OFFENBERGER: With laser breakdown of a gas target and long pulse times, hydrodynamic expansion gives a relatively large plasma volume. In this situation, the initial focusing is not important because the interaction occurs in the focal region with uniform underdense plasma around it at later times.

S.E. BODNER: What is the angular distribution of the Brillouin scattering, and could a change in angular distribution explain the saturation of backscatter?

A.A. OFFENBERGER: The detailed angular distribution has not been measured, though sample measurements show small scatter in directions other

than the backward direction. This is to be expected for the long-pulse laser beam, which creates a cylindrical column with radial beam trapping in the density minimum on axis.

K. PAPADOPOULOS: Do you have any measurement that indicates the power law of the non-thermal tails for electrons and ions?

A.A. OFFENBERGER: Not at present. A full X-ray energy spectrum has not been measured, chiefly because the total energy content of non-thermal X-rays is very small.

WORK ON LASER INTERACTION AND IMPLOSION AT CENTRE D'ETUDES DE LIMEIL

A. BEKIARIAN, E. BURESI, A. COUDEVILLE,
R. DAUTRAY, F. DELOBEAU, P. GUILLANEUX,
C. PATOU, J.M. REISSE, B. SITT,
J.M. VEDEL, J.P. WATTEAU
Centre d'études de Limeil,
Villeneuve St.-Georges,
France

Abstract

WORK ON LASER INTERACTION AND IMPLOSION AT CENTRE D'ETUDES DE LIMEIL.

Laser-matter interaction experiments at 1.06 and 10.6 μm were performed at fluxes of 5×10^{15} and 3×10^{13} W · cm^{-2}, respectively. At 1.06 μm the penetration depth of the absorbed energy, studied with the aid of stratified plane targets, is several thousand Å. 2-MeV Al^{11+} ions and 50–500-keV electrons were observed at 10.6 μm. Two types of implosion experiments were carried out with glass microballoons (diameter ~ 100 μm, thickness ~ 1 μm) containing about ten bars of DT at 1.06 μm and at absorbed energy densities of the order of 50 J · μg^{-1}. In the case of the Iris experiment, performed at 10^{13} W · cm^{-2}, implosion seems to be due to progressive ablation of the wall of the microballoon. The Coquelicot experiment was performed with the P.102 laser at several times 10^{15} W · cm^{-2} and with a pulse of 40–80 ps. From diagnostic tests, especially observation of the X-rays emitted, the following characteristics were deduced: energy absorbed by the target, 4 J; temperature and density of the compressed DT, 1 keV and 0.2 g · cm^{-3}; product $\rho r \sim 10^{-4}$ g · cm^{-2}; neutron yield, 10^5. To interpret these experiments, theoretical studies were performed on radiation pressure, particle transport, relativistic effects and implosion stability; one- and two-dimensional implosion codes have been developed. The implosion experiments will be continued with the Octal laser (700 J – 2 TW – 8 beams) whose shaped pulse can be varied from 50 ps to 1 ns.

1. LASER-MATTER INTERACTION EXPERIMENTS AT 1.06 μm AND 10.6 μm

At 1.06 μm the experiments are being pursued at higher flux with the P.102 laser (15 J; 40–80 ps; intensity on target ~5×10^{15} W · cm^{-2}; power contrast $> 10^6$). The energy deposition is studied on a thick, plane cryogenic target by observation, in particular, of the plasma expansion lobe and its evolution as a function of intensity, laser radiation polarization, and angle of incidence. The density profile of the expanded plasma is determined by interferometry at $2\omega_0$ and $4\omega_0$, and identification of the absorption mechanisms is attempted by spectrographic analysis of the plasma radiation [1, 2].

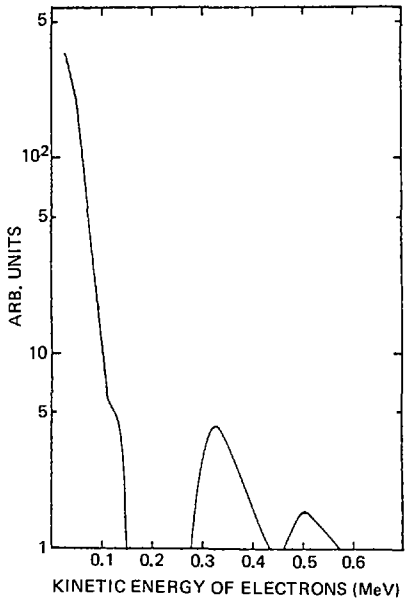


FIG.1. Spectrum of electrons emitted by aluminium through 25 μm of Be; $\lambda = 10.6$ μm; $\phi = 3 \times 10^{13}$ W·cm^{-2}; $\tau = 1.7$ ns.

Axial and radial electron conduction is studied with layered plane targets (deposition on glass substrate). Axial penetration is evaluated by measuring the intensity of the silicon lines for different thicknesses of aluminium deposition (600–7000 Å) on the front face of the glass layer: beyond a thickness of 2000 Å these lines are no longer detectable. Spatially resolved spectra taken tangentially to the target reveal the different behaviour of the various ion species, whose lines appear localized either near the surface (7.17 Å for Al^{12+}) or further within the expansion zone (7.75 Å for Al^{11+}) [3].

At 10.6 μm, the experiments are carried out with the M3 CO_2 laser (10 J; 1.7 ns; 3×10^{13} W·cm^{-2} on target; power contrast 2×10^5) and with targets of thick aluminium or thin polyethylene [4]. For intensities of 3×10^{13} W·cm^{-2}, Al^{11+} ions were observed with energies of the order of 2 MeV, depending strongly on the angle of incidence. At the same time, electrons are detected with an energy spectrum between 50 and 500 keV (Fig.1).

2. MICROBALLOON IMPLOSION EXPERIMENTS

Two types of microballoon implosion experiments at 1.06 μm were carried out with the C6 and P.102 neodymium-glass lasers at absorbed energy densities

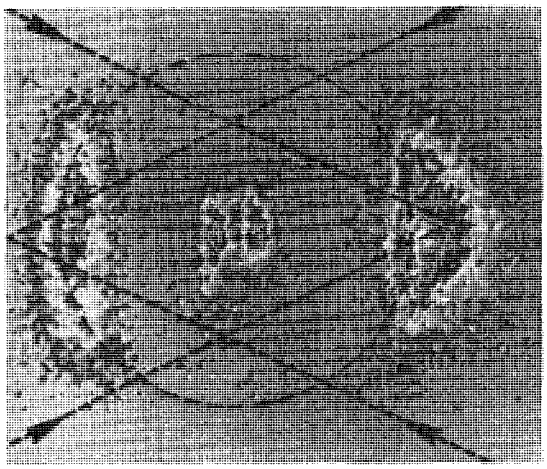


FIG.2. X-ray photograph of a microballoon through 250 μm of Be. Dia. 80 μm; thickness 0.8 μm; initial DT density 2 mg·cm^{-3}; 12 J absorbed; 80 ps. Initial positions of microballoon wall and laser beams are shown by dashed lines.

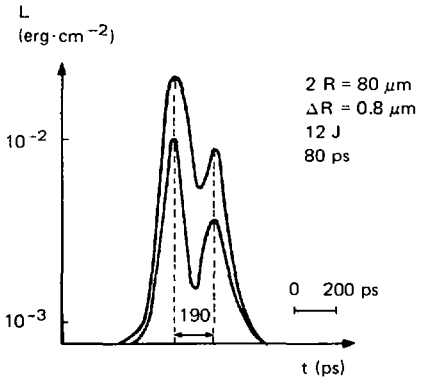


FIG.3. Time variation of X-ray emission from imploded microballoon.

in the neighbourhood of 50 J·μg^{-1}. In the case of the Iris experiment, the glass microballoon is imploded by four convergent beams; the duration of the pulse is 1.4 ns and the flux does not exceed 10^{13} W·cm^{-2}. There is relatively good agreement between the experimental results and the values given by a one-dimensional code, and implosion appears to be due to progressive ablation of the microballoon [5]. The Coquelicot experiment is carried out with a much shorter pulse, 40–80 ps, and with fluxes higher than 10^{15} W·cm^{-2}. The P.102 laser

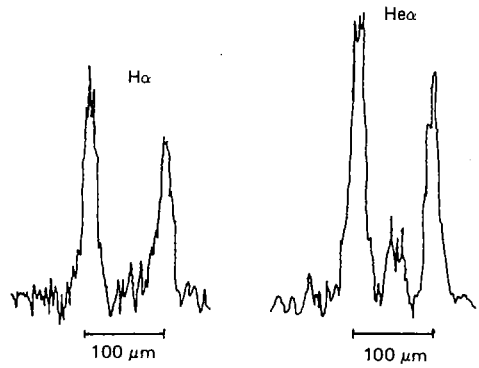


FIG.4. Spatial variation of intensity of the Hα and Heα lines of silicon along a diameter of the microballoon.

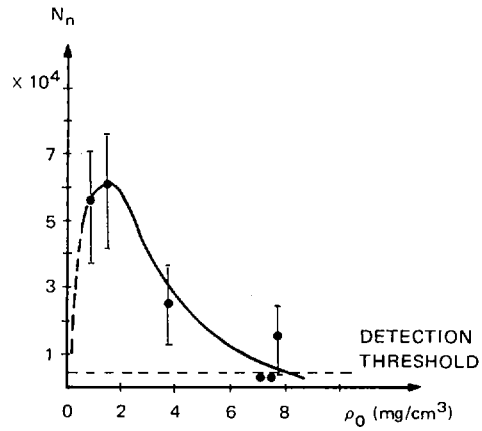


FIG.5. Variation of neutron yield as a function of the initial DT density. Dia. 80 μm; thickness 0.8 μm; incident power 500 GW.

beam is divided into two equal parts, which are focussed along a diameter on both sides of the microballoon (dia. 80 μm, thickness 1 μm) containing about ten bars of DT [6].

Figure 2 shows time-integrated X-ray emission from the plasma, filtered by a 250-μm-thick beryllium absorber, which stops photons with energies below 2 keV. With spatial resolution of the order of 5 μm one can discern the points of impact of the two beams on the microballoon, and the compressed core. It will be noted that the absorbed energy is not propagated beyond the region of deposition, which suggests that lateral electron conduction is ineffective in these

experimental conditions; X-ray emission is at a minimum at the centre of the microballoon where the compressed DT is found. The two-dimensional aspect does not permit accurate evaluation of the density of the compressed DT, but it is estimated at 0.2 $g \cdot cm^{-3}$ from the distance between the X-ray emission extrema [7].

Figure 3 shows the time variation of the X-ray emission – for the same spectral range as in Fig.2 – recorded with a streak camera (resolution of the order of 30 ps). The emissions from the core and from the corona are separated in time. The mean implosion velocity is deduced to be $2 \times 10^7 cm \cdot s^{-1}$. Figure 4 shows the intensity variation of Hα (6.18 Å) and Heα (6.65 Å) silicon lines along a diameter – obtained by means of a KAP crystal associated with a slit – for a microballoon 100 μm in diameter, with incident power of 500 GW. Finally, the variations in neutron emission as a function of DT initial density are shown in Fig.5 (dia. 80 μm; thickness 0.8 μm; incident power 500 GW).

From these experimental results one deduces the mean characteristics of the "exploding pusher" type of 2-dimensional implosion produced with the P.102 laser: incident energy 20 J; absorbed energy 4 J; temperatures of the corona 1 keV at $10^{22} cm^{-3}$ and of the core 1 keV; density of compressed DT 0.2 $g \cdot cm^{-3}$; product $\rho r \sim 10^{-4}$ $g \cdot cm^{-2}$; neutron yield $\sim 10^5$.

3. THEORY AND NUMERICAL SIMULATION

The preparation and interpretation of the above experiments are based on fundamental theoretical and numerical simulation work. On the question of interaction, this work was concerned with density profile modifications by ponderomotive force [8], with the generation of fast particles and magnetic fields [9], and with the influence of relativistic effects. To try to predict whether the absorption efficiency could be improved at very high flux, a thorough study of exact solutions of the Lorentz-Maxwell system in a homogeneous medium has been carried out [10]. A general method of approximation has been developed to study wave propagation in different cases [11]. In the inhomogeneous case, the spatial dependence of the wave in the neighbourhood of the critical surface is considerably modified when relativistic effects are taken into account.

To improve the numerical simulation of the implosion, studies are being carried out on equations of state and ionization models, opacities, and particle and radiation transport. As regards thermal conductivity, recent calculations suggest that the use of more flexible systems of hydrodynamic equations, such as the GRAD method of 13 moments, could improve the description of heat transfer without the need to adopt an ad-hoc flux limitation.

Several codes are developed on the basis of these studies. The one-dimensional code mentioned above has the following main characteristics: (a) Lagrangian code for two temperatures and a single fluid; (b) absorption of laser energy by

inverse bremsstrahlung with or without energy deposition at the cut-off density. The code also takes account of radiation pressure, ion and electron thermal conductivity (which may or may not be limited in flux), exchange of energy between these two populations, transport of suprathermal particles and of radiation by multigroup or MONTE CARLO methods, and thermonuclear reactions. In addition, a two-dimensional hydrodynamic code is being developed to obtain a better model of the absorption of laser energy by the target and to study, for example, the target illumination defects, lateral thermal conductivity, and the generation of magnetic fields.

Finally, numerical calculations on target implosion stability have been performed using the PERTUS Lagrangian perturbation code. At the same time, theoretical studies were carried out on the stability of the ablation zone. It is shown that there exists a generalized static criterion which includes previous instability criteria [12]. When the perturbations are adiabatic, they depend only on the entropy gradient ∇S, and the instability criterion is written $g \cdot \nabla S < 0$ (g is the acceleration of the front) instead of the usual criterion $g \cdot \nabla \rho > 0$, which neglects, in particular, the effect of compressibility. If we assume that the speed of sound is locally constant, the growth rates can be derived explicitly and it is noted that the very thin ablator shells ($R/\Delta R > 100$) are without doubt the seat of catastrophic instabilities, while moderate structure ratios of several tens are still acceptable.

4. LASERS, TARGETS AND DIAGNOSTICS

The Octal laser now in service comprises a series of amplifiers with ED_2 silicate glass rods developed by Cilas; the final stage has a diameter of 9 cm, a glass length of 2×18.5 cm and a gain of 4, with a pumping energy of 70 kJ [13]. This laser is driven either by a YAG mode-locked oscillator followed by a 10-channel "pulse stacker" producing a pulse of 50–600 ps, or by a single-mode oscillator giving a pulse whose duration after clipping is 200 ps to 1 ns with a risetime of 150 ps and a power contrast of 10^6. At the chain output Octal produces 2 TW in 200 ps and over 700 J in 600 ps. Octal is at the moment being used for an implosion experiment in which the 8 beams are synchronized at ±5 ps.

In connection with lasers the following subjects are being studied with industrial support:

A 12-cm neodymium-glass rod amplifier (CGE) – relatively uniform gain of 3 ± 0.08 for small signal;

Multi-dielectric layers (MATRA) resistant to 7 $J \cdot cm^{-2}$ at 1.4 ns;

An iodine laser chain (CGE).

Plane and spherical targets have been made specially for experiments; for example, plane glass targets 1 μm thick covered with a 500–7000-Å coating of aluminium.

Studies are also being performed on techniques for coating the microballoons: thin aluminium coating (less than 1 μm) by vacuum evaporation, chemical reduction, and electrochemistry (several micrometres of Ni or Au to within about 0.1 μm), and plastic coating by polymerization in a low-pressure electric discharge (up to 10 μm within about 0.3 μm).

For diagnostics, efforts are being made to increase the resolution and improve the processing of experimental results, as the following two examples illustrate:

(a) The TSN 505 streak camera (Thomson-CSF) has a sweep speed of 2 $cm \cdot ns^{-1}$, a spatial resolution of 4 pairs of lines per mm, and a time resolution of 5 ps; it can be fitted with UV, X and latterly S1 microchannel tubes. A camera employing a lamellar optic tube (LEP) is being developed and should make it possible to achieve resolutions of 10 pairs of lines per mm and 2 ps [14].

(b) The DATAIC system of automatic acquisition, treatment and visualization of streak camera images has an Isocon television tube coupled by optic fibres to the TSN 505 camera. With a laser pulse of 10 ps half-width, the system dynamics are better than 100 [15].

5. CONCLUSION

The interaction between radiation and matter was studied at 1.06 μm and 10.6 μm for a product of a few 10^{15} $W \cdot \mu m^2 \cdot cm^{-2}$: fast particles were detected and the absorbed energy penetration was estimated by spectrometry. The two types of implosion (by ablation or explosion of the wall of the microballoon) were attained by means of the C6 laser (1 ns) and the P.102 laser (100 ps), respectively, at absorbed energy densities of 50 $J \cdot \mu g^{-1}$. These implosion experiments will be continued with the Octal (700 J, 2 TW) laser, whose eight beams provide uniform illumination of the target and whose pulse-shaping will facilitate laser-target coupling. In addition, an effort will be made to increase the hydrodynamic efficiency of implosion by using more refined targets. Finally, for a better understanding of the experiments, numerical simulation will be progressively improved by better treatment of the absorbtion of laser radiation and the transport of absorbed energy and by using the two-dimensional code mentioned above.

REFERENCES

[1] SALERES, S., Contribution à l'étude des mécanismes d'interaction et de chauffage dans un plasma de deutérium créé par laser, Thesis, Paris (1977).
[2] DECROISETTE, M., et al., "Transfer processes and hydrodynamics in laser interaction", Proc. 10th Europ. Conf. on Laser Interaction with Matter, Palaiseau, 1976.
[3] COUTURAUD, J.C., et al. "X-ray spectroscopic studies in laser plasma experiments", Proc. Mtg. of Plasma Phys. Div. Am. Phys. Soc., Atlanta, 1977.
[4] BOCHER, J.L., et al. Fast particle emission from CO_2 laser-produced plasmas, Optics Commun. **24** (1978) 291.
[5] BILLON, D., et al., "Laser-driven implosion experiments at Limeil", Proc. 10th Europ. Conf. on Laser Interaction with Matter, Palaiseau, 1976.
[6] BILLON, D., et al., "Laser-driven implosion experiments of microballoons with nanosecond and picosecond laser pulse duration", Proc. 11th Europ. Conf. on Laser Interaction with Matter, Oxford, 1977.
[7] BILLON, D., et al., "Experimental results on implosion experiments performed at Limeil", Proc. Top. Mtg. on Inertial Confinement Fusion, San Diego, 1978.
[8] VIRMONT, J., et al. Density profile modification by light pressure in spherical geometry, Phys. Fluids **21** (1978) 567.
[9] MORA, P., PELLAT, R., Renormalized theory of magnetic field generation in resonance absorption, Phys. Lett. **66A** (1978) 28.
[10] DECOSTER, A., Non-linear travelling waves in homogeneous cold collisionless plasma, to appear in Phys. Rep.
[11] BOURDIER, A., et al., Relativistic effects on electromagnetic wave propagation in a cold inhomogeneous electron plasma, Phys. Lett. **64A** (1977) 292.
[12] SITT, B., Instabilités en phase linéaire dans les milieux stratifiés, CEP Rep. in preparation.
[13] BARDES, J., et al., "Status of high power at Limeil", Proc. 11th Europ. Conf. on Laser Interaction with Matter, Oxford, 1977.
[14] BOUTRY, B., et al., "Picosecond streak camera with a laminar optics image converter tube", Proc. 13th Int. Conf. Ultra Rapid and Photonic Cinematography, Tokyo, August 1978.
[15] CAVAILLER, C., et al., "Acquisition and automatic analysis system for streak cameras (DATAIC)", ibid.

DISCUSSION

J.P. BORIS: Do your *experimental* results on low-power one-dimensional ablation in the nanosecond pulse range shed any light on the Rayleigh-Taylor modes in the ablation layer? I understand that your code results show instability, but such calculations are suspect unless the zone sizes are smaller than or of the same order as the characteristic scales for the equilibrium ablation layer thickness, i.e. $\delta r \lesssim 0.1$ m.

J.P. WATTEAU: The resolution of the X-ray pictures we took of the IRIS nanosecond implosion experiment was too low (20 μm) to provide information on the development of instabilities in the ablation layer. The code results I

showed refer to the two-dimensional COQUELICOT implosion. This is a hydrodynamic code which does not include a treatment of ablation layer stability. Nevertheless, we do have a Lagrangian stability code which can be coupled to hydrodynamic codes, with proper mesh size – the importance of which you stress; and from the stability code we have found that for an aspect ratio $R/\Delta R$ of the order of 100, the growth rates are such that the shell implosion is unstable.

H. HORA: I have a question concerning the two-dimensional compression code. What delay time did you allow between the laser incidence and the thermalization, assuming that you are driving your compression thermally and not by non-linear forces? It is known (HORA, H., Aust. J. Phys. 29 (1976) 375) that this delay can be relatively long.

J.P. WATTEAU: The results I presented were the first obtained with our two-dimensional code. Up to now, the absorbed energy is deposited in the shell, proportionally to the mass ($1\ J \cdot ng^{-1}$). So we do not really take into account interaction phenomena in this rough simulation, which we intend to improve.

EXPERIMENTAL STUDIES OF INTERACTION AND TRANSPORT PROCESSES IN LASER FUSION*

F. AMIRANOFF, R. BENATTAR, R. FABBRO,
E. FABRE, C. GARBAN, C. POPOVICS,
A. POQUERUSSE, R. SIGEL**, C. STENZ,
J. VIRMONT, M. WEINFELD
Ecole polytechnique,
Laboratoire de physique des milieux ionisés,
Palaiseau,
France

Abstract

EXPERIMENTAL STUDIES OF INTERACTION AND TRANSPORT PROCESSES IN LASER FUSION.

The effect of laser wavelength and pulse shaping on interaction and the transport process is investigated. Experiments show that absorption increases with shorter wavelength, from 35% at 1.06 μm to 45% at 0.53 μm. The production of hot electrons is significantly reduced in short-wavelength experiments. The hot electron temperature determined from X-ray emission decreases from 8 keV at 1.06 μm wavelength to 2 keV at 0.53 μm. This indicates a better thermal electron transport at shorter wavelength. The measurement of burn-through depth has confirmed this result, showing that at 0.53 μm this depth is almost three times larger than at 1.06 μm. Experiments with different types of prepulse show that there is a difference between discrete and continuous prepulse in backscattering and refraction effects, in favour of the continuous pulse shaping. It is also observed that pulse shaping enhances lateral thermal transport.

INTRODUCTION

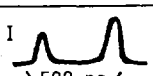
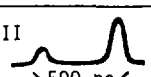
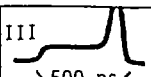
The problem of energy deposition and transport in laser-matter interaction experiments, in connection with inertial confinement fusion, is being investigated in many laboratories. These studies are fundamental in photon-driven compression experiments to defining the capability of lasers to be efficient drivers for inertial

---

* Work performed as part of the scientific programme of the Groupement de Recherches Coordonnées Interaction Laser Matière du Centre National de la Recherche Scientifique (Ecole Polytechnique, Palaiseau).

** On leave from Projektgruppe für Laserforschung, Garching, Federal Republic of Germany.

TABLE I. FRACTION OF LASER LIGHT REFLECTED IN MASSIVE POLYETHYLENE TARGET EXPERIMENTS

Angle of incidence	Pulse shape	0 	I  >500 ps<	II  >500 ps<	III  >500 ps<
0°	back reflected	8	12	12	9
	scattered	54	74	72	60
	Total	62	86	84	69
30°	back reflected	3	8	7	3.5
	specular	49	59	60	46
	Total	52	67	67	49.5
		%	%	%	%

Laser wavelength 1.06 μm. Intensity 210^{15} W·cm^{-2}. The main pulse is identical and 100 ps FWTM. The prepulse energy varies with the type: I 30%, II 10%, III 30%.

confinement fusion. Our work is concentrated on studies of the mechanisms which govern laser beam absorption by solid targets and the transport of the absorbed energy in high-density plasma. Among the physical parameters involved in these processes, the temporal pulse shape, laser wavelength and interaction geometry are very important, and our experimental studies have been pointed in this direction. Some results obtained in laser target irradiation experiments are reported here,in which the shape and composition of the targets, laser wavelength and pulse shape were varied in order to facilitate fundamental studies.

Our major laser facility in the Groupement de Recherches (GILM) is at present a neodymium glass laser (λ = 1.06 μm) made by Quantel, which gives an output energy of 10 J in a 100-ps FWHM pulse. A pulse stacker included in the laser chain allows continuous variation of the pulse shape within a time interval of 600 ps. The output beam can also be frequency-doubled with an energy of 5.5 J at 0.53 μm. Experiments have also been made at 10.6 μm with a long-pulse TEA-CO_2 laser with 40-J output energy.

The maximum light intensities on target are 3×10^{15} W·cm^{-2} at 1.06 μm, 10^{15} W·cm^{-2} at 0.53 μm, and 10^{12} W·cm^{-2} at 10.6 μm.

Experiments were performed mainly with massive flat targets of aluminium or polyethylene and with thin foils of polystyrene. In the latter case, the foil thickness varied from 0.03 μm to a few μm. Solid glass microspheres were used for hydrodynamic studies in spherical expansion geometry.

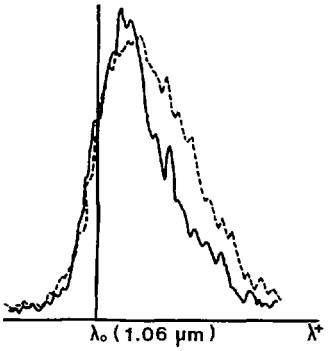


FIG.1. Effect of prepulse on the spectrum of backreflected light. Broken line: with 30% prepulse, $\Delta\lambda = 7$ Å. Solid line: without prepulse, $\Delta\lambda = 5$ Å. Al foil, 10° incidence.

Several diagnostics were installed on the experiments at 1.06, 0.53 and 10.6 μm. The optical energy balance, with spatial resolution, is obtained from pyroelectric detectors, and spectra of the refracted or back-reflected laser light can be made at the fundamental frequency or its harmonics. Optical interferometry with a Wollaston interferometer and schlieren photography are used to measure the electron density profile. For the CO_2 experiments a ruby laser is used as the probe beam, whereas for the neodymium experiments a fraction of the beam of the master oscillator is, after amplification, frequency-quadrupled and used as the probe. Ion time-of-flight analysis is made with charge-collectors protected for secondary emission. The continuum X-ray emission between 1 keV and 30 keV is analysed with a multichannel system consisting of PIN diodes and NaI scintillators coupled to photomultipliers. A pinhole X-ray camera with 6 μm resolution is used for plasma photography and a flat or bent-crystal X-ray spectrograph for line spectroscopy.

Automatic data acquisition and processing is in operation with a Camac interface and a Nova computer. At present, the signals of the charge-collectors are processed in this way.

INTERACTION EXPERIMENTS

Laser light absorption, still a matter of concern for laser fusion applications, has been studied in considerable detail with the main emphasis on the dependence of absorption on the laser wavelength and the dependence of collimated or Brillouin backscatter on the laser pulse shape. The former study, performed by frequency-doubling the laser to 0.53 μm, is motivated by efforts to build fusion lasers with output in the visible spectral range; the latter by the fact that, in general,

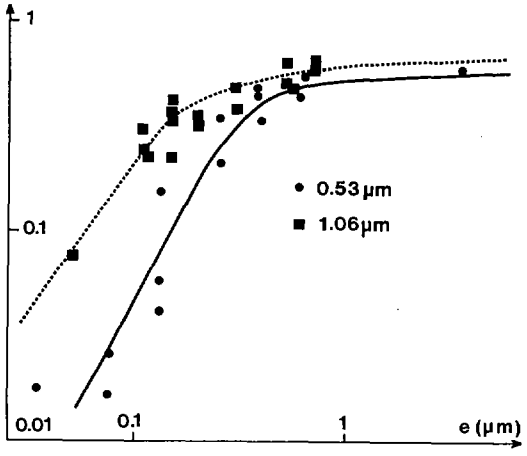


FIG.2. Reflection coefficient variation with foil thickness (e) for different laser wavelengths.

longer laser pulses than have yet been applied may be required in future applications, with the possibility that the reflection losses by stimulated scattering would increase catastrophically.

Results are presented in Table I. It appears that, for the pulse shapes investigated here, the losses by backscattering are much less important than in recent experiments with more widely spaced pulses [1]. We find, in fact, that a discrete prepulse somewhat enhances the collimated backscatter with correspondingly enhanced redshift in the spectrum (Fig. 1) compared to a clean pulse or plateau-like prepulse, and seems the least favourable pulse shape with respect to backscatter losses. Those, however, never exceed 12% for our F/1.5 focusing optics. It is interesting that a plateau-like prepulse, i.e. pulse shape, which approaches more the pulse shape often discussed for laser fusion, seems to be not particularly vulnerable to backscatter losses.

Table I also shows results for oblique incidence at 30° of p-polarized light. This angle is near the optimum angle for resonance absorption reported by other laboratories [2, 3]. We also find that, at this angle, absorption is enhanced. Most favourable are the clean pulse and the plateau-like prepulse, each with ~ 50% absorption.

A comparative study of absorption at 1.06 μm and 0.53 μm was made in a series of thin-foil experiments as shown in Fig. 2. Absorption was found to increase from 35% to 45% when changing to the shorter wavelength. Laser light absorption at 1.06 μm is well known to be accompanied by the production of fast electrons in the plasma with damaging effect on the performance of laser fusion targets. Hence, X-ray measurements were performed in these experiments at the same time.

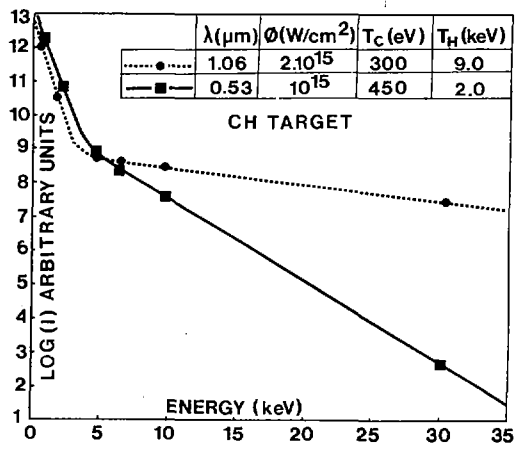


FIG.3. X-ray spectra at 1.06 μm and 0.53 μm.

For the 'cold electron' temperature T_c, not much change is observed between the two wavelengths (the somewhat surprising increase from 400 ± 50 eV at 1.06 μm to 500 ± 50 eV at 0.53 μm not exceeding the error bars). The change in intensity of the hard X-rays and the hot electron temperature T_h is very pronounced (Fig. 3). At $h\nu = 30$ keV the intensity diminishes by 10^5. At the same time, T_h diminishes from 7.5 ± 2 keV at 1.06 μm to 2 ± 0.4 keV at 0.53 μm. Thus, laser light absorption is not only enhanced at the shorter wavelength but is also less complicated by fast electron generation. One may speculate that absorption by inverse bremsstrahlung, which should not lead to fast electron generation, begins to contribute at the shorter wavelength.

It may be noted that a correspondence was found between T_h as evaluated from the X-ray measurements and the temperature evaluated from the fast ion signal of the charge-collectors. The collector signals indicate an exponential density decay of the form $\partial N/\partial V = \exp -v/v_0$, where v_0 is the isothermal sound velocity $v_0 = (Zk\,T_h/Mi)^{1/2}$. The temperature T_h determined in this way was very close to but slightly smaller than the temperature measured by the X-rays.

Expansion of the plasma corona was investigated directly by schlieren photography and interferometry. Experiments in spherical geometry were emphasised, to facilitate comparison with theory.

In CO_2 interaction with glass microballs of 180 μm diameter (Fig. 4(c), (e)), the density profile could be probed up to $n_e = 10^{20}\,cm^{-3}$ (ten times critical density) with the ruby laser light source. In Nd interactions with glass balls of 40 μm and 70 μm diameter (Fig. 4(d), (e)) the maximum density measured with the 4ω probe beam was not more than $n_e = 3 \times 10^{20}\,cm^{-3}$.

The density profile obtained in the Nd case shows an exponential decay with radius which is characteristic for a rarefaction wave. At $3 \times 10^{20}\,cm^{-3}$ the

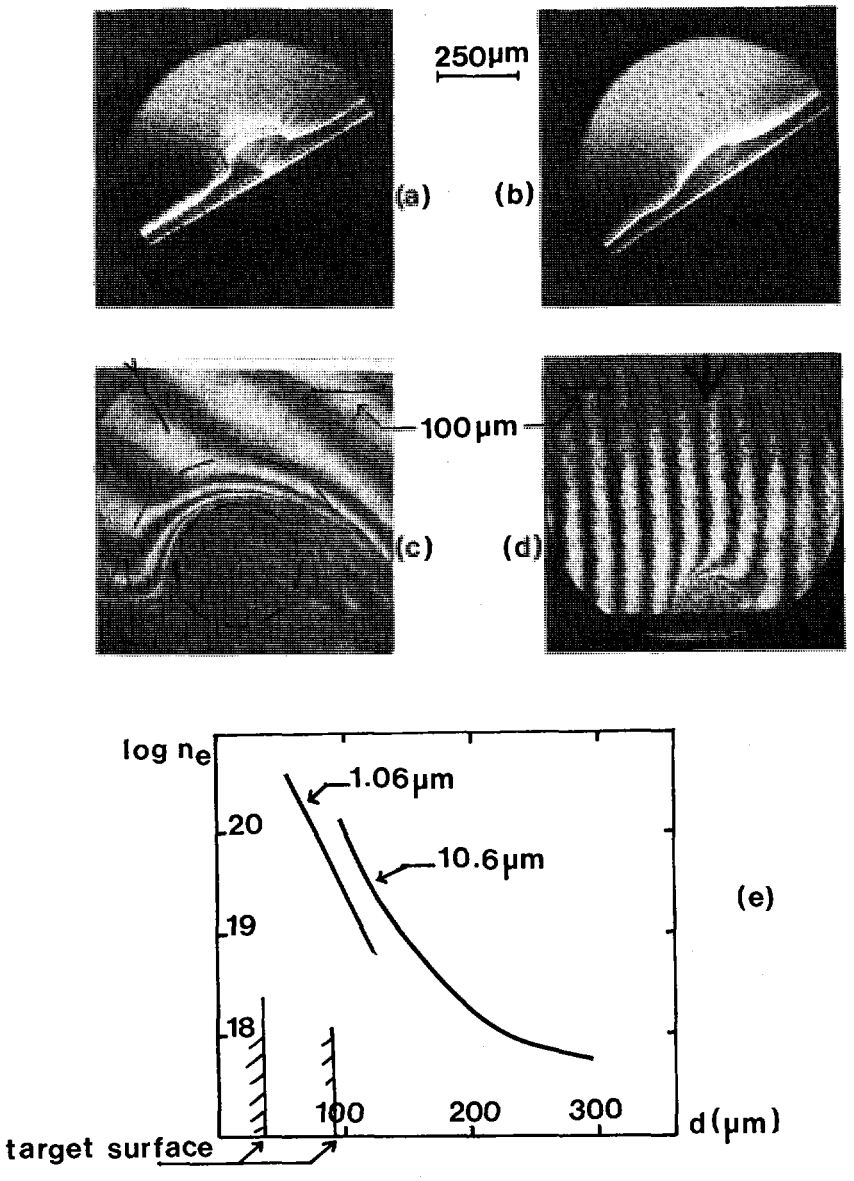


FIG.4. **Schlieren photography:** $\lambda = 1.06\ \mu m$; *100 ps; Al target* $- t = 1.08$ *ns.*
(a) 5.7 J, no prepulse; (b) 4.9 J, prepulse type III.
Interferometry: *(c)* $\lambda = 10.6\ \mu m$, $10^{12}\ W \cdot cm^{-2}$, $SiO_2\ \phi\ 176\ \mu m$, $t = 190$ *ns. (d)* $\lambda = 1.06\ \mu m$, *5.5 J, 100 ps,* $SiO_2\ \phi\ 70\ \mu m$, $t = 0$.
(e) Density profiles measured from interferograms (c) and (d).

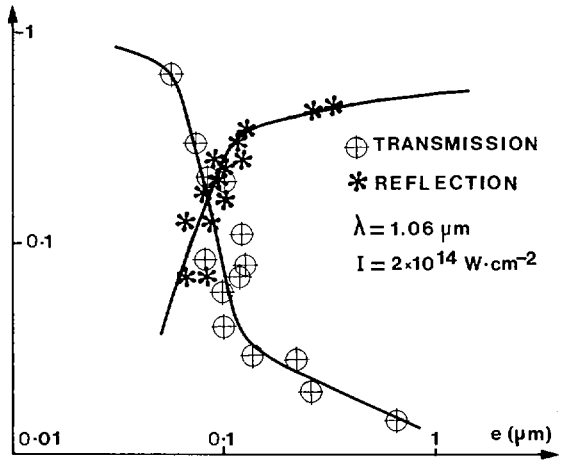


FIG.5. Transmission and reflection coefficient variation with foil thickness (e).

density gradient is 15 μm, the fringes disappearing abruptly towards the upper density side. This observation may indicate the onset of profile steepening in the vicinity of the critical density, but experiments with improved resolution (limited at present to 6 μm) are needed to confirm this.

For CO_2 interactions the density profile shows a tendency towards flatter, more stationary profiles [4], as is expected for these long-pulse experiments. The density gradient at the critical density is 30 μm, i.e. 3 λ0. A hydrodynamic explanation for the observed gradient may be sufficient, particularly since the interferograms show clearly that deviations from spherical symmetry remain significant in these one-sided spherical target irradiation experiments and lead to a more rapid density decay than predicted for a truly spherical expansion.

TRANSPORT EXPERIMENTS

The penetration of the thermal front in the target was determined in experiments using thin foils [5, 6] of polystyrene with oblique incidence, 30°. For ease of diagnostics, the p-polarization was used. The main parameter was the foil thickness, ranging from 0.03 μm to 3.5 μm. The experiment was conducted at 1.06 μm for two laser intensities: 2×10^{14} and 2×10^{15} W·cm^{-2} with 100 ps pulse, and at 0.53 μm, 10^{15} W·cm^{-2} with 70 ps pulse.

The diagnostics were: optical transmission and reflection of the foils; ion energy distribution in the front and in the rear of the foil; and intensity in X-ray emission. In Fig. 2 the foil reflections for the wavelength 1.06 μm and 0.53 μm are compared. The change in the slope of the curve occurs, respectively,

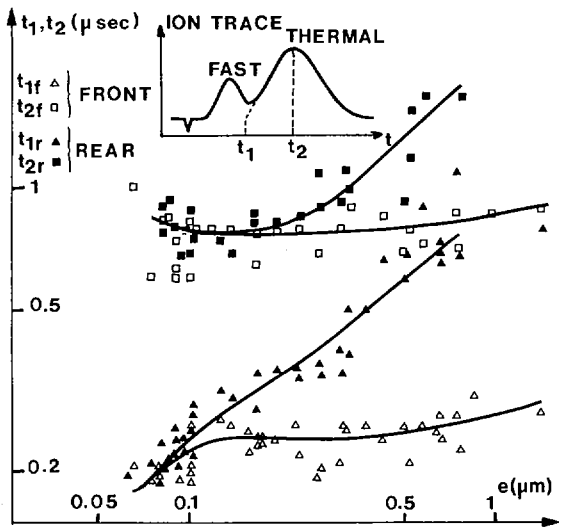


FIG. 6. t_1 and t_2 variation with foil thickness (e); $\lambda = 1.06\ \mu m$; $I = 2 \times 10^{14}\ W \cdot cm^{-2}$.

for a foil thickness of $0.15 \pm 0.05\ \mu m$ and $0.3 \pm 0.05\ \mu m$ for comparable laser flux. In Fig. 5, for a lower flux $2 \times 10^{14}\ W \cdot cm^{-2}$ at $1.06\ \mu m$, the change in reflection occurs for a foil thickness of $0.12\ \mu m \pm 0.02$, which is approximately the thickness at which the foils begin to be strongly opaque. This characteristic foil thickness provides an upper limit for the burn-through depth because the plasma has to expand after the burn-through before becoming transparent. Figure 6 gives typical results obtained from charge-collector signal. We have plotted here the dependence on foil thickness of parameters t_1 and t_2 as shown in Fig. 6: t_1 is the asymptotic value of the time of flight of the ion of the thermal ion component; t_2 is the time of the peak of this component. The collector is located 45 cm from the plasma. The value of these parameters is compared in the front (f) and in the rear of the foil (r).

Figure 7 gives results for $0.53\text{-}\mu m$ wavelength and $10^{15}\ W \cdot cm^{-2}$. Experiments have also been made at $1.06\ \mu m$ and $2 \times 10^{15}\ W \cdot cm^{-2}$. t_{1f} is expected to be smaller than t_{1r} when the thermal front no longer burns through the foil. At $1.06\ \mu m$ this occurs at a $0.1\ \mu m$ foil thickness for $2 \times 10^{14}\ W \cdot cm^{-2}$ and at approximately $0.15\ \mu m$ for $2 \times 10^{15}\ W \cdot cm^{-2}$. At $0.53\ \mu m$, burn-through is observed at $0.3\ \mu m$ for $10^{15}\ W \cdot cm^{-2}$. These results are in good agreement with the burn-through determination obtained from optical measurement. The thickness for which $t_{2f} < t_{2r}$ is larger. Comparison was made with numerical computation with a 1D hydro Lagrangian code. Fast electron transport was not taken into account; the flux limit coefficient was 0.05 and an absorbed flux of $10^{14}\ W \cdot cm^{-2}$. The values obtained for 95% absorption and $t_{1f} < t_{2r}$ were $0.2\ \mu m$ and $t_{2f} < t_{2r}$,

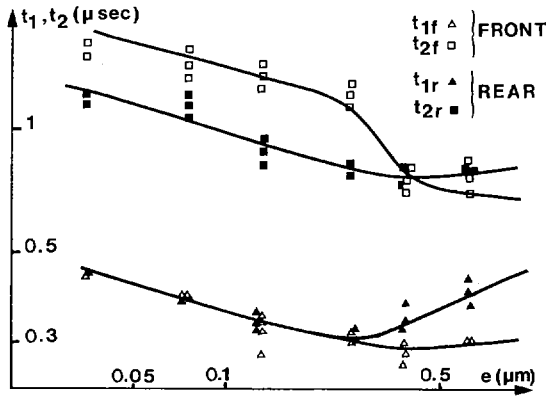


FIG. 7. t_1 and t_2 variation with foil thickness (e); $\lambda = 0.53$ μm; $I = 10^{15}$ W·cm^{-2}.

0.3 μm. These values are larger than the experimental determination discrepancy. This can be attributed to the 2D effect in transport and expansion which cannot be included in this code. However, the general behaviour with foil thickness of the t_1 and t_2 is very similar to both numerical and experimental results. Moreover, the calculations show that for much smaller thickness than the burn-through depth, t_T has to be smaller than t_f, which is effectively observed for 0.53-μm experiments, for experiments at 1.06 for 2×10^{15} W·cm^{-2}.

Finally, we discuss the effect of prepulse on interaction and transport. We had observed in previous experiments that a prepulse type III significantly reduces the formation of fast ions, decreases the hot electron temperature, and increases the number of thermal ions. This prepulse also decreases the intensity of hard X-ray near 1 keV. These effects are more effective at oblique than at normal incidence. Figure 4 shows that the prepulse has a lateral extension which is larger at the target. As a result, prepulse favours the transport parallel to the target, which reduces thermal flux inhibition and hot electron production. The type of prepulse also acts upon the X-ray emission; type I and type II have an intermediate behaviour between type III and the no-prepulse case. This is not entirely understood at present.

CONCLUSIONS

Our experiments have been devoted to the effects on interaction and transport mechanisms of laser wavelength and pulse shaping. Experiments at 1.06 and 0.53 μm have shown that absorption is favoured, as expected, at the shorter wavelength and increases from 35% to nearly 50% at laser intensities of 10^{15} W·cm^{-2}, showing an increasing efficiency of bremsstrahlung absorption.

However, absorption results obtained for CO_2 and long pulses show that, on flat targets, absorption is in the range of 30% near the absorption for 1.06 μm. This means that the effect of wavelength on absorption is very important in the visible or shorter wavelength. The major energy losses are not due to Brillouin backscattering but to refraction or sidescattering, even in flat targets.

The effect of wavelength on energy thermalization and transport is the most significant. Hot electron production is greatly reduced for the shorter wavelength, mainly as a result of a less inhibited longitudinal thermal transport. The penetration depth is approximately twice as large at 0.53 μm than at 1.06 μm.

The model for the isothermal rarefaction wave in the corona region seems to be confirmed by direct measurement of the electron density distribution below critical density. The effect of pulse-shaping on interaction and transport has been analysed. In pulse-shaping it appears that there is a difference between continuous and discrete prepulse. It does not seem that continuous pulse-shaping will greatly increase the collimated Brillouin backscattering.

Finally, the effect of pulse-shaping is to favour lateral thermal conduction, which could be favourable for isotropy of energy deposition in implosion experiments if the effect of refraction does not introduce major losses.

ACKNOWLEDGEMENTS

This work was performed as a part of the research programme of GILM, the CNRS group on laser-matter interaction. The authors are grateful to Dr. Pellat and his colleagues for fruitful discussions. They also wish to thank their collaborators for valuable technical assistance.

REFERENCES

[1] RIPIN, B.H., YOUNG, F.C., STAMPER, J.A., ARMSTRONG, C.M., DECOSTE, R., McLEAN, E.A., BODNER, S.E., Phys. Rev. Lett. **39** (1977) 611.

[2] MANES, K.R., RUPERT, V.C., AUERBACH, J.M., LEE, P., SWAIN, J.E., Phys. Rev. Lett. **39** (1977) 281.

[3] GODWIN, R.P., SACHSENMAIER, P., SIGEL, R., Phys. Rev. Lett. **39** (1977) 1198.

[4] GITOMER, S.J., MORSE, R.L., NEWBERGER, B.S., Phys. Fluids **20** (1977) 234.

[5] PEARLMAN, J.S., ANTHES, J.P., Appl. Phys. Lett. **27** (1975) 581.

[6] YOUNG, F.C., WHITLOCK, R.R., DECOSTE, R., RIPIN, B.H., NAGEL, D.J., STAMPER, J.A., McMAHON, J.M., BODNER, S.E., Appl. Phys. Lett. **30** (1977) 45.

DISCUSSION

A.G.M. MAASWINKEL: How does one obtain a mean T_e of 3–4 keV at 1.06 μm from flux limit considerations if one measures T_{cold} = 400 eV and T_{hot} = 7.5 keV at 10^{15} W·cm^{-2} intensity, with 30–40% absorption?

E. FABRE: The cold temperature refers to the plasma corona heated by the laser where absorption takes place mainly, in all probability, through resonance absorption at 1.06 μm. With a hot electron temperature of 7.5 keV, the flux limit considerations will be fulfilled.

W. KRUER: Can you infer the existence of transport inhibition from your experiments in which foils are irradiated?

E. FABRE: Comparison with numerical simulation with a flux limit of 20 gave thermal heat conduction slightly larger than the experimental data. These calculations were made at 1.06 μm.

DYNAMICS OF LASER-PRODUCED IMPLOSION OF GAS-FILLED MICROBALLOON TARGETS*

R.G. EVANS, M.H. KEY, D.J. NICHOLAS,
F. O'NEILL, A. RAVEN, P.T. RUMSBY,
I.N. ROSS, W.T. TONER, P.R. WILLIAMS,
M.S. WHITE
Science Research Council,
Rutherford Laboratory,
Chilton, Didcot, Oxon.

C.L.S. LEWIS, J.G. LUNNEY,
A. MOORE, J.M. WARD
Queen's University,
Belfast

T.A. HALL
Essex University,
Colchester, Essex

J. MURDOCH, J.D. KILKENNY,
T. GOLDSACK, J.D. HARES
Imperial College, London,
United Kingdom

Abstract

DYNAMICS OF LASER-PRODUCED IMPLOSION OF GAS-FILLED MICROBALLOON TARGETS.

Laser-produced compression of gas-filled microballoon targets has been produced by a two-beam Nd:glass laser with energies of up to 40 J per beam in a 100-ps pulse. The compressed plasma has been diagnosed by space-resolved, time-integrated X-ray spectroscopy and by observation of D-T fusion reaction products. Time-resolved measurements of the implosion dynamics have been made by X-ray streak photography with a time resolution of 20 ps and in a separate experiment by pulsed X-ray shadowgraphy (or radiography) with a time resolution of 100 ps. Evidence is presented for hydrodynamic instability and shell break-up in an exploding pusher implosion of a layered microballoon. A multi-layer plane target experiment has yielded a quantitative measurement of laser energy deposited into fast electrons.

---

* Work carried out at the Science Research Council's Central Laser Facility at the Rutherford Laboratory.

1. INTRODUCTION

The Central Laser Facility of the UK Science Research Council was set up in April 1976 to provide to British Universities a high-power laser system for studies of laser-plasma interaction and laser-produced compression of matter. The two-beam laser system was commissioned in April 1977 and compression studies began at the end of that month. In 1978 the laser system was improved by using the two 10-cm disk amplifiers in double pass mode, and energies of up to 40 Joule per beam have since been available.

The compression studies have involved focussing the two laser beams on small glass shell targets using two aspheric f/1 lenses. The targets are typically 70 μm - 100 μm diameter, 0.6 μm - 1.3 μm wall thickness and filled with various gases (Neon, Argon, Deuterium-Tritium) at pressures up to 87 atm.

Interpretation of the experimental data has been aided by computational modelling using the 1-D Lagrangian code MEDUSA[1]. The code has been developed at the Rutherford Laboratory beyond its published form to include suprathermal energy transport and the ponderomotive pressure of the laser beam.

2. IMPLOSION CORE PARAMETERS

2.1. Electron Density and Temperature

The electron density and temperature in the imploded core regions of Neon-filled glass microballoons have been deduced from X-ray spectra using a space-resolving crystal X-ray spectrometer. The details of the spectrometer have been described elsewhere[2]. The spectrometer has a space resolution of about 7 μm and a simultaneous spectral resolution of $\lambda/\Delta\lambda \approx 2000$. The instrument is sufficiently sensitive to record the spectrum of both line and continuum emission on a single laser shot. Fig. 1 shows a typical portion of the space-resolved spectrum showing the emission lines of Helium and Hydrogen-like Neon (Ne IX and Ne X) from the compressed gas.

The electron density and temperature of the imploded material may be deduced from a number of different analyses of the spectrum, but two of these are particularly direct. If the X-ray spectrum is sufficiently well exposed, the intensity of the continuum emission at frequency ν, $I_\nu \propto e^{-h\nu/kT_e}$, this leads to an unambiguous determination of the average electron temperature in the plasma. This metod may be used both for the imploded Neon and the Silicon in the imploded glass.

If the electron temperature is known approximately then the electron density may be deduced from the linewidths of Stark-broadened lines, in particular the Helium-like transitions Ne IX $3^1P_1 - 1^1S_o$ and Si XIII $3^1P_1 - 1^1S_o$. The Stark-broadening calculations were performed with a computer code developed by Richards[3] that included both electron impact and ion microfield broadening. The theoretical line profiles need to be corrected for the opacity of the plasma, using a simple homogeneous model, and the resulting agreement between theory and experiment is shown in Fig.2.

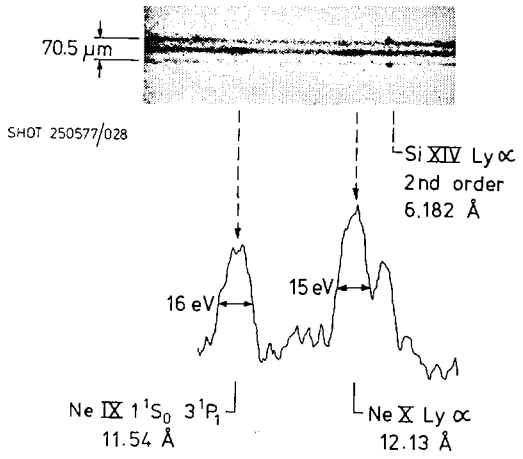


FIG.1. Space-resolved X-ray spectrum of imploded microballoon showing Stark-broadened emission lines of Ne IX and Ne X. (8.5-bar neon-filled microballoon; initial diameter 70.5 μm; wall thickness 0.82 μm.)

These methods of analysis may be applied to both Neon and Silicon in separate areas of the implosion core and typical results are summarised in Table I.

2.2. Ion Temperature

The observation of fusion reaction products, i.e. neutrons and alpha particles, from microballoons filled with equimolar Deuterium-Tritium is a measure of the quantity $\rho^2\langle\sigma v\rangle$ where ρ is the imploded D-T density and $\langle\sigma v\rangle$ is the average fusion reaction rate. The density of the compressed D-T was inferred by comparision with a target filled to the same density with D_2 + 5% Ne in which the implosion core could be diagnosed spectroscopically as described in section 2.1. Assuming that the ions in the compressed core have time to establish a Maxwellian energy distribution, then $\langle\sigma v\rangle$ may be related to the D-T ion temperature.

The neutron emission has been observed with an absolutely calibrated scintillator-photomultiplier detector, and the yield of alpha particles has been measured by the use of cellulose nitrate films. When subsequently etched, the α-particle tracks in the cellulose nitrate are visible under a microscope and may be counted. Both methods agree on the number of D-T fusion reactions per shot.

The calculation of ion temperature from the fusion yield was performed using a self-similar implosion-explosion model[4] and the result for a shot yielding 1.6×10^5 neutrons is $T_i \simeq 1$ keV.

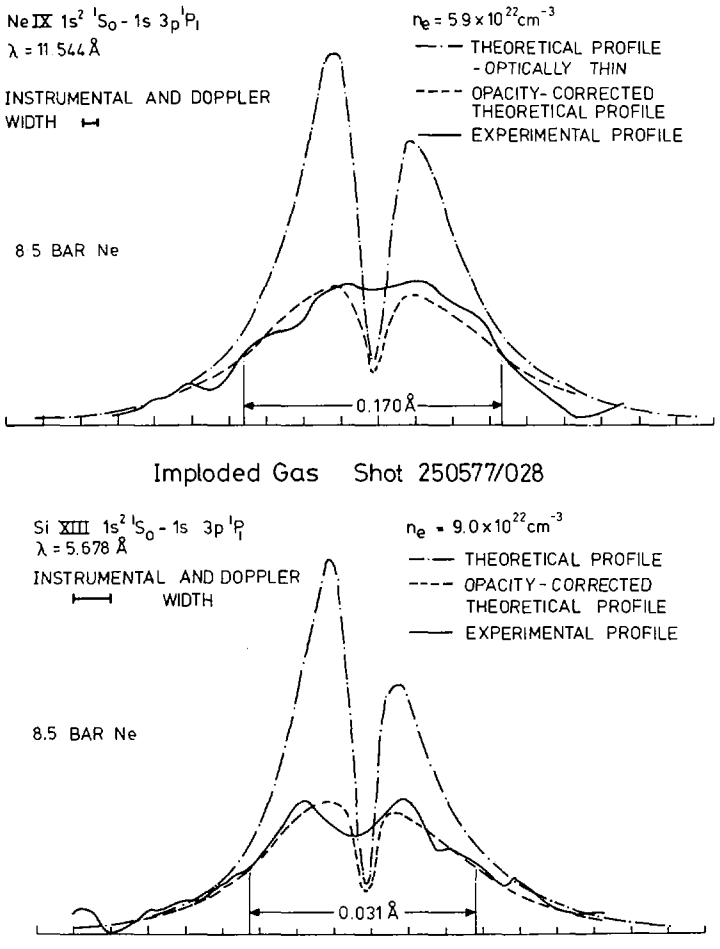


FIG.2. Measured and computed lineshapes of Ne IX and Si XIII from the implosion core of the plasma.

TABLE I. IMPLOSION CORE PARAMETERS: NEON-FILLED MICROBALLOON

	ρ(Neon)	ρ(glass)	Te(Neon)	Te(glass)
Experiment	0.23 g cm^{-3}	0.32 g cm^{-3}	500 eV	450 eV
MEDUSA	0.29 g cm^{-3}	0.45 g cm^{-3}	620 eV	610 eV

r = 33 μm Δr = 0.96 μm ρ_o = 8.5 mg cm^{-3} E = 18 J

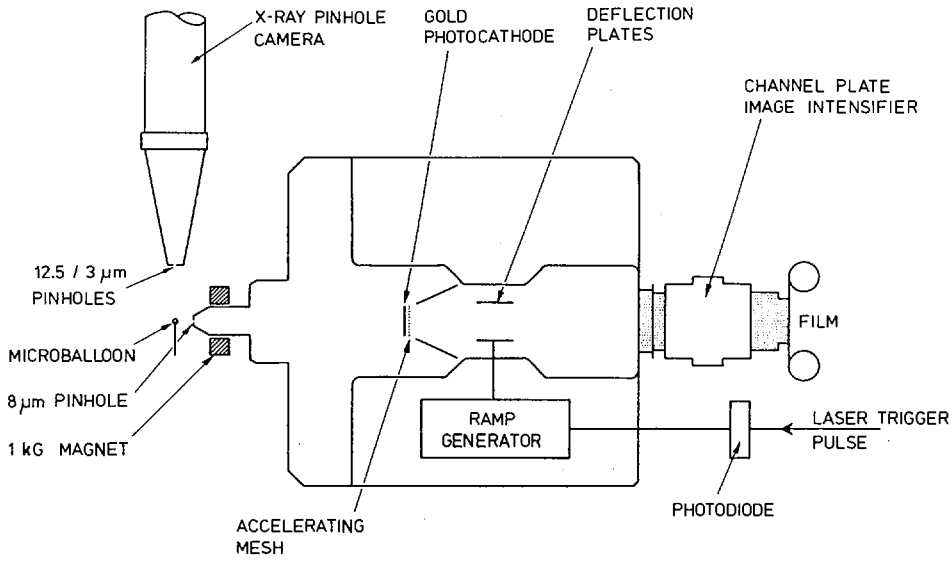


FIG.3. Schematic diagram of X-ray streak camera.

2.3. Computer Predictions

The MEDUSA code as referred to in section 1 has been used to model the particular implosions described above, and predicted values of the core parameters are included in Table I. The main adjustable parameter in the code is the partitioning of the absorbed laser energy between the thermal and suprathermal or 'hot' electrons. Best agreement with observed values is obtained by assuming that virtually all (i.e. > 90%) of the laser energy which is absorbed at the critical density surface is used to create 'hot' electrons. Only in this case does the implosion show the exploding pusher behaviour in which the centre of the shell remains almost stationary during the implosion. The values of electron density and temperature shown in Table I were calculated by a post-processor atomic physics routine that calculates time-integrated X-ray line and continuum emission and these are reduced in exactly the same manner as the experimental spectra. The maximum densities and temperatures in the computer model are higher than these average values by almost a factor of two.

3. IMPLOSION DYNAMICS

3.1. X-ray Streak Records of the Implosion History

The time variation of the X-ray emission from hot laser-produced plasmas is most readily studied using streak photography(eg. (5), (6)). The results reported here were obtained with a UK-developed X-ray streak camera outlined in fig. 3. The X-ray streak tube has a transmitting photocathode consisting of a 9-μm Beryllium substrate on which is deposited a gold layer of 150 Å thickness. The photocathode is most sensitive at an X-ray energy of about 1 keV and suitable filtering can increase this to about 1.4 keV.

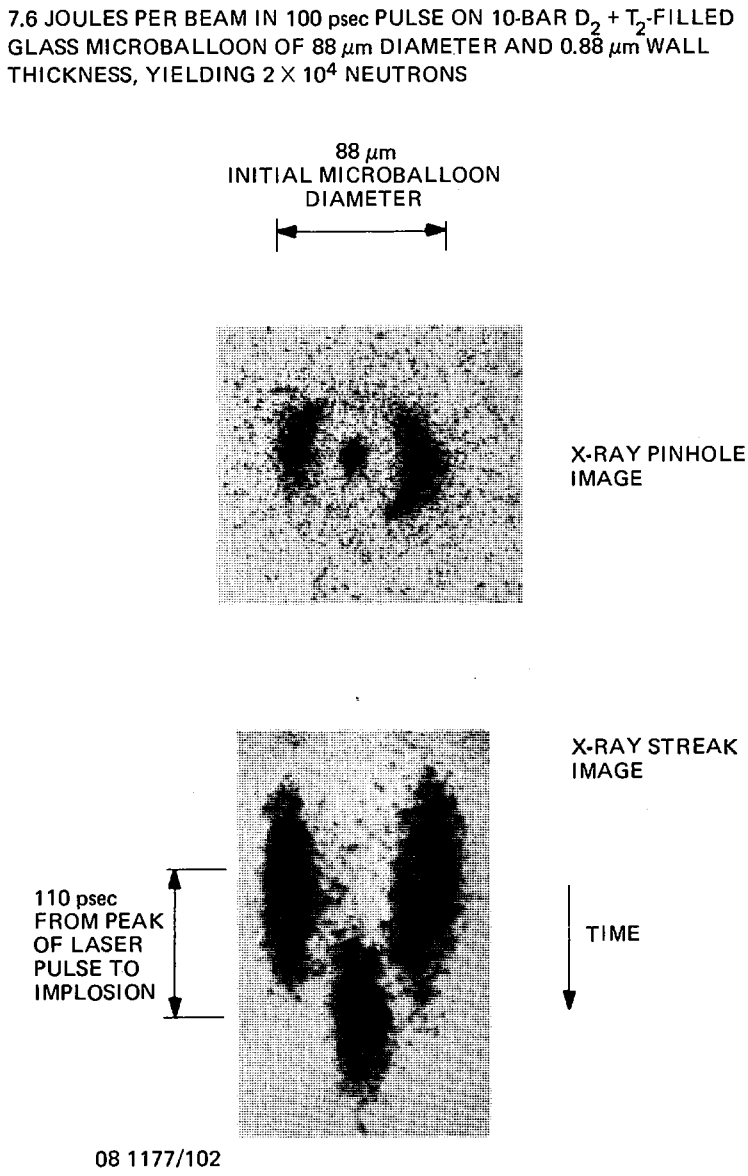


FIG.4. Time and space resolved X-ray emission from implosion of 10-bar D_2 + T_2-filled glass microballoon.

TABLE II. IMPLOSION TIMES

r (μm)	Δr (μm)	E (J)	t_{impl} (psec)
37.0	1.12	11.3	117
32.6	1.38	21.6	23
35.0	1.28	25.1	79
35.0	0.64	8.1	122
42.0	0.77	13.0	104
44.0	0.44	22.7	106
45.0	0.44	19.7	97

The X-ray streak camera viewed the microballoon target through a pinhole 8 μm diameter placed 1.5 cm from the target. An 11x magnified image of the target was thus produced on the photocathode. The whole image was streaked without using a further slit and this enabled both coronal and core regions of the plasma to be well exposed at the same time. A typical streaked image is shown in fig. 4, showing for comparison the time-integrated pinhole camera image.

For this method of whole image streaking, the time resolution Δt for a source of dimension Δx in the streak direction is simply $\Delta t = \Delta x/v$ where v is the streak speed. The time resolution achieved was 23 psec in the core and 60 psec for the coronal plasma. After correction for the instrumental resolution, the core plasma was observed to emit for 120 psec and the corona for 130 psec, both at greater than half the peak intensities. The coronal emission is essentially coincident with the laser pulse and has a similar temporal distribution. The delay between coronal and core emission was 110 psec for this particular shot and results for different targets are summarised in Table II.

These results were modelled with the MEDUSA code as described earlier. The code was used to model the effects of changing the shell thickness and the laser energy independently since the simple theory of exploding pushers would predict that the implosion time should scale as $(E/M)^{-\frac{1}{2}}$ where E is the useful absorbed energy (7) and M is the shell mass.

The results of the computer modelling shown in fig. 5 show that the implosion time can usefully be described by the single parameter E/M but that the implosion time measured from the peak of the laser pulse does not scale as $(E/M)^{-\frac{1}{2}}$. This is simply due to the fact that the peak of the laser pulse is not a good time reference for different values of E/M and it is better to measure the implosion time from the time when the inner wall of the shell has moved about 10% of its initial radius. With this definition of implosion time the scaling with E/M is much closer to the expected behaviour.

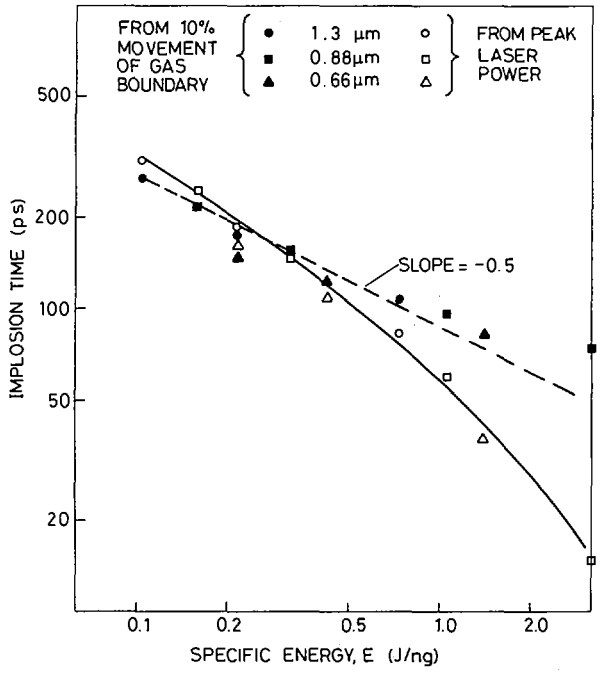


FIG.5. Variation of implosion time with specific energy.

In fig. 6 we show the comparison between the MEDUSA predictions (measured from the time of peak laser power) and the measured implosion times. In order to account for differences in shell radii, the implosion times have been scaled linearly with shell radius, normalised to shot 102. It may be seen that there is a qualitative agreement with the code predictions but an absolute discrepancy of a factor of about 2 in the values of E/M.

The code assumes absorption of laser energy by inverse bremsstrahlung together with a 10% dump at the critical density to simulate resonance absorption; the total effective absorption in the code is about 12%. In this particular experiment the absorption fraction was not measured but other measurements ((8), (2)) would suggest a figure of 17%. Another factor which may account for the discrepancy between theory and experiment is that the illumination of the microballoon is strongly concentrated at the two poles to about twice the mean, and the polar regions will be expected to implode faster than the equator, although the heating by fast electrons will tend to alleviate this asymmetry since they dominate the energy transport in exploding-pusher implosions.

For the sake of completeness we have included in fig. 6 the computer calculations for purely classical heat conduction and also for the case where the classical conduction is inhibited by a factor of 30 as suggested by some "burn-through" experiments. Clearly these cases which do not include fast electron energy transport show implosion times much longer than those observed experimentally.

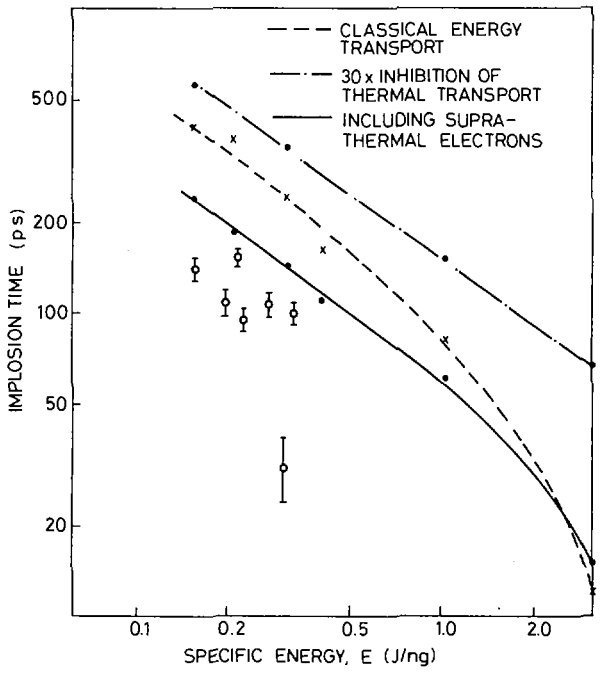


FIG.6. Comparison of measured and predicted implosion times for different descriptions of energy transport.

3.2. Pulsed X-ray Radiography

The experimental work described in the earlier parts of this paper have been concerned with the exploding pusher type of implosion in which there is considerable preheat of the fill gas prior to the implosion, resulting in densities of about 0.2 $g \cdot cm^{-3}$. Progress towards higher densities requires the reduction of the fast electron preheat and achieving a true ablative compression. A first step in this direction has been made by using the thickest available microballoon targets and using lower laser powers to reduce the amount of fast electron preheat. Such an implosion will be rather slow, taking a few hundred picoseconds to implode, and will not achieve very high temperatures. It will be too cool to radiate significantly in the X-ray region and so cannot be diagnosed by its X-ray emission. On the other hand it is possible to measure the X-ray absorption of the imploding plasma by viewing its geometric shadow as produced by an auxiliary pulsed source of reasonably hard X-rays.

The geometry of the experiment is shown in fig. 7. The glass microballoon target was filled with Neon at 87 atm. pressure. The implosion was produced by two beams each containing 3 J in a 100-psec pulse. The focussing was such as to achieve the best uniformity of illumination; the flux density on the poles of the target was about 2×10^{14} $W \cdot cm^{-2}$. A third beam containing about 5 J in 100 psec was delayed by up to 600 psec relative

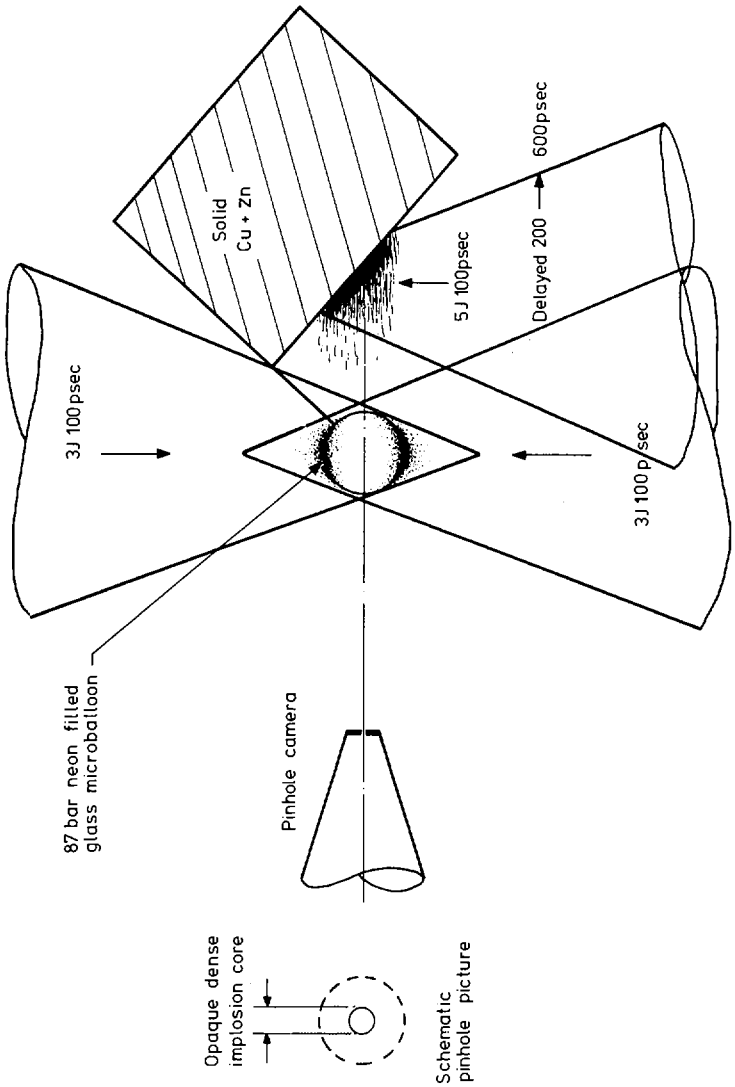


FIG. 7. Pulsed X-ray radiography of a high-density implosion.

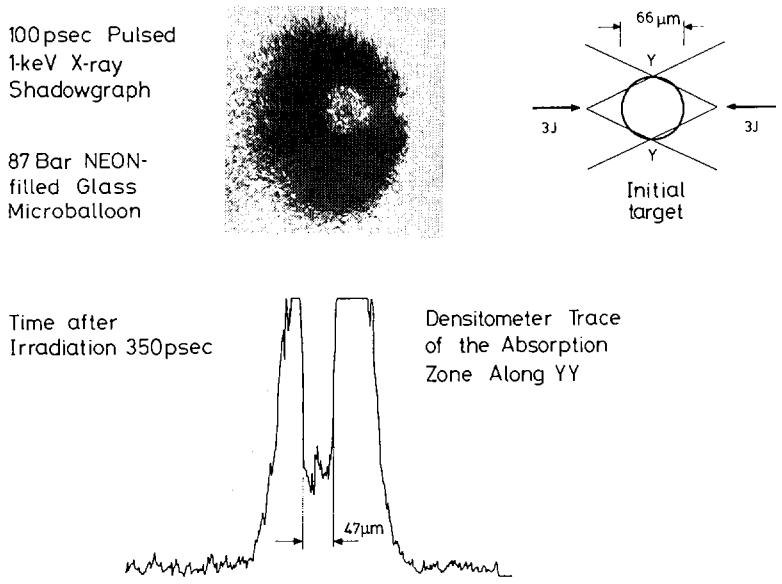


FIG.8. X-ray shadowgraph of 87-bar neon-filled microballoon 350 ps after laser irradiation.

to the main pulse, displaced slightly in angle and focussed by one of the main beam-focussing lenses onto a brass (Cu + Zn) target. The auxiliary beam was somewhat defocussed on the brass rod to provide an X-ray source rather larger than the size of the microballoon. The X-ray pinhole camera was set up to view the microballoon against the background of X-ray emission from the brass rod.

The pinhole camera image shown in fig. 8 was actually obtained on the first laser shot of this experiment with a delay time of 350 ps. As expected, it shows a well defined and reasonably circular shadow of the imploding microballoon against the diffuse X-ray emission from the brass rod. The shadow is less opaque at the centre, showing that at this time the imploding microballoon still has a pronounced shell structure.

A sequence of pictures varying the timing of the X-ray pulse is shown in fig. 9. It is seen that at 250 psec and 350 psec the shell structure is still present as evidenced by the central intensity peak. Maximum compression occurred between 460 psec and 570 psec and at 670 psec the plasma was beginning to expand again. In order to reduce these images to more quantitative data, the densitometer tracings were converted to intensity and the contribution of the polar X-ray emission of the microballoon was removed (this was measured in a separate experiment). A smooth intensity profile was fitted to the emission of the back-lighting plasma alone and from a comparison of these two intensity profiles the opacity of the imploding plasma as a function of position was derived. Examples of these opacity profiles are shown in fig. 10.

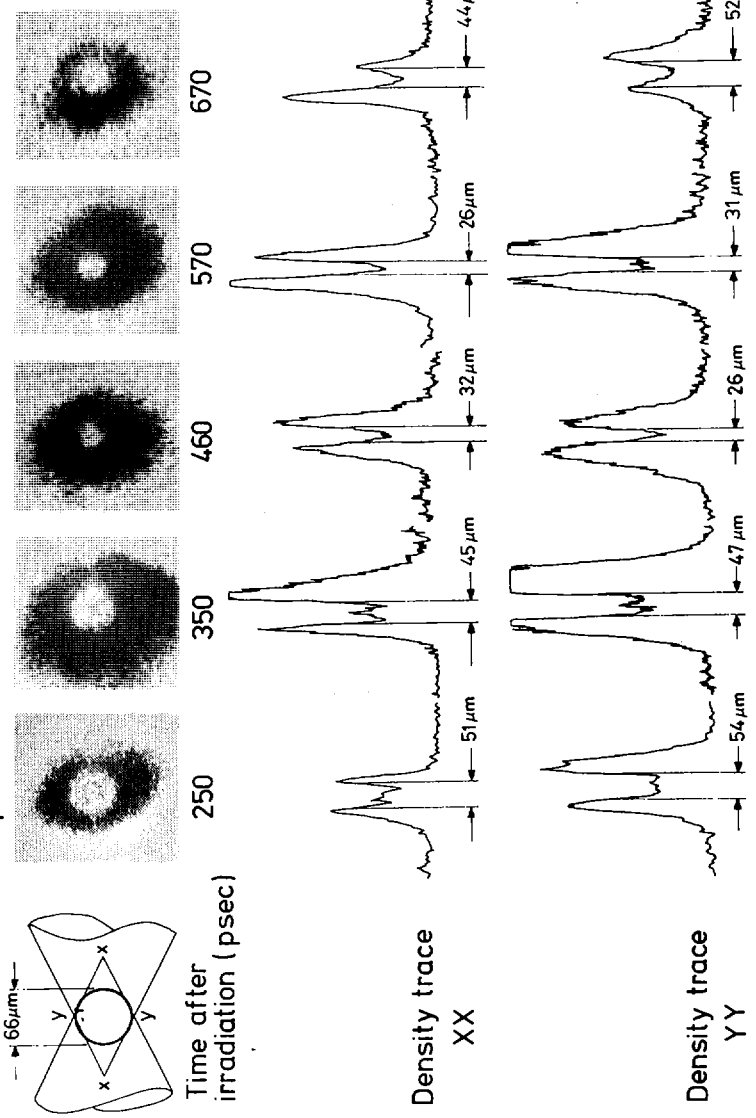


FIG. 9. Sequence of X-ray shadowgraphs at varying times after laser irradiation.

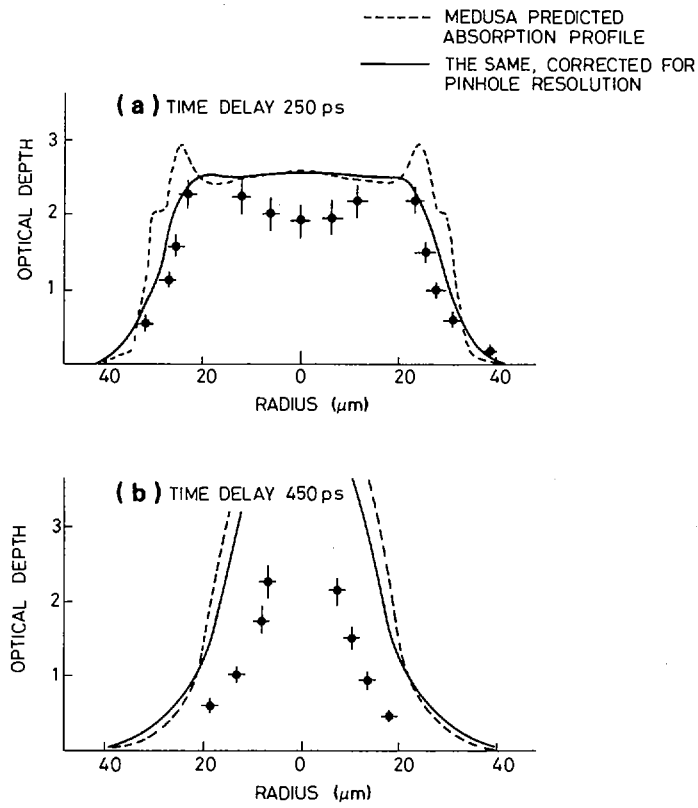


FIG.10. Measured and computed X-ray opacity profiles of 87-bar neon-filled microballoon: (a) 250 ps after irradiation; (b) 46 ps after irradiation.

The spectral quality of the probing X-rays was determined with an X-ray spectrometer in the position normally occupied by the pinhole camera. This showed the effective energy of the X-rays to be 1.5 keV. This energy is less than the ionisation threshold of He-like Silicon and so the dominant absorption is by Oxygen and Neon both of which will be predominantly in their Helium-like states at temperatures between 40 eV and 250 eV.

The MEDUSA code has been modified to calculate the integrated line of sight opacity of the plasma as a function of time assuming the above absorption mechanisms. The results are shown in fig. 10 and, for a realistic comparison with experiment, need to be convoluted with the spatial response of the pinhole camera. Clearly the agreement with the experimental data is good at a delay of 250 psec. At this time the plasma has not moved very much from the initial position of the microballoon and this demonstrates that the mechanisms postulated for the opacity are reasonable. At a delay of 460 psec the experimental data show the plasma to have compressed more than predicted by the code.

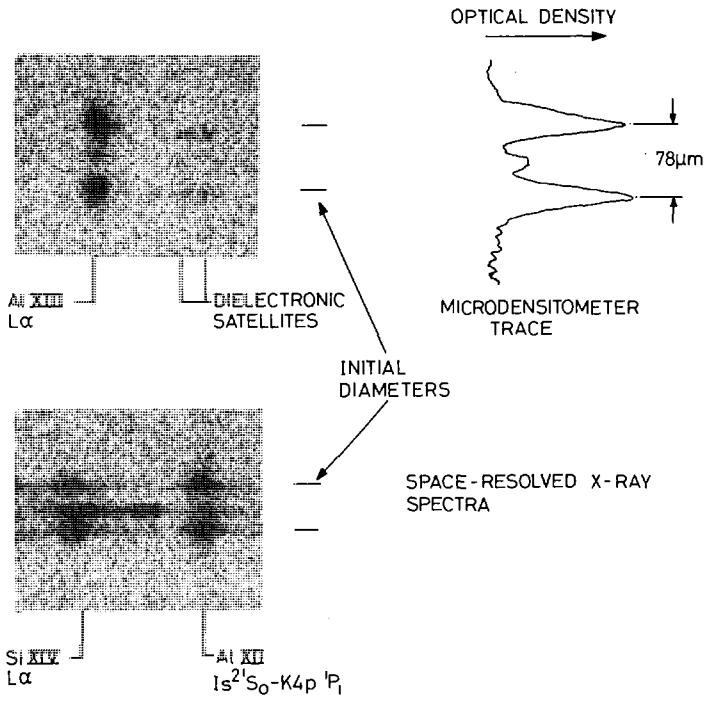


FIG.11. Space-resolved X-ray spectra of 1-μm wall-thickness microballoons, showing evidence of Al XII and Al XIII ions in the implosion core.

The code predictions of maximum compressed gas density are rather sensitive to the assumptions made about radiative losses in the plasma. The calculations presented here ignore radiative cooling and predict compressed gas densities of about 1 g · cm^{-3}. Including bremsstrahlung losses and a simple correction for reabsorption increases the predicted density to $\sim$ 5 g · cm^{-3} but delays the implosion by $\sim$ 200 psec, in marked disagreement with the experiment. Further analysis of this experiment is in progress including an improved treatment of radiative transfer.

To determine the compressed gas density from the experimental opacity profiles is difficult since it requires some assumption about the position of the gas-glass interface. In all the code runs the position of maximum observable opacity, i.e. optical depth $\tau \gtrsim 2$, occurs within the glass shell. If we assume that all the Neon originally in the target is compressed to within the opaque region at 450 psec delay, i.e. r $\simeq$ 8 μm, then the volumetric compression is about x 70 and the compressed gas density is about 4.5 g · cm^{-3}.

3.3. Hydrodynamic instabilities

In the exploding pusher mode the shell material which subsequently appears in the compressed core should come from the innermost 20% of the shell of empty glass microballoons, according to 1D and 2D simulations.

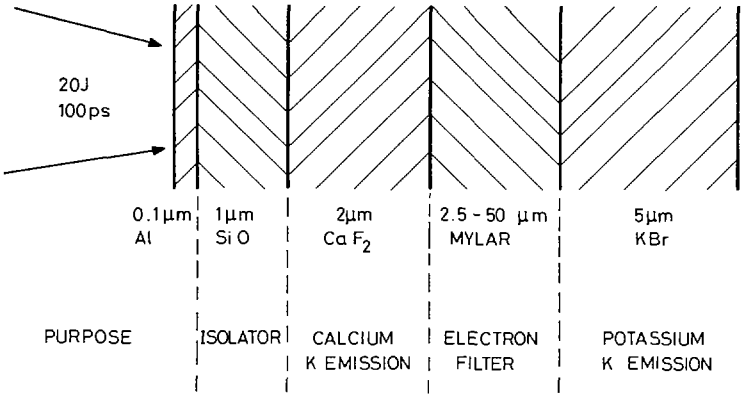


FIG.12. Multi-layer target for fast electron detection.

An earlier experiment at the Rutherford Laboratory (9) used glass microballoons of 1 μm wall thickness coated with 0.1 μm of aluminium, imploded by 20 J of laser energy. When the implosion plasma was observed with the space-resolving X-ray spectrometer (see Section 2) aluminium X-ray line emission was seen from the implosion core as well as from the shell.

In the earlier experiment there were two geometric possibilities which could have led to the observed spectra without actually requiring the aluminium to be in the implosion core. These were emission from the equator of the microballoon and from the fibre supporting the microballoon. These possibilities have now been eliminated by coating only the polar regions of the microballoon and re-mounting it on a clean fibre. The Aℓ XIII emission is still seen in the core as shown in fig. 11 and moreover the Aℓ XII $1s^2 - 1s4p$ emission line is appreciably Stark-broadened, indicating that the emission is from the dense implosion core. On both these shots there was essentially no prepulse ($< 10^{-5}$ of main pulse energy), which should exclude the possibility of target damage prior to the main pulse.

The possibility remains that shell break-up has occurred due to fluid instabilities even in an exploding pusher implosion, and an examination of a 1-D code simulation using MEDUSA does show a short period of possible Rayleigh-Taylor instability on the outside of the shell during the early part of the laser pulse.

4. HOT-ELECTRON GENERATION

In view of the importance of hot electron generation in both exploding pusher and ablative compression experiments, a plane layered target experiment has been performed to study the generation and transport of fast electrons. The structure of the multilayer targets is shown in fig. 12. Fast electrons are generated in the Aℓ layer by laser flux densities of $10^{14} - 10^{16}$ W.cm^{-2}. The SiO layer shields the subsequent layers from the thermal heat front. The fast electrons produce K α emission in the CaF_2 and K Br layers and the Mylar is a filter to reduce the fast electron energy. Both front and rear of the multilayer foil are viewed by space-resolving X-ray spectrometers which are absolutely calibrated.

Foils with varying thicknesses of Mylar are used to study the variation in K α emission from the back layer. Analysis of the data is still incomplete but K α emission from the back layer was observed with up to 25 μm of Mylar, and an absolute energy of 1 J in fast electrons of energies greater than 10 keV was observed with 20 J of laser energy on target.

ACKNOWLEDGEMENTS

We wish to acknowledge the leadership of Professor D. J. Bradley and members of the Laser Facility Committee in establishing the SRC Central Laser Facility, and the guidance of Dr. A. F. Gibson, Head of the Laser Division.

We wish to record our appreciation of the continuing support of the engineering, technical and secretarial staff of the Laser Division.

This work was supported entirely by the Science Research Council.

REFERENCES

[1] CHRISTIANSEN, J.P., ASHBY, D.E.T.F., ROBERTS, K.V., Comput. Phys. Commun. 7 (1974) 271.
[2] KEY, M.H., et al., 11th Europ. Conf. on Laser Interaction with Matter, Oxford, 1977, Paper IV (Rutherford Lab. Rep. RL-77-122/B).
[3] RICHARDS, A.G., submitted to J. Phys. B (1978).
[4] MAYER, F.J., JOHNSON, R.R., TANNER, D.J., Phys. Fluids **19** (1976) 2049.
[5] KEY, M.H., LAMB, M.J., LEWIS, C.L.S., SARCHSENMAIER, P., Optics Commun. **19** (1976) 393.
[6] ATTWOOD, D.T., COLEMAN, L.W., BOYLE, M.J., LARSEN, J.T., PHILION, D.W., MANES, K.R., Phys. Rev. Lett. **38** (1977) 282.
[7] STORM, E.K., LARSEN, J.T., Lawrence Livermore Lab. Rep. UCRL 79788 (1977).
[8] AHLSTROM, H.G., Lawrence Livermore Lab. Rep. UCRL 79819 (1977).
[9] KEY, M.H., et al., Inertial Confinement Fusion Meeting, San Diego, 1978, Paper No.WA7 (Rutherford Lab. Rep. RL-78-020).

Session M

INERTIAL CONFINEMENT III

Chairman

J.P. WATTEAU
France

RESEARCH ON ELECTRON-BEAM INERTIAL-CONFINEMENT THERMONUCLEAR FUSION

L.E. ARANCHUK, Yu.I. ARKHANGEL'SKIJ, M.V. BABYKIN,
K.A. BAJGARIN, E.I. BARANCHIKOV, A.V. BARTOV,
A.S. CHERNENKO, B.A. DEMIDOV, S.D. FANCHENKO,
A.V. GORDEEV, Yu.G. KALININ, Yu.V. KOBA,
V.D. KOROLEV, D.N. LIN, V.I. MIZHIRITSKIJ,
S.L. NEDOSEEV, A.M. PASECHNIKOV, V.S. PEN'KINA,
L.I. RUDAKOV, V.A. SKORYUPIN, V.P. SMIRNOV,
E.Z. TARUMOV
I.V. Kurchatov Institute of Atomic Energy,
Moscow,
Union of Soviet Socialist Republics

Abstract

RESEARCH ON ELECTRON-BEAM INERTIAL-CONFINEMENT THERMONUCLEAR FUSION.

Recent results of investigations into the problem electron-beam nuclear fusion at the Kurchatov Institute with Angara-1, Triton, Kalmar-1 and other devices are reviewed. In the experiments, it is shown possible to accelerate the shell material up to velocities of $(1-2) \times 10^7$ cm·s^{-1}. In current focusing experiments with Angara-1 (1 MeV electron energy, 330 kA total current) the following parameters are attained: maximum current density 3×10^7 A·cm^{-2}, maximum beam power 2.5×10^{11} W, power rise-time 30–35 ns, total energy deposition in the focused beam 15 kJ. – The diode impedance upon current focusing inside the plasma channel is found to be inexplicable by the Child-Langmuir vacuum current law so that growth of the turbulent plasma resistivity has to be assumed. The calculated ion-sound-instability-driven resistivity values agree with the experimental data. – The Angara-1 device with the 'Koltso' output device is used to simulate conditions of beam transport along cusp-trap magnetic field lines. The transport efficiency starting from the trap equatorial gap and all the way towards the calorimeter placed behind the end-on mirror is found to be up to 85%. The transport of a single beam along an inhomogeneous magnetic field used as a mock-up of the Angara-5 field is also studied. Energy transport in magnetic insulation transmission lines is being explored. The regime with ion-leakage current is tested by producing a plasma at the line anode. The ion-leakage current is shown not to destroy the magnetic insulation regime.

1. INTRODUCTION

In recent years, there has been a surge of optimism in regard to the feasibility of electron-beam-driven pulsed fusion with energy gain with an e-beam power of 10^{14} W. This optimism is based on computations performed at the USSR Academy of Sciences Institute of Applied Mathematics and at the I.V. Kurchatov Institute of Atomic Energy [1]. A similar optimism is expressed by physicists of the US Lawrence Livermore Laboratory [2]. To ignite pulsed fusion, one has to accelerate the inner shell of a spherical fusion target up to no less than 200 $km \cdot s^{-1}$, which requires a power flow density of no less than 10^{13} $W \cdot cm^{-2}$ on the target surface. This power density level has been achieved in the focused beam of the Kurchatov Institute Angara-1 device. Experiments have shown that a thin polyethylene shell was accelerated up to 100–150 $km \cdot s^{-1}$. With a sharply focused beam being stopped in the thin-metal anode foil, a reduction in the energy deposition length was observed, owing to the effect of the beam self-magnetic field penetrating inside the anode-bound plasma. By making use of the sharp focusing and the effect of deposition length reduction, it turned out to be possible to achieve an energy deposition of the order of 10^7 $J \cdot g^{-1}$ in a 15–20 μm metal (gold or platinum) foil.

Important results have also been achieved in e-beam and electromagnetic energy transports. It was shown that, because of the vacuum line magnetic self-insulation effect, the electric field strength could be increased up to 2–3 $MV \cdot cm^{-1}$, transmitting over 5 m a power of 3×10^{10} $W \cdot cm^{-2}$ with an efficiency of 80%. As the transport of ultimate power energy and e-beams towards the target constitutes one of the main problems of future fusion devices, the study of transport methods and efficiency should attract utmost attention in the next few years.

Relativistic electron beams are a rather simple and cheap energy source and provide a realistic option for reaching the threshold of inertial confinement pulsed fusion feasibility demonstration.

2. ANODE-METAL-FOIL HEATING BY A FOCUSED BEAM

The Triton, Angara-1, Kalmar-1 and NPR-2M devices were used to study thin-metal-foil heating by a focused electron beam. At the Triton device [3], the effect of the high-current beam-stopping-range reduction in thin foils was discovered, which is very important for the programme as a whole. The study of this effect was further continued at the Angara-1 device (Fig.1) with up to 1 MeV electron energy, 330 kA total current, up to 3×10^7 $A \cdot cm^{-2}$ current density and 2.5×10^{11} W maximum power (power rise-time 30–35 ns). The total energy within the beam focus was up to 15 kJ [4, 5].

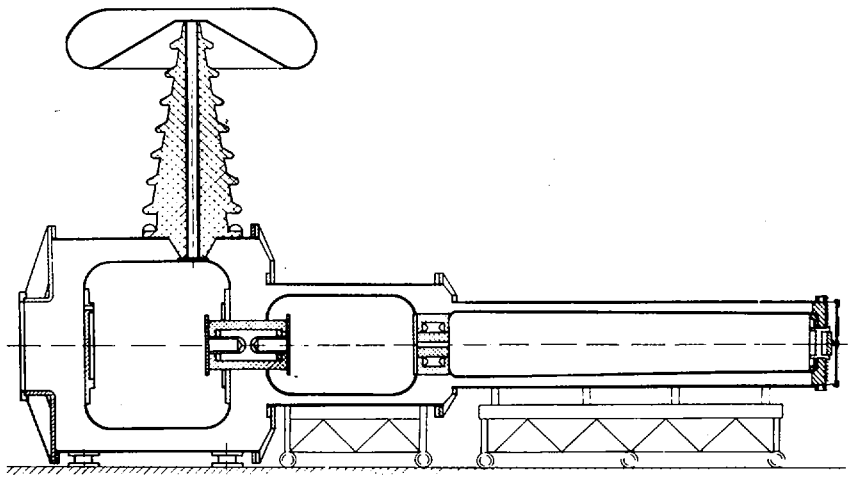


FIG.1. Lay-out of Angara-1.

To estimate the stopping length of the high-current beam in thin foils, experiments were carried out at the Angara-1 device in which a target consisting of two spherical gold segments of different thicknesses was irradiated. Both segments with a diameter of 4 mm were placed on opposite sides of a perforation in a 2-mm-thick anode plate.

The thickness of the frontal foil varied from 5 up to 45 μm, while the rear-side foil was kept at a thickness of 25 μm. The X-ray images of the foils were taken with two pinhole cameras at an angle of 90° to the beam axis. Pinhole image densitometry has demonstrated that the X-ray brightness of the 5-μm-thick frontal foil was comparable to that of the rear-side foil [5] (at 400 kV diode voltage and 200 kA current). For the sake of comparison, note that for single 400-keV electrons, the electron flux is attenuated by a factor of two in 15 μm of gold. Similar experiments carried out for 1 MV diode voltage yielded a twofold beam attenuation depth of 20 μm (instead of a 50-μm single-electron twofold attenuation depth). The experimental results are presented in Fig.2.

The reduction of the stopping length of a focused beam may be attributed to the lengthening of the electron path in the anode material plasma due to the magnetization by the beam self-magnetic field penetrating into the plasma (the electric field does not penetrate into the plasma). This makes it possible to use this material layer to stop the beam. One should, however, note that at the beam axis the electrons are not magnetized, so that in case the foil thickness is less than the single-electron stopping range, a part of the beam should be able to penetrate through the foil, which is, indeed, observed in experiments. This

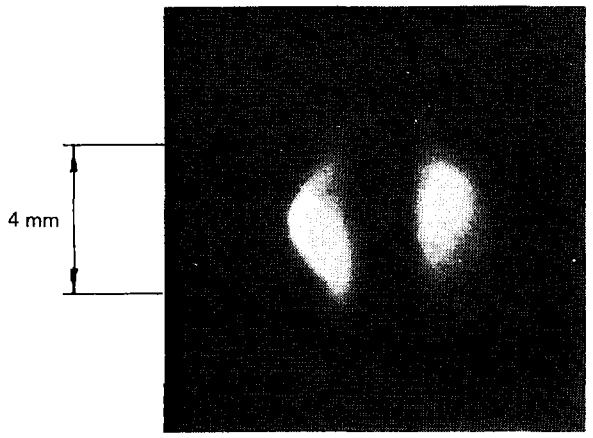


FIG.2. X-ray image of spherically shaped gold target. Diode voltage: 1 MV; thickness of frontal hemisphere: 20 μm; thickness of rear hemisphere: 50 μm. Both hemispheres produce comparable observed luminosities (instead of much less frontal-hemisphere luminosity expected in case of normal stopping range).

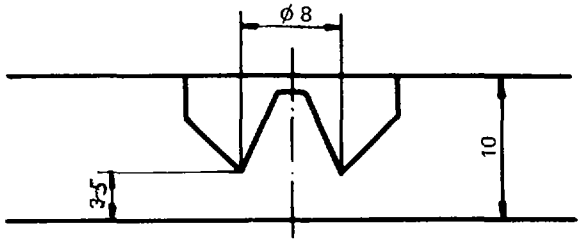


FIG.3. Shape of annular cathode protrusion (section). Anode to cathode plane distance 10 mm; the gap between cathode protrusion edge and anode is 3–5 mm.

point should be taken into account when thin-layer beam-heating experiments are performed.

To evaluate the gold-foil temperature due to focused beam heating, experiments were carried out in which the foil vapour expansion velocity was measured as a function of the foil density ranging from 5 μm up to 45 μm. This velocity was measured by making use of the time delay of light emission from a barrier put in the way of the vapour stream. The light was measured by a photomultiplier according to the scheme used previously in Ref.[3]. For a 5-μm-thick foil the velocity of gold vapour was up to 2.5×10^6 cm·s^{-1}.

3. DIODE CURRENT FOCUSING

To focus the current in high-current accelerator diodes, it is usual to make use of plasma channels produced with lasers, with dielectric and metal pins or cones. At the Angara-1 device, the current channel was produced by introducing metal protrusions of various shapes into the planar cathode-anode gap. Substantial progress was achieved by using an annular protrusion (Fig.3) resulting in a diode impedance reduction and a better diode line matching. Experiments were done to optimize the anode-cathode gap and the cathode protrusion dimensions. The gap between the protrusion edge and the anode was varied over a range of 2 to 10 mm, and the cathode protrusion diameter from 5 to 14 mm. The best results in energy deposition and sufficiently sharp focusing were obtained with 2.5–3.5-mm gaps and 7–8-mm cathode protrusion diameters. In addition, the depth of the central conical depression was also varied. When the depth was small (3–4 mm), the diode would be short-circuited very soon with dense plasma. Increasing the central depression depth would result in a lengthening of the plasma channel during the focusing stage and prevent diode short-circuiting during the total pulse duration of about 70–80 ns. With a current of 330 kA and an electron energy of 1 MeV, the current channel diameter was 1–2 mm. The channel radius was measured from X-ray pin-hole photographs (Fig.4) obtained with absorption filters of various thicknesses. The beam axis would not deviate by more than 0.5 mm from the cathode centre. Better matching and lack of diode short-circuiting improved the energy deposition in the diode. Figure 5 presents the oscilloscope traces of current and voltage together with the time dependence of diode power deposition computed from current and voltage. The peak diode power is 2.5×10^{11} W, the power build-up time is 30–35 ns, and the power build-up rate is 0.7×10^{19} W·s^{-1}. The power density in the focused beam reaches 10^{13} W·cm^{-2}. The total energy content in the focus was also evaluated by the size of the single-shot crater produced in the aluminium anode plate. The experimental data were compared with the computation results of Ref.[6]. In a 10-mm-thick aluminium anode plate, a perforation is produced with a 20-mm input and a 6-mm output diameter (Fig.6). Such an erosion approximately corresponds to a beam energy of 15 kJ.

In the studies of focusing as a function of cathode protrusions of various shapes, it was observed that the beam current and the energy deposition are very sensitive to the cathode protrusion geometry and to the protrusion-edge-anode gap, but quite insensitive to the gap between the anode and the planar part of the cathode. A special test was made with the latter gap being increased up to 3 cm, while the annular cathode protrusion was fixed to a 15-mm-diameter pole, so that the protrusion-edge-anode gap remained at a value of 3 mm. It was found that practically no change occurred in the diode total current and energy deposition in contrast with planar-diode theory, which predicts a diode impedance



FIG. 4. X-ray images of gold hemisphere obtained in one shot by means of end-on pinhole camera with 5 pin holes. The central image was recorded without filter; it shows the luminosity of the entire foil diaphragmed by the 4-mm-diameter anode aperture. The other images were obtained through copper filters 0.5, 1, 1.5 and 2 mm thick.

increase of up to 17 Ω. This indicates that, in our conditions, electron emission predominantly occurs from the cathode protrusion. The current value of 330 kA, with a channel diameter of 2 mm, is incompatible with the assumption of a vacuum current. We are then led to the assumption that the diode current is determined by the turbulent resistivity of the plasma channel [4, 5, 7]. A possible interpretation of diode operation in the presence of the plasma channel is the fact that the channel is unable to carry the short-circuit current because small-scale turbulence develops in the channel, resulting in an anomalously high resistivity [8]. In a relativistic electron gas, development of turbulence goes unimpeded, owing to a strong mixing of all oscillation modes. Thus, we may assume with sufficient confidence that the charge drift velocity in the plasma cannot substantially exceed the ion sound velocity

$$\frac{j}{ne} = \alpha c_s$$

where α is a numerical factor. If the plasma sheath is confined by the self-magnetic field, it can carry a current of

$$I = 10^3 \sqrt{V}/\alpha$$

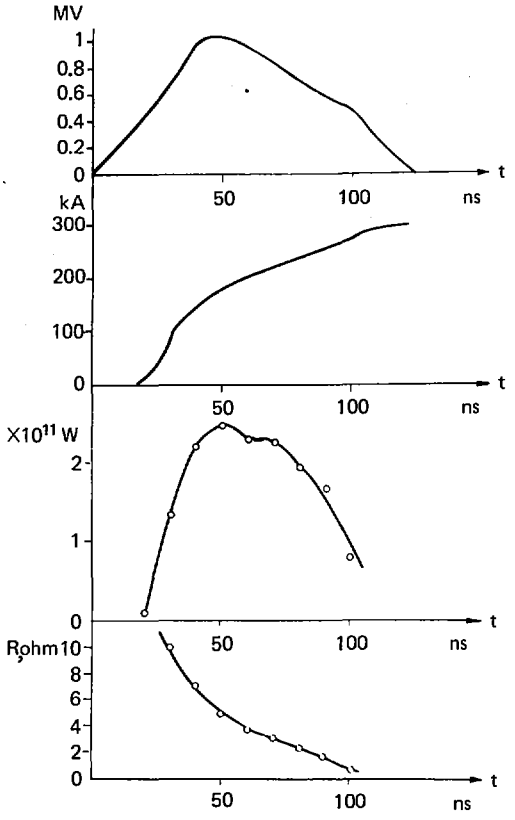


FIG. 5. Diode impedance and diode electric power (lower curves) computed from diode voltage (top oscillogram) and current (second oscillogram). The maximum power and total energy deposition in the diode were 2.5 X 10^{11} W and 15 kJ, respectively. The impedance was initially 10 Ω.

Assuming $\alpha \approx 3$, we obtain current values which agree with the experimental data by order of magnitude. This formula is remarkably independent of the diode geometry, i.e. of cathode-anode gap, cathode surface and plasma column shape, which is an important argument in favour of its validity. One should point out that the anode is not bombarded by an electron beam from the pinch but rather by a flux of relativistic electrons with a temperature proportional to the potential drop over the pinch length.

The Kalmar-1 device was used to study current focusing as a function of diode geometry and pre-pulse magnitude. Good focusing was achieved with a stainless-steel conical cathode, the base diameter of the cone being 70 mm

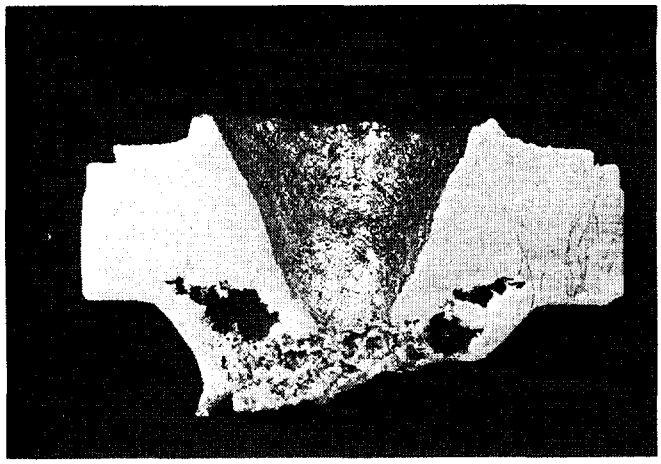


FIG. 6. One section of one-shot 10-mm-thick aluminium anode perforation. The damage size corresponds to an energy deposition of 15 kJ.

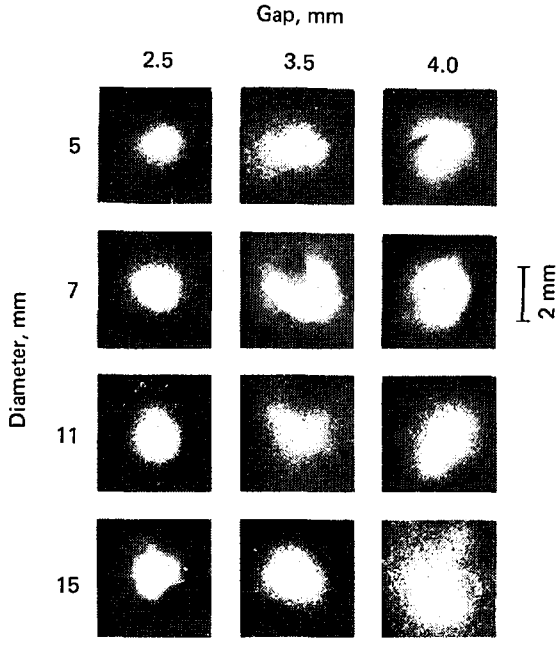


FIG. 7. Focusing spot diameter as a function of annular cathode protrusion diameter and cathode-anode gap; X-ray pinhole images.

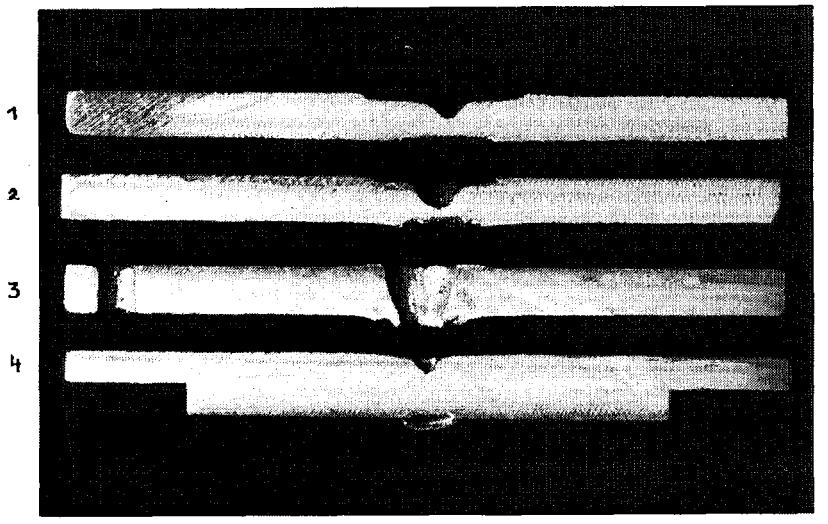


FIG.8. Aluminium anode plate sections. 1 – annular hollow-cone cathode with edge diameter 15 mm; 2 – cathode diameter 11 mm; 3 – cathode diameter 7 mm; one-shot anode perforation, anode thickness 6 mm in the cases 1, 2, 3; 4 – protruding cone anode, focus spot diameter 0.75–1 mm, but energy deposition lower than for annular hollow-cone cathode (anode thickness 8 mm).

an apex angle of 135°. Such a cathode provided focusing to a spot size not exceeding 1 mm precisely towards the centre of the anode. Sharp focusing was observed both with 1 and 10 percent pre-pulses. The focus current density was up to 10^7 A·cm^{-2}. The diode impedance was, however, substantially higher than the 1.50-Ω line output impedance so that it was not possible to match the diode with the line, and the energy deposition in the beam focus was no more than 2 kJ per pulse.

The largest energy deposition in the focus at Kalmar-1 was obtained by using the annular-protrusion-type cathode shown in Fig.3 and first used at Angara-1 [5, 7], with a protrusion diameter of 8 mm and a cone-shaped depression at the centre. The necessary condition of maximum energy deposition was found to be a small pre-pulse (1%). The gap between the cathode annular-protrusion edge and the planar anode was 2.5–4 mm, the protrusion diameter ranging from 5 to 40 mm. Pinhole image densitometry has shown that the best focusing is observed at a 2.5-mm gap, the focus diameter increasing from 1.5 to 6 mm, almost linearly with a protrusion diameter increase from 5 to 40 mm (Fig.7).

The aluminium anode plate damage was used to evaluate the energy deposition to the focus. The energy deposition reached a maximum, corresponding to 40%

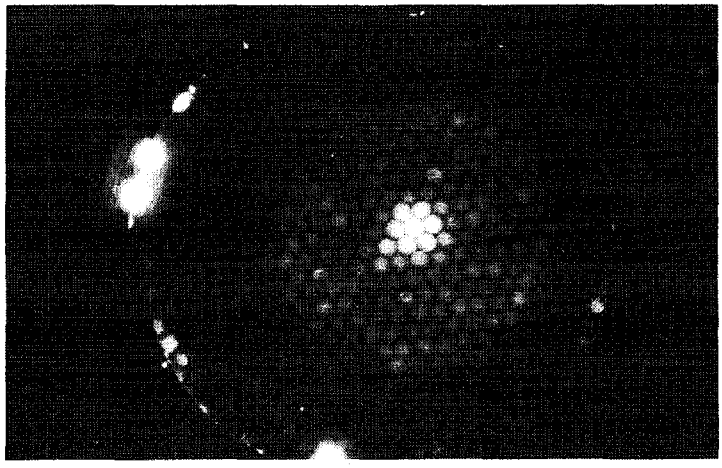


FIG. 9. X-ray bremsstrahlung profile in Kalmar-1 diode obtained with plastic-scintillator pinhole camera. The mosaic image structure is due to the microchannel intensifier plate in the image converter.

of the total energy deposition in the diode, at a cathode protrusion diameter of 7 mm (Fig.8). The decrease of energy deposition at a smaller protrusion diameter was due to worse diode-line matching, while at diameters in excess of 7 mm a substantial portion of the beam energy goes to the periphery of the focal spot, the deposition to the spot itself decreasing.

The focused beam produced, in one shot, a hemispherical crater at the inner surface of the aluminium anode (crater depth 5–5.5 mm) and in some cases perforated a 6-mm-thick aluminium anode. According to computation results [6], this represents a focus energy deposition of 3–4 kJ.

To establish the current profile across the anode, time-history experiments have been started at the Kalmar-1 device in which the diode bremsstrahlung was detected by scintillators. A plastic scintillator with nanosecond persistence time was either placed into an X-ray pinhole camera or directly applied to the anode. It was photographed through an image intensifier system. In the photographs, one of which is presented in Fig.9, we distinguish a several-mm-diameter central spot, corresponding to the previously observed sharp-focusing spot. This spot is surrounded by a much less intense X-ray halo. From photographs of scintillators either inserted in the X-ray pinhole camera or in direct contact with the anode, it follows that no X-ray radiation is observed from the 70-mm-diameter planar part of the cathode, i.e. practically all the electrons arrive at the anode inside the plasma streams produced around the protruding cathode part.

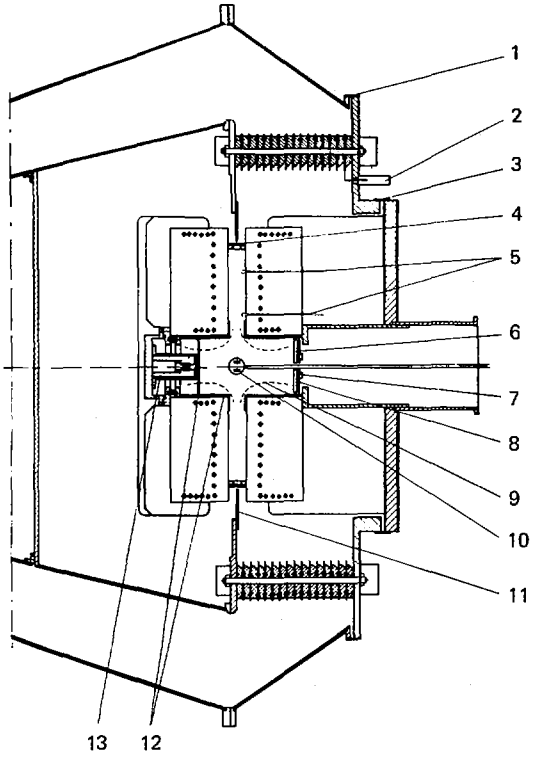


FIG.10. Koltso-1 experimental lay-out. 1 – major current shunt; 2 – voltage divider; 3 – minor current shunt; 4 – anode foil; 5 – magnetic probes; 6 – end-on calorimeter; 7 – dose meters; 8 – photographic paper; 9 – magnetic lines; 10 – spherical target with thermopair and dose meter ; 11 – cathode blades; 12 – polypropylene screens; 13 – pinhole camera.

The experimental data on diode current focusing by means of cathode protrusions have shown that this method provides a possibility of sharp focusing and outstanding power density of 10^{13} W·cm^{-2}. Besides, it was established that most of the electron emission occurred from the cathode protrusion and the diode current seemed to be hardly explicable by a Child-Langmuir vacuum current. Accordingly, the assumption was made that the diode impedance is determined by the plasma channel current with turbulent resistivity. This assumption is able to explain the observed phenomena qualitatively. However, at present there is no complete understanding of the plasma channel mechanisms; therefore, it is not possible to establish scaling laws, and it is rather difficult to predict the possibilities of using the present focusing method for higher-power beams.

4. HIGH-CURRENT BEAM TRANSPORT IN A MAGNETIC CUSP

An important problem of a future e-beam fusion reactor is beam transport from the diodes, which are to be placed at the exit ends of the magnetic insulation lines towards the target. One of the solutions studied in the present work consists in beam transport and focusing along cusp magnetic-field lines with subsequent trapping of electrons in the cusp, followed by their absorption at the target surface [9].

The trapping and absorption of electrons in a cusp trap provided with a central target was mocked up previously in a small-size trap (8-cm loop diameter) at the Ural device [10].

To study high-current beam transport along the cusp magnetic field in nearly full-scale conditions and to mock up one of the possible schemes of Angara-5 beam transport, the Koltso device has been built.

The Koltso device (Fig.10) has a high-voltage diode (voltage up to 1.5 MV, inner diameter 1.2 m) and is connected to the Angara-1 2.1-Ω output impedance forming line [7]. Inside the diode section, two 0.7-m-diameter coils are provided to produce a cusp magnetic field with a maximum field strength of 12 kOe both in the magnetic slit and the axial mirrors (4 ms magnetic-field half-period). In the equatorial plane of the magnetic trap, there are cathode blades, which are located around a 0.8-m ring and produce 12 electron beams. Each of the 0.5-mm-thick and 112-mm-long stainless-steel blades is separated by a distance of 13 mm from the 50-μm-thick titanium anode foil, isolating the diode vacuum space from the trap space (Fig.10). The total injected current was 350 kA for a maximum voltage of 700 kV (2 Ω diode impedance). The effective pulse length was 60 ns. In typical operation regimes, the field in the slit and the axial mirrors was 5 kOe, and the total beam energy in the diode was 9–10 kJ; the maximal energy reached in these experiments was 15–16 kJ. When passing through the anode foil, the beams would perforate it and produce a slit of up to 4 mm width, which depended on the air pressure in the trap volume.

Figure 10 presents the general lay-out of the experiment and shows some of the diagnostics. An unusual diagnostic method consisted in putting a 2-mm-thick polypropylene screen across the beam path (Fig.11). The beam was recorded through the effect of polypropylene foaming out at a sufficiently high energy deposition density. The solidified foam carries information on beam shape and position and, qualitatively, on the energy density.

The transport experiments were done over a range of air pressures from 2×10^{-3} up to 20 torr. The beam self-fields were weaker than the external magnetic field. In these conditions, one could not expect any considerable amount of non-adiabaticity or any significant extent of electron trapping in the cusp. The end-on calorimeter signal has shown that, in the absence of any probe (target) within the trap volume and at air pressures in the trap ranging

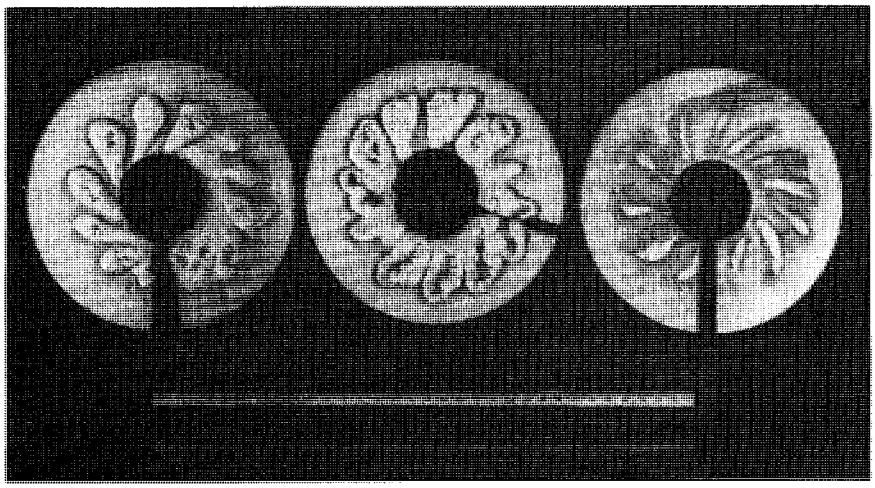


FIG.11. Beam signature on polypropylene screen, the screen thickness and the diameter being 2 mm and 15 cm, respectively. The sample with narrow beam signatures represents the case of vacuum in the trap volume, the next one was obtained at a pressure of 0.5 torr, the third sample represents a pressure of 20 torr. Maximum screen damage is seen at second sample (0.5 torr).

from 0.3 up to 0.5 torr, the total energy incident to the calorimeter was higher than 5 kJ when the energy of the beams in the diode was 13 kJ. One should take into account that each beam was split into two, the partial beams propagating along the magnetic axis in opposite directions, as well as that 10% of the energy was lost in anode foil evaporation. Then, the efficiency of transport of beams from the equatorial trap slit through the axial mirror (the magnetic force tube being turned over 90°) is 85% for a total transport distance of 0.5 m.

The beam signatures at the surface of the polypropylene sheet (Fig.11), which was 5 cm behind the axial mirror, 15 cm from the trap centre and perpendicular to the magnetic axis, indicate that the beams were propagating from the lateral slit all the way through the axial mirror along magnetic-force tubes. The shape of each beam at the anode foil exit was a band elongated along the equatorial slit. The signature of each beam at the end-on polypropylene sheet was wedge-shaped with the apex towards the centre, which is indicative of the beam profile evolution.

The curvature of the beam signatures is due to both the superposition of the external magnetic field and the self-magnetic field of the beams and also to electron drift in the non-homogeneous magnetic field. The beam energy transport to the end-on sheets (targets) was not substantially changed by increasing the

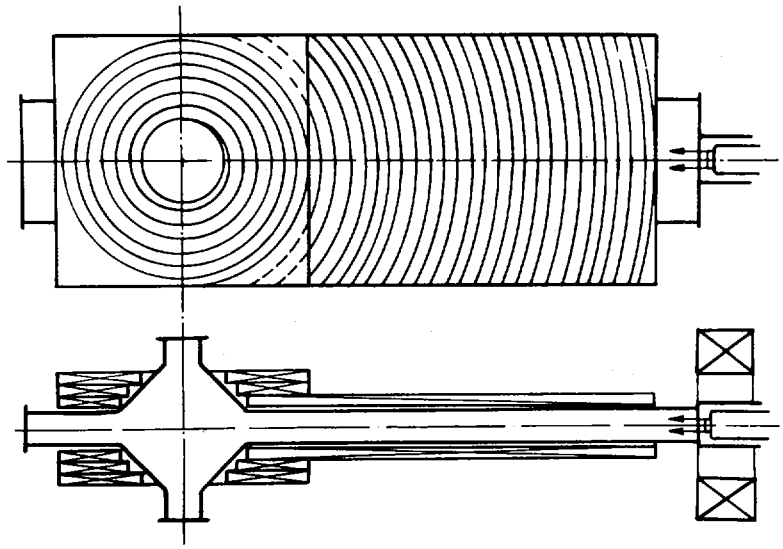


FIG. 12. Magnetic system, mocking up part of Angara-5 magnetic-field space. Circular sector lines indicate current loop curvature.

initial pressure from 0.3 up to 30 torr. The decrease of pressure down to 2×10^{-3} torr significantly lowered the energy deposition density, without altering the general character of beam signature profiles (Fig. 11).

Two interesting, but not yet completely clarified effects should be noted:

1. One could expect to see some broadening of individual beams with some degree of filling-up of the gaps between them. However, in the process of beam convergence all the way to the exit through the end-on mirrors the gaps between them subsisted.

2. The general beam profile over the end-on mirror plane was expected to have a central depression due to the trapping of part of the electrons with subsequent scattering into the loss cone. The actually observed profile with a large central gap and a large radius of annular flux in the mirror suggests, however, that some other effects seem to exist, resulting in the expansion of the annular electron profile.

An experiment was done to study the transport of one of the beams in a radially converging magnetic field. A model of the central part of the trap and of the planar transport section of the Angara-5 magnetic system was built, the mock-up scale being 1:2 in linear dimensions (Fig. 12). A 300-kV electron beam with a 120-kA current ($\nu/\gamma \sim 5$) and 60 ns pulse duration was produced in a region with a 5-kOe magnetic field 170 cm off the trap axis. The beam output cross-section was rectangular: 10 mm high and 35 mm wide. The magnetic coils

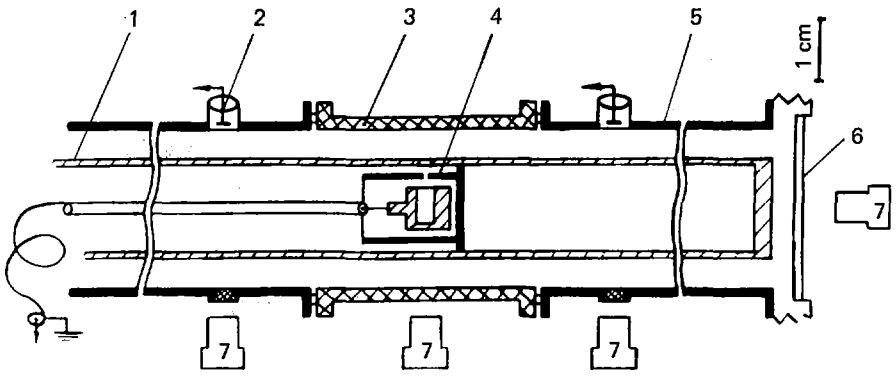


FIG.13. Diagram of a magnetic insulation line with anode plasma formation; 1 – negative electrode; 2 – electron leakage probe; 3 – dielectric insert; 4 – ion probe; 5 – positive electrode; 6 – Faraday end cylinder; 7 – X-ray detectors (PIN-diodes).

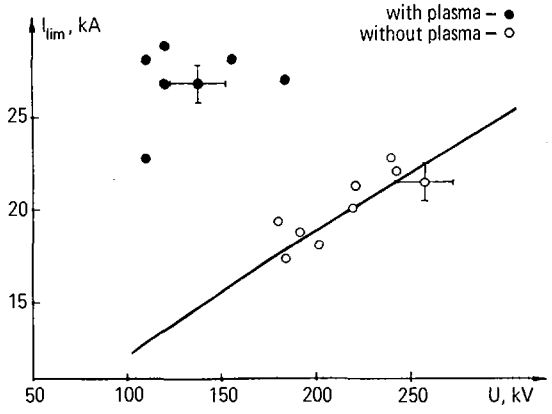


FIG.14. Limiting line current (suppressing electron leakage) with and without plasma. The solid line represents the theoretical curves.

were shaped such that the magnetic-field profile over the beam transport section was up to 10% identical with that of a perfectly symmetric cusp.

Experiments have shown that, in some gas pressure range, it was possible to transport the beams efficiently to the central trap boundary. For instance, at 0.5 torr air pressure, up to 80% of the beam energy was detected by a graphite calorimeter 30 cm off the trap axis. Energy measurements and beam signatures on thin foils put across the chamber indicated that the beam electron motion was in agreement with electron trajectories computed in single-particle approximation.

Consequently, the experiments have demonstrated the possibility of efficient propagation and convergence of individual beams in a magnetic field of vortex shape proposed in one of the fusion reactor schemes [9].

5. ELECTROMAGNETIC ENERGY TRANSPORT ALONG MAGNETIC INSULATION VACUUM LINES

In future fusion systems, the choice of a particular scheme of energy and beam transport to the target will depend upon transport efficiency and ultimate transmitted power flux. At present, magnetic insulation lines are regarded as the most efficient means of electromagnetic energy transmission to beam-generating high-voltage diodes [1]. At present, electric fields up to 3 $MV \cdot cm^{-1}$ and power flux densities up to 2×10^{10} $W \cdot cm^{-2}$ have been reached in such lines. These results were obtained with rather high-impedance lines on modest transmitted power levels. The realization of the Angara-5 device and of a future reactor requires an increase of the total power per line and a decrease of both line impedance and cross-section in order to bring the energy as close as possible to the target.

In uniform lines with low energy fluxes, the losses are determined by electron leakage currents arising during the transient process of self-insulation build-up. At high energy flux levels, the leakages produce a plasma sheath around the positive line electrode resulting in ion currents which are non-magnetized, contrary to the electron current, and in some modification of the self-insulation regime. To simulate this mechanism, experiments were done at the MS facility in which an anode-bound plasma was prepared inside the line by means of a surface discharge over a dielectric section inserted into the positive electrode gap (Fig.13). The co-axial line had the following dimensions: 2.6 cm outer electrode diameter, 1.6 cm inner electrode diameter, 40 cm total length, 10 cm dielectric insert length. Currents, voltages and electron leakage currents were measured by conventional means [11]. The ion current was measured with a negative bias collector put inside the negative line electrode. The total ion current amounted to 1–5 kA with a line current of 30 kA and a voltage of 200 kV.

Bremsstrahlung X-ray radiation measurements from the lateral wall of the co-axial indicated that the electron leakage currents in the region of ion flux and outside this region were comparable with, and did not exceed, those in a conventional line with no dielectric insert. The limiting current [12] required to suppress the electron leakage was, in this case, 1.5–2 times higher than that in the absence of ions (Fig.14). One should note that the limiting current increase was not a simple consequence of some additional leakage current since the ion current was lower than 10–20% of the total line current. The limiting current increase could reasonably be attributed to the modification of the electron layer due to an increase in the electric field. The increase of electric forces acting on the electron layer resulted from the field profile re-shaping due to the presence of plasma and of an ion current.

At large anode-cathode gaps in the line-end diode, some part of the electron stream impinges upon the side surface of the positive electrode at the line

output [11]. In the present case, this produced an anode-bound plasma observable via ion currents at the line output. Plasma was observed to be produced at an electron leakage energy deposition ot the stainless-steel side surface close to $100\ J \cdot g^{-1}$.

So, the experiments on energy transport along vacuum lines established the fact that ion leakage currents did not destroy the magnetic self-insulation regime.

6. CONCLUSIONS

The realization of pulse thermonuclear reactions, the construction of large Angara-5-type devices and their successful operation require the solution of the problems of beam focusing, of energy and beam transport to the target, of beam-thin-shell interaction, as well as the solution of some fusion target problems. All these problems will be studied in the next years. Although encouraging results have already been obtained, there are still many questions to be answered and serious physical and technological problems to be solved.

REFERENCES

[1] RUDAKOV, L.I., Fiz. Plazmy **4** (1978) 72.
[2] NUCKOLLS, J.H., Inertial Confinement Fusion Targets, paper presented at Top. Meeting Inertial Confinement Fusion, San Diego, California (February 1978).
[3] BOGOLYUBSKIJ, S.L., et al., Pis'ma Zh. Ehksp. Teor. Fiz. **24** (1976) 202.
[4] AFONIN, I.P., et al., All-Union Meeting on Engineering Problems of Controlled Thermonuclear Fusion, Leningrad (June 28–July 2, 1977).
[5] AFONIN, I.P., et al., in Engineering Problems of Fusion Research (7th Symp. Knoxville, October 1977).
[6] WIDNER, M.M., THOMPSON, S.L., Sandia Report, Sand-74-351.
[7] BABYKIN, M.V., et al., Technology of Inertial Confinement Experiments, IAEA – 200 (1977).
[8] ZAVOJSKIJ, E.K., RUDAKOV, L.I., At. Ehnerg. **23** (1967) 417.
[9] VELIKHOV, E.P., et al., Second IAEA Technical Committee Meeting and Workshop (Madison, Wisconsin, USA, October 1977).
[10] KOBA, Yu.V., et al., Pis'ma Zh. Ehksp. Teor. Fiz. **2** (1976).
[11] BARANCHIKOV, E.I., et al., in Research and Technology of Intense Ion and Electron Beams (2nd Int. Conf. Ithaca, USA, October 1977).
[12] GORDEEV, A.V., et al., Ann. N.Y. Acad. Sci. **251** (1975) 668.

DISCUSSION

V. NARDI: There are other machines which are very efficient sources of highly collimated electron beams at the terawatt power level, namely plasma

focus systems of a few kJ or more. Plasma focus systems have been producing electron beams for observation and study since 1972, at the Stevens Institute (Proc. High-Beta Plasma Conf., Garching (1972) 155 and Proc. 5th European Fusion Conf., Grenoble, II, 239) and at the Lebedev Institute (JETP Lett. **18** (1973) 5), and indeed more or less regularly from then on. The Lawrence Livermore Laboratory, T-Division, is at present using these electron beams to implode D-T pellets in a plasma focus (H_2) discharge with some success; 10^6-10^7 neutrons per shot have been reported. It would be interesting if you could compare performance, efficiency and/or costs (including operating costs) of your system with those of a plasma focus. By way of example, a plasma focus of approximately 5 kJ generates an electron beam of about 0.1 $TW \cdot cm^{-2}$ with an efficiency of 10% (ratio of electron beam to capacitor bank energy), as we have reported in paper U-3-3.

M.V. BABYKIN: Yes, plasma focus systems can be used to generate electron beams, and in one of our papers we have in fact described the plasma focus as a possible electron beam generator (BABYKIN, M.V., BARTOV, A.V., Kurchatov Institute of Atomic Energy Preprint 2253 (1972)). The disadvantage of the plasma focus lies in the fact that the locus of beam formation is not easily reproducible. Thanks to the use of a ring cathode with a conical recess, we succeeded in our experiments in creating a beam with a displacement of no more than ± 0.5 mm. Also, since there was no pre-pulse, we managed to obtain sharp focusing; and we were in fact the first to obtain power flux densities of 10^{13} $W \cdot cm^{-2}$ for a total energy in the beam of 12-15 kJ (BABYKIN, M.V., et al., Technology of Inertial Confinement Experiments (Proc. Advisory Group Meeting, Dubna, 1976), IAEA Technical Document (1977) 41).

At this Conference we have learned (see paper M-3) that G. Yonas and his colleagues at Sandia Laboratories have likewise succeeded in obtaining $10^{13} W \cdot cm^{-2}$ after eliminating the pre-pulse (using a similar cathode), as well as temperatures of up to 30 eV on the metal target surface.

As to comparisons of efficiency and cost, it seems to me that it would be premature to attempt them now. If the plasma focus system is to be used as a beam generator we will first have to develop special machines (higher-voltage, less inductive perhaps) in order to obtain the requisite short megavolt electron beams. The efficiency of electron accelerators can be as great as 50–60% (ratio of electron beam energy to capacitor bank energy).

V. NARDI: I agree of course that the random displacement from shot to shot of a localized electron beam source within an axial pinch 2 or 3 mm in diameter makes the task of hitting a pellet near the source somewhat difficult. On the other hand, the plasma focus electron beams are very well collimated and propagate over a long distance practically without diameter variations. The task of guiding a beam onto a target outside the plasma focus should not be unduly difficult.

M.V. BABYKIN: It might be of interest to mention here that the phenomena which occur in the plasma diode of which I was speaking a few moments ago appear

to be similar to what happens in the plasma focus. First a plasma channel is formed, and then turbulent resistivity sets in and the electron beam is created; however, these phenomena take place at a voltage of 1 MW in a small volume of plasma, and we can direct the beam to within 0.5 mm. The problem of transporting the beam onto the external target is extremely important and will no doubt be the subject of further study in the next few years.

DEVELOPMENTS IN SANDIA LABORATORIES PARTICLE BEAM FUSION PROGRAMME*

G. YONAS
and
THE SANDIA LABORATORIES PARTICLE
BEAM FUSION GROUP
Sandia Laboratories,
Albuquerque, New Mexico,
United States of America

Abstract

DEVELOPMENTS IN SANDIA LABORATORIES PARTICLE BEAM FUSION PROGRAMME.

Recent developments in the Sandia particle beam fusion programme are described. Requirements for reactors as well as methods for generating, focusing and depositing intense electron and light ion beams in targets specifically suited to particle beams are described.

REACTOR REQUIREMENTS

The high efficiency (several tens of percent) and relatively low cost ($\sim$ 10 \$/J) of intense, pulsed electron and light ion beam accelerators makes them ideal candidates for ICF ignition sources. Before one can convincingly demonstrate the utility of these drivers for future reactor needs, several critical physics and technology issues must be resolved. The beams in question must be focused, transported, and efficiently coupled to appropriate targets. Since this beam technology is naturally suited to pulses of several tens of nsec and focal radii of several mm, the resultant target mass necessitates ignition energies and power levels of $>$ 1 MJ and $\gtrsim 10^{14}$ W[1]. ICF reactor approaches depend to a large extent on driver efficiency which for economic reasons determines the pellet gain and yield as well as energy stored and transferred per pulse. Conceptual reactor studies cover a wide range from 1% efficient, .1000 MJ yield, 100 MJ storage, laser concepts to the $\lesssim$ 50% efficient, 25-50 MJ yield, few MJ storage particle beam concepts [2] (Fig. 1). Although the high efficiency low pellet yield approach will require multiple modules ($<$ 10) and higher repetition rates (10 Hz) to produce power economically, one of these relatively small modules ($\sim$ 100 MW_e) may more readily provide the basis for an experimental power reactor.

Since the technology of megampere particle beams was originally developed for single pulse applications, it is improtant to determine the feasibility of extending this approach to the needed repetitive pulse capability. Recent extended life tests of MV, flowing gas spark gap switches indicate a switch electrode lifetime of $\sim 10^9$ shots should be achievable [3], and economic analyses indicate that a comparable lifetime would not have an adverse impact on ultimate power cost [4]. The other aspect of repetitive pulsing is diode survival and given pellet yields in the 50 MJ range; the "in-diode" reactor concept [5] previously proposed would not be applicable. Methods have therefore been sought to transport beams over a distance of a few meters to a target within a reactor chamber.

This has led us to consider propagation of beams within multiple, magnetized plasma channels formed within a 50 torr to 1 atm pressure background gas. The size of the reactor chamber is then determined by the repetitive hoop stress in the first wall caused by the blast overpressure rather than x-ray and debris induced ablation which is eliminated by virtue of the buffer gas, and a chamber radius less than a few meters appears practical. In order to efficiently propagate several megavolt megampere electron or ion beams over

* Work supported by the US Department of Energy.

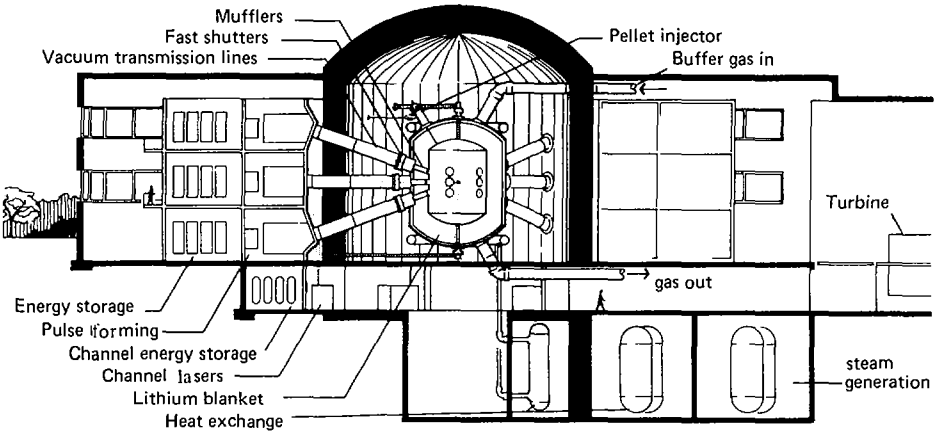


Figure 1. Compact 100 ME_e particle beam driven ICF reactor.

these distances at current densities $> 10^6$ A/cm^2 it is necessary to minimize ohmic dissipation by pre-forming a plasma with a conductivity $> 10^4$ mhos/m and containing a discharge current. The high conductivity plasma renders the E beam force free and the magnetic field of the discharge current must be $I_A \lesssim 17{,}000\ \beta\gamma$ [6], and for ions, the current is chosen to contain those ions injected with the maximum transverse velocity component. [7]. In both cases, the required current is $\sim 10^5$ A and the needed value of conductivity can be attained by a combination of channel preheating followed by beam heating of a low-Z gas by ohmic and collisional dissipation. We should note that the transverse pressure of the beam exceeds the magnetic pressure and the beam can be contained by the discharge magnetic field only if it is "frozen" into a background gas with high enough density to inertially confine the beam during its short lifetime. In order to produce a uniform channel, the discharge must be guided; fine tungsten wires have been used thus far in discharge initiation and a laser guided discharge is envisioned for reactors [2]. Dual beam transport and combination has been demonstrated on Hydra [8] and a 12 beam experiment is being prepared for Proto II to provide the basis for the 36 beam EBFA experiment, (Fig. 2).

TARGET RESEARCH

In order to employ targets which are compatible with energy intensive (rather than power intensive) capabilities of particle beam accelerators, various complex targets are being considered. One of these concepts involves a target containing preheated fuel together with magnetic fields for electron thermal conduction suppression [9]. Experimental tests of this concept using a CD_2 filament inside of a 3 mm diameter insulating shell showed initial feasibility of the concept [10], and extensions to higher power drivers are underway. First experiments with DT-gas-filled shells gave the expected characteristic neutron signature which compares well with the pulse shape expected from short-pulsed neutron source calibrations and Monte Carlo simulation of neutron transport in the shielded scintillator-photomultipliers. Additional experiments using Schlieren and spectroscopic techniques as well as correlation with 2-D MHD simulations have verified the preheat conditions created by an $\sim$ 10 kA and $\sim$ 1 μsec pre-pulse. 2-D Eulerian MHD simulations of the target implosion and compressional fuel heating agree with the 1-D predictions of fuel temperatures of .4 KeV and fuel densities of $\sim 10^{-2}$ g/cm^3 for an absorbed specific power of 4TW/g [11].

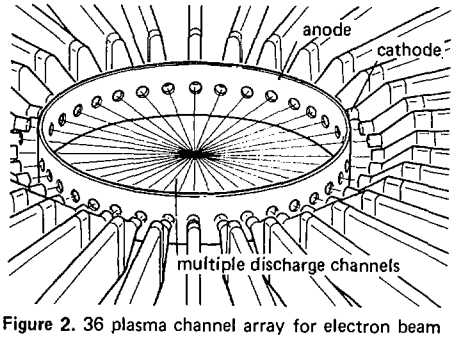


Figure 2. 36 plasma channel array for electron beam transport on EBFA.

These "magnetically enhanced" targets were originally thought to be limited to relatively low gains because of their low fuel mass, but in more recent target calculations, the addition of a cryogenic fuel layer has been found to increase the gain considerably without substantial power increases [1 and 12] (Fig. 3). The alpha-particle energy from the ignited fuel ignites the compressed cryogenic layer leading to a higher gain. The most interesting results follow for ion-driven targets which are ~ .5 cm in diameter and produce a gain of ~ 50 with an input power less than 50 TW.

A principal reason for the larger beam power and energy requirements for electrons as opposed to ions is the more penetrating nature of the electrons and the resultant Bremsstrahlung which can lead to pusher preheat and thus require ablators of substantial mass. Monte Carlo electron deposition calculations predict that for beams with $I \gg I_A$ there should be substantial deposition enhancement due to electron stagnation in the deposition region [13]. Recent experiments employing x-ray diodes and hard x-ray detectors on the Proto I accelerator (peak current density ~ 10 MA/cm^2) indicate peak temperatures > 15 eV in the focal region of a 6 μm thick Au foil. This is consistent with magnetically enhanced deposition with power/mass ≈ 50 TW/g enhancement of ⩾5. The target mounting geometry was found to strongly influence the quality of the beam focus and target coupling, and other geometries are being investigated to improve energy deposition. It was shown previously that spherical targets elevated from the anode on a short rod were not only uniformly irradiated [14] but in addition exhibited strong deposition enhancement [15]. In experiments on MITE [16], targets have been extended into the cathode (Fig. 4a) and have shown enhanced coupling with maximum temperatures of 25 eV in 6-μm-thick Au foils as detected by multiple XRD's with different filters (Fig. 4b). These results confirm the prospects for deposition enhancement [17,18] but also illustrate the coupled nature of electron focusing and deposition.

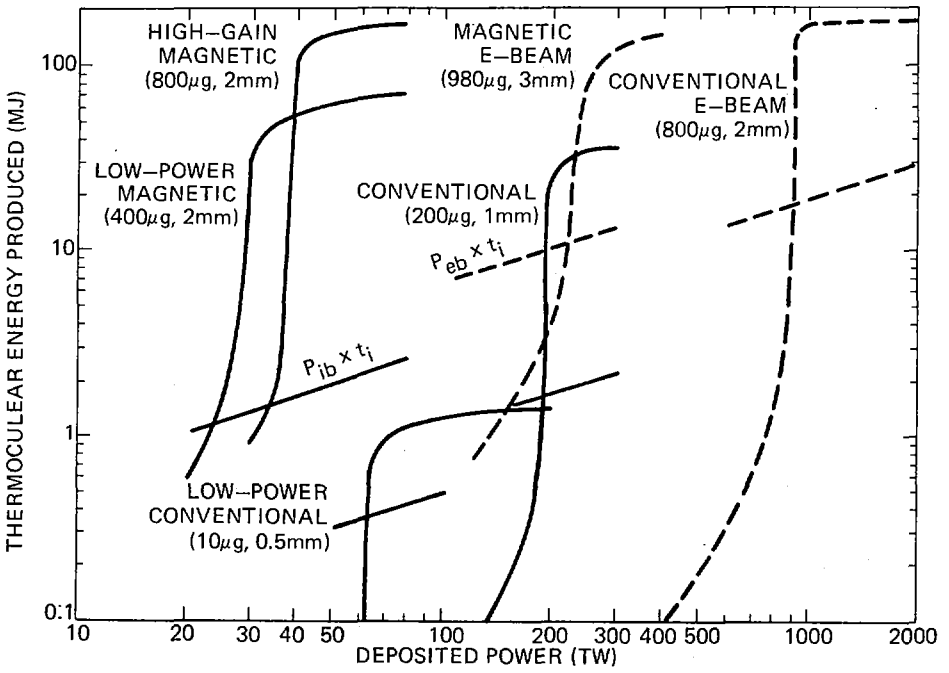


Figure 3. Predicted energy output vs deposited power for various electron and ion beam targets. The breakeven point is where the beam power implosion time product crosses the yeild curve. Ion beam calculations, solid; electron beam, dashed.

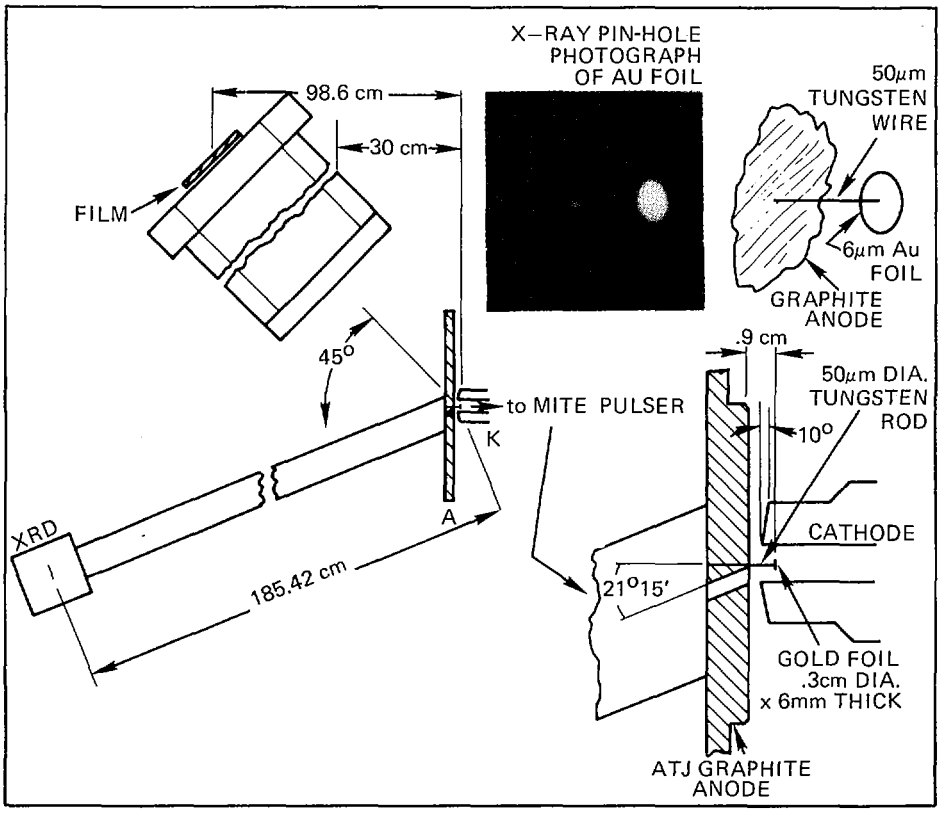
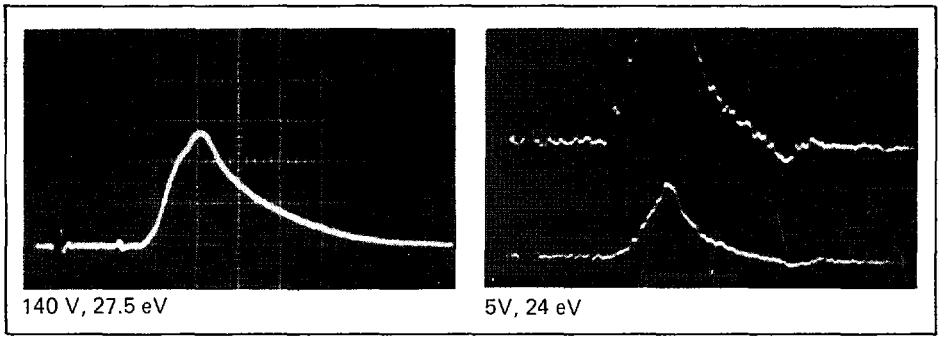


Figure 4(a) Electron beam diode/target mounting geometry. (b) XRD data for 6μm Au foil.



DRIVER DEVELOPMENT

In order to obtain sufficiently high current densities to carry out enhanced electron deposition experiments, an extensive series of diode optimizations has been carried out. The conclusion from this work is that high current densities ($> 10^7$ A/cm^2) and efficient focusing can be achieved by minimizing the cathode diameter, anode cathode gap, and diode pre-pulse level. An example of a useful cathode geometry which operates at the 4Ω level and producing $> 10^7$ A/cm^2 is shown in 5a with the current density distribution as determined with an x-ray pinhole camera in 5b. This diode is being used in deposition studies on Proto I.

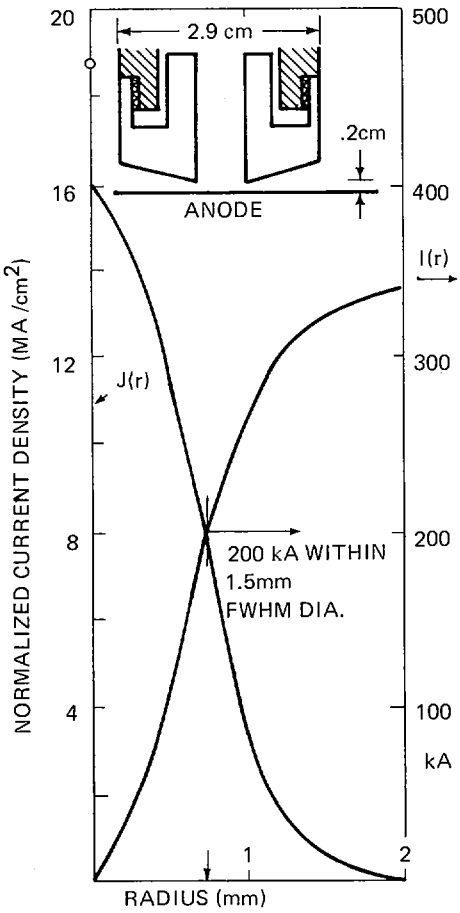


Figure 5 (a) Diode geometry for irradiating flat foil anode. (b) Current distribution as measured by x-ray pinhole photography.

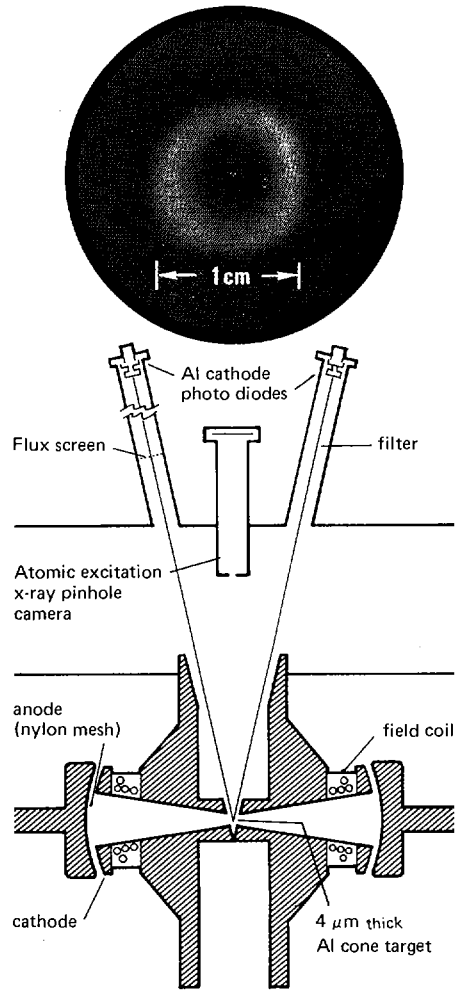


Figure 6a. Schematic of ion diode, diagnostics, and x-ray output from target.

Light ion beams have the advantage of providing efficient target coupling with low mass ablators without requiring enhancement over that for single particle collisions. Focusing of such beams, however, requires that the natural beam divergence angle be $< 1°$ so that simple geometrical focusing can be employed. The methods being considered for electron current suppression to achieve high ion production efficiency in intense beam diodes involve both electrostatic and magnetic methods. We are investigating the use of external field coils (Fig. 6a) to provide an elec-

tron suppressing magnetic field and the use of multiple plasma channels for beam transport and overlap as in Fig. 2. 2-D electron-ion particle simulations for this diode show that the magnetic field prevents electron leakage and that a strong virtual cathode forms with the extracted ion current density equal to 13 times the vacuum Child-Langmuir value based on the physical anode-cathode gap (Fig. 6b). Soft x-ray pin-hole photographs

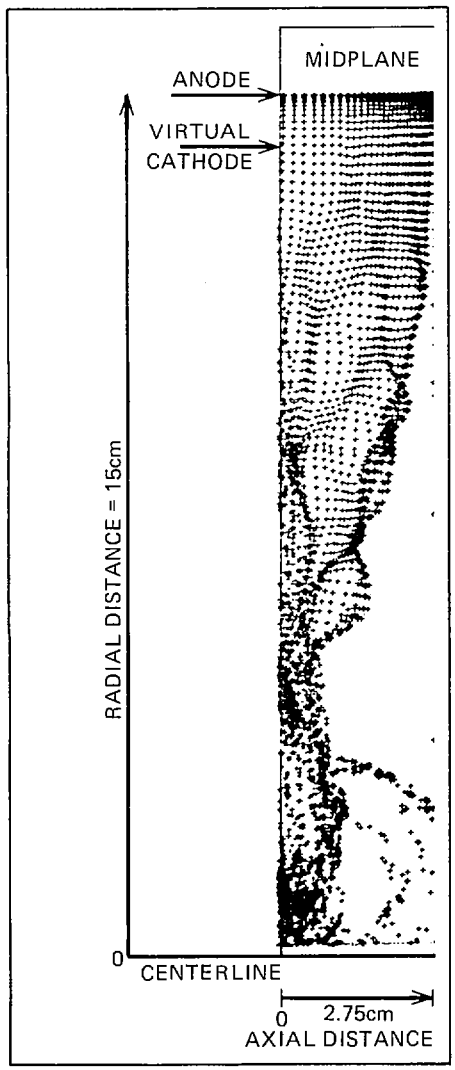


Figure 6b. Simulation of ion flow in diode shown in Figure 6a. Self-pinch of the 2 MeV, 280 kA ion beam is seen.

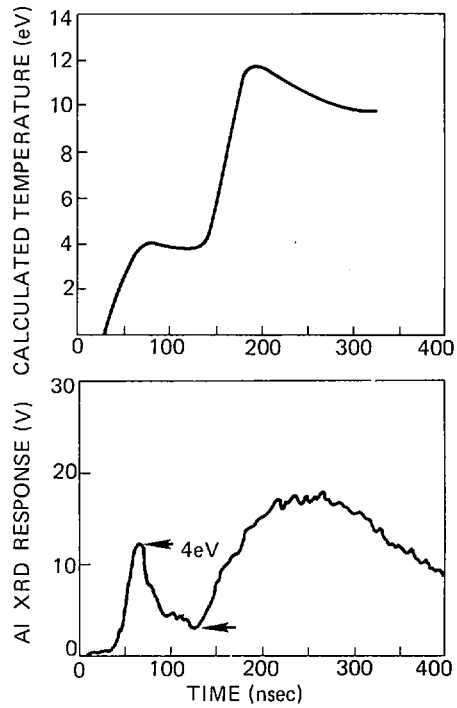


Figure 7. Observed Al x-ray diode signal plotted with the calculated midplane surface temperature on the inside of a 4 μm thick Al cone for 1 kJ of deposited ion energy.

of a conical target on axis show a focused beam and the XRD data indicate a current density of $\approx$ 25 kA/cm^2 (Fig. 7). These data indicate that current densities of 10^5 A/cm^2 are attainable from geometrical focusing and the additional needed factor of 100 in power density should be achievable by a combination of the following effects now under study at Sandia as well as at the Naval Research Laboratory and Cornell University: space-time bunching using a time-varying voltage; multiple beam overlap; reduced beam divergence and enhanced geometrical focusing; further increases in ion beam current density due to electron concentration within the diode.

In order to achieve the multi-megajoule beam levels needed with both the electron and ion approaches, we require the use of multiple, compact pulse-forming modules each in the 50-kJ range which can be arranged to deliver their energy within a few m of the target. Because of the large area insulators necessitated by the electrically weak insulator-vacuum interface, it has been found neces-

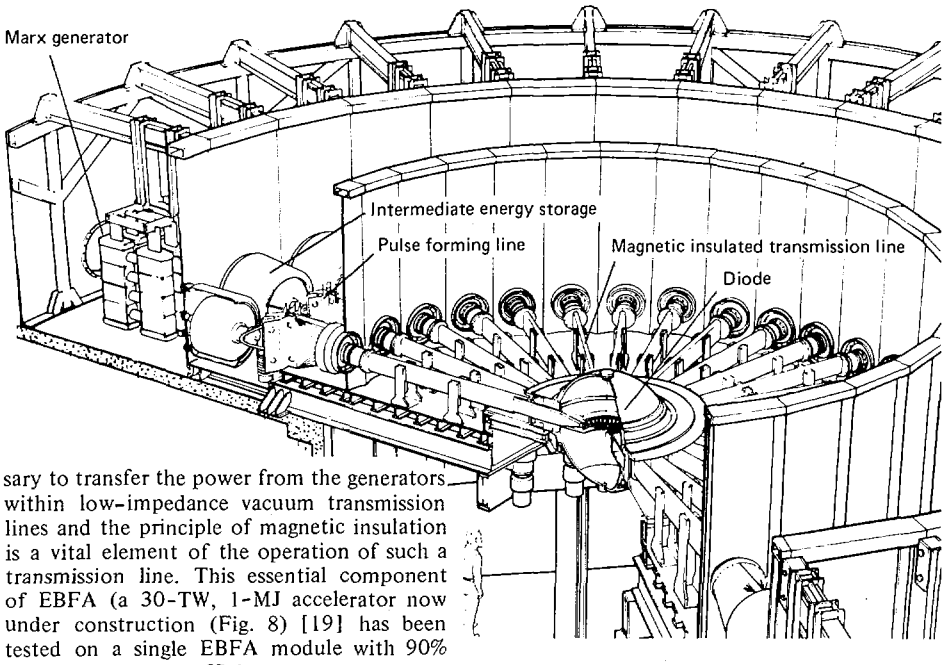
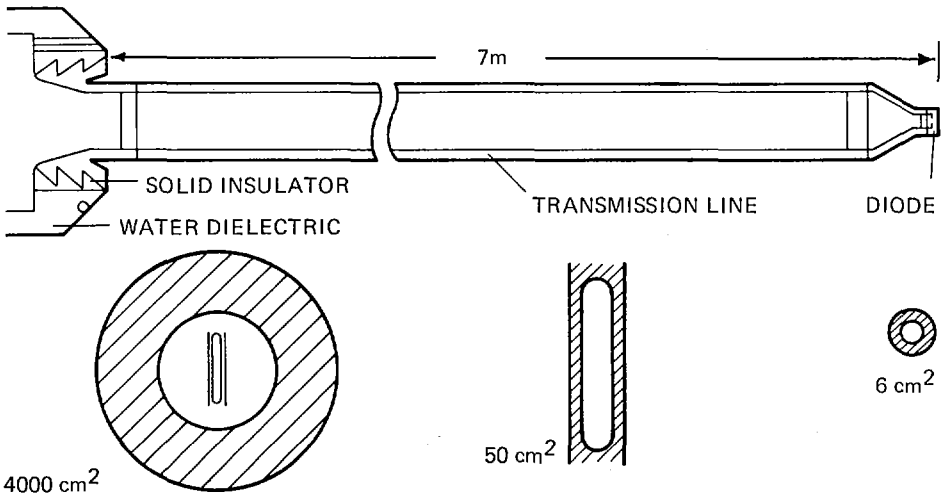


Figure 8. EBFA : 30 TW, 1 MJ, operational 1980.

sary to transfer the power from the generators within low-impedance vacuum transmission lines and the principle of magnetic insulation is a vital element of the operation of such a transmission line. This essential component of EBFA (a 30-TW, 1-MJ accelerator now under construction (Fig. 8) [19] has been tested on a single EBFA module with 90% energy transport efficiency at an average stress $> 10^{14}$ W/m^2 over the 7-m-long line with the only energy losses occurring due to pulse front erosion (Fig. 9). This energy loss

Figure 9a. Schematic of magnetically insulated transmission line experiment showing area through which ~ .7 TW is transmitted (cross hatched).



effect has also been simulated with a 2-D particle simulation code [20] and is well understood. By tapering the vacuum line near the diode, an electric field in excess of 600 MV/m and power density $> 10^{15}$ W/m^2 has been achieved and higher stress may be possible permitting direct connection of the vacuum line to the pellet [21].

Many of these concepts can be adequately explored with present accelerators and should provide the basic design data needed for use on EBFA which will become operational in 1980.

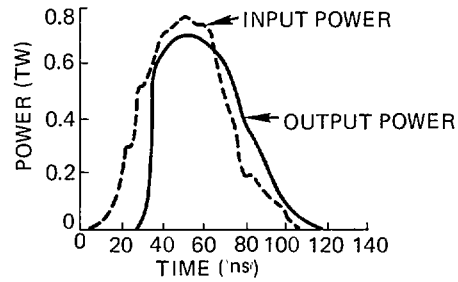


Figure 9b. Input and output power pulses.

REFERENCES

1. Sweeney, M. A. and Farnsworth, A. V. *IEEE Conference on Plasma Science.* Monterey, CA (1978).
2. Cook, D. L. and Sweeney, M. A. *Proc of Third ANS Topical Meeting on Tech. of Contr. Nucl. Fusion.* Santa Fe, NM (1978).
3. Buttram, M. T. and Rohwein, G. J. *13th Pulse Power Modulator Symp.* Buffalo, NY (1978).
4. Prestwich, K. R., Cook, D. L., and Yonas, G. *3rd ANS Topical Mtg. on Tech. of Contr. Nucl. Fusion.* Santa Fe, NM (1978).
5. J. R. Freeman et al., *Plasma Physics and Controlled Nuclear Fusion Research* Berchtesgaden. 1 (1976) 167.
6. Miller, P. A., Butler, R. I., Cowan, M., Freeman, J. R., Poukey, J., Wright, T. P., and Yonas, G. *Phys. Rev. Lett.* 39 (1977). 92.
7. Mosher, D. L. *IEEE Int. Conf. Plasma Science* Monterey, CA (1978).
8. Miller, P. A., Baker, L., Freeman, J. E., Mix, L. P., Poukey, J. W., and Wright, T. P. *Proc. of 2nd Int. Top Conf. on High Power Electron and Ion Beam Res. and Tech.*, Ed. by J. Nation and R. N. Sudan. Cornell U., Ithaca, NY (1977).
9. Widner, M. M. *Bull. Am. Phys. Soc.* 22 (1977). 1139.
10. Chang, J., Widner, M. M., Farnsworth, A. V., Jr., Leeper, R. J., Prevender, T. S., and Baker, L. *Proc. of 2nd Int. Conf. on High Power Elect., and Ion Beam Res. and Tech.* Ed. by J. Nation and R. N. Sudan. Ithaca, NY (1977).
11. Lindemuth, I. R. and Widner, M. M. *Annual Meeting on Theoretical Aspects of Contr. Thermonuclear Res.* Gatlinburg, TN. (1978).
12. Bangerter, R. O., and Meeker, D. L. *Proc. of 2nd Int. Top Conf. on High Power Elec. and Ion Beam Res. and Tech.* Ed by J. Nation and R. W. Sudan. Ithaca, NY. (1977).
13. Gilad, P., Kaplan, Z., Miller, S., Nardi, E., Peleg, E., and Zinamon, Z. *Proc. of 2nd Int. Top Conf. on High Power Elect. and Ion Beam Res. and Tech.* Ed. by J. Nation and R. W. Sudan. Ithaca, NY (1977).
14. Chang, J. S. T., Widner, M. M., Kuswa, G. W., Yonas, G. *Phys. Rev. Lett.* 34 (1975). 1266.
15. Clauser, M. J. Mix, L. P., Poukey, J. W., Quintenz, J. P., and Toepfer, A. J. *Phys. Rev. Lett.* 38 (1977). 398.
16. Chang, J. S. T., Mendel, C. W., Goldstein, S. A., and Quintenz, J. P. *IEEE Conf. on Plasma Sci.* Monterey, CA (1978).
17. Yonas, G., Poukey, J. W., Freeman, J. R., Prestwich, K. R., Toepfer, A. J., and Clauser, M. J. *Nucl. Fusion* 14 (1974) 731.
18. Bogolyubski,. et. al. *JETP Lett.* 24 (1976). 182.
19. Martin, T., Johnson, D. L., and McDaniel, D. H. *2nd Int. Top. Conf. on High Power Beam Elect. and Ion Beam Res. and Tech.* Ed. by J. Nation and R. W. Sudan. Ithaca, NY (1977).
20. Poukey, J. W., and Bergeron, K. D. *Appl. Phys. Lett.* 32. (1978). 8.
21. Rudakov, L. I. *Top. Mtg. on Inert. Conf. Fusion.* San Diego, Ca. WA 1-1. (1978).

DISCUSSION

C.C. BAKER: How do you propose to focus the beam on a target several metres away with repetition rates of, say, once per second?

G. YONAS: Electron or ion beam transport is to be carried out in preformed plasma discharge channels; these are to be initiated on a repetitive basis, a laser

being used for pre-ionization. Single and multiple beam transport has been demonstrated and experiments and analyses are continuing.

D.D. RYUTOV: The real reactor target should obviously be spherically symmetrical. But if the irradiation of such a target is also spherically symmetrical, you will have no magnetic field at all. How can you then rely on the enhanced energy deposition described in your paper?

G. YONAS: Enhanced electron deposition is expected to occur in the multiple discharge overlap region where the total discharge current $I_T \gg I_A$ (I_A being the Alfvén current). The degree of symmetry one can achieve is still an unanswered question.

R.N. SUDAN: In a Cornell experiment similar to but smaller in scale than the spherical ion diode experiment mentioned by Mr. Yonas, ion focusing was observed to follow ballistic trajectories with a divergence angle of $\lesssim 5$; the total ion current density increased by a factor of 50.

INERTIAL CONFINEMENT FUSION RESEARCH AT OSAKA
New developments in laser energy drivers, laser and REB fusion research

H. AZECHI, H. FUJITA, K. IMASAKI, Y. IZAWA,
Y. KATO, Y. KAWAMURA, M. MATOBA, K. MIMA,
S. MIYAMOTO, Y. MIZUMOTO, T. MOCHIZUKI,
S. NAKAI, K. NISHIHARA, H. NISHIMURA,
T. NORIMATSU, T. SASAKI, H. TAKABE, J.J. THOMSON*,
K. YOSHIDA, T. YAMANAKA, C. YAMANAKA
Institute of Laser Engineering,
Osaka University, Osaka,
Japan

Abstract

INERTIAL CONFINEMENT FUSION RESEARCH AT OSAKA: NEW DEVELOPMENTS IN LASER ENERGY DRIVERS, LASER AND REB FUSION RESEARCH.

The present approach to inertial confinement fusion is based on understanding the physics of beam-plasma interaction and implosion. The Institute of Laser Engineering, Osaka, is now pursuing project 'Kongoh' which includes the Gekko (glass laser) programme, the Lekko (CO_2 laser) programme and the Reiden experiment (REB), a scientific feasibility experiment. Lasers are the most developed energy drivers and are of great value in fundamental fusion research by implosion. REB has a good performance efficiency, and is suitable for a reactor scheme, while beam transport is rather cumbersome owing to plasma instability. Successful implosion experiments by glass microballoon have been performed. Interesting data on laser coupling have been obtained.

1. INTRODUCTION

The current objectives of inertial confinement fusion research are to obtain clear information on beam-plasma interaction and to demonstrate pellet compression which proves the scientific feasibility of this fusion scheme.

The Institute of Laser Engineering, Osaka (ILE), has three energy driver programmes: the Gekko glass laser system, the Lekko CO_2 laser system and the

---

* Permanent address: Lawrence Livermore Laboratory, University of California, Livermore, CA, USA.

TABLE I. HIGH-POWER LASER SYSTEMS AT ILE, OSAKA UNIVERSITY

	No. of beams	Total output energy	Completion year
Glass lasers			
Gekko II	2	200 $J \cdot n^{-1}$ 0.4 TW – 0.1 ns	1975
Gekko IV	4	2 $kJ \cdot ns^{-1}$ 4 TW – 0.1 ns	1977
Gekko XII	12	20 $kJ \cdot ns^{-1}$ 40 TW – 0.1 ns	1980
CO_2 lasers			
Lekko I	1	200 $J \cdot ns^{-1}$	1976
Lekko II	2	1 $kJ \cdot ns^{-1}$	1977
Lekko X	10	10 $kJ \cdot ns^{-1}$	1980

Reiden REB system. The use of different types of energy driver enables direct comparison of beam-plasma coupling data which reveals the interaction mechanism.

Implosion experiments by glass microballoon have been performed in conjunction with the data from computer simulation.

2. LASER ENERGY DRIVERS

One of the key issues of scientific feasibility experiments in laser fusion is to construct laser energy drivers delivering output energy of 100 kJ – 1 MJ. Among the several types of energy drivers, the laser is the most advanced tool for fusion research. Improving the efficiency of high-powered lasers is an important step towards realizing laser-fusion power reactors.

Table I summarizes high-powered laser systems for present and future laser fusion experiments at Osaka University. Based on the technologies developed for Gekko II and Lekko I, various schemes for improvements have been developed and are incorporated in Gekko IV and Lekko II. These improvements, with further developments, are being applied to higher energy lasers Gekko XII and Lekko X. Improvements of Nd:glass and CO_2 lasers are given below.

2.1. Gekko Nd : glass lasers

The efficiency of glass lasers is judged by pumping efficiency, energy storage in the laser glass and extraction of stored energy. Performance can be improved by the following methods:

(1) Uniform pumping, which improves pumping efficiency and increases stored energy.
(2) Suppression of parasitic oscillation in large-aperture amplifiers, which can increase the stored energy by more than 50%.
(3) Use of laser glass with a smaller non-linear refractive index, which improves extraction efficiency, since higher-intensity laser light can be propagated.
(4) Use of laser glass with larger emission cross-section, which improves extraction efficiency. This results in a high-gain laser system with fewer amplifier modules and is therefore simpler and more cost effective.

Phosphate laser glass, developed by the Hoya Glass Works in 1975, has the ideal properties of small non-linear refractive index and high-emission cross-section, and we have adopted it for our entire new glass laser system, Gekko IV. Since a laser amplifier with larger gain is more susceptible to parasitic oscillation, we have made special efforts to prevent parasitic oscillations in order to increase the stored energy.

The performance of the phosphate glass laser system Gekko IV, which has an 11-cm disc amplifier as the final amplifier, has been tested at various pulse widths. We have obtained focusable output powers of 1.2 TW and 1.0 TW per beam at 10 ps and 100 ps, respectively. Output energy of 500 J per beam at 1 ns was attained. This performance is almost comparable to a single arm of the silicate glass system, Shiva, when operated with a 15-cm dia. final disc amplifier. Comparison of the number of amplifiers and the final output aperture of the two laser systems clearly shows that the phosphate glass system (Gekko IV) is far more efficient, simple and cost effective than Shiva by more than factor of two.

The same principle will be applied to the larger glass laser system, Gekko XII, scheduled to be completed in 1980. Figure 1 is a photograph of the Gekko IV glass laser. Figure 2 shows the system diagram of the Gekko II and Gekko IV lasers.

2.2. Lekko CO_2 lasers

CO_2 lasers present many technical and physical problems in the construction of a high-powered and highly efficient fusion laser, and the ILE, at Osaka University, has endeavoured to develop high-powered CO_2 lasers. The development steps of the project are shown in Table I. Components have been developed and system design and performance investigated for construction of the 10-kJ Lekko X system.

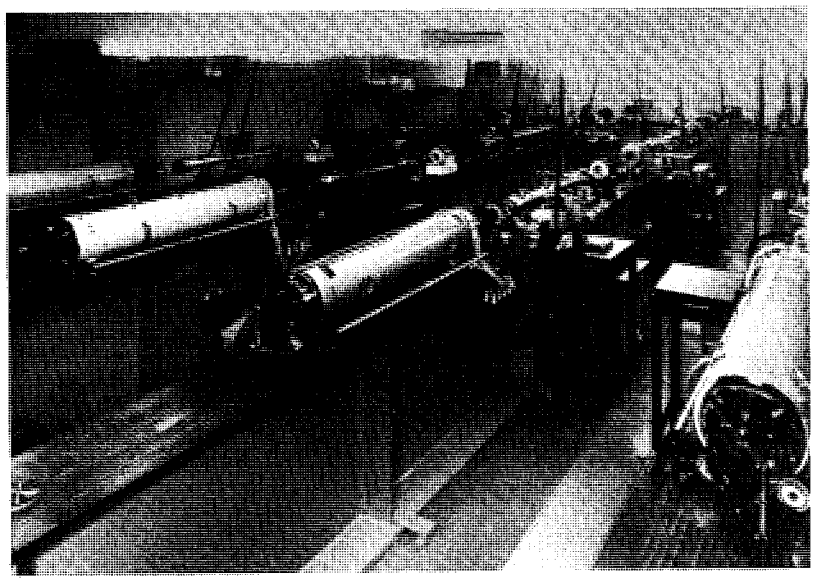


FIG.1. Gekko IV phosphate glass laser system. Energy 2 kJ, pulse 1 ns, power 4 TW in four beams.

Figure 3 shows the Lekko II CO_2 laser with the system diagram. The most relevant results are as follows:

(1) Efficient short-pulse energy extraction from an amplifier by multiline double-band amplification. Almost 100% energy extraction from the upper laser level was experimentally verified with a nanosecond laser pulse of nine lines in double bands.

(2) Investigation of a new type of laser gas containing only CO_2 and N_2. In an E-beam-controlled laser, laser gas without helium could be uniformly pumped and the operational E/P without arcing was increased. A very high gain coefficient of 10%/cm and high pumping efficiency of 4% were achieved with no He gas in the laser. These values are far greater than the normal gain coefficient of 5%/cm and pumping efficiency of 2% with He mixed gas.

(3) Development of a new p-Ge saturable absorber, with a wide absorption spectrum to cover all CO_2 laser lines and low saturation energy.

High-powered laser technology is progressing rapidly and it seems feasible to design a laser reactor system using these lasers conventionally.

3. LASER FUSION RESEARCH

Strong energy concentration and high peak power can at present only be attained by laser drivers. We have investigated both the laser-plasma interaction process and implosion. The wavelength scaling of laser interaction and target compression is a most interesting problem, and this is why we produced the Gekko systems (glass laser) and Lekko systems (CO_2 laser).

Pellet fabrication and design are also very important for obtaining efficient compression. The ILE has completed several techniques for gas-filled glass microballoons and polyethylene shell targets. Cryogenic targets are also being investigated.

To obtain reliable data, highly developed diagnostics with micrometer and picosecond space-time resolution are required. Several diagnostic techniques including computer aid are being cultivated by ILE in co-operation with industry.

3.1. Interaction

To understand interaction, it is necessary to study absorption of laser light by the plasma, light scattering, particle velocity distributions, energy transport through the plasma and spontaneous magnetic fields.

The data on coupling the CO_2 laser Lekko I to plasma show clearer features of plasma non-linearity than in the case of glass lasers. Several interaction experiments were performed with plane targets at a laser intensity of up to 10^{13} W·cm^{-2}.

Near the power of 10^{12} W·cm^{-2}, the resonance absorption becomes dominant, which is shown by (a) the fact that reflected patterns are strongly dependent on the laser light polarization; (b) the rapid generation of very fast ions; and (c) the fact that the p-polarization light is absorbed more strongly than the s-light. Figure 4 shows the directional distribution of the reflected light in the incident plane in the case of 35° oblique irradiation. As shown in Fig. 4(a), the s-light has a strong anisotropy of side-reflected light, which can be explained by the ripples on the critical density surface. The wavelength of the ripple was estimated as 29 μm, using a grating model. For the case of p-polarization, a dip in the specular cone as shown in Fig. 4(b) gives the optimum angle for resonance absorption. The density scale length was then estimated as 8.2 μm. These results are consistent with the scheme of resonance absorption enhanced by density steepening, and are fairly explained by our theoretical surface wave model described in Section 3.3.

3.2. Implosion

The ILE has performed implosion experiments using the Gekko II two-beam glass laser system, using glass microballoons 70 μm in diameter filled with

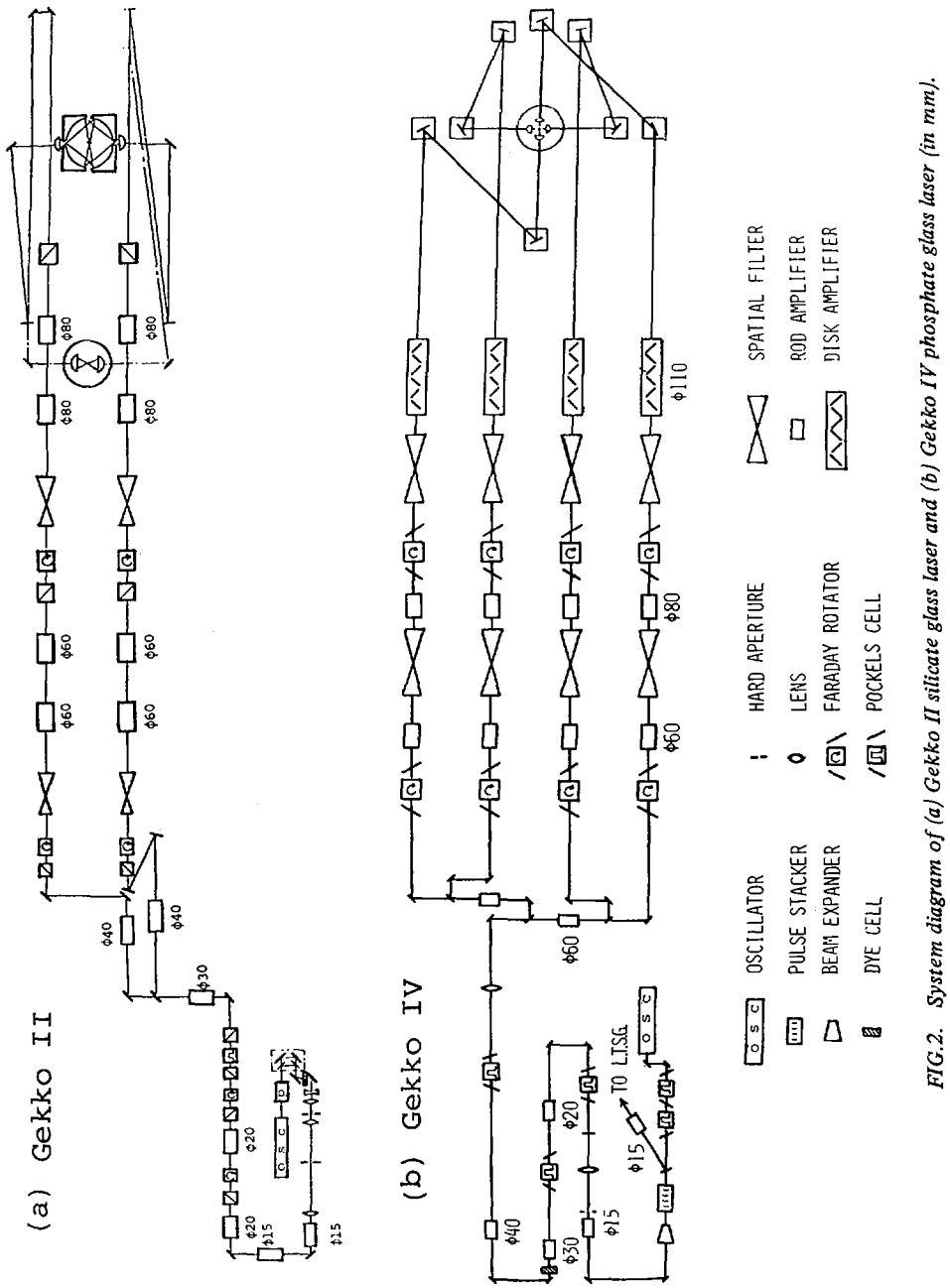
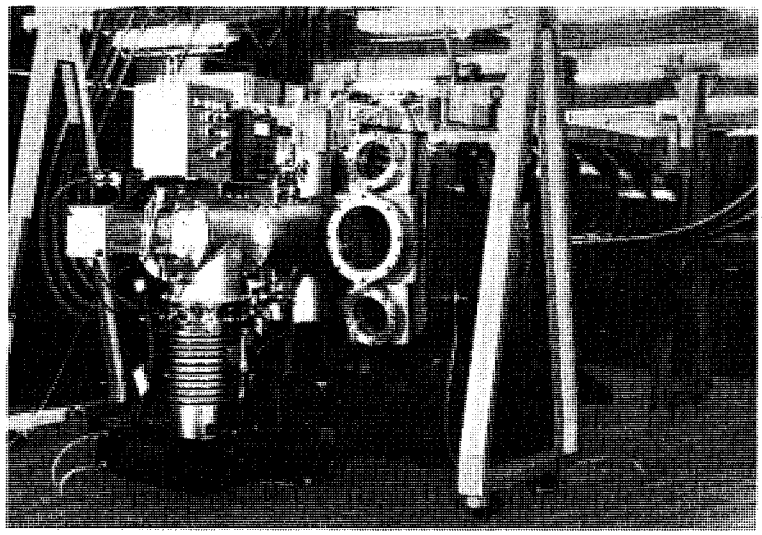
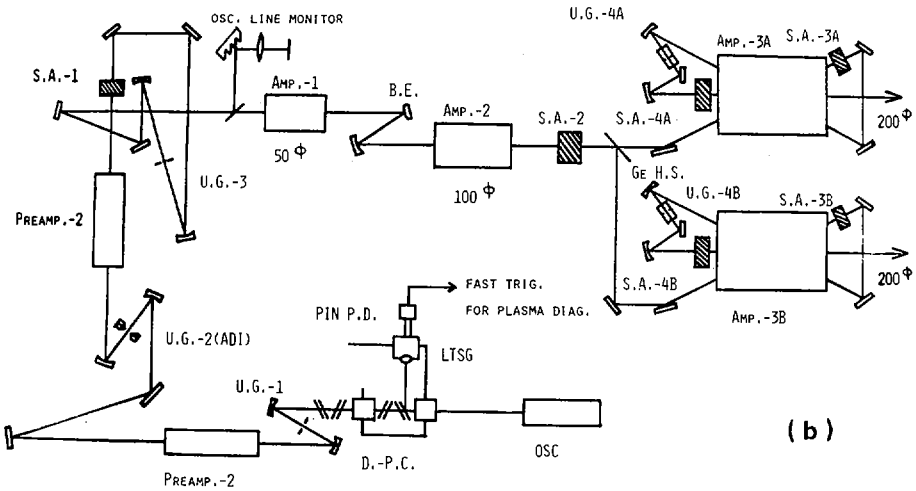


FIG.2. System diagram of (a) Gekko II silicate glass laser and (b) Gekko IV phosphate glass laser (in mm).



(a)



(b)

FIG.3. (a) Lekko II CO_2 laser and (b) its system diagram. Energy 1 kJ, pulse 1 ns in two beams.

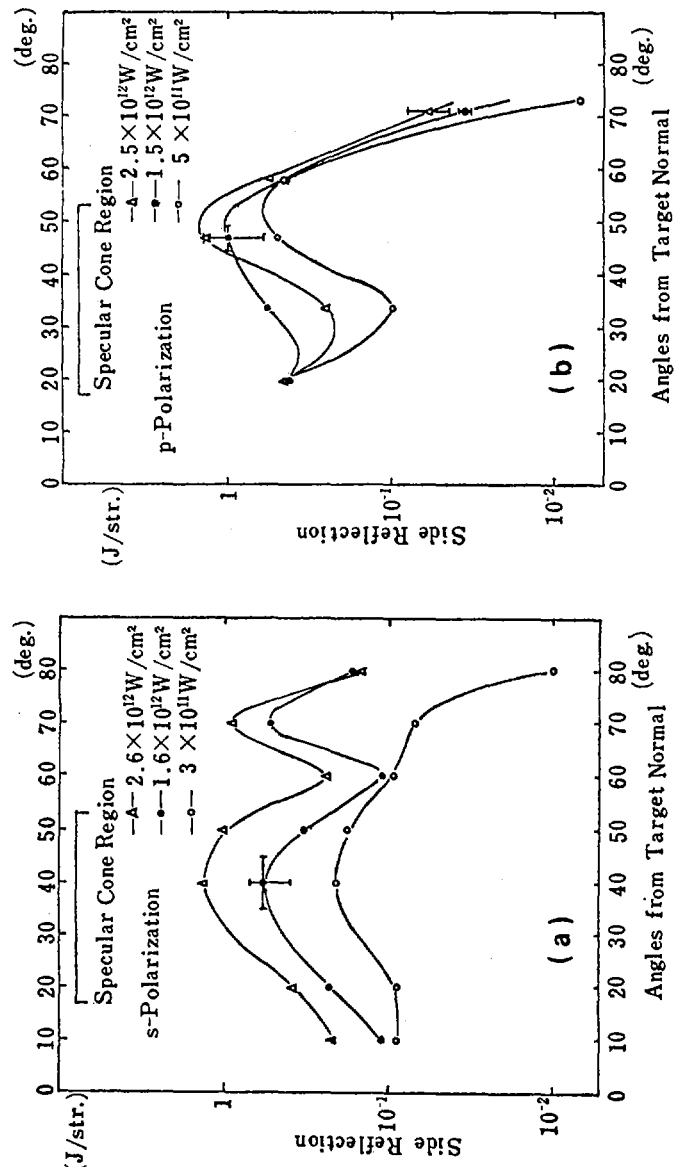


FIG.4. Directional distribution of reflected light from a polyethylene foil target by oblique irradiation of CO_2 laser light. (a) s-polarization light; (b) p-polarization light.

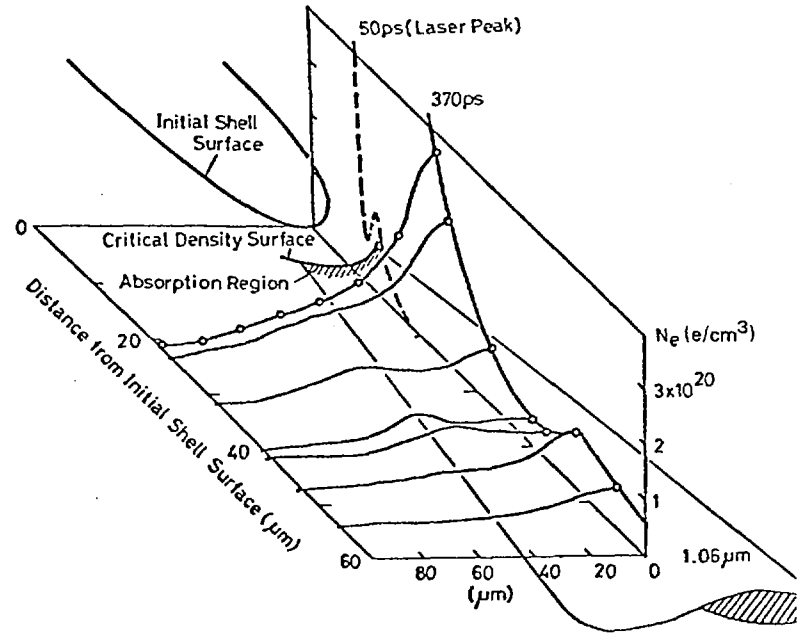


FIG.5. Density scale length of glass microballoon target measured by an interferometric method of second harmonic laser light.

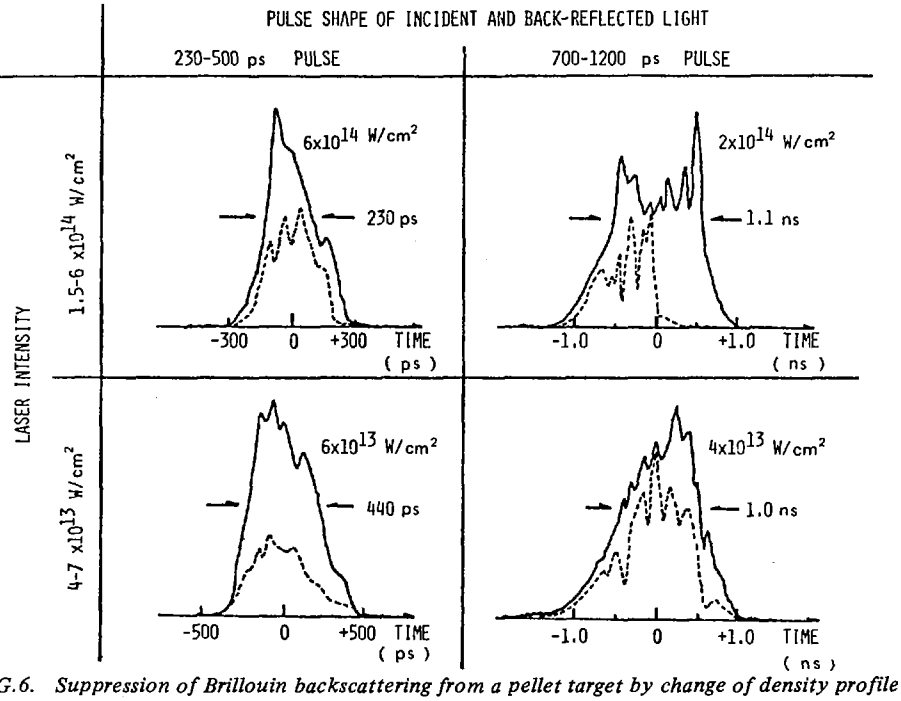


FIG.6. Suppression of Brillouin backscattering from a pellet target by change of density profile due to ponderomotive force of Gekko II glass laser.

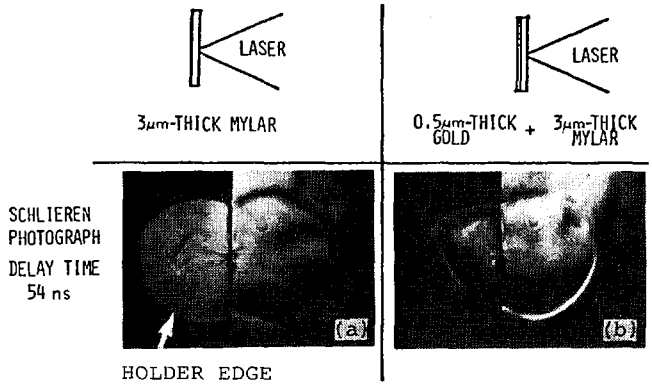


FIG. 7. Photograph of blast waves generated in 10-torr He by Gekko II laser. (a) Mylar target and (b) Mylar + gold target.

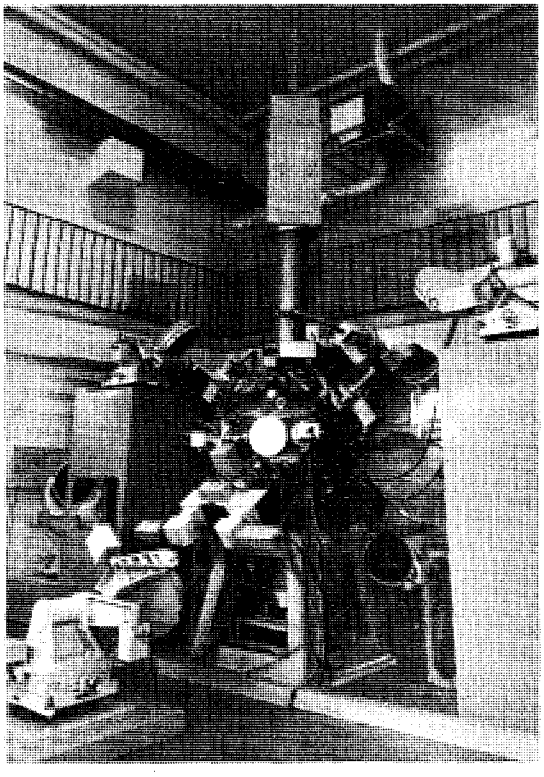


FIG. 8. Gekko IV target chamber for tetrahedral irradiation. Irradiation power is 4 TW.

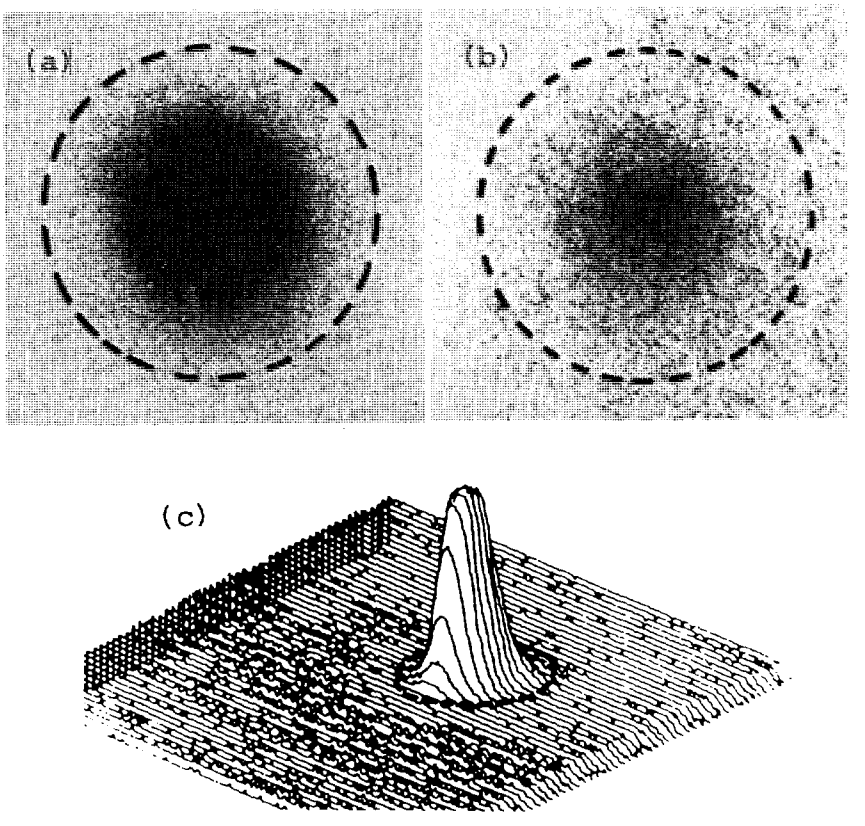


FIG.9. X-ray pinhole photographs of D_2-filled glass microballoon ((a) and (b)) and three-dimensional intensity profile (c). X-ray filter is (a) 75-μm Be and (b) 75-μm Be + 7-μm Al, Diameter of target: 70 μm.

20 atm D_2 gas. The exploding pusher mode was investigated by an F/1 optical system and a 4π irradiation crab shell. The incident laser energy 20 J (50 ps) was delivered as follows: 54% in scattered light; 7.7% in ion energy; 0.28% in X-ray and 8.0% in absorption. The spatial distribution of slow ions was isotropic, while fast ions greater than 10 keV were mainly scattered in the focus cone. The distribution of scattered light had two peaks, one backscattered in the focus cone and the other backscattered in the angle of 60°–80° from the laser beam. Compared to the CO_2 laser experiment of Fig. 4, the latter peak seems to correspond to scattering due to ripples of the cut-off density surface. The power dependence of electron temperature higher than 10 keV was $\phi^{1/2}$ and the lower component of 1–2 keV showed the $\phi^{2/3}$ dependence. The ion also had two components. The fast ions were driven by the same electrostatic potential.

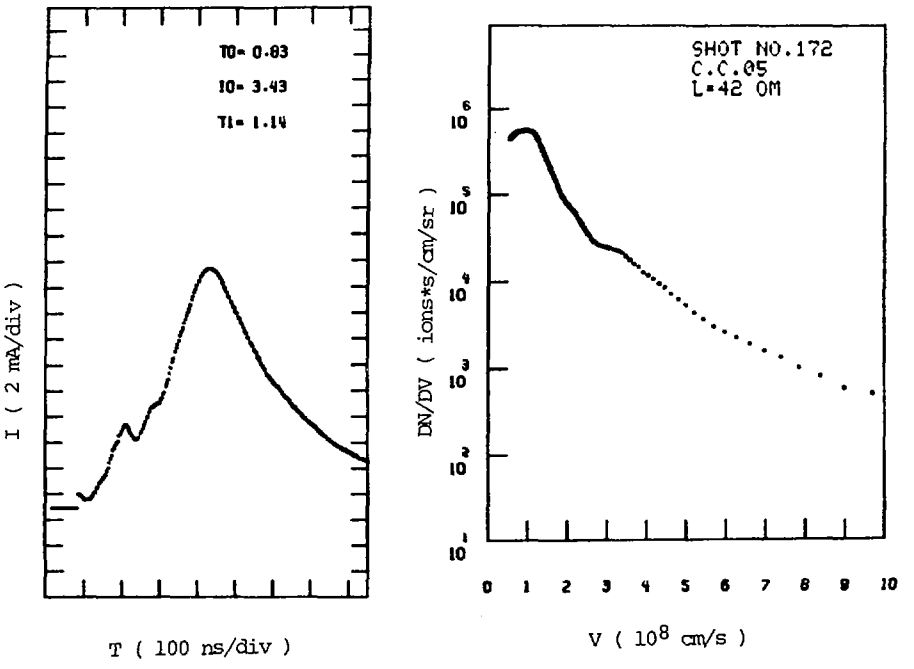


FIG.10. Ion energy distribution measured by ion collector at 35° from laser axis. Target is neon-filled glass microballoon 84 μm diameter with laser power of 2 TW.

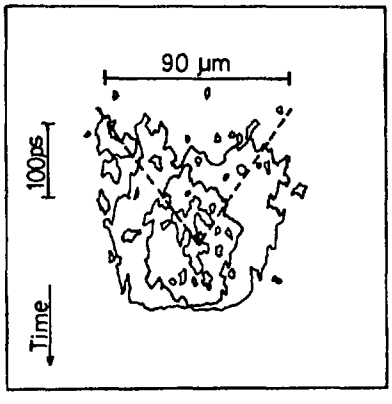


FIG.11. X-ray streak image of glass microballoon target. Target diameter 90 μm; magnification of pinhole camera 15; diameter of pinhole 10 μm; sweep speed 5.7 ps·mm^{-1} in phosphor screen; temporal resolution 20 ps; laser power. 2 TW.

The density profile of the pellet was measured by the time-resolved interference method to show a shelf formation. The scale length was estimated as 1–2 μm (Fig. 5). Propagation of the shock front was also observed.

Brillouin backscattering from a compressed glass microballoon target was measured. With a long laser pulse (1 ns) of sufficient power (10^{14} W·cm^{-2}), the backscattered light dropped in the middle of the laser pulse, as shown in Fig. 6; with a weaker laser pulse it did not decrease. This behaviour suggests that isentropic compression by a long laser pulse shows promise.

Energy transfer from the laser-absorbed layer to the pusher region was measured by the blast-wave method using a Mylar target 3 μm thick with and without a thin gold layer backcoat. When the gold layer was less than 0.2 μm thick, a jet stream with laser intensity higher than 5×10^{14} W·cm^{-2} occurred at the rear, as shown in Fig. 7(a). A blast wave occurred when the gold was more than 0.2 μm thick. These phenomena show that a gold layer seems to suppress the plasma instability due to fast electrons caused by resonance absorption. The energy transfer efficiency from the laser-absorbed region to the rear was 1–2% for the 0.5-μm gold-coated Mylar target at a laser intensity of 5×10^{14}–10^{16} W·cm^{-2}.

Using the Gekko IV glass laser, we compressed a glass microballoon pellet containing D_2 gas of 15 atm by four-beam tetrahedral irradiation (Fig. 8). The compression ratio was 200, given by an X-ray image of the core, as shown in Fig. 9. The neutron yield was about 10^7. The ion energy distribution measured by an ion collector at 35° from the laser axis is shown in Fig. 10. The electron temperature estimated from the velocity distribution was about 50 keV, which is higher than that estimated from the X-ray spectrum (20 keV). The implosion velocity was 3×10^7 cm·s^{-1} estimated from an X-ray streak image, as shown in Fig. 11. An X-ray spectrum of a neon-filled glass microballoon (Fig. 12) gave the parameters of the plasma core as $\rho = 7.6 \times 10^{-2}$ g·cm^{-3}; $\rho R = 1.7 \times 10^{-4}$ g·cm^{-2}; $N_e = 3.9 \times 10^{22}$ cm^{-3}; and $T_e = 430$ eV. A 1-D two-temperature compression code containing the high-energy electron effect was used to estimate an implosion process, which agrees fairly well with the experimental data.

3.3. Theory and simulation

Some physical problems in the field of laser-plasma interaction, energy transport and fluid dynamics of implosion and thermonuclear burning were investigated.

(a) Critical surface instability was studied to analyse anisotropic polarization-dependent angular distribution of the reflected light shown in Fig. 4. The side peaks in Fig. 4(a) are explained by the scattering due to the most unstable critical surface ripple. The absence of side peak for p-polarization can be related to the stability of the surface wave for p-polarization.

Reduction of stimulated Brillouin scattering (SBS) was also investigated for a plasma of a given scale length. If the damping rate of ion waves is constant, reflectivity increases monotonically with incident laser power. However, the ion heating due to ion waves and their non-linearity enhances the damping rate, leading to reduced reflectivity. We found the steady-state reflectivity included self-consistent ion heating and non-linear Landau damping; the results are plotted versus input laser power in Fig. 13. We solved the time-dependent ion temperature equation numerically and compared the results with recent SBS reflectivity measurements. Steady-state and time-dependent SBS reflectivity measurements shown in Fig. 6 may be explained by the enhanced damping of ion waves together with the decrease of density scale length due to ponderomotive force.

(b) Ratios of hot electron heat flux to the free-streaming heat flux were found self-consistently in the spherical geometry. Hot electron inward current induces cold electron return current, which generates ion wave turbulence. As a result of the ion wave excitation, the return current is reduced, and the hot electron inward current and then the inward heat flux are therefore suppressed. For a spherical plasma with an exponential density profile, the steady-state hot electron heat flux normalized by the free-streaming value F is shown in Fig. 14, from which diagram $F \cong 0.04\ n_{ho}/n_c$ is concluded.

(c) At the final stage of implosion, thermonuclear burning is ignited at the centre of the target. It is important to discover the ignition condition and the burning front characteristics. The ignition condition is on the scale of an initial burning region, λ. When $\lambda \geqslant \lambda_c$ (the critical length for ignition), the burning region starts to expand. The critical length, λ_c, is roughly several times α-particle range when a background temperature $T_i = T_e \cong 4$ keV. This condition means competition between α-particle heating and the energy loss due to the escape of α-particles and the electron thermal conduction. The development, propagation and structure of the reaction wave ignited at the centre were studied numerically. Typical spatial profiles of T_i, T_e, burning rate, Y, fluid velocity, etc.,in the burning region are shown in Fig. 15. Initially, $T_e = T_i$ is set 1 keV everywhere except the central region. At the centre, $r \leqslant 0.7\ \mu m$, $E_{inp} = 200$ J, is put in to ignite the thermonuclear burning. The profiles shown in Fig. 15 are for t = 4.6 ps after ignition.

4. REB FUSION

The energy deposition mechanism of an REB on a solid target is one of the most basic problems which must be investigated in REB inertial confinement fusion research. A proposed pellet design for REB fusion consists of a high-Z absorber on the pellet surface to dissipate the REB energy efficiently in a shorter

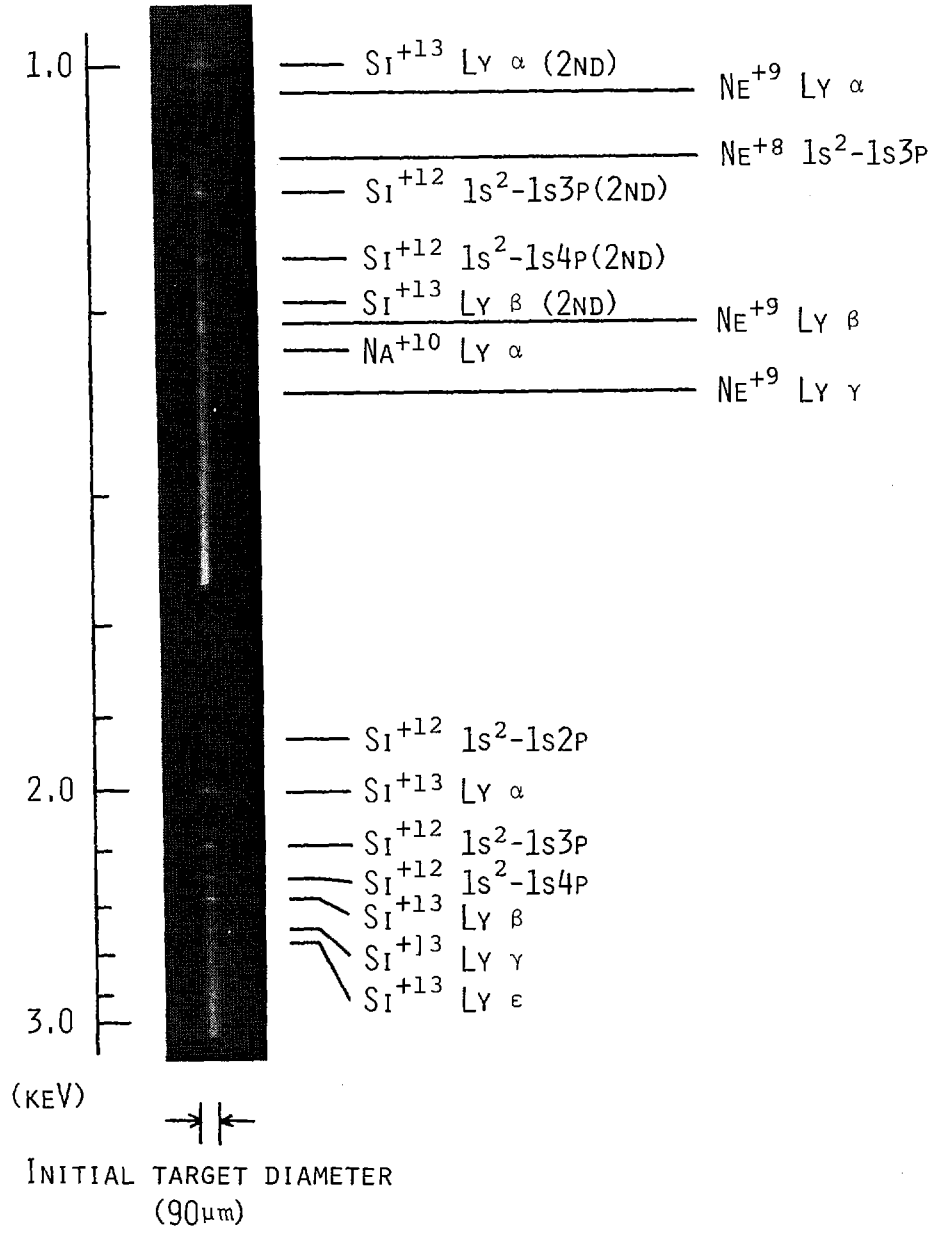


FIG.12. X-ray spectrum of a neon-filled glass microballoon. Target diameter 90 μm; shell thickness 0.93 μm; neon fill pressure 7 atm; laser pulse width 110 ps; total laser energy 256 J. A 25-μm-thick Be filter was used over the whole spectrum and a 6.5-μm-thick Al filter was added above 1.52 keV.

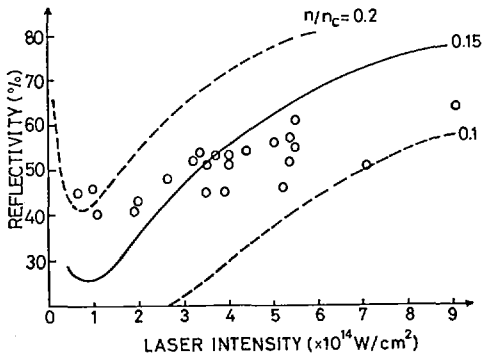


FIG.13. Power dependence of steady-state stimulated Brillouin scattering reflectivities for $n/n_c = 0.2$ and 0.1. Open circles represent reflectivities measured by Gekko II Nd-glass laser experiments.

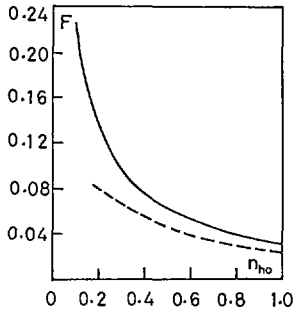


FIG.14. Hot-electron heat flux normalized by the free-streaming heat flux versus hot electron density normalized by the cut-off density. The solid line is for $T_\perp/T_r = 0.1$ and the broken line is for $T_\perp/T_r = 1$. $T_\perp/T_r$ is the temperature ratio between radial and perpendicular temperature.

range than the shell thickness. According to our experiments, however, a low-Z target can dissipate the REB energy more efficiently than a high-Z target. This result is consistent with a previously proposed interaction model which assumes kinetic two-stream instability in a corona region round the target.

4.1. Experimental results

The REB generator Reiden III was used to generate a tightly focused beam of 500 kV, 80 kA, 4×10^{10} W and 80 ns duration. The beam was focused on a thin foil target placed at the centre of the anode. The focal spot size was measured as 1.5 mm in diameter, and 80% of the total current was concentrated in the focal spot at about 70 ns after the onset of the main pulse.

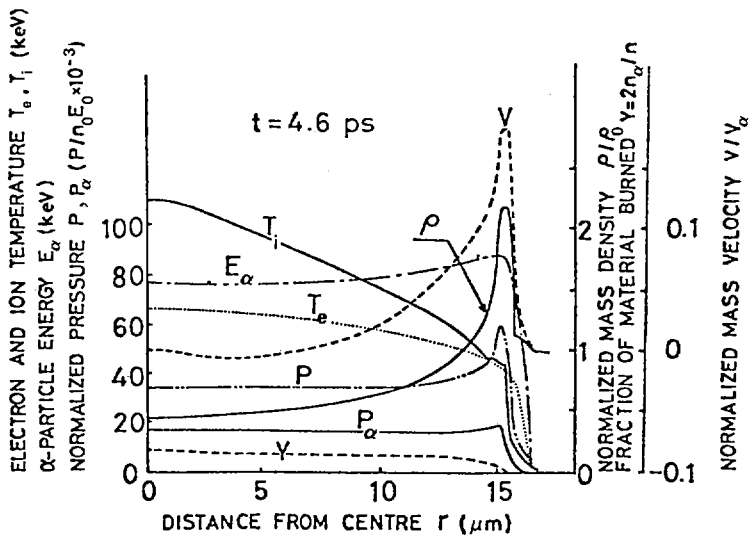


FIG.15. Structure of the thermonuclear reaction wave ignited at the centre of a pellet. Profiles of the various physical variables at 4.6 ps after ignition.

When a thin foil of CD_2 was used as a target, neutrons from the D-D reaction were observed even if the foil was very much thinner than the classical range of the electron beam. The neutrons were thermonuclear in origin. The estimated plasma temperature required to produce 10^9 neutrons and the electron temperature measured by X-ray were consistent and imply the existence of strong enhancement of energy deposition. Kinetic two-stream instability is excited in the corona plasma and dissipates the beam energy. According to this model, the fusion products such as protons and beam electrons must pass through the remaining target in order to be detected behind the target. The proton energy and its dependence on the target thickness are consistent with the model.

The energy distribution of the transmitted electrons was measured by employing an electrostatic particle energy analyser placed behind the target. The results are shown in Fig. 16. The estimated electron energy distribution due to Coulomb scattering through a 100-μm-thick polyethylene foil is given in Fig. 16(a). An experimental result using a 20-μm-thick polyethylene foil is shown in Fig. 16(b). Experimental data using 6-μm Ni-coated 20-μm-thick polyethylene foil is shown in Fig. 16(c). In Fig. 16(b), the lower energy component of the electrons begins to increase in magnitude, and the higher energy component decreases drastically 70 ns after the rise of the main pulse. This indicates the existence of anomalous losses of the focused REB. In the case of a laminar target with a high-Z coating, as shown in Fig. 16(c), such a large energy loss as in Fig. 16(b) was not observed. It should

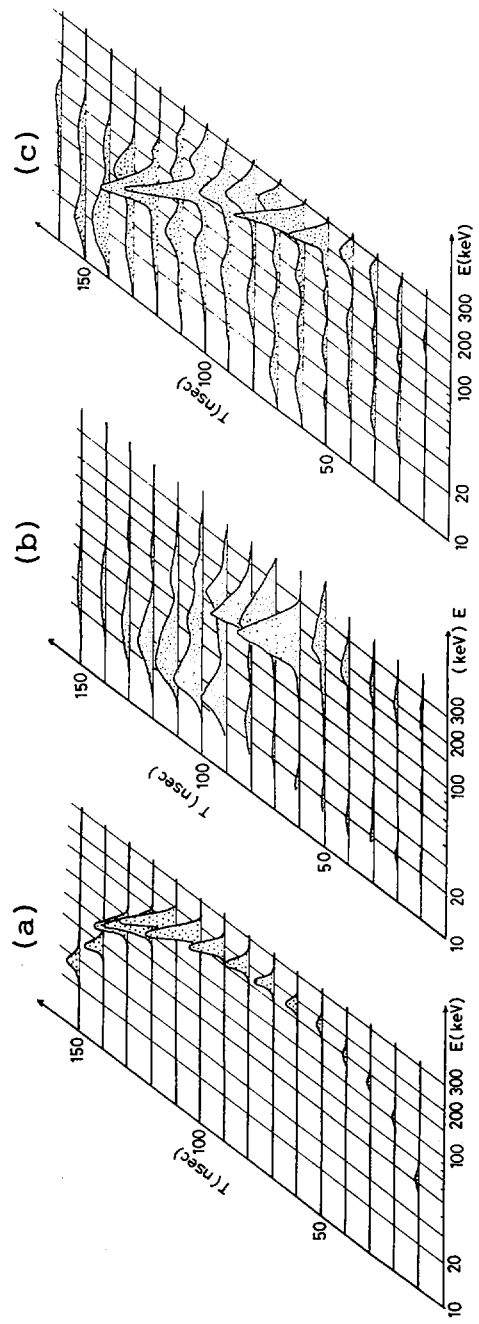


FIG.16. Energy dissipation of transmitted REB electron through various targets.
(a) Estimated Coulomb scattering by polyethylene target 100 μm thick;
(b) Polyethylene target 20 μm thick;
(c) Double layer target 6 μm Ni and polyethylene 20 μm thick.

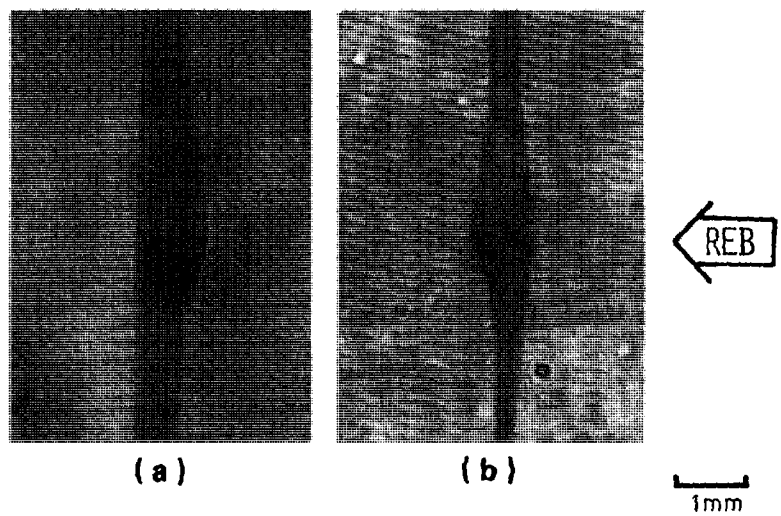


FIG.17. Interference pattern of (a) $(CH_2)_n$ target 100 μm thick and (b) Ni target 10 μm thick at the peak of REB pulse 100 ns, 2 kJ, 400 keV, by N_2 laser.

be noticed that the thin 6-μm nickel coating on the polyethylene base foil strongly reduces the loss of REB because the high-Z material can suppress the growth of the plasma instability.

Figure 17 shows the effective stopping of REB electrons in a low-Z target. The interference fringes were observed by nitrogen laser interferometry of 6-ns pulse width. At the peak of the REB pulse the electron cannot penetrate the 100 μm of polyethylene, in spite of the 500 μm classical range of the 400-keV electron. Density steepening also appears at the front of the target. A delayed protrusion on the rear surface was observed to expand with a sharp density boundary. It seems that the REB energy is dissipated in the corona region and drives a shock wave into the target. The results of computer simulation using our interaction model coincided well with the observed results. In contrast to the low-Z target behaviour, a high-Z target such as Ta expands more symmetrically and slowly in both sides, which shows the penetration of REB electrons through the target.

4.2. Development of REB

The Reiden series of REB generators were constructed at Osaka University. Most of the interaction experiments and the basic investigation of the implosion were performed with Reiden III (500 kV, 100 kA, 80 ns, 4 kJ). For pellet implosion experiments, Reiden IV, which can deliver REB of 1.7 MV, 1.7 MA, 30 ns and 100 kJ, is now under construction.

BIBLIOGRAPHY

INST. OF LASER ENGINEERING, OSAKA UNIV., Annual Progress Report on Laser Fusion Program 1977, ILE-APR-77 (1977).

YAMANAKA, C., in Top. Mtg. on Inertial Confinement Fusion, San Diego, 1978, paper D1.

YAMANAKA, C., IAEA Technical Committee Meeting on Progress in Inertial Confinement Fusion, San Francisco, 1978 (Rep. to be published by US Dept. of Energy).

AZECHI, H. et al., Phys. Rev. Lett. **39** (1977) 1144.

AZECHI, H. et al., Appl. Phys. Lett. **32** (1977) 216.

NAKAI, S., IMASAKI, K., YAMANAKA, C., in Plasma Physics and Controlled Nuclear Fusion Research 1976 (Proc. 6th Int. Conf. Berchtesgaden, 1976) Vol. 1, IAEA, Vienna (1977) 207.

NAKAI, S., YAMANAKA, C., et al., Phys. Rev. **A17** (1978) 1133.

DISCUSSION

H.J. HOPMAN: Could you explain why the measured REB distribution function does not show a broad plateau but instead seems to indicate coherent deceleration?

C. YAMANAKA: Perhaps it is because of the strong non-linear damping of plasma waves.

K. PAPADOPOULOS: Could you compare the energy deposition lengths based on the REB plasma interactions, as measured in your experiment, with those presented earlier by the Kurchatov and Sandia groups, which were based on magnetic field penetration in the target?

C. YAMANAKA: It follows from the estimated growth rate of the two-stream instability that the interaction length is a few millimetres. This can be measured on the basis of the interference pattern produced by the nitrogen laser.

P. AVIVI: Did the different frequencies of the lasers you used have any influence on the implosion and compression experiments?

C. YAMANAKA: The compression achieved with the Lekko II CO_2 laser was about 20 (volume ratio), with no neutron yield – presumably a consequence of poor focusing. The compression achieved with the Gekko IV glass laser was about 200, with 10^7 neutrons from the D-D reaction.

P.A. HOLSTEIN: Did I understand rightly that the power achieved in laser implosion with Gekko IV was 2 TW focused on the target? What is the pulse duration in such a shot?

C. YAMANAKA: Gekko IV can deliver 4 TW of focusable power in four beams in 100 ps.

Session V

INERTIAL CONFINEMENT IV

Chairman

C.M. STICKLEY
USA

Papers V-1-1 and V-1-2 were presented
by T.P. Donaldson as Rapporteur
Papers V-2-1 to V-2-3 were presented
by C.S. Liu as Rapporteur

LASER FUSION IMPLICATIONS OF RESONANCE ABSORPTION AND ASSOCIATED ELECTROSTATIC FIELD PRESSURE

T.P. DONALDSON, J.E. BALMER,
P. WÄGLI, P. LÄDRACH
Institut für angewandte Physik,
Universität Bern,
Bern,
Switzerland

Abstract

LASER FUSION IMPLICATIONS OF RESONANCE ABSORPTION AND ASSOCIATED ELECTROSTATIC FIELD PRESSURE.

Resonance absorption of laser radiation in plasma and some of its implications for laser fusion have been studied. The angular width of the resonance is shown to be broad enough to permit a non-critical incidence angle, which is important when laser radiation is focused onto the curved surface of a microsphere. For the range of parameters studied, the energy loss to non-thermal ions is found to be small. Modification of the electron density profile by the resonant electrostatic field pressure is shown to play an important role.

1. INTRODUCTION

It has recently been established experimentally[1-6] that resonance absorption of laser radiation in plasma[7-10] is an important process from the standpoint of Laser-Fusion[11]. This paper describes experimental and theoretical work made in order to reach a better understanding of the phenomenon and its implications for Laser-Fusion.

If laser radiation is focused onto the curved surface of a micro-sphere, it is important that the angular width of the resonance be sufficiently broad so that the change in incidence angle of the laser beam does not influence the radiation absorption. It is also important that most of the absorption be thermal, because non-thermal (ultra-fast[12]) particles transfer minimal momentum per unit energy to a fusion target, and therefore the energy they carry represents a loss of "useful energy".

Measurements have been made of the total laser energy absorbed, and it has been shown that, for 35 ps, 1.06μm, s-polarised laser pulses, with $I < 10^{14}\ W{\cdot}cm^{-2}$, inverse bremsstrahlung accounts for the absorption. This is low, less than 30% between $10^{13}\ Wcm^{-2}$ and $2X10^{14}\ Wcm^{-2}$. Resonance absorption can therefore play an essential role by increasing the total

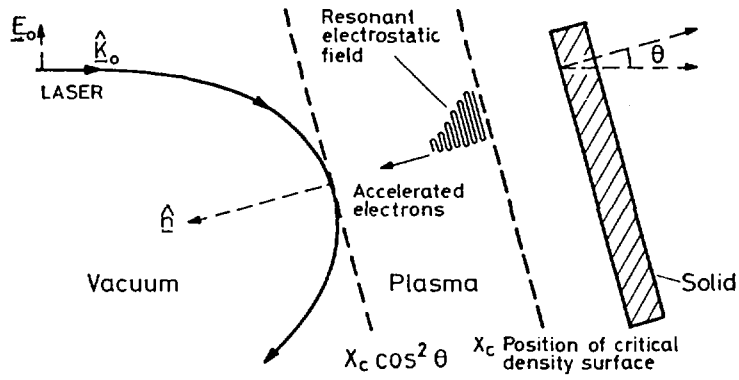


FIG.1. Schematic of particle acceleration by the resonant electrostatic field.

absorption of p-polarised laser radiation to > 60%[2]. Measurements of cold electron temperatures[2] and non-thermal (ultrafast) ion energies[12] show that it occurs over a broad range of angles, while measurements of X-ray spectra and ion fluxes have established that the non-thermal particles carry a fraction of the total absorbed laser energy. The roles of density profile modification and non-smooth critical surfaces are emphasised.

2. THEORY

Since laser-generated plasma is inhomogeneous, there is a density region (critical density) where a resonance exists between the laser frequency and the plasma frequency, over their respective bandwidths. If the laser electric field has a component in the direction of the plasma density gradient, then, under favourable conditions, the electromagnetic field of the laser can drive an electrostatic field in the resonance region (see Fig.1). This requires that the laser beam be incident at a finite angle to the density gradient, and therefore, since for short pulses the plasma expansion is one-dimensional, at a finite angle to the target normal. Due to refraction, the distance between the "turn-around point" of the laser beam and the critical density surface increases with increasing incidence angle, so that, if the angle of incidence becomes too large, the electromagnetic and electrostatic fields will decouple. This results in an optimum angle of incidence for the absorption of the laser radiation. The full derivation of this optimum can be found in Ginzberg[13]. The angle of incidence for maximum absorption, θ_{opt}, is given by: $\sin\theta_{opt} = (k_o L)^{-\frac{1}{3}}$ where L is the electron density scale length and k_o is the incident laser k vector. The electrostatic field driven at resonance (Fig.1) is very intense ($>10^9 Vcm^{-2}$)[12].

Assuming that inverse bremsstrahlung is the only other absorption mechanism, and assuming that field losses are due to

plasma wave convection, the spatially dependent electrostatic field E(x) can be written[14]:

$$E(x) = \frac{(1-\alpha)^{\frac{1}{4}} E_o \Phi(\tau) L \cos\phi}{(2\pi k_o L)^{\frac{1}{2}} (x^2 + \Delta^2)^{\frac{1}{2}}} \qquad (1)$$

where α is the inverse bremsstrahlung absorption coefficient, $\Phi(\tau)$ is the Ginzberg resonance function[13], ϕ is the E vector polarisation angle, and Δ ($=(\lambda_D^2 L)^{1/3}$) is the electrostatic field width, with λ_D as the Debye length. This field strongly perturbs the electron velocity distribution, and since it is highly localised, the effect on an electron depends on its velocity.

Electrons travelling faster than an escape velocity, v_{es}, can cross the field in a time less than one oscillation period and therefore fall through an accelerating DC potential. These constitute the long-wavelength Fourier components of the electrostatic field, with wavelengths greater than one field width, so that plasma wavebreaking occurs. They escape from the plasma with an equal amount of ionic charge (conservation of charge neutrality) and rapidly transfer their energy to the ions. These have been observed in several experiments[12,15,16]. They will be referred to as ultra-fast ions with energy ε_{uf}

$$\varepsilon_{uf} = \int_0^L E(x)\,dx \qquad (2)$$

On the other hand, electrons travelling slower than v_{es} experience an AC field. They constitute the short-wavelength Fourier components, with low phase velocities, and are Landau damped so that this part of the field energy is thermalised and the cold plasma electron temperature is enhanced. They also experience an acceleration, in this case due to ponderomotive force[17], but the maximum energy gained is less than 1 keV[18]. Ponderomotive force, which acts on the plasma as a whole, does play an important role, however, in steepening the density profile and thereby narrowing the electrostatic field width.

The fraction, f, of particles accelerated to high energies relative to thermal particles can be calculated by integrating over the background Maxwellian energy distribution function. The partition of energy, P, between the loss to fast particles and the thermal energy can be found in the same way;

$$f = 1.13 \frac{(\varepsilon_{es}/T_c)\exp(-\varepsilon_{es}/T_c)}{\Gamma(3/2)} \qquad (3)$$

$$P = 0.75(\varepsilon_{uf}/T_c)(\varepsilon_{es}/T_c)^{\frac{1}{2}}\exp(-\varepsilon_{es}/T_c) \qquad (4)$$

where $\varepsilon_{es} = \frac{1}{2} m_e v_{es}^2$, T_c is the background electron temperature and v_{es} was obtained by a rigorous treatment of Landau damping:

$$v_{es} = 0.88\,\pi\nu_o\Delta \qquad (5)$$

where ν_o is the frequency of the laser radiation.

A computer code, ZWERG, has been written[15] to model the experimental observations, and it is able to predict the effect of different laser/target parameters. In addition to equations (1) to (5), the code includes energy and momentum balance, equations (6) and (7). Absorption is by inverse bremsstrahlung and plasma resonance, while energy losses are by both thermal and non-thermal ion transport:

$$\left[\alpha+(1-\alpha)\frac{\phi^2(\tau)\cos^2\phi}{\pi}\right]I_o = g\frac{n_e T_c^{\frac{3}{2}}}{m_e^{\frac{1}{2}}} + f\frac{n_i \varepsilon_{uf}^{\frac{3}{2}}}{m_i^{\frac{1}{2}}} \qquad (6)$$

$$\rho du/dt = -\nabla n_e T_e + \frac{n_e e^2}{2m_e \omega_o^2}\nabla\langle E^2\rangle \qquad (7)$$

where g is a phenomenological factor derived from measurement of T_c, ρ is the plasma mass density, u is the plasma expansion velocity, n_e and n_i are the electron and ion number densities respectively and ω_o is the laser angular frequency. Steepening of the electron density gradient is described by inclusion of resonant electrostatic field pressure in the momentum balance.

A single ion species plasma expansion at the ion sound speed is assumed for the thermal ions, since friction between different ion species is high[19]. In the case of the non-thermal ions, however, protons are preferentially accelerated [12,20] because the resonant electrostatic field force is able to overcome the frictional forces. The average charge state, z, in the plasma was calculated using time-dependent ionisation equations[21]. It never exceeded 2.2, even at the maximum measured electron temperature of 400eV. This corresponds to a basic plasma cell of 8 protons, 5 helium-like carbon and 2 helium-like oxygen ions. Stages higher than helium-like are not reached, because the ionisation times from helium-like to hydrogen-like ions are always much longer than the laser pulse duration.

3. EXPERIMENTAL RESULTS

Experiments were made with 1.06μm, 35ps laser pulses, from the OUTIS system, focused onto plane perspex targets $(C_5O_2H_8)_n$. The focal diameter was ≃ 80μm, the focal depth was ≃ ±200μm and the surface smoothness of the target was better than λ/4. The polarisation plane was rotated, through the required angle, by a λ/2 plate. Hot and cold X-ray electron temperatures, T_h and T_c [2,22] were measured by the foil absorber method[23]. Ion emission energies, ε_{uf}[12,15], and ion fluxes were measured using Faraday detectors with electrostatic analysers. Specular plasma reflectivities, R, and plasma transmissivities, T, were measured by calibrated photodiodes[24]. Experiments were made over a range of incident laser intensity, I_o, laser incidence angle, θ, and polarisation angle, φ.

For θ = 0° the values of R (Fig.2), T and T_c, in the range I_o = 2×10^{11} Wcm^{-2} to 10^{14} Wcm^{-2}, are entirely consistent with laser energy absorption by inverse bremsstrahlung, as calculated by the computer code ZWERG. Up to 10^{14} Wcm^{-2} laser radiation was found to be reflected predominantly at the specular angle,

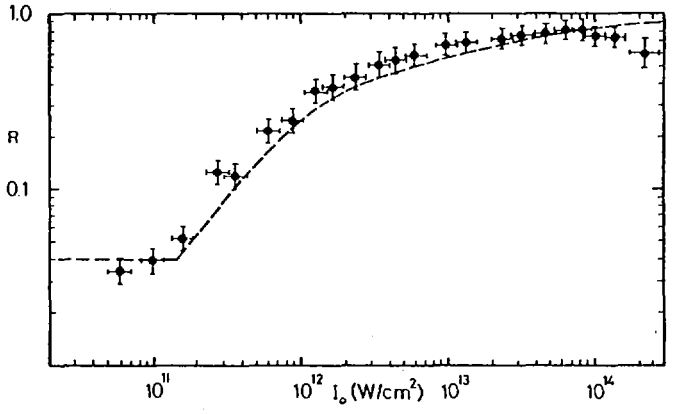


FIG.2. Specular plasma reflectivity, R, as a function of laser intensity, I_0. Points with error bars are measurements and the dashed line is the theoretical prediction for inverse bremsstrahlung absorption.

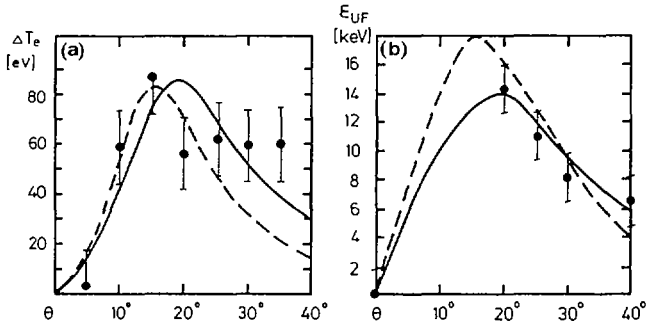


FIG.3. Variation of plasma parameters with incidence angle, for p-polarized 1.06 μm at 3×10^{13} W·cm^{-2}.
(a) Cold electron temperature enhancement, ΔT_e, due to Landau damping of the resonance electrostatic field;
(b) Non-thermal (ultra-fast) proton energy, ϵ_{uf}, due to field acceleration.
Solid and dashed lines are code predictions with and without profile steepening, respectively.

indicating that parametric side-scattering is negligible below this intensity. These reflectivities can therefore be taken, together with the measured transmissivities, as a measure of total laser energy absorption. It is seen from Fig.2 that reflectivity increases rapidly with increasing laser intensity until, above 10^{14} Wcm^{-2}, a small decrease, probably due to Brillouin side-scatter, is seen (I_{th} = 1.7×10^{14} Wcm^{-2} [25]). This therefore would not mean an increase in absorption.

When θ is non-zero, additional absorption occurs for p-polarised laser radiation. This leads to an increase in electron temperature and to the appearance of non-thermal ions with

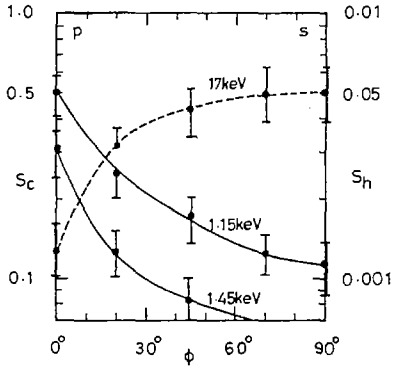


FIG.4. Cold and hot X-ray emission signals, S_c and S_h, in relative units, as functions of E-vector polarization angle, showing at p-polarization the cold signal (cold temperature) enhancement and the hot signal depletion.

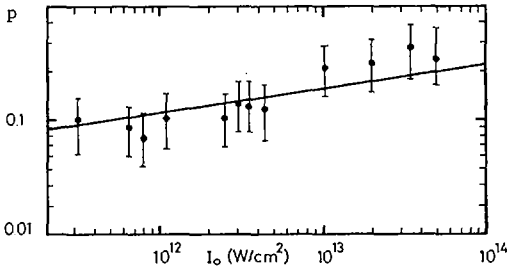


FIG.5. Ratio, P, of non-thermal proton energy to thermal plasma energy, as a function of laser intensity, I_0. Theoretical predictions are given by the solid line.

energies ε_{uf} > 10 keV. Using an electrostatic analyser, these were identified as protons, which are preferentially accelerated, due to their low m_i/z_i [20]. For $I_o = 3X10^{13}$ Wcm^{-2}, Fig.3(a) shows, as a function of θ, the measured electron temperature difference, ΔT_e, between the plasma generated by p- and s-polarised laser radiation. Fig.3(b) shows non-thermal proton energy as a function of θ, for p-polarisation. The maximum at $15^o \pm 5^o$, seen in Fig.3, is consistent with resonance absorption in a plasma with a density scale length L = 3 μm [2,12]. This value for L is in agreement with that calculated by ZWERG for measured R = 0.8, T = 0.1, T = 270 eV and z = 2.2.

Non-thermal protons are confined to an emission cone of $\pm 5^o$. They are seen only when the target surface is located within a range of ± 150μm of the focal plane, outside which the beam spread, $\Delta\theta$, reduces resonance absorption.

The acceleration and escape of particles with an initial velocity v > v_{es} will lead to a truncated velocity distribution[26]. Since the collision period for ultra-fast electrons is

much greater than their escape time, they will not contribute to the bremsstrahlung emission, and therefore a truncation should also be seen in the X-ray spectrum. Thin foils, 14.5μm and 29μm Be, monitored the thermal X-rays, while thick foils, 125μm Al and 500μm Al, monitored the hard X-rays. The cut-off energies were, respectively, 1.15 keV, 1.45 keV, 10 keV and 17 keV. The signals transmitted through each foil are plotted in Fig.4. as a function of E-vector polarisation angle, ϕ. The 10-keV signals are not shown because they are nearly equal to the 17-keV signals. As polarisation is varied from s to p, the thermal signals are enhanced due to Landau damping of the short-wavelength components, and the non-thermal signals are depleted due to wavebreaking of the long-wavelength components.

Fig.5 shows the measured ratios of non-thermal to thermal ion energy flux, P, obtained by integrating the ion emssion currents measured with the Faraday cup/electrostatic analyser, over the thermal and non-thermal peaks. These are compared with the theoretical values, calculated from equation(4) and they can be seen to be in good agreement, within the experimental errors.

4. DISCUSSION

For p-polarised laser radiation, with profile steepening included in the model, the ZWERG predictions are in good agreement with the experimental results. From Fig. 3(a) it can be seen that profile steepening[16,27-31] maintains the resonance for angles $\theta > \theta_{opt}$, so that the peak is broad, but this cannot account for all of the additional absorption. A non-smooth critical surface could also be important. Experiments made with roughened target surfaces (roughness $\simeq$ L) indicated, in this case, that the absorption was independent of the polarisation and incidence angles. Another effect that could be important but which has not yet been considered in detail is the change in density scale length during the plasma expansion.

Comparison of predictions shown in Fig. 3(b) indicates that profile steepening reduces the peak non-thermal ion energy slightly, by narrowing the width of the electrostatic field. It can be seen from equation(5), however, that this also increases the number of high-energy particles lost. The non-thermal ion loss relative to the thermal energy, P, shown by equation (4), is most strongly influenced by the term $\exp(-\varepsilon_{es}/T_c)$. Substituting equation (5), Δ and λ_D, the loss can be seen to be dependent on $\exp(-\nu_o L/T_c z_i)^{\frac{2}{3}}$. It is therefore expected to increase with laser wavelength and with profile steepening. The dependence on laser intensity is fairly weak, as can be seen from Fig.5.

For longer pulses a broader resonance field is expected. This would increase the ion energy but it would also increase the escape energy. Thus, although the energy of the escaping ions would be greater, the loss should remain approximately constant.

5. CONCLUSIONS

It has been demonstrated, at 1.06μm, that the electrostatic field spike accompanying resonance absorption accelerates non-thermal particles, predominantly of the lowest m_i/z_i. The angular width of the resonance is broad and this is partly

explained by steepening of the electron density profile, due to the associated electrostatic field pressure. However, another effect must be present, such as rippling of the critical surface which could grow from thermal fluctuations, or a time-dependent density scalelength. The energy loss to particles accelerated by the field is $\sim$ 25%, and therefore is not serious at 1.06μm. This loss is seen to depend weakly on laser intensity but it is predicted to be more strongly dependent on laser wavelength. Since these particles escape from the plasma, they do not contribute to the bremsstrahlung emission. Consequently,a truncated X-ray energy spectrum was seen at p-polarisation. In conclusion, these results indicate that resonance absorption is favourable for Laser-Fusion at 1.06μm.

REFERENCES

[1] DONALDSON, T P., HUBBARD, M., SPALDING, I.J., Phys. Rev. Lett. 37 (1976) 1348.
[2] BALMER, J.E., DONALDSON, T.P., Phys. Rev. Lett. 39 (1977) 1084.
[3] PEARLMAN, J.S., THOMSON, J.J., MAX, C.E., Phys. Rev.Lett. 38 (1977) 1397.
[4] MANES, K.R., RUPERT,V.C., AUERBACH, J.M., LEE, P., SWAIN, J.E., Phys. Rev. Lett. 39 (1977) 281.
[5] GODWIN, R.P., SACHSENMAIER, R., SIGEL, R., Phys. Rev. Lett. 39 (1977) 1198.
[6] LUTHER-DAVIES, B., Appl. Phys. Lett. 32 (1978) 209.
[7] ESTABROOK, K.G., VALEO, E.J., KRUER, W.L., Phys. Fluids 18 (1975) 1151.
[8] FREIDBERG, J.P., MITCHELL, R.W., MORSE, R.L., Phys. Rev. Lett. 28 (1972) 795.
[9] FORSLUND, D.W., KINDEL, J.M., LEE, K., LINDMAN, E.L., MORSE, R.L., Phys. Rev. A11 (1975) 679.
[10] DEGROOT, J.S., TULL, J.E., Phys. Fluids 18 (1975) 672.
[11] NUCKOLLS, J., WOOD, L., THIESSEN, A., ZIMMERMAN, G., Nature 239 (1972) 139.
[12] WÄGLI P., DONALDSON, T.P., Phys. Rev. Lett. 40 (1978) 875.
[13] GINZBERG, V.L., Propagation of Electromagnetic Waves in PLasma, Pergamon, Oxford (1970).
[14] BOYD, J.T.M, HEWITT, W.T., J.Phys.D. 10 (1977) 249.
[15] WÄGLI, P., DONALDSON, T.P., LÄDRACH, P., Appl. Phys. Lett. 32 (1978) 638.
[16] BOCHER, J.L., ELIE, J.P., MARTINEAU, J., RABEAU, M., PATOU, C., in Laser Interaction and Related Plasma Phenomena, edited by H.J. Schwarz and H. Hora (Plenum, New York, 1976), Vol.4.
[17] HORA, H., in Laser Interaction and Related Plasma Phenomena, edited by H.J. Schwarz and H. Hora (Plenum, New York, 1971), Vol.1, P383.
[18] SILIN, V.P., Pis'ma Zh. Eksp. Teor. Fiz. 21 (1975) 333 (JETP Lett. 21 (1975) 152).
[19] MULSER, P., Plasma Physics 13 (1971) 1007.
[20] DECOSTE, R., RIPIN, B.H., Phys. Rev. Lett. 40 (1978) 34.
[21] MCWHIRTER, R.W.P., in Plasma Diagnostic Techniques, edited by R.H. Huddlestone and S.L. Leonard (Academic Press, New York, 1965), chap. 5.
[22] DONALDSON, T.P., BALMER, J.E., WÄGLI, P., to be published.

[23] DONALDSON, T.P., Plasma Physics 20 1279 (1978).
[24] BALMER, J.E., DONALDSON, T.P., Seka, W., Zimmermann, J., Opt. Commun. 24 (1978) 109.
[25] LIU, C.S., ROSENBLUTH, M.N., WHITE, R.B., Phys. Rev. Lett. 31 (1973) 697.
[26] PEARLMAN, J., MORSE, R.M., Phys. Rev. Lett. 40 (1978) 1652.
[27] ATTWOOD, D.T., SWEENEY, D.W., AUERBACH, J.M., LEE, P.H.Y., Phys. Rev. Lett. 40 (1978) 184.
[28] AZECHI, H., ODA, S., TANAKA, K., NORIMATSU, T., SASAKI, T., YAMANAKA, T., YAMANAKA, C., Phys. Rev. Lett. 39 (1977) 1144.
[29] FEDOSEJEVS, R., TOMOV, L.V., BURNETT, N.H., ENRIGHT, G.D., RICHARDSON, M.C.,Phys. Rev. Lett. 39 (1977) 932.
[30] ZAKHARENKOV, Yu. A., ZOREV, N.N., KROKHIN, O.N., MIKAILOV, Yu.A., RUPASOV, A.A., SKLIZKOV, G.V., SHIKANOV, A.S., ZhETF Pis. Red. 21 (1975) 557.
[31] DONALDSON T.P., SPALDING, I.J., Phys. Rev. Lett. 36 (1976) 467.

FAST IONS IN LASER-PRODUCED PLASMA

N.E. ANDREEV, A.S. SHIKANOV, V.T. TIKHONCHUK,
Yu.A. ZAKHARENKOV, N.N. ZOREV

P.N. Lebedev Institute of Physics of the
USSR Academy of Sciences,
Moscow, Union of Soviet Socialist Republics

Abstract

FAST IONS IN LASER-PRODUCED PLASMA.

The effect of stream acceleration of ions with an energy of up to ~ 0.5 MeV was observed in experiments on power laser irradiation of spherical targets. A resonance ion acceleration theory allowing for a non-linear plasma-wave interaction in the critical-density region was proposed. The mechanism of ion acceleration was shown to result in the fast anisotropic ion propagation. The estimated values of energy and number of fast ions are in accordance with the experimental data.

1. EXPERIMENTAL RESULTS

Experiments were performed with the powerful laser device 'Kalmar' [1]. The laser radiation was focused from nine directions onto spherical glass targets with diameters varying from 80 to 200 μm. The targets were situated in the centre of a vacuum chamber, where the diameter of the laser beam was ~ 150 μm. The light energy was $E \lesssim 100$ J, the pulse duration $\tau \approx 2.5$ ns on the base level, and the flux density at the target, $q \sim 10^{14}$ W·cm^{-2}.

Interferometric measurements [2] carried out at pressures of $p \sim 10^{-6} - 1$ torr in the vacuum chamber showed a high symmetry of plasma corona expansion. But at higher residual-gas (D_2) pressure ($p \gtrsim 5$ torr) it was discovered [3] that, along with the spherical plasma expansion, there appeared some 'streams' of high directivity (Fig. 1), and during the first moments after the heating pulse, the velocity of the streams (up to $v \approx (2-3) \times 10^8$ cm·s^{-1}) significantly exceeded the velocity of plasma corona spherical expansion. The direction of 'stream' propagation and the number of streams changed from shot to shot, but the angle between any 'stream' direction and the nearest heating beam varied within $15° \lesssim \theta \lesssim 30°$.

The method of interferograms allowed us to draw the conclusion that the electron density n_e in the 'stream' corresponded to full ionization of the residual gas and increased with the gas pressure.

We used multi-frame schlieren photography [4] as a second method for the observation of residual-gas ionization region dynamics (up to ~ 300 ns). A typical

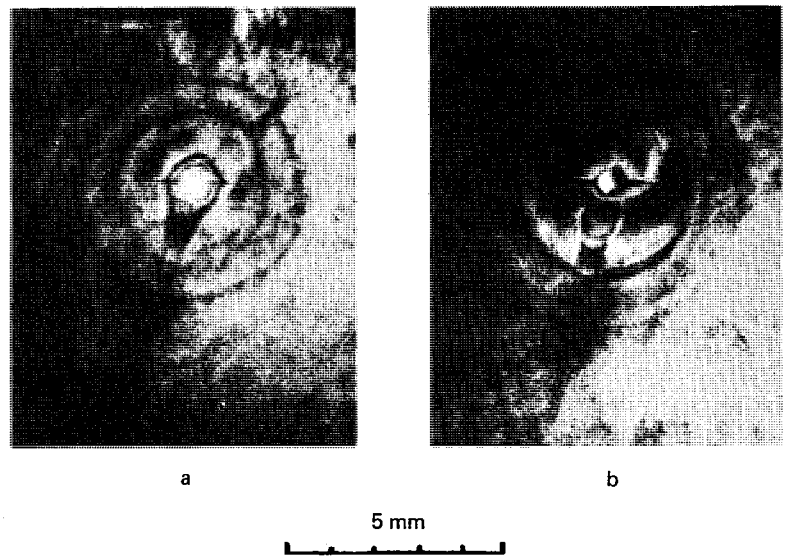


FIG.1. Interferograms of plasma expanding in deuterium ($p \approx 10$ torr). a) 3.1 ns, b) 5.4 ns.

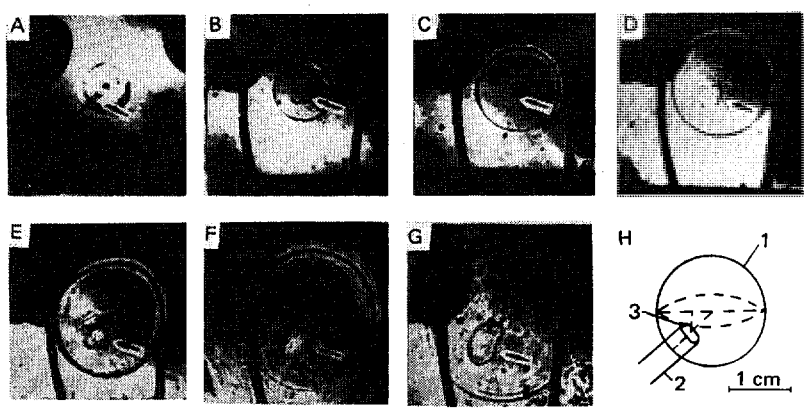


FIG.2. Laser plasma seven-frame schlieren photography, $p \approx 16$ torr. a) 12 ns, b) 20 ns, c) 48 ns, d) 92 ns, e) 136 ns, f) 226 ns, g) 316 ns, h) scheme of interaction of cylindrical (2) and spherical (1) shock waves; 3 is the ring compression region.

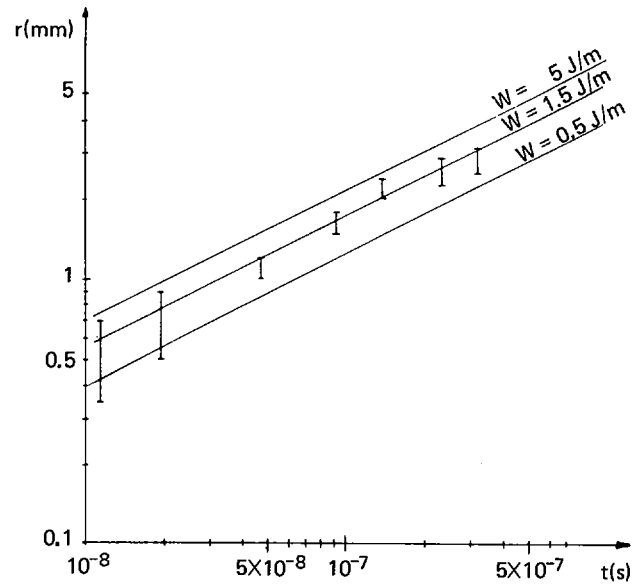


FIG.3. Experimental r-t diagram of cylindrical shock wave propagation (dots). Curves correspond to the blast wave scaling applied to different explosion energies W.

seven-frame schlieren photograph is presented in Fig. 2. The first frames demonstrate that the 'stream' diameter increases with time, which may be explained by the formation of a cylindrical shock wave expanding from the ionized gas region. 'Stream' visualization at later stages of observation was impossible because of the limited sensitivity of the method applied. The sensitivity was, however, sufficient to record a circular region of condensation resulting from the interaction of a cylindrical shock wave with a spherical one formed by isotropic plasma expansion (Fig. 2b–d). This region on the photographs has the shape of an ellipse whose eccentricity depends on the angle between the direction of observation and the 'stream' direction. It allowed us to determine both the spatial position of the 'stream' and an r-t diagram of the cylindrical shock wave expansion (Fig. 3). Its movement is satisfactorily approximated by the blast-wave scaling, $r = [\alpha(\gamma)\, W]^{1/4} \rho^{-1/4}\, t^{1/2}$, where W is the explosion energy, ρ the gas density, and $\alpha(\gamma)$ a coefficient depending on the ratio of the specific heats γ. This allowed us to determine W, which is usually equal to ~ 0.01 J·cm^{-1} (with $\sim 100\%$ accuracy). Such an accuracy is connected with some uncertainty of γ, which depends on the gas temperature behind the shock wave front and may change in time.

In the case of vacuum experiments ($p \sim 10^{-5}$ torr), the plasma expansion was investigated by means of a few charge collectors distributed in the chamber. In

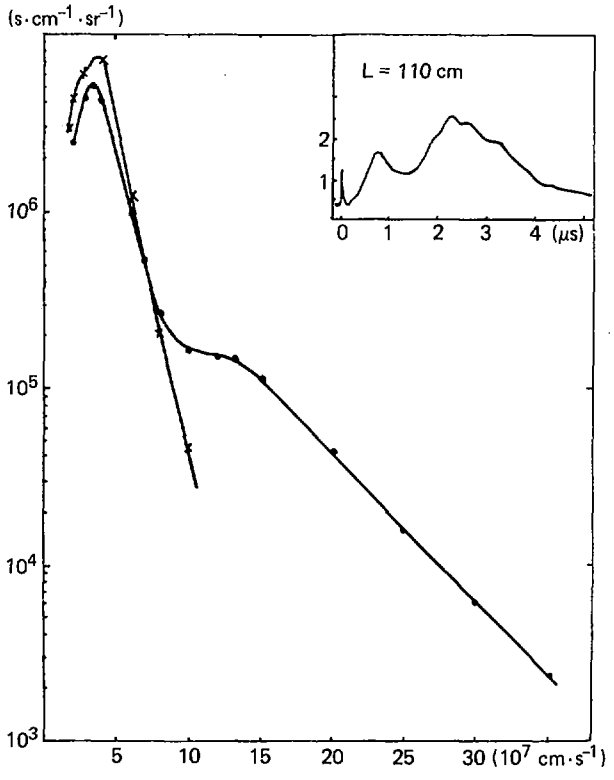


FIG.4. Ion-velocity spectrum from two charge collectors. Oscilloscope voltage trace for one of them is shown.

most of the shots, the ion current pulses corresponded to thermal ions ($v \leqslant 10^8$ cm·s^{-1}) only, and the same range of expansion velocities was obtained interferometrically. The number of ions per steradian in different directions varied by a factor of $\lesssim 1.5$, which was nearly equal to the measurement error. Nevertheless, in some shots, a group of ions with velocities $> 10^8$ cm·s^{-1} was observed, and, in contrast to thermal ions, their expansion was anisotropic. Figure 4 shows the ion-velocity spectrum, which was obtained from two charge collectors placed in the chamber at ~ 90° to each other. The voltage trace from one of them (shown in the inset) led to the discovery of a measurable quantity of fast ions with velocities of up to 3.5×10^8 cm·s^{-1}. The total number of fast ions ($v > 10^8$ cm·s^{-1}) incident on the collector was ~ 10^{10}, or ~ 5% of all plasma ions recorded. Their energy was ~ 40% of the total ion energy recorded in the solid angle. The mean fast-ion energy was ~ 280 keV.

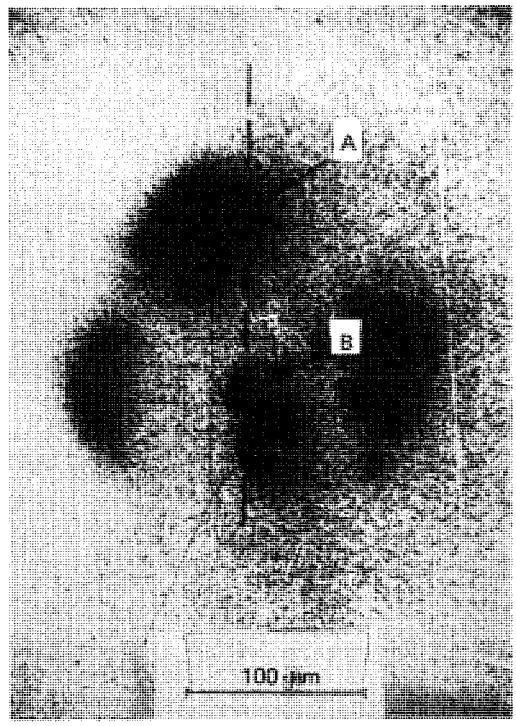


FIG.5. Plasma corona image in 2 ω radiation. Spectrograph slit position is shown by dotted line.

Thus, the collector measurements confirmed the anisotropic character of the fast-ion expansion and permitted us to obtain the velocity spectrum of these ions. But owing to the limited aperture, it was impossible to estimate, by this method, the total number of fast ions produced in the spherical plasma.

The use of high-speed optical methods in our experiments allowed us to estimate the total number of fast ions. The energy loss of a plasma ion with a velocity of $\sim 2.5 \times 10^8$ cm·s^{-1} in the ambient gas [5] is dE/dx $\sim$ 20 keV·cm^{-1}. The ratio of the cylindrical shock wave energy W to dE/dx may be regarded as an approximate measure of the total number of fast ions in the 'stream'. The mean value was 5×10^{12} ions, or 0.1%, of all the target ions. The total fast-ion energy equalled the stream energy and was $\lesssim 3\%$ of the absorbed laser energy.

There was no correlation between the occurrence of a stream and the re-arrangement of plasma X-ray (1–2 keV) luminosity. Nevertheless, a coincidence between the spatial position of the streams and the plasma second-harmonic emissivity maxima was observed. The size of these bright spots (Fig. 5) was close to the spatial resolution ($\sim$ 15 μm) of the applied optics. Simultaneously, in the

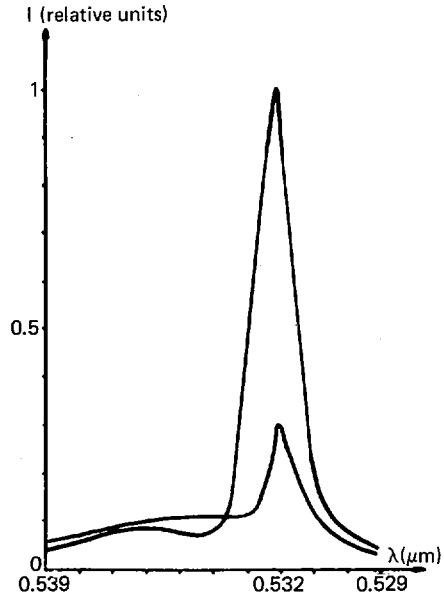


FIG. 6. 2 ω spectral intensity distributions at two plasma corona points (a and b) indicated by arrows in Fig. 5.

same direction as the second harmonic, images were taken, the spectrum near $\lambda = 0.53$ μm was recorded. The spectrum consisted of two components: the main one, which was 'red'-shifted up to some ångströms and an additional component in the form of a long-wavelength background. The interpretation of this behaviour was carried out in Ref. [6] and connected the main component with a linear transformation of the incident light wave into plasma waves in non-uniform plasma, and the additional component with parametric turbulence effects. Investigations of the second-harmonic spectrum along the target surface showed that, in the bright spots, a measurable increase of the main component, in comparison with other parts of the surface, occurred (Fig. 6).

2. RESONANCE ACCELERATION OF IONS IN LASER-PRODUCED PLASMA

The existence of accelerated ions cannot be explained in terms of the well-known theories because of their high energy and the small width of their angular distribution. An analysis of various mechanisms of acceleration shows that a resonant increase in the laser-beam electric-field amplitude in the critical-density region is the only mechanism resulting in a jet stream of the plasma.

The effect of resonance acceleration of ions in the critical-density region of the linear approximation on the pump radiation intensity was considered in the literature. The main theoretical principles were formulated in Ref. [7], and generalized in Ref. [8] for the case of a laser plasma of average pump intensities. Physically, the effect of resonance acceleration is connected with the increase in the electric-field component in the plane of incidence (p-component) at the point of plasma resonance ($\omega_{Le}(x) = \omega_0$), for the case of oblique incidence of the electromagnetic wave on an inhomogeneous plasma slab. In linear approximation, the maximum field amplitude in the resonance region E_* was determined [9]:

$$E_* = E_0 \Phi(\theta)(2\pi k_0 L)^{-1/2} \omega_0/\nu_{eff}$$

where E_0 is the vacuum amplitude of the p-polarized pump wave, Φ is the resonance function of the angle of incidence θ, $\Phi(\theta) \approx 1$ if $\theta \approx \theta_r \approx (k_0 L)^{-1/3}$, $k_0 = \omega_0/c = 2\pi/\lambda_0$, and L is the density scale length in the critical region. The effective collision frequency ν_{eff} is determined by the Coulomb collision frequency ν_{ei} and by the convection of plasma waves out of the resonance region:

$$\nu_{eff} = \max\{\nu_{ei}, \omega_0(r_D/L)^{2/3}\}$$

The width of the resonance peak Δx is also determined by ν_{eff}:

$$\Delta x = L\, \nu_{eff}/\omega_0$$

However, in the case of a hot plasma when

$$\nu_{ei} < \omega_0 (r_D/L)^{2/3}$$

the region where intense Langmuir waves exist is broader because the Langmuir waves leaving the resonance region can carry away energy at a distance of

$$\Delta x_L \cong 3\,(k_{st}\, r_D)^2\, L$$

to lower-density plasma regions where they are absorbed by electrons through the Cherenkov effect. For a Maxwellian distribution of electrons, $k_{st} \cong 0.3\, r_D^{-1}$. The abundant pressure of the electric field of the Langmuir oscillations pushes the plasma away from the critical-density region. The maximum energy of the accelerated ions is [8] given by

$$n_i M_i v_i^2 \cong E_*^2/4\pi$$

We find the domain of application of linear-theory formulas by realizing that the resonantly excited peak of Langmuir waves may be parametrically unstable. From

the stability analysis, it follows that the non-linear reconstruction of field structure may be neglected if

$$\frac{E_0^2}{4\pi n_c T_e} \lesssim 2\pi k_0 L \Phi^{-2}(\theta)\left(\frac{\nu_{eff}}{\omega_0}\right)^3 \max\left\{1, \frac{\nu_{eff}}{\omega_0}\left(\frac{\omega_{Le}}{\omega_{Li}}\right)^2\right\} \quad (1)$$

The electron non-linearities (self-crossing of trajectories [10]) represent a stronger restriction than Eq. (1) only for a very inhomogeneous plasma, when $L < r_D\, \omega_{Le}/\omega_{Li}$. This inequality cannot be fulfilled under the real conditions of Nd-laser-($\lambda_0 = 1\ \mu m$)-produced plasmas.

The development of an aperiodic instability leads to a further increase in the electric-field amplitude and, thus, to an increase in the energy of the accelerated ions. First, we shall find the initial scale of the aperiodic instability. For a short density scale length, $L < r_D\, \omega_{Le}^2/\omega_{Li}\nu_{eff}$, the plasma waves in the resonance region are subject to a hydrodynamic aperiodic instability in the region above the threshold where Eq. (1) is not valid. The initial scale k_a^{-1} of this instability is determined to be

$$k_a r_D \cong \frac{r_E}{r_D}\,\frac{\omega_{Li}}{\omega_{Le}}\,\frac{\Delta x}{r_D}$$

Since k_a^{-1} is much less than the peak width Δx, the parametric hydrodynamic aperiodic instability leads to a break-up of the resonance peak into several density wells (cavitons) where the Langmuir oscillations have been captured. The further development of these cavitons may be described by ignoring their mutual interaction. We obtain an estimate of the maximum energy of the accelerated ions from the maximum intensity of the Langmuir field in the caviton. We assume that the change in the total energy of the captured Langmuir field during the process of non-linear caviton evolution is small [11].

The minimum scale of caviton collapse, Δx_{min}, is determined from the condition of absence of Landau damping in the captured field. Thus, when $\Delta x_{min} \sim k_{st}^{-1}$, the Langmuir oscillations of shorter wavelength damp immediately, owing to the Cherenkov effect. The condition of energy conservation in the caviton leads to the following estimate of the maximum electric-field amplitude in the non-linear regime:

$$E_{max} \sim E_* (k_{st}/k_a)^{3/2}$$

For the case of a hot plasma, we can obtain the following estimate of the maximum Langmuir field density in the caviton:

$$\frac{E_{max}^2}{4\pi} \cong \frac{\sqrt{2\pi}}{\Phi(\theta)}\,(k_{st} r_D)^3\,\frac{(n_c T_e)^{3/2}}{E_0/\sqrt{4\pi}}\left(\frac{\omega_{Le}}{\omega_{Li}}\right)^3\left(\frac{v_{Te}}{c}\right)^{5/3}(k_0 L)^{-7/6}$$

The total number of cavitons in the critical-density region, $N \sim \Delta x_L\, k_a$, may be high because of the large dimension of the high-intensity field region Δx_L:

$$N \sim k_a \Delta x_L \sim \frac{3(k_{st} r_D)^2}{\sqrt{2\pi}} \Phi(\theta) \left(\frac{c}{v_{Te}}\right)^2 (k_0 L)^{3/2} \frac{\omega_{Li}}{\omega_{Le}} \frac{E_0}{\sqrt{4\pi n_c T_e}}$$

The caviton life-time $\tau \sim (k_a v_s)^{-1}$ is determined by the collapse time because the time Δt of dissipation of an a.c. electric field in a caviton is very small, $\Delta t \ll \tau$.

Now, we shall obtain the energy of an ion travelling through a structure of N non-stationary (collapsing) cavitons. The energy is acquired only by the ions contained in the caviton. For ions going through the caviton, we may consider the caviton to be a non-stationary potential barrier. An increase in the ion energy $\Delta\mathscr{E}_i \equiv \Delta(M_i v_i^2)$ is equal to the change in barrier energy during the time of flight, $\Delta t_i \sim (k_a v_i)^{-1}$, i.e.

$$\Delta\mathscr{E}_i \sim (\Delta t_i/\tau)\,(E_{max}^2/4\pi n_i) \sim (v_s/v_i)\,(E_{max}^2/4\pi n_i)$$

where v_s is the sound speed.

Therefore, after passing through one caviton, the ion assumes a small fraction of its total energy. But the maximum energy of the ion passing through all N cavitons is rather high:

$$\mathscr{E}_i \sim zT_e(NE_{max}^2/4\pi n_c T_e)^{2/3} \qquad (2)$$

where z is the average ion charge. The acceleration mechanism in question leads to a pronouncedly anisotropic ion stream because all cavitons are arranged in the direction of the density gradient. Ions that are directed at an angle to the gradient cannot be accelerated in all cavitons, and, therefore, their energies cannot be noticeably increased. The process of acceleration occurs in a very short time, of the order of the caviton collapse time. Note that the expression obtained for $\mathscr{E}_i$ depends weakly on the field intensity for the pumping wave because $N \sim E_0$ and $E_{max} \sim E_0^{-1}$. To obtain the total number of accelerated ions, we must know the plasma volume in which the cavitons exist. Its longitudinal size is Δx_L, and its transverse size depends on the square of the distance to the point S on the critical surface where the incident angle of radiation θ is close to the optimum one: $\theta_r \cong (k_0 L)^{-1/3}$. If the diameter of the laser beam cross-section at the target surface is larger than the target diameter, and $k_0 L \gg 1$, we may put $S \cong (R_c \theta_r)^2$, where R_c is the radius of curvature of the critical surface. The total number of accelerated ions is

$$N_i \cong \frac{3}{z}(k_{st} r_D)^2\, n_c\, L R_c^2\, (k_0 L)^{-2/3}$$

This formula should be considered to be the upper limit for the number of fast ions since not all ions acquire the maximum energy, Eq. (2). The energy of the 'stream' is given by

$$N_i \mathscr{E}_i \sim T_e n_c R_c^2 \lambda_0 (k_{st} r_D)^{16/3} (c/v_{Te})^{2/9} (\omega_{Le}/\omega_{Li})^{4/3} (k_0 L)^{5/9}$$

This equation depends implicitly on the pumping-field density through the hydrodynamic parameters only: $N_i \mathscr{E}_i \sim R_c^2 L T_e^{2/3}$. Because of the weak dependence on E_0, the stream energy should decrease with the pump energy.

In the experiment discussed ($T_e \cong 0.8$–1 keV, $L \cong 20$ μm, $R_c \cong 100$ μm, $z \cong 10$, $A \cong 20$) Eq. (1) is valid for $q_0 > 2 \times 10^{13}$ W·cm^{-2}. The fluxes used in the experiment, $q_0 \sim 10^{14}$ W·cm^{-2}, exceed this threshold value. According to Eq.(2), the maximum energy of the accelerated ions under the conditions of the experiment discussed is (T_e in keV) given by

$$\mathscr{E}_i \sim 20\, z^{1/3} A^{2/3} T_e^{8/9} (L/\lambda_0)^{2/9} \text{ [keV]} \tag{3}$$

which, with the parameters given above, amounts to a value of $\mathscr{E}_i \sim 1$ MeV, in agreement with the experimental data. Note that, by Eq. (3), the ion energy increases with the atomic weight of the target matter A and the average charge z.

The number of accelerated ions (L, R_c, λ_0 in μm)

$$N_i \sim 10^8 (L^{1/3} R_c^2 / z\, \lambda_0^{4/3})$$

under the conditions of experiment discussed is $\sim 10^{12}$. This value is slightly lower than the experimental one. However, taking into account the low accuracy of the experimental measurements of the total stream energy, and hence of the number N, we may consider the agreement of calculated and measured values to be satisfactory.

It is worth noting that, with increasing flux density of laser radiation, the energy of the accelerated ions in the plasma resonance (3) should be substantially increased. At the same time, the directivity pattern of fast ions should become wider because of the increasing steepness of the plasma density profile in the critical region. Fast C VI ions with an energy of ~ 0.5 MeV were discovered in the experiment [12] at a neodymium laser radiation flux density of $\sim 10^{15} - 10^{16}$ W·cm^{-2}. Energy and direction of emission of these ions can be also explained within the framework of the acceleration mechanism considered above.

It should be noted that the observed effect of ion acceleration cannot essentially distort the compression symmetry and may be used as a diagnostic method for measuring the plasma parameters in the critical-density region.

REFERENCES

[1] BASOV, N.G., KOLOGRIVOV, A.A., KROKHIN, O.N., RUPASOV, A.A., SHIKANOV, A.S., SKLIZKOV, G.V., ZAKHARENKOV, Yu.A., ZOREV, N.N., Laser Interaction and Related Plasma Phenomena, Vol. 4, Plenum Press, New York (1976).
[2] ZAKHARENKOV, Yu.A., RODE, A.V., SKLIZKOV, G.V., FEDOTOV, S.I., SHIKANOV, A.S., Sov. J. Quant. Electron. **4** (1977) 815.
[3] KROKHIN, O.N., SHIKANOV, A.S., SKLIZKOV, G.V., ZAKHARENKOV, Yu.A., in Phenomena in Ionized Gases (Proc. 13th Int. Conf. Berlin, 1977) 883.
[4] EROKHIN, A.A., ZAKHARENKOV, Yu.A., ZOREV, N.N., SKLIZKOV, G.V., SHIKANOV, A.S., Sov. Plasma Phys. **4** (1978) 648.
[5] NEMETS, O.F., GOFMAN, Yu.V., Nuclear Physics Reference Book, Naukova Dumka, Kiev (1975).
[6] BYCHENKOV, V.Ya., ZAKHARENKOV, Yu.A., KROKHIN, O.N., RUPASOV, A.A., SILIN, V.P., SKLIZKOV, G.V., STARODUB, A.N., TIKHONCHUK, V.T., SHIKANOV, A.S., Sov. JETP Lett. **26** (1977) 500.
[7] GUREVICH, A.V., SILIN, V.P., Sov. J. Nucl. Phys. **2** (1965) 280.
[8] SILIN, V.P., Sov. JETP Lett. **21** (1975) 333.
[9] GINZBURG, V.L., Electromagnetic Wave Propagation in Plasma, Nauka, Moscow (1967).
[10] EROKHIN, N.S., ZAKHAROV, V.E., MOISEEV, S.S., Sov. JETP **56** (1969) 179.
[11] GORIAEV, V.V., KINGSEP, A.S., RUDAKOV, L.I., Sov. Izvestiya Vuzov., Radiofizika, **19** (1976) 691.
[12] McLEAN, E.A., DECOSTER, R., RIPIN, B.H., STAMPER, J.A., BODNER, S.E., Appl. Phys. Lett. **31** (1977) 9.

DISCUSSION

ON PAPERS V-1-1 AND V-1-2

R. PETSCH: You say, in connection with the graph of reflectivity as a function of incident laser activity, that this is specular reflection. Your target is plane, and you have an incident angle of 0°. How can you be sure that this light is not due to Brillouin backscatter?

T.P. DONALDSON: We do not have Brillouin backscatter, because, if we angle the target at 20° so that specular reflection does not enter the focusing lens, we see only a very small backscatter signal. In any case the threshold for Brillouin backscatter, taking into account our plasma conditions, is calculated to be above 10^{14} W · cm^{-2}.

H. HORA: You mentioned that measurements of 1 MeV ions were found to be in agreement with calculations. What is the ion charge number?

T.P. DONALDSON: The average ion charge number, in the study by Andreev and co-workers (paper V-1-2), was 10. I must point out, however, that these 1 MeV ions are seen only in the high-energy tail of the fast-ion distribution function. The mean ion energy was lower.

H. MOTZ: I noticed that there was a high-temperature tail in the ΔT curve on your first slide, and I wonder how you account for it.

T.P. DONALDSON: We do not have any definite explanation for this. However, we find, when we include weak profile steepening in our theoretical calculations, that this could account for part of the high-temperature tail. Another possible explanation could be rippling of the critical surface, which would then allow more absorption at larger angles.

A. HASEGAWA: We have recently noticed that ion vortices may be formed in laser-pellet interactions – vortices which can accelerate the ions and form a magnetic field. Do you see any evidence that these might be a cause of density depletion and ion acceleration?

T.P. DONALDSON: We do not claim to see very great density depletion – only a weak profile modification. We do not know whether our experimental evidence for ion acceleration is consistent with ion vortices or not.

NON-LINEAR THEORY OF COLLECTIVE PROCESSES IN LASER-PELLET INTERACTION AND SOLITON GENERATION

H.H. CHEN, C. GREBOGI, C. S. LIU,
V.K. TRIPATHI
University of Maryland,
College Park, Maryland,
United States of America

Abstract

NON-LINEAR THEORY OF COLLECTIVE PROCESSES IN LASER-PELLET INTERACTION AND SOLITON GENERATION.

Soliton generation through the ponderomotive force effect of large- amplitude electrostatic waves generated locally around the resonance region is proposed as a saturation mechanism for collective processes occurring in laser-pellet interaction. The non-stationary behaviour is discussed in detail by following the growth and convection of solitons. Their physical significance, such as density modifications, is also discussed. Collective processes involving the interaction of plasma and ion waves with laser radiation dominantly affect the absorption and scattering of laser light and determine the efficiency of laser-pellet coupling. Because of the requirements of frequency and wavenumber matching, many collective interactions are localized in relatively narrow regions of the corona: the resonance absorption and parametric decay are localized near the critical layer, and decay into two plasmons and absolute Raman backscattering are localized near the layer of quarter-critical density. As a result of wave growth in a localized region, ponderomotive force tends to push the plasma out of the region of high wave intensity, leading to the formation of soliton and density cavity. The local reduction of the plasma density has two effects: (i) It gives rise to a non-linear frequency shift of the plasma wave which is proportional to $-|E|^2/16\pi n T$, the ratio of wave energy to the plasma kinetic energy. Thus when the wave grows to an amplitude sufficiently large for the non-linear frequency to become comparable to the growth rate of the parametric processes, the three-wave resonance becomes detuned and the parametric instability shuts off. (ii) It modifies the density profile, thereby affecting the growth of subsequent parametric instability. In this paper, the roles of soliton formation in the resonance absorption at critical density, parametric decay into two plasmons and Raman backscattering at quarter-critical density are discussed. Effects of a d.c. magnetic field on the resonance absorption processes are also discussed.

1. RESONANCE ABSORPTION [1–3]

Consider an electromagnetic wave $E_{in}=E_0\exp(ik_{0y}y+ik_{0x}x-i\omega_0 t)+c.c.$, obliquely incident onto a plasma slab with increasing density $n=n_0(1+x/L)$. The nonlinear equation for the slowly varying amplitude $E(x,t)$ of the driven Langmuir wave $\varepsilon(x,t)=E(x,t)\exp(-i\omega_p t+ik_{0y}y)+c.c.$ in a nonuniform

plasma near the critical density (x=0) is written in dimensionless form as [3,4]

$$i\frac{\partial E}{\partial t}+\frac{\partial^2 E}{\partial x^2}+2\left(|E|^2-\alpha x+\frac{i\Gamma}{2}\right)E=E_d\theta(t) \tag{1}$$

where $E_d=E_0\phi(s)/(2\pi k_0 L)^{1/2}$; $\phi(s)$ is the usual resonance function with $s=(k_0L)^{1/3}\sin\beta$; and $\beta=\tan^{-1}k_{0y}/k_{0x}$; $\alpha=1/2L$; $t=\tau-\omega_p y/3k_y v_e^2$ is the shifted time variable; Γ the collisional damping rate; and $\theta(t)$ is the Heaviside step function. The dimensionless variables are expressed in the unit of ω_{pe}^{-1} for time, λ_D for spatial length, and $4(\pi nT)^{1/2}$ for E. Without the nonlinear term, Eq. (1) can be solved analytically by Green's function technique,

$$E(x,t)=iE_d\int_0^t \exp\left[\frac{4i\alpha^2}{3}(t'-t)^3+(2i\alpha x+\Gamma)(t'-t)\right]dt' \tag{2}$$

Initially, i.e. $t\ll(3x/2\alpha)^{1/2}$, the wave convection is not important and we have

$$E(x,t)=\frac{E_d}{\alpha x-i\Gamma/2}\sin[(\alpha x-i\Gamma/2)t]\exp[-(i\alpha x+\Gamma/2)t] \tag{3}$$

which shows that the wave amplitude grows linearly in time and the width shrinks as t^{-1} for $|\alpha x-i\Gamma/2|\ll 1$. Asymptotically, i.e. $t\gg(3x/2\alpha)^{1/2}$, a steady state is attained when the linear growth is balanced by the convection. Near x=0, the amplitude is at the level

$$E_c\sim iE_d\pi(2\alpha)^{-2/3}[Gi(0)+iAi(0)] \tag{4}$$

where $d\sim\alpha^{-1/3}$ is the width of the main peak of the Airy function. Landau damping becomes important for $k\lambda_D\gtrsim 0(1)$ or $\alpha x\gtrsim 1$, beyond which the wave is heavily damped.

For $\omega_{pi}t_c<1$, or $(m/M)^{1/2}(L/\lambda_D)^{2/3}\ll 1$, convective saturation takes place much before the ions start to move by ponderomotive pressure. The linear Eq. (1) then treats properly the saturation until several ion plasma periods, after which the nonlinear term in Eq. (1) begins to play a role. We may therefore take the convectively saturated amplitude (4) as the initial wave amplitude and ask how does the nonlinearity change this initial amplitude after the ions start to move. For a given initial amplitude E(x,t=0), the condition for N-soliton formation is [5]

$$\pi(N+\tfrac{1}{2})\geq\int|E|dx\geq\pi(N-\tfrac{1}{2}) \tag{5}$$

Substituting the convectively saturated amplitude given by Eq. (4) into Eq. (5), and remembering that Landau damping limits the wave E_c to $x\leq L$, we find

$$\int|E_c|dx=E_cL=\frac{\pi E_d}{(2\alpha)^{5/3}}>N\pi \tag{6}$$

The final density scale length, L_f, can thus be obtained from Eq. (6) by setting $(2\alpha)^{-1}=L_f$ and requiring no further soliton generation:

$$L_f=\frac{1}{E_d^{3/5}}\sim\frac{(k_0L_f)^{3/10}}{p^{3/10}}\quad\text{or}\quad L_f\sim(k_0/p)^{3/7} \tag{7}$$

This scaling of the density scale length with incident power P is consistent with the result of numerical simulations [6].

We next consider the case of $\omega_{pi}t_c>1$, in which the scale length is so long that the convective saturation time is much longer than the ion plasma period. In this case the soliton forms before the wave convects out and the saturation of the linear growth is primarily due to the detuning of the resonant frequency by the soliton. Initially the wave amplitude grows according to Eq. (3) as the convection is unimportant. As it grows in amplitude, its width shrinks so that the integral $\int_{-\infty}^{\infty}|E|dx\simeq \pi E_d/\alpha$ is independent of time. Comparing it with Eq. (5), we obtain a threshold driving field for N-soliton formation:

$$N+\frac{1}{2} > E_d/\alpha > N-\frac{1}{2} \tag{8}$$

This threshold condition appears to explain the numerical calculation [4] and experimental observations [7] very well. On the other hand, soliton growth can be calculated by varying the soliton parameters. For one-soliton solutions, we have $E=Ac^{i\phi}$ with $A=2\eta(t)\,\mathrm{sech}2\eta(t)[x-x_0(t)]$ and $\phi=2[\xi(t)-\alpha t]x+\phi_0$. From Eq. (1), we obtain

$$\dot{x}_0=4(\xi-\alpha t),\quad \dot{\phi}_0=4[\eta^2-(\xi-\alpha t)^2] \tag{9}$$

and

$$\dot{\eta}=\frac{\pi E_d}{2}\,\mathrm{sech}\,\frac{\pi(\xi-\alpha t)}{2\eta}\cos[2(\xi-\alpha t)x_0+\phi_0],\ \text{and}\ \dot{\xi}=(\xi-\alpha t)\dot{\eta}/\eta \tag{10}$$

We observe two stages of soliton growth. The soliton grows first linearly in time with

$$\eta=\frac{\pi E_d t}{2},\quad \xi=\alpha t/2,\quad \phi_0=[\pi^2E_d^2-\alpha^2]\frac{t^3}{3}\ \text{and}\ x_0\simeq-\alpha t^2 \tag{11}$$

and then saturates when the phase shift due to nonlinearity detunes the soliton from the driver. The saturation time can be estimated by setting $2(\xi-\alpha t)\times x_0+\phi_0 t^3[3\pi^2E_d^2+2\alpha^2]/3\simeq\pi/2$, or $t_s\simeq E_d^{-2/3}$. The staurated η and ξ are then

$$\eta_s=E_d^{1/3}\quad\text{and}\quad \xi_s=\frac{\alpha}{2}E_d^{-2/3} \tag{12}$$

The solitons thus generated will then propagate down the density gradient and be damped by interacting with hot electrons. Since the energy carried away by the solitons is eventually absorbed by the plasma, we can calculate the absorption coefficient of the laser light due to direct soliton generation for this case of $\omega_{pi}t_c>1$:

$$a=\frac{4\dot{\eta}}{|E_0|^2c}=\frac{|\phi(s)|^2}{\pi}$$

The maximum value is about 30%. Recently, Shukla et al. [8] had done a similar calculation on the soliton growth at resonance absorption. Their results agree with ours when $E_d/\alpha=1$. However, they also calculated single soliton growth with $E_d/\alpha=100\gg1$, which is obviously incorrect since Eq.(8) shows clearly that in this case one should consider multi-soliton instead of a single soliton production.

In the presence of a dc-magnetic field, often generated from the laser-pellet interaction [9] itself, laser radiation can be linearly converted into upper hybrid wave [10]. We have investigated the wave conversion of an extra-ordinary mode normally incident onto a magnetoplasma with a linear density gradient, taking thermal effects into account [11]. We solve a coupled wave

equation by matching the asymptotic WKBJ solution with the solution in the resonance region and obtained an absorption coefficient:

$$A=4\alpha Ai^2(0)/\{[1+\alpha Ai^2(0)]^2+\alpha^2 Ai^2(0)Bi^2(0)\}$$

where $\alpha = \pi^2(\omega_c/\omega)^2 (L\omega/c)^{4/3}$, A_i and B_i are the Airy functions. $\omega_c=eB/mc$, and L is the density scale length. Maximum absorption of 67% occurs at $\alpha = 4$ more than double the value found previously for Budden profile and cold plasma [12], or the value for unmagnetized plasma. The large values of the absorption coefficient are due to thermal effects which cause (i) resonance broadening and (ii) convection of the electrostatic wave out of the resonance region.

2. TWO-PLASMON DECAY AT QUARTER-CRITICAL DENSITY

Consider an electromagnetic wave $\vec{E}=E_0\hat{y}\cos(k_0x-\omega_0t)$ normally incident on an inhomogeneous plasma with a density profile $n(x)=n_0(1+x/L)$. Near the quarter-critical density, it may decay into two plasma waves [13,14]. The growth rate of the plasma waves with $\lambda_D^{-1}>>k>>k_0$ is $\gamma_0=k_0v_0/2$ where $v_0=eE_0/m\omega_0$. The two unstable modes propagate almost oppositely, bisecting the right angle subtended by the incident wave vector $\vec{k}_0$ and polarization $\vec{E}_0$.

When the plasma waves grow to large amplitude they are unstable to modulations, driven by the ponderomotive force. Let two plasma waves generated by the decay process be $\vec{E}_1=\vec{E}_1(x,t)\exp(i\vec{k}_1\vec{r}-i\omega_1t)+c.c.$, and $\vec{E}_2=\vec{E}_2(x,t)\exp i(\vec{k}_2\vec{r}-\omega_2t)+c.c.$ where $\vec{E}_1$, $\vec{E}_2$ are slowly varying functions. The ponderomotive force due to the two plasma waves is

$$F_p = -\frac{\nabla e^2|\vec{E}_1+\vec{E}_2|^2}{m\omega_p^2} \approx \frac{-e^2}{m\omega_p^2}\nabla[|\vec{E}_1|^2+|\vec{E}_2|^2]$$

after averaging over the spatial scale of the order of the wavelength of the plasma waves. The nonlinear density variation due to this ponderomotive force can be obtained from the pressure-balance equation:

$$T\nabla\delta n_N = \frac{ne^2}{2m\omega_p^2}\nabla(|E_1|^2+|E_2|^2)$$

The nonlinear frequency-shift of the plasma waves is therefore

$$\delta\omega_{NL} = \omega_p\left(1-\frac{\delta n_N}{n}\right)^{1/2} \approx \omega_p\left(1-\frac{|E_1|^2+|E_2|^2}{16\pi nT}\right)$$

When it becomes comparable to the growth rate of the decay instability, the plasma waves are effectively detuned from the pump and the saturation sets in. Setting $E_1=E_2$ because of the Manley-Rowe relation, we anticipate therefore the saturated level of the plasma wave to be of the order $|E|^2/8\pi nT\simeq\gamma_0/\omega_p\approx\sqrt{3}v_0/2c$. The corresponding density fluctuation is

$$\frac{\delta n}{n} = k\lambda_D|E_s|/(nT)^{1/2} = \left(\frac{v_0}{c}\right)(k\lambda_D)$$

With this saturation level, we may estimate the absorption coefficient due to the two-plasmon decay process. We may define the anomalous collision frequency ν_* as $\nu_*|E_0|^2/2\pi=\gamma_0|E_s|^2/2\pi$. Because the two-plasma decay is localized within a resonant region whose width is $\ell=L\gamma/\omega_p$, the absorption coefficient can be written as

$$\varepsilon = \nu_*\ell/c = 3\pi v_e^2v_0(k_0L)/64c^3$$

which is less than 1% for a Nd-glass laser of 10^{14} watt/cm^2 incident on a plasma with 1 keV temperature and $k_0L=100$. This may account for the fact that there is no observable change in absorption of light when the $\frac{3}{2}\omega_0$ emission is enhanced by orders of magnitude [15]. We therefore conclude that the decay into two plasma waves is unlikely to contribute significantly to absorption of the laser light.

3. ABSOLUTE RAMAN BACKSCATTER AT QUARTER-CRITICAL DENSITY

For Raman scattering, the absolute instability at the quarter-critical density [16] region has the lowest threshold power due to plasma inhomogeneity and highest growth rate thus appears to be the most important. Because it is an absolute instability localized near the quarter-critical density where $\omega_0=2\omega_p$, both the scattered light wave and the plasma wave are trapped in the resonant region. As they grow up to sufficient amplitude, the ponderomotive force of these localized waves pushed the plasma out of the resonant region, creating a density cavity and forming a soliton. The local plasma frequency within the cavity is lowered by

$$\delta\omega_p = \omega_p \frac{\delta n}{n} = -\omega_p \frac{|E_p|^2+|E_s|^2}{16\pi nT}$$

where $|E_p|^2/16\pi$ and $|E_s|^2/16\pi$ are the energy density of the plasma wave and the scattering light wave respectively. Because of Manley-Rowe relation, we have $|E_p|^2 \sim |E_s|^2$. The three-wave resonance condition is therefore detuned when $\delta\omega_p$ gets large and the unstable growth of the instability is saturated at

$$\frac{|E_s|^2}{\pi} \sim \frac{\gamma_0}{\omega_p} = 2\frac{\nu_0}{c}$$

where $\gamma_0 = \frac{\nu_0}{c}\omega_p$ is the linear growth rate of the instability and $v_0 = c|E_0|/m\omega_0 c$ is the electron oscillating velocity in the laser field. We may estimate the reflection coefficient as

$$R \sim v_e^2/v_0 c$$

where v_e is the electron thermal speed.

More rigorously, we consider the following coupled nonlinear equations:

$$i N_t + N_{xx} + (|N|^2+|V|^2-2\alpha x) = i\gamma_0 \exp(ik_0 x)V^*$$

$$i V_t + a^2 V_{xx} + (|N|^2+|V|^2-2\alpha x) = i\gamma_0 \exp(ik_0 x)N^*$$

where N denotes the amplitude of the Langmuir wave, and V that of the scattered light wave, $a^2=c^2/v_e^2 \gtrsim 100$; $\alpha=1/L$ is the inverse density scale length.

This equation is solved iteratively. Without the driving terms on the right side, the equation allows a soliton solution. It is a Langmuir soliton

$$N = 2\eta \operatorname{sech} 2\eta(x-4\xi t+2\alpha t^2-x_0) \times$$

$$\exp i[2(\xi-\alpha t)x+4\eta^2 t+4/3\alpha(\xi-\alpha t)^3]$$

with light wave trapped in it:

$$V = \delta \operatorname{sech}^{s} 2\eta(x-4\xi t+2\alpha t^2-x_0) \times$$

$$\exp i[2(\xi-\alpha t)x+4\eta^2 a^2 s^2 t+4/3\alpha(\xi-\alpha t)^3]$$

where η, ξ are constants characterizing the amplitude and the speed of the soliton,

$$\delta = 4\eta/a\xi\eta \quad , \quad s=1/2(-1+\sqrt{1+\delta/a^2}) \sim 1/a^2$$

We then put in the driving term. The effect is the growth of the soliton

$$\dot{\eta} = \frac{\gamma_0 \pi}{a} \eta \operatorname{sech} \frac{k_0 - 4(\xi-\alpha t)}{4\eta} \cos x$$

$$[(\xi-\alpha t)\eta]_t = -\alpha\eta$$

$$\dot{\chi} = 4\eta^2 + 8(\xi-\alpha t)^2 - 4\alpha(4\xi t-2\alpha t^2-x_0)$$

The maximum amplitude of the soliton is obtained by setting $\chi \sim \pi/2$; we have

$$\eta_s^2 \sim \pi^2 \gamma_0/4a \quad \therefore \quad \frac{|E_s|^2}{8\pi nT} \sim \frac{v_0}{c} \frac{\pi^2}{2a}$$

in agreement with our earlier intuitive result.

REFERENCES

1. V. L. Ginzburg, The Propagation of Electromagnetic Waves in Plasmas, Pergamon, New York (1970) 2nd Ed.
2. J. P. Freidberg, R. W. Mitchell, R. L. Morse, and L. Z. Rudinski, Phys. Rev. Lett 28 795 (1972); A. D. Piliya, Tekh. Fiz. 36 818 (1966) (Sov. Phys.-Tech. Phys. 11 609 (1966), N. G. Denisov, Zh. Eksp. Teor. Fiz. 31 609 (1956) (Sov. Phys.-JETP 4 544 (1957).
3. H. H. Chen and C. S. Liu, Phys. Rev. Lett. 39 1147 (1977).
4. G. J. Morales and Y. C. Lee, Phys. Rev. Lett. 35 1016 (1974).
5. H. H. Chen and C. S. Liu, Phys. Rev. Lett. 37 693 (1976).
6. W. L. Kruer and K. G. Estabrook Fifth Anomalous Absorption Conference Ann Arbor, Michigan, 1977, J. M. Kindel and E. L. Lindman, Fifth Anomalous Absorption Conference, Ann Arbor, Michigan, 1977.
7. H. Kim, R. Stenzel and A. Y. Wong, Phys. Rev. Lett. 33 886 (1970).
8. P. K. Shukla and K. H. Spatschek, J. Plasma Phys. 19 387 (1978).
9. J. A. Stamper and D. A. Tidman, Phys. Fluids 16 2024 (1973); J. J. Thompson, C. E. Max and K. Estabrook, Phys. Rev. Lett. 35 663 (1975).
10. W. L. Kruer and K. G. Estabrook, Lawrence Livermore Laboratory Report No. UCLR-79127 (1977) (unpublished).
11. C. Grebogi, C. S. Liu and V. K. Tripathi, Phys. Rev. Lett. 39 338 (1977).
12. R. B. White and F. F. Chen, Plasma Phys. 16 565 (1974)
13. E. A. Jackson, Phys. Rev. 153 255 (1967); C. S. Liu and M. N. Rosenbluth Phys. Fluids 19 967 (1976); Y. C. Lee and P. K. Kaw, Phys. Rev. Lett. 32 135 (1974).
14. H. H. Chen and C. S. Liu, Phys. Rev. Lett. 39 881 (1977).
15. H. C. Pant, K. Eidman, P. Sachaenmaier and R. Sigel, Opt. Commun. 16 396 (1976).
16. D. W. Forslund, J. M. Kindel and E. L. Lindman, Phys. Rev. Lett. 30 739 (1973); J. F. Drake and Y. C. Lee, Phys. Rev. Lett. 31 1197 (1973).

WAVE ABSORPTION AND SUPERREFLECTIVITY OF LASER PLASMAS DUE TO ELECTROMAGNETIC STRUCTURE RESONANCES

K. SAUER, N.E. ANDREEV*, K. BAUMGÄRTEL
Central Institute for Electron Physics,
Academy of Sciences
of the German Democratic Republic,
Berlin,
German Democratic Republic

Abstract

WAVE ABSORPTION AND SUPERREFLECTIVITY OF LASER PLASMAS DUE TO ELECTROMAGNETIC STRUCTURE RESONANCES.

The interaction of normally incident electromagnetic waves of high intensity with an inhomogeneous plasma whose maximum density is above the critical one is investigated theoretically. Structure resonances can be formed self-consistently due to deformations of the plasma density profile which are produced by the ponderomotive force. During the resonance, the electromagnetic energy is temporarily trapped in a self-induced density cavity whereby the reflection coefficient decreases to values near to zero. Simultaneously, the absorption coefficient reaches a maximum of about 50%. The rest of the energy is re-emitted when the resonance is destroyed. In this moment, peak values of the reflection coefficient greater than one can occur. The characteristic properties of these structure resonances have been studied analytically using a linear model in which the resonant density cavity is approximated by a step-like density profile (caviton model).

1. INTRODUCTION

The understanding of the coupling of laser energy to target plasmas is important for laser fusion in order to optimize the light absorption. Considerable attention has been devoted to the study of resonance absorption of obliquely incident radiation in inhomogeneous plasmas (p-polarisation) where excitation and damping of electron plasma waves are the dominant processes [1-3].

Recently, another type of resonant absorption has been treated at *normal* incidence of the laser radiation [4-6]. The mechanism is based on geometrical or structure resonances which arise due to coherence effects. The two-step profile, investigated by Mayer et al. [5],

* Physical Institute, Academy of Sciences of the USSR, Moscow, USSR.

however, does not represent realistic dynamical situations because the ponderomotive force cannot produce or maintain such a profile self-consistently. Meanwhile, self-induced structure resonances associated with enhanced absorption have been observed in our dynamical calculations for the case of *normally* incident waves [6].

In this paper further theoretical results on the interaction of high-power electromagnetic waves with inhomogeneous plasmas are represented. Especially, it is shown that the dynamical process of the formation of resonant density structures is connected not only with enhanced absorption but also with superreflectivity ($|R|^2 > 1$) when the amplitude of the incident wave is high enough. This effect is caused by temporary trapping of the electric field energy in the self-induced resonant density structures and by the re-emission of the radiation when the resonance is destroyed. The basic resonance properties of such density structures which are produced self-consistently by the ponderomotive force can be analysed in the linear theory by means of an overdense step-like plasma density profile with a hole (cavity) near the boundary. It will be shown that for normal incidence this "caviton model" is more relevant to the problem of strong electromagnetic wave interaction with inhomogeneous plasmas than the two-step profile used before [5].

2. DYNAMICAL THEORY

We assume that an electromagnetic wave with the frequency ω_o penetrates parallel to the density gradient into an inhomogeneous plasma whose maximum density is above the critical one. The self-consistent wave-plasma interaction is an effect of the ponderomotive force which produces deformations of the plasma density profile which react back on the wave propagation properties.

The basic equations are i) the wave equation in the modulational representation for the (complex) electric field amplitude $E(x,t)$,

$$2\,i\,\omega_o \frac{\partial}{\partial t} E + c^2 \frac{\partial}{\partial x^2} E + \omega_o^2 \left[1 - \frac{1}{1+i\nu/\omega_o} \frac{n}{n_c}\right] E = 0 \qquad (1)$$

and ii) the hydrodynamic equations for the ions,

$$\frac{\partial n}{\partial t} + \frac{\partial}{\partial x}(n v) = 0 \qquad (2)$$

$$\frac{\partial v}{\partial t} + v\frac{\partial v}{\partial x} + \frac{c_s^2}{n}\frac{\partial n}{\partial x} = -\frac{c_s^2}{2}\frac{\partial}{\partial x}\left|\frac{v_E}{v_T}\right|^2 \qquad (3)$$

where we have used the following abbreviations:

$$n_c = \frac{\omega_o^2 m}{4\pi e^2}\ , \quad v_E = \frac{eE}{m\omega_o}\ , \quad v_T = \sqrt{\frac{kT_e}{m}}\ , \quad c_s = \sqrt{\frac{kT_e}{M}}$$

The ponderomotive force is included in the equation of motion as a source term. Dissipation of the high-frequency field is described by an effective collision frequency ν. Further, we introduce the following dimensionless quantities:

$$\tau = \sqrt{m/M}\,\omega_o t\ , \quad u = v_E/v_T\ , \quad \lambda_o = 2\pi c/\omega_o$$

The normalized amplitude of the incident wave is denoted by u_o.

The system of partial differential equations (1) - (3) is solved numerically with the help of difference schemes [7].

The density profile at the initial state (t=0) is assumed to be

$$n(x,t=0) = \begin{cases} n_{max}\exp(-x^2/a_o^2) & \text{for } x \leq 0 \\ n_{max} & \text{for } x>0 \end{cases} \qquad (4)$$

with a half-width a_o of the order of the vacuum wave length λ_o. Throughout the calculations a maximum density of $n_{max} \simeq 1.5\, n_c$ is assumed.

From the solution of eqs. (1) - (3) it is easy to calculate the reflection and absorption coefficient, respectively:

$$|R(t)|^2 = \left|\frac{u(x=0,t)}{u_o} - 1\right|^2$$

$$|A(t)|^2 = \frac{\nu}{\omega_o}\int_0^{k_o d}\frac{n(x,t)}{n_c}\cdot\frac{|u(x,t)|^2}{u_o^2}\,d(k_o x)\ , \quad k_o=\omega_o/c. \qquad (5)$$

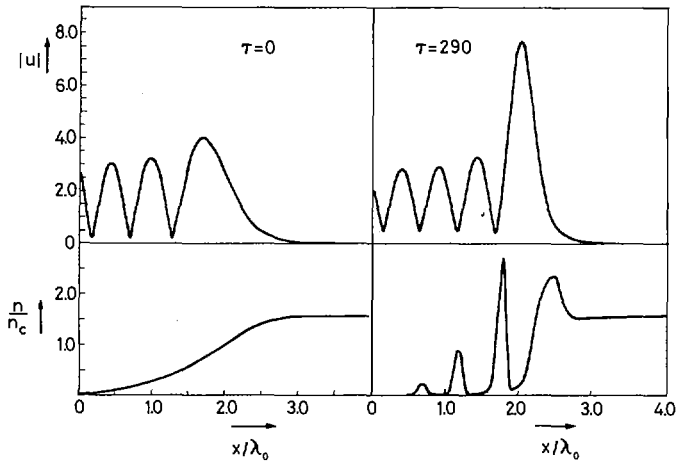


FIG. 1. Spatial dependence of the electric field amplitude and associated density profile at two significant times; $u_0 = 1.75$, $\nu/\omega_0 = 0.005$, $a_0/\lambda_0 = 1.5$.

Results of the numerical solution of our basic eqs (1) - (3) are shown in Fig. 1, in which both the spatial structure of the electric field amplitude and the density profile are plotted at two significant times. Here, the normalized amplitude of the incident wave is $u_0 = 1.75$. At the initial state ($\tau=0$) the undisturbed density profile is given by eq. (4) with $a_0 = 1.5\ \lambda_0$ and $n_{max} = 1.5\ n_c$. The spatial structure of the electric field amplitude for such density profile is obtained by solving the stationary wave equation and has an Airy-type pattern resulting from the superposition of the incident and reflected wave with $|R|^2 \simeq 1$. At later times the ponderomotive force of the inhomogeneous electric field leads to deformations of the density profile.

The second state ($\tau \simeq 290$) is characterized by a resonator-like density structure which is generated temporarily, providing an enhanced electric field in the middle of the created density cavity surrounded by two overcritical layers. The resonance properties of such density profiles will be studied in the next section by means of the "caviton model".

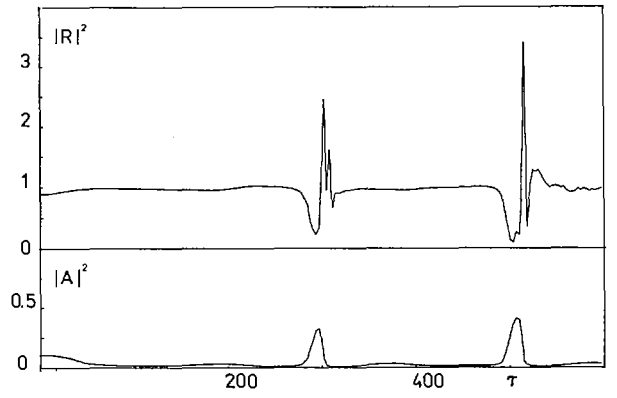


FIG. 2. Time history of the reflection and absorption coefficient (parameters as in Fig. 1).

As is to be expected, the enhancement of the electric field during the period of resonance is accompanied by temporal variations of both the reflection and absorption coefficient. The time history of both quantities is presented in Fig. 2. According to the upper curve in Fig. 2, the reflection coefficient, immediately after switching on the electromagnetic pulse, increases to a value close to one and is almost constant during the time τ_1 which is approximately given by $\tau_1 \simeq \pi/\beta$, where $\beta = v_T/c$ (see also [6]). After this time the reflection coefficient passes a minimum ($|R|^2 \simeq 10\%$) and afterwards jumps to a value $|R|^2 \simeq 3$. This means that the reflected energy is temporarily higher than the incident one. After a few oscillations, the reflection coefficient again assumes the starting value $|R|^2 \simeq 1$. During the resonance the absorption increases to about 40%.

Besides plasma heating, the observed effect of wave absorption and superreflectivity may play an important role in the case of target plasmas being used as a mirror in feedback laser systems as discussed in [8].

The occurrence of isolated peaks in the temporal evolution of the reflection coefficient is typical for plasmas with an initial (t=0) sharp boundary ($a_0 \lesssim 1.5\ \lambda_0$). For weaker density gradients near the critical point ($a_0 \simeq 5\ \lambda_0$) the reflection coefficient strongly oscillates for $\tau > \tau_1$ between $|R|^2 \simeq 0$ and $|R|^2 \simeq 2.5$.

Associated with these oscillations is enhanced absorption up to $|A|^2 \simeq 50\%$ at resonance. If a_o further increases ($a_o \simeq 10\ \lambda_o$) the isolated peaks merge into a broad absorption spectrum.

A balance equation for the temporal evolution of the electric quantities during the wave-plasma interaction can be derived from the wave equation (1) by traditional methods in the following form (transmission neglected):

$$0 = \frac{\partial}{\partial(\omega_o t)} \int_0^{k_o d} \frac{|u(x,t)|^2}{u_o^2}\, d(k_o x) + |R|^2 + |A|^2 - 1 \qquad (6)$$

[0,d] is the spatial interval covering the density profile.

Values $|R|^2 > 1$ are consistent with the balance equation (6) if the derivative of the integral with regard to time is different from zero. As discussed already in our earlier paper [6] , fast variations of the electric field energy occur on passing the electromagnetic structure resonance. Due to the formation of a resonant density structure, the plasma temporarily acts as a storage for the electric field energy. A short time later, when the resonance is destroyed, the non-absorbed energy is re-emitted as a short pulse whose intensity depends on the velocity with which the electric field energy changes.

To prove the balance equation (6), we have separately calculated the quantities

$$I(t) = \frac{\partial}{\partial(\omega_o t)} \int_0^{k_o d} \frac{|u(x,t)|^2}{u_o^2}\, d(k_o x) \qquad (7)$$

and

$$S(t) = |R|^2 + |A|^2 - 1 \qquad (8)$$

The results are shown in Fig. 3, where the temporal evolution of $|R|^2$, $|A|^2$, I and S is pictured for a interval around the resonance region. It can be seen that over the whole region $250 \leq \tau \leq 350$ the relation $I(t) = -S(t)$ is fulfilled, which is equivalent to the requirement of the balance equation: $I(t) + S(t) = 0$.

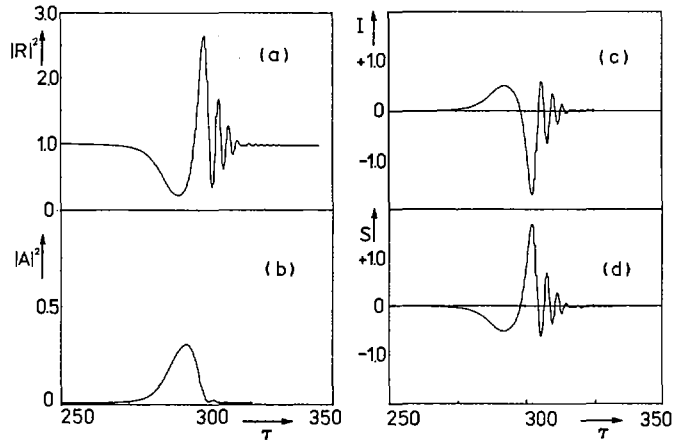


FIG.3. Numerical test of the balance equation (6). Temporal evolution of (a) the reflection coefficient, (b) the absorption coefficient, (c) the integral I (Eq.(7)), and (d) the quantity S (Eq.(8)) round the resonance.

3. CAVITON MODEL

The basic properties of the resonant density structures observed in our dynamical self-consistent calculations can be studied analytically with the help of the "caviton model". In this one-dimensional model drawn in Fig. 4, a step-like density profile is used consisting of two homogeneous overcritical plasma layers which are separated by an undercritical one.

In the cold collisional plasma approximation, the dielectric constant ε_j of each layer is given by

$$\varepsilon_j = 1 - \frac{n_j/n_c}{1+i\nu/\omega_o} \quad , \qquad j = 0,1,2,3 \qquad (9)$$

where n_j/n_c and ν_j are the plasma density normalized by the critical density and the collisional frequency, respectively, belonging to the j-th layer. The corresponding wave vectors k_j are determined by the dispersion relation

$$k_j^2 c^2 = \omega_o^2 \varepsilon_j \qquad (10)$$

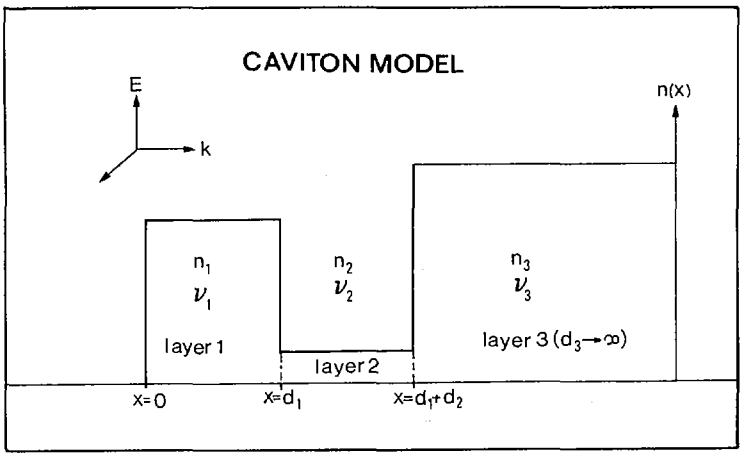


FIG.4. Caviton model consisting of two overcritical layers separated by an undercritical one.

In the vacuum region (j=0, ε_0=1) and in the first two layers, the electric field is a superposition of two waves propagating in opposite directions,

$$E_j(x) = A_j^+ \exp(ik_j x) + A_j^- \exp(-ik_j x) \quad , j=0,1,2 \qquad (11)$$

where A_0^+ and A_0^- are the amplitude of the incident and reflected wave, respectively. In the third layer there is no reflected wave, and hence

$$E_3(x) = A_3^+ \exp(ik_3 x) \qquad (12)$$

Using the condition that the electric and magnetic field must be continuous at the boundaries x = 0, x = d_1 and x = d_1 + d_2, we obtain for the reflection coefficient $R = A_0^-/A_0^+$ the relation

$$R = -\frac{F_+}{F_-} \qquad (13)$$

with the following abbreviations:

$$\begin{aligned} F_{\pm} = {} & E_+(1)\, E_+(2)\, K_{\pm}(1,0)\, K_+(2,1)\, K_-(3,2) + \\ & E_-(1)\, E_+(2)\, K_{\mp}(1,0)\, K_-(2,1)\, K_-(3,2) + \\ & E_+(1)\, E_-(2)\, K_{\pm}(1,0)\, K_-(2,1)\, K_+(3,2) + \\ & E_-(1)\, E_-(2)\, K_{\mp}(1,0)\, K_+(2,1)\, K_+(3,2) \end{aligned} \qquad (14)$$

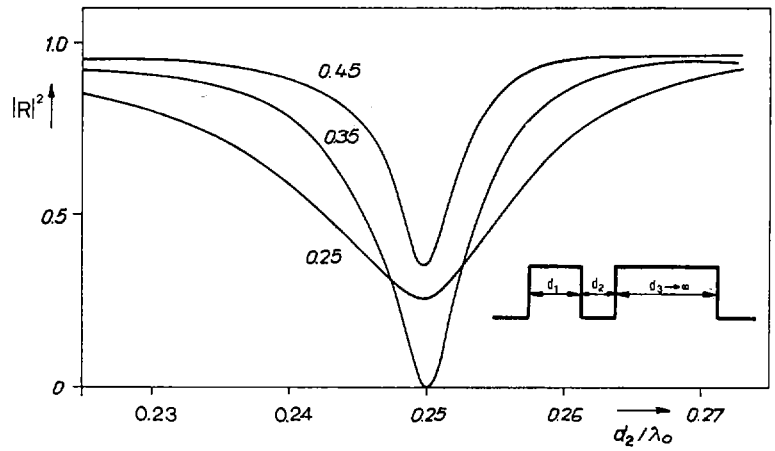


FIG.5. Resonance curves for the caviton model with $n_1 = n_3 = 2n_c$, $n_2 = 0$. *Reflection coefficient versus the distance* d_2 *normalized by the vacuum wavelength* λ_0. *Parameter is the width of the first layer in units of* λ_0; $\nu/\omega_0 = 0.01$.

and

$$E_{\pm}(j) = \exp(\pm i k_j d_j) \quad , \quad j = 1,2$$
$$K_{\pm}(l,m) = k_l \pm k_m \quad , \quad l = 1,2,3 \; ; \; m = 0,1,2 \qquad (15)$$

To demonstrate the resonance properties of our caviton model, we have treated the special case of the overcritical layers having the same density $n_1 = n_3 = 2\, n_c$ and the second layer being a vacuum region, i.e. $n_2 = 0$. For these conditions the power reflectivity $|R|^2$ is calculated in dependence on the width of the vacuum region d_2 in units of the vacuum wave length $\lambda_o = 2\pi/k_o$. The resonance curves are shown in Fig. 5; the parameter is the length of the first layer normalized by λ_o. The collisional frequency is assumed to be $\nu/\omega_o = 0.01$. As can be seen, the reflectivity has a minimum at a defined value d_2 and drops to zero if the length d_1 is chosen appropriately.

For small ν the resonance point d_2 does not depend on the length of the first layer. For decreasing values of the collisional frequency the resonance becomes sharper and is shifted to greater values of d_1. The curve in Fig. 6 represents the dependence $d_1 = f(\nu)$ for the resonance case, i.e. for $|R|^2 = 0$.

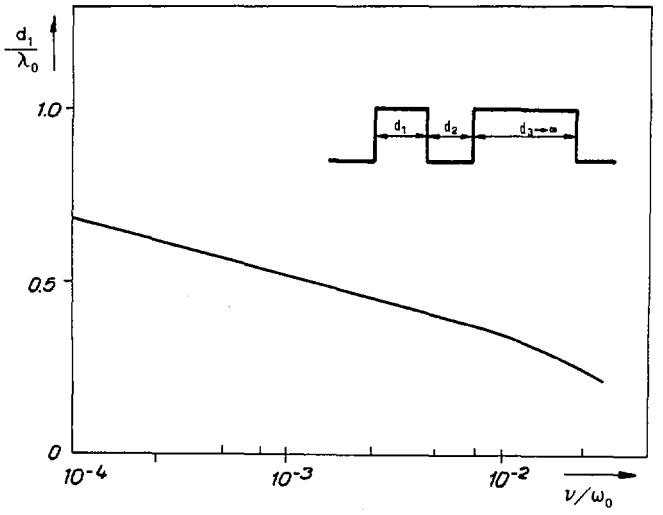


FIG. 6. Normalized width of layer 1 versus ν/ω_0 *for the resonance case, i.e.* $|R|^2 = 0$; $n_1 = n_3 = 2n_c$, $n_2 = 0$, $d_2/\lambda_0 = 0.25$.

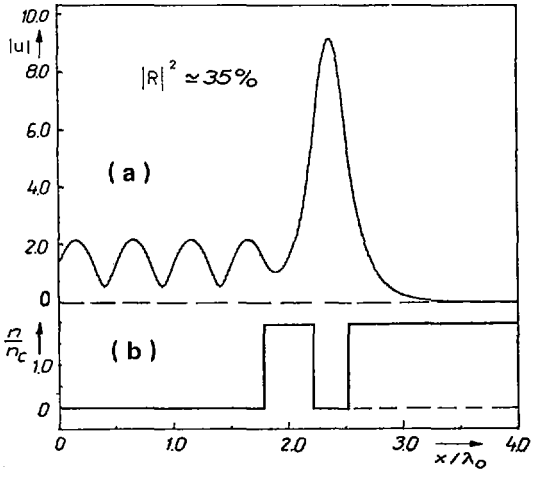


FIG. 7. Spatial dependence of the electric field amplitude (a) near resonance ($|R|^2 = 35\%$) *for the caviton model (b);* $\nu/\omega_0 = 0.01$.

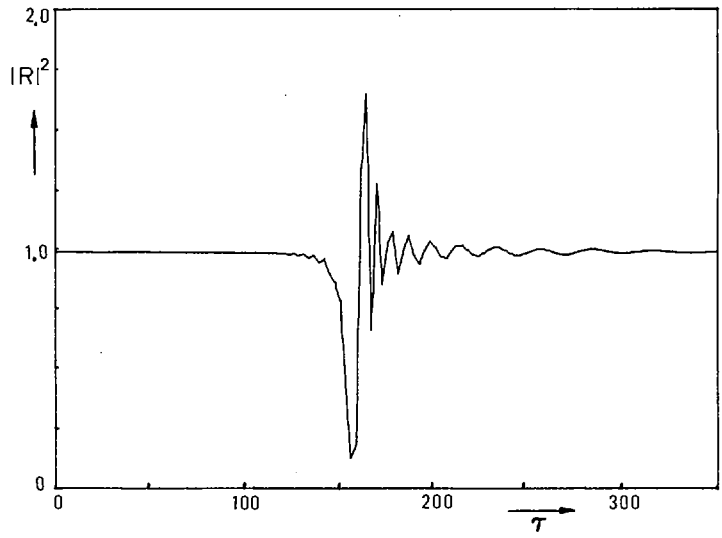


FIG.8. Time history of the reflection coefficient for the case when the width of the vacuum region d_2 *in the caviton model changes according to* $d_2 = c_s t$; $d_1 = 0.35\ \lambda_0$, $\nu/\omega_0 = 0.005$, $n_1 = n_3 = 2n_c$, $n_2 = 0$.

The structure resonance described above is an effect of the excitation and damping of eigenmodes (surface waves) propagating along the boundaries of the undercritical region (caviton). In the case of resonance the electric field in the caviton is strongly enhanced as in a resonator. The maximum amplitude increases with decreasing collisional frequency. For conditions near resonance ($|R|^2$ = 35%) the spatial profile of the electric field amplitude is shown in Fig. 7.

Finally, using the caviton model, we have investigated the temporal evolution of the reflection coefficient assuming the width of the caviton d_2 changes slowly with time. For this, d_2 is written as

$$d_2 = u \cdot t \qquad (16)$$

where the ion-sound velocity c_s is used as a characteristic velocity for density profile modifications. All the other parameters of the step-like density profile are fixed.

With such a time-dependent function n(t), the non-stationary wave equation (1) is solved numerically. The resulting reflection coefficient as a function of time is shown in Fig. 8, using the same

parameters as in Fig. 5: $d_1 = 0.35\ \lambda_0$, $n_1 = n_3 = 2\ n_c$, $n_2 = 0$, $\nu/\omega_0 = 0.005$. The resonance for these parameters is given by $d_2/\lambda_0 = 0.25$, which is, according to eq. (16), equivalent to a time

$$\tau_{res} = \frac{2\pi}{\beta} \quad 0.25 \quad , \quad \beta = v_T/c$$

i.e.

$$\tau_{res} \simeq 160$$

for $\beta = 0.01$ used in our case. On passing this resonance the reflection coefficient shows a similar behaviour as in the self-consistent calculations of Section 2. Thus, we have demonstrated that the strong temporal oscillations of the reflection coefficient with values greater than one are brought about by the formation of a structure resonance.

4. CONCLUSION

The results of our investigations can be summarized as follows. At the interaction of normally incident waves with an inhomogeneous plasma whose maximum density is higher than the critical one, resonant density structures can be formed self-consistently by the action of the ponderomotive force. The formation of structure resonances is connected with oscillations of the reflection coefficient whereby, after passing a minimum ($|R|^2 \simeq 0$), values greater than one ($|R|^2 \simeq 3$) can occur. During the resonance, the absorption reaches a maximum of about 50%. The temporal evolution of both the reflection and absorption coefficient is consistent with the predictions of a balance equation which can be derived from the (non-stationary) wave equation in the modulational representation. The density profile at the resonant state has a characteristic structure: two overcritical layers are separated by a cavity, in which the density is suppressed by the ponderomotive force of the strong localized electric field. The main characteristics of the self-induced structure resonances are contained in the caviton model in which a step-like density profile is used.

REFERENCES

[1] FORSLUND, D., KINDEL, J.M., LINDMAN, E.L., Phys. Rev. A 11 (1975) 679.

[2] ESTABROOK, K.G., VALEO, E.J., KRUER, W.L., Phys. Fluids 18 (1975) 1151.

[3] WONG, A.Y., "Electromagnetic wave interaction with inhomogeneous plasmas", in Laser Interaction and Related Phenomena , 4B, ed. Schwarz, Hora; Plenum Press, New York, London (1977).

[4] ALIEV, Yu.M., GRADOV, O.M., KYRIE, A.Yu., CADEZ, V.M., VUKOVIC, S., Pisma Zh. Ehksp. Teor. Fiz. 25 (1977) 351.

[5] MAYER, F.J., OSBORN, R.K., DANIELS, D.W., McGRATH, J.F., Phys. Rev. Letters 40 (1978) 30.

[6] SAUER, K., Phys. Letters 66 A (1978) 37.

[7] POTTER, D., "Computational Physics", Wiley, New York (1973).

[8] BOIKO, V.A., DANILYCHEV, V.A., ZVORYKIN, V.D., IVANOVA, T.G., HOLIN, I.V., CHUGUNOV, A.YU., Kvantovaya Elektronika 6 (1977) 1307.

THEORY OF CAVITONS IN LASER-IRRADIATED PLASMAS

K.H. SPATSCHEK, M.Y. YU, P.K. SHUKLA
Institut für Theoretische Physik,
Ruhr-Universität Bochum,
Bochum,
Federal Republic of Germany

Abstract

THEORY OF CAVITONS IN LASER-IRRADIATED PLASMAS.

Two problems associated with plasma density cavitation in laser fusion experiments are considered: The depression of density caused by mode-converted Langmuir waves in the critical region, and the localization of density caused by the radiation pressure of very-high-power laser light. In the first part, the propagation of an obliquely incident, p-polarized electromagnetic wave in an inhomogeneous plasma is discussed. Before effective damping of the mode-converted Langmuir wave electric fields can take place, non-linear effects dramatically modify the local density profile in a self-consistent manner. A rigorous theoretical calculation for the cavity formation, its development, and propagation out from the resonant layer towards the underdense region is presented. The mathematical procedure is based on a perturbation-theoretical solution of a driven, inhomogeneous, non-linear Schrödinger equation using the inverse-scattering technique. The results for large-scale density steepening are discussed. In the second part, the authors' theory is extended to high-power laser beams under construction where relativistic non-linearities originating from electron-mass variation may also become important. Furthermore, full electron and ion non-linearities are included in the plasma response and the relativistic ponderomotive foces, besides the non-linearities originating from the relativistic mass variation. For normally incident circularly polarized electromagnetic waves, corresponding to focused laser light, exact steady-state caviton solutions are reported. The new phenomenon of supersonic density humps is discovered.

I. INTRODUCTION

The propagation and absorption of laser light at the outer region of the corona as well as at the critical density crucially depends on the density profile. For large intensities, the density profile is changed selfconsistently through the radiation pressure and other nonlinear effects such as relativistic electron-mass variations. It is the aim of this contribution to calculate the plasma density cavitation in different regions which can occur in laser fusion experiments.

II. STEEPENING AT THE CRITICAL SURFACE

An obliquely incident p-polarized electromagnetic wave can tunnel from its turning point to the critical surface of a laser-irradiated plasma. The linear mode conversion process leads to

the build-up of Langmuir wave electric fields of very high intensity. The latter are driven by the electric field

$$\underset{\sim}{E}_d = (\underset{\sim}{H} \times \hat{e}_y) \approx \hat{e}_x E_o \phi(q)/(2\pi k_o L)^{1/2} \tag{1.1}$$

where E_o and $k_o = 2\pi/\lambda_o$ are the free space values of the laser electric field and the wave vector, L is the density gradient scale length, and $\phi(q)$ is the usual resonance function peaked around $q \approx 0.6$. Assuming that the scale length of variation of the electromagnetic wave is much longer than that of the driven Langmuir waves and that the plasma reacts adiabatically to the radiation pressure, one gets within the WKB-approximation for the total field $E = E_L + E_d$,

$$i\,\partial_t E + \frac{1}{2}\partial_x^2 E + (-\alpha x + |E|^2 + \frac{1}{2} i\nu)E = \frac{1}{2} E_d \tag{1.2}$$

where t, x, ν, E are normalized by ω_{pe}^{-1}, $3^{1/2}\lambda_{De}$, ω_{pe}, $(16\pi n_o T_e)^{1/2}$, respectively. ν is the collision frequency which accounts for the damping in a phenomenological way, and $\alpha = \lambda_{De}/2L$. The density variation follows from the solution for E through

$$\delta n/n_o = -|E|^2/8\pi n_o T \tag{1.3}$$

We first reduce the spatially inhomogeneous problem to an equivalent homogeneous one by using the transformation $u(x',t) = E \exp(i\psi)$, $\psi = \alpha x' t - \alpha^2 t^3/3$, and $x' = x + \alpha t^2/2$. Then (1.2) becomes

$$i\,\partial_t u + \frac{1}{2}\partial_x^2 u + |u|^2 u = -\frac{1}{2} i\nu u + \frac{1}{2} E_d \exp(i\psi) \tag{1.4}$$

where, for simplicity, we omit the primes on x. We solve this equation as an initial value problem treating the r.h.s. as a perturbation. It is easy to verify that eq.(1.4) can be written in the form [1]

$$i L_t + [L,A] = iR \tag{1.5}$$

where L and A are the same operators as in the Zakharov-Shabat problem, e.g.

$$L = \begin{pmatrix} i\partial_x & u^* \\ -u & -i\partial_x \end{pmatrix}, \text{ and } R = \begin{pmatrix} o & r^* \\ -r & o \end{pmatrix} \tag{1.6}$$

with $r = -\nu u/2 - i E_d \exp(i\psi)/2$.

The eigenvalue problem

$$L\varphi(x,t) = \lambda(t)\varphi(x,t) \tag{1.7}$$

yields together with (1.5)

$$(L-\lambda)(\varphi_t + iA\varphi) = -R\varphi + \lambda_t \varphi \tag{1.8}$$

Thus, the time dependence of the eigenvalue λ is given by

$$\lambda_t = \int \tilde{\varphi}^* R\varphi\, dx \Big/ \int \tilde{\varphi}^* \varphi\, dx \tag{1.9}$$

where $\tilde{\varphi}$ is a solution of the Hermitian adjoint eigenvalue problem. Introducing the Jost functions f and g as eigenfunctions of the eigenvalue problem (1.7) with the boundary conditions

$$g \to \begin{pmatrix} 1 \\ o \end{pmatrix} e^{-i\lambda x} \quad \text{as} \quad x \to -\infty, \qquad f \to \begin{pmatrix} o \\ 1 \end{pmatrix} e^{i\lambda x} \quad \text{as} \quad x \to +\infty \tag{1.10}$$

and remembering that if $\varphi = (\varphi_1, \varphi_2)$ is a solution of (1.7) then $\bar{\varphi} \equiv (\varphi_2^*, -\varphi_1^*)$ satisfies the system with λ^*, we define the scattering data $a(\lambda)$, $b(\lambda)$ by

$$\begin{aligned} g &= a\bar{f} + bf \\ \bar{g} &= \bar{b}\bar{f} - \bar{a}f \end{aligned} \tag{1.11}$$

$a(\lambda)$ can be analytically continued to the upper half-plane and, in particular, the zeros λ_j of $a(\lambda)$ in the upper half-plane are the discrete eigenvalues. Thus we have

$$g(x,\lambda_j) = c_j f(x,\lambda_j) \tag{1.12}$$

Solving (1.8) by the Green's function technique one obtains in the notation of Karpman and Maslov [1]

$$(\partial_t + iA) f(x,\lambda;t) = i \sum_s \left[\frac{c_s \alpha(\lambda_s,\lambda)}{a_s'(\lambda_s - \lambda)} f(x,\lambda_s;t) + \frac{c_s^* \bar{\alpha}(\lambda_s,\lambda)}{a_s'^*(\lambda_s^* - \lambda)} \bar{f}(x,\lambda_s;t) \right] - \frac{1}{2\pi} \int_{-\infty}^{+\infty} \frac{\bar{\alpha}(\mu,\lambda) f(x,\mu;t) + \bar{\beta}(\mu,\lambda) g(x,\mu;t)}{|a(\mu)|^2 (\mu - \lambda - i0)} d\mu + d_1 f + d_2 g \tag{1.13}$$

The coefficients α, $\bar{\alpha}$, β, $\bar{\beta}$ are defined as follows: $\alpha(\mu,\lambda) = \int \tilde{f}^*(x,\mu) R f(x,\lambda) dx$ and the coefficients $\bar{\alpha}$, β, $\bar{\beta}$ follow from α by the replacements $\tilde{f}^* \to \tilde{f}^*$, $f^* \to \tilde{g}^*$, $\tilde{f}^* \to \tilde{g}^*$, respectively. Then by considering the asymptotic values at $x \to \infty$ and $x \to -\infty$ one obtains in the usual way

$$\partial_t c_j = -2i\lambda_j c_j - \frac{i}{a_j'} \frac{d}{d\lambda} \left[\beta(\lambda,\lambda_j) c_j - \alpha(\lambda,\lambda_j) c_j^2 \right]_{\lambda = \lambda_j} \tag{1.14}$$

$$\partial_t a(\lambda,t) = i[a\bar{\alpha}(\lambda,\lambda) + b\alpha(\lambda,\lambda)] \tag{1.15}$$

$$\partial_t b(\lambda,t) = -2i\lambda^2 b + i[a\alpha^*(\lambda,\lambda) - b\bar{\alpha}^*(\lambda,\lambda)] \tag{1.16}$$

Instead of solving the complete inverse scattering problem, we now apply the adiabatic approximation, i.e. we assume that initially a soliton of the form

$$u_s = 2\eta \operatorname{sech} z \exp(i\frac{\mu}{\eta} z + i\delta), \quad z = 2\eta(x - \xi) \tag{1.17}$$

is present and only the parameters η, ξ, μ, and δ change with time. This assumption can be generalized to N-soliton situations.
Considering a situation where the convective saturation time is much longer than the ion plasma period, we find

$$\mu_t = (\pi E_d / 4\eta)\mu' \sin\delta' \operatorname{sech}(\pi\kappa/2) \tag{1.18}$$

$$\eta_t = -2\nu\eta - (\pi E_d/4)\sin\delta' \operatorname{sech}(\pi\kappa/2) \tag{1.19}$$

$$\xi_t = 2\mu' - (\pi^2 E_d/16\eta^2)\cos\delta' \sinh(\pi\kappa/2) \operatorname{sech}^2(\pi\kappa/2) \tag{1.20}$$

$$\delta_t = 2\eta^2 + 2\mu'^2 - (\pi^2 E_d/4\eta^2)\cos\delta' \sinh(\pi\kappa/2) \operatorname{sech}^2(\pi\kappa/2) \tag{1.21}$$

where $\kappa = \mu'/\eta$, $\mu' = \mu - \alpha t/2$, $\delta' = \delta - \alpha t\xi + \alpha^2 t^3/3$

We note that in the collisionless limit, Eqs.(1.18), (1.19) agree with those derived by Chen and Liu [2]. However, Eqs. (1.20), (1.21) show a new contribution which has not been considered previously. The new terms control the dynamics of the solitons in the field of the driver.

The numerical solution of the above set of equations shows the following behaviour. For a highly inhomogeneous plasma at first the soliton amplitude grows linearly with time. The subsequent saturation accompanied by damped relaxation oscillations occur when the phase shift due to nonlinearity detunes the soliton from the external driver. The growth of the soliton is limited when the phase locking is broken. At this stage, the hyperbolic secant function stops the oscillations to an exponentially small amplitude around the saturation level. Also the phasor saturates at a fairly small value and the soliton emerging from the resonance region moves down the density gradient of the unperturbed profile. It is essentially accelerated down the density gradient and the effect of the driver is negligible. The deepest cavity is created at the resonance layer and one then finds a progressively shallower density cavity moving down the density gradient.

However the results change qualitatively for a gentle density gradient when the external driver plays an important role. This is related to the conjecture that solitons behave like Newtonian particles and thus should experience a force in an external electric field. From our analysis it is evident that at early time the amplitude of the soliton increases, attains a maximum value, and then decreases abruptly leading to saturation without pronounced relaxation oscillations. This happens because the effects of the density gradient and the driver compete with each other. First, the amplitude is controlled by the cosine factor and later the secant hyperbolic dominates and damps the soliton amplitude to a small value. The solitons generated at the resonant layer propagate down the density gradient until that time when the soliton attains a maximum amplitude. Then the effect of the driver dominates over that of the density gradient. As a result, the soliton is retarded during the course of propagation. A similar behaviour has been observed by K.Brueckner [3] although the physical mechanism seems to be different there. Meanwhile the solitons saturate, having a small amplitude. When the amplitude is small, again the density gradient becomes important. Consequently, at late times the soliton propagates down the density gradient without changing shape. This feature appears in our investigation because we have simultaneously taken into account the effects of the driver and the density gradient in the expression for the position and hence the group velocity. This is actually inherent in the approximation based on the inverse scattering technique. It is of interest to point out that previous results obtained from the conservation laws do not predict such a fine structure in the soliton motion. The investigation of the generation and evaluation of many solitons under the action of an external driver and a density gradient is quite involved, nevertheless our present study of the dynamics of a single soliton solution is a prerequisite for future progress.

III. LOCALIZATION IN INTENSE LASER LIGHT

In this part, we consider the propagation of an intense circularly polarized electromagnetic wave in a collisionless plasma. The effects of relativistic mass variation, the relativistic ponderomotive force, as well as the fully nonlinear electron and ion dynamics within the fluid approximation are included. Our investigation thus extends beyond the existing works in which either the relativistic effects alone are treated, or a weak nonlinearity is assumed.

Consider a two-component electron-ion plasma in the presence of a circularly polarized electromagnetic wave in the form $\vec{A} = A[\hat{x}\cos(\omega_o t - k_o z) + \hat{y}\sin(\omega_o t - k_o z)]$, where $\vec{A}$ is the vector potential. For linear wave propagation, we have $\omega_o^2 = \omega_{pe}^2 + c^2k_o^2$, where ω_{pe} is the local electron-plasma frequency, and the other notations are standard.

We study the nonlinear interaction between the laser light and a warm, collisionless, relativistic electron-ion plasma. The basic equations are

$$\partial_t n_j + \nabla\cdot(n_j \vec{v}_j) = 0 \tag{2.1}$$

$$\partial_t \vec{p}_j + \vec{v}_j\cdot\nabla\vec{p}_j = e_j(\vec{E} + \vec{v}_j\times\vec{B}/c) - T_j\nabla\ln n_j \tag{2.2}$$

$$\nabla\cdot\vec{E} = -4\pi e(n_e - n_i) \tag{2.3}$$

$$\vec{p}_j = m_{jo}\vec{v}_j/(1 - v_j^2/c^2)^{1/2} \tag{2.4}$$

$$\partial_t^2\vec{A} - c^2\nabla^2\vec{A} = 4\pi c\vec{J} \tag{2.5}$$

where $\vec{J} \approx -n_e c\vec{v}_e$ is the total current density, and n_e is the slowly varying density produced by the low-frequency electrostatic perturbation ϕ induced by the laser field.

The equation governing the slowly varying electron density perturbation follows from (2.2):

$$\gamma\partial_t\vec{p}_e + (\vec{p}_e/m_o)\cdot\nabla\vec{p}_e = (e\gamma/c)\partial_t\vec{A} - (e/m_{eo}c)\vec{p}\times(\nabla\times\vec{A})$$
$$+ \gamma(e\nabla\phi - T_e\nabla\ln n_e) \tag{2.6}$$

where $\gamma^2 \equiv 1 + p_e^2/c^2m_{eo}^2$ and we have used $\vec{v}_e = \vec{p}_e/m_{eo}\gamma$.

Equation (2.6) is satisfied by

$$\vec{p}_e = m_{eo}c\vec{\psi} \tag{2.7}$$

together with a low-frequency momentum balance,

$$\tfrac{1}{2}\beta\nabla(\psi^2)/(1+\psi^2)^{1/2} = \nabla\phi - \nabla\ln n_e \tag{2.8}$$

where $\vec{\psi} = e\vec{A}/m_{eo}c^2$, $\beta = c^2/v_{te}^2$, $v_{te} = (T_e/m_{eo})^{1/2}$, and we have normalized ϕ by T_e/e, n by n_o, and the coordinates by λ_e, the electron Debye length. Note that due to the circular polarization, ψ^2 does not contain any high-frequency component. This allows us to separate the high- and low-frequency components of (2.6), as done in obtaining (2.7) and (2.8). Equation (2.5) and (2.8) together with the quasineutrality condition and the equa-

tions of motion for the ions, form a coupled set. As is well known, the linearized system is modulationally unstable. Accordingly, we look for the long-time asymptotic behaviour.

Within a modulational representation, we take the amplitude to vary slowly, namely

$$\vec{\psi} = \frac{1}{2}\psi(\tau,\zeta)(\hat{x} - i\hat{y})\exp(-i\omega_0 t + ik_0 z) + c.c. \qquad (2.9)$$

where $\partial/\partial\tau \ll \omega_0$. Thus, Eq.(2.5) becomes

$$2i\varepsilon\frac{\partial\psi}{\partial t} + i\alpha\frac{\partial\psi}{\partial\zeta} + \beta\frac{\partial^2\psi}{\partial\zeta^2} + \Delta\psi = \frac{n\psi}{(1+|\psi|^2)^{1/2}} \qquad (2.10)$$

where $\varepsilon = (m_e/m_i)^{1/2}(\omega_0/\omega_{po})$, $\alpha = 2c^2k_0^2/\omega_{po}^2\lambda_e$, and $\Delta = (\omega_0^2 - c^2k_0^2)/\omega_{po}^2$.
We are interested in the stationary solutions of the system. Accordingly, we write $n = n(\xi)$, and $\psi = \psi(\xi)\exp\{i[\theta(\tau) + \phi(\zeta)]\}$, where $\xi = \zeta - Mt$, and $M = V/c_S$ is the Mach number.
It follows from (2.10) that

$$\beta\frac{\partial^2\psi}{\partial\xi^2} + \delta\psi = \frac{n\psi}{(1+\psi^2)^{1/2}} \qquad (2.11)$$

where the nonlinear frequency shift δ is to be determined later and $\phi(\zeta) = \varepsilon M\zeta/\beta$.
From (2.8), one finds

$$\phi = \beta[(1+\psi^2)^{1/2} - 1] + \ln n \qquad (2.12)$$

where we have assumed the plasma to be unperturbed at infinity. Equations (2.12) and the equations governing the slow plasma motion give

$$(1+\psi^2)^{1/2} = (2\beta)^{-1}M^2(n^{-2} - 1) - \beta^{-1}\ln n + 1 \qquad (2.13)$$

Equations (2.11) and (2.13) can be combined and integrated, yielding

$$\frac{1}{2}\left(\frac{\partial n}{\partial\xi}\right)^2 + V(n;\delta,M) = 0 \qquad (2.14)$$

where the potential V is given by

$$V = \frac{[n - 1 + M^2/n - M^2 + \frac{1}{2}\delta\beta\psi^2]n^2\psi^2}{(1 - M^2/n^2)^2(1+\psi^2)} \qquad (2.15)$$

and $\psi^2 = \psi^2(n)$ is given by (2.13).

We are interested in localized solutions in which the electric field has a maximum at the location where the density perturbation is maximum. Therefore, we let $\psi = \psi_m$ and $n = N$ at $\xi = 0$, so that the nonlinear frequency shift is

$$\delta = 2(1 - N + M^2 - M^2/N)/\beta\psi_m^2 \qquad (2.16)$$

where ψ_m and N are related by

$$(1+\psi_m^2)^{1/2} = -(2\beta)^{-1}M^2(N^{-2} - 1) - \beta^{-1}\ln N + 1 \qquad (2.17)$$

Analysis of (2.14) shows that, for localized solutions to exist, the following conditions must be satisfied:

(i) $$(N-1)(1-M^2) < 0 \qquad (2.18)$$

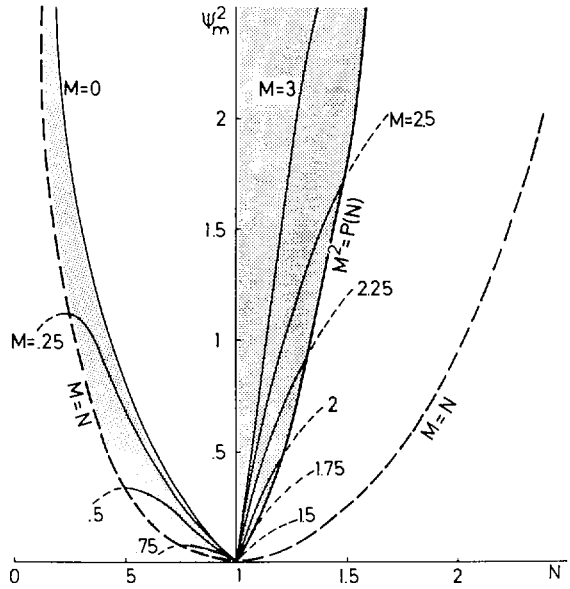


FIG.1. Relation between maximum amplitude ψ_m and the corresponding density (maximum or minimum) N for $\beta = 2$ and different Mach numbers M. Solitons exist only in the dotted areas. For $N < 1$, the region of existence is bordered by the $M = 0$ and $M = N$ lines, whereas for $N > 1$ the $M^2 = P(N)$ line representing condition (2.20) limits the area where supersonic solitons accompanied by density humps can appear.

(ii) $\delta < 1$ (2.19)

(iii) $1 - \delta(1 + \psi_m^2)^{1/2}/N < 0 \quad \text{for} \quad N > 1$ (2.20)

(iv) $M < N \quad \text{for} \quad N < 1$ (2.21)

The regions of existence of solitons are given in Figure 1. It can be shown from (ii) and (iii) that supersonic solitons of a given speed can appear only when β^{-1} is sufficiently large, while subsonic solitons can apppear for all β^{-1}.

A new phenomenon occurs when the effects of relativistic mass variation and ponderomotive force are included simultaneously. This is the appearance of supersonic solitary waves with density humps when the relativistic effects are sufficiently strong. Such a situation can occur because the relativistic mass increase dominates over the density increase associated with the density hump, the combined effect still being a net reduction of the local plasma frequency. Quantitatively, one can understand the above discussion by considering the small amplitude limit as follows. The local plasma frequency, including the

ponderomotive force modification of the density $n = 1 - \beta\psi^2/2(1-M^2)$ and the relativistic mass variation $m = m_o(1+\psi^2)^{1/2} \approx m_o(1+\frac{1}{2}\psi^2)$, is given by $\omega_{pe}^2 = [1 - \beta\psi^2/2(1-M^2) - \frac{1}{2}\psi^2]\omega_{po}^2$. Modulational instability and soliton formation is possible if the nonlinear frequency shift $\omega_{pe}^2 - \omega_{po}^2$ is negative, or $q \equiv \beta\psi^2/2(1-M^2) - \frac{1}{2}\psi^2 < 0$, which clearly allows the appearance of $M^2 > 1$ solitons as long as $\beta/|1-M^2| < 1$. On the other hand, in the nonrelativistic limit, which is realized by letting $\beta \to \infty$ while keeping $\beta\psi^2 = E^2/8\pi n_o T_e$ fixed, the above condition becomes $-\beta\psi^2/2(1-M^2) < 0$, so that only $M^2 < 1$ solitons can appear.

The time scales of the ponderomotive and relativistic effects are determined by the growth rates of the modulational instabilities associated with these effects. They are $|E_o|^2$ and $\beta^{-1}|E_o|^2$ for the ponderomotive and relativistic modulations, respectively. Here we took the purely growing mode ($M = 0$). Thus, when $\beta = c^2/v_{te}^2 \approx 1$, the two effects are equally important.

REFERENCES

[1] KARPMAN, V.I., MASLOV, E.M., Phys. Lett. 60A (1977) 307.

[2] CHEN, H.H., LIU, C.S., Phys. Rev. Lett. 39 (1977) 1147.

[3] BRUECKNER, K., "Plasma Physics" (Wilhelmsson, H., Ed.), Plenum, New York (1977) 9.

DISCUSSION

ON PAPERS V-2-1 TO V-2-3

H. HORA: You reported on the non-linear-force saturation of decay modes due to frequency shift. Absorption by this process was 10% in one case. Do you know of any case where it would be larger than 10%?

C.S. LIU: The absorption coefficient for two-plasmon decay is less than 1% for typical parameters of present experiments in laser fusion. It is important only for long-scale-length or relativistic plasmas.

P. MULSER: You treated the plasma at rest, whereas in fact a laser-produced plasma moves with considerable velocity. How would this influence soliton formation?

C.S. LIU: The group velocity of plasma waves near their turning points is less than the speed of sound, and the static approximation is justified. In general, however, plasma motion should be taken into account.

D.D. TSHAKAYA: You spoke of taking the relativistic dependence of electron mass on the field into account. Do you know of any experimental results which suggest that it is important to allow for the relativistic mass effect?

C.S. LIU: No, I know of no laboratory experiment at present where it would be important. It may be important in certain situations of interest in astrophysics and in connection with future high-power lasers.

THE UNITED STATES PROGRAMME IN HEAVY ION BEAM FUSION

T.F. GODLOVE, D.F. SUTTER
United States Department of Energy,
Washington, D.C.,
United States of America

Abstract

THE UNITED STATES PROGRAMME IN HEAVY ION BEAM FUSION.

Inertial confinement fusion relies on the rapid delivery of a large pulse of energy to a small heavy hydrogen mass, resulting in its compression and burn during a brief period of inertial confinement. Means that have been identified as promising for delivery of the required energy are lasers, electrons, light ions and, most recently, heavy ions. Although the requirements in terms of energy and power are similar for all delivery methods, the origin of the technology, the scientific and technical issues, and the projected characteristics of each method are quite different. Heavy ion fusion as a distinct programme in the USA has been funded since early 1977. In this paper the pellet requirements and potential advantages of the method are described, followed by a discussion of the various scientific and technical aspects of accelerator design and beam transport which are being studied so that a more complete evaluation can be made together with other pellet drivers in the mid-1980s.

1. INTRODUCTION

The basic contention of the proponents of heavy ion fusion (HIF) is that a technology exists which, having been developed for several decades, appears capable of being adapted to deliver the requisite beam to a pellet, using a particle which is well suited to the task. Evaluating this potential requires detailed examination of appropriate accelerator designs, ion/matter interactions, and various high-current beam phenomena. Overall power-plant topics, such as economic analyses and reactor design, are also important but, with the exception of some comments on the costs and scaling of high-energy accelerators, are beyond the scope of this paper.

Two major HIF workshops have been held, the first in 1976 [1] and the second in 1977 [2]. A third is scheduled for September 1978. Since the technology is that of high-energy accelerators, participants have been drawn largely from that community.

2. PELLET REQUIREMENTS

The study of an inertial confinement scheme must begin with consideration of target requirements. R. Bangerter has given the most recent summary of pellet design for heavy ions [3]. Typically, an optimum ion range is from 0.1 to

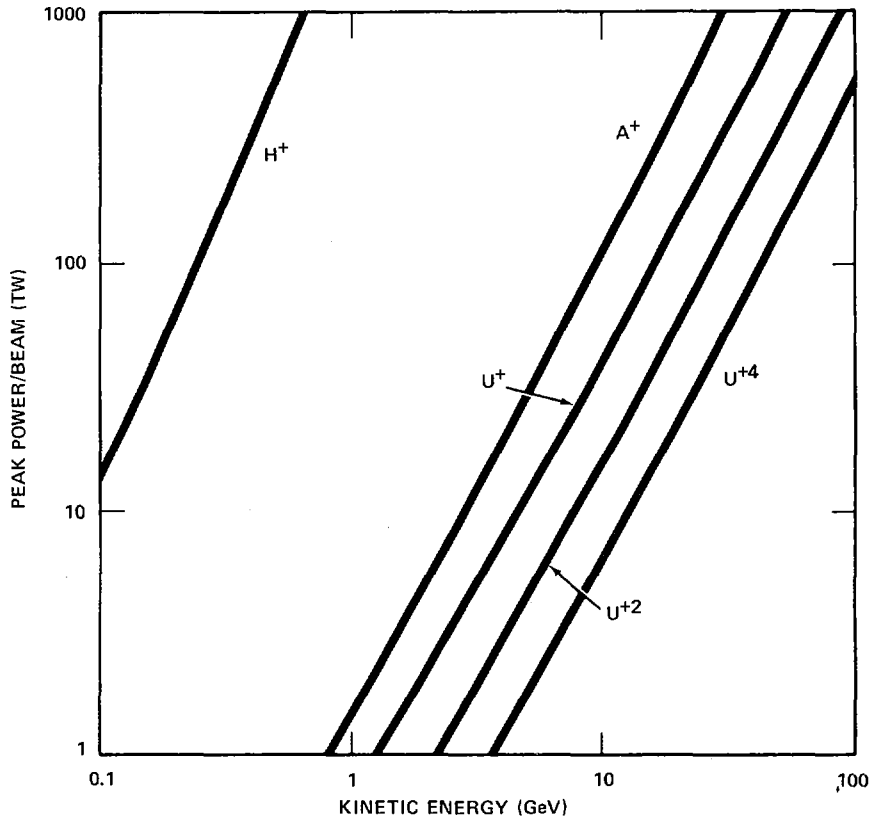


FIG. 1. Maximum peak power per beam line versus particle kinetic energy for several ion species and charge states, based on Eq.(1) using $\epsilon = 2$ cm·mrad and $B = 4$ T. Curves of this kind are derived from an equilibrium between the outward transverse force of the beam and the average external force due to periodic quadrupole focusing magnets.

1 g/cm^2. This dictates an ion energy from 1 GeV to several tens of GeV, depending on ion mass. The kinetic energy, together with the peak power and total pulse energy required, then determines the beam current. From the numerous self-consistent combinations of parameters which could be employed, a combination has been chosen to guide the HIF program, which is a compromise between high-confidence target design on the one hand and overly stringent accelerator requirements on the other. It has been dubbed the base case for a reactor target and leads to the following parameters for incident heavy ions such as bismuth or uranium:

Range - 0.6 g/cm^2 (20 GeV U ion)
Specific Energy Deposition - 20 MJ/g
Peak Power - 100 TW
Total Pulse Energy - 1 MJ (e.g. 100 TW x 10 ns)
Beam Diameter on Target (two beams) - 2.4 mm

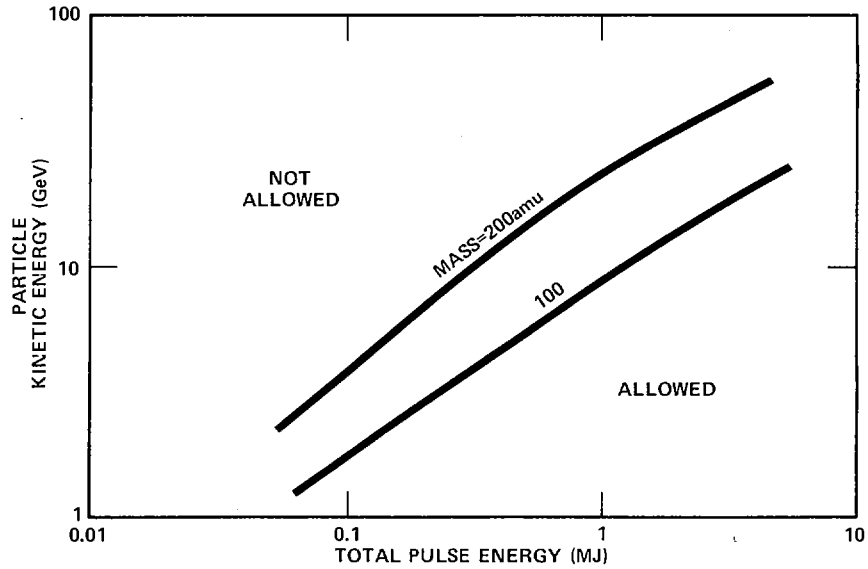


FIG.2. Maximum design particle energy versus total pulse energy on target for two values of ion mass, based on minimum required specific deposition of 20 MJ·g^{-1}. Other conditions: beam radius 1 mm; two beams; target material Pb at 2 g·cm^{-3} and 200 eV. Lower kinetic energy is permissible provided the correspondingly higher beam currents do not exceed other appropriate limits.

For these parameters the required peak beam current is 5 kA (2.5 kA per beam) for charge state 1. Although such currents are far beyond anything so far achieved with heavy ions, they are within the bounds of general beam transport theory. Figure 1 shows the beam power limit for quadrupole periodic focusing. It is seen that a power of 20 - 200 TW per beam is possible for 20 GeV. The number of beams is then determined by either this limit or by other considerations such as the accelerator design itself, whichever is more stringent.

In addition to the above requirements, strict limits are imposed on the beam emittance (product of rms angular divergence and rms radius) and momentum spread. These limits result from geometric considerations of the beam radius on target relative to the chamber radius (typically 10 m) and chromatic aberration in the final magnetic lens at the chamber wall.

An interesting feature of target design unforeseen in early studies is that the specific energy requirement sets an upper limit on the particle energy. This is because, for constant total energy and pulse length, higher kinetic energy implies longer range and reduced beam current, hence reduced specific deposition. Figure 2 shows the maximum allowed kinetic energy vs. total pulse energy, based on the range-energy curves used by R. Bangerter [3]. The curves do not represent a sharp upper limit, but nevertheless have a significant impact on accelerator design.

Both D. Mosher [4] and Bangerter [3] have studied the possible change in stopping power due to the reduced density and high temperature of the target material. No serious modifications are indicated. In any event, the beam parameters for a given desired target gain must be regarded as uncertain by about a factor of two pending more definitive target experiments at high power.

3. POTENTIAL ADVANTAGES

Advocates of HIF point out that it has a combination of advantages unique among pellet drivers. They are summarized as follows:

Target Coupling - As implied in Section 2, energy deposition by ions is an efficient, classical process, with no surprises expected for hot, dense matter. Only at energies well above those given in Figure 2 would nuclear fragmentation cause a potentially serious loss of energy.

Beam Propagation and Transport - The rigidity of high-energy heavy ions makes propagation in a reactor environment, or in long vacuum transport, appear to be tractable for the currents required. More detail is given in Section 5.

Electrical Efficiency - Estimates range from 10% to 40%, more than adequate in the context of current system studies.

Repetition Rate - The required rate for commercial power (1 - 10 Hz) has been demonstrated by a large number of operational accelerators.

Reliability - Large accelerators typically operate at 80% to 90% availability with lifetimes of decades.

4. ACCELERATOR DESIGN

While many of the beam parameters necessary to ignite an ICF reaction with heavy ions have been separately achieved in modern high-energy accelerators, no accelerator has ever produced heavy ion beams at the energy and peak current that will be needed in a HIF power plant. Studies over the last two years indicate that there are no fundamental physics questions related directly to accelerator technology which loom as potential obstacles to building a heavy-ion pilot plant (HIPP) driver in the 1 MJ, 100 TW range. However, there are a number of engineering questions which must be addressed before a cost-effective and technically optimized design can be completed.

Figures 3, 4 and 5 show representative examples of HIF accelerator configurations now being studied at Argonne National Laboratory (ANL), Brookhaven National Laboratory (BNL), and Lawrence Berkeley Laboratory (LBL), respectively [5, 6, 7]. The terms "accumulator", "rebuncher", or "multiplier" ring used in these descriptions refer to storage rings in which effective beam current multiplication occurs through multiturn injection or longitudinal ion bunch compression, or both in the same ring. Since the beam storage times in this application are extremely short compared to the storage times needed for high-energy physics, the magnet design parameters are considerably relaxed and are essentially the same as for synchrotron magnets.

The system utilizing synchrotrons as the principal accelerating element, shown in Figure 3, would produce a 0.8 mm beam spot radius of 20 GeV Xe^{+8} ions on a target pellet at the center of a 5 m radius target chamber. The use of synchrotrons and accumulator rings has two advantages over competing accelerator

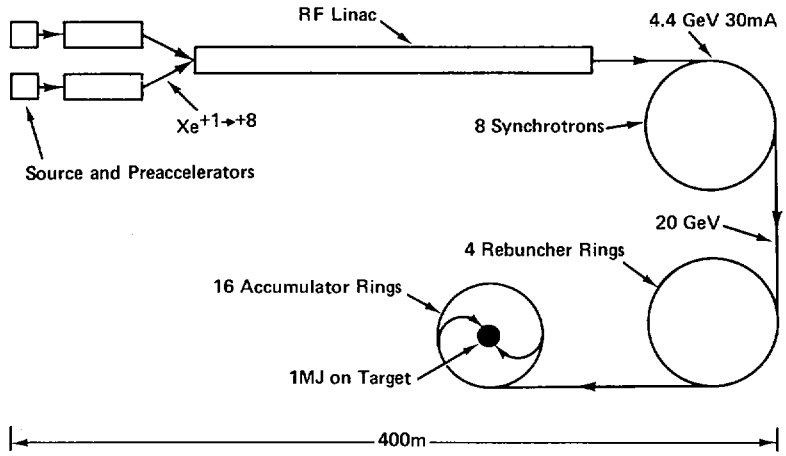


FIG.3. The Argonne National Laboratory conceptual design of a HIPP using rapid cycling synchrotrons (60 Hz) [5]. *Nine turns of 4.4-GeV Xe^{+8} ions from the 550-MV RF linac are injected into each of the synchrotrons. After acceleration to 20 GeV, the ions are transferred into the rebuncher rings and then into the sixteen storage rings where final charge accumulation and bunch compression takes place. 24 ion bunches are extracted from these rings and transported in two groups of 12 transport lines to the target chamber.*

methods: this approach seems to be less expensive by a significant margin, and there exists more accumulated engineering experience with synchrotrons than any other form of high-energy accelerator. However, the complexity of beam manipulations (transfer, timing and routing) must be taken into account, and the space charge limitation at injection in synchrotrons is more severe than in linacs. In addition, the problems of ion charge exchange, wherein an electron is transferred from one ion to another, creating a Xe^{+7} and Xe^{+9} pair which are lost, may be serious because of the long cycle time and is now under investigation. Because Xe^{+8} has a closed atomic shell, the problem is expected to cause a beam loss of only $\sim$ 10% for this design.

The high pulse repetition frequency of the eight rather small synchrotrons (magnetic radius 40 m), of 60 Hz, is well within the state-of-the-art. The Cornell Synchrotron, which is about three times larger, operates at 60 Hz. One of the concerns with synchrotrons is their low electrical conversion efficiency (line power to beam power) but, by using superconducting d.c. bias coils together with nonsuperconducting a.c. coils, ANL estimates that the efficiency can be raised to > 10%.

The conceptual design of a system using an RF linac and accumulator rings shown in Figure 4 operates at 15 Hz producing 10-MJ, 200-TW pulses 50 ns long. In this design the RF linac accelerates U^{+2} ions to the full energy of 20 GeV. The long linac is folded to conserve site space. A system of 8 multiplier/accumulator rings, in a configuration somewhat simpler than needed for the synchrotron/accelerator case, is used to provide current gain and pulse shaping before transport down two opposing sets of four transport lines each to the target. In this design as in the previous one, the final bunching process in the accumulator rings exceeds the space charge limit

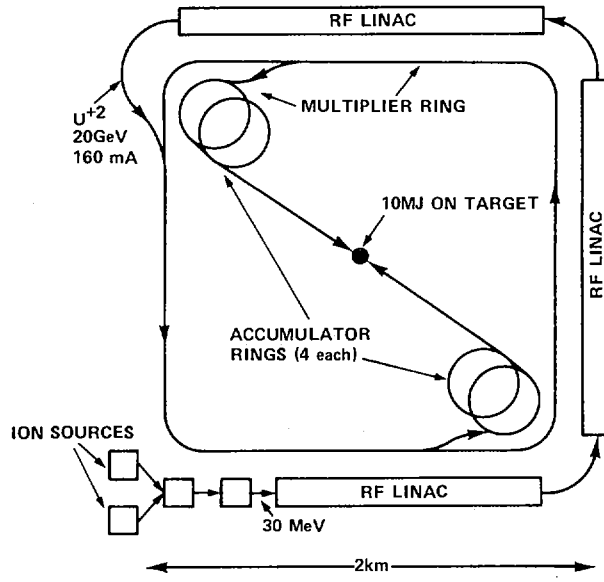


FIG.4. Conceptual design of a 10-MJ, 200-TW accelerator system developed at Brookhaven National Laboratory based on an RF linac [6]. *14 Wideroe, low-β linacs in a "tree" geometry feed a 10-GV RF linac that produces 160 mA of 20-GeV U^{+2} ions. After charge accumulation and rebunching in the large and small multiplier rings, beams are stored in 8 accumulator rings. Final bunch compression, which is initiated in these rings, requires the 1-km-long transport lines to complete the longitudinal collapse to 50 ns. This system operates at 15 Hz and is capable of providing beams to 5 reactor chambers.*

for circular machines, which is set by the limit that the tune[1] shift be < 1/4. The long (1km) beam transport lengths are needed to allow longitudinal collapse of the bunch to take place.

The simplest configuration (c.f. Figure 5), which is based on a linear induction accelerator (LIA), is the one for which there is the least engineering, operating and cost experience. U^{+1} ions are produced in a large-diameter ionization source, stripped to U^{+4} in the preaccelerator and, after acceleration through pulsed drift tube sections to ∿ 100 MeV, are injected into the iron core linear induction elements. Iron cores are used instead of ferrites at low energies in order to achieve the relatively long (∿ 5 μsec) pulse lengths needed to accelerate sufficient charge per pulse. As in all preaccelerator and low-velocity linac schemes, the chief limit to performance is space charge. The long pulse length and very large beam diameter (∿ 30 cm) possible in the pulse drift tube accelerator section permits the very large net currents at low energy which are needed to match optimally the current capability of the LIA at high energy and short pulse lengths. The high current capability of the

[1] "Tune" is the major synchrotron or storage ring circumference divided by the wavelength of transverse oscillations.

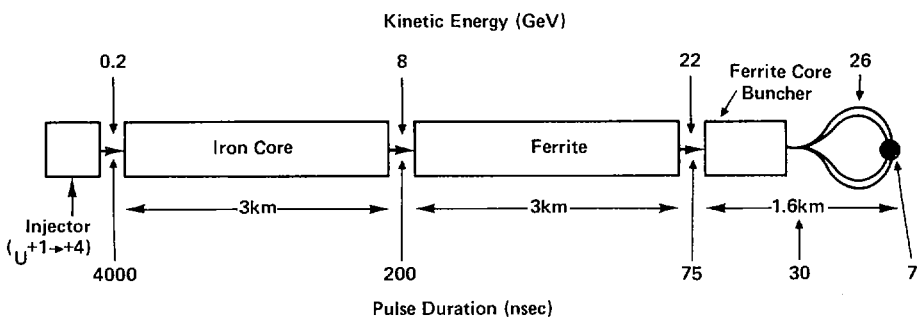


FIG.5. Lawrence Berkeley Laboratory's preliminary conceptual design of a HIPP based on linear induction accelerator (LIA) [7]. An injector consisting of a U^{+1} source, stripper ($U^{+1} \rightarrow U^{+4}$), and pulsed drift tube and induction modules (43 and 20 μs pulse duration) injects 14-MeV U^{+2} ions into the iron core LIA section. After 3 km the pulse length is 200 ns, allowing the use of ferrite core induction modules in the second 3-km section. A ferrite core buncher further compresses the beam longitudinally before splitting into 2, 4 or 8 beams for final transport to the target.

LIA eliminates the need for accumulator rings and results in considerable system simplification.

All LIA's built to date have accelerated electrons and have operated at peak currents in excess of 1000A. While positive ions have not been accelerated in these devices, there appears to be no obstacle to doing so. Because only a limited number of LIA's have been built, data on which to base costs is extremely limited, but the best estimates indicate that the LIA should be at least competitive with the RF linac methods.

The three conceptual designs described represent the three major design approaches now being studied intensively. None of these is in a clearly favored position for use in a HIPP, and the present engineering, prototyping, and cost studies will have to be completed before such a decision can be made.

5. BEAM TRANSPORT AND PLASMA EFFECTS

Three issues emerged early in the HIF program -- all associated with very high beam currents. They are:

(a) The limitations imposed by atomic collision processes, neutralization effects and potential beam instabilities during the propagation of the final beams in the residual gas of the reactor chamber, a distance of 5 to 10 meters.

(b) The limitations imposed by space charge forces during transport of an un-neutralized beam in the periodic focusing system of the accelerator proper and final transport up to the chamber. In this case long distances are involved, in high vacuum.

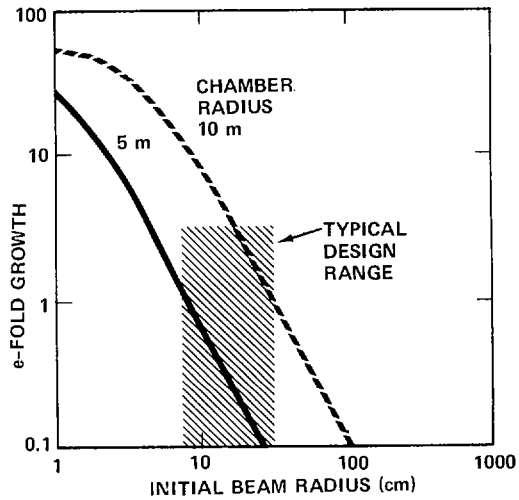


FIG.6. Number of e-foldings of the growth of filamentation instability at the pellet location versus initial beam radius at the chamber wall, for two chamber radii. Parameters used in the calculation: beam velocity c/2; beam power 25 TW; gas pressure 1 torr; plasma $T_e = 20$ eV; and electron density $n_e = 0.5\, n_0$. A focal spot radius of 1 mm is obtained assuming an initial transverse velocity, normalized to c/2, of 1.4×10^{-4} or 4×10^{-5}, respectively, for a 5- or 10-m chamber. The calculations, from Hubbard and Tidman [8], suggest an initial beam radius $\gtrsim 20$ cm for these parameters for the 10-m case.

(c) Is it possible to exceed the normal space charge limit in an accumulator ring during the transient operation, for final bunching into short pulses? Here the "normal" limit refers to a maximum change in tune of 1/4. This constraint on tune shift is more severe than case (b).

Space does not permit a critical review here. Instead we present some of the general conclusions and recent calculations.

For intermediate-to-high gas pressures ($> 10^{-1}$ torr) in a reactor chamber, the beam propagates in a charge-neutral and almost current-neutral condition due to rapid ionization and high plasma conductivity. Individual particles travel on nearly ballistic trajectories from a beam radius, typically > 10 cm at the reactor wall, to a small radius, < 1 cm, at the pellet. Stripping of most of the bound electrons of the beam ions is important and must be included except for very low pressure. At very high pressure, typically > 10 torr, scattering collisions dominate, reducing the growth of micro-instabilities, but increasing the rms radius of the beam to an unacceptable size.

The first stability question to be examined was the common resistive firehose instability. It was soon agreed that the growth of this instability is negligible for parameters of interest [1,2]. Figure 6 shows one example of calculations by Hubbard and Tidman [8] for a potentially more serious instability, that of filamentation. In this case the beam breaks up into a bundle of self-

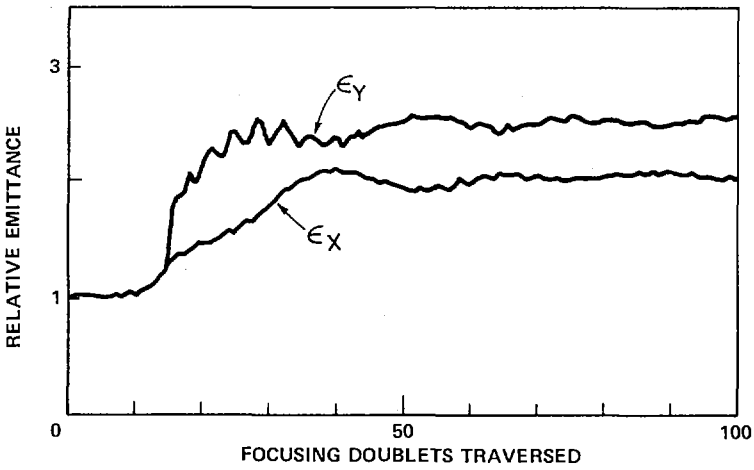


FIG. 7. Computer simulation of the growth in relative transverse emittance as a function of axial distance, measured as the number of quadrupole doublet periods traversed, for vacuum transport in a focusing channel. The run uses 16 K particles and assumes thin lenses with a phase advance of 90° per doublet, reduced to 30° by the assumed value of space charge. Note the growth and subsequent saturation. The difference between x and y emittance is presumed to be artificial.

pinched filaments as it nears the pellet. The calculations indicate that the growth (number of e-folds) is small except in extreme cases. However, it is clear that the system designer must be aware of these limitations. A conservative approach would appear to be: number of beams > 8 (often necessary for other reasons); initial radius > 20 cm; pressure < 1 torr.

The second issue, transport in a vacuum channel, has also received considerable attention. At the 1976 workshop A. Maschke submitted a formula which has been widely used in all of the accelerator design efforts. M. Reiser has given a recent review of the analytic theory with pertinent references [9]. The maximum beam power P that can be transported in a periodic magnetically focussed channel is, including space charge,

$$P = k\ (A/q)^{4/3}\ \varepsilon^{2/3}\ (\beta\gamma)^{7/3}\ (\gamma-1)\ B^{2/3} \qquad (1)$$

where A, q are the ion mass and charge state, $\beta = v/c$, $\gamma = (1-\beta^2)^{-1/2}$, B is the magnet pole tip field, and ε is the beam emittance divided by π. The constant k is about 2×10^{15} watts with B in Tesla and ε in meter-radians. This formula forms the basis for the curves of Figure 1 and shows the steep dependence on the particle energy via the relativistic factors $(\beta\gamma)^{7/3}\ (\gamma-1)$.

Equation 1 is a useful, perhaps even conservative, estimate of power-handling capacity of magnetic channels. However, the complete theory of space charge transport including stability has not been resolved even after decades of accelerator development. It is clearly a difficult problem, probably requiring large-scale particle simulation, but an area for potential cost savings if means can be identified for improved transport. To this end, I. Haber began a program in 1977 to adapt existing NRL computer codes, in

collaboration with others. Figure 7 shows some initial results from a recent report by Haber and Maschke [10]. The evolution of the x and y emittance, defined as the product of the rms values of transverse position and momentum, is plotted vs. axial distance measured in units of quadrupole doublet periods traversed. The behavior exhibits a rapid doubling of emittance but subsequent saturation. Future effort will include detailed examination of instabilities and inclusion of a distribution in longitudinal velocity.

The third space charge issue, transient violation of the limiting current in an accumulator ring, has received little attention. In some unpublished experiments using the Brookhaven AGS accelerator, a group led by A. Maschke succeeded in surpassing the limit by a factor of eight for a few turns using 200-MeV protons. In another set of experiments, also using the AGS, they achieved a bunching factor (initial bunch length/final bunch length) of 60:1 compared to the usual 10:1. These experiments are encouraging but need to be repeated under various conditions and extended.

6. ION SOURCES, PREACCELERATORS AND LOW-β LINACS

In addition to the accelerator system studies described in Section 4, an intensive development program is underway to design, build and operate sources of 10 to 15 MeV beams of heavy ions.

At Argonne National Laboratory, a Dynamitron high-voltage generator has been modified to accelerate 50 to 100 mA of Xe^{+1} to 1.5 MeV. The high-brightness source, which is being built by Hughes Research Laboratories, is to be mounted inside the high-voltage column, and the entire system is to be operated by September 1978. Design of an RF cavity for a 12.5-MHz Wideroe-type linac, but operating at $\lambda/4$ instead of $\lambda/2$, is essentially complete, and a 10-MV section using 10 of these cavities is planned for construction in 1979.

A slightly different approach is being followed at Brookhaven National Laboratory. A duoplasmatron-type ion source operating with a 750-kV Cockroft-Walton preaccelerator has produced a low-current beam of Xe^{+1} ions which were then accelerated to 1 MeV using a prototype 16.6-MHz linac cavity driven by a $\lambda/4$ resonator. In 1979 a 5-m-long, 2-MHz section of Wideroe linac will be constructed, which will be followed later by a similar linac section operating at 4 MHz.

The ion source, preaccelerator and low-velocity linacs described above are designed to meet the needs of the synchrotron and RF-linac-based accelerator configurations described in Section 4. The front end needs of the LIA are quite different, and LBL has developed a 1000-cm^2, 1-ampère, 50-kV CS^{+1} source. The source will be followed by several sections of pulsed drift tube accelerator powered by 500-kV Marx generators. To test the concept of contact ionization, LBL has already operated a 250-cm^2 source which produced $\sim$ 900 mA of CS^{+1} at 200 kV. In addition, LBL has developed a multiaperture Xe^{+1} plasma arc source operating at 35 mA for eventual use with a Cockroft-Walton preaccelerator.

As a result of the work described, it is expected that by the end of 1979 at least three sources of high-intensity and high-brightness ions will be operating in the 3 - 10 MV range. Tests with other ions and of high-current beam transport in long drift tube sections will then be undertaken.

TABLE I. COST ESTIMATES FOR TWO HEAVY ION FUSION DESIGNS

Reference	Arnold et al. [5]	Maschke [6]
Design Parameters	1 MJ, 100 TW, 1 Hz	10 MJ, 200 TW, 15 Hz
SUBSYSTEM	COST	COST
Linac, incl. sources	$ 50M	$532M
Synchrotrons	90M	not used
Intermediate rings	10M	40M
Final storage rings	50M	80M
Beam transport	30M	80M
Conventional facilities	25M	135M
TOTAL	$255M	$667M

7. COST SCALING

Meaningful cost estimates for heavy ion drivers could not be made until the accelerator design efforts reached an acceptable level of completeness. Early estimates ranged up to "several hundred million dollars" for a power plant driver of approximately 10 MJ size [11]. At the BNL workshop, costs for eight different specific subsystems ranging from injectors and various linac structures to final RF bunching and transport were analysed [12]. Table I gives a summary of the cost breakdown for two of the designs described in Section 4. Since the LBL design employs quite different components and is preliminary, it has not been included in Table I. The LBL group reports a preliminary cost, for 1-MJ, 150-TW, 1-Hz parameters, of about $475 M [7]. The costs as listed are in 1978 dollars and do not include site, detailed design, or contingency and, of course, do not include reactor chambers or any other non-driver costs.

We believe that the above costs effectively set limits on and illustrate the cost expected for a HIF power-plant driver. It should be emphasized in this connection that Maschke's design is an order of magnitude more powerful than the ANL and LBL designs, both in energy and repetition rate.

Although more design work is needed and the available designs need to be verified, it is clear that the cost scaling of HIF drivers is not the same as those modular drivers where increased energy is obtained by replication of high-power modules. Rather, we believe that HIF drivers scale, within limits, roughly as the square root of total energy. The basic reason is that the allowable beam current, hence power and total energy, increases rapidly with particle energy. This property is shown in Figure 1 for beam transport, but similar scaling occurs for accelerators in general. The inverse statement is that performance varies roughly as the cost squared.

The above scaling must be taken into account in system studies and economic analyses. For example, if target parameter requirements increase beyond those presently anticipated, the scaling is an advantage. On the other hand, if

potential users demand very small drivers, then it is a disadvantage. For application to a fusion/fission hybrid driver, the HIF technology would appear to be very attractive, since high pulse energy and high efficiency would match in a natural way with cheaper, low-gain pellets. While these diverse speculations may be premature, it is well to recognize the unique characteristics of HIF pellet drivers early in the program.

For brevity we have omitted detailed discussion of several important topics, notably longitudinal bunch compression, the optics of final focus, ion-atom cross-sections, and resulting vacuum requirements. These topics, except for the more recent studies, are discussed in the workshop proceedings [1,2]. Finally, we thank R. F. Hubbard, D. A. Tidman, I. Haber and A. W. Maschke for permission to use their results prior to publication.

REFERENCES

[1] (BANGERTER, R.O., et al., Eds), Final Report of the ERDA Summer Study of Heavy Ions for Inertial Fusion, July 1976, Lawrence Berkeley Lab. Rep. LBL-5543.

[2] (SMITH, L.W., Ed.), Proc. Heavy Ion Fusion Workshop, October 1977, Brookhaven Natl. Lab. Rep. 50769.

[3] BANGERTER, R.O., ibid., p.78.

[4] MOSHER, D., in Final Report of the ERDA Summer Study of Heavy Ions for Inertial Fusion, July 1976 (BANGERTON, R.O., et al., Eds), Lawrence Berkeley Lab. Rep. LBL-5543, p.39.

[5] ARNOLD, R.C., BURKE, R.J., FOSS, M.H., KHOE, T.K., MARTIN, R.L., Hearthfire Reference Concept #3: A Rapid Cycling Synchrotron System, Argonne Natl. Lab. Rep. ACC-6 (1978).

[6] MASCHKE, A.W., Conceptual Design of a Heavy Ion Fusion Energy Center, Brookhaven Natl. Lab. Rep. BNL 50817 (1978).

[7] LAWRENCE BERKELEY LABORATORY, Half-Year Report on the Lawrence Berkeley Laboratory Heavy Ion Fusion Program, Rep. LBL-7591 (1978).

[8] HUBBARD, R.F., TIDMAN, D.A., Filamentation Instability of Ion Beams Focussed in Pellet Fusion Reactors (June 1978), submitted for publication.

[9] REISER, M., Part. Accel. 8 (1978) 167; MASCHKE, A.W., Brookhaven Natl. Lab. Rep. BNL 20297 (1975).

[10] HABER, I., MASCHKE, A.W., Steady State Transport of High Current Beams in a Focused Channel, US Naval Research Lab. Memorandum Rep. 3787 (1978).

[11] KUSWA, G.W., in Final Report of the ERDA Summer Study of Heavy Ions for Inertial Fusion, July 1976 (BANGERTER, R.O., et al., Eds), Lawrence Berkeley Lab. Rep. LBL-5543, p.30.

[12] GRAND, P., et al., in Proc. Heavy Ion Fusion Workshop, October 1977 (SMITH, L.W., Ed.), Brookhaven Natl. Lab. Rep. BNL 50769, p.141.

DISCUSSION

H. HORA: Could you say a little more about pellet compression?

T.F. GODLOVE: The pellet design requirements for heavy-ion fusion, including compression, are similar to those applicable to laser fusion, apart from

the differences in coupling efficiency and in ion range that have to be taken into account. A recent summary of these questions is to be found in the paper of Bangerter cited by us as Ref. [3].

H. HORA: You mentioned the range of uranium GeV ions. How was the stopping power calculated: did you include plasma conditions and anomalous stopping power for high ion intensities?

T.F. GODLOVE: In the paper I mentioned a moment ago Bangerter calculated stopping power for GeV heavy ions under plasma conditions, namely for Pb at 2 $g \cdot cm^{-3}$ and 100 eV. D. Mosher has also examined the question. The differences, compared with cold matter stopping power, are small. I am not aware of any 'anomalous' stopping power for ion currents of interest.

I. ALEXEFF: What percentage of the energy contained in the hot plasma pellet is radiated by bremsstrahlung of the hot plasma electrons on the high-Z ions?

T.F. GODLOVE: I would expect the bremsstrahlung from the hot plasma electrons on the beam ions to be negligible, since the number of ions is many orders of magnitude smaller than the number of target atoms.

NUCLEAR FUSION BY CYLINDRICAL ION IMPLOSION

M. GRYZIŃSKI, J. APPELT, J. BARANOWSKI, M. BIELIK,
E. GÓRSKI, A. HORODEŃSKI, L. JAKUBOWSKI,
A. JERZYKIEWICZ, J. KURZYNA, J. LANGNER,
B. LIPIŃSKI, K. MELZACKI, Z. NAWROCKI, J. NOWIKOWSKI,
M. SADOWSKI, E. SKŁADNIK-SADOWSKA,
J. STANISŁAWSKI, K. SUDLITZ
Institute of Nuclear Research,
Otwock-Świerk,
Poland

Abstract

NUCLEAR FUSION BY CYLINDRICAL ION IMPLOSION.

The present status of investigations on ion-implosion fusion undertaken at the Institute of Nuclear Research, Świerk, Poland, in the early 1960s is presented. Since then several experiments on production of intense radially convergent ion beams have been carried out by means of cylindrical devices equipped with coaxial electrodes consisting of thin metal rods, placed symmetrically and parallel to the axis of symmetry. With these devices, supplied from condenser banks of energy 10 – 20 kJ operated at 30 kV initial voltage, deuteron beams have been produced in a few hundred nanosecond pulses with energy sometimes greater than 30 keV and intensity of the order of 10 kA. The production of energetic ions was accompanied by the production of neutrons, up to 5×10^8 n per discharge. It was found from X-ray observations that convergent ion beams are focused on the symmetry axis of the system so that the cross-section of the dense plasma is several millimetres in diameter. Investigations on a complete symmetric implosion by means of a 150-kJ device have begun.

1. INTRODUCTION

Research on controlled nuclear fusion by means of ion beams was undertaken at the Institute of Nuclear Research (INR), Świerk, Poland, some fifteen years ago [1, 2]. At that time production of a dense plasma by convergent ion beams and the generation of powerful beams by magnetically insulated low-pressure cylindrical discharges between 'particle transparent' (grid or multirod) electrodes were proposed (see Fig.1). The concepts of magnetic insulation and of three-dimensional implosion have been verified by a series of experiments [2 – 5]. It has been shown that, under properly chosen experimental conditions, plasma ions are efficiently accelerated by the radial electric field existing between

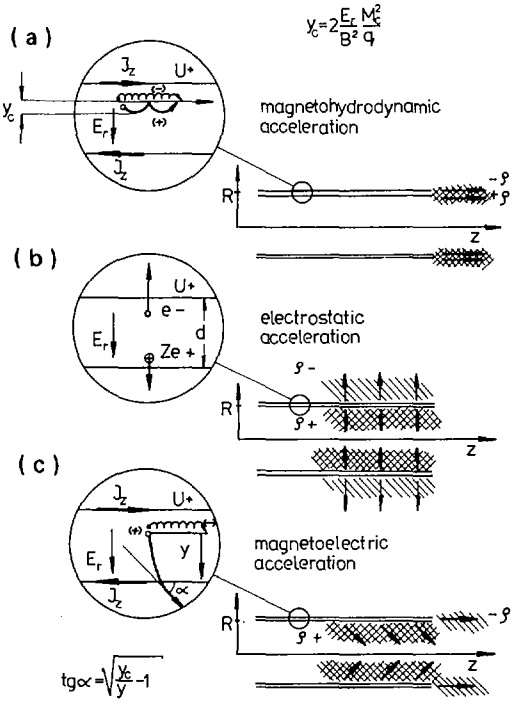


FIG.1. Three basic modes of acceleration of plasma particles in the system of two 'particle-transparent' co-axial electrodes conducting the axial current I_z at the initial potential difference U_0 [1].

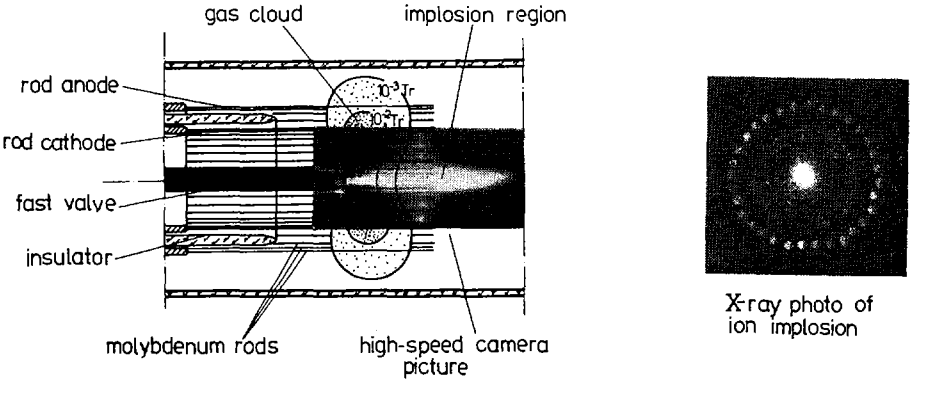


FIG.2. "One-side symmetry" ion-implosion experiment. A convergent ion beam is produced by a low-pressure discharge between co-axial grid-type electrodes.

the coaxial grid electrodes. As a result, at the axis of symmetry of the system, i.e. inside the cylindrical transparent cathode, a high concentration of plasma can be observed, as shown in Fig.2.

The advantages of using ion beams for nuclear fusion are now widely recognized and some laboratories are concentrating on the realization of ion beam-pellet experiments [6 – 11]. The main direction of ion-beam fusion research at the INR, Świerk, however, remains pure ion implosion, i.e. the generation of a dense plasma by the ion beams themselves. This paper presents some results of the ion-implosion studies recently performed at Świerk.

2. THEORETICAL BACKGROUND

The idea of ion-implosion fusion is relatively simple, and rough theoretical estimates present no great difficulties. Without going into details, such an evaluation of spherical ion implosion may be reduced to the following:

(a) The condition of the ideal implosion (which occurs when all the ions emitted in the interval of time

$$\Delta t = R_0 \left(2 \frac{q_i}{m_i} U_0\right)^{-1/2} \tag{1}$$

arrive at the centre of the sphere of radius R_0 at the same moment) can be given by the dependence:

$$U = U_0 \left(1 - \frac{t}{\Delta t}\right)^{-2} \tag{2}$$

where U_0 is the acceleration potential at $t = 0$; q_i and m_i are, respectively, the charge and the mass of the ions considered.

(b) The energy concentration criterion determining the possibility of the fusion reactor operation, is almost the same as for ion beam-pellet experiments. It can be written in the form:

$$E_Q \gtrsim K_E r_f^2 \quad \text{where } K_E \cong \begin{cases} 10\ \text{MJ} \cdot \text{cm}^{-2} \text{ for DT reaction} \\ 2 \times 10^3\ \text{MJ} \cdot \text{cm}^{-2} \text{ for DD reaction} \end{cases} \tag{3}$$

where E_Q is the energy of the imploding ion shell and r_f is the final value of the ion shell radius in cm.

(c) The ion current density criterion can be written as follows:

$$j_0 \cong \frac{K_j}{R_0 \kappa^2} \quad \text{where } K_j \cong \begin{cases} 10^{10} \text{ for DT reaction} \\ 2 \times 10^{13} \text{ for DD reaction} \end{cases} \tag{4}$$

and where j_0 is the initial ion current density in $A \cdot cm^{-2}$ and χ is the concentration factor given by

$$\kappa = \frac{R_0}{r_f} \tag{5}$$

In looking for a way to realize these conditions experimentally, two important ideas have been developed: magnetic insulation and magnetic compensation of defocusing properties of a perforated cathode [1]. The first idea is particularly important for the effective production of intense ion beams, and the second for improving the concentration factor κ.

The effective ion acceleration in a high-current gas discharge can be realized if:

(a) The collisional drift of electrons can be neglected in comparison with the $\vec{E} \times \vec{B}$ drift, i.e. if the initial gas pressure fulfils the condition:

$$p[\text{torr}] \ll 2 \times 10^{-4} \frac{B^2[G]}{E[V \cdot cm^{-1}]} \tag{6}$$

where E and B are, respectively, the mean values of the electric and magnetic field in the discharge; and

(b) The distance d between the electrodes is settled such that the ions moving in the electric field (produced by the potential difference) and the magnetic field (generated by the currents) can leave the inter-electrode volume. But electrons cannot do that, i.e. if

$$3 \lesssim \frac{B(G] \cdot d\,[cm]}{u[V]} \lesssim 100 \tag{7}$$

The condition of the magnetic compensation of the defocusing properties of a perforated cathode (since a perforation deforms the ideal symmetry of the electric field[1]) was analysed in detail for a cylindrical cathode made of thin

[1] Perforation of the cathode can be avoided by using very thin foil and acceleration of ions to very high energies. This method, however, seems unsuitable for our ion-implosion experiments.

parallel rods. A simplified analysis demonstrated that the best compensation can, in this case, be obtained if the current flowing in the rods is related to the potential difference between the anode and the cathode according to the formula:

$$I_0^2\,[A] = 5 \times 10^4\, U_0\,[V]\, n \frac{R}{d} \qquad (8)$$

where n is the number of rods forming a cylindrical cathode with radius R.

Since the topology of the magnetic field does not allow the construction of a device of ideal spherical symmetry, an investigation of the electrode shaping and the distribution of currents in the electrodes is under way, so that an almost spherical ion implosion may be achieved.

Equations (2) – (4) present the main direction of our efforts, while Eqs (6) – (8) demonstrate the method we want to use for solving the most important ion-implosion problems.

3. EXPERIMENTAL FACILITIES

To verify the theoretical predictions, a series of experiments on ion implosion was carried out, using several different facilities. All the devices were equipped with coaxial transparent electrodes consisting of thin metallic rods placed symmetrically and parallel to the axis of symmetry, but remarkable differences were introduced in geometrical dimensions and insulation of the electrodes, as well as in the energy of the supply systems.

In most cases the devices which we call RPI machines were equipped with electrodes consisting of 32 rods each. The rods were 0.8 mm – 1.7 mm in diameter and 100 – 180 mm long. The diameters of the external and internal electrode were, accordingly, equal to 65 and 45 mm in one version and 130 mm and 90 mm in the second. To feed the discharge condenser, banks of energies between 10 kJ and 20 kJ were used. To enable experiments to be made with an external magnetic field, one of the machines was equipped with additional windings supplied by an auxiliary condenser bank. Figure 3 shows such a machine.

The largest machine operated so far is the SOWA-150, which permits investigation of a fully symmetric implosion, as shown in Fig.4. This machine can be powered by two identical 57.5 μF, 50 kV, current pulse generators. The SOWA-150, with some diagnostic equipment, is shown in Fig.5.

All these ion-implosion machines were equipped with fast electromagnetic valves, which permitted rapid feeding of a definite amount of working gas.

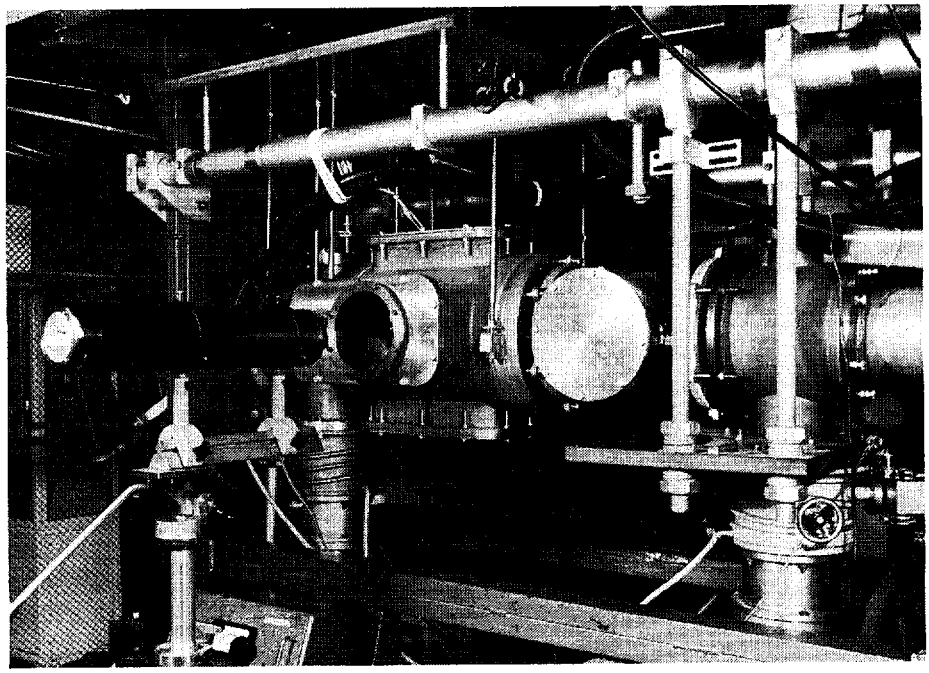


FIG. 3. One of the one-side symmetry devices.

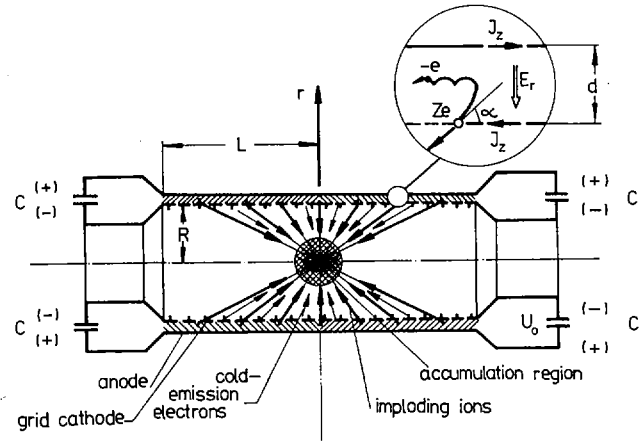


FIG. 4. Scheme of an ion-implosion experiment with mirror symmetry realized with SOWA-150 device as shown in Fig. 5.

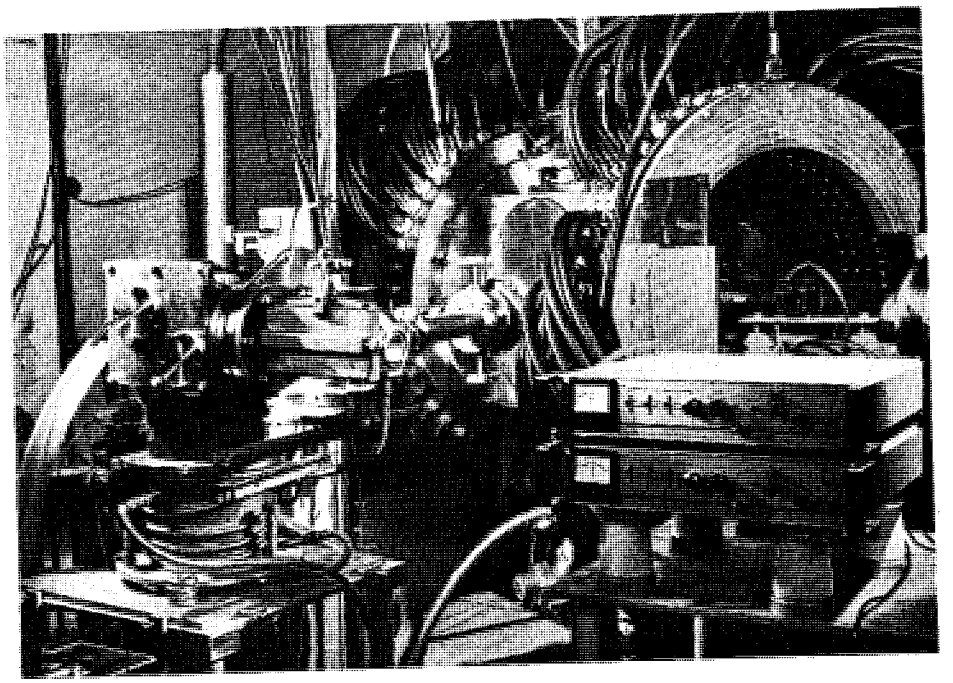


FIG. 5. The mirror symmetry device SOWA-150.

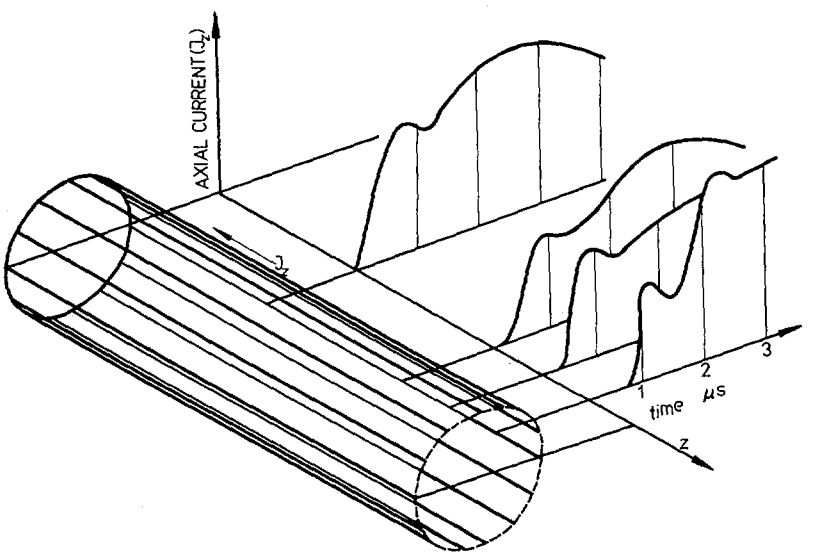


FIG. 6. Magnetic probe measurements showing the current flow along electrodes during discharge.

4. EXPERIMENTAL RESULTS

The principal aim of our investigations was an experimental, and at least qualitative, verification of the basic points of the cylindrical ion-implosion concept. Experimental studies carried out with the above devices concentrated on investigating magnetic insulation and the acceleration of ions, in addition to the study of the focusing properties of the cylindrical rod-type cathode and on space-charge neutralization. Some of the results obtained so far are as follows.

4.1. Magnetic insulation

Since resistivity of the discharge depends directly on the character of the electron current flow, the voltage and current measurements are of particular importance for the study of magnetic insulation. If gas conditions are adjusted to the mechanical and electrical parameters of the system investigated, i.e. if the gas pressure fulfils the relation (6), the discharge current wave forms become strongly deformed and large overvoltages can be observed. Depending on details of the system investigated, the current deformations and overvoltages can have very different forms.

To obtain more detailed information on the character of the electron current flow, some measurements with inner magnetic probes were carried out (see Fig.6), which made it possible to determine the magnetic cut-off displacement of the electron current front. Some information on the character of the electron current flow was also obtained from observations with a high-speed camera. The proper conditions, when the electron drift in the $\vec{E} \times \vec{B}$ fields plays a decisive role, can be identified by increased luminosity of the ends of the anode rods. If the discharge is realized with a heavy gas (e.g. argon or nitrogen) and bright spots of a strong electron emission are visible on the cathode rods, streams of electrons can be observed drifting in the $\vec{E} \times \vec{B}$ fields.

Valuable information on the magnetic insulation phenomenon can also be obtained from X-ray measurements. Such measurements were performed perpendicular to the symmetry axis of the device, and enabled the relation (6), which is directly related to the $\vec{E} \times \vec{B}$ electron drift, to be checked, showing that, at high gas densities, X-rays are produced mainly in the gas-cloud region, while at lower densities the production of X-rays is localized at the ends of the anode rods (see Fig.7).

4.2. Ion acceleration

To obtain information on the ions produced and accelerated in the ion-implosion devices, various mass and energy analysers were used, some of them absolutely calibrated. Time-integrated measurements were performed with a

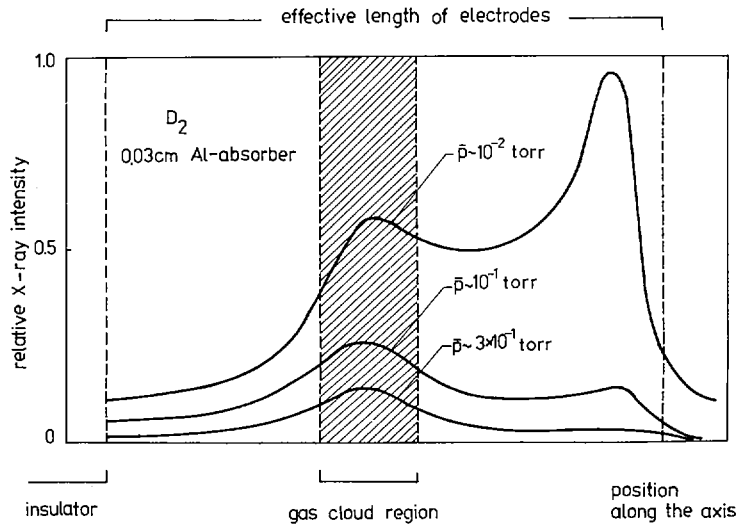


FIG. 7. Results of X-ray measurements demonstrating the dependence of the effectiveness of magnetic insulation on plasma density (initial gas pressure)

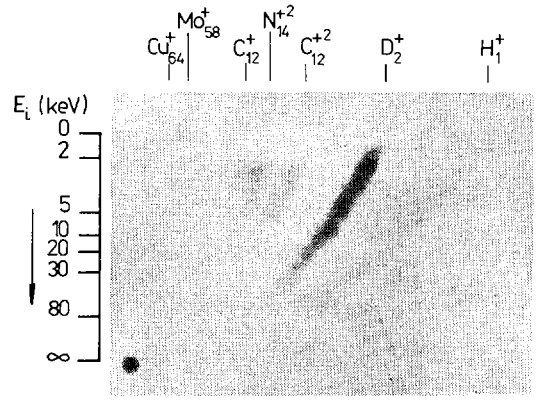


FIG. 8. Example of mass-energy spectrum of ions produced by a cylindrical, magnetically insulated plasma discharge.

Thomson spectrometer, and typical results are presented in Fig.8. Time-dependent measurements were carried out with various electrostatic mass-energy analysers (see Fig.9). These measurements were performed at different angles to the axis of the SOWA-150. Ions of energies up to a hundred keV were observed.

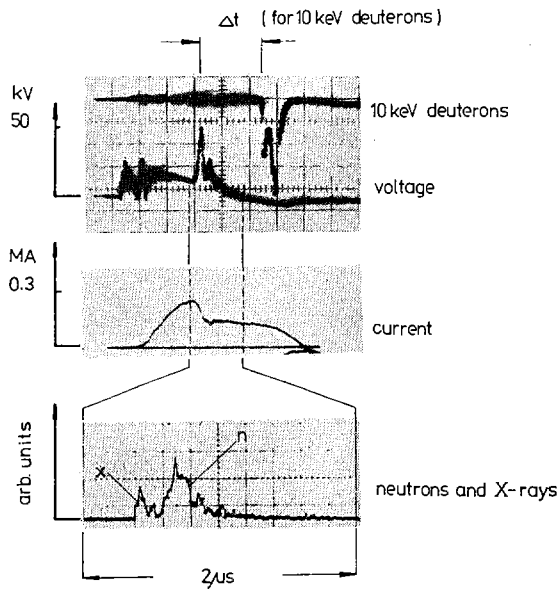


FIG. 9. Results of some time-dependent measurements performed using the ion-implosion experiments.

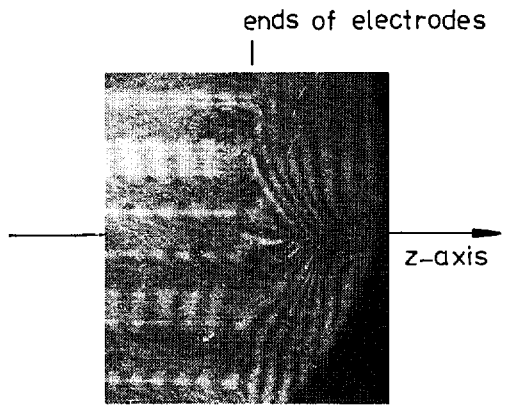


FIG. 10. An interferogram of the inertial cumulation phase observed in an ion-implosion experiment.

A rough estimate of the total ion flux gives ~ 6 kA from measurements with the Thomson spectrometer and about 15 kA from the electrostatic analyser. The flux of energetic neutrals, which can be seen as a zero-deflected beam on the Thomson spectrometer, seems to be rather low, sometimes one order of magnitude lower than the ion flux.

Direct evidence of the efficient production of energetic ions was also supplied by neutron measurements. The total outputs of neutrons generated in one shot, during experiments with some 15 kJ devices, were observed to reach 5×10^8, while the mean output of neutrons was found to be smaller by one order of magnitude. The neutron emission in time was also investigated (see Fig.9), and obvious correlations were found between the neutron yield, the value of overvoltages, and a character of the current deformations discussed above.

4.3. Focusing properties

Although information on the focusing properties of the ion-implosion devices can be obtained from high-speed camera observations and spectroscopic measurements, these methods are not very useful for the most interesting situations when the deuterium plasma is almost fully ionized, for which X-ray measurements give important information. To perform X-ray measurements in the ion-implosion devices, a multi-pinhole camera and a device equipped with various Ross filters and scintillators of different thickness were used for carrying out time and energy analyses.

The time-integrated pinhole camera pictures demonstrated a relatively good concentration of beams at the axis of the system investigated. The diameter of the X-ray focus was found to be of the order of a few mm (see Fig.2). Concentrations of plasma in the focus were measured by laser interferometry, showing concentrations up to 10^{18} cm^{-3} (see Fig.10).

In the experimental studies described here some attempts were also made to localize the neutron sources. The preliminary results obtained so far have demonstrated that a certain amount of neutrons are produced in the central region of the device. The majority of the neutrons seem at the moment, however, to be generated at the walls of the vacuum chamber.

Investigations on time-focusing are less advanced than those discussed here, but technical studies for construction of an appropriate supply system have already been undertaken.

4.4. Space-charge neutralization

To estimate the electron space-charge neutralization in the convergent ion beam, some probe measurements have been made, which showed that typical values of the potential drop inside the passive region of the ion-implosion device

do not exceed several kV. In some cases, however, spatial potentials up to 50 kV have been observed. One can conclude that a cold emission of electrons, which is accountable for the ion space-charge neutralization, changes accidentally within relatively wide limits.

It should be noted that the results presented here have been obtained with "one-side symmetry" devices. Measurements in a full symmetry (shown in Fig.4) have just begun. The main problem to be investigated with the fully symmetric device is that of z-focusing.

5. CONCLUSIONS

The experimental results presented (obtained so far with relatively small devices) and, in particular, the good radial convergence of ion beams of several kA as well as relatively high neutron yield (up to 5×10^8 neutrons per pulse), are consistent with the theoretical estimates and seem to warrant further investigation.

The results obtained seem to support the opinion that ion-beam fusion research can lead to a thermonuclear breakeven experiment faster than other methods, and the way from the breakeven experiment to the construction of a fusion reactor can be shorter than by other approaches.

Our ion-implosion method seems to have some advantages which could slightly shorten the long road to beam fusion.

REFERENCES

[1] GRYZIŃSKI, M., Institute of Nuclear Research Rep. INR 711/XVIII/PP, Warsaw (1966) (in Polish); Nukleonika **14** (1969) 679.

[2] GRYZIŃSKI, M., NOWIKOWSKI, J., SADOWSKI, M., SKŁADNIK-SADOWSKA, E., SUCKEWER, S., in Controlled Fusion and Plasma Physics (Proc. 2nd Europ. Conf. Stockholm, 1967) Paper No. THaC3; published in Plasma Phys. **10** (1968) 450.

[3] GRYZIŃSKI, M., NOWIKOWSKI, J., SUCKEWER, S., in Plasma Physics and Controlled Nuclear Fusion Research (Proc. 3rd Int. Conf. Novosibirsk, 1968) Vol.2, IAEA, Vienna (1969) 87.

[4] SKŁADNIK-SADOWSKA, E., GRYZIŃSKI, M., KURZYNA, J., SADOWSKI, M., in Plasma Accelerators (Proc. 3rd All-Union Conf. Minsk, 1976) 299.

[5] GRYZIŃSKI, M., NOWIKOWSKI, J., JAKUBOWSKI, L., Nukleonika **21** (1976) 1225.

[6] WINTERBERG, F., Phys. Rev. **174** (1968) 212, Plasma Phys. **17** (1975) 69.

[7] CLAUSER, M.J., Phys. Rev. Lett. **35** (1975) 848.

[8] CLAUSER, M.J., SWEENEY, M.A., in Electron Beam Research and Technology (Proc. Int. Top. Conf. Albuquerque, 1975) **1** (1975) 135.

[9] SHEARER, J.W., Nucl. Fusion **15** (1975) 952.

[10] POUKEY, J.W., FREEMAN, J.R., CLAUSER, M.J., YONAS, G., Phys. Rev. Lett. **35** (1975) 1806.

[11] FREEMAN, J.R., et al., in Plasma Physics and Controlled Nuclear Fusion Research (Proc. 6th Int. Conf. Berchtesgaden, 1976), Vol.1, IAEA, Vienna (1977) 167.

CALCULATIONS OF INERTIAL CONFINEMENT FUSION GAINS USING A COLLECTIVE MODEL FOR REHEAT, BREMSSTRAHLUNG AND FUEL DEPLETION FOR HIGHLY EFFICIENT ELECTRODYNAMIC LASER COMPRESSIONS

H. HORA*, R. CASTILLO, R.G. CLARK,
E.L. KANE, V.F. LAWRENCE, R.D.C. MILLER,
M.F. NICHOLSON-FLORENCE, M.M. NOVAK,
P.S. RAY, J.R. SHEPANSKI, A.I. TSIVINSKY
Department of Theoretical Physics,
University of New South Wales,
Kensington, New South Wales,
Australia

Abstract

CALCULATIONS OF INERTIAL CONFINEMENT FUSION GAINS USING A COLLECTIVE MODEL FOR REHEAT, BREMSSTRAHLUNG AND FUEL DEPLETION FOR HIGHLY EFFICIENT ELECTRODYNAMIC LASER COMPRESSIONS.

Inertial nuclear reaction gains are calculated for DT, HB(11) and DLi(6) using spherical hydrodynamics, losses by bremsstrahlung fuel depletion and an anomalous stopping power for calculating the reheat by the charged reaction products. Agreement exists with calculations based on semi-empirical stopping powers. The problem of the delay of thermal coupling for laser compression is being discussed by non-linear Coulomb interaction, instabilities and resonance absorption. The alternative laser compression by non-thermalizing non-linear (optical ponderomotive) force with dielectric swelling has been studied numerically. Guiding parameters have been reproduced and were used for compression by a CO_2 laser pulse in the ns range.

1. REACTION GAINS FROM INERTIAL CONFINEMENT

This section describes the recent results of calculations of nuclear reaction gains for a spherical plasma of initial volume V_o, initial density n_o, of fully ionized ions of charge Z, initial zero velocity, and initial temperature T_o given by equal-distributing an energy E_o to all particles. The early calculations at the time when the first paper on laser-fusion was published [1] were optimizations of the calculation of the nuclear reactions gains [2]:

$$G = \frac{\text{reaction energy}}{\text{input energy } E_o} = \frac{\epsilon_F}{E_o} \int dt d\tau n_i^2 \langle\sigma v\rangle / A \qquad (1)$$

gave plots of $G(E_o)$ for constant n_o with V_o as parameter. Envelopes of these plots arrived at optimum energies $E_o = kT_{opt} = 10.6$ keV for DT reactions and showed a decrease of E_o by the

* On leave at Dept. of Laser Physics, Institute of Applied Physics, University of Bern, Switzerland.

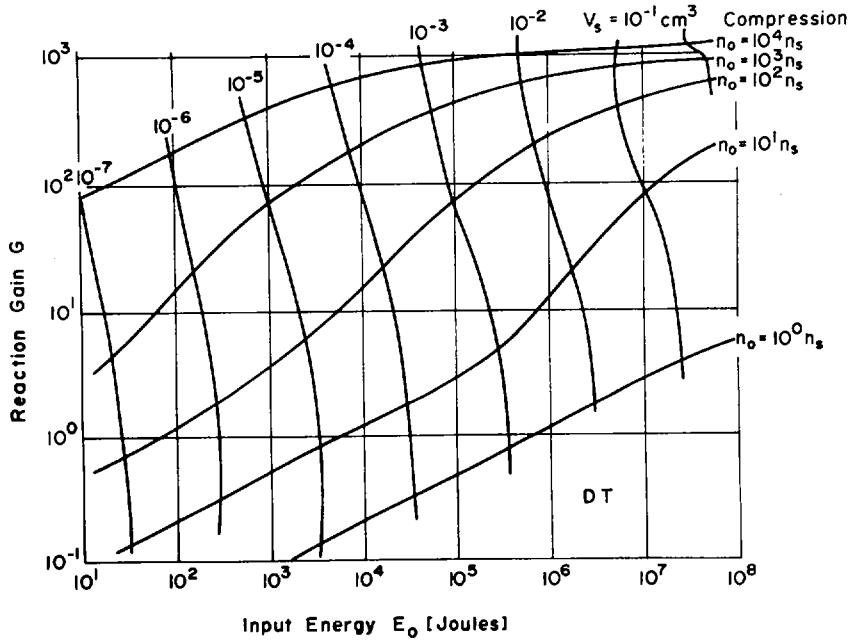


FIG. 1. Reaction gains G for DT depending on the input energy E_0 for various initial densities n_0 (multiples of solid-state density n_s), if solid-state volumes V_s before compression are being used.

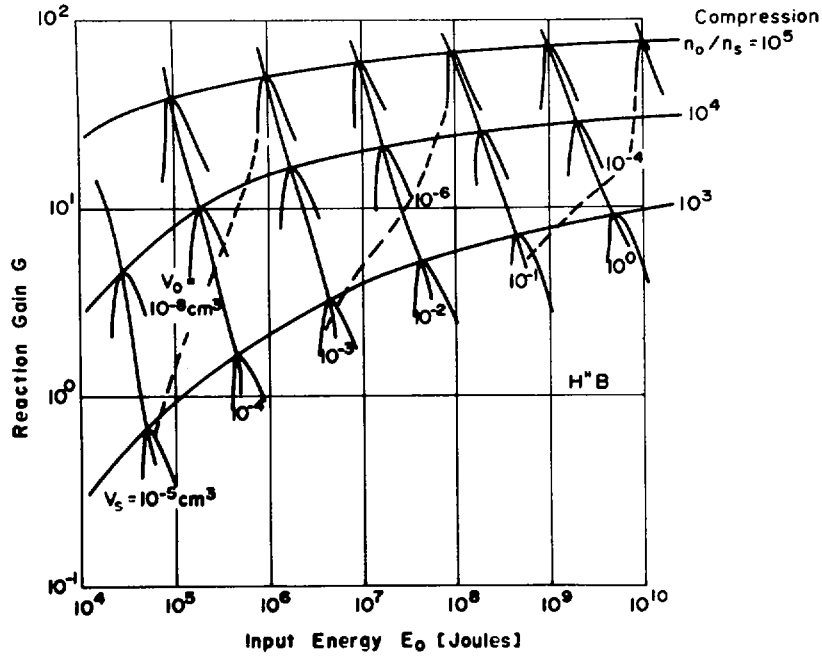


FIG. 2. Gains G for the HB(11) reaction as in Fig. 1.

square, if n_o increased to reach the same G. The general formulation for such V_o that T_{opt} was always reached was given in 1970 by Hora and Pfirsch [3]:

$$G = \left(\frac{E_o}{E_{BE}}\right)^{1/3} \left(\frac{n_o}{n_s}\right)^{2/3} \tag{2}$$

where for DT the break-even energy E_{BE} = 1.6 MeV and the solid-state density $n_s = 5.9 \times 10^{22}$ cm^{-3}. This formula is algebraically identical with Kidder's [4] formula to substitute the Lawson criterion for the dynamics of inertial confinement:

$$G = C_1 n_o R_o \quad , \quad C_1 = 1.66 \times 10^{-23} \text{ cm}^2 \tag{3}$$

where R_o is the radius of the initial volumes. The good agreement of the numerical constant was a confirmation for the fully different methods used for the derivation by several authors [5].

The formulas (2) or (3), however, neglected the losses by bremsstrahlung, the depletion of the fuel to arrive at saturation values of G for high E_o, and the reheat of the pellet by the reaction products which can even cause ignition and self-burning. The reheat process needs a sufficient description of the slowing-down length of charged nuclear reaction products (stopping power) in the plasma. To overcome discrepancies between the usually calculated stopping powers with the measured cases of MeV-electrons in high-density plasma, we used a collective model which was in agreement for electrons [6] and whose agreement for alphas [7] will be shown here. A discussion of the discrepancies in the earlier theories and reasons for the anomalous processes has been given by Hamada [8].

The results for DT are given in Fig. 1 where the gains G (E_o, n_o) are given. It is necessary to choose a volume V_s of the solid state before compression, where the relation between V_s and E_o defines the initial temperature T_{opt}. The left-hand drift of T_{opt} for increasing n_o is due to ignition. The calculation of the time dependence of the plasma temperature and its very sensitive dependence on the parameters has shown in detail [9] how the ignition works for surprisingly low initial temperatures of only 3keV and less. The full inclusion of bremsstrahlung (even for the pessimistic case of neglecting its self-absorption) and fuel depletion makes the calculation realistic.

Agreement of our results with the calculations of Nuckolls [10] can be seen from the following example: Nuckolls arrives at a gain of his definition of 40 for an energy input E_i of 200 kJ. In his case, only 5% of E_i (E_o = 10 kJ) are going into the compressed plasma of $n_o = 10^4 n_s$, which in our definition would result in his gain of 800. For same densities and E_o = 10 kJ we arrive at a gain of 720 which is in remarkably good agreement. Because of Nuckolls' use of stopping powers derived from macroscopic nuclear reactions [11], we conclude an indirect justification of the model of anomalous stopping powers we have used.

The gains for the hydrogen-boron(11) reaction at inertial confinement are given in Fig. 2. The parabolas are from the G calculation at varying E_o without optimized initial temperatures. The very sharp maxima correspond to the sensitivity in the choice of the parameters. Despite strong bremsstrahlung losses, we see ignition and self-burning from the left-hand drift of the V_s-curves. Based on a recalculation of the fusion cross-sections for the 2α-branch of the DLi^6 reaction [12] we calculated a similar diagram to Figs 1 and 2 and found maximum gains of less than 8 for 10^5 times solid-state densities. The V_s had a right-hand drift showing the predominance of bremsstrahlung and the absence of ignition and self-burning.

2. COMPLICATIONS IN LASER COMPRESSION AND NONLINEAR FORCES

The preceding considerations for inertial confinement are based on the assumption of instantaneously working compression which may be easily realized with particle beam compression. The calculations of Nuckolls with laser compression [10] needed an instantaneous action of the thermalization of the laser radiation necessary for driving the ablation. Under this view, our comparison in the preceding section on the pure inertial confinement will be justified.

The real problems with lasers, however, are connected with a delay time of the collisions, if the thermal ablation has to be used, and if not a nonthermalizing ablation-compression by electrodynamic nonlinear forces [13] is being used.

If neodymium-glass laser radiation of 10^{16} W/cm^2 and higher intensity hits DT, electron energies of 100 keV are measured by x-rays and same energies of fast ions are observed [14]. Electrons with a quivering energy of 100 keV in 10^{21} cm^{-3} density have a collision time of 1.3 nsec, while 50% of the laser energy had to be thermalized within less than 0.1 nsec [11]. This problem of a delay restricts neodymium-glass laser intensities to less than 10^{16} W/cm^2, while finally 10^{19} W/cm^2 energy flux densities have to be produced [15], as has been discussed before [16] on the basis of the quivering motion of electrons and the nonlinear absorption constant based on Coulomb collisions.

For the desired fast-thermalizing processes at high laser intensities, anomalous processes have been discussed as parametric decay instabilities [17] and resonance absorption [18], which can both be described by the nonlinear force [19] [20] in a similar way as the nonthermalizing transfer of optical energy into kinetic energy of plasma is a basically nonlinear force process. The nonlinear (optical ponderomotive) forces of direct interaction of electromagnetic radiation with plasmas was discussed for the case of laser radiation in 1967 by Hora, Pfirsch and Schlüter [21] where, for perpendicular incidence of radiation of frequency ω, vacuum electric field amplitude E_v, in an inhomogeneous plasma of a depth x with an electron density $n_e(x)$ corresponding to a (real) refractive index $\tilde{n}(x)$, a time-averaged nonlinear force density was produced:

$$f_{NL}=\frac{1}{8\pi}\frac{\partial}{\partial x}(-E^2-H^2)=-\frac{E_v^2}{16\pi}(1-\tilde{n}^2)\frac{\partial}{\partial x}\frac{1}{\tilde{n}}=-\frac{E_v^2}{32\pi}\frac{n_e}{n_{ec}^2(1-n_e/n_{ec})^{3/2}}\frac{\partial n_e}{\partial x} \tag{4}$$

which could be shown to be identical [16] with the result of microwaves [22]. The special action on gradients of the electron density, however, was a new aspect for lasers leading to the fact that the force is called also "intensity gradient force" [23].

To arrive at reasonable results for oblique incidence of laser radiation, the hitherto most general formulation of the nonlinear force [24] had to be derived by adding nonlinear terms to the usual two-fluid equation of motion:

$$f_{NL}=\frac{1}{c}\underline{j}\times\underline{H}+\frac{1}{4\pi}\underline{E}\,\underline{\nabla}\cdot\underline{E}+\frac{1}{4\pi}(\tilde{n}^2-1)\,\underline{E}\cdot\underline{\nabla}\,\underline{E}+\frac{1}{4\pi}(\tilde{n}^2-1)\,\underline{E}\,\underline{\nabla}\cdot\underline{E}$$
$$+\frac{1}{4\pi}\underline{E}\,\underline{E}\cdot\underline{\nabla}\,(n^2-1)\equiv A+B \tag{5}$$

j is the current density and H is the magnetic field strength of the laser radiation. It is important that terms of $\nabla\cdot E$ and $\nabla\cdot n^2E$ must not be neglected to produce the longitudinal E field in plasmas at oblique incidence of the waves [24] [20]. As long as the laser pulse length $\tau>(2\pi/\omega)10^3$, Poynting vectors can be neglected or added. If we use therefore

$$A=\frac{1}{c}\underline{j}\times\underline{H}+\frac{1}{4\pi c}(\tilde{n}^2-1)\frac{\partial}{\partial t}\underline{E}\times\underline{H} \tag{6}$$

$$B=\frac{1}{4\pi}\underline{E}\,\underline{\nabla}\cdot\underline{E}+\frac{1}{4\pi}\underline{\nabla}\cdot(\tilde{n}^2-1)\,\underline{E}\,\underline{E} \tag{7}$$

from the Maxwellian equations and from vector identities we find

$$A=-\frac{1}{4\pi}\underline{H}\times(\underline{\nabla}\times\underline{H})-\frac{1}{4\pi c}(\frac{\partial}{\partial t}\underline{E})\times\underline{H}=-\frac{1}{4\pi}[\frac{1}{2}\underline{\nabla}\,\underline{H}^2-\underline{H}\cdot\underline{\nabla}\,\underline{H}]-\frac{1}{4\pi c}(\frac{\partial}{\partial t}\underline{E})\times\underline{H}$$

$$B=\frac{1}{4\pi}\tilde{n}^2\underline{E}\cdot\underline{\nabla E}+\frac{1}{4\pi}\underline{E}\underline{\nabla}(\tilde{n}^2\underline{E})-\frac{1}{4\pi}\underline{E}\cdot\underline{\nabla E}=\frac{1}{4\pi}[\tilde{n}^2\underline{E}\cdot\underline{\nabla E}-\frac{1}{2}\underline{\nabla}\underline{E}^2+\underline{E}\underline{\nabla}\cdot(\tilde{n}^2\underline{E})]-\frac{1}{4\pi c}\underline{E}\times\frac{\partial}{\partial t}\underline{H}$$

and by adding A and B

$$f_{NL} = \underline{\nabla} \cdot [\underline{\underline{T}} + \frac{\tilde{n}^2 - 1}{4\pi} \underline{E}\,\underline{E}] - \frac{1}{4\pi c} \frac{\partial}{\partial t} \underline{E} \times \underline{H} \qquad (8)$$

where

$$T = \frac{1}{4\pi} (\underline{E}\,\underline{E} + \underline{H}\,\underline{H} - \frac{1}{2} (\underline{E}^2 + \underline{H}^2)\, \underline{\underline{1}})$$

we found a force density given by Landau and Lifshitz [24] for nondispersive media. Formula (8) is therefore of more general validity, e.g. for the dispersive plasma [24].

The nonlinear forces can dominate the thermokinetic pressure above 10^{14}W/cm^2 for Nd-glass or above 10^{12}W/cm^2 for CO_2 lasers [25]. The swelling by a factor $1/|\tilde{n}|$ of the laser intensity (energy density) or of the radiation pressure or of the effective wavelength, causes a resonance-like electrodynamic explosion of plasma as the momentum balance [24] [26] has shown, resulting also in a photon momentum of half of that of Abraham and that of Minkowski [27]. Numerical studies have shown that a density minimum (caviton) is being generated, discovered by Shearer, Kidder and Zink [28] and reproduced by many others [29] [30]. These minima and the steepening of the density profile [31] have been observed experimentally first by Zakharenko et al. and then by other groups [32]. The linear Z-dependence [16] of emitted fast ions as observed [33], or of MeV ions [34] including relativistic self-focusing [35], are evident for the nonlinear force actions. The generation of magnetic fields in laser-plasmas can be explained by the nonlinear force [36]. While the inclusion of absorption (complex refractive index) has been evaluated for perpendicular incidence [24], Stamper has derived an additional term from a formulation (5) which could be further generalized [37]. The immediate action of the nonlinear force to electrons in tenuous plasma has been demonstrated experimentally [38] where the quivering electron motion is transferred into translative energy.

The observation of strong-swelling dielectric nonthermal explosion by the nonlinear force and of cavity generation could be studied in very transparent microwave experiments [39] and the behaviour of the dominating energy density in Langmuir oscillations at strong swelling was confirmed as soliton process [40]. The little bit larger solitons of the total energy density behave similarly [41] [42].

3. PARAMETRIC DECAY AND RESONANCE ABSORPTION

The general theory of parametric decay instabilities by the nonlinear forces was given by F.F. Chen [19] after the theory was given analytically for microwaves [43] and by a numerical model [17]. Early saturation of these processes has been observed [44] and the arguments have been pointed out by Bobin, et al [45] that these processes and therefore the considered fast thermalization of this type do not dominate for Nd-glass laser intensities above 10^{16}W/cm^2.

Another process for a very fast heating is the resonance absorption, which was described by the macroscopic picture using the nonlinear force in the following way: after the oblique incidence of plasma waves on an inhomogeneous plasma had been used [24] to derive the nonlinear terms in the most general formulation of the nonlinear force, Eq. (5), the generated standing wave at oblique incidence with linear polarized E oscillating parallel to the plane of incidence was causing a striated motion of plasma [20]. Depending on the magnetic Reynolds number, within one half wavelength depth, the plasma was upstreaming, and downstreaming within the next half. Relative velocities corresponded to ion energies of 10 keV and more. Helmholtz-Kelvin instabilities will have thermalized the turbulent motion to fast generation of high temperatures. This process is most effective for angles of incidence from 25° to 30° and is absent for perpendicular incidence. This result of 1972 [20] was identical with a single particle code calculation [18], arriving at maximum action for the same polarization and incidence, "whatever process damps oscillations there" [46]. It has to be underlined that the microscopic picture needs expensive simulations and only preliminary results exist for the significant physical effects [46], while our macroscopic theory [20] explains the anomalous heating in a straightforward way. A combination of macroscopic and microscopic processes should not be excluded, and it should be taken into account that in the present laser-pellet experiments this resonance absorption (or striated motion) process may be dominant and may provide the necessary conditions for the fast

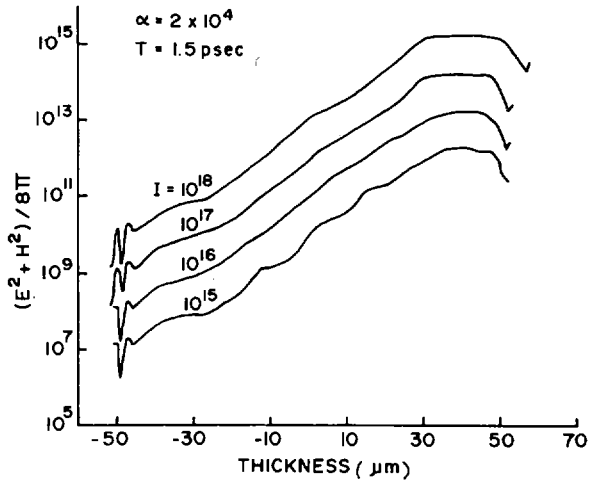


FIG.3. For an $\alpha = 2 \times 10^4$ cm^{-3} bi-Rayleigh initial 100-eV electron density from -50 to $+50$ μ, irradiated by a Nd:glass laser of varying intensity I, the energy densities shown $(E^2 + H^2)/8\pi$ are produced at a time $t = 1.5$ ps.

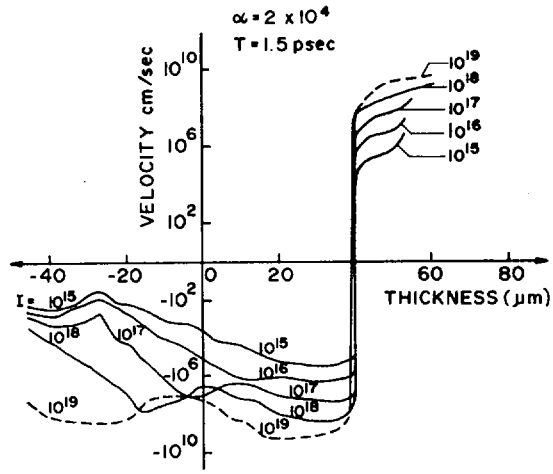


FIG.4. The initially resting plasma has received a velocity profile at 1.5 ps in the case described in Fig.3.

thermalization of the Nuckolls compression. Single experiments at plane targets for 25° incidence gave evidence of the fast heating. The necessary generation of a standing wave pattern for the striated motion may be the reason why a prepulse caused thermal ions only, while irradiation without prepulse showed the Z-dependent nonlinear force acceleration of ions [47]. However, it is remarkable that the two-beam irradiation of pellets by the Argus laser [14] and the similar experiments at KMS did not show the polarization dependence simultaneously with good compression. In both experiments the angle of incidence was nearly zero, and it may be suggested that all the effects of 100-keV fast ions and the transfer of 70% of laser energy into these ions, discovered by F.Meyer in 1973 [33], and the compression might have been caused by immediate nonlinear force acceleration without preceding thermalization.

4. MOTION BY NONLINEAR FORCES

After we were aware that the fast thermalization of laser radiation for the Nuckolls compression of plasma for laser intensities above 10^{16} W/cm^2 for Nd-glass (above 10^{14} W/cm^2 for CO_2) laser seems to be possible neither by nonlinearized Coulomb processes nor by parametric decay instabilities, and not by resonance absorption if there is a perpendicular incidence of the radiation, we studied the nonlinear force acceleration of plasma for neodymium-glass-laser pulses of 1 to 10 psec duration. To provide initial plasma densities of very low reflection, to avoid standing waves and macroscopic Brillouin instabilities, we used Rayleigh profiles with a real part of the refractive index of the kind: $\tilde{n}_R = 1/(1+\alpha x)$, where $\alpha \ll 2\omega/c$, otherwise strong reflection will occur. This profile [13] has the preference that the acceleration from Eq. (4),

$$\frac{d}{dt} v = -\frac{E^2 \alpha}{16\pi n_{ec}} \qquad (9)$$

is constant for the whole profile of the plasma. We used a very general hydrodynamic code for the equations of conservation of momentum (with thermokinetic and nonlinear forces) and energy with different ion and electron temperatures, and thermalization of laser radiation based on complex nonlinear optical constants [25]. The boundary condition of incident laser radiation was for a $\sin^2(\pi t/\tau)$ rising laser pulse being then constant of an intensity I. Initial plasma temperatures were T_i = 100 eV or of this order; initial electron density for DT was a bi-Rayleigh profile, starting from zero at x = 50μ to a maximum at x = 0 with an $\tilde{n}_R$ and symmetrically dropping to x = -50μ. Connection with a low-density plasma provided closed boundary conditions by absorption. τ was 1 psec and we plotted, e.g. for 1.5 psec, the values of $(E^2 + H^2)/8\pi$ (Fig. 3) and the resulting velocities (Fig. 4). Thick blocks of compressing plasma (negative velocities) reached velocities of more than 10^8 cm/sec for subrelativistic intensities of 10^{18} W/cm^2 of Nd glass lasers, though the swelling (Fig. 3) was only in the order of 25. The total energy ϵ transferred to the compressed block increased by $\epsilon \sim I^{1.8}$ on the intensity showed a highly nonlinear electrodynamic (non-thermal) absorption. Varying α, T_i, I, indicated the expected influence of Coulomb collisions, the gasdynamic motion and ion heating by adiabatic compression. For times up to 5 psec, reflection rose, causing standing waves, pushing plasma to the nodes and driving a macroscopic Brillouin instability as described before [30, p. 71]. The generation of density minima (cavitons) was seen as usual. The possibility of postponing the instability was explored numerically, however, for Nd-glass lasers; the nonlinear force compression will have to use pulses of 2 to 8 psec, otherwise the thermalizing processes would interfere. The transfer of quivering motion into kinetic ion energy and the block-like acceleration of the Rayleigh profiles had been reproduced by the numerical results.

There may be difficulty in generating 4-psec Nd-glass laser pulses as the Argus pulses were about ten times longer [14], or the main energy of the Nuckolls pulses [10] was within 60 to 100 psec. The existing largest CO_2 lasers with their 1-nsec pulses are fully in the range for the nonlinear force compression, as the 5 psec for Nd glass correspond to 0.5 nsec for CO_2.

5. CONCLUSIONS FOR CO_2 LASER COMPRESSION

We would not easily have been able to consider CO_2 lasers for efficient fusion by nonlinear force compression if the results of Fig. 1 were not available. As we are now able to use a compression of one hundred times solid-state density only for an ignition, we no longer have problems with too low a density and temperature of the cut-off-dense initial shell to be nonlinearly accelerated and adiabatically heated by compression, described as follows.

The laser pulse should be of 4×10^5 Joules and 0.3 nsec duration (longer pulses may be considered too, but we have to be on the safe side with respect to the Brillouin process [30]. Of this energy we shall transfer 50% into a plasma of density 100 n_s and 3.5 keV temperature resulting in a 100 gain (Fig. 1) or producing 2×10^7 Joules nuclear energy. The target is a DT gas of 10^{19} cm^{-3} atom density limited by a sphere of 2.62 cm radius of a thin CD_2 film and by a photo explosive thin rigid shell of 1 cm radius. A short prepulse plasmatizes the CO_2 and explodes the inner shell, and the expanding plasma reaches a bi-Rayleigh-like density of $\alpha = 1.9 \times 10^3$ cm^{-1} when the main pulse is incident. The intensity at the radius of the shell center is 3.2×10^{13} W/cm^2. The quivering electron motion near the vacuum has an average kinetic energy $\epsilon_{kin} = 335$ eV only. 50% of the laser energy goes to the ablating exterior and 50% into the compression. The acceleration is $a = \epsilon_{kin}\,\alpha/m_i = 2.43 \times 10^{17}$ cm/sec^2. Within 0.3 nsec, a velocity of 7.32×10^7 cm/sec, corresponding to 7.0 keV ion energy, is being reached using the approximation which was based on the very detailed numerical studies described in Section 4. After the laser pulse, the inner half of the plasma will collapse and, assuming nearly adiabatic initial conditions, the density of 10^{19} cm^{-3} will be increased to 5.9×10^{24} cm^3 at compression. A necessary condition is that the temperature of the gas at the time of incidence of the main pulse has to be between 0.5 and 1 eV depending on the Saha equilibrium of ionization to provide an adiabatically reached temperature of 3.5 keV at maximum compression.

The very little thermalization during the interaction of the main pulse is due to the fact that the quivering energy will be swelling to 10^4 eV and more. As the dimension of the pellet is sufficiently large, angles of incidence of the radiation of less than 3° can be assumed to avoid any resonance absorption. For the nonlinear acceleration, the variation of the incidence does not change the symmetry [24]. The parameters mentioned, however, are only the global values of a detailed numerical calculation.

REFERENCES

[1] N.G. Basov and O.N. Krokhin, 3rd Int. Conf. Quantum Electronics, Paris 1963 (Dunod 1964), Vol. II, p.1373. [2] H. Hora, Inst. Plasmaphys. Garching Rpt. 6/23 (July 1964). [3] H. Hora and D. Pfirsch, 6th Int. Conf. Quantum Elect., Kyoto, 1970, Digest p.11. [4] R.E. Kidder, Nucl. Fusion 14 (1974) 797). [5] H. Hora, Nucl. Inst. Methods 144 (1977) 17. [6] E. Bagge and H. Hora, Atomkernenergie 24 (1974) 143. [7] P.S. Ray and H. Hora, Nucl. Fusion 16 (1976) 535. [8] T. Hamada, Aust. J. Phys. (to be published). [9] H. Hora and P.S. Ray, Z. Naturforsch. 33A (1978). [10]. J.H. Nuckolls, Laser Interaction Rel. Plasma Phen. (Plenum) 3B (1974) 399. [11] J.H. Nuckolls, IAEA Tech. Com. Inertial Confin. Meet. Livermore 6th Feb. 1978. [12] R.G. Clark, H. Hora, P.S.Ray and E.W.Titterton, Phys.Rev. C18 (1978) 1127. [13] H.Hora, Sov.J.Quantum Elect. 6 (1976) 154. [14] V.R. Manes et al, J. Opt. Soc. Am. 67 (1977) 717; R.A. Haas et al, Phys. Fluids 20 (1977) 322. [15] J.L. Emmett et al, Scient. Am. 230 (6) (1974) 24. [16] H. Hora, Aust. J. Phys. 29 (1976) 375. [17] P.K. Kaw, J. Dawson, W. Kruer, C. Oberman and E. Valeo, Sov. J. Quantum Elect. 1 (1973) 205. [18] J.P. Freidberg et al, Phys. Rev. Lett. 28 (1972) 795. [19] F.F. Chen, Laser Interaction Rel. Plasma Phen. (Plenum) 3A (1974) 291. [20] H. Hora, Phys. Fluids 17 (1974) 939. [21] H. Hora, D. Pfirsch and A. Schlüter, Z. Naturforsch. 22A (1967) 278. [22] A.V. Gapouov and M.A. Miller, Sov. Phys. JETP 7 (1958) 168. [23] M.A. Stroscio, 10th Int. Quantum Electron Conf. Atlanta 1978, paper I, 11. [24] H. Hora, Phys. Fluids 12 (1969) 182. [25] H. Hora, Opto-Electro 2 (1970) 201.[26] J.D. Lindl and P.K. Kaw, Phys. Fluids 14 (1971) 371. [27] R. Klima and V.A. Petrzilka, Czech. J. Phys. 1322 (1972) 896; V.A. Petrzilka, ibid 1326 (1976) 151; H. Hora, Phys. Fluids 17 (1974) 1042. [28] J.W. Shearer, R.E. Kidder and J.W. Zink, Bull. Am. Phys. Soc. 15 (1970) 1483. [29] K.A. Brueckner, Laser Interact. Rel. Plasma Phen (Plenum) 4B (1977) 891. [30] H. Hora, Laser Plasma and Nuclear Energy (Plenum, 1975). [31] P. Mulser and C. van Kessel, Phys. Rev. Lett. 38 (1977) 902. [32] Yu. A. Zakharenkov et al, Sov. Phys. JETP 43 (1976) 283; M.E. Marhic, Phys. Fluids 18 (1975) 857; R. Fedosejev, M. Richardson et al, Phys. Rev. Lett. 39

(1977) 932; H. Azechi, C. Yamanaka et al, ibid p.1144. [33] D.C. Slater, Appl. Phys. Lett. 31 (1977) 196; F.J. Mayer et al, Phys. Rev. Lett. 40 (1978) 30; P. Wägli and T.P. Donaldson, Ibid 40 (1978) 875. [34] A.W. Ehler, J. Appl. Phys. 46 (1975) 2464; M. Siegrist, B. Luther-Davies and J.L. Hughes, Opt. Comm. 18 (1976) 605. [31] H. Hora, J. Opt. Soc. Am. 65 (1975) 882; H. Hora, E.L. Kane and J.L. Hughes, J. Appl. Phys. 49 (1978) 923. [36] J.A. Stamper and S.E. Bodner, Phys. Rev. Lett. 37 (1976) 435. [37] R.D.C. Miller, 1st Aust. Laser Conf. 1978, Digest p. 123. [38] B. Luther-Davies, B.W. Boreham, J.L. Hughes and M.J. Hollis, 10th Int. Conf. Quant. El., Atlanta 1978, paper I, 7; J.L. Hughes, Invit. paper, 9th Conf. Nonl. Opt. Leningrad June 1978; B.W. Boreham et al, Conf. Raref. Gases, Cannes, July 1978. [39] H.C. Kim, R.L. Stenzel and A.Y. Wong, Phys. Rev. Lett. 33 (1974) 886. R.L. Stenzel, Phys. Fluids 19 (1976) 865. [40] H.-H. Chen and C.-S. Liu, Phys. Rev. Lett. 37 (1976) 693; ibid 39 (1977) 881. [41] J.F. Lam, B. Lipman and F. Tappert, Phys. Fluids 20 (1977) 1176. [42] R.M. Godfrey, Hon. Thesis, UNSW 1978; M.Y. Yu and K.H. Spatschek, Z. Naturforsch. 29A (1974). [43] K.Nishikawa, J. Phys. Soc. Japan 24 (1968) 916. [44] R.L. Dewar, Phys. Fluids 16 (1973) 431.[45] J.L. Bobin et al, J. Physique 38 (1977) 769. [46] R.C. Maloye and R. Morse, Phys. Fluids 21 (1978) 143. [47] B. Luther-Davies and J.L. Hughes, Phys. Lett. A58 (1976) 399.

DISCUSSION

P. MULSER: Have your 'collective' effects been taken into account in numerical calculations (e.g. in LASNEX), and is this the reason for the good agreement between your analytical results and LASNEX?

H. HORA: I gather from Nuckolls (see our Ref. [11]) that they use experimental stopping powers derived from explosions. The agreement of these values with our calculations is the basis of our confidence, as we had to develop stopping powers for the difficult conditions of very strong interaction. The usual Fokker-Planck calculations are only for very small perturbation and can differ from our values by orders of magnitude (see Ref. [7]).

Session X

FUNDAMENTAL PROCESSES AND NEW TRENDS

Chairman

C.N. WATSON-MUNRO
Australia

Papers X-4-1 and X-4-2 were presented
by J.M. Dawson as Rapporteur

LOW-ASPECT-RATIO LIMIT OF THE TOROIDAL REACTOR: THE SPHEROMAK*

M.N. BUSSAC†, H.P. FURTH+, M. OKABAYASHI+,
M.N. ROSENBLUTH†, A.M.M. TODD+
Institute for Advanced Study,
Princeton, New Jersey
and
Plasma Physics Laboratory,
Princeton University, Princeton, New Jersey,
United States of America

Abstract

LOW-ASPECT-RATIO LIMIT OF THE TOROIDAL REACTOR: THE SPHEROMAK.

The ideal and resistive MHD stability properties of a class of toroidal plasma configurations ("spheromaks") having internal toroidal and poloidal fiels and external poloidal fields are considered. The reactor advantage of the spheromak is two-fold: (1) The maximum field strength at the external coils is about half the field at the plasma centre, rather than twice, as in a tokamak. (2) A roughly spherical blanket can be used, rather than a blanket that links the plasma topologically. – Taylor's criterion, which ensures stability against both ideal and resistive modes, has been applied to force-free spheromaks of unity aspect ratio. In the presence of a loosely fitting external conducting shell, oblate spheromaks are stable against all modes except short-wave surface kinks (which are an artifact of the idealized current density profile). The Mercier criterion gives a β-limit below 1%; however, at aspect ratio $\gtrsim 1$, the β-limit for representative spheromak models rises into the range 2–4%. The Mercier analysis has been confirmed by Balloon Code studies. The ideal MHD Pest Code is being applied to spheromaks of various aspect ratios and current density profiles. Ideal-MHD stability can be obtained in the presence of a loosely fitting conducting shell.

1. INTRODUCTION

An ideal magnetic fusion reactor would combine the best features of tokamaks and mirror machines: i.e., closed magnetic field lines and a coil-blanket topology that does not link the plasma. In fusion research to date, the dominant objective has not been reactor optimization, but the demonstration of scientific feasibility under the constraint of available experimental technology. In this feasibility competition, the tokamak has emerged in first place and now seems likely to evolve into the first fusion reactor system. In the longer term, considerations of pure economics will

* This work was supported by the US Department of Energy Contracts EY-76-C-02-3073 and E(11-1)-3237.

† Institute for Advanced Study, Princeton, New Jersey 08540, USA.

+ Plasma Physics Laboratory, Princeton University, Princeton, New Jersey, 08540, USA.

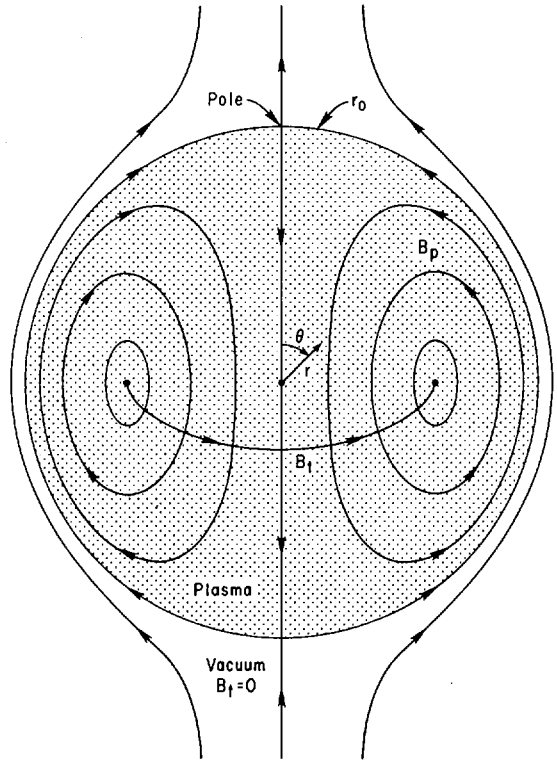


FIG.1. Idealized spheromak configuration ($b/a = 1$, $\alpha = 1.0$, $\delta = 0$).

dominate and may favor a quite different solution. Looking towards this ultimate solution, it is logical to undertake a survey of ideal reactor possibilities without reference to near-term experimental feasibility. In particular, it is logical to look for MHD-stable configurations having closed toroidal flux surfaces, with external coil systems that require only poloidal-field coils. The low-aspect-ratio limit of this family of configurations, which we call "spheromaks ", is illustrated in Fig.1 (see also Table I).

Configurations of the spheromak type were first studied theoretically in an astrophysical context [1,2]. An experimental investigation in the fusion context is described in Ref. [3]; related configurations were studied in Ref. [4]. Extensive MHD equilibrium analyses were carried out in Ref. [5]. Recently a number of authors have drawn attention to the merits of the spheromak configuration [6,7]. The high-aspect-ratio limit of the spheromak family is the familiar "stabilized pinch" [8] with null external toroidal field. The principal aim of the present study is to survey the MHD stability properties of the spheromak family in the range of low aspect ratio and to deduce some guidelines governing hypothetical reactors of this type.

TABLE I. PARAMETERS OF THE SPHEROMAK OF FIGURE 1

B_t on Magnetic Axis	B_{to}
B_p at $r = 0$	$1.38\,B_{to}$
B_p at $r = r_c$, $\theta = \pi/2$	$0.56\,B_{to}$
B_p at $r = \infty$	$0.38\,B_{to}$
Toroidal Current I_t	$0.24\,r_c B_{to}$
Poloidal Current I_p	$0.30\,r_c B_{to}$
Magnetic Energy $W_t = W_p$	$0.051\,r_c^3 B_{to}^2$
q on Magnetic Axis	0.82
q on Separatrix	0.72

[Units are electromagnetic (emu).]

2. EQUILIBRIUM CONFIGURATIONS

The special force-free model $\vec{J} = (k_o/4\pi)\vec{B}$, where k_o is constant in space, lends itself to a straightforward analytic treatment [1,2]. The solutions corresponding to this model can be expressed in the general form

$$\nabla^2\Psi + k_o^2\Psi = 0$$
$$\vec{B} = \vec{r}\times\nabla\Psi + \frac{1}{k_o}\nabla\times(\vec{r}\times\nabla\Psi) \tag{1}$$

where $\vec{r}$ is the spherical radial coordinate. We then have

$$\vec{B} = \sum b_{m,n} e^{in\phi}\left[\left(m(m+1)P_m^n\frac{j_m}{k_o r}\right)\hat{r} + \hat{\theta}\left(\frac{in}{\sin\theta}P_m^n j_m - \sin\theta\,P_m^{n'}\frac{1}{k_o r}\frac{d}{dr}rj_m\right) + \hat{\phi}\left(\sin\theta\,P_m^{n'}j_m + \frac{in}{\sin\theta}P_m^n\frac{1}{k_o r}\frac{d}{dr}rj_m\right)\right] \tag{2}$$

Here we have used the ψ-components $\psi_{m,n} = e^{in\phi}j_m P_m^n$, where $j_m(k_o r) = J_{m+1/2}(k_o r)/(k_o r)^{1/2}$, and $P_m^n(\cos\theta)$ are the associated Lengendre functions. The classical spheromak equilibrium solution illustrated in Fig. 1 is obtained for $n = 0$, $m = 1$. The radius of the plasma sphere is given by $r_c = 4.493/k_o$.

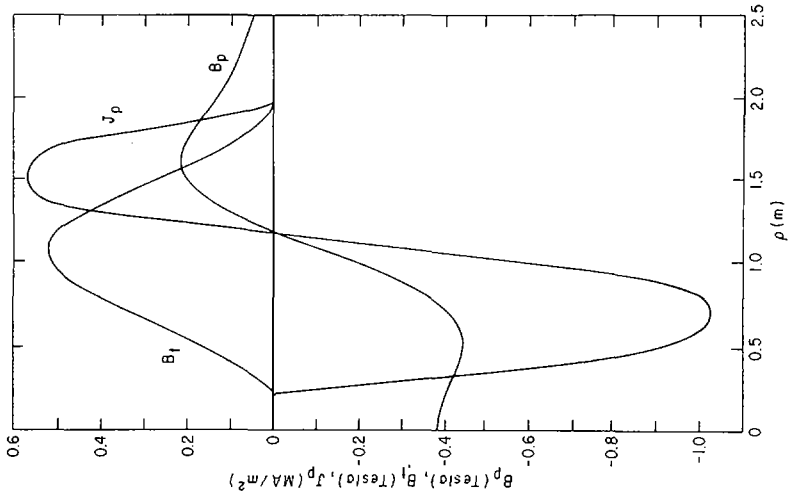


FIG.2(b). Field and current profiles in the horizontal midplane ($I_t = 1.0$ MA).

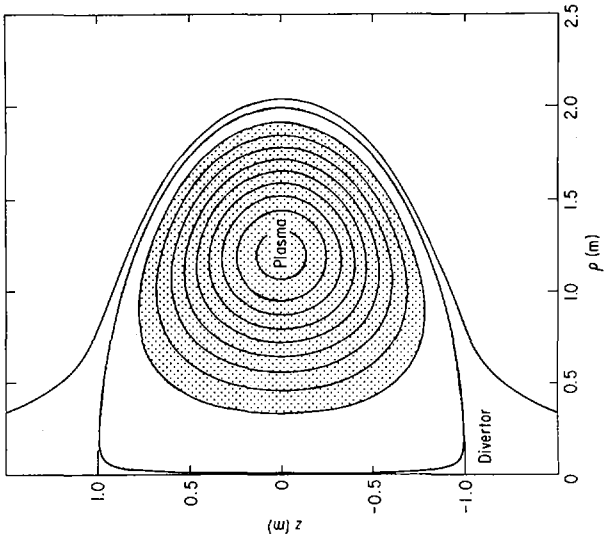


FIG.2(a). Oblate spheromak ($b/a = 0.5$, $\alpha = 1.3$, $\delta = 0.05$). Plasma current flows only in the shaded area.

We will assume either a close fitting shell at $r = r_c$, or a vacuum region $r > r_c$ characterized by

$$\vec{B} = \nabla\{\sum e^{in\phi}[ar^m + br^{-(m+1)}]P_m^n\} \tag{3}$$

with an outer shell at $r = r_s$. Figure 1 corresponds to the case $r_s >> r_c$; the continuity of $\vec{B}$ then implies a uniform vertical field at large r. Some parameters characterizing this configuration are given in Table I.

The superior stability properties of configurations satisfying $\vec{J} = (k_o/4\pi)\vec{B}$ in the absence of a vacuum region, have been pointed out in Ref. [9]. In the practical case, for which an external vacuum region is required, equilibria where the current density drops sharply from $(k_o/4\pi)\vec{B}$ to zero at the plasma edge turn out to be far from optimal. Furthermore, our primary objective is to depart from the force-free case and maximize the MHD-stable ß-value.

Our analysis has, therefore, been extended to more general types of spheromak configurations than that of Fig. 1. Among the possible solutions of Eq. (1), we have treated prolemaks (vertically elongated prolate spheroids with shape factor $b/a > 1$) and oblimaks (oblate spheroids with $a/b > 1$) as well as doublimaks. The shear of the spheromak can be improved dramatically by providing a current-free central hole (cf. Fig. 2). Finite-ß configurations have been introduced into the analysis, as well as into related computer studies. In the computer studies, we have further generalized the current distribution relative to Eq. (1) by using the Grad-Shafranov equation (in cylindrical coordinates) in the form

$$\frac{\partial^2\psi_p}{\partial z^2} + \rho\,\frac{\partial}{\partial\rho}\,\frac{1}{\rho}\,\frac{\partial\psi_p}{\partial\rho} = 4\pi^2\rho^2\,\frac{dp}{d\psi_p} + k_o^2\psi_p^{2\alpha-1} \tag{4}$$

where ψ_p is the poloidal magnetic flux. [For $p \equiv 0$, the solutions of Eq. (4) coincide with those of Eq. (1) when $\alpha = 1$; for $\alpha > 1$, the current profiles are centrally more pe ked.] Figure 2 shows a computer equilibrium solution having current profiles and stability properties that are considerably more practical than those of the configuration in Fig. 1.

Further generalizations of the equilibrium solution could be introduced by providing some external toroidal field [10] through passage of a weak axial current or by applying external helical windings.

3. MHD STABILITY

The instability modes of principal interest can be studied analytically by utilizing the configuration of Fig. 1 and introducing nonsphericity, finite-ß, etc. as small perturbations. In particular, this approach lends itself to the application of Taylor's stability criterion [9], which has the merit of ensuring stability against both ideal and finite-resistivity modes. The ideal-MHD beta limit is calculated from the Mercier criterion [11].

The finite-ß stability of more general configurations, such as that of Fig. 2, has been studied numerically by means of the Mercier criterion and the Balloon code [12]. Conventional resistive and ideal MHD kink mode

analyses have been carried out in the high-aspect-ratio limit, and have been compared with the results of the Taylor analysis and the PEST code [13]. An assessment has been made of resistive flute mode stabilization by non-MHD effects.

3.1 Taylor Analysis

Using an equilibrium solution that satisfies Eq. (1), we look for energy-minimizing perturbations under the constraint of constant $K = \int \vec{A} \cdot \vec{B}\, d^3r$, where $B = \nabla \times \vec{A}$. K is conserved in both ideal and finite resistivity MHD stability theory. As pointed out in Ref. [9], energy-minimizing perturbations inside the plasma continue to satisfy $\vec{J} = (k_o/4\pi)\vec{B}$; thus they are represented by the components of Eq. (2). It is then straightforward to show that the classical spheromak equilibrium solution of Fig. 1, if placed inside a fixed shell ($r_s = r_c$), represents the lowest-energy state relative to all perturbations except the $n = 1$ "tilting" mode, which is only marginally stable. For the fixed-boundary prolemak, this tilting mode becomes unstable; for the oblimak it becomes positively stable. The oblimak is thus in the elite class of absolutely "Taylor-stable" configurations, along with the constant-current-density tokamak and the reverse-field pinch. (The ideal MHD calculation for the case $r_s = r_c$ yields the same tilting mode and stability condition as Taylor's criterion.)

In the more practical case where a vacuum region surrounds the plasma, we must compare the energy-minimizing $\vec{B}_{1c}$-perturbations on the interior of the conducting plasma [Eq. (2)] with the $\vec{B}_{1v}$-perturbations in the vacuum region [Eq. (3)], to determine whether the resultant imbalance of pressure across the plasma surface reinforces or opposes the surface displacement. Specifically, we require for stability

$$\delta E = \int \sin\theta \; d\theta \, d\phi \; \xi(\theta,\phi) \vec{B}_o \cdot (\vec{B}_{1v} - \vec{B}_{1c}) > 0 \qquad (5)$$

where $\vec{\xi} = \xi(\theta,\phi)\hat{r}$ is the surface perturbation, and the perturbed field must remain tangent to the perturbed surface; i.e., $\vec{B} \cdot \nabla r_c = 0$.

The case $n = 0$ is special, since the conservation of K is not insured by the symmetry of the mode, and we must utilize the K-constraint explicitly. Minimizing Eq. (5), we then find that all $n = 0$ perturbations are stable, except for a vertical displacement in the absence of any conducting shell (i.e., $r_s = \infty$), which is marginally stable. Vertical displacements are positively stable in the oblimak, but are unstable for the prolemak, unless stabilized by a loose-fitting shell, with $\sigma \equiv (r_s/r_c) - 1$ of order $|1/\varepsilon|$, where $a/b = 1 + \varepsilon$.

For $n = 1$, we have the trivial possibility of a horizontal displacement, which in the standard spherical case is marginally stable for $r_s = \infty$ (or positively stable for the prolemak and unstable for the oblimak unless a shell with σ of order $1/\varepsilon$ is used). Much more important is the $n = 1$ tilting mode: In the absence of a shell at $r_s = r_c$, there can now be a free-boundary mode where the plasma surface tilts and is compressed at the displaced poles while being decompressed at the former location of the poles. The stability condition for oblimaks is given approximately by $\sigma < 0.2\varepsilon$. Prolemaks are stable against this surface-tilting mode, but of course remain unstable against the fixed-boundary interior-tilting mode previously described.

Modes with $n > 1$ have been evaluated quantitatively only for the spherical case. We find that surface kinks localized near the poles are unstable for all n in the absence of a conducting shell. For $n = 2$ the stability condition is $\sigma < 0.15$. For large n, the condition is $\sigma < 0.75/n$. The higher-n modes, however, should disappear when a less sharp-edged equilibrium current distribution is used [i.e., for $\alpha > 1$, rather than $\alpha = 1$; cf. Eq. (4)], and would in any case be suppressed, for realistic plasma parameters, by finite-gyroradius effects.

The overall conclusion is that a null-β oblate spheromak resembling Fig. 1, but with shape factor $a/b \sim 2$, can be completely stable for a conducting shell radius about 1.15 times the plasma radius.

3.2 Mercier Analysis

To obtain an idea of finite-β stability limits of the configurations that have been studied analytically, the Mercier criterion is evaluated on the basis of the null-β field configurations. This treatment would be inappropriate to tokamaks, where $\beta << \beta_p \sim 1$ so that one cannot neglect the finite-β effects on the equilibrium field or the ballooning effects on the interchange perturbations; since $\beta \sim \beta_p << 1$ for the spheromak, however, the Mercier analysis turns out to give accurate results. The criterion [11] can be written in the form

$$\left(\frac{1}{q}\frac{dq}{d\psi_p}\right)^2 + \frac{dp}{d\psi_p}\,G(\psi_p) \geq 0 \qquad (6)$$

where $G(\psi_p)$ is the negative gradient of the magnetic well — and is normally positive (destabilizing). The marginally stable profile $p(\psi_p)$ is obtained by integrating Eq. (6) with the equality sign. Defining $\beta_o = 8\pi p_o/B_{to}^2$ on the magnetic axis, one finds the disappointing limiting value of $\beta_o \sim 10^{-3}$ for the spheromak of Fig. 1. The problem is that q varies only from 0.82 to 0.72 between the magnetic axis and separatrix, so that the shear-stabilization term in Eq. (6) is weak. (The shear does become singular at the plasma edge, but no pressure drop can be supported across the separatrix.) The result can be improved by various nonspherical shaping effects: an oblimak of shape factor $a/b \sim 2$ is found to have $\beta_o \sim 8 \cdot 10^{-3}$; addition of doublimak terms also improves β_o. The most dramatic benefit, however, is produced by excluding plasma currents from a central hole (cf. Fig. 2), so that q vanishes at the plasma edge, greatly increasing the shear on the plasma interior. The analysis then shows that β_o increases linearly with the excluded flux fraction $\delta = \Delta\psi_p/\psi_p$, saturating at $\beta_o \sim 0.15$ for the limiting case of a large hole (i.e., the cylindrical pinch case).

A survey of the detailed dependence of β_o on δ, as well as on α and on the shape factor has been carried out as a part of the computational program. As illustrated in Fig. 3, oblate spheromaks with $b/a \sim 0.6$ give the maximum values of β_o and of $\langle\beta^*\rangle_o = 8\pi\langle p^2\rangle^{1/2}/B_{to}^2$. Specializing to an oblimak separatrix for which $b/a = 0.6$, we see in Fig. 4 that $\langle\beta^*\rangle_o$ rises dramatically with δ. The dependence on the current peaking parameter α is shown in Fig. 5, where we have further specialized to $\delta = 0.05$. Configurations with fairly rounded current distributions, such as that in Fig. 2 have $\langle\beta^*\rangle_o$-values of ~0.02. Much higher betas can be realized for $\alpha < 1$, but the pressure gradient then becomes localized near the plasma edge; for $\alpha < 0.7$ the q-profile actually becomes nonmonotonic, so that

the pressure profile must be peaked off-axis. While these low-α configurations have extremely favorable β-limits, they also give rise to kink instabilities related to the sharp-edged current profiles (see below). In practice, a compromise value of α, in the range $\gtrsim 1$, must be chosen to achieve optimum overall stability.

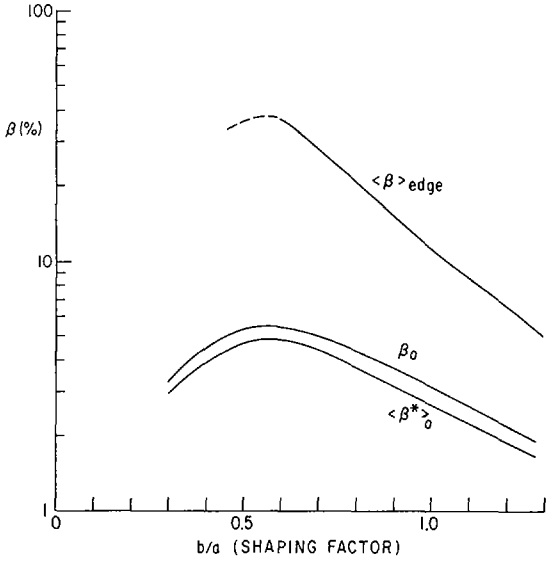


FIG.3. MHD β-limit as a function of b/a (α = 1.0, δ = 0.05).

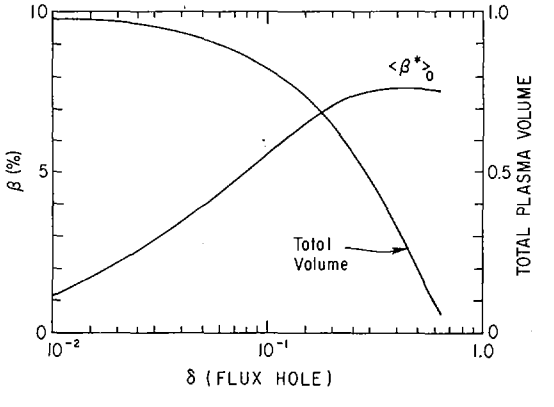


FIG.4. MHD β-limit as a function of δ (b/a = 0.6, α = 1.0).

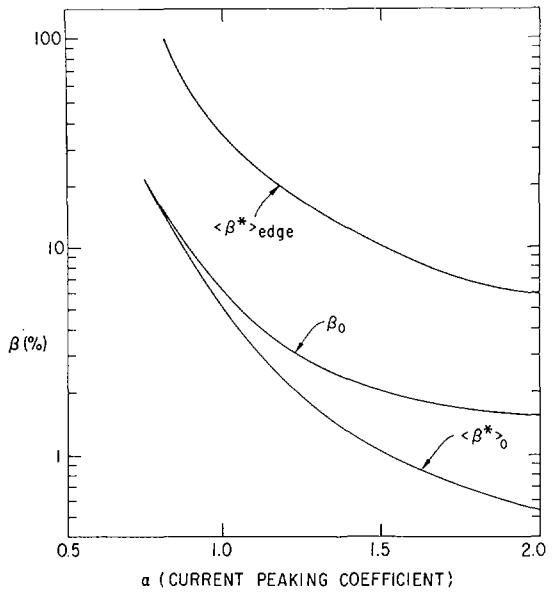


FIG.5. MHD β-limit as a function of α (b/a = 0.6, δ = 0.05).

TABLE II. BETA LIMITS IN SPHEROMAKS AND TOKAMAKS

	Spheromak	Tokamak
B_{to}	$\sim 2.5B_{coil}$	$\sim 0.5B_{coil}$
$\langle\beta^*\rangle_o$	2 - 4%	5 - 10%
$\langle\beta^*\rangle_{coil}$	13 - 25%	1.3 - 2.5%

The maximum-β configurations derived from integration of Eq. (6) have been tested by means of the Ballon code [12], which carries out a self-consistent finite-beta analysis of interchange modes. The results agree well with the Mercier analysis. In addition it is found that the Mercier beta limit is encountered only for very high-n modes; in the presence of realistic finite-gyroradius effects, the stable beta-values will thus tend to be somewhat higher than those shown in Figs. 3-5.

From a practical reactor point of view, the beta-measure of principal interest is not β_o or $\langle\beta^*\rangle_o$, but $\langle\beta^*\rangle_{edge} = 8\pi\langle p^2\rangle^{1/2}/B^2_{edge}$, since B_{edge} is roughly equal to the magnetic filed B_{coil} that must be supported by the external coil system. A relevant comparison of spheromak and tokamak β-values is made in Table II. (It should be noted, of course, that $\langle\beta^*\rangle_o$ can also become a critical factor, as in the example of excessive synchrotron radiation cooling when $\langle\beta^*\rangle_o \lesssim 0.01$.)

3.3 Resistive and Ideal MHD Kink Mode Analysis

The conventional analyses for null-β resistive and ideal MHD stability can be carried out straightforwardly in the limit of low aspect ratio; i.e., for the cylindrical pinch. (The analyses for a closely related reverse-field pinch solution have been carried out in Refs. [13] and [14], respectively.) The model $\vec{J} = (k_o/4\pi)\vec{B}$ now gives a spheromak-like equilibrium configuration where $B_{zo} = BJ_o(k_o r)$, $B_{\theta o} = BJ_1(k_o r)$, for $r < r_c$, and $B_{zo} = 0$, $B_{\theta o} = BJ_o(k_o r_c)r_c/r$ for $r > r_c$. The plasma boundary r_c is taken at the first null of B_{zo}, so that $k_o r_c = 2.405$. The sharp discontinuity of B'_{zo}, and thus of the axial current density, at r_c, has a strongly destabilizing effect. For $r_s = \infty$, the finite-resistivity $m = 1$ instability is unstable over the whole range of $|k|$, the most dangerous modes having $k/k_o < 0$. For $k/k_o < -1/2$, the singular point falls into the plasma, so that the ideal-MHD $m = 1$ mode becomes localized outside the singular point, and tends to be suppressed as $|k|$ increases, while the resistive mode persists. For small $|k|$, the singular point disappears from the plasma and the ideal MHD mode is dominant. Modes with $m > 1$ are stable in both the resistive and ideal MHD analyses. The $m = 0$ mode is peculiar in that the singular point falls on r_c. In the ideal MHD analysis, the $m = 0$ mode is positively stable; this would correspond to our earlier assumption (Section 3.1) that $\vec{B}$ remains tangential to the perturbed plasma surface. In the finite-resistivity treatment, the $m = 0$ mode would be only marginally stable — but the assumption of a sharp-edged current distribution with a resistive surface entails inconsistency in the definition of the equilibrium.

Several approaches are appropriate for stabilizing the high-aspect-ratio spheromak against the $m = 1$ mode. A very loose-fitting shell $r_s \lesssim 1.7 r_c$ will eliminate the ideal MHD modes. The resistive modes are much more difficult to suppress. Even a close-fitting stabilizing shell with $(r_s/r_c) - 1 \equiv \sigma << 1$ can provide stability only against wave numbers up to the limit $|kr_c| < 0.9/\sigma$. The remaining high-k resistive modes are due to the discontinuity of the edge current density that is characteristic of Taylor's model when extended to the case $r_s > r_c$; they will tend to disappear in configurations where the edge current density is a smoother function of r. Thus a combination of profile-smoothing and shell-stabilization will be required to provide complete stability against resistive and ideal kinks. A computational study, designed to maximize σ consistent with resistive kink stability, is being carried out using the tearing-mode code of Ref.[15].

In relating the cylindrical pinch results to the low-aspect-ratio spheromak analysis of Section 3.1, one can readily verify, first of all, that the Taylor analysis applied to the cylindrical case gives a stability condition that is mathematically identical with the condition for simultaneous stability of the resistive and ideal MHD modes. In addition, the gross features of the instability in the cylindrical case are seen to be very similar to those in the low-aspect-ratio case of Section 3.1. Presumably, the Taylor modes in the latter case can also be classified as either finite-resistivity or ideal modes, depending roughly on whether the singular surface falls well into the plasma ($n >> 1$) or not ($n \sim 1$).

In order to extend the ideal MHD treatment over the entire range of aspect ratios, the PEST code [16] has been adapted to the spheromak configuration. Initial computations for $\alpha = 1$ and aspect ratio ~6.7 show that complete stability is achieved with a conducting shell of $\sigma \lesssim 1$, in good agreement with the ideal MHD analysis for the cylindrical case. As the aspect ratio is reduced, a new form of kink instability develops.

To extend the ideal-MHD treatment over the entire range of aspect ratios, the PEST code [16] has been adapted to the spheromak configuration. Initial computations for $\alpha = 1$ and aspect ratio ~6.7 show that complete stability is achieved with a conducting shell of $\delta \leqslant 1$, in good agreement with the ideal-MHD analysis for the cylindrical case. As the aspect ratio is reduced, a new form of kink instability develops. More extensive studies will be needed to establish the optimal relationship between aspect ratio, α-value, and stabilizing-shell design.

3.4 Resistive Flute Mode

The average magnetic-well gradient [cf. the quantity $-G$ in Eq. (6)] is necessarily destabilizing at the plasma surface, where B_t vanishes, and is found to be destabilizing at all radii for standard spheromak configurations, such as those in Figs. 1 and 2. In nonideal MHD theory, the spheromak is therefore unstable against the "resistive-G" flute mode [17]. For representative plasma parameters of a spheromak reactor or medium-high-temperature experiment, however, the growth-rate of resistive-G modes becomes small compared with the diamagnetic drift frequencies; accordingly, finite-gyroradius and collisional-ion viscosity effects [18] must be taken into account.

Results of a computational analysis of resistive stability are reported in Ref. [19]. For a spheromak geometry where the density scale height r_h, the mean radius of curvature $\bar{R}_c$, and the shear length L_s are all roughly of the same order, stability depends mainly on the parameter $\nu_o = \nu_{ei}/\omega_{*e}$, where ν_{ei} is the electron collision frequency, and ω_{*e} is the drift frequency. Assuming a D-T plasma with $T_e \sim T_i$, and $r_h/\bar{R}_c \sim 0.2$, $L_s \sim \bar{R}_c$ one finds that the stability condition is roughly $\nu_o \lesssim 300$. Under typical spheromak reactor plasma conditions, the resistive-G mode should thus be stable by a wide margin; nonetheless, it could play a significant role during the process of plasma formation, if the starting plasma has low temperature and high density. The principal danger from curvature-driven modes in the spheromak geometry would be expected to come from non-MHD phenomena in the highly collisionless regime — notably the trapped-ion mode.

4. EXPERIMENTAL REALIZATION

A basic barrier to the small-scale experimental demonstration of high-temperature confinement in pinch-type configurations is the scaling of the electron streaming paramter $v_{stream}/v_{thermal} \propto T^{1/2}/I\beta_p$, which implies that a certain minimum current level is required in order to guard against microscopic instability. This consideration is far more serious for spheromaks, where $\beta \sim \beta_p \ll 1$, than for tokamaks, where $\beta \ll \beta_p \sim 1$.

The low-aspect-ratio spheromak has the advantage, relative to the conventional pinch, of permitting high current to be attained for smaller total magnetic energy and plasma volume; it has the disadvantage of calling for radically innovative techniques of plasma formation. At this point, three principal formation methods have begun to be explored experimentally.

A. Coaxial Gun Injection. When a radial magnetic field component is set up at the nozzle of a coaxial rail gun, the emerging B_t-driven plasma ring is transformed into a spheromaklike entity [3]. The plasma can then be decelerated and captured in a mirror field.

B. Theta-Pinch Field Reversal. Reversal of the axial field is a standard technique in theta-pinch experiments [20,21]. An interior toroidal field could be established by passing an axial current pulse during the process of field reversal.

C. Pulsed Electron Beam. Short-pulse injection of a cylindrical shell of helically directed relativistic electrons along an axial guide field generates both poloidal and toroidal fluxes, so as to form an elongated prolemak [8]. The beam pulse serves to ionize the background gas, so that the magnetic fluxes remain frozen in the plasma after the beam particles have escaped.

A number of other approaches appear promising. It may prove advantageous to combine concepts (A) and (B) in the form of a radially directed two-ring-electrode rail gun, which pinches an axial magnetic field radially inward, with subsequent axial-field reversal. Adiabatic compression could be applied in conjunction with various spheromak formation methods, to enhance the initial investment in magnetic and plasma energy. Configurations resembling Fig. 2, but linked by a toroidal-field-generating axial conductor could be used to approach the spheromak from the side of low-aspect-ratio pinches or tokamaks.

In order to realize small-scale spheromak configurations with sufficiently extended field-decay times so as to permit a significant assessment of MHD stability, the low-temperature impurity-radiation cooling limit on β_p must be overcome. For this purpose, intense short-pulse auxiliary heating may prove to be important. Both neutral-beam and rf-heating have an additional potential for driving directed plasma currents that could maintain the spheromak configuration in steady state. As in the case of the steady-state, ion-beam-driven tokamak [22], or the field-reversed mirror machine [23], the establishment of a net toroidal plasma current is hindered by an electron drag current, which cancels the ion current unless either $Z_{eff} > 1$ or there is a modulation of magnetic field strength along the direction of current flow; furthermore, counter-injected beams are required to preserve the toroidal balance of mechanical momentum [22]. The use of axial injection to generate the additional poloidal current component required for the spheromak is a relatively simpler task: in this case, the electron drag current is strongly damped by mirror trapping, and the axial mechanical thrust can be balanced magnetically.

5. REACTOR EMBODIMENTS

Spheromak reactor design considerations are essentially different from present-day experimental considerations. For example, the achievement of low values of $v_{stream}/v_{thermal}$ is no longer a critical concern in reactor plasma size. There are two principal reactor alternatives: (A) a pulsed spheromak, which must generate sufficient fusion energy during the field-decay process so as to multiply the initial investment in magnetic field and plasma energy; (B) a steady-state spheromak with a plasma-driving mechanism that is sufficiently efficient so that the associated dissipation does not exceed the fusion power production. In the absence of experimental information, assumptions about $n\tau_E$ in spheromaks must be quite speculative; however, since magnetic field dissipation is of such importance and is likely to remain classical in spheromaks, some general conclusions can be drawn.

5.1 Large Transient Spheromak Reactor

The resistive decay time of a field configuration satisfying $\vec{J} = (k_o/4\pi)\vec{B}$ is given by $\tau_M = 2\pi/k_o^2\langle\eta\rangle$ where $\langle\eta\rangle$ is the average resistivity weighted by J^2. (For the spheromak of Fig. 1, we have $\tau_M = 0.31r_o^2/\langle\eta\rangle$.) The plasma energy balance can be written as

$$\frac{\beta W_M}{\tau_{Eo}} \sim \frac{W_M}{\tau_M} + P_H + \frac{W_M Q_M}{5\tau_M} \qquad (7)$$

where W_M is the stored magnetic energy, τ_{Eo} is the basic plasma energy confinement time, W_M/τ_M is the ohmic heating power, P_H is an auxiliary heating (or cooling) term, and $W_M Q_M/5\tau_M$ is the alpha-particle heating power in a D-T reactor with $Q_M = \int P_F\, dt/W_M$.

If $\tau_{Eo} < \beta\tau_M$ during the heating phase, then $P_H > 0$ is required to reach ignition. For neoclassical transport, one would have $\tau_{Eo} \sim \tau_M/\beta$, so that $\tau_{Eo} >> \beta\tau_M$. In such a case, auxiliary cooling rather than heating would be required; i.e., the plasma energy confinement time would actually have to be reduced below its normal value τ_{Eo}.

Following ignition, the τ_{Eo}-term drops out of the energy balance if $\tau_{Eo} > \beta\tau_M(1 + Q_M/5)^{-1}$. In that case, the reactor Q-value simply equals Q_M, so that the scaling law is $Q \propto \beta^2 I^2/\langle\eta\rangle$, without reference to the plasma $n\tau_{Eo}$.

TABLE III. REPRESENTATIVE PARAMETERS FOR A LARGE SPHEROMAK IGNITION REACTOR WITH RESISTIVELY DECAYING CURRENTS

Minor Radius	125 cm
B_{to}	120 kG
B_{edge}	40 kG
I	70 MA
$T_e \sim T_i$	20 keV
n	$2 \cdot 10^{14}$ cm^{-3}
$\langle\beta^*\rangle_o$	2%
τ_M	~10 min
Magnetic Energy Storage	$\sim 2 \cdot 10^3$ MJ
Fusion Yield per Pulse	$\sim 2 \cdot 10^5$ MJ
Q_M	$\sim 10^2$

TABLE IV. REPRESENTATIVE PARAMETERS FOR A SMALL SPHEROMAK TCT REACTOR WITH BEAM-DRIVEN CURRENTS

Minor Radius	25 cm
B_{to}	120 kG
B_{edge}	50 kG
I	6 MA
$T_e \sim T_i$	20 keV
n	$2 \cdot 10^{14}$ cm^{-3}
Plasma $\langle\beta^*\rangle_o$	2%
τ_M	20 sec
V_{Beam}	150 keV
I_{Beam}	100 A
Beam $\langle\beta^*\rangle_o$	4%
Fusion Power	40 MW
$Q_R = Q_{TCT}$	2.5

Some representative parameters of a pulsed spheromak reactor are shown in Table III. Reasoning from tokamak experimental results, one may suppose that the condition $\tau_{Eo} \gtrsim 10$ sec (for auxilary heating to be unnecessary during temperature build-up) will not be met, whereas the condition $\tau_{Eo} \gtrsim 0.5$ sec (for magnetic energy rather than plasma energy losses to impose the main limitation on Q) may well be met, so that $Q \sim Q_M$.

5.2 Small Steady-State Spheromak Reactor

In an optimized D-T reactor, the ratio of P_F to the required current-driving power can be written in the form

$$Q_R \sim 40\varepsilon_I \beta^2 I^2 T^{3/2} \tag{8}$$

where I is in MA, T is in units of 10 keV and ε_I is the energetic efficiency of the steady-state current-driving method, relative to current generation by a static toroidal E-field. Even if the plasma ignites, the effective reactor Q-value cannot exceed Q_R.

If the neutral-beam current-driving method is used, the scaling of ε_I is such that Q_R can never be much above unity, for parameters of practical interest. To do even this well, calls for β-values (plasma plus beam) in the ≳5% range, so that a medium-high spheromak aspect ratio is required (cf., Fig. 4). If Q cannot be large, it is logical to think in terms of a two-component (or TCT) reactor [24], as in Table IV. The advantage is that the reactor unit size can then be made quite small: for the example given, the quality of plasma confinement becomes unimportant if $\tau_{Eo} > 50$ msec. It is of incidental interest to note that a TCT spheromak of size comparable to the example in Table IV could achieve $Q > 1$ even in the face of Bohm diffusion.

The most useful spheromak reactor prospect, of course, would arise from the development of efficient current-driving methods (possibly using rf to maintain an energetic-electron current). In that case, a steady-state reactor of moderate size could attain high Q-values.

ACKNOWLEDGMENT

The authors acknowledge useful discussions with Drs. D. L. Jassby, G. Laval, P. H. Rutherford and S. Yoshikawa.

REFERENCES

[1] LÜST, R., SCHLÜTER, A., Z. Astrophys. 34 (1954) 263.
[2] CHANDRASEKHAR, S., in Proc. of the National Academy of Sciences 42 (1956) 1.
[3] ALFVÉN, H., in Proc. 2nd Int. Conf. on Peaceful Uses of Atomic Energy 31 (1958) 3; LINDBERG L., JACOBSON, C. T., Phys. Fluids Suppl. (1964) S44; WITALIS, E., Plasma Physics 13 (1971) 507.
[4] BOSTICK, W. H., WELLS, D. R., Phys. Fluids 6 (1963) 1325; WELLS, D. R., et al., Phys. Rev. Lett 33 (1974) 1203.
[5] MORIKAWA, G. K., et al., Phys. Fluids 12 (1969) 1648; 13 (1970) 497; 14 (1971) 781.
[6] KOLOC, P. M., Bull. Am. Phys. Soc. 22 (1977) 1152; 21 (1976) 1194.
[7] SETHIAN, J. D., et al., Phys. Fluids 21 (1978) 1227.
[8] ROSENBLUTH, M. N., in Proc. 2nd Int. Conf. on Peaceful Uses of Atomic Energy 31 (1958) 85.
[9] TAYLOR, J. B., in Pulsed High Beta Plasmas, Pergamon, Oxford (1976) 59.
[10] YOSHIKAWA, S., Bull. Am. Phys. Soc. 8 (1963) 298.
[11] GLASSER, A. H., GREENE, J. M., JOHNSON, J. L., Phys. Fluids 18 (1975) 875.
[12] DOBROTT, D., et al., Phys. Rev. Lett. 39 (1977) 943.
[13] VOSLAMBER, D., CALLEBAUT, D. K., Phys. Rev. 128 (1962) 2016.
[14] GIBSON, R. D., WHITEMAN, K. J., Plasma Physics 10 (1968) 1101.
[15] GLASSER, A. H., FURTH, H. P., RUTHERFORD, P. H., Phys. Rev. Lett. 38 (1977) 234.
[16] GRIMM, R. C., GREENE, J. M., JOHNSON, J. L., in Methods of Computational Physics 16, Ed. J. Killeen, Academic Press, New York (1976) 253.
[17] FURTH, H. P., KILLEEN, J., ROSENBLUTH, M. N., Phys. Fluids 6 (1963) 459.
[18] COPPI, B., ROSENBLUTH, M. N. in Plasma Physics and Controlled Nuclear Fusion Research (Proc. 2nd Int. Conf. Culham, 1965) Vol. 1, IAEA, Vienna (1966) 617.

[19] BUSSAC, M. N., ROSENBLUTH, M. N., RUTHERFORD, P. H., WHITE, R. B., to be presented at the American Physics Society, Division of Plasma Physics Meeting, Colorado, 1978.
[20] ES'KOV, A. G., et al., in Plasma Physics and Controlled Nuclear Fusion Research (Proc. 5th Int. Conf. Tokyo, 1975) Nuclear Fusion Supplement (Translations Volume), IAEA, Vienna (1975) 155; in Controlled Fusion and Plasma Physics (Proc. 7th Europ. Conf. Lausanne, 1975) I, 55.
[21] LINFORD, R. K., PLATTS, D. A., SHERWOOD, E. G., to be published.
[22] OHKAWA, T., Nuclear Fusion 10 (1970) 185.
[23] BALDWIN, D. E., RENSINK, M. E., Comments on Plasma Physics and Controlled Fusion IV (1978) 55.
[24] DAWSON, J. M., FURTH, H. P., TENNEY, F. H., Phys. Rev. Lett. 26 (1971) 1156.

DISCUSSION

I.R. JONES: Have any experimental methods been proposed for setting up the *toroidal* field profile and, if so, what are they?

H.P. FURTH: A number of possible approaches are listed in our paper. The first experimental realization was reported by Alfvén in 1958, at the Second International Conference on the Peaceful Uses of Atomic Energy. The toroidal field, in this case, was the driving field of a Marshall gun. The poloidal field was added by a fringe-field structure at the end of the gun.

K.V. ROBERTS: Do you assume that the field configuration would sustain itself automatically, as is found experimentally in the Reversed-Field Pinch?

H.P. FURTH: Alfvén's group reported an anomalous conversion between the toroidal and poloidal fluxes, which is reminiscent of the phenomena found in the Reversed-Field Pinch. If we do not rely on anomalous phenomena, the main problem of a steady-state spheroid would be that of maintaining the poloidal field. Here one encounters the same difficulties as in the case of the steady-state tokamak and the reversed-field mirror machine. If this problem can be solved, the maintenance of the toroidal flux becomes relatively easy.

P.J. TURCHI: Would it be possible to use this configuration for field-shaping at the end of a high-beta plasma, such as a theta-pinch, to achieve a cusp-ended system (in the manner of the Centaur experiment)? In this way, a high-beta plasma (~ 0.9) could be stably confined. The cost of the low-beta end regions could be amortized by extending the length of the high-beta region. Cusp end losses would be moderate at very high magnetic fields, and electron conduction losses could be handled by techniques similar to those proposed for mirror systems.

H.P. FURTH: This is an interesting idea. The proposed configuration may well be stable.

BOUNDARY LAYER ANALYSIS OF COLD-BLANKET SYSTEMS*

B. LEHNERT, B. BONNEVIER,
J.R. DRAKE, A. KUTHY, D. OHLSSON,
E. TENNFORS, B. WILNER
Royal Institute of Technology,
Stockholm,
Sweden

Abstract

BOUNDARY LAYER ANALYSIS OF COLD-BLANKET SYSTEMS.

Theoretical analysis of the partially ionized boundary layer of a magnetized plasma indicates that a cold-blanket state exists only within restricted ranges of such parameters as the power input, the ion density, and the β-value. In tokamaks, cold-blanket operation is likely to require total β-values of at least a few per cent. Experimental investigations show that the plasma core density increases with the imposed power input, as long as the plasma is permeable to neutral gas. On the other hand, at large enough power inputs and ion densities to sustain an impermeable plasma, the core density becomes weakly dependent on both the power input and the neutral wall density. The boundary layer thickness then decreases as the power input increases. All these features are at least in qualitative agreement with theory.

1. INTRODUCTION

The "cold-blanket" (or "cold-mantle") state of a quasi-steady magnetically confined plasma is defined in this paper as one in which a fully ionized hot plasma core becomes separated from surrounding walls by a partially ionized boundary layer, within which the temperature remains at a few electron volts. We consider a cylindrical plasma column of radius a, being immersed in an axial magnetic field $\vec{B}$, and define the characteristic features of the system as outlined in Fig.1. The boundary layer of this model [1] has a thickness $x_b \ll a$, and the plasma temperature T adopts the value $T_b \simeq 5\times10^4$K at its inner "edge" $r = r_b$. In the layer the plasma density n drops from the value n_b at $r = r_b$ to $n(a) \ll n_b$ at the wall, whereas the density $n_{nf} \simeq n_n$ of fast neutrals drops from n_{na} near the outer "edge" to a value

---

* Section 1 is by all the authors;
Sections 2 and 3 are by B. Lehnert, and
Section 4 is by the remaining authors.

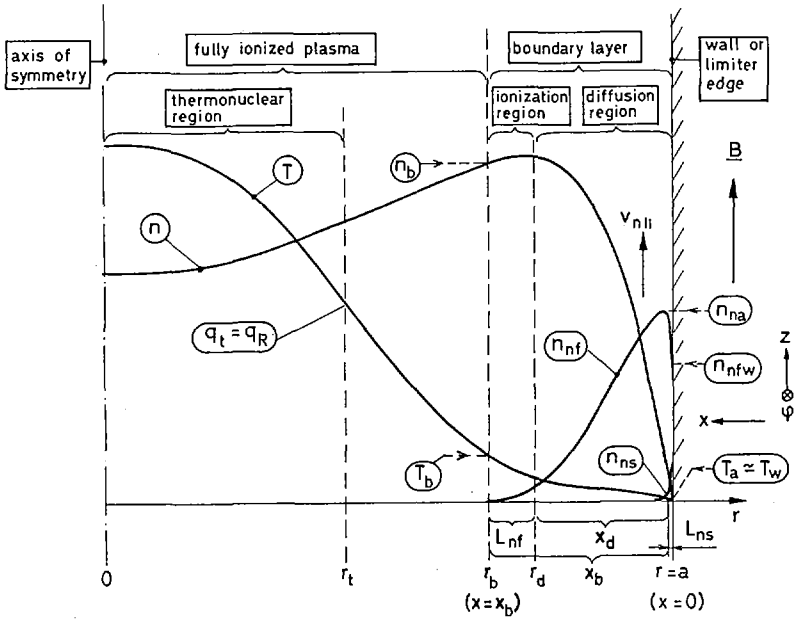


FIG. 1. Outline of a quasi-steady fully developed cold-blanket system.

$n_{nf}(r_b) \ll n_{na}$ at $r = r_b$. This analysis divides the boundary layer into an outer "diffusion region" $r_d < r < a$ (or $0 < x < x_d$) and an inner "ionization region" $r_b < r < r_d$ (or $x_d < x < x_b$). In the former region the ionization rate ξ remains much smaller than both its "saturation" (maximum) value $\xi_{max} \simeq 10^{-14}$ m^3/s and the ion-neutral collision rate ξ_{in}. In the latter region ξ increases to the point where the penetration length of neutrals $L_{nf}(T_b, n_b)$ becomes small compared to the system dimensions, and the neutral gas density decreases rapidly in the positive x direction.

2. BALANCE EQUATIONS OF THE BOUNDARY LAYER

In the present analysis of a steady state, the particle and momentum balance are treated in terms of a simplified model where the plasma and neutral gas temperatures are approximated by a constant mean value T_m. Introducing the particle fluxes $\Gamma(x) = -nv_x$ and $\Gamma_n(x) = n_n v_{nx}$ of plasma and neutral gas, it is easily seen that $\Gamma = \Gamma_n$ and that the maximum values of these fluxes are $\Gamma(0) = \Gamma_n(0) \equiv \Gamma_a$ at $x = 0$. We further adopt the parameters $n_B = k_B B = c_a k_{Bc} B$, $k_{Bc} = 1/[n_c m(\xi_{in} + \xi)]^{1/2}$ with the classical resistivity n_c, $m = m_i + m_e$, $N = n/n_B$, $N_n = n_n/n_B$, $G = \Gamma/\Gamma_a = \Gamma_n/\Gamma_a$,

$s = [m(\xi_{in} + \xi)\Gamma_a/2kT_m]x$, and c_a being a coefficient representing neoclassical or anomalous diffusion. The balance equations then lead to an expression for dN_n/dN being independent of G. This yields a solution of N_n in terms of N. With the asymptotic normalized density values $N_{na} \equiv N_n(x = 0)$ and $N_b \equiv N(x_b)$ of neutrals and ions at each side of the boundary layer, we obtain $N_n \simeq 2(N_b^3 - N^3)/3$; $N_{na} \simeq 2N_b^3/3$ for $N_b \ll 1$ (case I), and $N_n \simeq 2(N_b - N)$; $N_{na} \simeq 2N_b$ for $N_b \gg 1$ (case II). In case (I) the plasma pressure gradient is balanced mainly by diffusion due to Coulomb collisions, whereas the same gradient is balanced mainly by plasma-neutral gas friction in case (II).Especially for Pfirsch-Schlüter diffusion, $n_{na} = 2(1 + q^2)n_b^3/3k_{Bc}^2B^2$ in case (I) and $n_{na} = 2n_b$ in case (II). Consequently, neutral boundary layer densities n_{na} of the order of $n_b \propto \beta B^2$ should become available in tokamaks only at strong magnetic fields B and comparatively large beta values β.

The particle and momentum balance equations, and the associated plasma impermeability condition with respect to neutral gas penetration, are not sufficient to specify a cold-blanket state, but have to be combined with the heat balance. Integration of the heat balance equation over the interval $0 < x < x_b$ yields

$$\Delta Q_b = Q_b - (C_\xi + C_s)/x_b - (C_\eta + C_R)x_b \qquad (1)$$

where Q_b is the heat per unit area and time flowing into the layer at $x = x_b$ from the fully ionized region; C_ξ represents the plasma particle loss due to diffusion across the layer being compensated by a corresponding ionization and heating work on the incoming neutral gas; C_s stands for the heat shunted away across the layer by conduction; C_η represents the excitation radiation loss; and C_R the bremsstrahlung and cyclotron radiation losses. With subscripts $(_b)$ and $(_m)$ referring to $x = x_b$ and to meanvalues in the layer, these coefficients become:

$C_\xi = 4s_b(W + 3kT_b)kT_m/m\xi_{inm} \equiv c_\xi s_b$ with W as the ionization work, $s_b = N_b^2/2$ and $\varrho n2$ in cases (I) and (II), $C_s = c_{sn}N_{na}/(N_{na}+N_b) + c_{si}k_B^2N_b^2$ with $c_{sn} \simeq 75(kT_m)^{3/2}(\pi/m)^{1/2}/64\sigma_{nnm}$ and $c_{si} \simeq 5k^2T_m^2g\nu_{iim}m_i/4e^2n_b$ where σ_{nn} is the neutral-neutral collision cross-section, ν_{ii} the ion-ion collision frequency, and $g \simeq 1$ a factor associated with the heat conductivity across $\vec{B}$. Further, $C_\eta = c_\eta k_B^2B^2N_bN_{na}$ with

$$c_\eta \simeq \int_0^{x_b} \frac{3}{2}(nn_n/n_b n_{na})kf_{exc}\xi_{en}T dx/x_b, \quad \text{and} \quad C_R = c_{br}k_B^2B^2N_b^2 + c_{cr}k_B B^3 N_b$$

$$\text{with} \quad c_{br} \simeq \int_0^{x_b} k_{br}Z^2(n/n_b)^2\sqrt{T}\, dx/x_b \quad \text{and} \quad c_{cr} \simeq \int_0^{x_b} k_{cr}(n/n_b)T dx/x_b.$$

The equilibrium state is given by $\Delta Q_b = 0$. When $\Delta Q_b > 0$ there is a heating power excess which tends to increase the ionization degree and shrink the layer thickness x_b, whereas $\Delta Q_b < 0$ leads to a heating power deficit which tends to decrease the ionization degree and expand the layer thickness x_b. At fixed values of Q_b and of the C-coefficients in Eq. (1), the equilibrium leads to the two solutions:

$$x_b = (x_{b1}, x_{b2}) = \frac{Q_b}{2(C_\eta + C_R)} \{1 \mp \left[1 - 4(C_s + C_\xi)(C_\eta + C_R)/Q_b^2\right]^{1/2}\} \tag{2}$$

of the layer thickness. Only x_{b1} given by the minus sign corresponds to a stable heat balance. This can be seen from $\Delta Q_b = -[(C_\eta + C_R)/x_b](x_b - x_{b1})(x_b - x_{b2})$.

3. EXISTENCE CONDITIONS FOR COLD-BLANKET OPERATION

Two limits determine the possible range of Q_b for cold-blanket operation in equilibrium. Thus when

$$Q_b < Q_{bmin} = 2[(C_s + C_\xi)(C_\eta + C_R)]^{1/2} \tag{3}$$

the losses cannot be balanced by the power input, and the partially ionized layer is spread out, thus tending to cover the entire plasma body. The limit Q_{bmin} corresponds to a maximum possible layer thickness:

$$x_{bmax} = x_b(Q_b = Q_{bmin}) = [(C_s + C_\xi)/(C_\eta + C_R)]^{1/2} \tag{4}$$

On the other hand, when Q_b increases, there is a corresponding decrease of x_b, but only down to the limit where x_b becomes comparable to the penetration length $L_{nf} \simeq [kT/m\xi(\xi_{in} + \xi)n^2]^{1/2} \equiv 1/\sigma_{cf}n$ at $x = x_b$ in Fig.1. Thus when Q_b becomes too large to be balanced by the losses within a cold boundary layer, the diffusion region of Fig.1 becomes replaced by the ionization region, and the cold-blanket is replaced by a plasma having a wall temperature of the order of or larger than T_b. This occurs when

$$Q_b > Q_{bmax} = Q_b(x_b = x_{bmin}) \tag{5}$$

where Q_{bmax} corresponds to the minimum layer thickness

$$x_{bmin} = x_{blmin} = L_{nf}(T_b, n_b) = 1/n_b\sigma_{cf}(T_b) \tag{6}$$

The lower and upper input limits Q_{bmin} and Q_{bmax} of a well defined cold-blanket state and the corresponding maximum and minimum values x_{bmax} and x_{bmin} of the layer thickness are related by $F \equiv Q_{bmax}/Q_{bmin} = (f/2)+(1/2f)$ where

$$f \equiv x_{bmax}/x_{bmin} = \left[(C_s+C_\xi)/(C_\eta+C_R)\right]^{1/2} n_b\sigma_{cf}(T_b)$$

$$= \begin{cases} \sigma_{cf}\left(\frac{1}{2}c_\xi + \frac{2}{3}c_{sn}+c_{si}k_B^2\right)^{1/2} / \left[\frac{2}{3}c_\eta + (c_{br}/N_b^2)+(c_{cr}B/k_BN_b^3)\right]^{1/2} & \text{(I)} \\ \sigma_{cf}\left(c_\xi \ell n 2 + \frac{2}{3}c_{sn}+c_{si}k_B^2N_b^2\right)^{1/2} / \left[2c_\eta+c_{br}+(c_{cr}B/k_BN_b)\right]^{1/2} & \text{(II)} \end{cases} \tag{7}$$

Here $f \geq 1$ by definition, and $F \geq 1$. For such a state to exist within a wide domain of parameter space it is therefore necessary that $f >> 1$ and $F >> 1$.

Transport theory can be used to express the power input in the form $Q_b = C_bN_b^2/a$ where C_b is a coefficient depending on the special transport law being assumed. In particular, when $N_b << 1$ and $C_\eta >> C_R$, the lower input limit leads to the existence condition

$$n_ba < (n_ba)_{lower} = \left[3C_b^2/8c_\eta\left(\frac{2}{3}c_{sn} + c_{si}k_B^2\right)\right]^{1/2} \tag{8}$$

and the upper input limit to

$$n_ba > (n_ba)_{upper} = (n_ba)_{cf}c_b/\left(\frac{2}{3}c_{sn} + k_B^2c_{si}\right) \tag{9}$$

where $(n_ba)c_f \equiv 1/\sigma_{cf}$ can be considered as an impermeability "limit" defined by $L_{nf}(T_b, n_b) = a$.

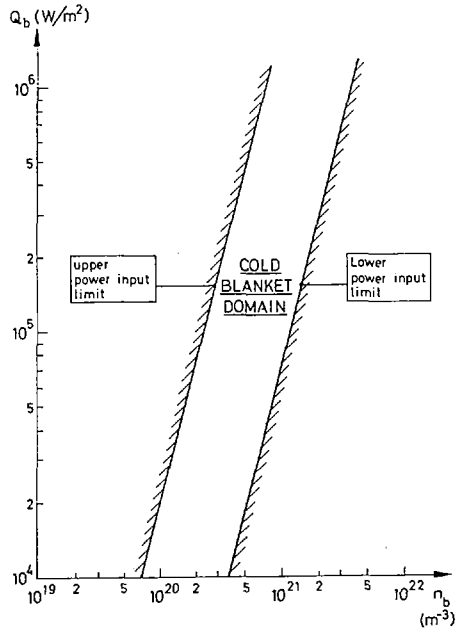


FIG.2. The domain of existence of a cold-blanket system, as defined by the lower and upper power input limits. The power input Q_b is treated as an independent variable; $\beta = 3 \times 10^{-2}$ and normalized density $N_b > 10^{-2}$.

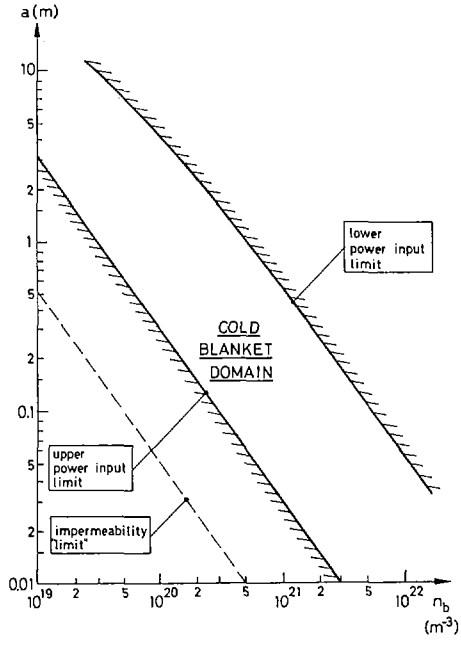


FIG.3. Similar to Fig.2, but with a power input depending on N_b and of the radius a, as defined by the coefficient C_b.

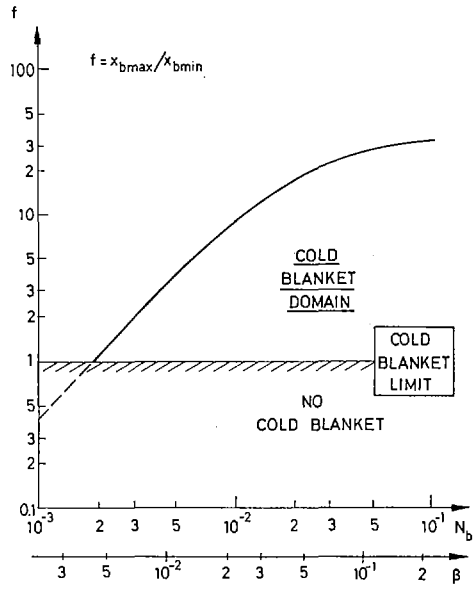


FIG.4. The ratio $f = x_{bmax}/x_{bmin}$ as a function of N_b at $B = 3$ T.

Two numerical illustrations are now given for hydrogen with $q = 3$, $T(r = 0) = 10^7$K, $nT^{-\alpha} = $ const. within the region $0 < r < r_b$, $\alpha = 1/4$, and $C_b = 3 \times 10^6$W/m. First, when choosing $\beta = 4\mu_0 nkT/B^2 = 3 \times 10^{-2}$ at $r = 0$, the upper and lower input limits define regions of a cold-blanket state as shown by Fig.2 with Q_b as independent variable, and by Fig.3 with Q_b expressed through the coefficient C_b. Second, with $B = 3$ tesla, the limits of the cold-blanket domain behave as seen from Fig.4. In this particular case there is no cold-blanket at all when $N_b < 2 \times 10^{-3}$ and $\beta < 4.5 \times 10^{-3}$. In a highly collisional plasma with $c_a = 1$, the results differ only slightly from those of Figs 2-4.

Even if there is some uncertainty in the approximations and coefficients of the present analysis, the latter thus indicates that the domain of cold-blanket operation is restricted in parameter space, as given by $f > 1$. At a fixed magnetic field strength this domain shrinks at decreasing beta values and increasing radiation losses. In tokamaks cold-blanket operation is likely to require total beta values of at least a few per cent.

It has finally to be added that a moderately large wall interaction may sometimes take place even when x_b tends to become smaller than $L_{nf}(T_b, n_b)$.

4. EXPERIMENTS

In this section we present the results of experiments performed in a plasma with typical peak densities of $3.5 \times 10^{21} m^{-3}$ and temperatures of 0.5 - 7 eV. This range of parameters includes the transition from a permeable to an impermeable plasma and is therefore suitable for cold-blanket studies. The plasma core was impermeable at power input levels P above a certain value P^*. For $P > P^*$, the plasma profile exhibited the three regions of Fig.1, with a local density peak in the region where most of the ionization occurred, i.e. where L_{nf} fell below 5×10^{-3} m. In Fig.1 the density and temperature at this point are defined as n_b and T_b. In this experimental section we use n_{pk} for the local peak value of the density and T_{pk} for the temperature at this density peak for all power levels. Therefore n_{pk} and T_{pk} correspond to n_b and T_b in Fig.1 only when the plasma core is impermeable, i.e. when $P > P^*$.

We shall discuss the following observations in detail:

A. The transition from an impermeable to a permeable plasma was marked by a change in the dependence of n_{pk} on P. For $P < P^*$, we observed $n_{pk} \propto P$, but for $P > P^*$, we observed n_{pk}(i.e. n_b) independent of P.

B. For $P > P^*$, T_{pk} was roughly constant at 2.5 eV and corresponded to T_b in Fig.1. However, for $P < P^*$ we observed $T_{pk} \propto P$.

C. The boundary layer thickness, x_{pk}, defined here as the distance from the density peak to the plasma edge, increased with decreased P. This indicates the dominant energy transport term was convection of enthalpy.

D. The scaling of n_b versus neutral pressure n_{na} at the wall was consistent with the model discussed in Sec.2 where $n_b = (3n_{na}k_B^2B^2/2)^{1/3}$.

The experiments were carried out on the F I rotating plasma device [2], having a purely poloidal spherator magnetic field configuration. The azimuthal $\vec{E} \times \vec{B}$ rotation velocity is sheared and therefore the plasma is heated through ion viscosity. This provides technique for coupling high power inputs, up to 10^8 W/m^3, to the plasma. The device has the disadvantage that particle and energy transport parallel to $\vec{B}$ give losses to the internal ring support. However, in the experiment discussed here, the rotation parameters and $\vec{B}$ were such that transport perpendicular to $\vec{B}$ dominated and the particle containment scaled classically like B^2.

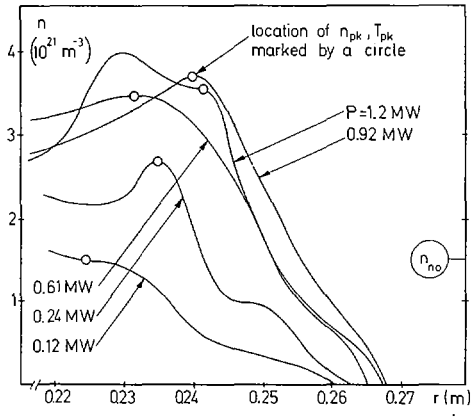


FIG.5. Radial density profiles for various power input levels.

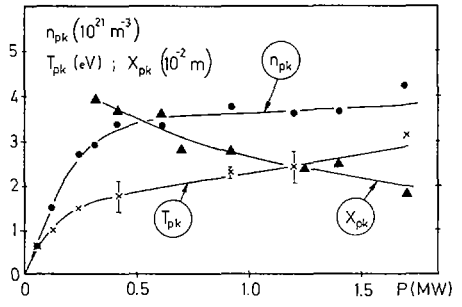


FIG.6. Curves of n_{pk}, T_{pk} and x_{pk} versus P at a filling density $n_{n0} = 1.5 \times 10^{21}\ m^{-3}$.

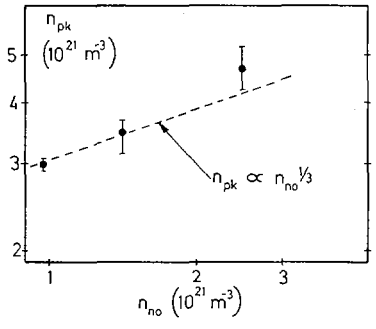


FIG.7. Curve of n_{pk} versus n_{n0} for $P > P^*$.

We studied radial density profiles (laser interferometry) and radial temperature profiles (Thomson scattering and H-line spectroscopy). These profiles were taken on the equatorial plane of the internal ring between the ring surface (major radius r = 0.19 m) and the outer vertical wall of the vacuum chamber at r = 0.28 m. The cold-blanket discussed here was located between the dense plasma core and the limiter at r = 0.265 m.

The discharge consisted of two phases. In the first phase a fully ionized plasma was produced during a 250-μsec "burnout" discharge with very high power levels, up to 10 MW, sufficient to overcome the radiation loss barrier. This barrier makes the attainment of fully ionized dense plasmas with modest power inputs difficult [3]. In phase 2, the discharge was sustained in a quasi-steady state at reduced power inputs.

In Fig.5 we show density profiles for decreasing phase-2 power inputs. The transition from an impermeable to a permeable plasma core occurred at about $P^* \simeq 0.5$ MW. For $P > P^*$, the magnitude of n_{pk} was fixed, but the position moved spatially so that x_{pk} increased with decreased P. These dependences of n_{pk} and x_{pk} on P are shown in Fig.6. For $P > P^*$, when n_{pk} was fixed in magnitude, the observed scaling of x_{pk} with P is consistent with a simple model in which the dominant energy loss term is perpendicular transport of enthalpy. The energy balance of Eq. (1) has the simplified form:

$$P/A_\perp \propto Q_b \simeq (W + 3kT)\Gamma \simeq C_\xi/x_{pk} \qquad (10)$$

where $A_\perp$ is the surface area through which the plasma flux Γ passes. We take Q_b proportional to P because we are uncertain of the division between energy transport inward to the ring and outward to the blanket. Also, there may be some power losses not coupled to the plasma. We have observed that n and T in the boundary layer are independent of P for $P > P^*$, and this means that $C_\xi = 2n^2\eta_c kT(W + 3kT)/B^2$ is only weakly dependent on P. Therefore the observed inverse scaling of x_{pk} with P is consistent with Eq. (10) which considers only perpendicular enthalpy transport.

In Fig.6 we also show the temperature, T_{pk}, at the moving density peak versus P. Note that T_{pk} was roughly constant for $P > P^*$, although the maximum temperature in the fully ionized core was as high as 7 eV at the highest power inputs.

The data of Figs 5 and 6 were taken with a fixed magnetic field strength of about 0.5 T and with a neutral H-atom filling density $n_{no} = 1.5\times10^{21}m^{-3}$. The experiments were repeated with filling densities of $n_{no} = 1.1\times10^{21}m^{-3}$

and $2.8\times10^{21}m^{-3}$. The scaling of n_{pk} versus filling pressure is shown in Fig.7. Here we have $P > P^*$ so n_{pk} corresponds to n_b. We see that n_{pk} was a weak function of n_{no}.

In these experiments the plasma volume ($2 \times 10^{-2}m^3$) was only about 20% of the vacuum volume, so the build-up of the plasma density caused only a small decrease in n_{no} at the wall and we can take $n_{no} \simeq n_{na}$. The weak dependence of n_{pk} on n_{no} is consistent with the predicted scaling $n_b \propto n_{na}^{1/3}$. The value for the coefficient defined in Sec. 2 relating n_b and $n_{na}^{1/3}$, which was calculated assuming resonant charge exchange as the dominant momentum transfer process at 2.5 eV, was 50% greater than the observed coefficient. However,we point out that this calculated coefficient is a rough approximation and we stress that the important observation is the weak dependence of n_b on n_{na}.

REFERENCES

[1] LEHNERT, B., Nucl. Fusion 8 (1968) 173; 13 (1973) 958; Nucl. Instrum. Methods 129 (1975) 31; Royal Inst. of Technology, Stockholm, Rep. TRITA-PFU-77-08 (1977).

[2] BERGSTRÖM, J., HOLMBERG, S., LEHNERT, B., "Rotating plasma experiments", Plasma Physics and Controlled Nuclear Fusion Research (Proc. 2nd Int. Conf. Culham, 1965) Vol.1, IAEA, Vienna (1966) 341.

[3] SCHÜLLER, F.C., GOEDHEER, W.J., ORNSTEIN, L.T.M., ENGELMANN, F., SCHEP, T.J., in Proc. Fusion Fueling Workshop, Princeton, US Dept. of Energy, Conf. 771129 (1978) 75.

DISCUSSION

R.W. CONN: Can the attributes of a gas blanket be obtained over a wider range of parameters if one does not attempt to establish the blanket in steady state? We have, for example, considered periodic gas puffing and numerical modelling in tokamaks which indicates this to be true.

B. LEHNERT: Yes, in principle you are right, though I am for the moment not sure how this would work under various experimental conditions. As far as the parameter ranges of our laboratory experiments in Stockholm are concerned, the relaxation time of the boundary layer balance seems to be of the order of 100 μs.

B. GREEN: In the first part of your presentation you showed a number of apparently algebraic relations between quantities in different radial regions of your model. As the problem is basically differential in nature, would it not be right to say that all your relations are essentially *implicit*? If this is the case, how can you *explicitly* solve for quantities such as the boundary layer thickness?

B. LEHNERT: With regard to the particle and momentum balance, the relations between n_b and n_{na} at each side of the boundary layer are, in fact, independent of the profile shapes in the first approximation; this was also found in an earlier paper by Dr. J. Rem at Jutphaas. With regard to the heat balance, certain profiles of density and temperature have been assumed. These results should be taken as a first approach to the problem, indicating the existence of the lower and upper power input limits of cold-blanket operation. For refinements, a more rigorous approach is certainly needed. This would have to be developed by means of computers, thereby also including experimentally determined cross-sections for impacts.

R.A. KRAKOWSKI: Gryczkowski, Oliphant and I have worked on this problem of the dependence of neutral and ion density in two related computations. They published (OLIPHANT, T.A., GRYCZKOWSKI, G.E., KAMMASH, T., Nucl. Fusion **16** (1976) 263) a discussion of neutral-gas blanket behaviour in theta-pinches, and Gryczkowski and I applied the same technique to investigate the feasibility of a lithium evaporative first wall operating in conjunction with a dense thermonuclear plasma. The processes modelled in these analyses included an MHD description of plasma, charge-exchange cross-sections/processes, Franck-Condon processes, surface evaporation models, dynamic pump-out of neutral gas volume, alpha-particle heating, and so on.

COMPUTER SIMULATION OF HEAT TRANSPORT ON A $2\frac{1}{2}$-D MODEL AND INVESTIGATIONS OF LARGE-SCALE PLASMA SIMULATIONS ON THE CHI COMPUTER

J.M. DAWSON, T. KAMIMURA*, H. NAITOU*,
R.W. HUFF, C.C. WU
Center for Plasma Physics and Fusion Engineering,
University of California,
Los Angeles, California,
United States of America

Abstract

COMPUTER SIMULATION OF HEAT TRANSPORT ON A $2\frac{1}{2}$-D MODEL AND INVESTIGATIONS OF LARGE-SCALE PLASMA SIMULATIONS ON THE CHI COMPUTER.

Two aspects of computer simulation of plasma are investigated: the simulation of heat transport across a magnetic field for a thermal electron plasma (fixed ions), and the use of highly parallel microprogrammable computer architecture for plasma simulation. In the first investigation it was found that heat can diffuse slower than particles owing to the averaging of fluctuating electric fields by large Larmor orbit particles. Details are given. In the second investigation this computer architecture was found to be very cost effective and capable of greatly reducing the cost of plasma simulation. Examples are given.

I. INTRODUCTION

The problems of plasma and heat transport across a magnetic field due to collective effects are fundamental to magnetic confinement of a plasma. One means for investigating these problems is through computer simulation. In this paper we discuss two aspects of this: the first is an investigation of heat transport across a magnetic field using a two-dimensional model; the second is an investigation of the use of a new computer architecture in combination with microprogramming (the CHI Computer) to achieve more effective plasma simulation.

The investigation of heat transport employed a two-and-one-half dimensional (two space coordinates and three velocity coordinates) electrostatic particle model with mobile electrons, fixed uniform ions density and a fixed magnetic field. The model is illustrated in Fig. 1. Heat and particle transport were measured in an essentially thermal plasma. One of the principal results of this investigation was that there are situations under which heat transport is slower than particle transport. This occurred when particle

---

* Institute of Plasma Physics, Nagoya University, Nagoya, Japan.

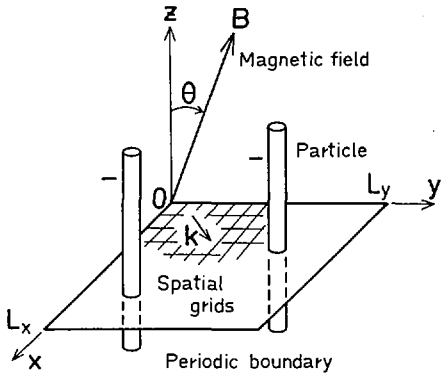


FIG. 1. 2½-dimensional plasma model.

transport was dominated by convective diffusion [1]. The reason for the effect was the following. The convective motion in the plasma is associated with E × B drifts produced by charged flux tubes; low-energy particles have small Larmor radii and move with the full E × B velocity; high-energy particles have large Larmor orbits which pass through a number of charged flux tubes and thus, to some extent, average out the E × B drifts. The high-energy particles are thus transported less rapidly. We may note that this result has significance for thermonuclear reactors since it shows that large Larmor radius particles are less effected by low-frequency relatively short wavelength turbulence than small Larmor radius particles. The ions, and particularly the hot ions, have the largest Larmor radii and should thus diffuse the slowest. These are the particles it is most important to confine and this effect could particularly play a role for two-component operation [2]. Present experimental evidence on tokamaks, that electron heat transport is anomalous while ion transport and hot-ion confinement agree with neoclassical theory [3], are consistent with this. While the present results were obtained for electrostatic fluctuations, similar effects should occur for fine-scale magnetic fluctuations; here the crucial scale length is probably the banana width.

The second part of this paper deals with experimentation with a micro-programable machine which is capable of handling large particle and fluid models at speeds comparable to those of the largest existing machines at a small fraction of the cost. We have run million-particle problems for a model similar to that used in the heat transport studies at speeds somewhat in excess of what a CDC-7600 will do. Similar performance is found on large MHD calculations [4].

II. HEAT CONDUCTION STUDIES [5 - 9]

The model used for the heat conduction studies is a two-and-one-half dimensional (two positions and three velocities) electrostatic dipole expansion code [5], with fixed magnetic field shown in Fig. 1. While in general the magnetic field can be tilted at an arbitrary angle to the z-axis as shown, for most of these studies it was taken parallel to the z-axis and the model reduces to a two-dimensional one. The ions constitute a uniform

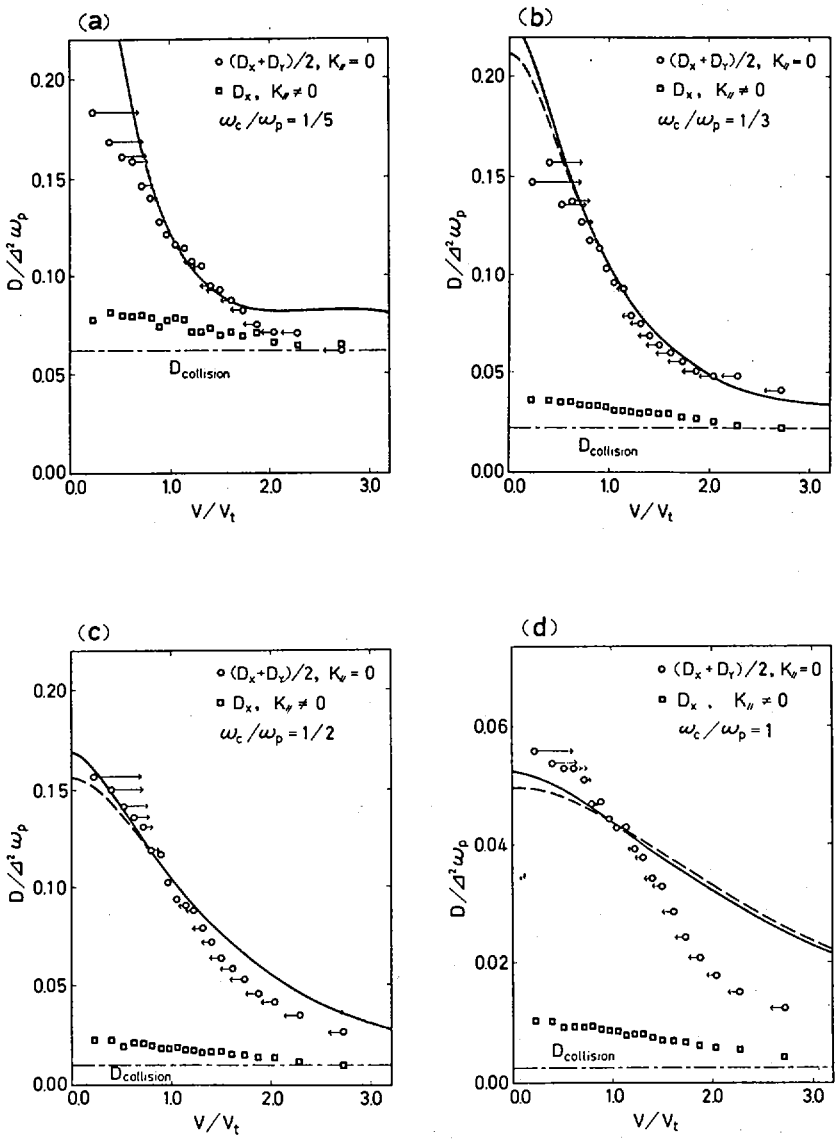


FIG.2. Velocity-dependent diffusion coefficient versus velocity.

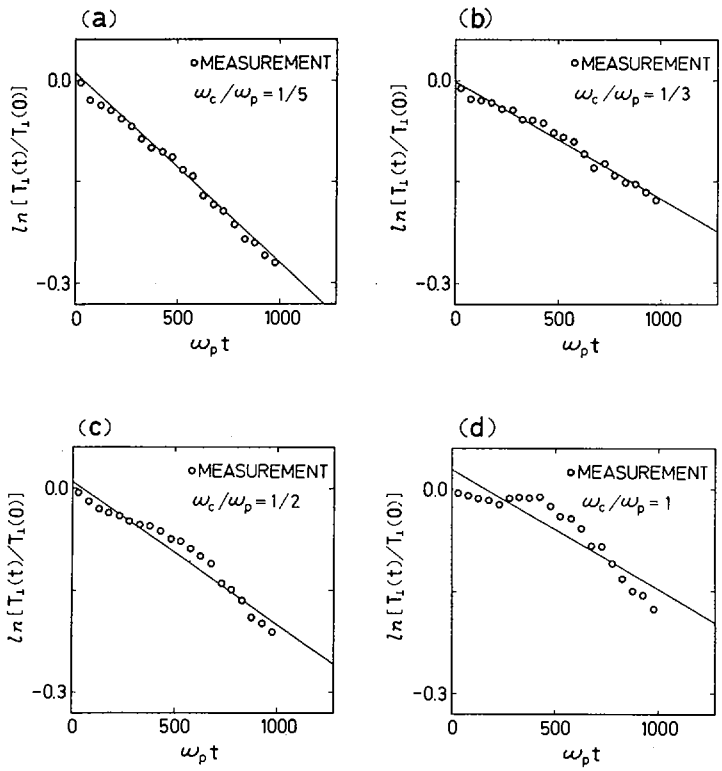


FIG. 3. Thermal diffusion.

fixed background; the mobile electrons are modelled by finite-sized particles with a Gaussian charge distribution [5]. The full Lorentz force is used in advancing the electrons. Periodic boundary conditions are used.

Two types of runs were made: for the first a thermal equilibrium plasma of uniform density and temperature was used; in the second a slight temperature variation in the x-direction was initially imposed. Runs of the first type were used to compute the particle diffusion by computing the mean square displacement of the guiding centers perpendicular to B of a large number of test particles; the diffusion coefficient as a function of velocity could be determined by choosing the test particles to be in a narrow velocity range. In this way we verify that the more energetic particles diffuse more slowly than lower energy particles. Runs of the second type were used to compute the thermal diffusion coefficient assuming that the temperature evolved according to a simple diffusion equation.

For the thermal plasma a series of runs were made with systems-size 64^2 grid spacings, electron number equal 65,536, particle size equal 1, Debye length equal 2, magnetic field strengths of ω_c/ω_p=1, 1/2, 1/3, 1/5, $n\lambda_D^2$=64, time step 0.2, and collision times of $\omega_p t$=10^4 and total run times of $\omega_p t_{end}$=400. Velocity-dependent diffusion coefficients D(v) are shown in Fig. 2. The horizontal coordinates of the open circles correspond to the

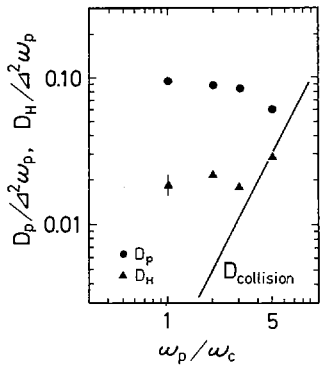


FIG.4. Particle and thermal diffusion versus magnetic field.

initial averaged velocities of the particles while those of the ends of the arrows starting from the circle correspond to the averaged final velocities. The change in the averaged velocities are due to the classical collisional relaxation processes in velocity space. The square points are obtained by tilting B away from the z-axis so as to largely short out the convective modes [2] and are close to the values predicted from collision theory. The curves are predicted by a theory which is developed in a more complete treatment of this study [9].

We now turn to the results of the cases in which there was a temperature gradient in the x-direction. Initially the temperature was given by

$$T(x) = T_o[1 - 0.1 \cos 2\pi x/L_x] \quad (1)$$

The time evolution of the temperature for the $k_x=2\pi/L_x$, $k_y=0$ mode (cosine component) was followed. Assuming that the evolution of the temperature follows a diffusion type equation, we obtain the heat diffusion coefficient from the expression

$$D_H = \left(\frac{L_x}{2\pi}\right)^2 \frac{\partial}{\partial} \ell nT \quad (2)$$

Runs were made for the following parameters: $L_x \times L_y = 64\times64$; $N_e = 65,536$; particle size = 1; Debye length = 1; $n\lambda_D^2 = 16$; $\omega_c/\omega_p = 1, 1/2, 1/3, 1/5$; collision frequency = $4\times10^{-4}\omega_p$; time step $\omega_p \Delta t = 0.2$; and the length of run was $1000\ \omega_p^{-1}$.

Figure 3 shows the results of these simulations. The damping of ΔT is generally linear although at the higher fields some sinusoidal fluctuations are superposed on the damping; these may be associated with large-scale vortex motion which has a very long relaxation time.

Figure 4 shows the heat and particle diffusion coefficient vs. ω_p/ω_c. We see that the particle diffusion rate is as much as a factor of five times larger than the heat diffusion rate, particularly at high magnetic fields. These results are consistent with our results for D(v). This effect should be even more pronounced if comparison were made for ions which have larger

TABLE I. COMPUTER PERFORMANCE COMPARISONS

	IBM 360/91	CHI SYSTEM
PARTICLE CODE		
Time/Particle Push:	Assembly Code	
CPU	55 μs	13 μs
I/O	- -	0.6 × 24 μs
Overall	55 μs	15 μs
10^6 Particles, 4000 Timesteps:		
Time	61 Hr	16 Hr
Cost	50 k$	0.3 k$
3D MHD CODE	Fortran (H-Compiler)	
Time/Gridpoint	230 μs	100 μs
64^3 System, 4000 Timesteps:		
Time	33 Hr	13 Hr
Cost	27 k$	0.28 k$

Larmor radii. We should note that the heat diffusion is a macroscopic process involving averages over many particles, while the particle diffusion as measured here is a microscopic process involving the diffusion of test particles. In a plasma the electrons could not diffuse away and leave the ions behind. However, for heat transport where cold electrons can diffuse in to replace hot ones, the test particle results are probably reasonably correct and the conclusion that the ion heat transport will be less affected by micro-turbulence than that for electrons should be valid.

III. ADVANCED COMPUTER ARCHITECTURE

Three large plasma simulation models are being run on the recently installed Culler-Harrison Inc. (CHI) computer system at UCLA: (1) A 2½-dimensional electrostatic particle code with constant magnetic field plus mirroring. (2) a 2½-dimensional MHD fluid code with spatially dependent resistivity. (3) A 3-dimensional MHD fluid code with constant resistivity. Performance results are presented in Table I , in terms of computing time per particle or gridpoint update, as well as overall timing and cost for typical million-particle and 64×64×64-gridpoint systems. These results demonstrate that the CHI type of highly parallel architecture can yield a two-order-of-magnitude decrease in cost relative to large general-purpose computers such as the IBM 360/91 or the CDC 7600. Programming costs, even for these first codes on the CHI computer, have been less than the costs of single large runs on a general-purpose computer. Since hundreds of runs are anticipated, inclusion of programming cost does not alter our conclusion

regarding a two-order-of-magnitude cost advantage of the CHI computer. The principal implication is that the CHI computer system, or another of similar structure, permits running many large plasma simulations which would otherwise not be feasible due to excessive cost. This should prove to be a very powerful tool for the CTR program.

REFERENCES

1. H. Okuda and J. M. Dawson, Phys. Fluids 16 408 (1973).

2. J. M. Dawson, H. P. Furth, F. H. Tenney, Phys. Rev. Lett. 26 1156 (1971).

3. C. C. Daughney, Princeton Plasma Physics Laboratory Report, PPPL-1442, May 1978.

4. J. M. Dawson, R. W. Huff and C. C. Wu, UCLA Plasma Physics Group Report PPG-334 (1978).

5. W. L. Kruer, J. M. Dawson and B. Rosen, J. Comp. Phys. 13 114 (1973).

6. T. Kamimura, J. M. Dawson, B. Rosen, G. J. Geller, R. D. Levee and G. Ball, UCLA Plasma Physics Group Report PPG-248 (1975).

7. A. B. Langdon and C. K. Birdsall, Phys. Fluids 13 2123 (1970).

8. H. Okuda and C. K. Birdsall, Phys. Fluids 13 2123 (1970).

9. H. Naitou, T. Kamimura and J. M. Dawson, Institute of Plasma Physics, Nagoya University Report (1978), submitted to the Physical Society of Japan.

TURBULENT CONVECTIVE TRANSPORT IN A PLASMA

A.S. BAKAJ
Physico-Technical Institute of the
Ukrainian SSR Academy of Sciences,
Kharkov,
Union of Soviet Socialist Republics

Abstract

TURBULENT CONVECTIVE TRANSPORT IN A PLASMA.

It is shown that as a result of the build-up of various instabilities with $\tau_{NL} < \tau_{QL}$ (τ_{NL} is the characteristic non-linear interaction time and τ_{QL} is the quasi-linear time), correlations are found between the fields and the particle motion, and a state of moderate turbulence is established. In this case the transport is of a turbulent convective character. The kinetic equations for moderate turbulence are derived and analysed. Investigations are made of cases of kinetic, current-convective and drift instabilities. Aspects of anomalous transport in toroidal traps are discussed.

1. INTRODUCTION

Convective transport is an extremely important factor in plasmas since the long-lived electromagnetic field perturbations generate convective cells in the particle phase flow. Examples of convective cells are given in Figs 1 and 2. In a turbulent plasma the particle flows are random although they may form ordered convective structures resulting in turbulent diffusive transport more rapid than that generated by spatially homogeneous turbulence. It is demonstrated in the present investigation that at the non-linear stage when the instability-generated waves interact among themselves more vigorously than with the excited macro-inhomogeneity, the flows become ordered and a state of moderate turbulence is established. The kinetic equations for moderate turbulence are obtained from which, in various limiting cases, the equations for strong, weak and degenerate turbulence are recovered. An analysis is made of the turbulence generated by kinetic, current-convective and drift instabilities.

2. LAMINAR AND TURBULENT STATES OF MOTION

It is useful to classify the plasma states on the basis of the scale of correlations. We shall assume that L is the scale of the instability-generating

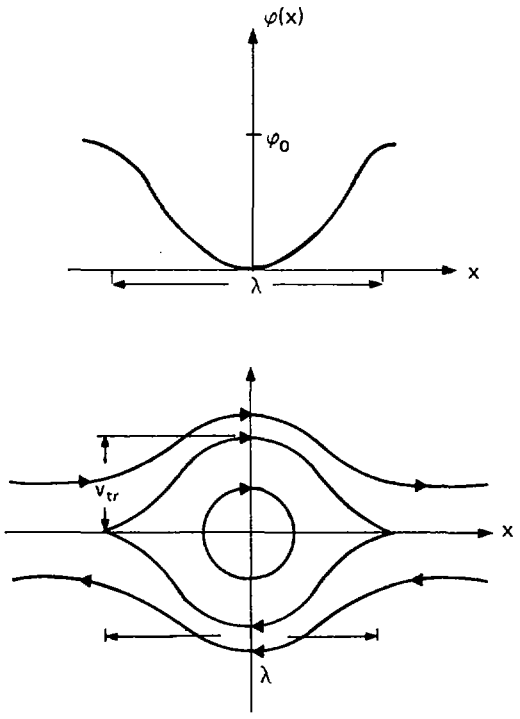


FIG. 1. Phase flow distorted by a one-dimensional potential well. Characteristic parameters of convective cell: λ, $v_{tr} = (\ell e \varphi_0/m)^{\frac{1}{2}}$, $\tau = \lambda/v_{tr}$.

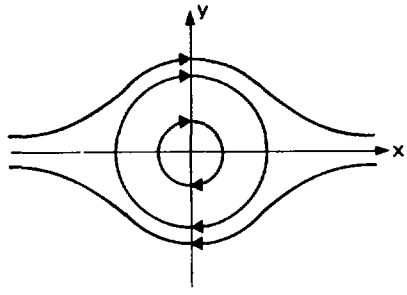


FIG. 2. Convective cell formed by two-dimensional potential perturbations $\varphi = \varphi(x, y)$ *in a magnetic field* $B = B_z$. *The current lines coincide with the equipotential lines. Parameters:* λ, $v = c \nabla_\perp \varphi B_z^{-1}$, $\tau = \lambda/v$.

macroinhomogeneity; λ is the main microinhomogeneity scale (for example, in hydrodynamic turbulence, the scale of the energy range vortices); $\epsilon\lambda$, with $\epsilon \ll 1$, is the dimension of the small-scale microinhomogeneities; $\tau_{QL} = \tau_{int}(\lambda,L)$ is the quasi-linear time which is the reciprocal of the quasi-linear growth rate of the instability resulting from the interaction between the microinhomogeneities and the macroinhomogeneity; $\tau_{NL} = \tau_{int}(\lambda;\lambda)$ is the characteristic non-linear interaction time of the microinhomogeneities; $\tau_c = \tau_{int}(\lambda;\epsilon\lambda,\lambda,L)$ is the correlation time, i.e. the time in which the correlation between motions on the scale λ is destroyed as a result of interaction with small-scale microinhomogeneities and also with main-scale macro- and microinhomogeneities.

The states of plasma motion depend on the ratios between the characteristic times. When $\tau_{NL} \to \infty$ and $\tau_c \to \infty$, the flow is laminar (Fig.3a).

The build-up of instabilities amplifies the fluctuation microinhomogeneities over the characteristic time τ_{QL} and $\tau_c \lesssim \tau_{QL}$. A state of weak turbulence is established when $\tau_c \sim \tau_{QL} \ll \tau_{NL}$. The current lines are stochastic but for some time do not differ appreciably from straight lines (Fig.3b). As the microinhomogeneities increase, τ_{NL} decreases and when $\tau_{NL} \sim \tau_{QL} \sim \tau_c$, a state of strong turbulence is established (Fig.3c). Strengthening of the interaction between the microinhomogeneities when $\tau_{NL} \ll \tau_{QL}$ may strengthen the correlations and result in the formation of ordered convective flows. The plasma is then transferred to a state of moderate turbulence (Fig.3d). If the fields are completely correlated, $\tau_c \to \infty$ and $\tau_{QL} \to \infty$, a state of degenerate turbulence is established (Fig.3e). Characteristic conditions of degenerate turbulence are found when the dimensions of the microinhomogeneities (convective cells) begin to exceed the macroinhomogeneity scale.

Our problem involves deriving the kinetic equations for moderate turbulence generated by various types of instability and describing the turbulent convective transport typical of this state.

3. KINETIC INSTABILITY

We shall analyse the evolution of turbulence excited by the kinetic instability of a one-dimensional velocity-smoothed electron beam. As was demonstrated in Refs [1–3], when

$$\Omega_{tr} > \gamma_{QL} \quad \text{or} \quad \tau_{NL} < \tau_{QL} \approx \tau_c \tag{3.1}$$

where Ω_{tr} is the trapped-particle oscillation frequency and γ_{QL} is the quasi-linear growth rate, correlations between the field and the particle motion are established and strengthened, such that the quasi-linear relaxation is replaced by moderately

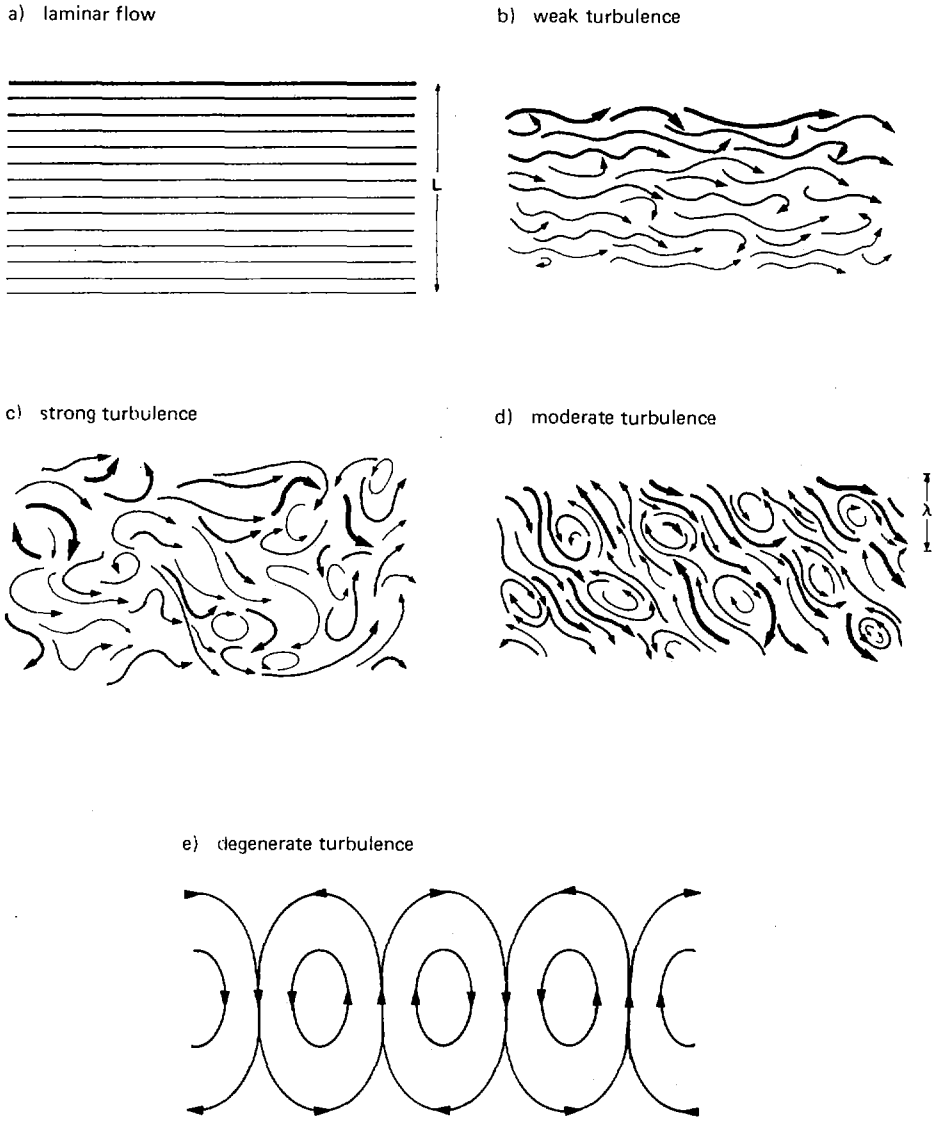


FIG. 3. Laminar and turbulent flows:
a) laminar flow, $\tau_c \to \infty, \tau_{NL} \to \infty$;
b) weak turbulence, $\tau_c \sim \tau_{QL} \ll \tau_{NL}$;
c) strong turbulence, $\tau_c \sim \tau_{QL} \sim \tau_{NL}$;
d) moderate turbulence, $\tau_{NL} < \tau_c, \tau_{QL}$;
e) degenerate turbulence, $\tau_{NL} < \infty, \tau_c \to \infty$.

turbulent relaxation. In this case the field decomposes into coherent packets with the characteristic correlation between the amplitude E and the spatial extention ℓ:

$$\ell \approx \ell_{int} = \pi v_{ph}/\Omega_{tr} = 2\pi v_{ph}/kv_{tr} \quad v_{tr} = 2(eE/km)^{1/2}, \quad \Omega_{tr} = (ekE/m)^{1/2} \qquad (3.2)$$

where v_{ph} and k are the average phase velocity and the wave vector of the packet; e and m are the electron charge and mass. The packets form an ordered structure in the (x, v_{ph}) space, resulting in the establishment of ordered convective flows in the phase plane. In this case, attention is focused on the derivation and analysis of the kinetic equations for moderate turbulence.

The distribution function $\bar{f}(v, t)$ averaged over x, used in quasi-linear theory, is inadequate to describe ordered particle phase flows. On the other hand, Vlasov's equation yields a too detailed description of the process. To go over correctly to a more approximate description of the process, we need to investigate the evolution of the distribution function on the main scale (v_{tr}, ℓ_{int}, $\tau_{NL} = \ell_{int}/v_{ph}$), averaging over all the smaller scales. For this purpose, we shall analyse the evolution of the distribution function in the region of resonant interaction with the packet. Let E_k be the amplitude of the packet. In addition to the field of the packet, we shall allow for the existence of fluctuating fields (these generate small-scale phase-flow inhomogeneities) and also for the non-resonant influence of other packets on the resonant phase flow. The particles interact resonantly with the packet over the section of phase surface $|v - v_{ph}| < v_{tr}$, $x_0 < x < x_0 + \ell$, where $(x_0, x_0 + \ell)$ is the region of spatial localization of the packet. We shall assume that $v_{ph} > v_{the}$ (v_{the} is the electron thermal velocity) and neglect the packet group velocity. When $\Omega_{tr} \gg \gamma_{QL}$, the effect of the fluctuating fields and of non-stationarity may be regarded as a small perturbation. When the fluctuating fields are neglected, the particle phase trajectories in the wave system at rest are defined by the constant-energy equations:

$$W = \frac{mv^2}{2} + e\varphi_k \cos kx, \quad \varphi_k = E_k/k$$

When $-W_0 < W < W_0$, $W_0 = e\varphi_k$, the particles are trapped and when $W > W_0$, the particles are untrapped. In Fig.4 the trapped- and untrapped-particle trajectories are separated by the separatrix. An important characteristic of the particle motion is the oscillation frequency in the wave field, $\Omega = \Omega(W)$. It has been established that this value differs negligibly (by not more than 25%) from Ω_{tr} when $W_0 < W < 0.7\ W_0$, but alters rapidly when $|W - W_0|W_0^{-1} < 0.3$, vanishing when $W = W_0$. To describe the evolution of the distribution function in the region of localization of the packet, neglecting the fluctuating fields and subject to slowly varying amplitude ($\gamma_{QL} \ll \Omega_{tr}$), it is sufficient to know the particle trajectories (see Refs [4, 5]). The fluctuating fields result in a mixing of the

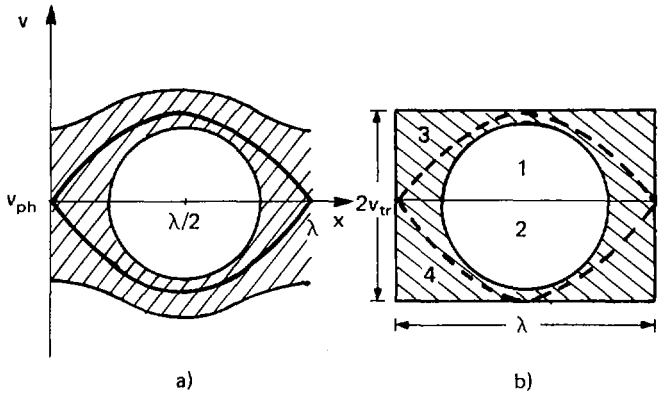


FIG.4. a) Phase flow element. Turbulent flow zone shown hatched. b) Splitting of the region of resonant interaction with a packet into sections.

trajectories, the influence of these fields being non-uniform in different sections of the phase plane as a result of interference with the packet field. This influence is substantial in the vicinity of the separatrix for two reasons: firstly, the frequency $\Omega(W)$ is low and thus the mixing time as a result of quasi-linear diffusion is shorter than or comparable with the average value of $\Omega^{-1}(W)$; secondly, in the vicinity of the separatrix the distribution function exhibits a larger than average velocity gradient since, at this point, particle trajectories initially separated by $\Delta v \sim v_{tr}$ are adjacent. Thus, the distribution function varies considerably more rapidly as a result of quasi-linear diffusion than in other sections of the phase surface. The region of turbulent flow in the vicinity of the separatrix is shown hatched in Fig.4.

Thus, the particle flow can be divided into two sections, a regular trapped-particle flow, for which turbulent mixing over the length ℓ_{int} is negligible, and a turbulent flow undergoing strong mixing. On this basis, we divide the resonance region into sections as shown in Fig.4b. Here, sections 3 and 4 are filled by the turbulent phase flow and sections 1 and 2 are filled by the 'regular' phase flow, with sections 1 and 3 lying above v_{ph} and sections 2 and 4 lying below. In accordance with this division, we introduce the four distribution functions $f_i(x, v, t)$, $i = 1, 2, 3, 4$ as follows:

$$f_i(x, v, t) = \frac{1}{S_i(v)} \int_{S_i} f(x', v', t)\, dx'\, dv' \tag{3.3}$$

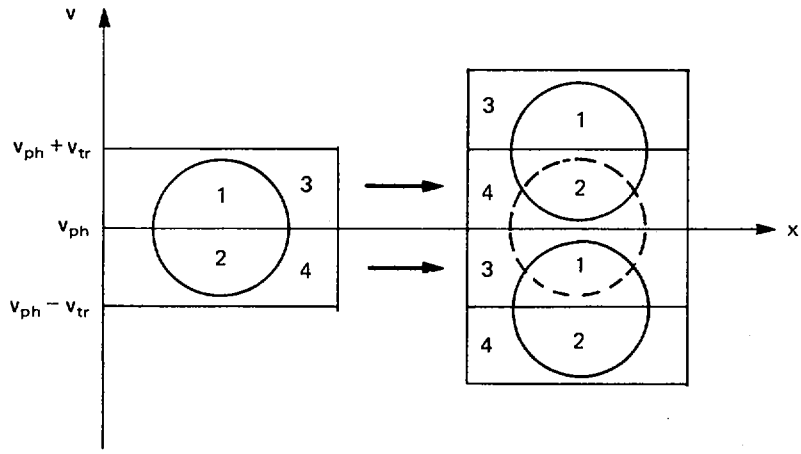


FIG. 5. Schematic representation of the resonant regions of neighbouring packets and particle transitions from one packet to another.

where integration is performed over the area of the i-th section, integration over x′ being performed within one wavelength, including the co-ordinate x.

In the absence of fluctuating fields the area inside the separatrix is $S_{tr} = 4v_{tr}\lambda/\pi$ and that outside the separatrix is $S_{ntr} = 2v_{tr}\lambda(1 - 2/\pi)$.

If turbulent mixing is allowed for we may assume that

$$S_{tr} \approx \left(1 - \frac{\tau_{NL}}{\tau_{QL}}\right) S_0 = \left(1 - \frac{\pi\gamma_{QL}}{\Omega_{tr}}\right) S_0, \quad S_0 = 2v_{tr}\lambda$$

$$\times S_{ntr} = (1 - \xi_{tr})\, S_0 \equiv \xi_{ntr}\, S_0 \tag{3.4}$$

The areas of the sections $S_i(v)$ are thus defined by

$$S_{1.2} = \xi_{tr}\, S_0/2, \quad S_{3.4} = \xi_{ntr}\, S_0/2$$

The distribution function averaged over x is expressed in terms of f_i as follows:

$$\bar{f}(v, t) = \tfrac{1}{2} \langle [\xi_{tr} (f_1(x, v, t) + f_2(x, v, t)) + \xi_{ntr} (f_3(x, v, t) + f_4(x, v, t))] \rangle_x \tag{3.5}$$

where the angular brackets denote averaging over x.

We define $f_i(v, t)$ as the i-th distribution function at the beginning of the packet $x = x_0$, averaged over all the packets with the phase velocity $v_{ph} = v$,

$$f_i = \langle f_i(x_0, v, t)\rangle_{x_0}$$

and we shall define $\tilde{f}_i(v, t)$ as an analogous distribution function at the distance ℓ_{int} from the beginning of the packet:

$$\tilde{f}_i(v, t) = \langle f_i(x_0 + \ell_{int}, v, t)\rangle_{x_0}$$

The correlation between the functions f_i and $\tilde{f}_k$ may readily be obtained from the character of the particle phase trajectories described above. As a result of strong mixing, we have the following equations for $f_{3,4}$:

$$\tilde{f}_{3,4}(v, t) = \tfrac{1}{2}\,[f_3(v, t - \tau) + f_4(v, t - \tau)] \tag{3.6}$$

Since the trapped particles in sections 1 and 2 oscillate at almost identical frequencies and, at the distance ℓ_{int} from the beginning of the packet, undergo approximately half of a complete oscillation (τ_{NL} is equal to half the oscillation period), particles from section 1 are transferred to section 2 and conversely. As a result, we have:

$$\tilde{f}_1(v, t) = (1 - \eta)\, f_1(v, t - \tau_{NL}) + \eta\, f_2(v, t - \tau_{NL})$$

$$\tilde{f}_2(v, t) = \eta\, f_1(v, t - \tau_{NL}) + (1 - \eta)\, f_2(v, t - \tau_{NL}) \tag{3.7}$$

where η is the mixing coefficient due to the scatter of the particle oscillation frequencies (it is readily estimated that when $W < 0.7_0$, we have $\Delta\Omega/\Omega \sim 0.1$) and the influence of the fluctuating fields. When $\gamma_{QL} \ll \Omega_{tr}$, it can be assumed that $\eta \approx 2\Omega/\Omega \approx 0.2$.

It can be seen from Eq.(3.7) that the distribution function at a distance ℓ_{int} from the beginning of the packet has a derivative of approximately equal absolute value to the derivative at the beginning of the packet but of opposite sign. Thus, waves with phase velocities such that $|v'_{ph} - v_{ph}| < v_{tr}$ are attenuated within the packet whilst the spatial extension of the packet remains equal to ℓ_{int} with increasing amplitude [1]. In addition, waves with phase velocities v'_{ph} separated from v_{tr} by v_{ph} have growth rates larger than the average quasi-linear

[1] We note that the narrowing of a beam-amplified packet with increasing amplitude is the reverse process to the spatial stretching of a high-intensity packet attenuated by resonant particles whose initial distribution function has a negative derivative, observed in Ref.[4].

value within the packet [1]. This results in ordering of the packets in (x, v_{ph}) space: the phase velocities of adjacent packets are shifted by approximately v_{tr} (Fig.5). As a result of this ordering, particles from sections 1 and 3 of a packet with phase velocity v_{ph} are transferred to sections 2 and 4 of a neighbouring packet with phase velocity $v_{ph} + v_{tr}$ and particles from sections 2 and 4 are transferred to sections 1 and 3 of a packet with phase velocity $v_{ph} - v_{tr}$. We can introduce the probabilities $\xi_{ik}(v_{ph}, v'_{ph})$; i, k = 1, 2, 3, 4 for the transition of particles from the k-th section of interaction with a packet of phase velocity equal to v_{ph} to the i-th section of interaction with a packet of phase velocity equal to v'_{ph}. Calculation of ξ_{ik} reduces to calculation of the relative overlapping of the areas of i-th and k-th sections of adjacent packets, allowing for the phase coherence of these packets. Without giving details of the calculations of the appropriate areas and their ratios, we shall give an estimate of ξ_{ik} obtained for $\tau_{NL} \ll \tau_{QL}$ correct to within terms of the order of $\partial v_{tr}/\partial v$, which may be neglected if the amplitudes of the adjacent packets differ negligibly. In this case, we have

$$\begin{aligned}
&\xi_{21}(v, v + v_{tr}) = 1 - \xi_{23}(v, v + v_{tr}) \approx \xi_{12}(v, v - v_{tr}) \\
&= 1 - \xi_{14}(v, v - v_{tr}) \approx \xi_{43}(v, v + v_{tr}) = 1 - \xi_{41}(v, v + v_{tr}) \\
&\approx \xi_{34}(v, v - v_{tr}) = 1 - \xi_{32}(v, v - v_{tr}) \approx 0.8
\end{aligned} \tag{3.8}$$

Applying the probabilities ξ_{ik}, we can express the distribution functions $f_i(v \pm v_{tr}, t)$ in terms of $f_k(v, t)$. We then have:

$$\begin{aligned}
f_1(v - v_{tr}, t) &= \xi_{12}(v, v - v_{tr})\, \tilde{f}_2(v, t - \delta\tau) + \xi_{14}(v, v - v_{tr})\, \tilde{f}_4(v, t - \delta\tau) \\
f_3(v - v_{tr}, t) &= \xi_{32}(v, v - v_{tr})\, \tilde{f}_2(v, t - \delta\tau) + \xi_{34}(v, v - v_{tr})\, \tilde{f}_4(v, t - \delta\tau) \\
f_2(v + v_{tr}, t) &= \xi_{21}(v, v + v_{tr})\, \tilde{f}_1(v, t - \delta\tau) + \xi_{23}(v, v + v_{tr})\, \tilde{f}_3(v, t - \delta\tau) \\
f_4(v + v_{tr}, t) &= \xi_{41}(v, v + v_{tr})\, \tilde{f}_1(v, t - \delta\tau) + \xi_{43}(v, v + v_{tr})\, \tilde{f}_3(v, t - \delta\tau)
\end{aligned} \tag{3.9}$$

where $\delta\tau = \delta\ell/v$, and $\delta\ell$ is the average distance between adjacent packets. By order of magnitude, $\delta\ell$ is comparable with ℓ_{int}.

Eliminating the functions $\tilde{f}_i$ from Eq.(3.9) by means of Eq.(3.7), we obtain the required system of kinetic equations. This system must be supplemented by the boundary conditions and the equation for the packet amplitudes.

Let v_1 and v_2 be the upper and lower limits of the average phase velocities of the main-scale packets. Bearing in mind that particles from sections 1 and 3

of a packet with phase velocity v_1 are transferred to sections 1 and 3 of an adjacent packet with the same phase velocity, and similarly, that particles from sections 2 and 4 of a packet with phase velocity v_2 are transferred to sections 2 and 4 of the nearest packet with the same phase velocity, we obtain:

$$f_{1,3}(v_1, t) \approx f_{1,3}(v_1, t - \delta\ell_1/v_1)$$

$$f_{2,4}(v_2, t) \approx f_{2,4}(v_2, t - \delta\ell_2/v_2) \tag{3.10}$$

Here, $\delta\ell_{1,2}$ are the average distances between packets with phase velocities $v_{1,2}$ approximately equal to $\ell_{int}(v_{1,2})$.

The equation for v_{tr} is readily obtained from Eqs (3.7), (3.9) and the energy conservation law. Expressed in differential form this equation takes the form:

$$\frac{\partial v_{tr}}{\partial t} = \frac{v^3}{\tau_{NL}\, v_{tr}} [2\, \xi_{tr}\, (1 - \eta)\, F_- + (1 - \xi_{tr})\, \Phi_-] \tag{3.11}$$

where

$$F_\pm(v, t) = \tfrac{1}{2} [f_1(v, t) \pm f_2(v, t)]$$

$$\Phi_\pm(v, t) = \tfrac{1}{2} [f_3(v, t) \pm f_4(v, t)] \tag{3.12}$$

The system of difference equations (3.7) and (3.9) can be reduced to differential equations in the following important limiting cases:

1. Let

$$v_{tr} \ll |v_1 - v_2|,\ |v_{tr}\, \partial F_-/\partial v| \ll F_+,\ 2F_- \tag{3.13}$$

In this case, from Eqs (3.7) and (3.9), by expanding with an accuracy up to linear terms and allowing for Eq.(3.13), we have

$$\tau \frac{\partial F_+}{\partial t} = \frac{\partial}{\partial v} (w v_{tr}\, F_-) + (1 - \xi_\parallel)\, (\Phi_+ - F_+) \tag{3.14}$$

$$\tau \frac{\partial F_-}{\partial t} + 2(1 - w) F_- = \tfrac{1}{2} v_{tr} \frac{\partial}{\partial v} [(1 + \xi_{21}) F_+ + (1 - \xi_{21})\, \Phi_+] \tag{3.15}$$

$$\tau \frac{\partial \Phi_\pm}{\partial t} = \tfrac{1}{2} \frac{\partial}{\partial v} \{ v_{tr} [\Phi_- + 2\, (1 - \xi_{43})\, (1 - 2\eta)\, F_-] \}$$
$$+ (1 - \xi_{43})\, (F_+ - \Phi_+) \tag{3.16}$$

$$\Phi_- \approx \tfrac{1}{2} v_{tr} \frac{\partial}{\partial v} [(1 + \xi_{43}) \Phi_+ + (1 - \xi_{43}) F_+] + 2(1 - \xi_{43})(1 - 2\eta) F_- \quad (3.17)$$

$$\tau = \tau_{NL} + \delta\tau, \; w = \tfrac{1}{2} [1 + \xi_{21} (1 - 2\eta)] \quad (3.18)$$

It can be seen from Eqs (3.14) and (3.16) that the difference $F_+ - \Phi_+$ decreases with the time constant $\tau(2 - \xi_{21} - \xi_{34})^{-1}$. Allowing for this, and for the correlation between $\bar{f}$ and F_+, Φ_+, Eq.(3.5), for $\bar{f}$ we obtain from Eqs (3.14) and (3.16)

$$\frac{\partial \bar{f}}{\partial t} = \frac{\partial}{\partial v} \left\{ \frac{v_{tr}}{\tau} [2 \xi_{tr} w + \xi_{ntr} (1 - \xi_{43})(1 - 2\eta)] F_- + \frac{v_{tr}}{\tau} (1 - \xi_{tr}) \Phi_- \right\} \quad (3.19)$$

To within the same accuracy, Eqs (3.13) and (3.14) give

$$\tau^2 \frac{\partial^2 F_-}{\partial t^2} + 2(1 - w) \frac{\partial F_-}{\partial t} = w_{tr}^2 \frac{\partial^2 F_-}{\partial v^2} \quad (3.20)$$

This equation describes the evolution of the inhomogeneity of the distribution function F_- and takes the form of a dissipative wave equation. When $w \to 1$, the term with the first derivative describing the dissipation vanishes whilst when $w \to \frac{1}{2}$, it is a dominant factor. The inhomogeneity 'attenuation' time is, as can be seen from Eq.(3.20), given by

$$\tau_r = \tau (1 - w)^{-1} \quad (3.21)$$

and, on time scales shorter than this, the relaxation of a velocity-smoothed beam may become oscillatory as was observed in various numerical experiments [2, 3, 7–9].

Equation (3.19) is an analogue of the quasi-linear kinetic equation. It is readily shown that when $w \to \frac{1}{2}$ ($\eta \to \frac{1}{2}$), Eqs (3.11) and (3.19) are converted into equations for 'strong turbulence' (or re-normalized quasi-linear equations [10] which, in the limit $v_{tr} \to 0$, are then converted into quasi-linear equations [11, 12]. When $\eta \to \frac{1}{2}$, it follows from Eqs (3.15)–(3.17) that

$$F_+ (v, t) = \Phi_+ (v, t) = \bar{f}(v, t); \; F_- (v, t) = \Phi_- (v, t) = v_{tr} \, \partial \bar{f}(v, t)/\partial v \quad (3.22)$$

On substituting Eq.(3.22) into Eqs (3.11) and (3.19), we obtain a quasi-linear system in which the coefficients are the same as the known values if it is assumed that

$$\tau_{NL} = \tau = 1 \; b/\pi \Omega_{tr} \quad (3.23)$$

2. In the other limiting case when the microinhomogeneity scale is equal to or greater than the macroinhomogeneity scale, i.e. $v_{tr} \gtrsim \Delta v$, the average phase velocities of all the packets are approximately equal. The kinetic equations in this case are derived from Eq.(3.10) if we assume $v_1 = v_2 = \bar{v}$ ($\bar{v}$ is the average phase velocity of the packets) and take the following form:

$$F_+(\bar{v}, t) \approx F_+(\bar{v}, 0); \Phi_+(\bar{v}, t) \approx \Phi_+(\bar{v}, 0)$$

$$F_-(\bar{v}, t) = (1-\eta) F_-(\bar{v}, t - \bar{\tau}); \ \bar{\tau} = \tau_{NL} + \delta\bar{\ell}/\bar{v} \tag{3.24}$$

These equations describe the state of degenerate turbulence. The coefficient η describes mixing due to the difference between the trapped-particle oscillation frequencies. These equations specifically describe the evolution of a BGK wave with a non-equilibrium initial distribution function, particular cases of which were analysed by Mazitov [13] and O'Neil [4]. To confirm this, we give the particular solution of Eq.(3.24) for $\bar{\tau} = \tau$, Eq.(3.23), in the form:

$$F_-(\bar{v}, t) = F_-(\bar{v}, 0)\, e^{-\frac{\eta t}{\tau}} \cos(\bar{\Omega} t) \tag{3.25}$$

where

$$F_-(\bar{v}, 0) = v_{tr}\, \partial\bar{f}/\partial v \Big|_{v=\bar{v}}, \ \bar{\Omega} = \pi/\tau$$

This solution can be obtained by approximating the results obtained in Ref.[4]. In particular, for the growth rate we obtain from Eqs (3.25) and (3.11):

$$\gamma_{NL}(t) = \gamma_{QL}(0) \exp(-\eta t/\tau) \cos(\bar{\Omega} t) \tag{3.26}$$

The equations for moderate turbulence describing the inhomogeneities of the distribution function and allowing for the correlation of the particle motion also express the idea of the generation and substantial influence of the macroparticles on the relaxation of the non-equilibrium distribution function formulated and applied to develop the macroparticle relaxation theory in Refs [14–17]. The inhomogeneities described by the functions F_- and Φ_- can be considered to be macroparticles in the sense of Refs [14–17] with the main scale $\Delta v = v_{tr}$, $\Delta x = \lambda$. An important parameter is the macroparticle life-time τ_d.

On the basis of Eqs (3.14)–(3.20), τ_d can be estimated as follows: The characteristic attenuation time of Φ_- is equal to τ, and the attenuation time of F_- [see Eq.(3.21)] is equal to $\tau(1-w)^{-1}$. Thus, depending whether it starts from sections 1 and 2, or 3 and 4, the macroparticle life-time will be given by, respectively,

$$\tau_d^{(tr)} \approx \tau(1-w)^{-1} \text{ and } \tau_d^{(ntr)} \approx \tau \tag{3.27}$$

For the average life-time, we have from Eq.(3.27)

$$\bar{\tau}_d = \tau\left(1 + \frac{w}{1-w}\ \xi_{tr}\right) \tag{3.28}$$

On comparing Eqs (3.27) and (3.28) with the expressions for τ_d obtained in Refs [14–17], it can be seen that our value of τ_d is several times higher than that obtained in Ref.[16] (after Dupree, $\tau_d \approx (kv_{tr})^{-1}$) where the field correlation was neglected, but is lower than that estimated in Refs [14, 15] where an exponential law of decreasing pair correlation was obtained.

The value of τ_d obtained in numerical experiments [2, 3] agrees with the estimates made above.

Another important property of the equations for moderate turbulence should be noted: they establish a correlation between the macroinhomogeneity and the perturbations of the distribution function. In particular, it follows from Eq.(3.15) that in the quasi-steady-state limit when $|\tau\dot{F}_-| \ll F_-$ that

$$F_- \approx \frac{v_{tr}}{2(1-w)}\ \frac{\partial \bar{f}}{\partial v} \tag{3.29}$$

Correlations of this type (3.29) form the basis of the phenomenological approach in turbulence theory based on the introduction of the mixing length. The mixing length is described as the coefficient of proportionality of the average inhomogeneity fluctuations.[2] In our case, for trapped particles, it can be seen from Eq.(3.29) that the mixing 'length' is given by

$$v_{mix}^{(tr)} = \frac{v_{tr}}{2(1-w)} \tag{3.30}$$

For untrapped particles, we have $v_{mix}^{(ntr)} \approx v_{tr}$ and for the average value of v_{mix} we obtain the following expression:

$$\bar{v}_{mix} = \frac{v_{tr}}{2}\left[1 + \frac{w}{1-w}\ \xi_{tr}\right] \tag{3.31}$$

[2] This approach was first adopted in the theory of hydrodynamic turbulence by Prandtl. It was applied in the theory of plasma turbulence by B.B. Kadomtsev [18].

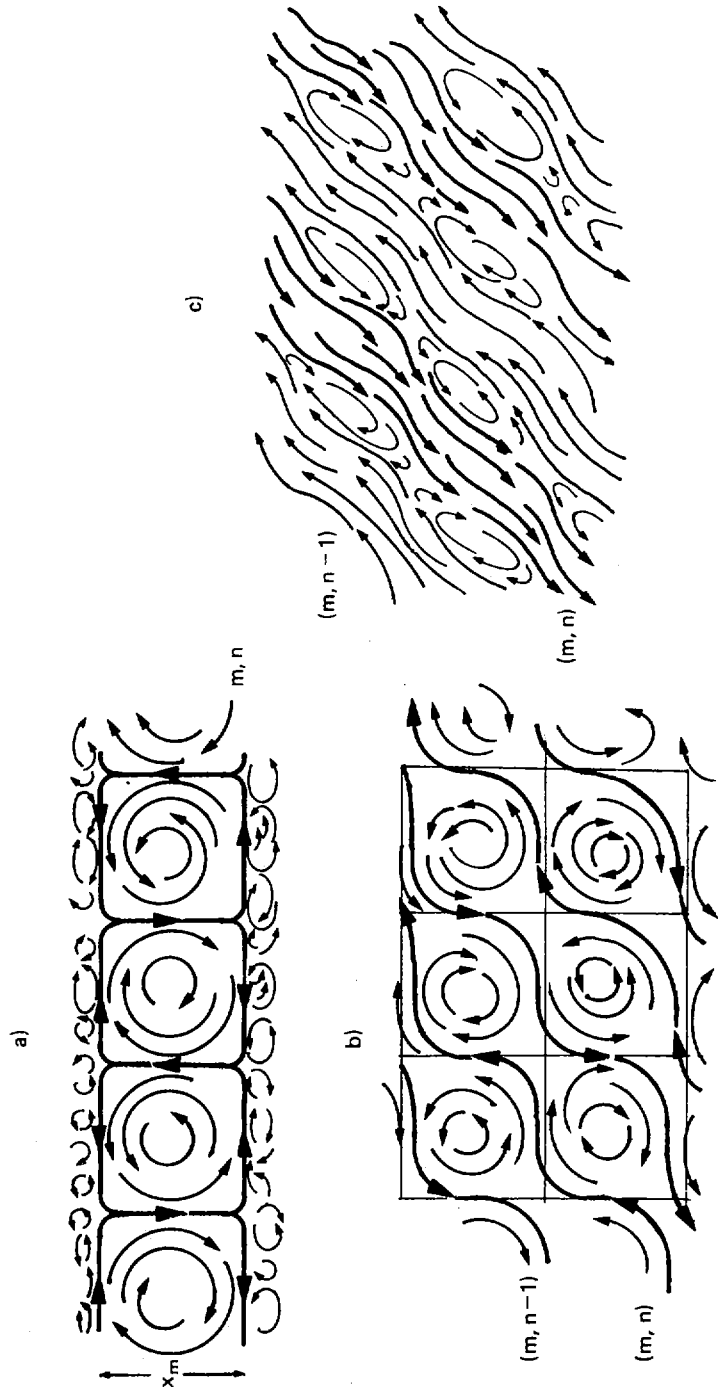


FIG. 6. a) Isolated chain of convective cells; b) the overlapping cells are ordered and mutually amplifying and c) forming ordered convective flows.

4. CURRENT-CONVECTIVE INSTABILITY

We shall now analyse the current-convective instability. The formation of convective cells at the non-linear stage of this instability was investigated in Ref.[19]. The problem involves constructing the kinetic equations which allow for the interaction of the convective cells with one another. As will subsequently become apparent, in the development of the current-convective instability a moderately turbulent state is also established with its characteristic turbulent convective transport.

We shall analyse the development of the current-convective instability in a homogeneous plasma situated in a sheared toroidal magnetic field with the temperature gradient $\partial T/\partial r < 0$. As shown in Ref.[19], thermal convective cells are formed in the vicinity of resonant magnetic surfaces at the non-linear stage, with the characteristic dimensions, velocity and convection time given by

$$x_m = r\,\xi^{1/3}\,m^{-2/3},\ v_m = 2\,A\tilde{T}/x_m,\ \tau_m = x_m/v_m \tag{4.1}$$

where

$$\xi = A\,|\partial T/\partial r|\,r^{-3}\,\alpha^{-1},\ A = q\,c\,E_0\,(d\sigma/dT)/q'B_\theta\sigma\ \ \alpha = \chi_\parallel\,\theta^2\,r^{-4}$$

$\tilde{E_0}$ is the constant electric field intensity, $\tilde{T}$ is the temperature perturbation, q is the safety factor, c is the speed of light, B_θ is the poloidal magnetic field intensity, σ is the conductivity, θ is the shear and $\chi_\parallel$ is the longitudinal thermal conductivity. The resonant surfaces are numbered by the pair of indices (m, n). The average instability growth rate is given by

$$\gamma_m \approx -\,2A\,(\partial T/\partial r)\,x_m^{-1} \tag{4.2}$$

The characteristic distance between resonant surfaces with cells of comparable size is given by [19] $\Delta_m \approx q^2/q'm$. Since only the largest cells make a major contribution to the transport, provided that they overlap, equating x_m and Δ_m, we find that the main scale of the cells is governed by the number $m_0 \approx (q^2/q'r\xi^{1/3})^{3/4}$.

At the initial stage of the instability, thermal convection develops near the resonant surfaces and is amplified by the average temperature gradient, the flows developing from the initial fluctuations being uncorrelated for the various surfaces. At the non-linear stage when the convective flows significantly alter the temperature distribution, the overlapping cells substantially influence each other. At this stage, the cells undergo spatial ordering and convective flows are formed (see Fig.6). Such ordering is advantageous: the instability is amplified

since the local temperature gradient increases and, on the other hand, the ordering increases the heat transport. In addition to the main-scale cells, the small-scale cells are also unstable, $m_0 < m' < m_c$ (m_c is the smallest scale of the instability determined by the thermal conductivity [19]) and these make the convective flows turbulent.

The kinetic equations for moderate turbulence can be expressed in the form:

$$T_1(r, t) = w_0 T_1 (r - x_0, t - \tau_0) + (1 - w_0) T_2 (r, t - \tau_0)$$

$$T_2(r, t) = (1 - w_0) T_1 (r, t - \tau_0) + w_0 T_2 (r + x_0, t - \tau_0) \qquad (4.3)$$

where T_1 and T_2 are the average temperatures in the ascending and descending fluxes, $\tau_0 \approx \sqrt{2} x_0/v_0$ and v_0 is determined by Eq.(2.1) in which $x_0 = x_{m0}$, $T = T_+ = (T_1 + T_2)/2$, $m = m_0$, $\tilde{T} = T_- = (T_1 - T_2)/2$, should be substituted, w_0 is the probability of the flow element remaining in the ascending (descending) flow after a circuit of the cell. An element is transferred from one flow to another as a result of small-scale turbulent transverse transport to which contributions are made by collisions and small cells with $m' \ll m_0$, and also as a result of the disorder in the convective flow structure which is found, for example, if the values m(r) and $m(r + x_0)$ of adjacent overlapping cells differ slightly. Thus, if $|m(r) - m(r + x_0)| = \delta m$, ascending and descending flows with respect to r are mixed on average by the value $\eta \approx \delta m/m_0$. The probability w_η allowing only for such mixing is given by

$$w_\eta = 1 - \eta \equiv 1 - \delta m/m_0 \qquad (4.4)$$

Mixing as a result of small-scale turbulence can be estimated as follows: The temperature perturbation $\tilde{T}$ decreases exponentially with the characteristic spatial scale x_0, as is known from solution of the thermal conductivity equation,

$$\tilde{T}(t + \tau_0) = \tilde{T}(t) \exp\left(-\frac{\pi^2 \chi_{\perp c} \tau_0}{x_0^2}\right) \qquad (4.5)$$

where $\chi_{\perp c}$ is the thermal conductivity resulting from the small-scale turbulence and collisions. The expression for $\chi_{\perp c}$ is given in Ref.[19] and may be estimated by using the following relationship:

$$\chi_{\perp c} \approx x_{m'}^2 \gamma_{m'}/\pi^2, \; m' \ll m_0 \qquad (4.6)$$

obtained from the condition of turbulent suppression of small-scale instabilities [18] On the other hand, neglecting the spatial variation of $T_{1,2}$ over distances

of the order of x_0, we have from Eq.(4.3):

$$T_-(t + \tau_0) = 2(1 - 2w)\, T_-(t) \tag{4.7}$$

On comparing Eqs (2.5) and (2.7), we obtain an expression for w:

$$w = \frac{1}{2}\left[1 + \exp\left(-\frac{\pi^2 \chi_\perp \tau_0}{x_0^2}\right)\right] \tag{4.8}$$

The total probability w_0 is obtained by multiplying Eqs (4.4) and (4.8):

$$w_0 = \frac{1-\eta}{2}\left[1 + \exp\left(-\frac{\pi^2 \chi_{\perp c} \tau_0}{x_0^2}\right)\right] \tag{4.9}$$

System (4.3) differs from the system of kinetic equations (3.14)–(3.17) only by the absence of terms describing the turbulent component of the flow. Replacing Eqs (2.3) by differential equations, we obtain

$$\tau_0 \frac{\partial T_+}{\partial t} = \frac{1}{r}\frac{\partial}{\partial r}\left(r \frac{w_0 x_0}{\tau_0} T_-\right) \tag{4.10}$$

$$\tau^2 \frac{\partial^2 T_-}{\partial t^2} + 2(1 - w_0)\,\tau \frac{\partial T_-}{\partial t} = x_0 \frac{\partial T_+}{\partial r} \tag{4.11}$$

which are similar to Eqs (3.19) and (3.20). In particular, it follows from these equations that

$$T_- \approx \frac{x_0}{2(1 - w_0)} \frac{\partial T_+}{\partial r} \tag{4.12}$$

$$q_{\perp T} = \frac{w_0}{4(1 - w_0)^2}\, x_0^2\, \gamma_0 \frac{\partial T_+}{\partial r} \tag{4.13}$$

Here, $q_{\perp t}$ is the transverse thermal flux.

It can be seen from Eq.(4.12) that the temperature gradient reaches $\sim 2T_-/x_0 \sim T_+' (1 - w_0)^{-1}$, which is a factor of $(1 - w_0)^{-1}$ larger than the average temperature gradient and equal to this gradient in the absence of order, i.e. when $w_0 = \frac{1}{2}$. It follows from Eq.(4.12) that the mixing length is given by

$$\ell_{mix} = \frac{x_0}{2(1 - w_0)} \tag{4.14}$$

and may achieve values many times larger than x_0.

The thermal conductivity of a strongly turbulent plasma is estimated from Eq.(4.6) in which m_0 should be substituted for m′:

$$\chi_{\perp o}^{(ST)} \approx x_0^2 \, \gamma/\pi^2$$

If the factor near T_+' in Eq.(4.13) is considered as the moderately turbulent thermal conductivity $\chi_{\perp o}^{(MT)}$, we have

$$\chi_{\perp o}^{(MT)} \approx \frac{w_0}{(1 - w_0)^2} \chi_{\perp o}^{(ST)}$$

It can thus be seen that ordering substantially increases the transport coefficients.

We note that ordering of overlapping cells may be considered as the excitation of quasi-modes [20], the only difference being that it takes place at the non-linear stage as a result of interaction of the cells. At the linear stage, amplification of the fluctuating perturbations is observed.

5. DRIFT INSTABILITY

Convective transport of plasma particles as a result of the development of drift instability takes place as a result of the drift waves exciting weakly attenuating convective cells. Transport due to convective cells, excited as a result of thermal fluctuations, was studied by Dawson and Okuda in Ref.[21]. Diffusion due to convective cells excited by drift waves produced as a result of drift instabilities was studied theoretically and numerically in Refs [22–24]. In Ref.[24], an investigation was also made of the excitation of convective cells by Alfvén waves. Interaction of convective cells and their coalescence to form larger cells was observed numerically in Ref.[22]. We also note the numerical experiments, the results of which are reviewed by N. Sato [25], in which it was observed that the onset of drift instability resulted in the formation of ordered convective flows in the direction of the density gradient rather than in turbulent mixing of the particle flows. Mention should also be made of a numerical experiment [28], where a similar pattern was observed in the development of the trapped-particle instability. These results indicate that the non-linear stage of the drift instability is characterized by a transition to a stage of moderate turbulence with rapid turbulent convective transport. The kinetic equations for moderate turbulence established as a result of the onset of the drift instability are derived below and the particle transport coefficient is determined.

The characteristic parameters of the problem are as follows. The macro-inhomogeneity scale is equal to the plasma radius. The drift oscillations build up near the resonant surfaces and the radial width of the zone of localization is equal to

$$x_0 \approx \rho_i \frac{T_e}{\theta T_i} \tag{5.1}$$

where ρ_i is the ion Larmor radius, θ is the shear, and $T_{e,i}$ are the electron and ion temperatures.

The distance between the resonant surfaces is given by

$$\Delta_m \approx q^2/q' m^2 \approx aq/m^2 \tag{5.2}$$

This relationship was obtained, as in the previous section (see Ref.[19]) allowing for substantial interaction between modes with similar values of m.

From the condition of overlapping of the cells, equating Eqs (5.1) and (5.2), we obtain

$$m_0 \approx \left(\frac{aq\theta}{\rho_i} \frac{T_i}{T_e}\right)^{1/2} \tag{5.3}$$

which determines the main scale of the convective cells.

As a result of interaction, the neighbouring overlapping cells analysed in detail in the previous section are ordered and mutually amplifying. In this case, ordered radial convective particle flows are observed. Let n_1 and n_2 be the average ion densities in the ascending and descending flows, and by analogy with Eq.(4.3), allowing for the interaction of the convective cells with the drift waves, as described in Refs [23, 24], we obtain

$$\tau \frac{\partial n_+}{\partial t} = \frac{1}{r} \frac{\partial}{\partial r} \left(rw \frac{x_0}{r} n_- + r j^d\right), \quad n_\pm = \tfrac{1}{2}(n_1 \pm n_2) \tag{5.4}$$

$$\tau \frac{\partial n_-}{\partial t} + 2(1-w)n_- = x_0 \frac{\partial n_+}{\partial r}$$

$$+ \sum_{\vec{k}_1 - \vec{k}_2 = \vec{k}^c} V^{m_0}_{\vec{k}_1 \vec{k}_2} n^d_{k_1} n^d_{\vec{k}_2} \tilde{\delta}(\omega_{k_1} - \omega_{k_2}, \tau) \tag{5.5}$$

Here, $\tau = x_0/v^c$, and v^c is the radial drift velocity in the convective cell given by

$$v^{\tilde{c}} = \frac{c\ \nabla_y\ \varphi^c}{B} \approx \frac{cm_0\ \varphi^c}{rB} \tag{5.6}$$

φ^c is the potential perturbation related to the density perturbation by

$$\varphi^c = \frac{T_e}{e}\ \frac{\delta n}{\bar{n}} = \frac{T_e}{e}\ \frac{n_-}{n_+} \tag{5.7}$$

and j^d is the particle flow due to drift turbulence.

The second term in Eq.(5.5) describes the interaction of the convective cells with the drift waves. The drift wave amplitudes n_k^d and expressions for the interaction coefficient $V^m_{\vec{k}_1, \vec{k}_2}$ can be found in Refs [23, 24]. The function $\tilde{\delta}(\omega_1 - \omega_2, \tau)$, Eq.(5.5), implies that only drift waves with similar frequencies, $|\omega_1 - \omega_2|^{-1} \gtrsim \tau$, contribute to the interaction.

Systems (5.4) and (5.5) should be supplemented by the drift wave equation:

$$\frac{\partial n_k^d}{\partial t} = \gamma_k\ (n_+)\ n_k^d + \sum_{\vec{k}_1 - \vec{k}^c = \vec{k}} V^{m_0}_{\vec{k}\vec{k}_1}\ n^d_{\vec{k}_1}\ n_-\ \tilde{\delta}\ (\omega_k - \omega_k, \tau) \tag{5.8}$$

Here, γ_k is the quasi-linear drift wave growth rate.

The probability w is defined by an expression similar to Eq.(4.9):

$$w = \frac{1-\eta}{2}\left[1 + \exp\left(-\frac{\pi^2 D_\perp \tau}{x_0^2}\right)\right] \tag{5.9}$$

In this case, the drift waves and small-scale cells contribute to the diffusion coefficient $D_\perp$. Since the attenuation of the cells $\sim k^2 D_\perp$ increases with decreasing size, transport due to small-scale cells is weak and thus $\tau D_\perp / x_0^2 \ll 1$.

It can be seen from Eqs (5.4), (5.5) and (5.9) that the drift instability develops as follows: Drift waves are first excited and these then excite convective cells when their amplitudes are sufficiently large. By interacting with each other, the convective cells become ordered and mutually amplifying and give rise to anomalously fast transverse plasma transport. It can be seen from Eq.(5.9) that the influence of the convective cells (flows) on the drift waves should result in a phase correlation and the establishment of a certain quasi-equilibrium distribution in the drift wave system by virtue of the second term on the right-

hand side. In addition, the decrease in the average density gradient $\partial n_+/\partial r$ as a result of the transport reduces $\gamma_k(n_+)$ and restricts the drift instability.

Equations (5.4) and (5.5) yield expressions for the density perturbation and the transverse particle flow:

$$n_- \approx \frac{x_0}{2(1-w)} \frac{\partial n_+}{\partial r} \tag{5.10}$$

$$j = j^c + j^d, \; j^c = \frac{w x_0}{\tau} n_- \tag{5.11}$$

Here, j^c is the flux due to convective transport.

Equations (5.10) and (5.11) yield an expression for the diffusion coefficient:

$$D_\perp^c = \frac{w}{2(1-w)} x_0 v^c \approx \frac{w}{2(1-w)} \frac{m_0 x_0}{r} \left| \frac{n_-}{n_+} \right| D_B$$

$$\approx \frac{w}{4(1-w)^2} \frac{m_0 x_0^2}{rL} D_B \tag{5.12}$$

where $D_B = \rho_i (T_i/m_i)^{\frac{1}{2}}$ is the Bohm diffusion coefficient.

The transport due to the drift waves can be described by the familiar expressions [18]:

$$j^d = D^d \frac{\partial n_+}{\partial r}, \; D^d = \sum_k \frac{c^2 |\varphi_k^d k_y|^2}{B^2} \frac{\gamma_k}{\omega_k} \tag{5.13}$$

6. MAGNETIC DRIFT

Drift and tearing instabilities may result in splitting of the resonant magnetic surfaces, i.e. in radial displacements of the magnetic field lines in the vicinity of the unperturbed surfaces by a certain value δ_B determined by the geometry of the unperturbed magnetic field, the hydrodynamic parameters of the plasma [26, 27] and the amplitude of the perturbations. The transverse projection of the split surfaces takes the form of two-dimensional convective cells. If the dimensions of the convective cells are greater than the distances between the resonant surfaces, $\delta_B \gtrsim \Delta_m$, they overlap. The magnetic convective cells may become ordered as a result of the establishment of correlations between the

unstable waves generated by these cells at the moderately turbulent stage (see previous section), and the degree of ordering of the magnetic convection is governed by the degree of correlation between the plasma drift and convective motion. Thus, the characteristic transverse mixing length of the magnetic field lines in the overlapping cells may be given by

$$\ell_{mix} = \frac{\delta_B}{1 - w} \tag{6.1}$$

which considerably exceeds the splitting width of the magnetic surfaces.

Magnetic drift may be the main mechanism for the anomalously high transverse electron thermal conductivity observed in tokamaks. Moreover, the transverse electron thermal conductivity at the moderately turbulent stage may be appreciably higher than the values obtained in Ref.[26] by virtue of Eq.(6.1).

Existence and size of the magnetic convective cells in different plasma states require special investigation. A detailed discussion of this aspect is outside the scope of the present paper.

REFERENCES

[1] BAKAJ, A.S., Dokl. Akad. Nauk SSSR **237** (1977) 1069.
[2] BAKAJ, A.S., SIGOV, Yu.S., Dokl. Akad. Nauk SSSR **237** (1977) 1326.
[3] BAKAJ, A.S., SIGOV, Yu.S., Preprint No.52, Institute of Problems of Mechanics, Academy of Sciences of the USSR (1977).
[4] O'NEIL, T., Phys. Fluids **8** (1965) 2255.
[5] GALEEV, A.A., SAGDEEV, R.Z., in Problems of Plasma Theory (LEONTOVICH, M.A., Ed.) Vol. 7, Atomizdat (1973).
[6] DENAVIT, J., SUDAN, R., Phys. Rev. Lett. **28** (1972) 404.
[7] DAWSON, J., SHANNY, R., Phys. Fluids **11** (1968) 1506.
[8] MORSE, R., NIELSON, C., Phys. Fluids **12** (1969) 2418.
[9] BISKAMP, D., WELTER, H., Nucl. Fusion **12** (1972) 89.
[10] DUPREE, T., Phys. Fluids **9** (1966) 1773.
[11] VEDENOV, A.A., VELIKHOV, E.P., SAGDEEV, R.Z., Nucl. Fusion. Supplement **2** (1962) 465.
[12] DRUMMOND, W., PINES, D., Nucl. Fusion. Supplement **3** (1962) 1049.
[13] MAZITOV, R.K., Prikl. Mekh. Tekh. Fiz. **1** (1965) 27.
[14] KADOMTSEV, B.B., POGUTSE, O.P., Phys. Rev. Lett. **25** (1970) 1155.
[15] KADOMTSEV, B.B., POGUTSE, O.P., Phys. Fluids **14** (1971) 2470.
[16] DUPREE, T., Phys. Rev. Lett. **25** (1970) 789.
[17] DUPREE, T., Phys. Fluids **15** (1972) 334.
[18] KADOMTSEV, B.B., in Problems of Plasma Theory (LEONTOVICH, M.A., Ed.) Vol.4, Atomizdat (1964).

[19] KADOMTSEV, B.B., POGUTSE, O.P., in Problems of Plasma Theory (LEONTOVICH, M.A., Ed.) Vol.5. Atomizdat (1967).
[20] ROBERTS, K., TAYLOR, J.B., Phys. Fluids **8** (1965) 315.
[21] OKUDA, H., DAWSON, J., Phys. Fluids **16** (1973) 408.
[22] CHENG, C., OKUDA, H., Phys. Rev. Lett. **38** (1977) 708.
[23] CHENG, C., OKUDA, H., Preprint, PPPL-1397 (1977).
[24] SAGDEEV, R.Z., SHAPIRO, V.D., SHEVCHENKO, V.I., Piz'ma Zh. Ehksp. Teor. Fiz. **27** (1978) 361.
[25] SATO, N., Comments on Plasma Phys. and Controlled Fusion **11** (1977) 185.
[26] CALLEN, J., Phys. Rev. Lett. **39** (1977) 1540.
[27] RECHESTER, A., ROSENBLUTH, M., Phys. Rev. Lett. **40** (1978) 38.
[28] SAISON, R., WIMMEL, H., SARDEI, F., Plasma Phys. **20** (1978) 1.

DISCUSSION

ON PAPERS X-4-1 AND X-4-2

A. HASEGAWA: Would you care to comment on the recent statement by Dupree that test particle diffusion is different from density diffusion? It seems that test particle diffusion can occur by $\vec{E} \times \vec{B}$ drift, but that density diffusion can occur not by $\vec{E} \times \vec{B}$ drift only, but by other processes as well.

J.M. DAWSON: Test particles, density and heat all diffuse at different rates. In fact, every different velocity class diffuses at a different rate, as can be seen from our calculations. We had expected that heat diffusion would be roughly equal to test particle diffusion because test particles carry their heat with them as they diffuse. However, our calculation shows that energetic test particles diffuse more slowly than low-energy particles, and so heat diffuses more slowly than particles.

A. HASEGAWA: What is a typical scale size of the vortices in Bakaj's theory?

J.M. DAWSON: I believe the scale size in Bakaj's theory is that of the locally fastest-growing mode.

A.SYKES: Is it possible to do fully 3D point particle simulations, rather than the $2\frac{1}{2}$D rod simulations, and if so what differences in the diffusion results would you expect?

J.M. DAWSON: Okuda and I did 3D particle simulations about five years ago. If the magnetic field lines are closed the same type of convective cells occur as in the 2D model and the same type of phenomena should also take place. If the lines are ergodic, the convective cells short out and the diffusion drops to near the collisional level. However, instabilities and inhibition of current flow parallel to B (such as can be produced by mirroring) can lead to low-frequency E fields and a similar result should occur.

W. HORTON: You explain an interesting mechanism by which the particle diffusion may exceed the thermal diffusion. However, the $2\frac{1}{2}$D drift wave simulations by Okuda and co-workers show that the electron thermal transport exceeds the particle transport by an appreciable factor. In addition, as the shear increases, the density fluctuations and the particle diffusion decrease, but the thermal transport remains largely unchanged. What could be the reason for these different observations?

J.M. DAWSON: Our calculations show that particles with small Larmor radii are transported faster than those with large Larmor radii. Since the ions have relatively large Larmor radii, they will be diffused relatively slowly by the turbulence. The diffusion of the plasma as a whole is primarily determined by the ions; the electrons cannot diffuse away and leave the ions behind. However, hot electrons can be diffused out and replaced by cold electrons diffusing in.

The rapid electron diffusion produced by the turbulence would result in rapid electron heat transport and would be completely consistent with our calculations. We have not considered the sheared-magnetic-field case, but I suspect that fine-scaled turbulence would still be allowed by a highly sheared field and that the electrons would respond to it. However, again, the ions would not respond because of their large Larmor radii.

EXPERIMENTS ON PLASMA CONFINEMENT BY RELATIVISTIC-ELECTRON-BEAM RING

A. MOHRI, K. NARIHARA, T. TSUZUKI,
Y. KUBOTA, Y. TOMITA, K. IKUTA,
M. MASUZAKI*
Institute of Plasma Physics,
Nagoya University,
Nagoya,
Japan

Abstract

EXPERIMENTS ON PLASMA CONFINEMENT BY RELATIVISTIC-ELECTRON-BEAM RING.

Toroidal magnetic configurations maintained by intense relativistic-electron-beam ring currents were experimentally demonstrated to be capable of confining hot plasma of density 6×10^{13} cm^{-3}. The lifetime of the ring was longer than 1 ms and the toroidal current higher than 30 kA. The ion temperature rose from 100 eV to 300 eV during major radial compression. Ring current of more than 150 kA was attained by injecting a beam into denser plasma. A diode composed of a metal cathode and a plasma-anode was used for the injection of electron beams.

1. INTRODUCTION

Toroidal magnetic configurations formed by intense relativistic-electron-beam (REB) currents offer many advantages for plasma confinement. Since the toroidal beam current can be generated in the plasma by injecting electron beams from outside, no space is necessary in principle for equipment driving the toroidal current, and low aspect ratio of toroidal configuration is therefore realizable. REB rings can be formed very rapidly by short-pulse REB injection, and the formation time observed experimentally was shorter than 1 μs [1]. The system can safely pass over dangerous unstable states which may lie on the way to a final stable state, e.g. a state of low safety factor. A highly paramagnetic configuration like the stabilized pinch or the reversed-field pinch may thus be formed without difficulty in a short period. The β-value of the plasma confined in this configuration is promisingly higher than that in tokamaks. Furthermore, three-dimensional adiabatic compression is effectively applicable by increasing the

* Permanent address: Faculty of Science, Kanazawa University, Kanazawa, Japan.

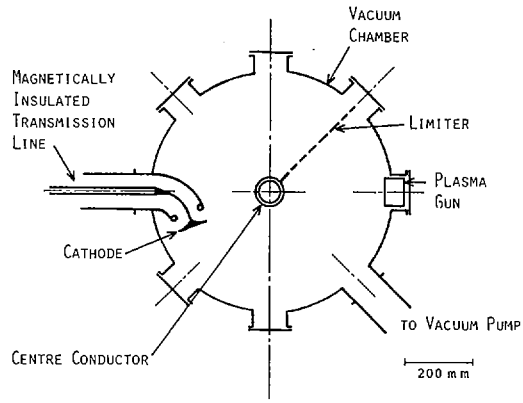


FIG.1. Top view of toroidal chamber of SPAC-V.

vertical magnetic field, whence particle energies of the beam electrons can be clamped or increased and the plasma can be heated.

To investigate this concept, experiments using a series of toroidal devices called SPAC have been carried out. The present report concerns new experimental evidence of the formation of intense REB rings in SPAC-V, together with some characteristics of the REB ring and the confined plasma with and without compression. Throughout the experiment, a new injection method using a 'plasma-anode' was adopted which improved the efficiency of the injection.

2. EXPERIMENTAL APPARATUS AND INJECTION METHOD

The experimental apparatus consists mainly of a toroidal device, SPAC-V, a high-voltage pulse generator, Phoebus-II, for REB generation, and diagnostic instruments. Figure 1 shows the schematic structure of SPAC-V. The toroidal field is generated by the current in a single-centre conductor set along the major axis of the torus. Current up to 500 kA is fed through an impedance transformer from a capacitor bank. Time variation of the toroidal field is adjusted by changing the turns ratio of the transformer and/or the resistance of the clamping circuit. Vertical magnetic field coils are of the Bitter type and generate 10 kG maximum. Using the rising phase of the vertical field, we can compress the ring towards the major axis of the torus. Its risetime is 1.2 ms. The decay index of the vertical magnetic field is chosen so as to stabilize the positional instability of the beam ring. The vacuum chamber, made of thin stainless steel, is flat-cylinder shaped, has inner diameter 72 cm and inner height 18 cm. Other components of the device are made of non-metallic materials to minimize the field error due to Foucault currents.

Phoebus-II is equipped with an oil-immersed Marx generator (21 kJ, 2 MV) and a 6-Ω pulse-forming line with a gas switch. The duration of the output pulse is 80 ns. To inject a REB into the toroidal chamber, we used a conventional magnetically insulated transmission line (MITL) together with a new injection method which we call plasma-anode (Fig.1). The MITL is of coaxial type, with characteristic impedance 20 Ω. At the end of the MITL, which is inserted inside the vacuum chamber, a cathode of Cu-W or stainless steel is connected to the inner conductor of the MITL through a small aperture at the end of the outer conductor. The vacuum chamber is filled with a hydrogen plasma by a plasma gun before the REB injection so that the plasma contacts both the cathode and the chamber wall. When the outer conductor is electrically in contact with the chamber, the electrons are accelerated in a plasma sheath formed between the cathode and the plasma when the negative-pulsed voltage is applied on the cathode. This mechanism is very similar to beam generation in a plasma-filled diode [2]. The plasma-anode is superior to the conventional foil-anode in that there is no need to exchange foils and thus a repetitive operation becomes possible. Owing to the thin sheath, fairly high current density is obtainable for the REB without causing a pinch, and the beam electrons are ejected in the same direction.

While this plasma-anode is working, the cathode has a high negative potential to the plasma, so that the induced return current of the plasma cannot flow towards the cathode, and the current is forced to take its path towards the chamber wall along magnetic field lines. Masking of the poloidal field due to the return current is impeded effectively and the REB-current poloidal field quickly appears. Consequently, the fast rise of the magnetic force on the beam, which is caused by the image current on the wall, makes the beam orbit shrink inwards [3]; the decay of the momentum of the beam electrons due to the energy transfer from the beam kinetic energy to the energy of the self-magnetic field also gives rise to the drift of the beam towards the major axis of the torus. These motions, as well as the usual drift of the beam in the external magnetic field [4], settle the beam on the equilibrium position of a REB ring.

In this experiment, the cathode was 4 – 6 cm in diameter and the plasma density in front of the cathode surface was $3 - 8 \times 10^{13}$ cm^{-3}. Figure 2 shows observed waveforms of the cathode potential V_D, the emitted REB current I_D, and the diode impedance Z_D, for different plasma densities. At the beginning of pulse voltage application, the impedance was lower than in the subsequent phase because the plasma sheath grew with time, and the current rise was faster than the voltage rise. The difference in risetime is well suited to magnetic insulation in MITL.

3. LONG-LASTING RING

To have a long-lasting REB ring, the electron kinetic energy of the beam ring should remain high enough even after the ring has been formed. During

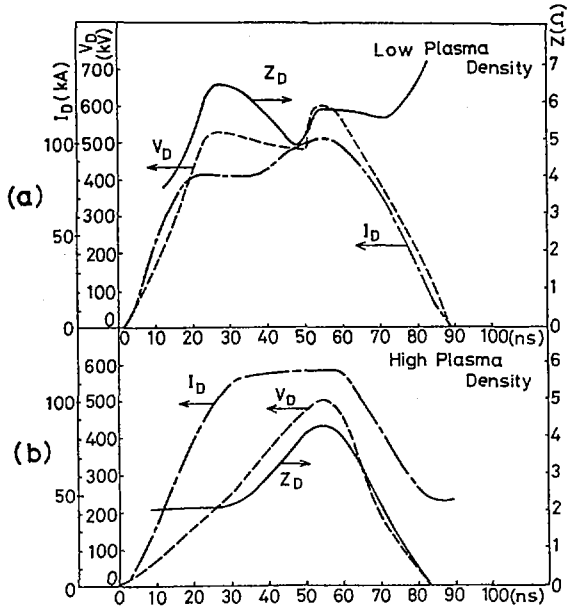


FIG.2. Characteristics of REB diode using plasma-anode:
(a) case of lower plasma density 3×10^{13} cm^{-3};
(b) case of higher plasma density $\sim 10^{14}$ cm^{-3}.

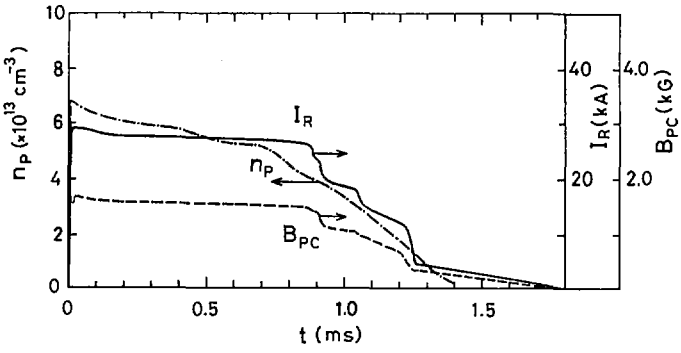


FIG. 3. Time variations of ring current I_R, *poloidal magnetic field at the centre conductor* B_{PC}, *and plasma density* n_p *in the case without adiabatic compression.*

formation of the ring, part of the initial kinetic energy of the injected beam is consumed by the creation of the poloidal magnetic field. Since the energy of the poloidal field is proportional to the square of the net current of the ring and the output energy of the REB source is limited, injection of energetic electrons at a relatively low current is essential for a long-lived ring. Alternatively, the diode should be operated at a fairly high impedance. The density of the pre-injected hydrogen plasma was chosen to be 3×10^{13} cm^{-3}, and Fig.2(a) shows characteristics of the diode in that case. The accelerating voltage V_D and the beam current I_D were nearly 500 kV and 80 kA, respectively, and the total injected energy $\int V_D \cdot I_D dt$ was 2.6 kJ. Experiments described in this section were made with the diode under these conditions.

The vertical magnetic field B_v reaches its peak 0.86 ms after the start and then decays with the time constant of 3.2 ms. The decay time constant of the toroidal magnetic field B_t was chosen to be 1.3 ms. When a REB ring continues for more than 1 ms, characteristics of the plasma and the REB ring itself are subject to the timing between B_v and B_t and to time variations of their field strengths. Two typical operating cases are presented as follows.

3.1. Case of constant major radius

A REB was injected 300 μs before the peak of the vertical field when the toroidal field became maximum, where $B_t = 3.7$ kG and $B_v = 560$ G at the major radius R = 15 cm. Figure 3 shows time dependences of the ring current I_R, the poloidal magnetic field on the centre conductor B_{PC}, and the mean plasma density n_p for the diameter of the plasma column $2a \cong 10$ cm. The ring current reached 28 kA 0.5 μs after the REB injection, from which the self-magnetic energy of the ring current was nearly 130 J, 5% of the total injected energy. Until a series of fast dampings appeared in the ring net current 0.9 ms after injection, I_R and B_{PC} decayed at the same rate, $\langle I_R/\dot{I}_R \rangle \cong \langle B_{PC}/\dot{B}_{PC} \rangle \approx 7.5$ ms, and n_p decreased as $\langle n_p/\dot{n}_p \rangle \approx 2.5$ ms. This decay rate cannot be explained by the classical Coulomb collision damping of the beam velocity; other damping mechanisms should be taken into account. Bursts of X-rays were emitted from the chamber wall at every fast damping, accompanied by line emissions of impurities. Plasma density decreased faster once the damping occurred.

The hydrogen plasma supplied by the gun was only partially ionized, but immediately after the REB injection the density increased to 7×10^{13} cm^{-3}. Spectral lines of neutral hydrogen atoms faded out 100 – 150 μs after injection, while impurity lines CI, ..., CIV, OI, ..., OV decreased considerably in intensity within 150 – 200 μs. The confined plasma was therefore in a highly ionized state. Figure 4 shows the time variation of the ion temperature of oxygen deduced from the Doppler broadening of an OVI line. Error of measurement was mainly due to shot-to-shot variation in the line emission. The ion temperature

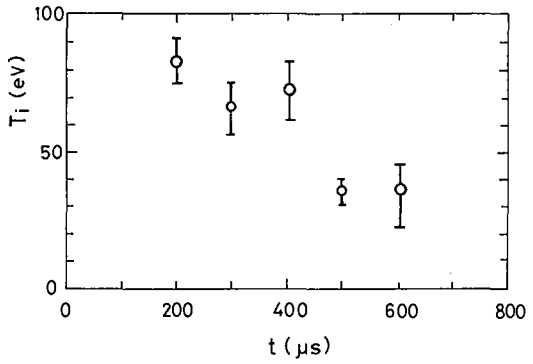


FIG. 4. Time variations of temperature of O^{+5} in the case of Fig. 3.

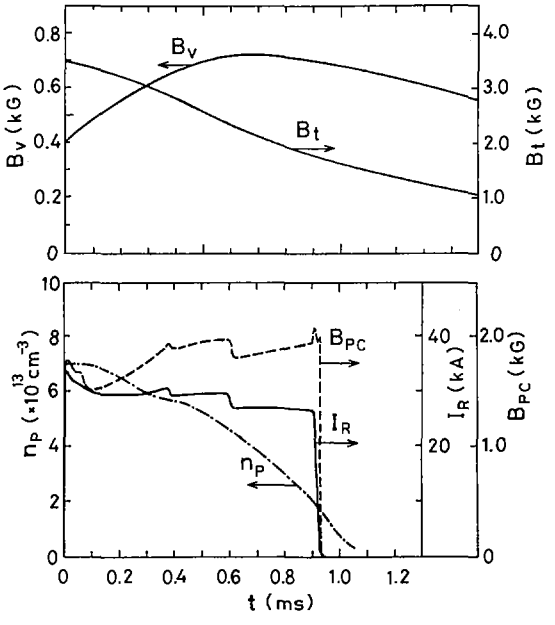


FIG. 5. Time variations of I_R, n_p, B_{PC}, toroidal magnetic field B_t and vertical magnetic field B_v during adiabatic compression.

gradually decreased from 80 eV to 40 eV for 600 μs. Since the proton temperature of the pre-injected plasma was lower than 10 eV, the ions must have been heated by the REB. The major radius of the REB ring was maintained nearly constant by matching the decay rate of B_v with I_R, while the toroidal magnetic field decayed from 3.7 kG to 2.5 kG for 600 μs. Temperature cooling due to decompression of the toroidal field pressure is estimated to be 26% in this case. The observed decrease of the ion temperature was nearly 50%. The heat loss rate towards the outside must therefore have been larger than the rate of heating by the electrons of the REB ring.

3.2. Case of weak compression

A REB was injected into the increasing vertical field to apply major radius compression to the REB ring, as shown in Fig. 5. The period available for compression was nearly 600 μs during which the vertical field changed from 400 G to 700 G. The toroidal field reached its peak at the injection and decayed exponentially.

During compression the major radius of the REB ring R decreased at the rate $dR/R(t = 0)dt \cong 6 - 7 \times 10^2\ s^{-1}$, while the REB ring current I_R increased a little until the first small damping appeared, and then decayed stepwise, followed by hard X-ray bursts and emission of impurity lines. At the times of these dampings, no noticeable oscillation with azimuthal mode about the magnetic axis was observed in the poloidal magnetic field. The decay rate of the plasma density became faster after the dampings occurred.

The major radius of the REB ring decreased by 30% during compression but the toroidal magnetic field decreased in the time. From the conservation of the toroidal magnetic flux inside the plasma column, the minor radius of the column can be said to have remained nearly constant during compression, and the increment of the plasma temperature by this compression is therefore estimated to be 16% for 300 μs. Figure 6 shows the time dependence of the ion temperature which was deduced from the Doppler broadening. The ion temperature was about 100 eV at the initial stage and rose to 300 eV 300 μs afterwards. Taking into account the temperature relaxation between the plasma ions and the oxygen ions, the temperature increment of plasma ions must be as large as 200 eV. The increase of temperature is larger than that expected from adiabatic compression. This suggests the presence of mechanisms for plasma ion heating.

The energy distribution of hard X-rays, produced by the bombardment of the energetic electrons on the limiter and the chamber wall, was measured for information on the energy increase of the beam electrons. Immediately after injection, the higher edge of the X-ray energy was at about 600 keV and it increased up to 1 – 1.2 MeV. From the conservation of canonical angular momenta of beam electrons, the increase of the electron energy is estimated to be about 400 keV, which agrees with the experimental result.

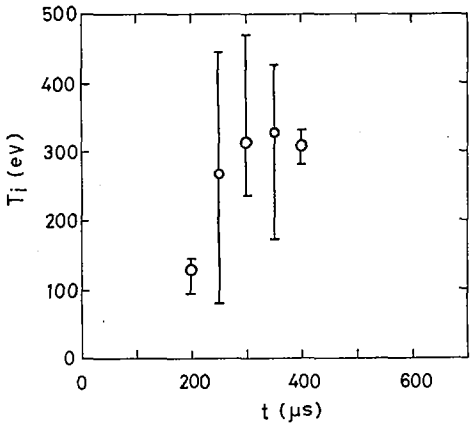


FIG. 6. Time variations of temperature of O^{+5} in the case of Fig. 5.

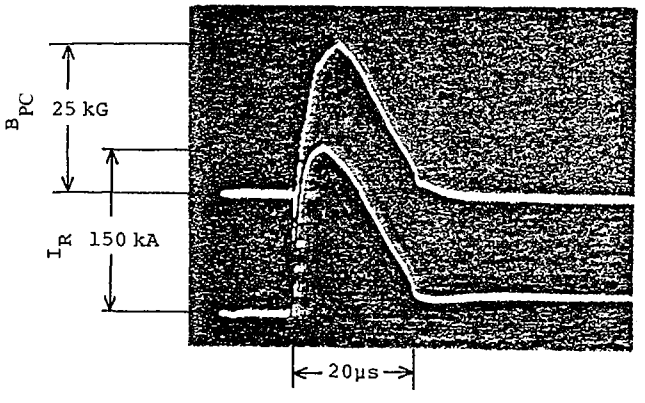


FIG. 7. Waveforms of B_{PC} and I_R in the case of high-current ring.

4. GENERATION OF HIGH-CURRENT RING

A REB of total energy 3.3 kJ was injected into a dense plasma with density nearly 10^{14} cm^{-3}. The area of the cathode was increased to 60 cm^2. In this case, the diode impedance decreased while the injection current increased to about 130 kA. Figure 7 shows a typical waveform of the REB ring current generated in this way. The total current reached 150 kA but the lifetime was as short as 20 μs. The toroidal field was 2 kG at R = 18 cm, so that the safety factor at the surface q_a was nearly 0.1. In this case the strength of the vertical magnetic field was too weak to hold the current ring in equilibrium, and the ring expanded fast.

For a longer ring lifetime it will be necessary to have a fast rise of the external vertical field or an effective conducting shell on the outer side. Hard X-rays were scarcely observed in this case, which means an efficient transfer of the kinetic energy of the injected electrons to the magnetic energy. The poloidal magnetic energy was estimated at about 2 kJ. More than 60% of the injected energy is thought to be spent on generation of the poloidal field.

5. CONCLUSION

It has been shown experimentally that toroidal magnetic configurations for plasma confinement are formed and maintained by REB currents higher than 30 kA with a lifetime of about 1 ms; i.e. the electrons travelled about 300 km through the plasma. A new diode consisting of a cathode and a plasma-anode was developed and found useful for pulse injection of the REB into toroidal plasma. By REB injection, a partially ionized plasma serving for the plasma-anode became a fully ionized hot plasma and was confined by the REB ring formed. Adiabatic compression raised the electron energy of the beam as well as the ion temperature of the confined plasma, though the compression ratio was small. The ion temperature attained was 300 eV. The maximum toroidal current was 150 kA but its lifetime was 20 μs. To increase the lifetime, faster rise of the external vertical field or an effective conducting shell would be needed.

ACKNOWLEDGEMENTS

The authors would like to thank Professors K. Takayama and A. Miyahara for their continuous encouragement. Thanks are also due to K. Ukegawa and S. Miyake for technical support.

REFERENCES

[1] MOHRI, A., MASUZAKI, M., NARIHARA, K., TSUZUKI, T., YAMANAKA, K., IKUTA, A., in Plasma Physics and Controlled Nuclear Fusion Research 1976 (Proc. 6th Int. Conf. Berchtesgaden, 1976) Vol.3, IAEA, Vienna (1977) 395.

[2] MILLER, P.A., POUKEY, J.W., WRIGHT, T.P., Phys. Rev. Lett. **35** (1975) 940.

[3] MOHRI, A., IKUTA, K., MASUZAKI, M.J., J. Phys. Soc. Jpn. **42** (1977) 1025.

[4] BENFORD, J., ECKER, B., BAILEY, V., Phys. Rev. Lett. **33** (1974) 1275.

DISCUSSION

J.U. GUILLORY: Could you say a bit more about the time history of the beam and plasma currents in your first experiment?

A. MOHRI: Our injection method has the advantage of impeding the plasma current – that is, the return current which is induced at injection. The net current is observable only from the magnetic probe measurement; its rise-time was 0.5 μs.

H.H. FLEISCHMANN: I have two questions which are somewhat related. In contrast to our experiments, you have a situation in which the maximum Larmor radius of your fast electrons in the toroidal or vertical field is small compared with the ring radius. Can you get from your data (magnetic fields, radius, etc.) an indication of what percentage of your ring current is carried by fast electrons?

A. MOHRI: The major radius of the ring is determined from the force balance between the expanding force (hoop force) and the force due to the vertical field. The beam electrons flow nearly along the field lines.

H.H. FLEISCHMANN: Assuming your T_e to be comparable to the measured $T_i > 100$ eV, the resistive decay time of your ring currents could be comparable to your measured decay times. Do you have any conclusion concerning T_e?

A. MOHRI: We have not succeeded in measuring the electron temperature, so I cannot quote an exact value. It could be more than 100 eV. If we assume such a value, the toroidal β might be more than 4% and the poloidal β 25%.

Session I

TECHNOLOGY AND REACTOR CONCEPTS I

Chairman

P.E. REBUT
CEC

A REVERSED-FIELD-PINCH REACTOR WITH SUPERCONDUCTING WINDINGS

R. HANCOX, C.R. WALTERS*
United Kingdom Atomic Energy Authority,
Culham Laboratory,
(Euratom/UKAEA Fusion Association),
Culham, Oxon.,
United Kingdom

Abstract

A REVERSED-FIELD-PINCH REACTOR WITH SUPERCONDUCTING WINDINGS.

The use of superconducting windings in a pulsed reversed-field-pinch fusion reactor is considered. A conductor consisting of many insulated and transposed niobium-titanium composite strands contained in a steel conduit, force-flow cooled with liquid helium, allows low-pulsed field losses to be achieved together with continuous electrical insulation. The power losses at cryogenic temperature are evaluated and the resultant refrigeration power is shown to be a factor 6 less than the Ohmic dissipation in the equivalent normal windings. The reactor parameters are optimized for minimum station capital cost, and the recirculating power fraction is estimated to be 21% ($Q \sim 12$). Some of the outstanding engineering problems in such a reactor are highlighted.

1. INTRODUCTION

The Reversed-Field Pinch is an axisymmetric toroidal confinement system which has the advantage, compared with the tokamak, of a high value of the ratio β of plasma pressure to magnetic pressure. To see whether this advantage would lead to significant benefits in a reactor, a conceptual design study of a 600-MW(e) Reversed-Field-Pinch reactor [1-5] was undertaken in 1976/77. Pulsed operation was assumed without refuelling during the burn, and copper magnetic field windings were used. The parameters of the resulting design, which was optimised for minimum station capital cost, are shown in the first column of Table I. A conclusion of the study was that the energy multiplication factor of the whole system, defined as the ratio of the useful thermal power generated to the net electrical power recirculated was low ($Q \sim 6$), corresponding to a high recirculating power fraction ($\varepsilon \sim 42\%$). This level of recirculating power, which is higher at less than full power operation, is unacceptable and significantly increases the station capital cost. Since more than half the recirculating power was due to ohmic dissipation in the magnetic field windings, it is of interest to consider whether the use of superconducting windings might be a feasible alternative and, if so, what improvement would be obtained by their use.

---

* SRC, Rutherford Laboratory, Chilton, Oxon.

TABLE I. PARAMETERS FOR REVERSED FIELD PINCH REACTORS WITH NORMAL AND SUPERCONDUCTING MAGNETIC FIELD WINDINGS

	Normal	Superconducting
Net output power (MW(e))	600	600
Gross thermal power (MW(th))	2500	1900
First wall radius (m)	1.75	1.5
Major radius (m)	16	14.5
Toroidal plasma current (MA)	19	17
Duration of burn (s)	27	25
Duration of full cycle (s)	40	37
Energy multiplication factor, Q	5.9	11.8
Recirculating power fraction, ε (%)	42	21

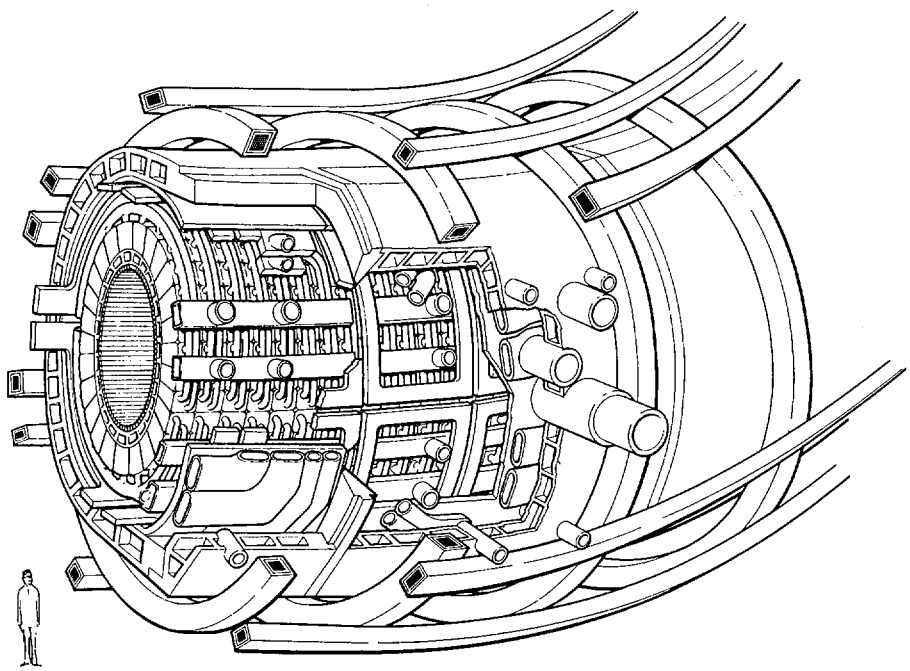


FIG. 1. Artist's impression of a 600-MW(e) reversed-field-pinch reactor with superconducting windings. The structure supporting the windings is not included.

The revised reactor design has the parameters shown in the second column of Table I. The first-wall radius and major radius are slightly reduced compared with the original design, but the thickness of shielding between the breeding blanket and windings is greater. The reactor structure is illustrated in Figure 1.

2. SUPERCONDUCTING WINDINGS

The use of large ($\sim$ 8 GJ) pulsed ($\tau_{rise} \sim 0.5$ s) superconducting magnets, as envisaged in this reactor, is beyond the present state of the art in superconducting magnet design. However, several large steady-state ($\sim$ 100 MJ) bubble-chamber magnets are in operation and small prototype pulsed magnets ($\sim$ 0.1 MJ, $\tau_{rise} \sim 0.25$ s) for use in accelerators have been built and tested, and there does not appear to be any reason why suitable windings could not be developed. The major areas of concern are the pulsed field losses and thermal stability of the superconductor, together with adequate electrical insulation in a highly stressed and pulsed structure in which fatigue may occur. A significant advantage in this application is that protection of the winding in the event of a transition from the superconducting to the normal state is provided by the already existing energy transfer system which is capable of discharging the magnetic energy in less than one second.

To reduce the pulsed field losses in the superconductor and its associated stabilizing material, the winding is constructed from a transposed cable, each strand of which is an insulated multi-filamentary composite of superconducting filaments in a copper matrix. To facilitate production, the strands may alternatively be sub-cables consisting of copper wires soldered around a central multi-filamentary composite. At the relatively low fields required in the Reversed-Field-Pinch reactor the superconductor is assumed to be niobium-titanium, although the use of A15 compounds such as niobium-tin in filamentary form is not excluded. The components of the pulsed field losses are the hysteresis loss in the superconducting filaments, losses due to coupling between filaments in both the transverse and longitudinal components of the magnetic field and eddy current losses in the normal matrix and conductor structure. These may be evaluated on the basis of previously derived equations [6,7], and acceptable losses obtained by a suitable choice of the filament and strand diameters and optimisation of the twist pitch of the filaments to minimise the sum of the coupling losses. A significant reduction in these losses is obtained by bunching the filaments close to the strand axis. Table II shows calculated losses in a suitable conductor, which consists of strands of 1.2 mm diameter containing 1600 superconducting filaments of 10 μm diameter twisted with a pitch of about 5 mm, and capable of carrying a current of 125 A in a magnetic field of 4 T.

Practical experience of magnet performance suggests that the complete conductor should be cryostatically stabilised, and therefore it must be designed to allow intimate contact between the liquid helium coolant and the copper matrix. Since a high-current conductor will contain many strands in a transposed cable, this is most conveniently achieved by means of a conduit which encloses the strands and through which supercritical helium is pumped[8]. Continuous unperforated insulation is then possible, which is essential in a pulsed magnet. This arrangement also simplifies epoxy resin impregnation of the winding which is required for mechanical rigidity. Optimisation of the conductor design [9] involves adjusting all the parameters so that the maximum possible thermal disturbance can be absorbed. In the present design this results in ratios of the cross-sectional areas of superconductor to copper of 0.13 and of helium coolant to total conductor of 0.60, and a helium velocity of 0.5 m/s. A helium temperature rise of 3.6 K/km, due to pulsed

TABLE II. PULSED FIELD LOSSES IN THE SUPERCONDUCTING WINDINGS

		Toroidal field coils (J/MA·m)		Poloidal field coils (J/MA·m)	
Hysteresis in superconductor	T	84		66	
	L	36		30	
			120		96
Coupling losses	T	51		32	
	L	51		32	
			102		64
Eddy current losses:					
in the copper matrix	T	212		102	
	L	9		11	
			221		113
in the conduit	T	36		17	
	L	1		2	
			37		19
in the reinforcing strip	T	32		17	
	L	0		0	
			32		17
	TOTAL		512		309

The losses, averaged over the volume of the windings and for one full cycle, are shown for the transverse (T) and longitudinal (L) components of the magnetic field.

field and pumping losses, imposes a limit of 500 m on the length of conduit between the helium inlet and outlet manifolds. The complete conductor, capable of carrying 30 kA in a magnetic field of 4 T, contains 243 strands in a 1-mm thick stainless steel conduit which compacts the cabled strands by 15% as it is drawn over them to an overall size 31 x 31 mm. The current density within the conduit is then 44 A/mm^2.

The general arrangement of the windings is similar to that adopted in the previous Reversed-Field-Pinch reactor study. The reactor is divided into segments, whose length is determined by the requirement that the conducting shell behind the first wall should have a minimum length equal to four times the plasma radius. To reduce the toroidal field ripple at the plasma surface, two toroidal field coils are required for each segment. Each toroidal field coil provides a maximum of 2.8 MA·turns with an inductive voltage of 0.2 kV/turn. Use of a single 30-kA conductor in 6 double pancakes of 16 turns allows the helium inlet and outlet manifolds to be sited on the outside of the windings. The total inductive voltage is 20 kV/coil, with a maximum turn-to-turn voltage of 3.2 kV. The innermost poloidal field coil carries the highest current, providing 4.6 MA·turns with an inductive voltage of 2.5 kV/turn, and by using four 30-kA conductors in parallel the maximum inductive voltage is limited

TABLE III. CONTRIBUTIONS TO THE RECIRCULATING POWER IN THE REACTOR

	Toroidal field coils	Poloidal field coils
Losses at 4 K (kW)		
Conductor pulsed field losses	26	21
Conduit pulsed field losses	2	1
Reinforcing strip pulsed field losses	2	1
Helium pumping losses	5	6
Current leads	9	12
Mechanical supports	9	3
Nuclear heating	8	2
Thermal radiation	1	2
TOTALS	62	48
	110	
Losses at room temperature (MW)		
Refrigerator power	32	
Energy to establish RFP configuration	32	
Unrecovered thermal and magnetic energy	47	
Switching losses	17	
Auxiliary supplies	38	
TOTAL	166	

The losses are integrated over one whole cycle and expressed as an average power.

to 60 kV during normal operation or 85 kV if the circuit is energised in the absence of a plasma. The heat leak to the toroidal and poloidal windings through all the current leads is 21 kW.

The magnet windings are made strong enough to support hoop stresses by the use of the steel conduit and by adding additional steel within the winding. The toroidal field coils are shaped and prestressed to produce uniform tensile stress throughout the winding at the maximum operating magnetic field, thus minimising the additional steel required in the winding and the local stresses transferred to the central support column. Shear stresses still remain in the plane of each toroidal field winding due to the reaction between it and the poloidal field. The forces on the windings are transmitted to a room-temperature structure by 50-mm-long fibreglass supports in compression, giving a heat leak of 5 W/MN. The radial force on each toroidal field coil is 10 MN and the sum of the twisting forces to be withstood is 54 MN, the sum of the vertical forces on the poloidal field windings is 800 MN, and all these result in a total heat leak of 12 kW. The rigidity of the resin-bonded windings is such that the supports may be spaced up to 3 m apart.

The various thermal losses which must be removed from the cryogenic environment are shown in Table III, based on the final reactor parameters derived in the next section, and amount to a total of 110 kW for the whole reactor. The total refrigeration power required at ambient temperature, assuming 25% of Carnot efficiency, is 32 MW, which is a factor of 6 less than

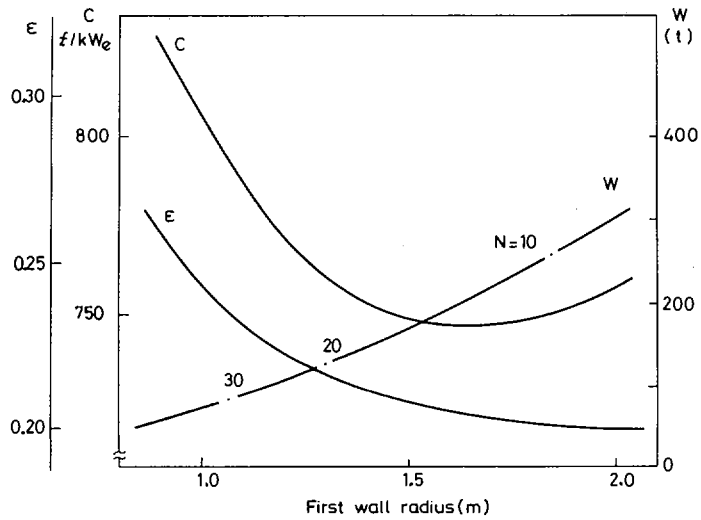


FIG.2. Variation of station capital cost C and recirculating power fraction ε with first-wall radius for a fixed net output power of 600 MW(e), together with the estimated weight W of the removable part of each of the N segments from which the reactor is constructed.

the ohmic dissipation in the reactor with normal windings. The additional costs of the superconductor, refrigerators, cryostats and the more complex conductor are estimated to be less than the cost of copper saved, which is greater than £100/kW(e), due to the higher current density in the superconducting windings.

3. REACTOR PARAMETERS

The introduction of superconducting magnetic field windings requires further changes in the reactor design, of which the most important are the requirement for additional shielding between the reacting plasma and the windings and the need for additional energy storage to allow removal of the magnetic energy in case of a magnet quench. The opportunity has also been taken of adding detail in some points of the design, resulting in further minor changes. These changes then require a re-optimisation of the reactor parameters, leading to a revised estimate of the capital cost and recirculating power fraction.

The shielding thickness specified in the original Reversed Field Pinch conceptual reactor design with copper windings operating at a temperature of 100°C was fixed on the basis of resistivity changes in the copper due to nuclear transmutations and of radiation damage in the inorganic insulation. With superconducting windings operating at a temperature of 4 K the resistivity changes in the copper stabilising material will be more pronounced, organic insulation is used, and the nuclear heat deposited in the windings must be reduced, so that more shielding is required. Preliminary studies suggest that a total of 1.0 m of shield will be required; of which the first section is incorporated within the breeding blanket cells at high temperature, the

cooled intermediate section is replaceable and the outer section forms the permanent structure and vacuum vessel of the reactor. The plasma-stabilising coils are situated in the intermediate shield region. The total thickness of the first wall, conducting shell, breeding blanket, stabilising coils, coolant ducts, and shielding is now estimated to be 2.10 m on the inner side of torus and 2.60 m on the outer side.

The variation of station capital cost for a fixed net output power of 600 MW(e) is shown in Figure 2 as a function of the first-wall radius, and it is seen to have a very broad minimum. As in the original study, the final choice of parameters is affected by the constraint that the weight of the removable part of each reactor segment should be kept within reasonable limits to ease remote-handling requirements, but since the thickness of the removable part of the shield has been increased this requirement is now more severe. Whilst a range of possible solutions exists, a first-wall radius of 1.5 m has been chosen as the basis of the revised parameters. This reduction in first-wall radius is consistent with additional calculations of the time required to reach ignition by ohmic heating alone in which thermal conduction losses from the plasma are included in a simple form and which show the necessity of an increased current density in the plasma.

The most significant improvement in the reactor parameters is the increase in the energy multiplication factor Q from 5.9 to 11.8, corresponding to a reduction in the recirculating power fraction to 21%. There is a corresponding reduction in station capital cost of around £200/kW(e), mainly due to the reduced gross output power and the reduced mass of the magnetic field windings. The largest remaining contributions to the recirculating power, as seen in Table III, are the energy lost when the Reversed-Field-Pinch configuration is established by self-reversal at the beginning of each cycle and the thermal and magnetic energy associated with the plasma which cannot be recovered at the end of each burn. The effects of these losses could only be significantly reduced by the introduction of plasma refuelling during the burn and quasi-steady-state operation. The possibility of achieving this in a Reversed-Field-Pinch reactor will depend on whether solutions can be found to the problems of refuelling without disturbing the magnetic field configuration, exhausting unburnt fuel and reaction products from the plasma and limiting the influx of impurities from the walls. These physics questions have not yet been considered in sufficient detail to provide conceptual solutions which could form the basis of a further reactor study.

4. OUTSTANDING PROBLEMS

Taken together this and the previous study indicate the possible form and parameters of a Reversed-Field-Pinch reactor. They also highlight many of the uncertainties and problems which must be resolved before substantial progress can be made towards a more realistic reactor design. With the physics model adopted in these studies, which requires the establishment of the Reversed-Field-Pinch configuration by self-reversal and control of the plasma temperature at a low level without plasma expansion during the burn, the main physics uncertainties are the possibilities of operating at sufficiently high plasma current densities to obtain ignition by ohmic heating without adversely affecting the particle confinement, of controlling the plasma temperature, and of stabilising the plasma with only a thin conducting shell and external stabilising coils. These questions were considered previously [2,3] and have not changed in the present study. There are equally severe engineering problems three of which are outlined below.

The requirement for constant plasma temperature during the burn results in 20% of the energy released in the reactor being deposited directly upon the first wall. The integrity of this wall under cyclic thermal stresses sets a limit on the mean wall loading at which the reactor can operate and hence on the overall power density and capital cost. The use of a membrane wall constructed from a niobium-zirconium alloy tubing is believed to allow the highest power loading, and a mean neutron wall loading of 1.5 MW/m^2 was chosen for the present design to give sufficient margin between the induced thermal stresses and the yield stress of un-irradiated material and allow for the effects of non-uniformity, welding and radiation damage. The use of stainless steels or titanium alloys under these conditions appears to be out of the question. In the present concept it is also necessary to re-weld each section of the first wall in situ after a maintenance operation, and, whilst a means of achieving this without affecting the heat removal capability of the wall at the location of the weld has been devised, it is a complex operation which is made more difficult by the limited access through the vacuum ports.

Behind the first wall, the copper or aluminium stabilising shell must be as close to the plasma as possible and is therefore in front of the breeding blanket. Up to 25% of the power released in the reactor is deposited in this shell which must be maintained at a temperature below 200 to 300°C. Since the breeding blanket operates at temperature of 550°C for high thermal efficiency, there are four concentric regions of very different temperature - the first wall, shell, blanket and shield - requiring thermal insulation between each. Coolant pipes must also pass from each of the inner three regions through those behind, and be thermally insulated from them. Finally, the whole structure must be sub-divided electrically into regions, with dimensions typically 0.5 m, to reduce eddy current losses due to the pulsed magnetic fields. The engineering development of such a structure capable of reliably withstanding pulsed thermal and magnetic loads in a radiation enivironment will require considerable ingenuity.

Finally, the design of the magnet support structure has not yet been considered. This structure, which must withstand the centering and twisting forces on the toroidal field magnets and the vertical forces on the poloidal field windings, will be at ambient temperature and must support the windings through distributed cryogenic supports. The structure must also be strong enough to withstand the forces which will be generated by any fault condition. On the other hand, the structure must allow reasonable access to all parts of the reactor for coolant pipes and diagnostics and must be removable between the toroidal field windings which will be moved for reactor maintenance. Compared with the reactor with normal windings, this structure is more complex because of the need to transmit forces from 4 K to ambient temperature through supports which allow for significant differential contraction when the winding is cooled to its operating temperature.

5. CONCLUSIONS

The use of superconducting windings for a Reversed-Field-Pinch reactor appears feasible, and a specific conductor design has been proposed. The pulsed field loss in the conductor can be reduced to a level where it is comparable to the sum of the other heat leaks into the cryogenic environment of the windings. The thermal leak into the windings through mechanical supports appears acceptable, although no detailed design of the support structure has been undertaken. The total refrigeration power required is estimated to be 32 MW, which is a factor 6 less than the joule losses in the equivalent normal coils used in the previous Reversed-Field-Pinch reactor

study. As a result the recirculating power fraction is reduced to 21%, corresponding to an energy multiplication factor Q ∿ 12. A more accurate evaluation of these numbers requires better physics information from future experiments. Several severe engineering problems remain, including thermal fatigue in the first wall, the complex shell and blanket structure and the need for a demountable magnet support structure.

ACKNOWLEDGEMENTS

The authors gratefully acknowledge major contributions to this Reversed-Field-Pinch reactor study by colleagues from Culham Laboratory and AERE, Harwell. The suggestion that superconducting windings should be considered was made by A.A. Newton and G. Rostagni during discussions at the IAEA Workshop on Fusion Reactor Design, Madison, 1977.

REFERENCES

[1] HANCOX, R., et al., UKAEA Preprint CLM-P501 (1977).
[2] LAWSON, J.D., UKAEA Report CLM-R171 (1977).
[3] HANCOX, R., and SPEARS, W.R., UKAEA Report CLM-R172 (1977).
[4] HOLLIS, A.A., and MITCHELL, J.T.D., UKAEA Report CLM-R173 (1977).
[5] BOBBIO, S., et al., Padua University Report Upee 77/05 (1977).
[6] WILSON, M.N., and WALTERS, C.R., Rutherford Laboratory Report RL-76-038 (1976).
[7] WALTERS, C.R., Rutherford Laboratory Report RL-77-131/A (1977).
[8] HOENIG, M.O., et al., Proceedings of the 6th International Cryogenic Engineering Conference, Grenoble (1976) 310.
[9] DRESNER, L., I.E.E.E. Transactions MAG-13 (1977) 670.

DISCUSSION

K.H. SCHMITTER: What would be the critical energy multiplication factor required to obtain zero net output?

R. HANCOX: As we have indicated in the introduction to our paper, the energy multiplication factor Q falls as the net output power is reduced. With the assumptions used in this study, Q = 2.5 gives zero net power with 100 MW(e) gross output from the generators.

K.H. SCHMITTER: Do the losses quoted for the pulsed superconducting coil system include transfer and storage losses (transfer into and storage in the energy storage device)?

R. HANCOX: During the off-period between burns the energy is stored in the superconducting windings of the reactor. The storage losses are therefore small, but are included in the evaluation. The losses during energy transfer are included in the switching loss.

A. PANT: What kind of storage/transfer system do you envisage, and what instantaneous power levels do you anticipate?

R. HANCOX: The energy transfer system, using a homopolar generator, is similar to that used in the original design and described by S. Bobbio and

co-workers – see our Ref.[5]. The energy in the poloidal field windings is 8 MJ, and is transferred in 0.5 s.

A. PANT: An energy transfer of 8 MJ of magnetic energy in 0.5 s would imply an instantaneous power level of 16 GW which has to be handled by the transfer/commutator system. This value is considerably larger than the reactor output of 600 MW(e), so that a *transfer* system more complicated than the *output* system would be required – a common feature of pulsed reactors.

R. HANCOX: The energy transfer problem in such systems is well recognized. It is greater in the superconducting reversed-field pinch reactor because of the increased thickness of shielding and because provision must be made for removing all the energy in the windings in the event of a magnet quench.

R.P. ROSE: What helium refrigerant conditions did you assume for the superconductors – supercritical He or two-phase flow?

R. HANCOX: Supercritical helium cooling of the superconducting magnets was assumed.

A. GIBSON: What are the requirements imposed on the conducting shell in this type of reactor; for instance what size of penetration is possible? What is the design solution adopted for the shell in your concept?

R. HANCOX: The requirements imposed on the shell have been discussed in detail by J.D. Lawson (see our Ref.[2]). In the present reactor design it is only possible to include 25 mm of copper or 50 mm of aluminium, giving a time constant of 0.9 s which is equal to the current rise-time, and even so tritium breeding and useful heat recovery in the blanket are affected. The effectiveness of such a shell, its minimum length, and the acceptability of penetrations are all questions which must be resolved in future experiments.

SYSTEMS STUDIES AND CONCEPTUAL REACTOR DESIGNS OF ALTERNATIVE FUSION CONCEPTS AT LASL*

R.A. KRAKOWSKI, R.L. HAGENSON, R.L. MILLER, R.W. MOSES
University of California,
Los Alamos Scientific Laboratory,
Los Alamos, New Mexico,
United States of America

Abstract

SYSTEMS STUDIES AND CONCEPTUAL REACTOR DESIGNS OF ALTERNATIVE FUSION CONCEPTS AT LASL.

Results are presented from systems studies of four promising alternative (non-tokamak) fusion reactor concepts: the reversed-field pinch, the linear theta pinch, the fast-liner reactor, and the toroidal bi-cusp (Tormac). An emphasis is placed on physics and energy-balance constraints, and crucial technologies and economic implications are quantitatively addressed.

1. Introduction

Although the strength of the world-wide fusion effort rests with the rapid and successful advances in Tokamak physics, reactor studies have illuminated crucial problems associated with large size, low power density, magnetics and beam technologies, materials limitations and remote maintenance, and the attendant uncertainties of economics and reliability. These results, therefore, have prompted a careful re-examination of the physics requirements and general approach taken by Tokamak reactor designers [1], as well as prudently generating an examination of less understood, alternative confinement approaches [2-4].

Depending upon the confinement scheme considered, systems studies of alternative concepts range from simple physics analyses, based on Lawson-like criteria, to detailed multi-man-year conceptual designs. With few exceptions most reactor studies of alternative concepts fall into the less formalized part of this spectrum. As part of an effort to place certain alternative concepts onto a common physics, technology and costing basis, the Los Alamos Scientific Laboratory (LASL) has been designated as a center for alternative concepts systems studies. Reactor concepts that have been recently examined at LASL are: the Reversed-Field Pinch Reactor (RFPR), the Linear Theta-Pinch Reactor (LTPR), the Fast-Liner Reactor (FLR), and the toroidal bicusp (Tormac). Interim but self-consistent

* Work performed under the auspices of the US Department of Energy.

TABLE I. RFPR-II INTERIM DESIGN SUMMARY: AIR-CORE POLOIDAL TRANSFORMER, SUPERCONDUCTING COILS

Definition	Value
First-wall radius (m)	1.5
Major radius (m)	12.8
Plasma current (MA)	20.0
Current density (MA/m^2)	5.4
Fuel burnup fraction	0.48
Lawson parameter (10^{20} s/m^3)	40.6
Toroidal coil energy (GJ)	2.33
Poloidal coil energy (GJ)	3.15
Burn time (s)	21.3
Cycle time (s)	26.3
14.1-MeV neutron current (MW/m^2)	2.46
Engineering Q-value	6.5
Net efficiency	0.34
Thermal power (MWt)	2950
Power density[a] (MWt/m^3)	0.90
Gross electric power (MWe)	1180
Net electric power (MWe)	1000

(a) Based on volume enclosed by and including superconducting coils.

TABLE II. LTPR INTERIM DESIGN SUMMARY: REENTRANT ENDPLUG[a]

Definition	Value
First-wall radius (m)	0.5
Length (m)	150.
REP radius (m)	5.0
Implosion field (kV/mm)	0.1
Compression field (T)	8.0
Fuel burnup fraction	0.06
Lawson parameter ($10^{20}s/m^3$)	27.0
Compression time (ms)	30.
Burn time (ms)	300.
Cycle time (s)	12.5
14.1-MeV neutron current (MW/m^2)	2.0
Engineering Q-value	4.7
Net efficiency	0.32
Thermal power (MWt)	2652.
Power density[b] (MW/m^3)	0.8
Gross electric power (MWe)	1060.
Net electric power (MWe)	835.

(a) Based on 10 times cross field thermal conduction in REP regions.
(b) Based on volume enclosed by and including compression coils.

TABLE III. INTERIM FLR OPERATING POINT: LOW YIELD CASE

Definition	Value
Initial liner radius (m)	0.2
Initial liner thickness (mm)	3.0
Liner length (m)	0.2
Initial azimuthal field (T)	13.0
Initial liner energy (GJ)	0.34
Liner Q-value	10.7
Pure fusion yield (GJ)	3.56
Enhanced fusion yield (GJ)	3.92
Engineering Q-value	3.94
Cycle time (s)	10.0
Net efficiency	0.30
Total thermal power (MWt)	430.
Power density[a] (MWt/m^3)	5.8
Gross electric power (MWe)	172.
Net electric power (MWe)	129.

(a) The system power density is based on the total volume enclosed by a 2.6-m radius containment vessel of 0.3-m wall thickness.

reactor designs for each of these alternative concepts are presented, and the assumptions and weaknesses associated with the physics basis for each are quantified.

The assessment of alternative fusion concepts is a continuing process; although the four concepts summarized herein offer certain advantages, it should not be inferred that these concepts are necessarily more desirable than the (evolving) Tokamak or the other ~ 20 alternative approaches that have been proposed. Clearly, many of the alternative approaches to magnetic fusion are related. Thirteen of these concepts have been evaluated under the uniform procedures described in Ref. [3], and the depth to which each has been examined theoretically, experimentally, and in a systems study context varies widely. The four concepts reported herein, therefore, represent only a beginning of a uniform and comprehensive sorting process, which ultimately must be reinforced by a more supportive but selective experimental program.

2. The Reversed-Field Pinch Reactor (RFPR)

A series of iterative, comprehensive reactor embodiments for the RFP have recently been generated [5-8]. The RFP is a high-beta ($\beta_\Theta \simeq 0.4$-0.5) toroidal device of arbitrary aspect ratio with a plasma current density j_z that is sufficient to achieve ignition by ohmic heating alone; confinement is provided primarily by the poloidal field B_Θ with the concomitant economy of magnetic field and ease of magnet design. A conducting shell or external conductors would eliminate MHD modes with wavelengths in excess of the minor radius r_w. Unlike q-stabilized systems ($q = 2B_z/\mu_0 j_z R > 1$), in which unstable MHD modes require wavelengths in excess of the major circumference, considerably higher current densities are possible with the shear-stabilized (for local modes), $q<1$ RFPR. A 1-2 T toroidal bias field B_z is trapped in the plasma, which during the toroidal current rise is reversed outside the plasma to give the high shear needed to satisfy the Mercier criterion [9].

Potential problems include startup, which may necessitate the plasma passing through unstable MHD states (like Tokamaks). A conducting shell adjacent to the first wall must have an electrical skin depth equivalent to the ~ 0.1-s startup time. The startup time is taken as $\sim 10\%$ of the energy containment time (~ 1 s for a reactor), which is consistent with diffusion scaling [10]. External conductors subsequently maintain stability during the burn phase; for long feedback times (0.1 s) and a tractable number of modes to be stabilized, this approach appears technically feasible [11].

The dynamic burn model, plasma and engineering energy balances, and stability/equilibrium criteria upon which the RFPR design is based have been described [5-7]. Both technological and economic considerations [6] point to a long-pulsed (0.1-s rise-time, 20-30 s burn period) batch-burn operation using an air-core, superconducting system. Earlier RFPR designs were based upon programmed quench or fuel burn-out as a means of beta control. The long-pulse operation more recently adopted [6,7] invokes an anomalous radial energy loss equivalent to ~ 200 Bohm diffusion times, and burnups of $\sim 50\%$ are achieved in ~ 20 s. A typical burn trajectory (time dependence of $F = B_z(r_w)/\langle B_z \rangle$ and $\Theta = B_\Theta(r_w)/\langle B_z \rangle$) is in accordance with predictions for a high-beta, minimum-energy configuration [12]. Table I summarizes key design parameters [6].

The MHD stability during the extended burn times required for a significant energy gain presents a major uncertainty for the projection of any magnetic confinement scheme into the reactor regime. Alfvén propagation speeds of $\sim 10^7$ m/s for reactor parameters imply that the plasma will rapidly seek out a minimum energy state. As for the Tokamak, the existence of minimum energy states lends considerable credibility to the RFP approach. The degree to which the burn trajectory must follow the predictions of minimum-energy calculations is presently unknown. Until experiments prove otherwise, reactor-scale times which encompass 10^8 - 10^9 MHD growth times probably will require operation close to a minimum energy state, despite the fact that detailed stability computations show stability exists far from a minimum-energy state [10].

3. Linear Theta-Pinch Reactor (LTPR)

The problems and promise of Linear Magnetic Fusion (LMF) have recently been reviewed [13]. Although excessive plasma lengths are required to sustain the plasma against free-streaming endloss, the attractions of LMF remain: proven heating methods, neutrally stable plasma equilibrium, high plasma density, accessible and convenient geometry, high engineering power density. Conceptual LMF reactor designs reflect a rich array of potential heating and axial confinement options [13], and the results of the LTPR studies summarized herein represent only one example of LMF possibilities.

Were it not for the plasma endloss, the heating and (radial) confinement principles for the LTPR would be identical to those envisaged for the toroidal Reference Theta Pinch Reactor [14]. A pre-ionized D-T gas is heated by a fast ($\sim$ 1-μs) implosion to $\sim$ 1 keV; the preheated plasma is subsequently compressed adiabatically to ignition, and a burn cycle occurs along a plasma-radius/temperature trajectory determined by the dynamics of an energetic, high-beta plasma. The LTPR study invokes the re-entrant endplug (REP), wherein the endloss particles and energy are directed by a small radius-of-curvature conduit to a second, parallel plasma column. The plasma within the REP region may not necessarily be in "toroidal" equilibrium and will be subject to anomalous cross-field transport losses (assumed here to be ten times classical values).

Typical LTPR reactor parameters, determined by the time-dependent axial burn code 1DRBURN, are depicted in Table II. Both the implosion and adiabatic compression coils are located outside the 0.5-m radius first wall and 0.4-m thick blanket, operate near 300 K, and require 0.9 GJ and 44 GJ of pulsed energy, respectively; reversible recovery of the adiabatic compression energy at 95% efficiency is specified. The 300-ms burn relieves considerably the problems associated with pulsed thermal loading of the first wall, energy-transfer/storage and magnet stress [14]. The present uncertainties of the REP approach, the close coupling of the implosion preheating to the reactor core (high-voltage insulated blanket) and the need for an efficient energy-transfer/storage system present crucial issues for the LTPR.

4. Fast-Liner Reactor (FLR)

The use of magnetically-driven metallic liners for the adiabatic compression of D-T plasmas to thermonuclear conditions has been studied by a number of investigators [15-19]. The LASL approach follows that of the Kurchatov group [16] and emphasizes fast (10^3 -10^4 m/s) destructive implosions of thin metallic shells.

The FLR concept [19] combines the favorable characteristics of inertial confinement and heating with the more efficient energy transfer associated with magnetic approaches. A small cylindrical liner is imploded radially to $\sim 10^4$ m/s by self-magnetic fields resulting from large axial currents driven through the liner. The liner implodes onto a $\sim$ 0.5 keV, $\sim 10^{24}$ m^{-3} D-T plasma that is initially formed in or injected into the liner. As the liner implodes in 20-40 μs, adiabatic compression raises the plasma to thermonuclear temperatures, and a vigorous burn ensues for 2-3 μs. During the implosion the plasma pressure is confined inertially by the metal liner and endplug walls. An imbedded azimuthal magnetic field provides magnetic insulation against radial and axial thermal conduction. FLR studies have focused primarily on the development of realistic plasma/liner models and the burn optimization based thereon [19]. On the basis of physics design curves derived from these optimizations, the interim FLR operating point summarized on Table III has evolved.

The major engineering and technology problems in order of perceived importance are: a) plasma preparation, b) the economics of destroyed leads and liner, c) containment, d) the switching and transfer of energy (0.5 GJ, 20-30 μs), and e) frequent (10-20 s) liner and leads replacement. Each of these issues is briefly addressed. Four possible plasma preparation schemes are considered: co-axial (Marshall) gun injection, shock-tube injection, exploding D-T threads, and in-situ plasma formation by electron or laser beams. The destroyed leads structure would represent the major but tenable (less than 30% of electricity cost) recycle cost. An interleaved leads structure has been optimized on the basis of realistic recycle cost for the conductor and for insulator refabrication. Detailed structural analyses of the blast vessel and blast mitigation by intervening coolant spray have been made with some basis in experimental fact, these studies indicating that nearly spherical vessels of 2.5-3.0 m radius and 0.2-0.5 m wall thickness would perform adequately under a 10-y fatigue constraint. The rapid energy transfer suggests the use of slow ($\sim$ 0.1 s) homopolar motor/generators switched into a storage inductor; the storage inductor would be rapidly switched through a transfer capacitor into the time-varying liner inductance. Reversible recovery of this energy is not required.

Depending upon the degree to which these uncertainties can be resolved, the FLR promises a number of significant merits: aside from the difficult pulsed ETS requirements, the FLR conceptually is a simple device that promises relatively small and economical fusion power. The physics of confinement and heating is a unique hybrid of inertial and magnetic approaches to fusion, which ideally would demonstrate the positive aspects of both. Lastly, if the fast-liner approach can be made to work, breakeven and reactor-like conditions would be demonstrated in small and economical sizes at a relatively early date.

5. Toroidal Bicusp Reactor (Tormac)

Like the Tokamak and the RFP, the Tormac [20,21] is a toroidal device that confines plasma on combined poloidal and toroidal magnetic fields. By opening the outer poloidal field regions, however, the Tormac creates an absolute minimum-B configuration that is MHD-stable for large aspect ratio and plasma beta. The resulting toroidal line cusps support plasma on both closed field lines (high-beta bulk plasma) and open field lines, the latter being enhanced by mirroring effects in the sheath region [20].

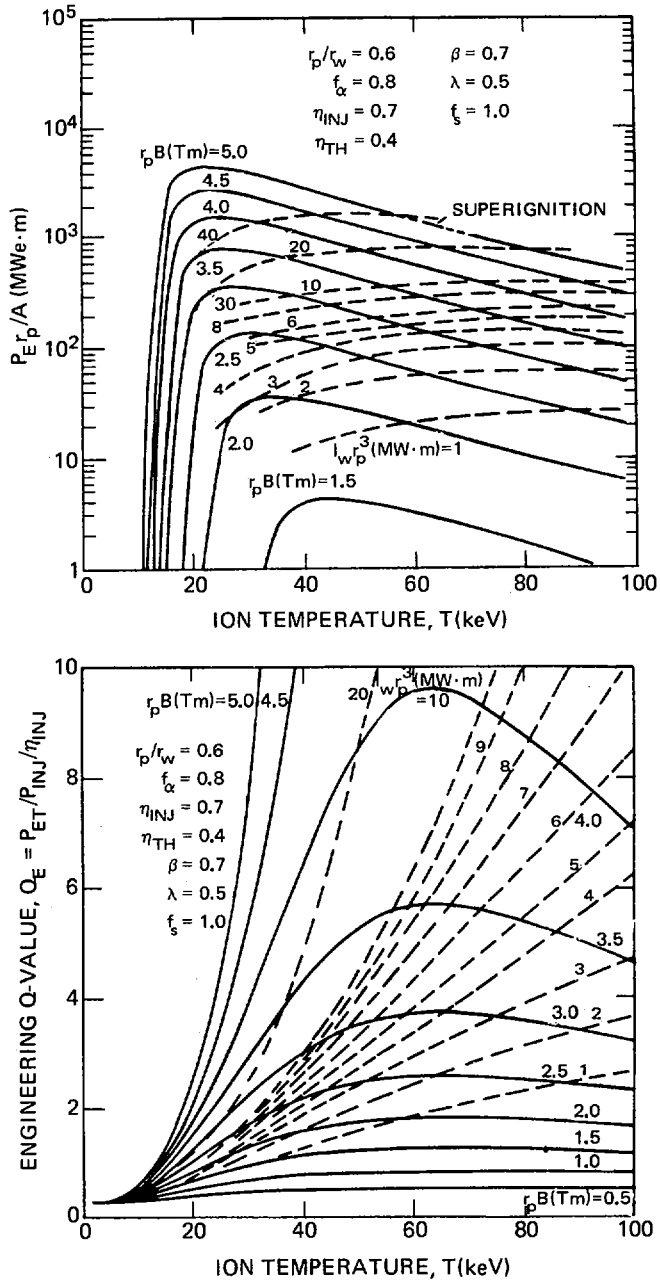


FIG. 1. Dependence of Tormac engineering Q-value Q_E and net power P_E(MWe) on ion temperature T(keV), product of plasma radius r_p(m) and cusp field B(T), and 14.1-MeV neutron wall loading I_w(MW/m^2) for the α-particle trapping efficiency f_α, injection efficiency η_{INJ}, thermal conversion efficiency η_{TH}, total beta β, electron-to-ion temperature ratio λ, and sheath thickness in ion gyroradii f_s shown.

The bulk toroidal plasma would be surrounded completely by a sheath of mirror-confined plasma, and the composite particle/energy loss time τ_ℓ should equal that of an ion-ion collision time τ_{ii} increased by the number of sheath inventories contained in the bulk plasma; this factor is $\sim r_p/\Delta_s$, where r_p is the plasma minor radius and Δ_s is the sheath thickness; Δ_s should be no greater than a few ion gyroradii ρ_i. Given that $\tau_\ell \simeq \tau_{ii}(r_p/\rho_i)$, relatively small, high-beta, and possibly steady-state reactor embodiments can be projected [22,23].

Under the assumption of a steady-state that is sustained by beam injection with efficiency η_{INJ}, design curves of the kind illustrated in Fig. 1 have been generated as a function of the indicated variables [23]. For instance, if $Q_E = 4$ is selected for $T = 65$ keV, then $r_p I_w = 4$ MW·m and $r_p B = 3.1$ T·m. Furthermore, if $I_w = 4$ MW/m^2, then $r_p = 1.0$ m, $B = 3.1$ T, and the net power P_E(MWe) equals 130A, where $A = R/r_p$ is the plasma aspect ratio. Hence, for $A \simeq 4$, net powers of 520 MWe systems are predicted. Lower recirculating power fractions $1/Q_E$ can be achieved by moving along the iso-$r_p I_w$ curves to higher temperatures and $r_p B$ values; more efficient, low-power systems result by allowing increased wall loading I_w or increased fields B.

Generally, moderate decreases in β can be compensated by modest increases in B, which for the sample case is already quite small. Increases in sheath thickness, as reflected by $f_s = \Delta_s/\rho_i$, degrade the Tormac reactor performance (Q_E, P_E), as do decreases in f_α. Arguments can be made [22], however, that τ_ℓ can be enhanced by a factor $(n/n_s)^2$, where n is the bulk plasma density, and n_s is the sheath density. Better theoretical sheath models that are substantiated by experimental evidence are required before this issue can be resolved. A clearer understanding of the mirror-confined sheath physics as well as the startup, achievement, and maintenance of the Tormac field/plasma configuration represent topics of future reactor study. On the basis of the assumed parameters and present knowledge, however, the "field" of point designs represented on Fig. 1 appear promising from the viewpoint of high Q_E, low to modest P_E and steady-state operation for reactors of small physical size (r_p,R), low fields and acceptable wall loading.

6. Summary Conclusions

Reactor projections of four confinement alternatives have been discussed. Although considerably different in themselves, these concepts share two common features: a) relative compactness and high beta, and b) a weak experimental basis relative to the Tokamak. These four concepts represent the full range from fast pulsed (FLR), to pulsed (LTPR), to long pulsed (RFPR), to nearly steady state (Tormac). Unresolved questions of stability can be identified for each: shear stabilization for the RFPR; equilibrium/stability in the curved re-entrant endplug for the LTPR; microturbulence and enhanced transport for the FLR; and the attainment of a stable absolute minimum-B confinement vis à vis the sheath for Tormac. The technology requirements for both the RFPR and the Tormac appear considerably easier than anything proposed to date for the Tokamak; the technological difficulties associated with the pulsed FLR and LTPR approaches must ultimately be weighed against the economic advantages of high power density and simple geometry. Variations on each concept, such as a driven steady-state solenoid for the LTPR or a fueled steady-state mode for the RFPR, should not be ruled out. Lastly, significant changes in the Tokamak reactor embodiment that embrace characteristics of the

alternative concepts should not be ignored, given the achieved and projected experimental/theoretical effort and successes for the Tokamak. A major goal for systems studies, in general, and studies of alternative concepts, in particular, is to induce this kind of iterative and evolutionary change in all conceptual fusion power systems.

References

1 DAVIES, N. Anne (ed.), "Workshop on Improving the Tokamak Reactor Concept," July 13-14, 1978, Washington, DC.

2 DAWSON, J.M., CHEN, F.F. (eds.), Elec. Power Res. Inst. Rept. EPRI ER-429-SR (May, 1977).

3 DECKER, J.F., Trans. Amer. Nucl. Soc. 27 41 (1977).

4 AMHERD, N.A., "EPRI Alternative Fusion Concepts Evaluation" (to be published as Electric Power Research Institute Rept., 1979).

5 HAGENSON, R.L., KRAKOWSKI, R.A., THOMASSEN, K.I., in Fusion Reactor Design Concepts (Proc. Workshop, Madison, 1977), IAEA, VIENNA (1978) 337.

6 HAGENSON, R.L., KRAKOWSKI, R.A., 3rd ANS Top. Meeting on the Tech. of Controlled Nucl. Fus., Santa Fe, NM, (May 9-11, 1978).

7 HAGENSON, R.L., KRAKOWSKI, R.A., 10th Symp. on Fus. Tech., Padova, Italy (Sept. 4-8, 1978).

8 HANCOX, R., SPEARS, W.R., UKAEA Rept. CLM-R 172 (1977).

9 MERCIER, C., Nucl. Fus. 1 47-53 (1960).

10 BAKER, D.A., DiMARCO, J.N., USERDA Rept. LA-6177-MS (1975).

11 LAWSON, J.D., UKAEA Rept. CLM-R 171 (1977).

12 NEWTON, A.A., LI YIN-AN, LUNG, J.W., YEUNG, B.C., Pulsed High-Beta Plasmas, 323-328, Pergamon Press, Oxford (1975).

13 KRAKOWSKI, R.A., 3rd ANS Top. Meeting on the Tech. of Controlled Nucl. Fus., Santa Fe, NM (May 9-11, 1978).

14 KRAKOWSKI, R.A., MILLER, R.L., HAGENSON, R.L., Proc. 2nd Top. Meeting on the Tech. of Controlled Nucl. Fus., 1, 359, Richland, WA (Sept. 21-23, 1976).

15 SHEARER, J.W., CONDIT, W.C., Energy Storage, Compression and Switching, 105, Plenum Publishing Corporation, NY (1977).

16 ALIKHANOV, S.G., et al., Plasma Physics and Controlled Nuclear Fusion Research (Proc. 6th Int. Conf. Berchtesgaden, 1976) Vol. 3, IAEA, Vienna (1978) 517.

17 BOOK, D.L., et al., ibid. 507.

18 RIOUX, C., JABLON, C., Nucl. Fus. 15 425 (1975).

19 MOSES, R.W., KRAKOWSKI, R.A., MILLER, R.L., 3rd ANS Top. Meeting on the Tech. of Controlled Nucl. Fus., Santa Fe, NM (May 9-11, 1978).

20 BOOZER, A.J., Pulsed High Beta Plasmas, 387, Pergamon Press, Oxford (1976).

21 LEVINE, M.A., et al., paper CN/37/E/4, this conference

22 BROWN, I.G., KUNKEL, W.B., LEVINE, M.A., Nucl. Fus. 18 6 761 (1978).

23 KRAKOWSKI, R.A., MILLER, R.L., HAGENSON, R.L., USDOE Rept. LA-UR-78-745 (1978).

DISCUSSION

R.W. CONN: One of the claims made on behalf of these designs is that they have significant advantages for reactor purposes. Yet the RFPR has a conducting shell near the plasma, or large stabilizing windings; the fast liner has problems of linear injection, connecting leads etc. every ten seconds, and so on. Thus the significant advantages relative to tokamaks are not all that obvious. Could you say where exactly you believe they lie?

R.A. KRAKOWSKI: Advantages common to the four concepts we have considered are very high β and relative compactness. Associated with these characteristics is the potential for higher *engineering* power density and the promise of lower power costs. Another related advantage that all four concepts are thought likely to have – a significant advantage, but one which it is difficult to quantify – is connected with the small, open and modular characteristics of key reactor components. First-wall and blanket replacement times of a few days can be considered, rather than the hundreds of days anticipated for the relatively massive monoliths that tokamaks seem likely to become (see paper I-4, for example). Three of the four concepts rely on 'conventional' heating techniques (Ohmic heating or adiabatic compression) rather than requiring exotic neutral-beam or RF heating schemes. In addition, none of the four concepts requires yet-to-be-proven divertors or gas-puffing systems for impurity control, whereas divertors represent a serious problem of technology where tokamaks are concerned.

On the other hand, as we have said, those advantages – which boil down essentially to simplicity of reactor operation – may be offset to some extent by the necessity of developing new and perhaps difficult technologies. The problems raised in your question have in fact been anticipated in our paper, but they should not be considered as being all in the same class: for instance, the need to have a conducting first-wall shell in RFPR is not thought to be as serious a matter as the economics problem associated with the FLR liner/leads.

The general question of power density need not exercise us so much, but *engineering* power density at an acceptable wall loading represents an important economic indicator; this is shown, among other things, by the attempts in recent tokamak designs to improve the engineering power density. Any fusion scheme which promises high power density, while at the same time using proven heating methods in relatively open and accessible geometries with a modest investment of energy, certainly holds out significant advantages for reactors. The purpose of this work was to determine whether the advantages we thought we saw could survive a quantitative systems study. As you have seen, in some instances the advantages withstood the test and appeared to be real while in other instances new problems were identified which may prove to be quite serious.

H.H. FLEISCHMANN: What penalties in the form of higher wall loadings do you expect to have to pay in order to obtain the higher power densities quoted for some of these concepts?

R.A. KRAKOWSKI: The relationship between *engineering* power density, $P_{TH}(MW \cdot m^{-2})$, and first-wall loading, $I_w(MW \cdot m^{-2})$ depends on the specific system and is not necessarily one-to-one. *Engineering* power density is defined here as the total thermal power divided by the total volume enclosed by the major reactor core structure, including coils. For instance, a system with a wall radius b(m) and a blanket and coil thickness Δb(m) has a ratio of engineering power density to wall loading given approximately by $P_{TH}/I_w = 2Mb/(b + \Delta b)^2$, where $M \cong 1.2 \rightarrow 1.4$ is the 14.1-MeV neutron energy multiplication. The dependence of P_{TH}/I_w on b shows a maximum at $b = \Delta b$, where $(P_{TH}/I_w)_{max} = M/b = M/\Delta b$; hence, systems with smaller b or Δb would operate at higher power densities for the same wall loading. Systems that require superconducting coils, and hence Δb values that are $2 - 3$ times greater than required solely by energy recovery constraints, must operate at lower P_{TH} for a given I_w. The cost impact of increased wall loading to achieve higher power density, or the lower power losses associated with the use of superconducting coils (and thicker blankets), must be weighed against the cost impact of increased or decreased thermal power density. This issue is further complicated in the case of the FLR concept, where, to first order, I_w and P_{TH} are decoupled and power densities in excess of $5 - 10\ MW \cdot m^{-3}$ can be achieved within the containment vessel. Problems such as thermal cyclic fatigue in the LTPR or blast confinement in the FLR present constraints not incorporated into the model described above – constraints which in some circumstances dominate the simple geometric arguments. This is seen, for instance, in the LTPR and RFPR designs, which both have $b \sim \Delta b$, different values of b, the same wall loading ($\sim 2\ MW \cdot m^{-2}$) and the same power density ($\sim 1\ MW \cdot m^{-3}$).

THE ELMO BUMPY TORUS (EBT) REACTOR*

N.A. UCKAN, D.B. BATCHELOR, E.S. BETTIS,
R.A. DANDL, C.L. HEDRICK, E.F. JAEGER,
D.G. McALEES,† D.B. NELSON, L.W. OWEN,
R.T. SANTORO, D.A. SPONG, T. UCKAN,
H.L. WATTS, H.T. YEH
Oak Ridge National Laboratory,
Oak Ridge, Tennessee

L.M. LIDSKY, J.S. HERRING, R.E. POTOK
Massachusetts Institute of Technology,
Cambridge, Massachusetts,
United States of America

Abstract

THE ELMO BUMPY TORUS (EBT) REACTOR.

The EBT concept provides a uniquely simple basis for a steady-state modular fusion reactor. Inclusion of recent advances from plasma research has led to a new, smaller design. Critical physics issues are discussed and dimensionless parameter scalings are explored.

1. INTRODUCTION/SUMMARY

The experimental results from the EBT [1] have motivated a consideration of the EBT concept as the basis for a potential reactor [2]. The EBT combines many of the most attractive features of both tokamaks and mirrors into an attractive reactor configuration: steady-state operation, potential for high beta, large aspect ratio, modular construction, favorable geometry for ease of maintenance, modest technology requirements, high Q value, and economic potential.

Since the first round of EBT Reactor (EBTR) designs [2] there has been considerable progress in design improvement. Recent designs which incorporate the increased understanding from plasma reserach lead to smaller reactors with easier and practical maintenance [3].

EBT is a large aspect ratio device. In our earlier reactor designs [2] the large aspect ratio (with a large toroidal major radius as well) led to plants with comparatively large total energy output, usually in the range of 1000 to 2000 MW of electrical power for a conventional wall loading of 1 MW/m^2. On the

* Research sponsored by the Office of Fusion Energy (ETM), US Department of Energy, under contract W-7405-eng-26 with the Union Carbide Corporation.

† Exxon Nuclear Co., Inc., Bellevue, Washington, USA.

TABLE I. CHARACTERISTIC EBT REACTOR PARAMETERS

	Previous Designs [2,3]	New Design
Plasma radius (m)	1.0	1.0
Mirror ratio	1.8	2
Magnetic field (midplane/mirror) (T)	2.5/4.5	2.5/5
Aspect ratio	30-60	20-30
Number of sectors	24-48	16-24
Number of ARE coils	none	2/sector
η, aspect ratio enhancement[a]	0	$\sim$2
Particle density (m^{-3})	1.2×10^{20}	$\gtrsim 1.4 \times 10^{20}$
Ion/electron temperature (keV)	15	15
Toroidal plasma beta (%)	$\sim$25	20-35
F, anomalous enhancement factor[b]	1-100	1-50
Neutron wall loading (average) (MW/m^2)	1-1.5	1-3
Total fusion power [MW(e)]	1000-2000	500-1500
Cold zone (m)	0.2	0.2
Blanket thickness (m)	0.6	0.6
Shield thickness (m)	0.55	0.55
Coil inner radius (TF coil) (m)	3.0	3.0
Coil inner radius (ARE coil) (m)	-	4.2
Neutral beam energy (keV)	100-150[c]	100-150[c]
Neutral beam power (MW)	50-200[c]	30-100[c]
Microwave frequency (GHz)		
Toroidal plasma	$\sim$120	$\sim$120
Hot electron annuli	$\sim$70-90	$\sim$60-80
Microwave power (MW)		
Toroidal plasma	50-200[c]	30-100[c]
Hot electron annuli	5-10	3-6

[a] See text for definition.

[b] See text for definition.

[c] A toroidal plasma will be heated to ignition conditions using either microwaves or neutral beam injection. Power required for ignition and beam energy depends on the startup scenarios.

other hand, the large aspect ratio provides very simple engineering and design requirements because of good access and small force loading asymmetries. However, by using relatively low current field shaping coils in a smaller device, an increase in the effective aspect ratio appears possible through symmetrizing effects. These coils are called aspect ratio enhancement (ARE) coils and provide the same improvement of the confinement that occurs when the major radius is increased [4]. An enhancement factor of two to three seems achievable. The first test of these coils will be made on the EBT-SA experiment [1,5].

The following set of design constraints is specified in order to select a reference design: from the utilities point of view, power output is limited to 500-2000 MW(e); neutron wall loading is in the range of 1-3 MW/m^2 from wall lifetime considerations; the mirror ratio required for annulus formation is typically $\sim$2:1 [5]; the limiting toroidal plasma beta (β_T) is in the range of 20-40% [6]; the required aspect ratio for plasma confinement is greater than 10; an aspect ratio enhancement factor from ARE coils is in the range of 1-3 [4]; and the device should be capable of ignition and should use, if possible, $\sim$150-keV Tokamak Fusion Test Reactor (TFTR) neutral beams or $\sim$120-GHz EBT-II microwave sources for toroidal plasma heating and $\sim$60- to 70-GHz EBT-II microwave sources for sustaining the annuli. On the basis of trade-off studies among the plasma physics requirements and uncertainties, engineering design, and technological capabilities, a self-consistent set of plasma parameters and a range of machine characteristics are obtained, as given in Table I. In view of the uncertainties involved, plausible estimates have been made to retain flexibility so the system can accommodate changes as the physics and technology evolve with time. The essential features of the EBTR are described below; however, greater emphasis has been given to the plasma physics issues.

2. PHYSICS BASIS

The EBT is a toroidal, non-axisymmetric magnetic configuration which confines a non-current-carrying toroidal core plasma by a number of toroidally linked mirrors. The configuration is stabilized by using the "minimum-B" properties of annular high-beta, hot electron plasmas formed by microwave heating in the midplane of each mirror section. Both theoretical studies [6] and experiments [1,5] on the EBT device have demonstrated the existence of a macroscopically stable plasma confinement regime.

The plasma physics areas which determine the EBTR operating characteristics are: (1) particle orbits and magnetic equilibrium, (2) plasma stability (macro- and micro-), (3) transport scaling, and (4) heating. Although considerable uncertainty remains about the behavior of the plasma under conditions necessary for a reactor, an analysis of the dimensionless parameters scaling indicates that the extrapolation of the present experimental results [1] becomes encouragingly feasible.

2.1 Equilibrium and Particle Orbits

The blanket and shield which surround the plasma chamber in a reactor make efficient use of the magnetic fields more difficult than in the present experimental device. Special attention has been placed on the equilibrium requirements and the efficient use of the volume within the vacuum chamber of the reactor. Two- and three-dimensional, self-consistent, finite beta equilibrium calculations are used to examine particle orbits and stability. Finite beta and ambipolar electric fields make significant changes in the particle orbits. Also, the toroidal curvature of the magnetic field results in an inward shift of drift orbits. This shift is largest for high energy particles with $v_{\parallel}/v \sim 1$.

Two methods have been used to improve the particle confinement. In the earlier studies, a displaced aperture inner wall design provided the required improvement via recentering the drift orbits and increasing the useful bore of the torus [2]. In the latest designs, supplementary coil configuration has been used to reduce dispersion in the drift orbits just as would increased aspect ratio. These coils, called aspect ratio enhancement (ARE) coils, hold the promise of increased plasma performance in a smaller EBT reactor with an acceptable power level at relatively low cost.

2.2 Stability

The viability of EBT as a reactor requires the stable confinement of a toroidal plasma with a density of $\sim 10^{20}$ m^{-3} and a temperature on the order of 10-15 keV. A hot electron population (annuli) with $T_e \gtrsim 100$ keV is crucial to the stability. The annulus density, however, is only about 10^{18} m^{-3}, a small fraction of the total electron density. In the EBT the stable behavior of the plasma relies on the presence of both hot (annuli) and warm (toroidal) species. In the experiment, this is shown by the transition from stable to unstable behavior when the hot electron density becomes either too large or too small [1].

In an EBT reactor, it is desirable that the toroidal plasma beta be at least 10-20%. Plasma instabilities are one of the physical processes which can limit beta, and among these the MHD instabilities could be especially dangerous because they can carry the plasma rapidly to the wall. The stability and beta limitations of the toroidal plasma have been studied by using a modified energy principle [6]. In this model the hot electron ring is treated as an external rigid current which contributes to the static force balance but is unaffected by the perturbed plasma or fields. It is shown [6] that the toroidal core plasma can be macroscopically (MHD) stable, provided the hot electron rings (annuli) have sufficient pressure to produce a minimum in the magnetic field. Once a magnetic well has been established by the annuli (at threshold value of annuli beta, $\beta_C \sim 5$-15%), the beta limit of the toroidal plasma (β_T) can be comparable to the beta of the annuli ($\beta_A \lesssim 50\%$). With $\beta_T \lesssim \beta_A$, the plasma is stable to all modes encompassed by guiding center or ideal MHD theories. The shape of the hot electron annulus affects β_C, but calculated values lie in the range of 5-15% for a broad class of an assumed annulus configuration. Figure 1 shows the results for two different configurations. The modes which limit toroidal beta are pressure-driven ballooning interchanges. Since the results shown in Fig. 1 are extremely encouraging for an EBT reactor, no further attempt has yet been made to optimize the annulus configuration.

Experimental confirmation of these optimistic toroidal beta predictions is not possible in the present device [1] because β_T is limited by heating and transport considerations to $\sim 0.5\%$. However, the threshold value of β_A at $\sim$8-10% does agree with an abrupt change in experimental operating conditions: transition from the noisy-mode to the quiet-mode of operation [1].

The stability of hot electron rings requires a Vlasov treatment because the characteristic drift frequencies can be comparable to or greater than the ion cyclotron frequency. Analysis of the Vlasov-Maxwell equations shows that the hot electron drift waves are stabilized by interference between the responses of fast drifting electrons and the slowly drifting ions [7]. Recent calculations [8] treat the stabilization of modes characteristic of the hot electrons by interaction with cold electrons or ions and indicate that the rings are stable if the ratio of the cold to hot electron density is sufficiently high (e.g., ~ 10).

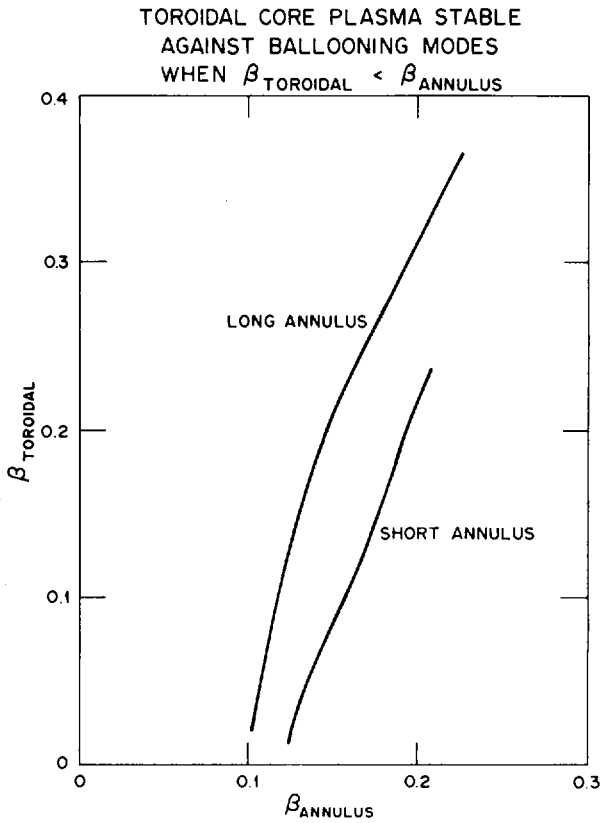


FIG.1. Maximum toroidal beta for MHD stability.

A similar Vlasov model [9], considering low frequency localized MHD modes characteristics of the warm species, has been used to explore the validity of the rigid annulus MHD model discussed earlier. It was shown that future experiments will be in the rigid annulus regime where the results of the Vlasov-Maxwell equations will reduce to those of MHD.

While more work clearly needs to be done, some conclusions can be drawn from the results to date: there is a symbiotic relationship between the toroidal core plasma and the hot electron rings; and the toroidal core plasma provides the cooler electrons to stabilize the rings, while the hot electron rings provide the minimum-B necessary to stabilize the toroidal core plasma.

Stable operation of a reactor will require that the hot electrons achieve a temperature comparable to that in the present device [1,5] and a pressure profile of sufficient steepness to produce large ∇B drifts. Near the outer edge of the annuli, the presence of the high density toroidal core plasma and

line tying can provide the stability within the context of MHD. Some small volume of cold edge plasma may be required for stability and may also be useful in screening impurities from the central portion of the plasma, as observed in EBT-I [1].

An initial survey has also been made of possible microinstabilities which might affect reactor operation [10]. The stability criteria for these modes are similar to those obtained from the energy principle. It is interesting to note that because EBT relies upon strong magnetic gradients rather than rotational transform for single particle confinement, the stability criteria for these dissipative modes reflect the magnetic gradient (and minimum-B) much more strongly than the related criteria for tokamaks. It is encouraging that the qualitative requirements on density and temperature profiles of these modes are automatically provided by neoclassical transport, which appears to govern the operation of EBT-I [1,11] and is assumed applicable to future devices because of the constancy of most of the dimensionless parameters (see Sect. 2.5).

2.3 Transport Scaling

The latest neoclassical transport theory description of EBT losses and correlation with experiment are discussed in detail in Ref. [1]. Plasma confinement in EBT depends on the modification of the toroidal vertical drift, $v_T \sim T/eBR_T$, by the poloidal ∇B and EXB drifts (produced by bumpiness in the toroidal field and by the ambipolar electric field). The particle orbits are approximately circular, with the center of the orbit displaced from the mirror axis by an amount ΔX which is the ratio of the toroidal to poloidal drift velocities, $\Delta X = v_T/\Omega$ where

$$v_T = \frac{mv^2}{2eBR_T}\left(1 + \frac{v_\parallel^2}{v^2}\right)$$

$$r\Omega = \frac{mv^2}{2eBR_c}\left(1 + \frac{v_\parallel^2}{v^2}\right) + \frac{E_r}{B}$$

R_T and R_c are the toroidal and mirror radii of curvature, and E_r is the radial electric field. This displacement acts as a basic step size for diffusion of particles and energy. The diffusion coefficient in a simple case is given as [12]

$$D \sim \left\langle \frac{\nu(\Delta x)^2}{1 + \nu^2/\Omega^2} \right\rangle \sim \left\langle \frac{\nu R_c^2 a^2/R_T^2}{(1 + \nu^2/\Omega^2)(1 \pm eR_cE/T)^2} \right\rangle$$

where ν is the effective collision frequency. The electrons in the present experiment are in the collisionless regime ($\nu/\Omega < 1$), as would be the ions in a reactor. In this regime the plasma confinement time is given by

$$\tau \sim \left(\frac{R_T}{R_c}\right)^2 \nu^{-1} \sim \nu^{-1} A_{eff}^2 \sim \nu^{-1} A^2(1 + \eta)^2$$

which gives $\tau \propto A_{eff}^2$. Here A_{eff} is the effective aspect ratio of the system and A is the conventional mechanical aspect ratio (R_T/a). By cancelling out lowest order toroidal effects with ARE coils, enhancement in the effective aspect ratio could be possible ($\eta = 0$ without ARE coils and $\eta \sim 1$-2 with ARE coils [4]).

Transport rates in EBT depend sensitively on the radial ambipolar field (E_r) in contrast to other toroidal devices [11]. The field improves overall confinement of the system. In the present neoclassical transport model [11], the field is calculated self-consistently by equating electron and ion fluxes. Predictions of this model appear to be in good agreement with experimental observations [1]. In a reactor, this field may be strongly influenced by alpha particle containment properties. The azimuthal ambipolar field (E_θ) leads to an EXB drift which can partially cancel or add to (depending on the sign) the vertical drift caused by toroidal curvature. This may become important in a reactor plasma with neutral beam heating. Improvement in confinement may be possible by external control of E_θ by beams or other means. Presently, this field is chosen [13] so that particles with $v_\parallel = 0$ in the midplane are centered in the bore, as is suggested by experiment.

At present, there is uncertainty in the extrapolation of this model to reactor conditions and refinement of the model is necessary. However, approximate constancy of the dimensionless parameters influencing the transport (see Sect. 2.5) gives encouragement and lends some credibility to the extrapolation process.

2.4 Plasma Heating

The heating of an EBT reactor plasma by microwaves and neutral beams has been studied in some detail [14]. Although past and present EBT experiments use electron cyclotron heating (ECH) for formation of the hot electron rings and for heating of the bulk (toroidal) plasma, an EBT reactor and future experiments may use neutral beams as well as ECH, or a combination of both, for heating of the toroidal plasma. After the plasma is heated to ignition, the bulk heating would be turned off, but the ring heating would have to be sustained throughout the steady-state operation.

The ECH is a comparatively well understood technique which has been demonstrated successfully in EBT-I [1,5], tokamaks, and other devices. The questions of spatial energy deposition and accessibility (to both the ordinary and extraordinary modes) were considered for a reactor plasma, and it was found that the ordinary mode penetrates and is absorbed [14]. Microwave frequencies required for a reactor are $\sim$120 GHz for the toroidal plasma heating and $\sim$60-70 GHz for the ring formation. These frequencies are similar to the requirements of the proposed EBT-II experiment, and an aggressive microwave development program is under way [5].

Because energetic particles having large pitch angle ($v_\perp >> v_\parallel$) are well confined in EBT, perpendicular injection of neutral beams appears very attractive. The possibility of perpendicular injection coupled with the large aspect ratio and relatively small plasma minor radius ($\sim$1 m) for an EBT reactor means that neutral beams of moderate energy (of TFTR type, $\sim$150 keV) could be sufficient [14]. Neutral beam heating may also provide flexibility in tailoring profiles for optimum stability and confinement, as mentioned earlier. However, a pure beam heated EBT plasma might have different thermal stability properties than a plasma heated by ECH. One possible difference is the complicated crescent shaped drift orbits which occur near regions in configuration and velocity space where the poloidal drift frequency passes through zero [13]. Mirror and toroidal

TABLE II. DIMENSIONLESS PARAMETERS

		EBT-I	EBTR	CRITICAL VALUE
Annulus beta	β_A	0.2-0.4	0.3-0.5	$>\beta_{threshold} \sim$ 8-10%
Toroidal core beta	β_T	$3\text{-}5 \times 10^{-3}$	$\gtrsim 25 \times 10^{-2}$	$\lesssim \beta_A$
Ratio of gyroradii to plasma radius	ρ_e/a	10^{-3}	10^{-4}	
	ρ_i/a	2×10^{-2}	4×10^{-3}	
Ratio of cold (toroidal) to hot (annulus) electron density	n_c/n_h	$\sim$10	>10	
Field errors	$\delta B/B$	$\lesssim 10^{-4}$	$\lesssim 10^{-6}$	$\lesssim \rho/R_T$
Aspect ratio	A	10	20-60	>10
Ratio of electron to ion temperature	T_e/T_i	$\gtrsim 3$	$\sim$1	
Ratio of electron plasma frequency to cyclotron frequency	ω_{pe}/ω_{ce}	$\lesssim 0.7$	$\sim$0.8	
Ratio of ambipolar potential to temperature	$\lvert e\phi/T_j \rvert$ j=e or i	$\sim$1	$\sim$1(?)	
Collisionality	ν_e/Ω_e	0.1	0.5	<<1
	ν_i/Ω_i	0.15	0.015	

curvature, finite beta, and radial electric fields make general statements difficult, but it is encouraging that large aspect ratios yield fairly well centered drift surfaces. Theoretical studies are under way to determine the properties of beam heated EBT plasmas.

2.5 Dimensionless Parameter Scaling

The experimental results from EBT-I [1] have motivated plans for constructing larger scale EBT's and detailed reactor studies. Since it is necessary to predict the plasma properties in these systems, experimental data in some cases must be extrapolated as much as an order of magnitude. As mentioned in previous sections, uncertainty remains in the detailed extrapolation, especially near reactor conditions. While the EBT experiment and theory are evolving together, a less detailed and simpler approach based on dimensionless parameter scaling is warranted. The dimensionless parameters which influence stability and transport are listed in Table II for EBT-I [1] along with those projected for an EBT reactor and any known critical values of each, if any. A comparison of these parameters shows that the following dimensionless parameters are either the same

or in the direction of increased stability and/or improved confinement: annulus beta (β_A); ratio of gyroradii to various scale lengths [$(\rho/L)_{e,i}$ with L = a, (d ln Ω/dr)$^{-1}$, (d ln n/dr)$^{-1}$...]; field errors ($\delta B/B$); aspect ratio (A); ratio of cold to hot electron density (n_c/n_h); ratio of electron to ion temperature (T_e/T_i); ratio of electron plasma frequency to cyclotron frequency (ω_{pe}/ω_{ce}); and ratio of ambipolar potential to temperature ($e\phi/T$). The approximate constancy of these dimensionless parameters, which are known to influence stability and transport, is very encouraging, and the extrapolation of the present experimental results to EBTR has more certainty than might be inferred from the change in magnitude in T, n, and τ. The beta of the toroidal core plasma (β_T) and, to a lesser extent, the collisionality are the factors which change appreciably; their importance and uncertainties for reactor scale plasmas remain to be resolved in future experiments.

3. PLASMA DESIGN AND ANALYSIS

Steady-state plasma parameters are obtained from consistent solution of the equilibrium, plasma particle, and power balance equations [15]. As mentioned in previous sections, the scaling laws which will ultimately apply to the EBTR plasma are uncertain. A simulation model which retains the essential physics of the known phenomena has been developed [15] to assess the plasma behavior. Although in the present EBT device plasma transport seems to be governed largely by neoclassical processes [1,11], hypothesized anomalous transport losses are appended to the plasma simulation model in order to test the sensitivity of EBTR parameters. It is shown in Ref. [15] that the projected parameters for EBTR given in Table I are flexible enough to accommodate anomalous losses one to two orders of magnitude greater than the present neoclassical losses at the operating point before ignition fails. A range for the anomalous enhancement factor, F, [15] over the neoclassical transport for the cases studied here is also given in Table I.

Power requirements to sustain the stabilizing annuli need to be examined in detail, although preliminary calculations show that this may not be a problem because the ring plasma occupies a relatively small volume [2]. In steady state, the annulus power balance is $P_{\mu A} = P_{\tau A} + P_{BA} + P_{CA}$, where $P_{\tau A}$ is thermal conduction and convection, P_{BA} is bremsstrahlung losses, P_{CA} is synchrotron (cyclotron) radiation, and $P_{\mu A}$ is the microwave power required to sustain the annulus. The calculations show that the synchrotron emission from Maxwellian hot electron annulus would amount to a few tens of kilowatts per sector at worst, compared to some tens or hundreds of kilowatts of transport losses [2]. It is important, however, that this subject be reviewed frequently as more information becomes available about the annuli (and their scaling laws) from the future experiments.

An attractive feature of the EBTR is its steady-state operation, which requires fueling and divertor capability. This requirement is not unique to EBT since it applies to all large systems where the burn time will exceed the particle containment time. In EBT-I, impurities do not accumulate in the central region of the plasma because of the short confinement of impurities in the surface plasma and shielding by the ring (annuli) electric field [16]. Future experiments may continue as in EBT-I or show that the EBTR will require residue removal and impurity control mechanisms. In the latter event, toroidal or bundle divertors have been considered [2].

4. ENGINEERING DESIGN

Conceptual design of the EBTR is based on the modular concept. Each module consists of one superconducting magnet coil, two ARE coils, a shield

of articulated cylindrical units, and multiple blanket modules (roughly conforming to the plasma shape), as well as vacuum pumping and microwave injection ports.

4.1 Magnetics

The magnetic field in recent EBTR designs is produced by twenty four 6-m-bore NbTi superconducting coils for an aspect ratio = 30 system (for aspect ratio = 20, 16 such coils are required). The peak design fields are 8.5 T at the coil, 5 T at the magnet throat, and 2.5 T at the midplane, which gives a mirror ratio of 2. In order to increase the effective aspect ratio of the system, two ARE coils (normal copper or superconductor) per section are added. These field shaping coils are relatively low current (6-10% of the current in the TF coils) and are expected to improve the confinement [4]. Although access is restricted by the ARE coils, adequate space remains for other auxiliaries.

Because of the large aspect ratio, the magnetic field is reasonably uniform at the coils and the magnetic forces are nearly symmetrical. All coils are circular in shape and are made of tightly wound pancakes with pool-boiling cooling. Cryostability of the magnet is achieved by building up monolithic multifilamentary NbTi composite with formed copper strips. Four conductors are wound in parallel to maintain a reasonably small conductor and large heat transfer surface and are interleaved in a spiral fashion in such a way that inductances are equalized and the total current is evenly divided between conductors. It is important that the field errors be small in EBT, and the winding scheme adopted gives lower field errors than if only one conductor is used.

4.2 Blanket/Shield Systems

For the blanket, the following material choices and design constraints have been suggested [17]:

- stainless steel (modified 316) for all structures,
- metallic normal lithium as the fertile material,
- high pressure gaseous helium as coolant,
- first wall temperatures limited to 400°C,
- high pressure helium coolant doubly contained for protection of blanket buckets,
- thin first wall to handle surface energy deposition.

The blanket is divided into segments both poloidally and toroidally. There are nine toroidal segments in one module, and each segment consists of 12 sections arranged in a circular frame. The blanket is of uniform thickness, 60 cm, for all segments. In order to contain the high pressure helium and prevent damage to the blanket sections, double wall (concentric) cooling tubes are coiled in the sections. Helium gas at 70 atm is circulated through the blanket to remove the heat for steam generation. The entire blanket structure is 316 stainless steel with a small addition of titanium. The shield sections are made of stainless steel containers (tanks) filled with stainless steel spheres around which borated water is circulated for heat removal. These tanks are divided into appropriate shapes and sizes to permit access to the blanket with relative ease.

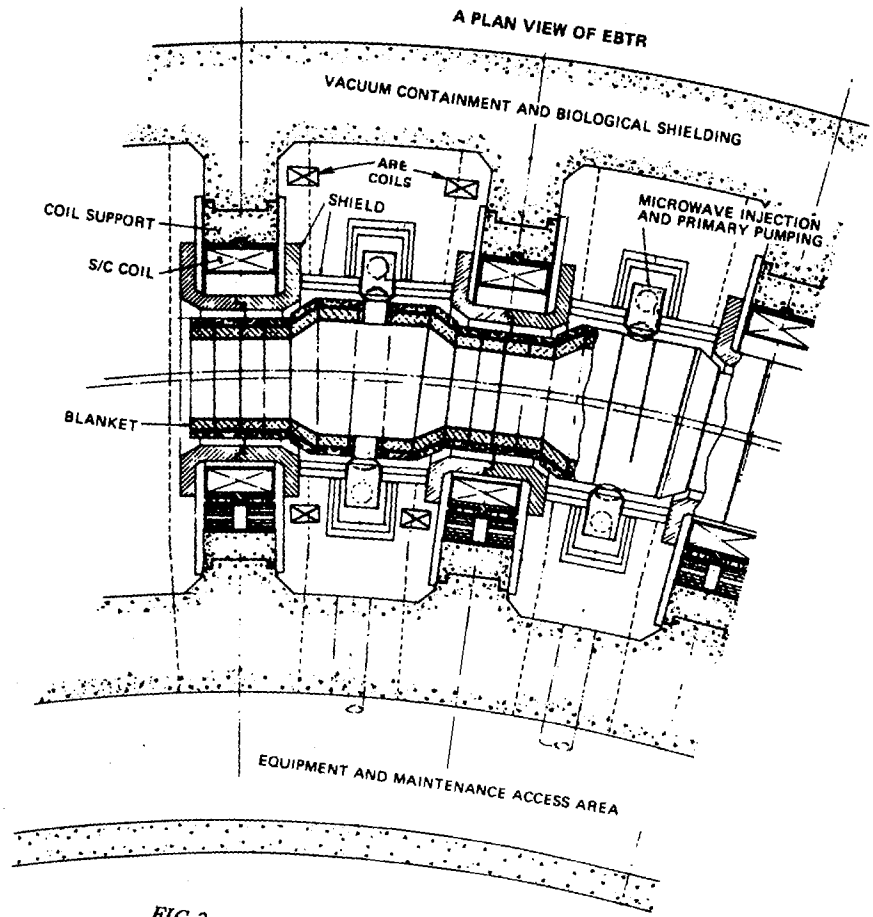


FIG.2. A plan and section elevation view.

The blanket assembly recovers 96% of the neutron and secondary gamma ray energy in the form of heat [18]. Approximately 4% of the energy is deposited in the shield and the remainder ($\sim 10^{-3}$–10^{-4}%) is deposited in the magnet assembly. The total heating rate in the blanket is 13.5 W/cm^3 and drops off to 0.34 W/cm^3 at the front of the shield. The shield reduces the nuclear heating by nearly four orders of magnitude, and at the front of the magnet assembly the peak heating is down to 5.8×10^{-5} W/cm^3.

Natural lithium is used as the fertile material in the blanket. The tritium breeding ratio is 1.3 tritium nuclei per incident neutron, with 56% of the breeding resulting from neutron reactions with ^{6}Li.

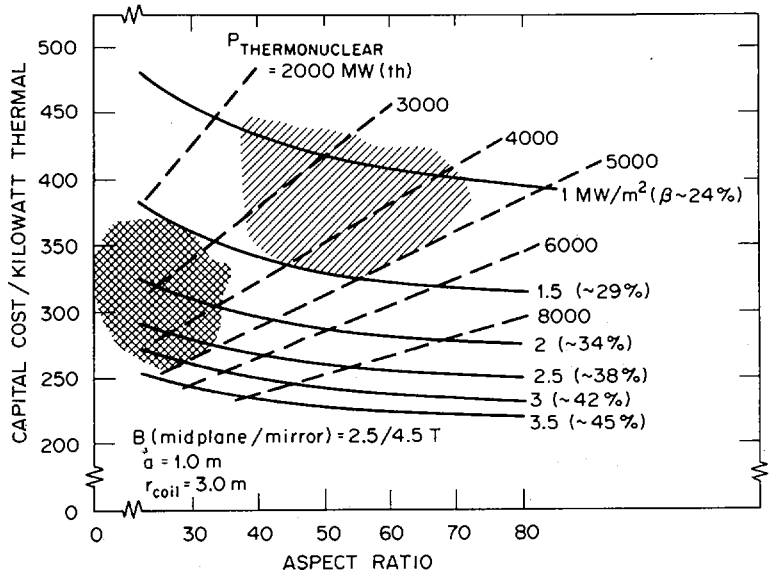


FIG. 3. The capital cost per kilowatt thermal versus aspect ratio for several values of neutron wall loading, and fusion power output for fixed plasma radius, coil size, and magnetic field strength. Capital cost ranges for earlier (hatched) and recent (cross-hatched) designs are shown.

4.3 Plant Design

The torus is assembled in a concrete moat which is evacuated to provide secondary vacuum enclosure for the machine. This vacuum environment greatly simplifies the assembly procedure; more importantly, it eases the remote maintenance problem and substantially lowers the structural cost. An important safety advantage when the reactor is sectioned into modules is that a lithium spill fire in a single section would be oxygen-limited, with the result that the maximum cell overpressure and cell gas temperature would be restricted to safe values [19].

The plasma region is maintained at a lower pressure than the moat by two vacuum pumping ports between each TF coil. Microwave injection is made through these same vacuum ports. The vacuum system for the plasma region is located in tunnels running radially under the moat. A plan view of the components of the torus is shown in Fig. 2. The large area encircled by the moat is used for microwave generators and power supplies, cryogenic refrigerators, primary heat exchangers, and other equipment.

5. ECONOMIC ANALYSIS

In order to establish the economic potential of the EBTR, two independent system costing models have been developed [20], one of which is based on the model developed for the tokamak system [21]. The results of the two models, which are discussed in detail in Ref. [20], are in general agreement and predict capital costs at approximately $300-400/kW(th). Figure 3 shows capital costs as a function of aspect ratio, wall loading, beta, and power output for fixed plasma

radius and magnetic field. Since the efficiency of the power conversion system varies and has yet to be demonstrated, cost estimates are given on the basis of dollars per kilowatt thermal instead of dollars per kilowatt electric. Capital cost ranges for earlier and recent designs are also indicated in Fig. 3. Additional cost savings of about 10-20% are realized with ARE coils in the latest designs.

In comparing the EBTR cost to the tokamak reactor cost [21], savings are realized from the lack of poloidal coil and driving systems and the economic gain of continuous operation. These costs do not include the increased maintenance cost associated with the more complex systems and operating cycles or the savings from ease of maintenance in the EBT geometry. The EBT concept appears competitive both among fusion reactor concepts and among different power plants.

ACKNOWLEDGMENTS

The authors gratefully acknowledge the entire ORNL EBT theoretical and experimental staff for their valuable input and L. A. Berry, J. D. Callen, R. A. Dory, and N. H. Lazar for many helpful discussions and continued support.

REFERENCES

[1] DANDL, R. A., et al., paper IAEA-CN-37/L-4 (this conference); and Plasma Physics and Controlled Nuclear Fusion Research (Proc. 5th Conf. Tokyo, 1974), II, IAEA, Vienna (1975) 141.
[2] UCKAN, N. A., et al., Oak Ridge National Laboratory Report ORNL/TM-6084 (to be published); MCALEES, D. G., et al., Oak Ridge National Laboratory Report ORNL/TM-5669 (1976).
[3] UCKAN, N. A., et al., paper presented at the 3rd Topical Meeting on the Technology of Controlled Nuclear Fusion, Santa Fe, New Mexico, May 9-11, 1978 (to be published).
[4] OWEN, L. W., et al., in Proc. Annual Controlled Fusion Theory Conf., paper D26 (1978).
[5] DANDL, R. A., et al., Oak Ridge National Laboratory Reports ORNL/TM-4941 (1975) and ORNL/TM-5451 (1976).
[6] NELSON, D. B., HEDRICK, C. L., Oak Ridge National Laboratory Report ORNL/TM-5967 (1977).
[7] GUEST, G. E., et al., Phys. Fluids 18 (1975) 871.
[8] DOMINGUES, R. R., BERK, H. L., Lawrence Livermore Laboratory Report UCRL-79268 (1977); and Phys. Fluids 21 (1978) 827.
[9] NELSON, D. B., to be published.
[10] BATCHELOR, D. B., et al., Oak Ridge National Laboratory Report ORNL/TM-6318 (1978).
[11] JAEGER, E. F., et al., Phys. Rev. Lett. 40 (1978) 866.
[12] KOVRIZHNYKH, L. M., Zh. Eksp. Teor. Fiz. 56 (1969) 877 [Sov. Phys.-JETP 29 (1969) 475].
[13] HEDRICK, C. L., et al., paper presented at the Controlled Fusion Theory Meeting, Gatlinburg, Tennessee, April 1978.
[14] UCKAN, N. A., BATCHELOR, D. B., Oak Ridge National Laboratory Report ORNL/TM-6346 (1978).
[15] UCKAN, N. A., HEDRICK, C. L., Oak Ridge National Laboratory Report ORNL/TM-6019 (1977).
[16] LAZAR, N. H., private communication; WARDEN, E. S., MOOS, H. W., LAZAR, N. H., Oak Ridge National Laboratory Report ORNL/TM-5899 (1977).

[17] BETTIS, E. S., et al., in Proc. 7th Symp. Engineering Problems on Fusion Research, II (1977) 1453.
[18] SANTORO, R. T., BARNES, J. M., Oak Ridge National Laboratory Report ORNL/TM-6085 (1978).
[19] DUBE, D. A., et al., paper presented at the 3rd Topical Meeting on the Technology of Controlled Nuclear Fusion, Santa Fe, New Mexico, May 9-11, 1978 (to be published).
[20] WOO, J. T., UCKAN, N. A., LIDSKY, L. M., in Proc. 7th Symp. on Engineering Problems of Fusion Research, I (1977) 681.
[21] STEINER, D., et al., Oak Ridge National Laboratory Report ORNL/TM-5813 (1977).

DISCUSSION

B.G. LOGAN: What is the perimeter length in your latest reactor design – that is, 2π times the major radius?

N.A. UCKAN: In the latest design the major radius of the reactor is 30m; so the perimeter length is $30 \times 2\pi$.

IMPACT OF TECHNOLOGY AND MAINTAINABILITY ON ECONOMIC ASPECTS OF TOKAMAK POWER PLANTS

M.A. ABDOU, C.C. BAKER, J. BROOKS,
R. CLEMMER, C. DENNIS, D. EHST, K. EVANS,
S. HARKNESS, R. KUSTOM, V. MARONI,
D. SMITH, H. STEVENS, L. TURNER
Fusion Power Program,
Argonne National Laboratory,
Argonne, Illinois

G.M. FULLER, H.S. ZAHN
McDonnell Douglas Astronautics Company,
St. Louis, Missouri,
United States of America

Abstract

IMPACT OF TECHNOLOGY AND MAINTAINABILITY ON ECONOMIC ASPECTS OF TOKAMAK POWER PLANTS.

Results of system studies on the primary energy conversion, energy storage and transfer, tritium and vacuum subsystems of a tokamak reactor are presented. These results quantify the impact of technology choices and maintainability on the economics of tokamak power plants. It is found that the expensive refractory alloys must offer a factor of three or greater advantage in lifetime compared to stainless steel in order that their costly development should have a reasonable benefit-to-cost ratio. Five reactor concepts are analysed in terms of their scheduled maintenance requirements for replacing the first wall and blanket. The total downtime is found to vary from ~100 days to 500 days for a single replacement of the entire first wall and blanket. Substantial reduction in the power supply requirements and costs over previous estimates seems possible. The emergency air detritiation system is found to be a major cost item.

1. INTRODUCTION

The successful development of a new energy source depends on the effort and time required for new technology developments and the economics of the commercial units. In the case of fusion energy, even for a single confinement approach such as the tokamak, there are a variety of design concepts and a wide range of potential choices for the major features of a power reactor.

TABLE I. REFERENCE REACTOR PARAMETERS

Thermal power, MW	4950
Neutron wall load, MW/m^2	4
Major radius, m	7.3
Maximum toroidal field, T	9
$\bar{\beta}_t$, %	8
Inner blanket/shield thickness, m	1
Outer blanket/shield thickness, m	1.3

TABLE II. REFERENCE PARAMETERS FOR THE HEAT TRANSFER AND TRANSPORT SYSTEM

Structure Material in the Blanket and Primary Loop	Stainless Steel	Vanadium Alloy
Primary coolant	Lithium	Lithium
Intermediate/cycle	Na/steam	Na/steam
Maximum structure temperature, °C	500	620
Steam temperature, °C	292	442
Thermodynamic efficiency, %	30.1	34.4
Net electric power, MW	1420	1630
Blanket structure, vol.%	10	8
Number of coolant loops	4	4
Unit cost for first wall and blanket structure, $/kg	30	440
Cost of first wall and blanket structure, M$	16	138
Cost of the primary loop:		
Pumps and pump drives, M$	43	3 × 43
IHX, M$	34	3 × 34
Pipes (installed), M$	17	3 × 17

Systems studies provide a means to help resolve some of these choices. The purposes of this paper are: 1) to describe some important results from an integrated systems studies effort at Argonne National Laboratory [1]; and 2) to describe the results of a comparison study on developing maintainability in fusion power systems performed at McDonnell Douglas Astronautics Company [2]. The paper is limited to the work on tokamak power plants.

2. FIRST WALL AND BLANKET SYSTEM

The maintainability of the first wall/blanket is a critical factor in determining the economics of the power reactor. A successful design and technology development strategy must focus on the goal of reducing the economics impact and requirements of the maintainability for the first wall/blanket. The most effective means to achieve this goal are: 1) to reduce the frequency of required replacement, i.e. by increasing the lifetime of the structural material; and 2) to reduce the downtime and cost associated with the first wall/blanket replacement. These two means are discussed, respectively, in Sections 2.1 and 2.2 below.

2.1. Selection and Development of the Structural Material

The only suitable structural material with an existing qualified industry is stainless steel. Recent studies [3,4] indicate that the first-wall life for stainless steel may be limited to an integral wall loading of $\sim$ 3-5 MW•yr/m^2 at a maximum operating temperature of $\sim$ 500°C. It is therefore necessary to explore the possibility of developing advanced structural materials with better material properties. The refractory alloys offer a good potential. A major disadvantage of the refractory alloys is a high material plus fabrication cost compared with stainless steel. Therefore, a fundamental question that needs to be resolved is whether the costly development of refractory alloys will result in a pay-off in terms of lower cost of energy. This study attempts to answer this question by comparing the economics of stainless steel and the refractory alloys as structural materials in tokamak reactors.

A reference lithium-cooled reactor whose major parameters are shown in Table I was selected. Two cases were considered. The first employs stainless steel as the structural material with conventional materials throughout the heat transfer and transport system. In the second case, a vanadium alloy is employed in the first wall, blanket structure, and primary coolant loop piping and pumping. "Switching" of materials from vanadium to conventional materials is made in the intermediate heat exchanger (IHX) such that the primary coolant is always in contact only with the refractory alloy. The intermediate coolant loop, steam generators, and turbines are built with conventional, relatively inexpensive materials. The reference parameters for the two cases are shown in Table II.

A meaningful comparison of stainless steel and refractory alloys must carefully consider several key variables. The first is the lifetime of the structure. Our analysis shows that the lifetime of stainless steel for the operating conditions discussed here is $\sim$ 3 MW·yr/m^2. The lifetime of the vanadium alloy is longer but it cannot be predicted with good accuracy and is parameterized in this study. The second key variable is the total downtime required to replace the first wall and blanket structure. This downtime is essentially a weighting function for the importance of the longevity of the structural material. The magnitude of the downtime is extremely design-dependent. Table III shows the estimated downtime for replacement of the first wall and blanket in several conceptual designs. This downtime exceeds 100 days and can be as long as 500 days. Another key variable is the cost of the structural material. Table II shows the cost assumptions used in this study. The cost data for stainless steel were derived from the detailed work of the Prototype Large Breeder Reactor (PLBR). We have chosen the highest estimate projected for the cost of the vanadium alloy.

TABLE III. ESTIMATED DOWNTIME REQUIRED FOR REPLACEMENT OF THE FIRST WALL AND BLANKET IN SEVERAL CONCEPTUAL DESIGNS

Module Concept/Design	Downtime (days)
Large Module Concept	
UWMAK-I (remote maintenance)	354
CULHAM (remote maintenance)	128
Intermediate Module Concept	
UWMAK-III (remote maintenance)	112
UWMAK-III (partially contact operations)	111
Small Module Concept	
GA-DPR (remote maintenance)	558
GA-DPR (partially contact operations)	544
ORNL-DPR (remote maintenance)	131

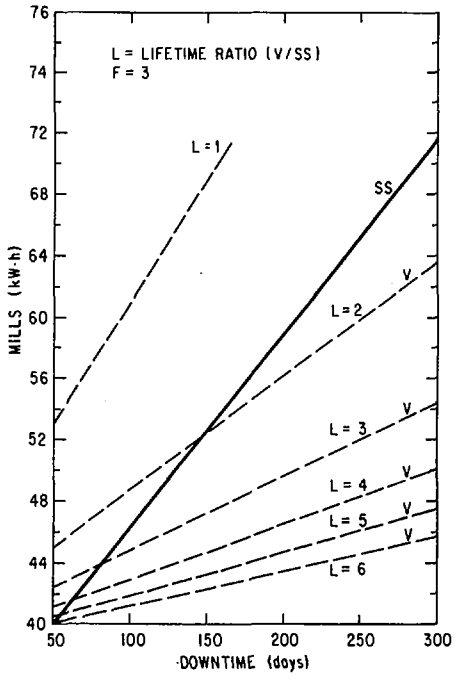


FIG. 1. Dependence of the cost of energy on the downtime for stainless steel structure and vanadium structure with lifetime ratio in the range 1–6.

Figure 1 shows the cost of energy as a function of downtime for the reference reactor with the above assumptions for stainless steel and vanadium alloy. The cost of energy for the vanadium case is shown for several values of L, the ratio of the lifetime of the vanadium alloy to that of stainless steel. The results in this figure show that: a) If the downtime is short, 50 days or less, the vanadium alloy is required to offer a factor of six or greater better life in order to be economically competitive with stainless steel. Therefore, the benefits of using a refractory alloy in this case will depend mainly on the lifetime advantage in excess of 20 MW•yr/m^2. Since lifetimes much longer than 20 MW•yr/m^2 cannot be assured prior to an extensive and costly experimental irradiation program, these short downtimes - if achievable - may render the development program for the expensive refractory alloys unwarranted. b) If the downtime is long, > 100 days, a significant saving in the cost of energy can be achieved by using the vanadium alloy provided that it offers a factor of 2.5 or more improvement in the lifetime of the first wall and blanket structure compared to stainless steel.

Table III shows that the downtime in tokamak reactors is most likely to greatly exceed 100 days. Furthermore, the available data [5] for vanadium and other refractory alloys, albeit limited, suggest strongly that these alloys are very likely to have a lifetime much greater than three times that of stainless steel. In addition, this study analysed the worst case for the refractory alloys in terms of the cost associated with their use. Therefore, one can conclude from this analysis that the benefit-to-cost ratio of a vanadium alloy, or a similar structural material, development program is high.

2.2. Scheduled Maintenance Requirements

In a recent maintainability analysis [2] of tokamak reactor concepts, the cost of scheduled maintenance for the first wall/blanket was assessed for both completely remote operations and partially contact (hands-on) operations. Existing conceptual designs were selected for analysis. These consisted of three baseline designs: large module concept - UWMAK-I; intermediate module concept - UWMAK-III; and small module concept - General Atomic Demonstration Power Reactor (DPR). Two alternate designs were also chosen. These are: the alternate large module - Culham Mark II concept; and the alternate small module - Oak Ridge Cassette concept. Major differences exist in the techniques required for accessing the first wall/blanket modules for the five concepts. In addition, the concepts, as defined in this study, employ different approaches to controlling plasma impurities.

In order to compare the impact of scheduled maintenance activities, candidate reactor designs were normalized to the same thermal power level, 5000 MW. The integral neutron wall load limit was set at 5 MW•yr/m^2. Downtimes were estimated for each concept as a function of the fraction of the first wall/blanket modules replaced per outage. Plant availability was estimated based on the scheduled first wall/blanket replacement downtimes plus an allowance for balance-of-plant scheduled shutdowns (28 days per year) and for all plant unscheduled shutdowns (65 days per operating year). These availability data are presented in Fig. 2. In some designs, a number of the accessing activities are of the same duration independent of the number of modules removed. For these designs, as the wall fraction replaced approaches 1.0, the relative effect of accessing time diminishes, resulting in the hyperbolic shape to the curves.

Of the five reactor candidates, the Culham concept possesses the highest availability, 74%, achieved with a replacement wall fraction per outage of 1/3.

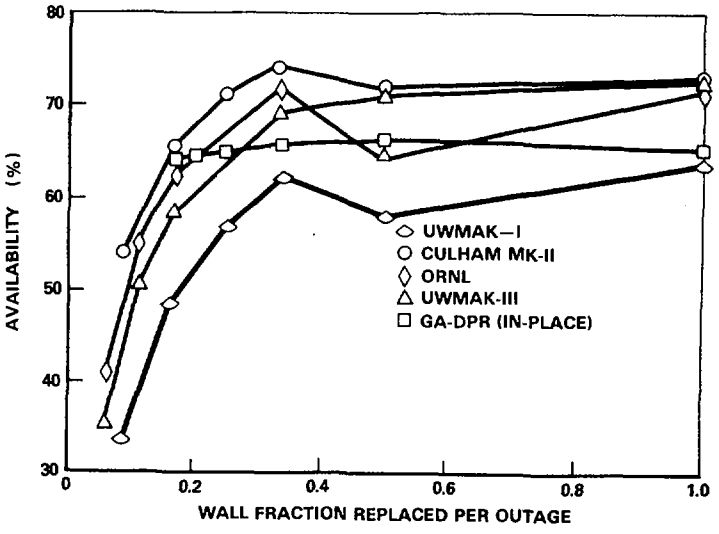


FIG.2. Plant availability factor as a function of wall fraction replaced per outage.

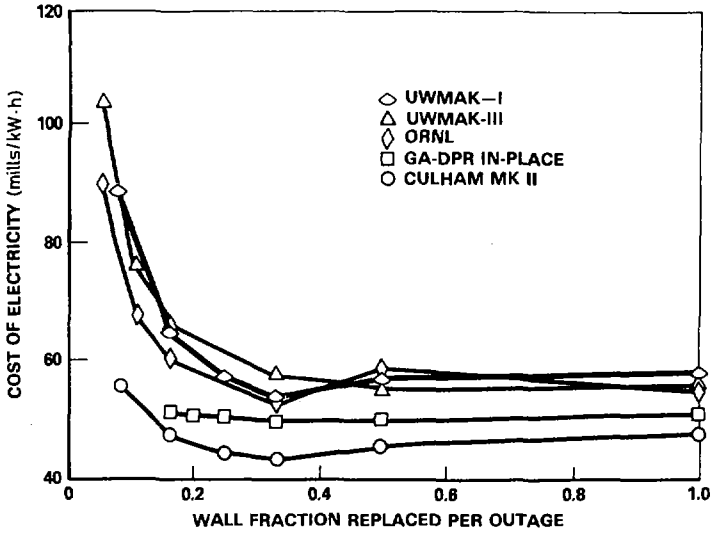


FIG.3. Cost of electricity as a function of wall fraction replaced per outage.

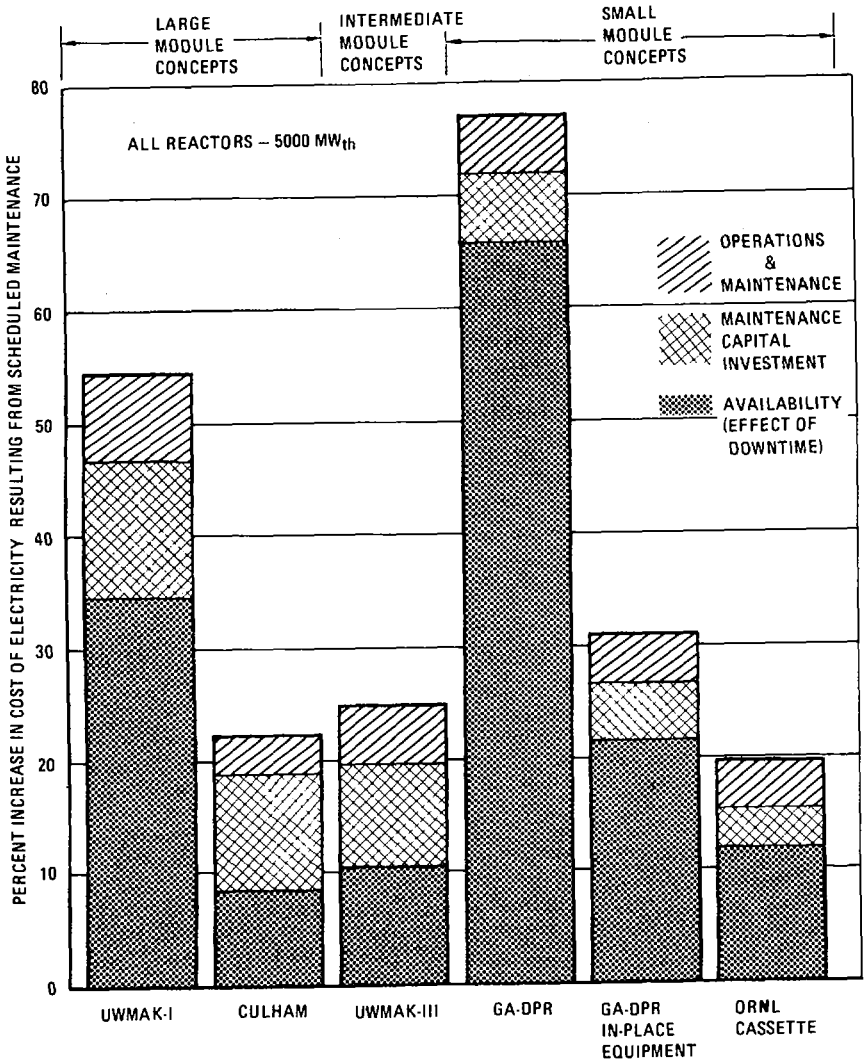


FIG.4. Impact of scheduled maintenance on cost of electricity (comparison of normalized reactors).

The impact of scheduled maintenance requirements on the cost of electricity is shown in Fig. 3. The elements affecting the cost of electricity are: maintenance equipment cost, maintenance facility cost, initial spares cost, labor and materials for replacement and refurbishment and plant availability. These data illustrate the dominant effect of availability.

The impact of scheduled maintenance for each of the five concepts is shown in Fig. 4. The impact is shown as a percentage increase to the cost of electricity relative to a plant designed for no reactor scheduled maintenance.

The total impact is made up of the annual operations and maintenance costs, the maintenance capital investment and the effect of availability. The wall fraction replaced per outage employed in this comparison is that fraction which results in the minimum cost of electricity for a particular concept. Availability is the dominant factor in all but the cases of Culham Mk-II and UWMAK-III. Examples of all three first-wall blanket module size categories - large, intermediate and small - have maintenance impacts in the 19-31% range. Three of these are below 26%.

The conclusions from this maintainability study can be summarized as follows: a) First-wall/blanket replaceable module size is not a discriminator in terms of minimizing the effect of scheduled maintenance on the cost of electricity; b) the wall fraction replaced per outage should be 1/3 or greater to minimize the effect of scheduled maintenance on the cost of electricity; c) the total effect of scheduled maintenance on the cost of electricity can probably be kept below 26% for commercial tokamak power systems; d) selection of design approaches for maintainability should be based on a careful evaluation of developmental and operational risks associated with the required remote maintenance equipment; and e) the use of partial contact (hands-on) techniques for scheduled maintenance operations resulted in improved availability for each of the three baseline reactor concepts. For two of the concepts, however, increased shielding costs and labor costs offset the benefit from availability. Unscheduled outage situations (reliability) should be given careful attention in ongoing tokamak power system studies.

3. POWER SUPPLY AND ENERGY STORAGE REQUIREMENTS

This section is concerned with analysing the power supply and energy storage system requirements for commercial tokamak fusion reactors. This activity is performed using an integrated systems approach whereby reactor design constraints and power supply characteristics are fully coupled to a detailed plasma burn cycle simulation code and to MHD equilibrium codes.

A conceptual design of a typical commercial tokamak reactor has been developed to serve as a test bed for the present study. This reactor has a 7-m major radius, a non-circular plasma cross-section (b/a = 1.3) and parameters of I_p = 11.6 MA, B^{TFC} = 8.6 T and β = 7%. The thermal output of the plasma is about 2300 MW. The ohmic heating (OH) coils are solenoidal with a midpoint radius of 2.5 M. The equilibrium field (EF) coils are located outside the TF coils and are decoupled from the OH coils. All coils are superconducting.

Several types of power supply/energy storage systems were examined ranging from the conventional, presently available, to those needing development. In general, substantial reductions in the power supply requirements and costs seem possible over previous estimates [1], because of a number of cost-saving techniques made plausible by some encouraging information from present tokamak experiments. Figure 5 shows the voltage and current waveforms for a burn cycle when a conventional power supply system is used. In this example both the OH and EF coils are driven by a thyristor type rectifier/invertor power supply both operating out of a motor-generator-flywheel (MGF) set. For the case shown, the OH current is ramped up in a time "Δt_{OH}" = 8 s. Neutral beam heating (100 MW) is applied from 8-15 s to bring the plasma to an ignited equilibrium. Some beam power ($\sim$ 15 MW) is also applied during the first and last second of the cycle to overcome some of the radiation losses due to oxygen impurities. Shutdown is accomplished by first reducing the DT fuel density and the plasma temperature (not shown) and then ramping

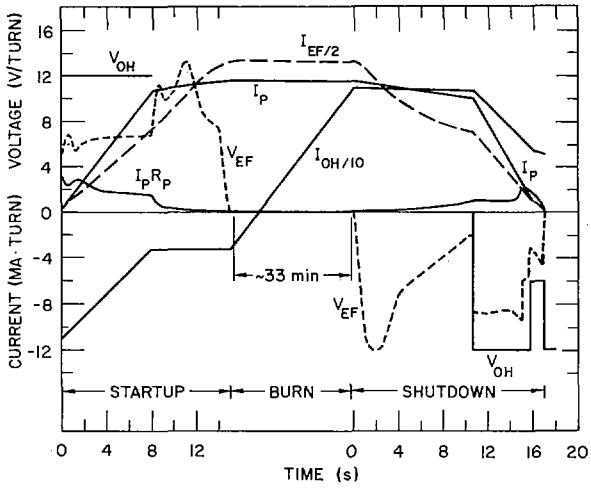


FIG.5. Voltage and current waveforms for a typical burn cycle using MGF set and thyristor OH and EF supplies.

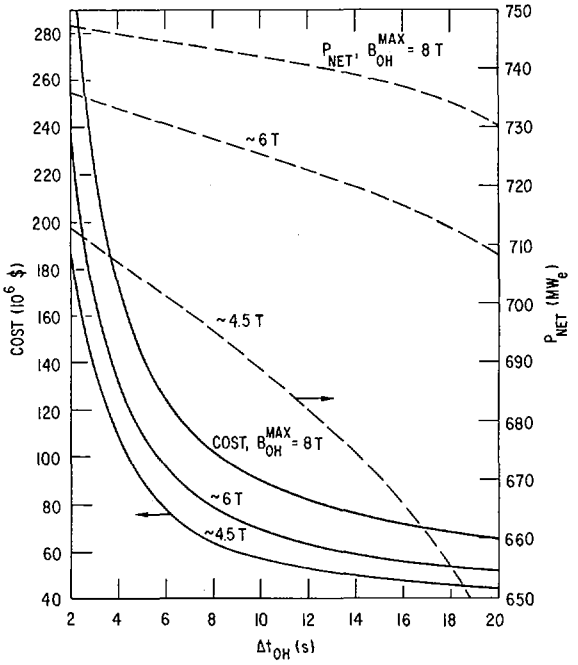


FIG.6. Power supply/energy storage system cost and net electrical power from the plant, as a function of OH startup ramp time, Δt_{OH}, and OH design field, B_{OH}^{MAX}.

down the OH current to bring down the plasma current and terminate the discharge. During the burn cycle the EF current must be adjusted in a way requiring active control of the EF voltage, as shown. For this example, the maximum power supply requirements are OH power = 1330 MVA, EF power = 351 MVA, and MGF stored energy = 12.8 GJ.

The effect of different startup densities, beam power levels, confinement scaling, impurity concentration, and several other parameters on the power supply requirements has been examined in detail. The most important single parameter has been found to be the OH startup ramp time. Figure 6 shows the cost of the power supply/energy storage system, for the conventional system described above, as a function of the ramp time, and for three assumed values of the maximum OH design field. This cost covers the MGF set and the OH and EF supplies but does not include the neutral beam supply. Figure 6 also shows the net electrical power from the reactor as a function of Δt_{OH} and B_{OH}^{MAX}. This net power takes into account the different burn times and duty factors obtainable as a function of the available OH flux swing. As shown, the cost is very sensitive to Δt_{OH} for short times. Previously, a range of Δt_{OH} = 2-4 s was considered optimum because shorter ramp times impose very high $\dot{B}$ and power levels while longer ramp times resulted in excessive resistive volt-second losses. Operation in this 2-s window tended to favor the use of a homopolar generator for the OH system because the cost of a homopolar generator is basically determined by the energy transferred and not the power level, exactly the opposite characteristic of a thyristor supply. Recent plasma physics experimental results that point to classical resistivity (no anomaly), less oxygen contamination and ease of low-density startup have now substantially extended what appears to be a feasible range of Δt_{OH}. Longer ramp times still use more resistive volt-seconds but not by an excessive amount. For these longer times, the power supply system cost is estimated in the $\sim$ 60-100 \$M range.

4. TRITIUM AND VACUUM SYSTEMS

The major effects of the tritium and vacuum systems on overall plant design obtained in our study are summarized below.

Fractional burnup has a substantial effect upon tritium inventories. The total tritium inventory in a 3000 MW(th) plant is in excess of 50 kg if the fractional burnup is 1.0%. Under these conditions, a breeding ratio of 1.20 is required for a doubling time of 5 years. The inclusion of an active impurity-removal mechanism on a tokamak, such as a divertor or a gas blanket, could result in a fractional burnup of the order of 1% or less [6]. On the other hand, if the fractional burnup is 2% or higher, tritium inventories will be 35 kg or less and a breeding ratio of 1.10 is sufficient to double the inventory in five years or less.

An item of considerable significance, from the standpoint of both safety and costs, is the emergency air detritiation system (EDS). The costs of such systems are primarily due to the reactor building volume and the permissible cleanup time. Our earlier studies [7] showed that the cleanup time should be no longer than about 48 hours. The required speed to attain this is about 0.5% of the reactor building volume per minute. Further, since the unit costs are about \$20 000 per m^3/min, the cost of the EDS is about \$100 per m^3 of reactor building. Since this is roughly half the cost of the reactor building itself, the EDS is a significant cost driver.

Compound cryopumps are assumed to be the primary torus vacuum pumps. A significant finding was that, because of the conductance losses imposed by the cryocondensation surfaces ahead of the helium cryopumps, the required helium pump speed may be in excess of the required DT pump speed.

Neutral beams require very high pumping speeds. It was found that the neutral beam vacuum system was a high-cost item [typically, 30-50 million dollars for a 3000 MW(th) reactor]. Getter pumps cost about the same as cryopumps for this application.

REFERENCES

[1] ABDOU, M. A., et al., "ANL Parametric Systems Studies," Argonne National Laboratory, ANL/FPP/TM-100 (1977).
[2] ZAHN, H. S., et al., "Developing Maintainability for Tokamak Fusion Power Systems," USA-DOE Report, COO-4184-4 (1977).
[3] FULLER, G. M., et al., "Fusion Reactor First Wall/Blanket Systems Analysis," McDonnell Douglas Astronautics Company-St. Louis, to be published as EPRI report.
[4] ABDOU, M. A., HARKNESS, S. D., et al., "The Establishment of Alloy Development Goals Important to the Commercialization of Tokamak-Based Fusion Reactors," Argonne National Laboratory, ANL/FPP/TM-99, and McDonnell Douglas Astronautics Company, MDCE-1743 (November, 1977).
[5] MATTAS, R. F., SMITH, D. L., "Model for Life-Limiting Properties for Fusion Reactor Structural Materials," Nuclear Technology 40 2 (1978).
[6] BADGER, B., et al., "UWMAK-III, A Non-circular Tokamak Power Reactor Design," University of Wisconsin, UWFDM-150 (1976).
[7] CLEMMER, R. G., et al., "Simulation of Large Scale Air Detritiation Operatings by Computer Modeling and Bench-Scale Experimentation," Argonne National Laboratory, ANL/FPP-77-3 (1977); also, Proc. 7th IEEE Symposium on Engineering Problems of Fusion Research, IEEE Publ. No. 77CH1267-4-NPS (1977).

DISCUSSION

F.R. SCHWIRZKE: Could you say what processes were assumed to limit (primarily) the life-time of the first wall? Was it structural damage induced by the neutron flux, or surface damage and impurity release due to plasma-wall interactions such as sputtering, blistering and so on?

C.C. BAKER: This study assumed a separate first wall and was concerned mainly with blanket life-time, as the blanket will probably be more difficult to replace than the first wall. The effects considered in connection with blanket life-time included radiation damage and the consequences of pulsed reactor operation. First-wall life-times and plasma-wall interactions do not have any direct effect on the blanket replacement time.

R.W. CONN: The first-wall temperature in the stainless-steel cases is assumed to be 500°C. It is possible to lower the first-wall temperature to 300–400°C and thereby achieve a substantial life-time increase. The outlet temperature of the coolant at the back of the blanket, where the neutron flux is low, can still be 500°C, so that the thermal efficiency would be preserved.

What impact would this have on your conclusions regarding the potential advantages of vanadium alloys relative to steels?

C.C. BAKER: This point was not explicitly considered in your study. However, I would expect that longer stainless-steel life-times would decrease F and increase L for conditions under which refractory alloys would compare favourably with stainless steel.

R.A. KRAKOWSKI: Could you say a little bit about the possible cost advantages of concepts that are sufficiently compact and modular to permit maintenance or replacement times of the order of days rather than hundreds of days – the range you have quoted for your tokamak studies?

C.C. BAKER: First, I doubt whether any fusion reactor concept would have replacement times of the order of days. I am certainly not aware of any. Secondly, as was mentiond earlier, the increment in the cost of electricity for the maintenance activities required by tokamak reactors can probably be kept to less than 25%. Therefore, other reactor concepts would have to be within 25% of the estimated cost of tokamak reactors to be in the same cost regime.

R.S. PEASE: Can you say specifically why the vanadium alloys used for your studies are believed to be more resistant to radiation damage than stainless steel?

C.C. BAKER: Life-times are determined by several factors, including radiation damage and resistance to pulsed reactor operation. The known mechanical properties of vanadium clearly indicate that it is more resistant to pulsed wall loadings. Irradiation data are not abundant, but the information available suggests that swelling and related effects will be much slighter than in stainless steel.

NEUTRAL-BEAM INJECTOR RESEARCH AND DEVELOPMENT WORK IN THE USA*

R.V. PYLE, W.R. BAKER, K.H. BERKNER, C.F. BURRELL, C.F. CHAN, W.S. COOPER, K.W. EHLERS, W.G. GRAHAM, D.B. HOPKINS, W.B. KUNKEL, D.J. MASSOLETTI, K.A. MILNES, H.M. OWREN, J.A. PATERSON, L. RUBY, R.R. SMITH**, J.W. STEARNS, W.F. STEELE, D.P. YEE
Lawrence Berkeley Laboratory (LBL), Berkeley, California†

O.A. ANDERSON, W.L. BARR, D.H. BIRDSALL, D.R. BRANUM, K.R. DeVORE, T.J. DUFFY, G.W. HAMILTON, E.B. HOOPER, Jr., R.W. MOIR, T.J. ORZECHOWSKI, L.C. PITTENGER, P. POULSEN, T.L. ROSSOW, M.E. SMITH
Lawrence Livermore Laboratory (LLL), Livermore, California†

M. GROSSMAN, C. LAM, R. LARSON, R. McKENZIE-WILSON, K. PRELEC, Th. SLUYTERS
Brookhaven National Laboratory (BNL), Upton, New York

G.C. BARBER, W.R. BECRAFT‡, C.W. BLUE, W.K. DAGENHART, R.C. DAVIS, C.A. FOSTER, W.L. GARDNER, H.H. HASELTON, J. KIM, C.M. LORING, M.M. MENON, S.L. MILORA, S. PONTE, P.M. RYAN, D.E. SCHECHTER, S.W. SCHWENTERLY, W.L. STIRLING, C.C. TSAI, J.H. WHEALTON, R.E. WRIGHT
Oak Ridge National Laboratory (ORNL)§, Oak Ridge, Tennessee
United States of America

* Work done under the auspices of the United States Department of Energy.
** Princeton Plasma Physics Laboratory, Princeton, New Jersey.
† University of California.
‡ General Electric Company, Oak Ridge, Tennessee.
§ Operated by Union Carbide Corporation for the United States Department of Energy.

Abstract

NEUTRAL-BEAM INJECTOR RESEARCH AND DEVELOPMENT WORK IN THE USA.

Neutral-beam injector research and development at the Brookhaven National Laboratory, Lawrence Berkeley and Lawrence Livermore Laboratories, and at Oak Ridge National Laboratory is described. – All neutral-beam systems for present and near-term applications are based on the acceleration and neutralization of positive ions. The research and development is carried out at LBL/LLL and ORNL. Present emphasis at LBL/LLL is on 80 to 120 kV systems for the mirror programme and for the TFTR and D III tokamaks. Present emphasis at ORNL is on 40 to 80 kV systems for the PLT, ISX, and PDX, and 80 to 200 kV systems for LPTT and TNS tokamaks. – Injectors for the future experiments and reactors may operate at energies of 200 keV or higher, especially for mirror machine applications, where positive-ion-based efficiencies will be very low, assuming no energy recovery. Research on negative-ion-based systems with potentially high efficiencies is carried out at BNL and at LBL/LLL and ORNL. The first demonstration of a high-power neutral beam based on negative ions is planned for 1980.

1. INTRODUCTION

The US neutral beam injector research and development work is carried out primarily at Department of Energy (DOE) Laboratories; The Brookhaven National Laboratory (BNL), The Lawrence Berkeley and Livermore Laboratories (LBL/LLL), and The Oak Ridge National Laboratory (ORNL).

High-power neutral beam systems based on positive-ion acceleration and neutralization have produced effective heating in recent confinement experiments [1, 2, 3]. For near-term applications, multi-megawatt neutral beam systems with particle energies up to 120 keV are in the testing phase. Systems using negative ions, for increased efficiency at high energies, are in the research phase, but are receiving increasing emphasis for applications in the mid-1980's. The development of suitable test facilities has been the pacing item in our program; four test stands with multi-megawatt capabilities at voltages above 100 kV are in operation or nearing completion.

2. NEUTRAL BEAM INJECTORS BASED ON POSITIVE IONS

2.1 LBL/LLL Neutral Beam Work

The Lawrence Laboratories Neutral-Beam Development Group's positive-ion-based work [4] proceeds along two lines: The first is required for the near-term applications: The presently identified applications, 2XIIB, TMX, MFTF, TFTR, and D III, require injection at energies up to 120 keV, ion currents per module up to 80 A, and pulse lengths to 0.5 sec. We have achieved 120 kV, 0.5 sec operation of a fractional-area (14 A) TFTR prototype source, and have tested a full-size TFTR source to 120 kV and 65 A for 20 ms. Half-second testing of the full-size TFTR source will begin in September 1978, when the High Voltage Test Stand (HVTS) is fully operational (section 4.4).

A first model of a fractional area, MFTF/DIII 80 kV source has been operated with 80 kV, 14 A, 0.5-sec pulses. No basic problems with the source designs have shown up; full-scale module tests will start soon. (The overall design and construction of the full-scale MFTF source has been carried out by MFTF personnel.)

The second part of our program is devoted to development for longer-term applications. The next few years will be devoted to increasing efficiency (ion species, gas, electrical), pulse length, energy (to 150 kV), and reliability. All of these items require major advances over present technology.

As part of this program we are developing a new generation of plasma sources with improved ion and electron confinement by cusp magnetic fields at the walls. These sources should have improved electrical efficiency and should produce ion beams with an enhanced atomic ion fraction. We are also developing the technology necessary for direct recovery of the energy of that portion of the beam which remains un-neutralized. The experiments to date, carried out with a 1 kW, 15 keV steady-state beam, gave 70% recovery efficiency. Electrostatic as well as magnetic fields were used for electron suppression. Recovery of a single species 10 keV H^+ beam using magnetic electron suppression gave over 85% recovery efficiency. Scaled up experiments on a 50 kW, 105 keV beam is underway with recovery efficiency over 20% initially, but decaying during the 500 msec pulse. The collector self-biased to a voltage over 75 kV. In the area of long-pulse operation, we are developing cathodes with d.c. capability, and have undertaken a computational analysis of secondary particle trajectories in the accelerator structure, which, together with experimental measurements, should permit us to identify and reduce the dominant heating mechanisms.

We are developing, through industrial vendors, techniques for manufacturing sources that are to be entirely hard sealed. Recently a method for brazing rectangular ceramic insulators to metal electrodes has been developed at LBL for use on the ion accelerators for TFTR [5].

New approaches to the design of electronics [6] and computerized controls [7] are included in the program.

2.2 ORNL Neutral Beam Work

The ORNL Plasma Technology Section participates in a variety of fusion plasma heating activities. Neutral beam injection systems have been designed for use on several state of the art tokamaks (PLT, [8] ISX, [9] PDX, LPT and TNS). The development and qualification of four PLT injection systems was recently completed with operating parameters of 0.75 MW (1 MW) neutral beam power per injector utilizing hydrogen (deuterium) extraction. Initial operation of four systems on PLT at about 2 MW neutral power produced record tokamak ion temperatures of about 5.5 keV.

ISX and PDX ion sources have been operated at plasma parameters consistent with 100 A extraction. A complete 100 A source is being assembled. The PLT injection system has been upgraded in pumping and will transport 50-60 keV neutral beams for pulses of 0.5 sec (0.1 sec) for PDX (ISX). The PDX system is in fabrication and assembly. LPT and TNS are in the conceptual phase and half-scale ion sources are under test in the 100 kV range, which will soon be extended to 150 keV.

An intense research and development program with modified three-grid duoPIGatron source [10] provided a dense (400 mA/cm^2), uniform (±5%), and quiescent (±10%) plasma from which 70 amperes of positive ions have been extracted at 40 kV. The source has also been operated using deuterium under similar conditions. Permanent magnets have been placed around the 2nd anode region to produce a cusp field which confines the plasma in a highly uniform manner. The source operation is characterized by moderate filament and arc power requirements, high gas efficiency (70%) and a high degree of reliability. The arc efficiency has been measured to be about 1 kW for every ampere of extracted beam. Although the source has generally been operated for pulse durations of 100 ms at 10% duty cycle, it has near dc capabilities, and 40 A pulses of 500 ms duration have been extracted. A smaller source has been operated for 10 s at 200 mA/cm^2.

An outstanding feature of the ORNL source is its ability to provide very high atomic yields, 85%. The high energy atomic fraction plays an important part in beam penetration and power deposition in a tokamak plasma. Control of the ion species will provide means of controlling the beam penetration to match the varying tokamak plasma density.

Initial experiments in energy recovery employing crossed magnetic field blocking of the electrons from the gas charge exchange cell have proved successful. The un-neutralized component is collected at ground potential. Energy recovery has been measured to be (40 ± 20)%. A 200 keV, 100 A positive ion source with c.w. capability and energy recovery is in the design stage. The entire 200 keV beam line is being redesigned to insure a high efficiency system. Such a positive ion system with direct recovery efficiency of 80% might well satisfy the injector requirements for heating future reactor size tokamaks.

Future research and development plans also include simplifying and increasing the reliability of 40 to 80 keV injector systems.

Computer simulations [11] are available and are found to be an extremely valuable aid in every phase of this program, both in predicting and verifying systems performance.

3. NEUTRAL BEAM INJECTORS BASED ON NEGATIVE IONS

3.1 BNL Negative Ion Activities

The objective of the BNL program is to develop multiampere (equivalent) high-energy injection systems based on direct extraction from negative ion plasma sources. Two types of direct extraction negative ion plasma sources have been extensively investigated, namely the magnetron source and Penning type source. Several improvements were implemented on these sources, which are basically of the cold cathode type operating in a mixture of deuterium gas and cesium vapor. These improvements (independent cesium vapor control, constant gas flow during the beam pulse, cooling of the cathode) together with extensive probe and spectroscopic studies of the plasma parameters (such as plasma and gas densities as well as atom energy distributions) enabled us to improve our fundamental knowledge of the negative ion creation and to construct a multiampere negative ion plasma source for extracted beam currents between 1-2 A in beam pulses up to 50 ms [12].

Negative ion acceleration and beam transport are being studied on a 150 kV test stand. Two accelerator systems have been investigated, the

close coupled geometry in which 1 A beams have been accelerated across a 2 cm accelerating gap and a system with the accelerator separated from the source and extractor by a bending magnet. Beam transport studies include the effects of space charge neutralization and beam focussing by means of a quadrupole doublet.

Neutralization of negative ion beams will initially take place with gas jets, being the simplest neutralizer to realize with relatively high (up to 60%) neutralization efficiency. A CO_2 effusive gas jet was constructed and its gas-dynamical properties analyzed.

3.2 LLL/LBL Negative Ion Activities

The LLL/LBL negative ion development effort is oriented toward longer-term applications requiring efficient neutral beam systems at energies well above 120 keV. Most of these systems probably will require the production and acceleration of large currents of negative ions. Two of our goals are the demonstration of a 200 kV, 5 A (D^o), long pulse system by 1980, and a 400 kV, 20 A (D^o), dc system by 1983.

The production of negative hydrogen ions by double charge exchange in cesium or other vapors offers the possibility of being scalable to arbitrarily large currents and long pulse lengths. We start with a 1 keV D^+ beam, of which somewhat more than 1 A passes through a cesium charge-exchange cell. The measured conversion efficiency is about 20%, in reasonable agreement with the value of 24% obtained in an atomic collision experiment. The plasma produced in the charge exchange cell is greatly reduced by flow transverse to the propagating (1 keV) beam, so the random electron current is less than the beam current. A 100 mA negative deuterium beam produced in this way has been accelerated to 60 keV. The accelerator was designed to yield good beam optics over a wide range of currents; in the present case $\pm 2.5^o$ divergence was obtained [13].

The production of beams by this method requires the propagation of low energy positive and negative ions distances of order of a meter in a low gas pressure environment. Analysis of the background plasma indicates that for such a case, space charge effects tend to expand positive ion beams significantly. This is reflected by difficulties in obtaining high quality, 1 keV D^+ beams. The analysis also shows that negative ion beams should be weakly confined by the space charge forces, and the low energy negative ion beam is observed to propagate with low divergence. Analysis of angular scattering in the charge-exchange process shows that the effect is small at 1 keV, but may become important at low beam energies.

Alternative techniques for producing negative ions are being studied, including surface and volume production in plasmas confined by magnetic-multipole fields.

3.3 ORNL Negative Ion Activities

The ORNL negative ion program is directed toward small scale experiments to develop negative ion plasma generators. Simultaneously, we are making a complete neutral beam line study for both positive and negative ion based systems in order to evaluate the relative merits of each and thereby determine a realistic efficiency for each system as a function of beam energy.

Two experiments, both employing direct negative ion extraction, are under study. The first utilizes the duoPIGatron ion source with a system of cesiated chevrons or vanes, on which the positive ions in the plasma generator impinge, placed directly above the extraction grids. Both electric and magnetic fields are used to reduce the flow of electrons to the grids. One ampere of unanalyzed beam has been extracted from this source. The second experiment utilizes a Calutron ion source employing a hot filament Penning discharge. Positive ions from the discharge are accelerated into a cesiated molybdenum surface which has independent temperature control. The arc discharge voltage, the energy of the positive ions striking the molybdenum surface and the cesium oven temperature are all independently controlled, which permits determination of optimum source performance. Preliminary results from the source have been achieved in both a pulsed mode, about 100 msec, and a c.w. mode, about 20 sec. About 60 ma/cm^2 of H^- have been observed in pulsed mode. For the c.w. mode, limitations in the arc power supply required lower discharge power and consequently lower output current, about 30 ma/cm^2. The gas efficiency in the c.w. mode was measured to be 4%.

Future plans are to extend either or both of these sources to 1 A H^- output and design a 10 A version for extraction at 50 keV. At this time, a complete beam system will be developed based on criteria determined from the system studies now under way. Beam systems of 100's keV are also being contemplated. However, the extracted beam density will be limited to approximately 100 ma/cm^2.

4. TEST FACILITIES

4.1 General

A large part of our effort in recent years has been the development of suitable test facilities. In the process of designing and constructing them it has been necessary to develop new concepts and components for the high power electronic circuits, and new diagnostic techniques. Two neutral beam facilities (HVTS at LLL, NBSTF at LBL) will have sufficient neutron shielding to permit extensive operation with deuterium.

4.2 BNL Facilities

A 1 ampere, 150 kV, 0.01 second, cryopumped facility is operating, and a 10 A, 250 kV, 0.1 sec, test stand is under construction.

4.3 LBL Facilities

Two beam lines with 120 kV electronics, one capable of operating at 15 A, 0.5 s, the other at 65 A, 30 ms, are in operation. Electrical, thermal, and optical diagnostics with on-line data analysis are used. Computer control of power supplies for semi-automatic source conditioning is installed. The Neutral Beam System Test Facility (NBSTF) for testing TFTR components and systems (120 keV, 65 A, 0.5 sec) will start operation early in 1979. It will be converted to a general Research and Development Facility about three years later.

4.4 LLL Facilities

A 100 kV, 1 A, 10 ms test stand is operational, and the High-Voltage Test Stand (HVTS) with 200 kV, 20 A, DC, or 120 kV, 65 A, 30 s, or 80 kV, 80 A, 30 s capability is nearly operational.

4.5 ORNL Facilities

The Medium Energy Test Facility has been used to test PLT beam line systems and is currently in use for R & D ion sources and system tests for ISX and PDX beam lines. It is a cryopumped system with electrical, thermal and optical diagnostics. A 60 kV, 60 A, 2 sec (10% duty cycle) power supply is presently in use. Modifications are under way to upgrade to 80 kV, 100 A, 20 s. It will be further modified to 120 kV, 100 A, 30 s capability in about 1 year. A PDP-11/40 is used for computer monitoring of the entire beam line on a shot basis. A study is under way to extend this to a computer controlled system.

A second test facility in operation is the High Energy Test Facility. This is a 7 M long diffusion pumped system with a 168 kV, 50 A, 20 sec (10% duty cycle) power supply. Design modifications are under way to convert to cryopumping and increase the beam energy capability to 200 keV. This facility has identical diagnostic and computer capability as the Medium Energy Test Facility.

REFERENCES

[1] SIMONEN, T. C., et al., Seventh International Conference on Plasma Physics and Controlled Nuclear Fusion Research, Innsbruck 1978, paper IAEACN-37/J-1.

[2] MURAKAMI, M, et al., "Plasma Confinement and Impurity Flow Reversal Experiments in the ISX-A Tokamak", Seventh Internation Conference on Plasma Physics and Controlled Nuclear Fusion Research, Innsbruck 1978, paper IAEA-CN-37-N-4.

[3] STODIEK, W., et al., Seventh Internation Conference on Plasma Physics and Controlled Nuclear Fusion Research, Innsbruck 1978, paper IAEA-CN-37/C-3.

[4] The Positive Ion Portion of the LBL/LLL Neutral Beam Program Workshops on Neutral Injectors, Culham, England, June 26-30, 1978.

[5] PATERSON, J. A., et al., "The Design and Fabrication of an Ion Accelerator for TFTR-Type Neutral Beam Systems". Proceedings of the 7th Symposium on Engineering Problems of Fusion Research, Knoxville, Tennessee 1977.

[6] HOPKINS, D. B., et al., "The Lawrence Berkeley Laboratory Power Supply System for TFTR Neutral Beam Source Development", ibid., pg., 1570.

[7] SHALZ, L. L., et al., "A Computer Based Diagnostic and Control System for a 120 keV Neutral Beam Test Stand", ibid., pg. 1549.

[8] DAGENHART, W. K., et al., "Development and Testing of the ORNL/PLT Neutral Beam Lines for the Princeton Large Torus", IEEE 7th Symposium on Engineering Problems of Fusion Research, Knoxville, Tennessee (1977).

[9] STIRLING, W. L., et al., "The New ORNL Neutral Beam Transport System," IEEE 7th Symposium on Engineering Problems of Fusion Research, Knoxville, Tennessee (1977).

[10] TSAI, C. C., et al., "DuoPIGatron Ion Sources for PLT Injectors," IEEE 7th Symposium on Engineering Problems of Fusion Research, Knoxville, Tennessee (1977).

[11] WHEALTON, J. H., et al., "Optics of Single-Stage Accelerated Ion Beams Extracted from a Plasma," Rev. Sci. Instrum. 48, No. 7, 829 (1977).

[12] PRELEC, K., "Development of H^- Sources at Brookhaven National Laboratory, Proceedings of the Symposium on the Production and Neutralization of Negative Hydrogen Ions and Beams, Brookhaven National Laboratory, September 26-30, 1977, pg. 11.

[13] HOOPER, E. B., Jr., ANDERSON, O. A., ORZECHOWSKI, T. J., and POULSEN, P., "Sixty keV D^- Beams Using Double Charge-Exchange System," Proceedings of the Symposium on the Production and Neutralization of Negative Hydrogen Ions and Beams, Brookhaven National Laboratory, September 26-30, 1977, pg. 11.

Session R

TECHNOLOGY AND REACTOR CONCEPTS II

Chairman

J.F. CLARKE
USA

Papers R-5-1 and R-5-2 were presented
by P.E. Stott as Rapporteur

CONCEPT OF TOKAMAK-TYPE REACTOR WITH HIGH-TEMPERATURE BLANKET

N.N. VASIL'EV, V.E. LUKASH, A.V. NEDOSPASOV,
L.B. NEFEDKINA, V.G. PETROV, M.Z. TOKOR
Institute of High Temperatures of the
USSR Academy of Sciences, Moscow
B.N. KOLBASOV, D.K. KURBATOV, V.V. ORLOV,
V.I. PISTUNOVICH, G.E. SHATALOV
I.V. Kurchatov Institute of Atomic Energy, Moscow,
Union of Soviet Socialist Republics

Presented by B.B. Kadomtsev

Abstract

CONCEPT OF TOKAMAK-TYPE REACTOR WITH HIGH-TEMPERATURE BLANKET.
A design study for a tokamak reactor with a high-temperature blanket is presented. It is expected that such a reactor, whose structure is more complicated than that of a low-temperature one, may be used as a source of high-temperature heat as well as for, e.g. hydrogen production from water. Parameters of such a device are given.

INTRODUCTION

Some time ago, the Institute of High Temperatures of the USSR Academy of Sciences, in co-operation with the Kurchatov Institute of Atomic Energy, developed the concept of a tokamak reactor with high-temperature blanket. Such a reactor can probably be used as a source of high-temperature heat for electric power plants with highly effective energy conversion as well as for technological purposes, such as hydrogen thermochemical production from water.

1. FUSION POWER PLANT WITH MHD GENERATORS

The TVE-2500 project completed in 1976 was based on the use of MHD generators to convert the thermal energy produced by a tokamak reactor into electricity. The purpose of this project was to evaluate the characteristics of the main equipment (first of all, those of a fusion reactor) as well as to study the feasibility of high-efficiency conversion systems at such power plants [1].

The major characteristics of the plant are summarized in Table I.

Electric power is generated by two MHD units, either of them comprising the MHD generator proper, a steam generator with a steam turbine, a compressor, auxiliaries and heat equipment.

TABLE I. MAJOR PARAMETERS OF FUSION POWER PLANT WITH MHD GENERATORS

1. Electric output (net) (MW)	2410
2. Efficiency	0.5
3. Working fluid (neon + 0.05% Cs) at the MHD generator inlet	
Temperature (K)	2000
Pressure (bar)	9.3
4. Operating mode	base load
5. Plant area (excluding sanitary-protective zone) (km^2)	0.3

TABLE II. MAJOR PARAMETERS OF FUSION REACTOR FOR MHD POWER POWER PLANT

1. Type of reactor	Circular-chamber tokamak with ignition
2. Thermal output (MW)	4800
3. First-wall neutron flux (14.2-MeV neutrons) ($n \cdot cm^{-2} \cdot s^{-1}$)	0.7×10^{14}
4. Magnetic field on axis (T)	5.0
5. Plasma heating method	Injection of hot neutrals (E = 600 keV, I = 200 A)
6. Re-fuelling method	DT pellet injection
7. Exhausting method	a) divertor b) turbulent plasma blanket
8. Operating cycle parameters(s)	
Burning phase	4000
Pause	50
9. First-wall material	molybdenum
10. Blanket composition	$LiAlO_2$ + C + ZrC + stainless steel
11. Tritium breeding ratio	0.93

TABLE III. PLASMA PARAMETERS OF FUSION REACTOR FOR MHD POWER PLANT

1. Minor plasma radius (m)	4.4
2. Aspect ratio	2.7
3. Poloidal beta	1.35
4. Stability factor	2.5
5. Temperature (keV)	
Ions	13
Electrons	14.5
6. Density (m^{-3})	
Fuel	1.25×10^{20}
Helium	1×10^{18}
7. Confinement time(s)	
Particles	4.8
Energy	2.9
8. Burnup (%)	2
9. Total thermal energy of plasma (GW)	2.4

The major characteristics of the reactor are listed in Table II.

The calculations of plasma parameters have been carried out in a zero-dimensional approach. It has been obtained that the so-called "self-maintaining" ignition mode could be realized by means of turbulent plasma behaviour due from trapped-particles instabilities. The time necessary for a startup of the reaction is 13–15 s. The results of the plasma parameter calculations are shown in Table III.

Re-fuelling is accomplished by injection of DT ice pellets with a velocity of 10 $km \cdot s^{-1}$. Acceleration estimates have shown that the re-fuelling system energy consumption equals 3–5 MW.

Two methods of unburned-fuel and ash evacuation from the reactor chamber have been considered in the project:

a) Use of a poloidal divertor with a single X-point;

b) use of a turbulent-plasma blanket.

In the latter case, it has been shown that if somehow plasma turbulence can be created in the near-wall layer, the energy of the particles bombarding the wall may be decreased below the sputtering threshold of the wall material.

Exhausting of the chamber, in this case, can be accomplished through a number of ports in the wall. The necessary perforation factor equals ~2%.

Neutronic calculations of the reactor have been conducted by means of the analysis described in Refs [2, 3].

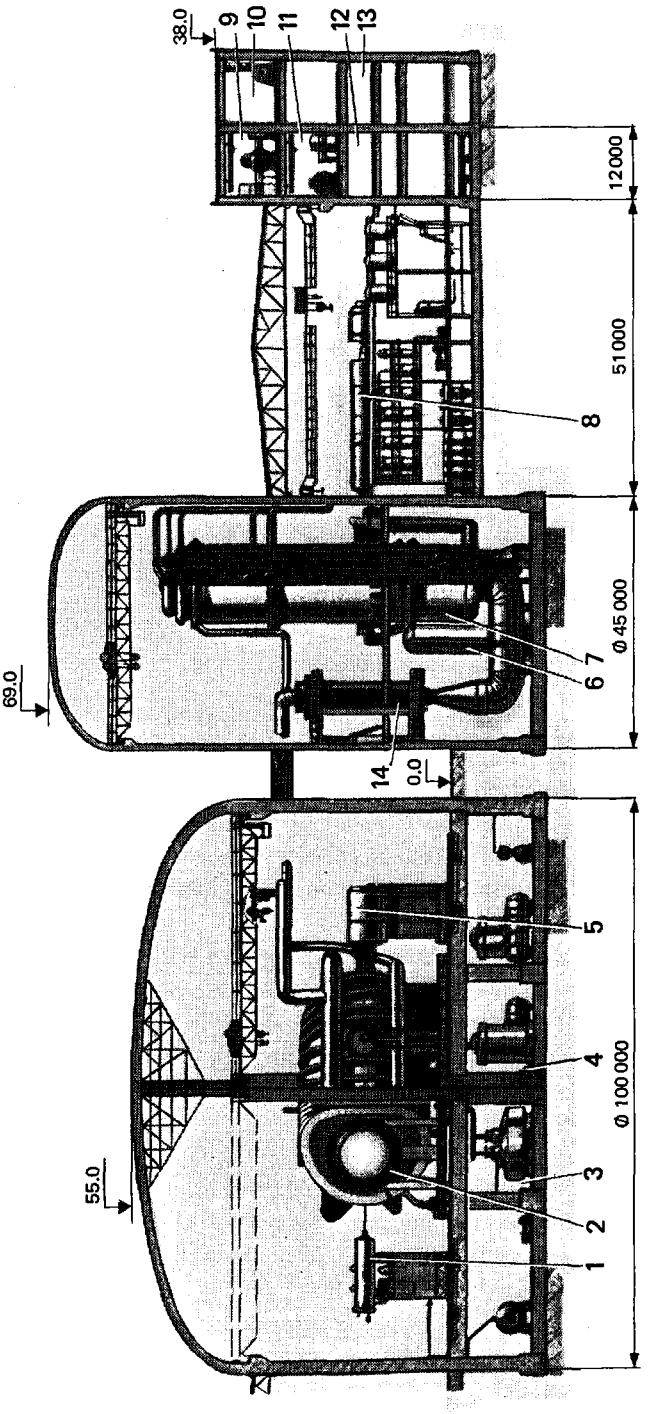


FIG.1. Lay-out of TVE-2500 plant: 1 – fuel injection gun; 2 – tokamak-type reactor; 3 – tritium injection recovery system box; 4 – cryogenic system box; 5 – injector of neutrals; 6 – heat sink; 7 – steam generator; 8 – steam turbine; 9 — de-aeration room; 10 – venting gallery; 11 – de-activation service room; 12–13 control boards; 14 – MHD generator.

The reactor structure is chosen to be a modular one. The number of modules equals 36. The toroidal magnetic field is produced by 36 D-shaped coils. Nb_3Sn stabilized by copper and re-inforced by stainless steel is used as superconducting material. The same material is used for transformer and divertor windings, etc.

A so-called "separate" lay-out of the plant main equipment is chosen in the TVE-2500 project (see Fig.1). This type of lay-out simplifies the solution of the radiation safety problem during repair and routine maintenance which can be probably much more complicated than that for modern plants with fission reactors.

2. FUSION POWER-TECHNOLOGICAL PLANT FOR THERMOCHEMICAL HYDROGEN PRODUCTION FROM WATER

One of the problems to be solved for future energetics is the problem of large-scale and cheap hydrogen production from water. This hydrogen may be used as a suitable energy carrier as well as a raw material for chemical industry and for synthetic fuel production. Such a large-scale hydrogen production will demand sufficient energy consumption. The analysis carried out has shown that in this case it can be worth the expenses to use thermochemical cycles directly converting thermal into chemical energy.

Reported in this paper are some results of a feasibility study of the tokamak reactor with high-temperature blanket for the purposes mentioned above.

The analysis has been completed for the thermochemical cycle proposed by C. Marchetti and G. De Beni in 1970 [4]:

$$C + H_2O \rightleftharpoons CO + H_2$$

$$2\,Fe_3O_4 + CO \rightleftharpoons C + 3\,Fe_2O_3$$

$$3\,Fe_2O_3 \rightleftharpoons 2\,Fe_3O_4 + \frac{1}{2}\,O_2$$

(The necessary temperature level for the last reaction is about 1500°C.)

The technological scheme of the plant is depicted in Fig.2. It is assumed that such a plant would generate electricity together with hydrogen production.

The characteristics of the reactor have been chosen by using experience acquired in the design of the TVE-2500 project.

Helium was chosen as a primary-loop coolant. An intermediate heat exchanger is provided in the schematic to eliminate radioactive products penetration from the coolant into the technological loop. Even if we assume that this heat exchanger is made of heat- and corrosion-resistant steels, it seems doubtful whether the temperature level of the heat-exchanging surfaces will

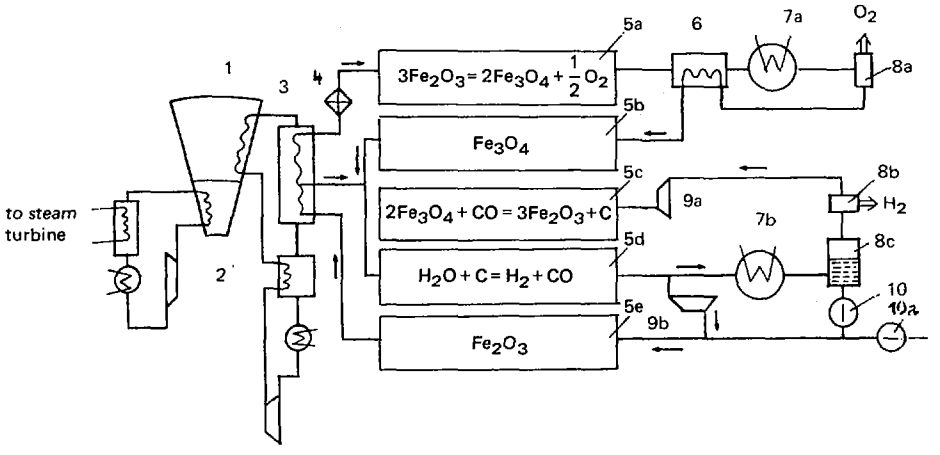


FIG.2. Power-technological schematic of plant: 1 – high-temperature zone of tokamak-type reactor blanket; 2 – low-temperature blanket zone; 3 – heat exchanger; 4 – plasmatron; 5a–5e – chemical vessels — heat regenerator; 6 – recuperator; 7a–7b – heat sinks; 8a–8c – separating systems; 9a–9b – compressors; 10–10a – water pumps.

TABLE IV. MAJOR CHARACTERISTICS OF HIGH-TEMPERATURE FUSION REACTOR FOR HYDROGEN PRODUCTION BY MEANS OF WATER DECOMPOSITION

1. Thermal output (GW)	6.86
2. First-wall neutron flux (14.2-MeV neutrons) ($n \cdot cm^{-2} \cdot s^{-1}$)	2.1×10^{14}
3. Typical size:	
Major radius of torus, R (m)	10
Minor radius of torus (m)	2.2
Ellipticity	2
Minor radius of plasma, a (m)	2
4. Toroidal magnetic field on axis (T)	5
5. Stability factor	2.5
6. Poloidal beta	3.58
7. Confinement time(s)	
Particles	1.5
Energy	1.18
8. Maximum magnetic field in toroidal coils (T)	11
9. Number of toroidal field coils	16

exceed 1200°C. Considering this fact, an additional electric-arc heating is provided in the water vapour of the technological loop. Decreasing the primary-loop coolant temperature down to 1200–1400°C (compared to the TVE-2500 project) allows the structure of a blanket to be simplified. Estimates show that the efficiency of this plant can reach 40%.

A preliminary analysis of the reactor plasma parameters has been carried out by means of a zero-dimensional turbulent-plasma model. It revealed that the use of a so-called "finger-ring" plasma shape can lead to operating modes with ignition characterized by high first-wall specific leading and moderate levels of thermal output. To obtain such modes it is necessary to use a turbulent plasma blanket as described in Ref.[5].

More detailed computations of steady-state modes have been performed by means of a one-dimensional time and space model of turbulent reactor plasma [6]. It has been assumed for the computation that energy and particle transfer is due to turbulent diffusion resulting from the development of thermal-drift [8] and trapped-particle instabilities [7]. The effect of magnetic field ripples has also been considered [9].

The characteristics of the reactor are listed in Table IV.

CONCLUSION

The design study results reported in this paper concern only a few of several possible ways of using a high-temperature fusion reactor.

The results show that, from the point of view of structure, such a reactor is more complicated than an ordinary low-temperature one, aiming at the production of electricity by means of a steam power cycle.

The development of units and aggregates for such a reactor (in particular, the blanket) is also more difficult and costly, but this complication may be worth the expense if the use of a high-temperature reactor were to solve the power-technological problems and in particular were to provide high-temperature heat, the proportion of which in the total energy balance at the beginning of 21st century is expected to be rather high. Furthermore, the experience to be gathered in developing the high-temperature technology in the energetics of the 20–30 years to come (open-cycle MHD generators, high-temperature gas-cooled fission reactors, etc.) will, to a considerable extent, be useful in the design of a high-temperature fusion reactor.

REFERENCES

[1] VASIL'EV, N.N., LUKASH, V.E., NEDOSPASOV, A.V., et al., Thermonuclear Power Plant with High-Temperature tokamak-type reactor, All-Union Conf. Energy Problems of Thermonuclear Reactors, Leningrad (1977).

[2] MARIN, S.V., MARKOVSKIJ, D.V., SHATALOV, G.E., Ehnerg. Transport 6 (1976).
[3] KURBATOV, D.K., SHATALOV, G.E., VASIL'EV, N.N., NEDOSPASOV, A.V., Tritium Regeneration and Energy Generation in the Reactor Blanket of a Thermonuclear Power Plant with Direct Conversion of Heat into Electrical Energy (with MHD Converter), Preprint IAEh-2670 (1976).
[4] DE BENI, G., MARCHETTY, C., Hydrogen 9 2 (1970) 16.
[5] VASIL'EV, N.N., NEDOSPASOV, A.V., PETROV, V.G., TOKOR, M.Z., Heat and Particle Transport to the Wall of a Tokamak Reactor, in Controlled Fusion and Plasma Physics (Proc. 8th Europ. Conf. Prague, 1977).
[6] VASIL'EV, N.N., LUKASH, V.E., One-Dimensional Model of Reactor Tokamak Plasma, Preprint 7-017 (1977).
[7] KADOMTSEV, B.B., POGUTSE, O.P., Nucl. Fusion 11 (1971) 67.
[8] KADOMTSEV, B.B., POGUTSE, O.P., Turbulent Processes in Toroidal Systems, Problems of Plasma Theory, Atomizdat (1967) 209.
[9] DNESTROVSKIJ, Yu., KOSTOMAROV, D.P., LYSENKO, S.E., Nucl. Fusion 15 (1975) 1185.

DISCUSSION

R.A. KRAKOWSKI: In certain respects – minor radius, beta, total power and so on – the designs you have been discussing are about twice as conservative as recent tokamak designs in the United States. Do you think this conservatism is a consequence of the special, non-electrical applications of these designs, or of some basic difference in design philosophy between the American and Soviet design groups?

B.B. KADOMTSEV: No, I think that the more conservative plasma parameters used here were chosen simply to make this part of the conceptual design more reliable.

D. PALUMBO: Why were circular cross-sections chosen for the reactor which is to generate electric power and elongated cross-sections for the other two reactors?

B.B. KADOMTSEV: Non-circular cross-sections were chosen for the concepts incorporating divertors.

C.C. BAKER: What fusion concepts other than tokamaks have you considered for hybrid and high-temperature blanket applications?

B.B. KADOMTSEV: Preliminary consideration has been given to mirrors, laser fusion and relativistic electron beams.

C.C. BAKER: How does the cost of the hybrid-bred fissile fuel compare with the cost of fissile fuel from fast breeder fission reactors?

B.B. KADOMTSEV: Hybrid-bred fissile fuel has, by itself, a higher cost than the fuel produced by fast breeders, but in addition to this fuel the hybrid reactor will produce electric energy, so that the net product is expected to be economically acceptable.

K.H. SCHMITTER: Neutron-induced damage to the first wall in a high-temperature reactor might be very serious. What kind of first-wall material did you select and what was the estimated life of the first wall?

B.B. KADOMTSEV: Molybdenum is the material that has been proposed for the first wall, but its life-time in this application is not certain as yet.

F.L. RIBE: You say that plutonium production is more efficient than the production of ^{233}U, but I believe this would not be true of a 'mixed' blanket in which the 14-MeV neutrons are first multiplied in ^{238}U. Outside the inner region of the blanket, consisting of ^{238}U, there is a thorium region in which the neutrons are captured to produce ^{233}U. Let me refer you to paper R-4 in this connection.

TOKAMAK TNS STUDIES*

P.H. SAGER, Jr.
(GA TNS Study Team),
General Atomic Company,
San Diego, California

M. ROBERTS
(Oak Ridge TNS Study Team),
Oak Ridge National Laboratory,
Oak Ridge, Tennessee,
United States of America

Abstract

TOKAMAK TNS STUDIES.

Studies are being carried out at General Atomic Company and Oak Ridge National Laboratory to develop conceptual designs of tokamak fusion reactors for the TNS (The Next Step) programme. The primary purpose of these studies is to identify technical problems and to develop solutions to them. The TNS studies, initiated in 1976 under the sponsorship of the US Energy Research and Development Administration, have been directed to the development of designs of reactors which achieve ignition and plasma burns sufficiently long to study burn dynamics. The ORNL study has resulted in the design of a reactor with a D-shaped plasma which has a major radius of 5.0 m, a minor radius of 1.2 m, and a plasma elongation of 1.6. A toroidal β of 5% is achieved by adopting a flux-conserving mode of operation. The General Atomic design is based on the use of a Doublet plasma cross-section to achieve high β. This reactor design has a major radius of 3.6 m, a minor radius of 0.95 m, and a plasma height-to-width ratio of 2.7. Both designs have a plasma volume of approximately 225 m^3 and a peak power in the 700–1000 MW(th) range. The current ORNL TNS reactor is designed for a plasma burn of 16 seconds, and the GA reactor is designed for a burn of 30 seconds. While the ORNL reactor is designed for a comparatively modest duty factor of 0.05, the GA reactor is designed for a duty factor of 0.5 and includes a blanket and power conversion system to produce a nominal amount of electric power. The costs of the current TNS reactors are estimated to be in the range of US $400 – US $600 million without escalation and specific supporting research and development.

1. INTRODUCTION

During the period 1974 - 1976, scoping [1-3] and conceptual design studies [4-6] were conducted for a tokamak experimental power reactor (EPR) at Argonne National Laboratory, General Atomic Company, and Oak Ridge National Laboratory.

* Work supported by US Department of Energy; GA Contract EY-76-C-03-0167, Project Agreement 38, ORNL Contract W-7405-ENG-26.

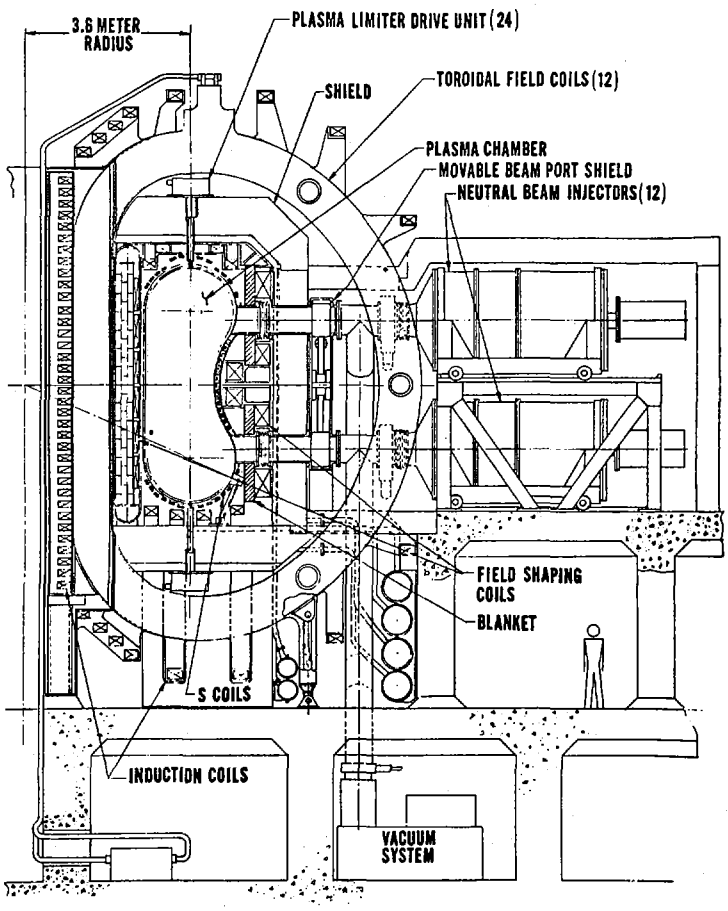


FIG.1. General Atomic 3.6 m TNS reactor.

In these studies, the characteristics of experimental power reactors designed to produce electrical power in a power reactor mode were derived [7], along with construction schedules and cost estimates. The results of these studies indicated that an EPR would cost of the order of $1 billion without escalation and supporting R&D. Moreover, in order to meet the target operational date in the mid-to-late 1980s, a decision to proceed with the EPR program would have had to be made immediately. It was concluded that the risks were too great to embark on such an ambitious program without further experimental information and an examination of alternatives.

Accordingly, in 1976 TNS (The Next Step) study programs were started at General Atomic and Oak Ridge National Laboratory under the sponsorship of the U.S. Energy Research and Development Administration. During the first year of this study, a range of design options and a variety of physics and technology problems were explored [8,9,10]. These studies led to the identification of the reactor concepts currently under study.

The primary purpose of the current studies is to identify technical problems and to develop solutions and/or to identify R&D requirements to provide solutions to these problems. Accordingly, the designs currently adopted for these studies primarily represent frames of reference for identifying problems and exploring solutions.

The basic objectives adopted for the TNS design are in both cases to: 1) achieve ignition and plasma burns sufficiently long to study burn dynamics, and 2) serve as a forcing function for development of fusion power reactors. In addition, in the General Atomic design, provision is made to generate a nominal amount of electrical power.

2. OVERALL REACTOR DESIGNS

The overall reactor designs currently being explored at General Atomic and at Oak Ridge National Laboratory are depicted in Figs 1 and 2, respectively. A comparison of the major design parameters for these designs is presented in Table I.

The main differences between the two reference designs are the plasma configuration and major radius. In the case of the ORNL design, a "Dee"-shaped plasma is used and, with an appropriate ignition margin, a major radius of 5.0 meters is required. It is expected on theoretical grounds that stability can be maintained at a somewhat higher total beta with the "Doublet" plasma used in the GA design due to the greater elongation and the existence of a separatrix. Also, the transport is somewhat reduced with the Doublet plasma. As a result, a substantial ignition margin can be achieved with a major radius as small as 3.6 meters.

3. PLASMA CHARACTERISTICS

The plasma characteristics for the current TNS designs are listed in Table II. While the major and minor radii are somewhat larger for the ORNL design than for the GA design, the plasma volumes are almost exactly the same due to the larger total cross-section of the Doublet plasma.

The basic GA plasma parameters were determined by a self-consistent parametric analysis, which accounted for engineering constraints and was based on a realistic model of the plasma characteristics. Using this analysis, the plasma major radius, minor radius, and on-axis toroidal field were established. The plasma elongation was determined by optimizing the MHD equilibrium and stability features, the basic point of issue being the ability to shape and control high-beta plasmas.

Given B_T, R, a and K, a minimum β was found for ignition of the order of 4% for either Alcator scaling or trapped ion scaling. The quoted ignition β of 5% provides for some physics margin and allows more flexibility in selecting the ignition point in density/temperature space. The 6%-burn β-value allows for a post-ignition thermal excursion to a higher-temperature, thermally stable burn equilibrium. Both values are well below the β-limits imposed by ballooning modes or by transport with achievable auxiliary heating power. The quoted plasma current, I_p = 11.4 MA, is the current corresponding to a safety factor q of 2.5 at the plasma edge.

The quoted mean electron density, $\bar{n}_e = 1.9 \times 10^{20}$, and mean ion temperature, $\bar{T}_i$ = 7.7 keV, are results from a zero-D calculation assuming a parabolic temperature profile, a somewhat flatter density profile, and an average β of 6%

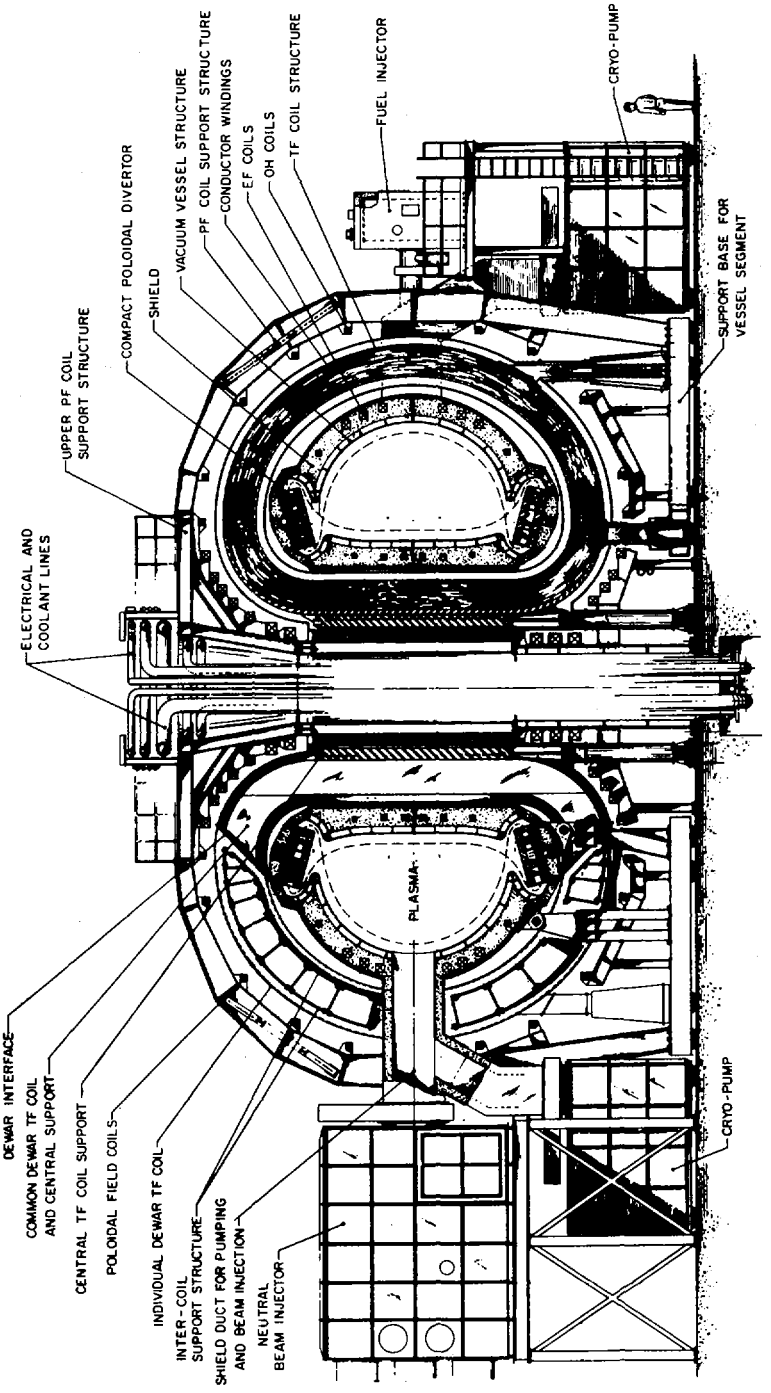


FIG. 2. Oak Ridge National Laboratory TNS baseline configuration.

TABLE I
TNS MAJOR DESIGN PARAMETERS

	GA	ORNL
Major radius, m	3.6	5.0
Minor radius, m	0.95	1.2
Plasma height-to-width	2.7	1.6
Toroidal field, tesla		
At coil	10.0	10.9
On-axis	5.1	5.3
Plasma thermal power		
Peak, MW	960	700
Burn time, sec	30	16
Duty factor	0.5	0.05
Electrical power generated, MW	20	N.A.

during burn. It was assumed that the burn equilibrium will be controlled in such a way as to maintain a central ion temperature of 15 keV. Averaging over the profiles, and including the contributions of electrons, ions and alpha particles, these parameters correspond to $\beta = 6\%$. The confinement time, $\tau_E = 3.7$ s, was then determined from the parameters using Alcator scaling. Radial transport code simulations give results in very close agreement to the 0-D simulation with the exception that a thermal runaway ensues if no explicit burn control mechanism is adopted.

One-tenth trapped ion mode scaling in 0-D calculations was used by ORNL. Studies using a 1-D analytic solution showed that the density profile solution of the transport equations leads to an equivalent global loss rate, $\langle D_{TIM} \rangle$, no larger than $D_{TIM}/10$. The effect of the density profile on $\langle D_{TIM} \rangle$ was also investigated, and it was shown that fueling profiles peaked toward the plasma edge, tending to flatten the density profile, which in turn reduces the trapped ion loss rate. Recent calculations at ORNL reveal D-shaped equilibria which are stable with respect to the internal ballooning modes at β-values of $\sim 5\%$ for TNS-like tokamaks. For a tokamak with aspect ratio equal to 2.4, stable $\bar{\beta}$ values up to 12% have been found. With shaping and profile optimizations, current estimates of the stable $\bar{\beta}$ limit are between 5% and 10% for the ORNL TNS.

4. DESIGN FEATURES

The design features of the GA and ORNL TNS reactors are compared in Table III. Significant differences evolved, due in part to differences in the plasma cross-section adopted. With the General Atomic Doublet design, for example, a large premium is placed on the radial space between the plasma chamber and the inboard sections of the toroidal field coils. As a result, economic trade-offs led to the selection of a very dense, highly effective shield material, tungsten, in the inboard region.

TABLE II
PLASMA CHARACTERISTICS

	GA	ORNL
Major radius, m	3.6	5.0
Minor radius, m	0.95	1.2
Plasma elongation	2.7	1.6
Aspect ratio	3.8	4.2
Toroidal beta		
Ignition, %	5.0	2.5
Burn, %	6.0	5.0
Assumed $Z_{effective}$	2.0	1.2
Plasma current, MA	11.4	4.3
Mean electron density, m^{-3}	1.9×10^{20}	1.3×10^{20}
Mean ion temperature, keV	7.7	13.0
Energy confinement time, s	3.7	1.8
Plasma volume, m^3	225	227.6
Total fusion power, MW	960	700

A difference in impurity control is also noted. A compact poloidal divertor was adopted for the ORNL design, while a passive impurity control system comprised of carbon liner plates in the inboard area of the chamber and a carbon coating applied directly to the chamber wall in the outboard area were adopted for the GA design.

Water-cooled copper coils were selected for the OH-coils of the ORNL design, while a superconducting coil was adopted for the OH-coils of the GA design. The superconducting coil involves additional development and therefore an element of additional risk, but it does result in substantial savings in parasitic power.

Twenty Nb_3Sn superconducting coils are used for the toroidal field coil system in the ORNL design. The GA design, on the other hand, utilizes twelve NbTi superconducting coils. While niobium-tin coils involve more development than niobium-titanium coils, parametric studies indicate a substantial savings in system cost. Parametric studies at both GA and ORNL reflect that a minimum cost reactor is achieved with about 20 toroidal field coils. In the case of the smaller GA reactor, however, access considerations dictated the use of a smaller number of coils at a modest cost penalty.

Studies of various startup scenarios at ORNL indicate that the plasma can be effectively heated by neutral beams in the 150 - 200 keV range. Accordingly, neutral beams with positive ion sources are used in the ORNL design. Studies at GA, on the other hand, based on a different set of assumptions and a different

TABLE III
DESIGN FEATURES

Feature	GA	ORNL
Plasma chamber		
Cross-section	Doublet	Dee
Material	Inconel 625	Stainless steel
Impurity control	Passive — Low-Z liner plates and wall coating	Compact poloidal divertor
Blanket	20 cm stainless steel, water-cooled	Not applicable
Shielding	Inboard: tungsten Top, bottom, and outboard: lead, stainless steel, boronated water	Stainless steel, boronated water, integral with plasma chamber
Poloidal coil system	Water-cooled copper stabilization and field-shaping coils Air core NbTi OH coil	Water-cooled copper PF and EF coils Air core, water-cooled copper OH coil
Toroidal field coils	12 superconducting NbTi coils	20 superconducting Nb_3Sn coils
Plasma heating	54 MW 500 keV negative-ion neutral beams	50 MW, 150 - 200 keV, positive-ion neutral beams
Vacuum pumping	Cryosorption pumps	Cryosorption pumps

assessment of risks involved, indicate that beam energies in the range of 500 keV are required and therefore beams with negative-ion sources are specified. R-f heating is also being considered for the TNS program.

5. MAINTENANCE

The need for remote maintenance is recognized in current TNS studies, and provisions are made in the designs to accomplish repair and replacement using remotely controlled devices.

Two basic approaches are being pursued by the two design teams. In the ORNL design, provisions are made to remove a segment comprising one-tenth of the basic reactor, including two of the TF-coils (Fig. 3). This approach has the advantage of permitting the replacement of a large segment of the reactor, but involves the cutting and disconnect of a large number of joints.

The design approach being pursued at General Atomic involves more localized operations. Provisions are made for removing segments of the shield, blanket, and plasma chamber individually. The toroidal field coils are normally left in place and would be removed only in the event of a failure in the coils themselves.

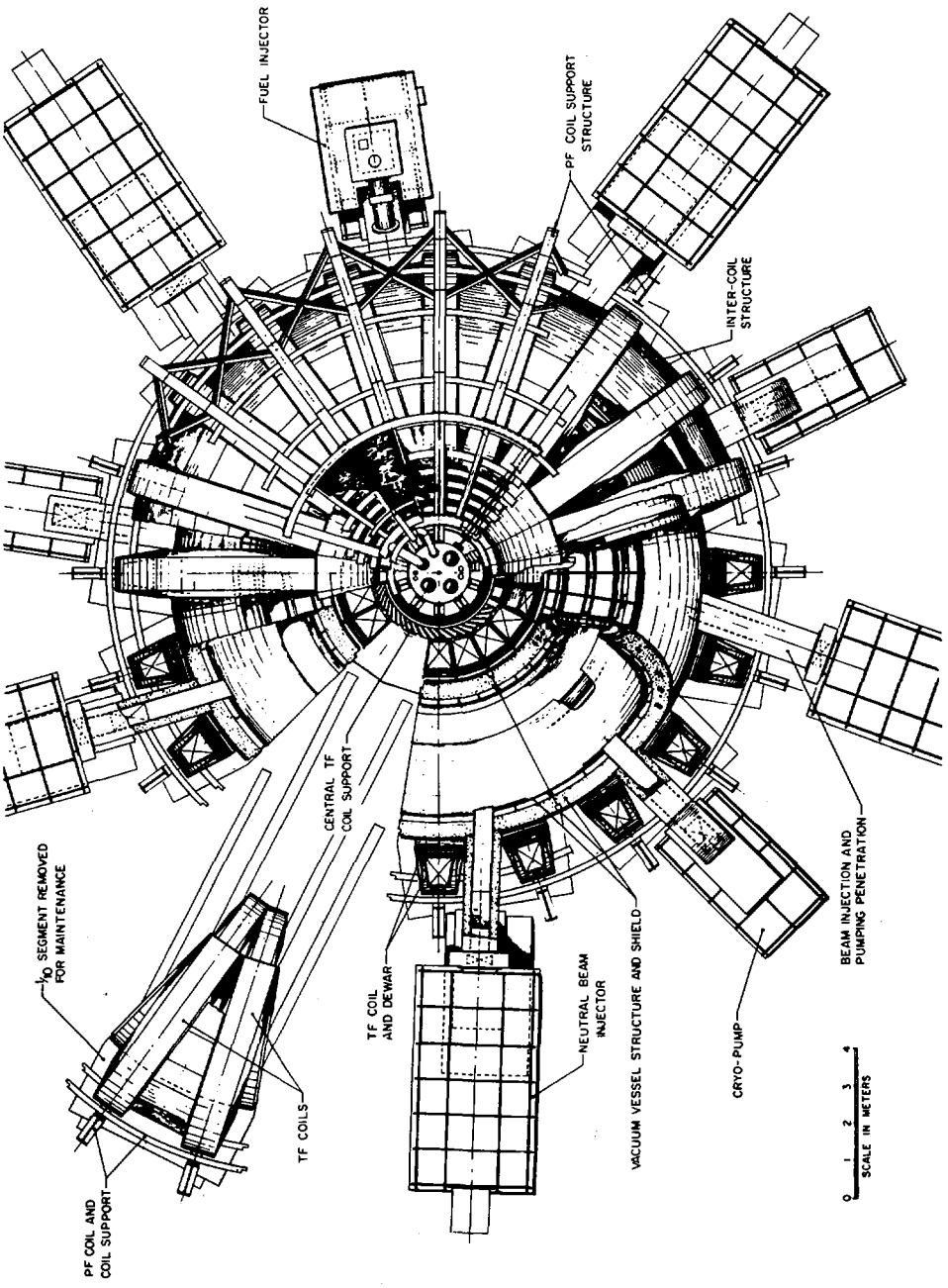


FIG. 3. Oak Ridge National Laboratory TNS remote maintenance concept.

6. CONCLUSIONS

The TNS studies being pursued at General Atomic and Oak Ridge National Laboratory have proved valuable in providing a focus for fusion R&D as well as defining the design characteristics and relative costs of candidate reactor. systems.

It is apparent that if the TNS is designed as an ignition machine, it will be substantially larger (3.6 - 5.0 m major radius, $\sim$ 1.0 m minor radius) than the TFTR and will cost in the range of $400 - $600 million without escalation and supporting R&D.

Additional studies and R&D are required in order to establish firmly the design characteristics and features of the TNS. In particular, additional information is required to establish the basic configuration of the plasma cross-section. Additional information is also needed to select the impurity control system, the type of superconducting toroidal field coil, the basic type of OH-coil, and the type of plasma heating system.

Programmatic studies should also be continued to establish the basic objectives and schedule of the TNS program. Of particular concern is whether or not the generation of electric power needs to be included as a requirement.

REFERENCES

[1] STACEY, W. M., JR., *et al.*, "Tokamak Experimental Power Reactor Studies," Argonne National Laboratory Report ANL/CTR-75-2 (1975).

[2] GAC FUSION ENGINEERING STAFF, "Experimental Power Reactor Conceptual Design Study — 12-Month Progress Report for the Period July 1, 1974, through June 30, 1975," General Atomic Company Report GA-A14534 (1975).

[3] ROBERTS, M., BETTIS, E. S., "Oak Ridge Tokamak Experimental Power Reactor Study Reference Design," Oak Ridge National Laboratory Report ORNL/TM-5042 (1975).

[4] STACEY, W. M., Jr., *et al.*, Tokamak Experimental Power Reactor Conceptual Design," Argonne National Laboratory Report ANL/CTR-76-3 (1976).

[5] BAKER, C. C., et al., "Experimental Power Reactor Conceptual Design Study — Final Report for the Period July 1, 1974, through June 30, 1976," General Atomic Company Report GA-A14000 (1976).

[6] ROBERTS, M., "Oak Ridge Tokamak Experimental Power Reactor Studies — 1976," Oak Ridge National Laboratory Report ORNL-TM-5572 through -5577 (1976).

[7] STACEY, W. M., Jr., BAKER, C. C., and ROBERTS, M., "Tokamak Experimental Power Reactor Studies," (*Proc. 6th Int. Conf. on Plasma Physics and Controlled Nuclear Fusion Research, Berchtesgaden, 1976*) Vol. 3, IAEA, Vienna (1977) 255.

[8] "GAC-ANL TNS Scoping Studies, Status Report for FY-77," General Atomic Report GA-A14614, Vols. I - XI (1977).

[9] "Draft Program Plan for TNS - The Next Step After the Tokamak Fusion Test Reactor," ORNL/TM-5982 through -5984 and WFPS/TME-004 (1977).

[10] "Oak Ridge TNS Program: Context, Scope, and Baseline Design of the FY 1978 Activities," ORNL/TM-6201 (1978).

DISCUSSION

A. GIBSON: We heard this morning that the β values around 10% mentioned by you for the Doublet configuration would require the presence of a perfectly conducting shell (or equivalent device) in close proximity to the plasma. Have you addressed yourself to the problem posed by this requirement in your design study?

P.H. SAGER, Jr.: In the General Atomic design we have provided stabilization coils outside – but in close proximity to – the plasma chamber. These are essentially passive coils which respond to any instability in the plasma.

B. GREEN: On the basis of the plasma physics data used in the 'self-consistent' designs you presented, how much additional heating power will be required?

P.H. SAGER, Jr.: Our studies indicate that approximately 60 MW of beam power are required for the General Atomic TNS reactor.

H.P. FURTH: I should like to pursue the line of questioning begun by Dr. Gibson. You replied to him that the TNS designs contain stabilizing coils that provide some semblance of conducting-shell stabilization. What I want to ask, then, is whether these coils are designed merely to give vertical stability, or whether they are capable of stabilizing a variety of kink modes – something which would be necessary, according to this morning's lectures, in order to achieve the high beta values that you have been mentioning.

P.H. SAGER, Jr.: We expect the stabilization coils incorporated in the General Atomic design to respond to the vertical modes which our studies indicate to be the critical ones. The plasma chamber is a double-wall continuous structure which responds to kink instabilities with fast growth rates. What the effect of kink modes with slower growth rates will be is a question we have not yet gone into.

J.P. GIRARD: My question relates to your choice of the air-core transformer to induce the plasma current. Have you considered using the iron-core transformer, which, as the JET group have shown, presents many advantages?

P.H. SAGER, Jr.: Early parametric studies indicated that total plant costs would be very sensitive to the major reactor radius, varying approximately as the square of the major radius. Given the higher fluxes that can be attained with air-core transformers, it is possible to minimize the major radius, so that the total cost of the air-core design is less than that of a design using an iron-core transformer.

J.P. GIRARD: The characteristics of the ORNL TNS seem to be quite similar to JET. What ought to be the next step, in your opinion? Should it be a study of the blanket, for example?

P.H. SAGER, Jr.: The objectives of the TNS programme are being examined concurrently with the studies of various reactor concepts. Among the

possibilities being considered are ignition of DT plasmas, burns sufficiently long to study burn dynamics and fuelling, a high total number of burns, high duty factor, and electric power production. In addition, it is anticipated that the reactor will provide a basis for the integration of certain systems likely to be used in subsequent power reactors, such as superconducting toroidal field coils, and will serve as a test facility for various materials and engineering concepts requiring a power reactor environment. The two reactor designs presented here have features which would allow them to be developed for the whole span of objectives under consideration.

TANDEM MIRROR REACTORS*

B.G. LOGAN, W.L. BARR, D.J. BENDER,
G.A. CARLSON, W.L. DEXTER,
J.N. DOGGETT, R.S. DEVOTO, J.F. FINK†,
T.K. FOWLER, G.W. HAMILTON, D. LAPPA,
J.D. LEE, W.D. NEEF, Jr., A.A. MIRIN,
R.W. MOIR, M.A. PETERSON, M.E. RENSINK
Lawrence Livermore Laboratory,
University of California,
Livermore, California,
United States of America

Abstract

TANDEM MIRROR REACTORS.

Preliminary designs of tandem mirror fusion reactors burning D-T fuel and of fusion-fission (hybrid) tandem mirrors producing both fissile fuel and electricity have been made. For the hybrid reactor, it is found that, by using stream-stabilized, 2XIIB-like plugs and by injecting 200-keV deuterium beams into a tritium-plasma target confined electrostatically in the solenoid (two-component operation), a useful Q (fusion power/injection power) near unity is obtained. The D-T tandem reactor parameters are optimized to obtain the minimum capital cost per kW(e) net. For $200/kW(e) of 1200-keV neutral-beam injection power in the plugs and a solenoid cost of about $3 million per metre length, the optimum Q is near 5. To allow for more expensive injector costs, a higher D-T reactor Q of 10 is obtainable with either increased power output or decreased neutron wall loading. Fokker-Planck calculations show steady-state $Q \approx 5$ for D-D tandem reactors burning only deuterium fuel and its reaction products, with most of the charged-particle fusion power recovered in a direct converter.

INTRODUCTION

Since the introduction of the tandem mirror concept two years ago by Dimov et al.[1] and independently by Fowler and Logan [2], the feasibility of tandem mirror reactors (TMR's) in terms of power density, magnetic fields, injector energies, and cost has largely been undetermined. We report here our preliminary evaluations of the economic and technical requirements for both D-T TMR's and fusion-fission (hybrid) TMR's. We have calculated significant Q (fusion power/injection power) values ($Q \approx 5$) for D-D TMR's, and so are also examining the possibilities for D-D reactors.

---

* This work was performed under the auspices of the US Department of Energy by the Lawrence Livermore Laboratory under contract number W-7405-ENG-48.

† On loan from Westinghouse Electric Corp.

We have identified several reactor components—high-field Nb_3Sn magnets for the end mirror cells (plugs), high-energy, negative-ion-based neutral injectors, and solenoid blankets suitable for low neutron wall loading — which will be needed in all TMR's, and which will require extensive development. In addition, for several plasma physics questions crucial to TMR's —beta limits due to MHD ballooning instability in the solenoid, radial diffusion, and microstability of the plugs—theory (Refs. [2] and [3]) is not yet sufficiently quantitative to impose constraints on reactor design. However, we have not yet found technical design problems or existing theoretical stability requirements that could not be accommodated in a suitable TMR design; therefore, we are sufficiently encouraged to continue our theoretical and experimental investigation of this concept.

Previous work [1] showed that a TMR Q can be made arbitrarily large (even to ignition) by making the fusion plasma density in the solenoid sufficiently small compared to that in the plugs and the volume of the solenoid sufficiently large compared to the volume of the plugs. Limits on Q are imposed by the combination of an economic limit on reactor power output, a minimum solenoid plasma density n_c to achieve an adequate fusion power density, and a maximum plug plasma density n_p that can be confined with the highest practical magnetic fields. Balancing the cost of recirculating power with the cost of the solenoid and blanket, we find minimum reactor capital cost per kilowatt of net electric power ($/kW) at a typical $Q \approx 5$ for 1000 MW(e) net power output. If neutral-beam injector costs were twice as high, and solenoid blanket and coil costs half as expensive as our initial estimates, the optimum Q would increase up to ≈ 10. The tradeoff between Q, fusion power density, and reactor size determines the optimum parameter values for all tandem reactors — hybrid, D-T, and D-D.

HYBRID TANDEM MIRROR REACTOR

We know that if fissile materials are added to fusion reactor blankets, then economic power balance can be obtained with fusion Q's as low as 1 to 2, depending on the energy multiplication by fission in the blanket. Alternatively, adding fertile materials to the blanket allows one fusion hybrid reactor to supply fissile fuel to five or more fission reactors; the economics would then also allow fusion Q's of order unity. Because of their simple cylindrical geometry and low solenoidal magnetic fields, TMR's are ideally suited to accommodate the more complex blankets and maintenance of hybrids.

We have selected a two-component mode of operation for a hybrid TMR to minimize plasma confinement and technology requirements. In this mode, energetic deuterium beams ($\sim$200 keV) are injected into a low-temperature tritium plasma target confined electrostatically in the solenoid. As with two-component operation of tokamaks [5], a fusion Q = 1 can be obtained with electron temperature T_e as low as 6 keV. Because the tritium plasma can have a much lower temperature than the reacting deuterons, two-component operation permits energy balance with a much larger loss rate of the tritium target than fusion with Maxwellian D-T plasma as considered by the Kurchatov group [6]. This in turn allows stream-stabilization of loss-cone modes in small plugs a few ion gyroradii in size, as presently done in 2XIIB [7]. Thus, a two-component tandem hybrid does not require classical ion confinement in the plugs, which can therefore be very small.

The electron temperature that controls Q is determined by the tritium end loss rate required for stream stabilization of the plugs. Measurements [8] of the minimum flux J_{min} of low-energy ions streaming through the midplane of the mirror-confined ions in 2XIIB at a ratio of plasma radius to gyroradius $r_p/\rho_i \approx 2$ indicate a flux

$$J_{min} \approx 1.84 \times 10^{-14} \frac{n_p T_e^{3/2}}{\sqrt{A_i}(R_p - 1)\bar{E}_p} \quad A/m^2 \qquad (1)$$

where A_i is the mass number of the streaming ions, R_p is the plug mirror ratio (enhanced by finite beta) and $\bar{E}_p$ is the average plug ion energy. (All energies and potentials are in keV, lengths are in metres, and densities are in m^{-3}.) Recent 2XIIB experiments [9] indicate improved ion confinement as r_p/ρ_i is increased up to 7, so we believe the streaming ion flux can be smaller than Eq. (1) by a factor of at least 10 for larger hybrid TMR plugs with $r_p/\rho_i \approx 12$. Since the plugs have negligible volume and the solenoid tritium flux dominates the end loss, the electron energy balance in this system is given approximately by

$$\frac{n_D(\bar{E}_D - \frac{3}{2}T_e)\pi r_c^2 L_c}{\tau_{ei}} \approx 2\pi r_p^2 \left(\frac{J_{min}}{10}\right)(\phi_e + T_e) \qquad (2)$$

where n_D and $\bar{E}_D$ are the deuterium component density and average energy, r_c and L_c are the solenoid radius and length, r_p is the plug radius, τ_{ei} is the Spitzer electron-ion equilibration time, and ϕ_e is the solenoid potential confining electrons (ϕ_e = 5 to $6T_e$, typically). As the left-hand side of Eq. (2) is largely the required solenoid beam injection power, Eqs. (1) and (2) can be used to estimate that injection powers of order ~300 MW can sustain $T_e \approx 6$ keV with plug densities $n_p \approx 5 \times 10^{20} m^{-3}$, radii $r_p \approx 0.16$ m and energies $\bar{E}_p \approx 200$ keV sufficient to plug a solenoid producing ~10 MW/m of fusion power. With tritium ion cooling by charge exchange in a gas-feed source, we find that small density ratios $n_p/n_c \approx 2$ to 3 give electrostatic confinement of tritium ions for typically 10^2 to 10^3 transit times. This reduction in tritium loss compared to free flow allows the hybrid TMR to reach T_e = 6 keV with less injection power at much lower magnetic field than required with unstoppered solenoids [10].

Using a zero-dimensional model coupling standard rate equations for energy transfer between hot deuterons, alphas, cold tritons, and electrons, we have evaluated the dependence of Q in the two-component tandem hybrid on solenoid length L_c, injection energy E_{inj} (same E_{inj} for plugs and solenoid), and plug midplane field B_{0p}. The deuterons and alphas are assumed to be mirror confined for a cooling time on the tritons and electrons. The triton electrostatic lifetime is calculated using analytic formulas by Pastukhov [11] with solenoid potential well depths $\phi_c = T_e \ln(n_p/n_c)$ adjusted to give a total tritium loss rate of $2\pi r_p^2(J_{min}/10)$. The plug ions are assumed to have $\bar{E}_p = E_{inj}$ and a lifetime = τ_{ei} in the presence of ion-cyclotron fluctuations as in the 2XIIB experiment. Sample tests of this simple model with Fokker-Planck calculations give the same Q values within 10%.

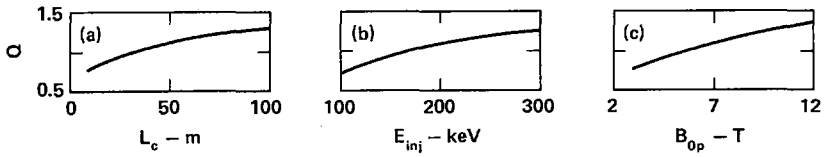


FIG. 1. Q for the two-component tandem hybrid as a function of (a) solenoid length L_c, (b) solenoid and plug injection energy E_{inj}, and (c) plug vacuum midplane field B_{0p}. In each, plug beta $\beta_p = n_p \bar{E}_p/(B_{0p}^2/8\pi) = 0.7$. Solenoid beta $\beta_c = 0.8$, and plug vacuum mirror ratio $R_{p\,vac} = 1.3$.

TABLE I. EXAMPLE PARAMETER VALUES FOR A Q = 1.1 TWO-COMPONENT TANDEM HYBRID REACTOR

Parameter	Value
Solenoid length, L_c	50 m
Solenoid radius, r_c	0.37 m
Solenoid electron density, n_c	1.7×10^{20} m^{-3}
Solenoid deuterium density, n_D	6.3×10^{19} m^{-3}
Solenoid tritium density, n_T	1.1×10^{20} m^{-3}
Electron temperature, T_e	6.0 keV
Injection energies, E_{inj}	200 keV
Solenoid field, B_c	1.8 T (β_c = 0.8)
Plug field, B_{0p}	7.0 T (R_p = 2, β_p = 0.7)
Plug density, n_p	$4.6 \times 10^{20} m^{-3}$
Plug radius, r_p	0.16 m (r_p/ρ_i = 12)
Fusion power	410 MW
Neutron wall loading, (at 1-m wall radius)	1 MW/m^2

The results for Q as a function of L_c, E_{inj}, and B_{0p} are shown in Figs. 1(a) through (c). With L_c limited to less than 100 m for a practical power output, E_{inj} less than 300 keV for efficient trapping, and B_{0p} less than 12 T for Nb_3Sn plug magnets ($R_{p\,vac}$ = 1.3), Figs. 1(a) through 1(c) show that two-component hybrid TMR's will be limited to $Q \lesssim 1.5$. As one example, Table I gives parameters for a hybrid TMR with reduced technology requirements (L_c = 50 m, E_{inj} = 200 keV, B_{0p} = 7 T).

D-T TANDEM MIRROR REACTORS

Our preliminary study [12] of D-T TMR's was designed to determine the optimum parameters for minimum cost of power and to assess the sensitivity of reactor cost to variable limits imposed by economics and technology, e.g., net power output, plug injection energy, and plug magnetic field strength. The most important result of that study, summarized in Fig. 2, is that reactor cost ($/kW) minimizes at a $Q \approx 5$ with a recirculating power fraction of 43% for a fixed power output of 1000 MW(e). The main reason for this result is that the 100-m-long solenoid and blanket form the single most expensive reactor component ($3.2 million/m), while our initial estimate for the 1200-keV neutral-beam injector cost per injected kilowatt of $200/kW(e) is probably too low by a factor of at least 2.

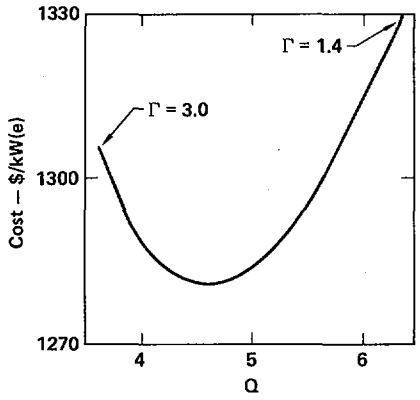


FIG.2. D-T reactor capital cost per kW(e) net as a function of Q = fusion power/injection power. The parameter Γ is the solenoid neutron wall loading in MW·m^{-2}. In all cases, $\beta_c = 0.7$, $\beta_p = 1.0$, $R_{p\,vac} = 1.07$, and net power = 1000 MW(e).

Note in Fig. 2 the decrease in neutron wall loading Γ with increasing Q. The cost of recirculating power balances the cost of the solenoid only at high Γ , which is obtainable only at relatively low Q and high recirculating power.

To understand the constraint on Q imposed by power density in TMR's, consider the following general expression for Q:

$$Q = \frac{P_{fusion}\, V_c}{P_p\,(1 - f_p)\, 2V_p + P_c\, V_c} \tag{3}$$

where V_c and V_p are the solenoid and plug volumes, respectively; where

$$P_{fusion} = \frac{1}{4}\, n_{ic}^2\, \langle \sigma v \rangle_{DT}\, E_F \tag{4}$$

is the fusion power density in the solenoid with D-T ion density n_{ic}, D-T fusion reaction rate $\langle \sigma v \rangle_{DT}$ $(m^3 \cdot s^{-1})$, and fusion energy release E_F = 17600 keV; where

$$P_p = \frac{n_p^2\, E_{inj}}{(n\tau)_p} \tag{5}$$

is the plug injection power per unit volume with a plug ion confinement $(n\tau)_p$; and where

$$P_c = P_p\, f_p \left(\frac{2V_p}{V_c}\right) + P_e \tag{6}$$

is the solenoid input power per unit volume with an external injection power P_e per unit of solenoid volume. The fraction f_p of plug injection power that is transferred to the solenoid electrons by plug ions cooling on electrons and lost at average energy $\bar{E}_L$ is given by

$$f_p = \frac{E_{inj} - (\bar{E}_L + \phi_e + \phi_c + T_e)}{E_{inj}} \tag{7}$$

We can define a solenoid power amplification

$$Q_{sol} = \frac{P_{fusion}}{P_c} \tag{8}$$

and, noting that Q increases monotonically with Q_{sol}, we can restrict our attention to the scaling of Q_{sol}. For energy balance in the solenoid, we require

$$P_c = \frac{n_{ic}^2}{(n\tau)_c}\left(\phi_e + T_e + \phi_c + T_c + \frac{3}{2}T_c \frac{\langle\sigma v\rangle_{cx}}{\langle\sigma v\rangle_i}\right)$$

$$- \frac{1}{4} n_{ic}^2 \langle\sigma v\rangle_{DT}\left[E_{\alpha 0} f_{\alpha E} - 2\bar{E}_r(1 - f_{\alpha E}) - \frac{3}{2} T_c f_{\alpha t}\right.$$

$$\left. -2\left(\frac{3}{2} T_c \frac{\langle\sigma v\rangle_{cx}}{\langle\sigma v\rangle_i} + \phi_e + T_e\right)(1 - f_{\alpha t})\right] \tag{9}$$

where T_c is the ion temperature, $\langle\sigma v\rangle_{cx}/\langle\sigma v_i\rangle$ is the ratio of charge exchange to ionization, $E_{\alpha 0} = 3520$ keV is the initial alpha energy, $f_{\alpha E}$ is the fraction of alpha energy transferred to the ions and electrons, $\bar{E}_r$ is the mean reacting ion energy, and $f_{\alpha t}$ is the fraction of alphas that thermalize in the potential well. We assume that the thermal alphas diffuse out radially to a cold boundary layer by classical collisions with the D-T ions [13], allowing steady-state operation at a fractional thermal alpha density of

$$C_\alpha \equiv \frac{n_\alpha}{n_{ic}} \approx 4.5 \times 10^{19} f_{\alpha t} \langle\sigma v\rangle \sqrt{T_c}\, r_c^2 B_c^2 (1 - \beta_c) \tag{10}$$

where B_c is the solenoid field in teslas and β_c is the solenoid beta. The fraction $f_{\alpha t}$ of alphas escaping radially carry out only 3/2 T_c energy per alpha while the fraction $(1 - f_{\alpha t})$ scattering out the ends carries out two electrons with $2(\phi_e + T_e)$ energy per alpha. The product of D-T ion density and confinement time $(n\tau)_c$ in Eq. (3) is given approximately by [14]:

$$(n\tau)_c \approx \frac{(n\tau)_{ii}}{(1 + 4C_\alpha)}\, g(R_c)\left(\frac{\phi_c}{T_c}\right)\exp\left(\frac{\phi_c}{T_c}\right) \approx \frac{7.8 \times 10^{10} T_c^{3/2}}{(1 + 4C_\alpha)} \left(\frac{n_p}{n_c}\right)^{T_e/T_c} \ln\left(\frac{n_p}{n_c}\right)^{T_e/T_c} \tag{11}$$

where $(n\tau)_{ii}$ is the D-T ion self-scattering time, $\phi_c = T_e \ln(n_p/n_c)$ and solenoid electron density $n_c = n_{ic}(1 + 2C_\alpha)$. By Eqs. (9) and (11), we see that Q_{sol} (and so also Q) increases monotonically with $(n\tau)_c$ and the parameter $(n_p/n_c)T_e/T_c$.

Clearly, to enhance the ratio T_e/T_c any auxiliary heating in a subignition solenoid should be selective to electrons. For the same reason, charge-exchange ion cooling benefits confinement. After that, Q can be increased only by increasing n_p/n_c, and since n_p is limited by plug magnetic fields and beta, the solenoid density n_c must decrease, reducing fusion power density as n_c^2. Economic Γ can be recovered at larger r_c, but then total power output increases.

By shortening the transition length between solenoid and plugs, we may induce nonadiabaticity for the hot alphas so that $f_{\alpha t} \to 0$. By solving Eq. (9) together with ion energy balance for the density ratio n_p/n_c, giving $Q_{sol} = 5$, we obtain nearly the same $n_p/n_c \approx 4$ at $T_e = 60$ keV with $f_{\alpha t} = 0$ as with the classical scattering value $f_{\alpha t} \approx 0.7$. Thus, hot alphas need not be confined at this value of Q_{sol}. To obtain a $Q_{sol} = 20$, however, containment of most hot alphas is essential, so that near ignition is achieved.

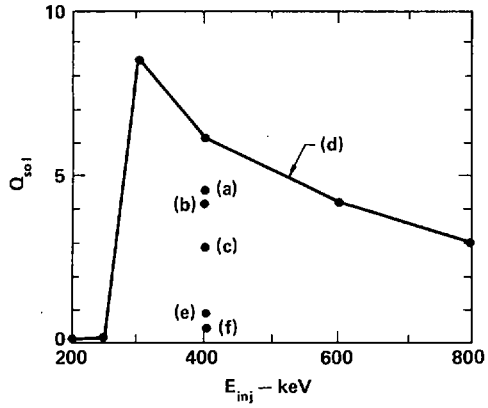
To allow for higher neutral injector costs, Q must be increased in order for the recirculating power fraction to be reduced. Example parameter values (not optimized) for a 1000-MW(e) D-T reactor with $Q_{sol} = 20$ and overall Q = 10, are given in Table II. Tritium plug ion confinement and hot alpha thermalization are derived from two-dimensional Fokker-Planck calculations. Thermal alpha fractions are determined by Eq. (10). Direct electron heating is assumed to provide an added power input P_e to the solenoid, such that $P_e V_c/(P_e V_c + 2P_p V_p) \equiv f_e = 0.6$. We assume equal generation efficiency, trapping efficiency, and cost per injected kilowatt for the direct electron heating as for the neutral beams. We assume lower values for B_{0p} and E_{inj} in Table II than in Ref. [12], exploiting direct electron heating which allows $f_p \approx 0$. We assume that small additional neutral-beam injections in field ripples near the outer plug mirrors raise the outer mirror densities to n_c so that plug ions see only a potential of magnitude ϕ_c. We find that $\sim$3 MW of additional injection in outer field ripples can increase the plug $(n\tau)_p$ by a factor of 2, depending on E_{inj}, through reduction of the local plug ambipolar potential. Combined generation and trapping efficiencies of 60% are assumed for both neutral-beam injection and direct electron heating, resulting in a recirculating power fraction of 27%. Because the solenoid is more than twice as long ($L_c = 240$ m) as at Q = 5, solenoid cost/m must be reduced by a factor of at least 2 for this reactor example to be near optimum with injected power costs of \$400/kW(e). We believe solenoid cost/m can be so reduced if the blanket design is optimized for low power density.

D-D TANDEM MIRROR REACTORS

Because of linear geometry and because ions exiting from the solenoid have a directed kinetic energy due to a plug potential that is large compared to their thermal temperature, the tandem mirror system is ideally suited to efficient direct conversion of the fusion energy released in

TABLE II. EXAMPLE PARAMETER VALUES FOR A Q_{sol} = 20, Q = 10, 10^3 MW(e) D-T TANDEM REACTOR

Parameter	Value
Solenoid length, L_c	240 m
Solenoid radius, r_c	1.6 m
Solenoid electron density, n_c	5.5 x 10^{19} m^{-3}
Thermal alpha fraction, C	0.1
Electron temperature, T_e	50 keV
Solenoid ion temperature, T_c	34 keV
Solenoid field, B_c	1.6 T (β_c = 0.9)
Plug density, n_p	5.5 x 10^{20} cm^{-3}
Plug field, B_{0p}	12.0 T (R_p = 2.6, β_p = 1.0)
Plug radius, r_p	0.47 m (r_p/ρ_i = 30)
Plug injection energy, E_{inj}	600 keV
Plug injection current, I_{inj}	150 A (total, incident)
Neutron wall loading, Γ (at 1.9-m wall radius)	0.60 MW/m



	n_p/n_c	f_e
(a)	25	0
(b)	20	0.09 (Reference case)
(c)	20	0.6
(d)	30	0
(e)	20	0
(f)	30	0 (No α diffusion loss)

FIG.3. Solenoid power amplification factor Q_{sol} for a D-D reactor as a function of deuterium neutral-beam injection energy into the solenoid E_{inj}, and for the listed plug/solenoid density ratios n_p/n_c and direct electron heating power fractions f_e. The product of solenoid radius and plasma internal field $r_c B_c \sqrt{1-\beta_c} = 1$ m·T. The solenoid plasma mirror ratio $R_c = 20$.

charged particles. To exploit this unique advantage, we consider a catalyzed D-D fuel cycle in which the ^{3}He and T reaction products are burned to increase the charged-particle fraction of fusion energy release to 64%. Because high electron temperatures are needed to confine the fuel electrostatically, synchrotron radiation must be suppressed by a very high solenoid beta ($\beta_c \geq 0.9$), which prevents the charged-particle fusion energy from ultimately being radiated to the walls rather than being directly converted. Such high betas may be possible if one localizes radial density and potential gradients to a thin surface boundary layer.

Using a multispecies Fokker-Planck code, we have calculated the steady-state, two-dimensional velocity space distribution functions $f_i(v,\theta)$ for the five ion species (D, T, ^{3}He, α, p) involved. Fuel ion

TABLE III. EXAMPLE PARAMETER VALUES FOR A $Q_{sol} = 4.3$ D-D TANDEM REACTOR (Solenoid only)

Particle	Mean energy (keV)	Density ($10^{18} m^{-3}$)
Electrons	200	47
Deuterons	288	29
Tritons	358	0.6
^3He	295	4.3
^4He	438	2.4
Protons	2687	3.7

Parameter	Value
Plug/solenoid density ratio, n_p/n_c	20
Direct electron heating fraction, f_e	0.09
Deuteron injection energy, E_{inj}	400 keV
Solenoid mirror ratio, R_c	20
Electron confining potential, ϕ_e	865 keV
(Solenoid radius) x (plasma internal field), $r_c B_c \sqrt{1 - \beta_c}$	1 m·T

losses by fusion burnup in D-D, D-T, and D-^{3}He reactions appear as isotropic sources for the reaction products at their appropriate energies. The electron temperature is determined by a rate equation that includes ion-electron energy transfer, relativistic synchrotron and bremsstrahlung radiation loss, and end losses of $\phi_e + T_e$ for each ion charge lost. Escaping ^3He and T ions are reinjected into the solenoid for complete burnup. Thermal alpha ash is assumed to have a classical radial diffusion time [13]

$$\tau_{\alpha r} = 3.9 \times 10^{21} \sqrt{\bar{E}_D}\, r_c^2 B_c^2 (1 - \beta_c)/(n_i \ln \Lambda)$$

where $\bar{E}_D$ is the mean deuteron energy, n_i is the density of $Z = 1$ ions, and $\ln \Lambda$ is the Coulomb logarithm.

The results for Q_{sol} are shown in Fig. 3 as a function of the deuterium injection energy in the solenoid, and for various density ratios n_p/n_c and electron heating power fractions f_e. Note that significant $Q_{sol} \approx 4$ to 5 can be achieved with several values of E_{inj} and n_p/n_c. For sufficiently long solenoids, the overall Q, including plug power, can approach Q_{sol}. As expected, the improvement of Q_{sol} with increasing n_p/n_c shows the beneficial effect of a deeper potential well for the ions. Also, a small amount of electron heating ($f_e = 0.09$) benefits Q_{sol}, but with too much electron heating ($f_e = 0.6$), the increased electron energy losses lead to lower Q_{sol}. A set of solenoid parameter values for $f_e = 0.09$ is given in Table III. We have not yet attempted to carry out a complete reactor design based on this case, but it should be noted that the power recovered in a direct converter (charged fusion power minus radiation losses) is 2.3 times the solenoid injection power, so a simplified reactor design may be possible if we eliminate thermal energy recovery in the blanket.

REFERENCES

(1) DIMOV, G. I., ZAKAIDAKOV, V. V., KISHINEVSKII, M. E., Fiz. Plazmy 2 (1976) 597.
(2) FOWLER, T. K. LOGAN, B. G., Comments Plasma Phys. Controlled Fusion Res. 2 (1977) 167.
(3) BALDWIN, D. E., et al., Paper IAEA-CN-37-J-4. these Proceedings.
(4) RYUTOV, D. D. et al., these Proceedings.
(5) DAWSON, J. M., FURTH, H. P., TENNEY, F. H., Phys. Rev. Lett. 26 (1971) 1156.
(6) GRIBOV, Y. V., CHUYANOV, V. A., Kurchatov Institute of Atomic Energy Rep. 44/1454 (1978).
(7) COENSGEN, F.H., et al., Phys. Rev. Lett. 35 1501 (1975).
(8) MOLVIK, A.W., Bull. Am. Phys. Soc. 22 1144 (1977).
(9) SIMONEN, T. C., et al., Paper IAEA-CN-37-J-1, these Proceedings.
(10) POST, R. F., et al., Phys. Rev. Lett. 31 (1973) 280.
(11) PASTUKHOV, V. P., Nucl. Fusion 14 (1974) 3.
(12) MOIR, R. W., et al., University of California, Lawrence Livermore Laboratory Rep. UCRL-52302 (1977).
(13) LONGMIRE, C. L., ROSENBLUTH, M. N., Ann. Phys. (N.Y.) 1 (1957) 120.
(14) COHEN, R. H., et al. (to be published in Nucl. Fusion).

DISCUSSION

R.W. CONN: What physics changes were made in going from Q = 5 to Q = 10? Are the technology requirements for plugs and beams the same at Q = 5 or 10?

R.G. LOGAN: What we did to get Q = 10 was, essentially, to increase the ratio of plug density to solenoid density, and also to include the effects of thermal alphas. This reduced the neutron wall loading, increasing centre cell length for the same reactor power output (1000 MW(e) net). At the same time, we used 60% electron heating with half the energy of neutral beams (600 keV) and lower plug fields (12 T), which eases technology requirements.

B. LEHNERT: In your calculations of Q, have you taken the plasma heat losses along the magnetic field lines into account?

R.G. LOGAN: Yes. The positive ambipolar potential of the plugs, which electrostatically confines ions in the centre cell, also confines electrons in the system. But, also, one must prevent the emission of cold secondary electrons from the wall. We believe our direct converter designs would be suitable for this purpose.

H. CONRADS: Could you please give the ratio of the cost of the reactor to the overall cost of the power plant for your design?

R.G. LOGAN: I am sorry, I do not remember that cost ratio. However, it is given in our reactor study report (Livermore Report UCRL-52302, July 1977).

R.A. KRAKOWSKI: Engineering power density (power per unit volume enclosed by the confinement system, i.e. the magnets) per unit wall loading

shows a dependence on geometry which predicts an optimum (maximum) at a first-wall radius equal to the blanket thickness. Let me refer you to the discussion on paper I-2 in this connection. Have you varied these geometric factors in your overall optimization procedure?

R.G. LOGAN: Yes. The various blanket, shield and coil costs were scaled with radius to minimize the cost of power at a fixed reactor power of 1000 MW(e) net.

FUEL PRODUCTION CHARACTERISTICS OF FUSION HYBRID REACTORS*

R.P. ROSE, T.C. VARLJEN
Westinghouse Electric Corporation,
Pittsburgh, Pennsylvania

F.L. RIBE, N.J. McCORMICK, G.C. VLASES, G.L. WOODRUFF
University of Washington,
Seattle, Washington

V.L. TEOFILO, B.R. LEONARD, Jr., D.T. AASE, R.T. PERRY, S.C. SHULTE
Battelle,Pacific Northwest Laboratories,
Richland, Washington

S.C. BURNETT, K.R. SCHULTZ, R.H. BROGLI, D.W. KEARNEY
General Atomic Company,
San Diego, California,
United States of America

Abstract

FUEL PRODUCTION CHARACTERISTICS OF FUSION HYBRID REACTORS.

The potential role of hybrid systems in the production of fuel for fission reactors is examined in the context of a possible serious fuel shortfall developing early in the next century. Various proliferation-resistant fuel-cycle options are considered, including the use of the Th/^{233}U fuel cycle and the Refresh Concept. It is concluded that the fusion hybrid reactor has a high potential to extend fuel resources for nuclear power stations. The hybrid concept also appears to offer the flexibility to operate with a variety of fuel-cycle options. Furthermore, a demonstration of fissile-fuel production in a hybrid based on the tokamak concept appears to be a feasible near-term goal.

1. INTRODUCTION

The need for development of advanced energy technologies has received world-wide attention during the past decade. It is clear that nuclear energy

* Work performed under the following contracts:
Westinghouse: DoE Contract EG-77-C-02-4544, EPRI Contract RP473-1, University of Washington/Battelle, PNL: DoE Contract EN-77-3-01-6173, General Atomic: DoE Contract EY-76-C-03-0167.

must assume a key role in satisfying energy needs to avoid excessive dependence on dwindling supplies of fossil fuels. However, growth of the nuclear power industry is limited since there is insufficient uranium ore to sustain widespread use of nuclear convertor reactors for much beyond the 20th Century. The chief candidate to extend the nuclear option is the Liquid Metal Fast Breeder Reactor (LMFBR). Technology for the LMFBR is presently available and its timely implementation could extend nuclear fuel supplies for centuries. Because of these factors, concerted efforts have been made to develop and deploy the LMFBR, not only in the USA, but in all the technologically advanced nations of the world. Concerns have been voiced in the USA, however, with regard to the availability of sufficient fissile material for breeder reactor startup inventory. These concerns arise, in part, because of the reduced rate of future LWR deployment which has been forecast in revised projections during the past several years. Recent studies by the Electric Power Research Institute[1] suggest that the ability to deploy breeders as rapidly as desirable to assure adequate energy availability may be limited by a shortage of fissile fuel needed for startup inventory. We believe this to be an unduly pessimistic assessment. However, the imperative need for the breeder to ensure the long-term viability of the nuclear option suggests that the development of an alternate source of fissile material to assure an adequate startup inventory would be a prudent investment. The fusion hybrid appears to be the leading candidate to provide this source of fissile material because of its prolific fuel production characteristics.

The fusion hybrid reactor appears to have a unique potential to help meet the rapidly expanding fuel needs of nuclear fission options and thus to ensure that we can avoid any shortfall in energy resources. Our studies, as well as those of other investigators both in the USA and abroad, indicate that the hybrid concept has the potential to produce very large quantities of fuel for fission power plants. Typical results suggest that a single hybrid facility may refuel from 5 to 15 nuclear plants of 1000 MWe capacity, depending on the specific hybrid concept and the nuclear fuel cycle selected. Fuel from a hybrid facility could also make up shortages in startup inventory for fission breeder reactors if these shortages should, indeed, develop. In addition, these studies indicate that the fusion hybrid has basic generic differences as compared to fission reactors. Typical fission reactors produce 2.5-3 neutrons per fission. One of these neutrons is used to sustain the nuclear reaction, i.e. to maintain the reactor in a critical state - and a second neutron must transmute a fertile nucleus to replace the fissile atom consumed in the reaction. Thus, less than one neutron is typically available to account for leakage, for parasitic losses, and to produce a net surplus of fissile material. In contrast, the fusion hybrid is comprised of a subcritical fertile lattice driven by a fusion neutron source. Therefore, it is not necessary for the fission reaction to sustain itself. Furthermore, high-energy fusion neutrons can produce 4-5 neutrons per fission, which affords a cascading effect to supply a surplus of neutrons for transmutation of fertile nuclei to fissile materials. These characteristics account for the high potential of the fusion hybrid as a fuel production facility.

Concerns regarding the effect of plutonium utilization on nuclear proliferation have recently been expressed by the current Administration in the USA. As a result, the Administration has initiated the International Nuclear Fuel Cycle Evaluation (INFCE) and Nonproliferation Alternative Systems Assessment Program (NASAP) studies to examine alternate nuclear fuel cycle scenarios. Results of these studies should be available in the Fall of 1979 and will have an influence on decisions regarding future fuel cycles for nuclear reactors. There is a broad-based consensus on the object of these proliferation concerns.

No responsible party wants to see nuclear weapons material fall into the hands of an unstable or irresponsible national government or subnational group. There is a significant area of disagreement, however, in the means of satisfying these proliferation concerns. Those experts with the most extensive first-hand knowledge of the nuclear power industry, as well as many responsible statesmen in the USA and abroad, conclude that plutonium can and should be utilized for LWR's and breeders with adequate institutional controls on reprocessing to ensure a high degree of proliferation resistance by extensive safeguards. Initial engineering studies of the fusion hybrid concluded that the uranium-plutonium fuel cycle is the choice which offers the potential for the most abundant production of fissile fuel[2]. This fuel cycle also offers the benefits of the most extensively developed technology in fuel fabrication and reprocessing. Thus, the fusion hybrid can serve as a source of fissile material for the fuel cycle that technical experts in nuclear fission consider to be the best choice for LWR and fast-breeder reactor systems. More recently the attention to alternate fuel cycles in the NASAP and INFCE studies has prompted consideration of these fuel cycles for various reactor systems, including the fusion hybrid. The hybrid appears to offer the flexibility for the production of fissile material in a wide variety of these alternate fuel cycles. In particular, the hybrid affords a means of producing U-233 from thorium without the consumption of natural fissile material which is required for U-233 production in a fission reactor. However, the ultimate assessment of alternate fuel cycles involves a much broader set of considerations than those addressed in hybrid studies to date. Thus, the entire fuel cycle must be assessed in some detail before meaningful conclusions on alternate approaches can be developed. With the above points in mind, the remainder of this paper describes recent hybrid work performed at Westinghouse, The University of Washington/Battelle PNL, and General Atomic.

2. ASSESSMENT OF ALTERNATE HYBRID REACTOR SYSTEMS

The goal of the studies performed by The University of Washington and Battelle PNL is to evaluate fusion-fission nuclear energy systems[2] which may reduce perceived risks of nuclear weapons proliferation while satisfying short- and long-term needs for nuclear energy. Other considerations are the technological, resource, economic, environmental and safety factors.

Hybrid reactors could produce power as well as fuel to extend the fuel supply for fission reactors. Several studies[3,4,5] have already shown that fuel-producing hybrids capable of fueling multiple burner-converters can serve a useful function in the perceived marketplace by the year 2000. However, these studies conclude that hybrid breeders must produce and sell power at least sufficient to offset the power consumed by the devices in order to compete in the marketplace. The sale of fissile material probably requires chemical processing of the blanket to recover the fuel, although recycle without reprocessing may be possible[6].

Fusion Drivers Based On Inertial And Magnetic Confinement

On the basis of present information, hybrid systems based on the laser and electron-beam-driven pellet systems, the tokamak, the classical mirror, the linear theta pinch, the laser-heated solenoid and the imploding liner were reviewed. These systems were assessed in terms of the following requirements: electrical energy and tritium-breeding self-sufficiency; fuel production to support a sufficient number of fission burner converters; and acceptable neutron wall loading and/or blanket power density. Based upon this assessment,

the fusion driver systems which were retained for characterization and evaluation include the laser inertial confinement system with high-gain pellets, the tokamak, the classical mirror with yin-yang magnets, and the linear theta pinch.

Hybrid Blankets Requiring No Reprocessing

These hybrid blanket concepts are analogous to the LWR once-through system with verified spent-fuel storage. The principal application for these types of blanket appears to be for the hybrid reactor to produce saleable electricity or synthetic fuels (e.g. hydrogen). The fuel cycle would utilize either uranium (natural or enrichment tails) or thorium in the blanket region of the reactor to multiply the energy of fusion-produced neutrons through fissioning of the uranium or the thorium. The spent uranium or thorium would be cooled and shipped to a secure repository for storage and ultimate disposal.

Compared with the LWR once-through system, these hybrid blanket concepts eliminate the need for enrichment requirements but require similar safeguards for the spent fuel. They can also have markedly improved resource utilization since they can utilize depleted uranium or thorium. However, they appear to be economically inferior since they involve plants with significantly greater capital costs[5].

Hybrid Blankets Requiring Reprocessing and Recycle of Fissile Materials In Fission Reactors

These hybrids extend natural resources by converting uranium and/or thorium to fissile material. The applications include hybrid blankets which produce only fissile material for sale to support fission reactors as well as those which produce both fissile material and electricity (or synthetic fuel) as saleable products. Variants on the blanket fuel cycle include use of uranium, thorium, or mixtures of both. For concepts involving recycling of plutonium to fission reactors, it has been suggested by some that the reprocessing and fuel refabrication facilities be located in an International Nuclear Center (INC) and co-processing and/or spiking of the final fuel be performed. Location of the hybrid within the INC would be advisable only if the hybrid blanket initially contained fissile material. Resource utilization is favorable since use can be made of depleted uranium and thorium and recycled plutonium. The hybrid system would be attractive economically because of the large number of thermal fission reactors it could support[4,5].

Thorium blanket concepts which utilize the recycling of U-233 denatured fuels to fission reactors may also involve locating the reprocessing and refabrication activities in an INC. In this case, the fission reactor fuel probably will be denatured by mixing with U-238. This concept has high resource utilization since it makes use of thorium and recycled U-233 which can produce relatively high conversion ratios in the thermal fission reactors. However, the economics may not be as attractive as plutonium recycling because of poorer hybrid breeding performance.

A potentially more attractive hybrid blanket is one in which depleted uranium and recycled plutonium are used for neutron and energy multiplication and in which U-233 is then bred in a thorium region[7]. Such a design incorporates the superior performance of U-238 and Pu-239 in a high-energy spectrum while producing U-233, a superior fuel for thermal reactors.

3. THE U-233 REFRESH CYCLE CONCEPT FOR HTR FUEL

As previously noted, concern by the present U.S. Administration about questions of nuclear proliferation has prompted international reexamination of these issues through the International Nuclear Fuel Cycle Evaluation (INFCE) Study. This international interest in alternate nuclear fuel cycles provides a unique opportunity for fusion power. Because the fusion neutron source is essentially independent of the breeding blanket, hybrid reactors have the flexibility to use a wide variety of blanket fuel materials and fuel cycles. Studies at the General Atomic Company, in cooperation with the Lawrence Livermore Laboratory, have been aimed at utilizing this flexibility with the U-233 Refresh Cycle Concept for HTR fuel.

Concept

The U-233 Refresh Hybrid Power System consists of a hybrid fusion reactor in which U-233 is produced from thorium, and several thermal fission reactors in which the Th/U-233 fuel is used without reprocessing. Because of its high burnup capabilities, fuel based on high-temperature gas-cooled reactor (HTR) technology is used. A preliminary evaluation of the U-233 Refresh Cycle Concept[6] concluded that the idea is technically feasible. The results of the more detailed studies reported here confirm those optimistic projections.

Results

The objectives of this study were to evaluate the HTR fuel materials irradiation limits, to investigate the nuclear performance of fusion reactor blanket designs, to study the fuel cycle of burner reactors using the fusion-bred fuel without reprocessing, and to determine the characteristics of a symbiotic fusion-fission power system based upon the Refresh Cycle Concept. The full range of HTR fuel design possibilities was considered for use in the hybrid blanket, including use of coated thorium fuel particles only with no graphite. Lithium-6 was added to depress the thermal flux and prevent the bred U-233 from being burned out and also to produce tritium to fuel the fusion reactor. Low C/Th ratio blankets have the highest uranium production rate but also experience more fast fluence to reach the 4% minimum concentration in thorium needed to operate the HTR without reprocessing the fuel. By use of reduced fuel temperature in the hybrid blanket this concentration can be achieved within presently expected fuel fluence limits. The uranium consumption of an HTR operating on the Refresh Cycle and the effect of using the fuel for multiple enrichment-depletion cycles were studied. The uranium consumption is high ($\sim$400 kg/GWe-yr) compared to that of a high conversion ratio HTR ($\sim$130 kg/GWe-yr) due to the amount of fissile fuel retired with the no-reprocessing concept. The use of several passes through the breeder and burner reactors before the fuel is retired does not reduce consumption significantly due to the effect of a large fission-product inventory after several cycles. The present calculations indicate that a fusion hybrid reactor could support from 2 to 3 HTR burner reactors of equal thermal power without reprocessing using the U-233 Refresh Cycle.

4. PROSPECTS FOR A NEAR-TERM DEMONSTRATION OF FISSILE FUEL PRODUCTION

With the foregoing points in mind, it is logical to ask how soon fusion might be utilized for the production of fissile fuel. The conclusion to date of studies conducted at Westinghouse is that the demonstration of the requisite technology to utilize fusion neutrons for the production of nuclear fuel

could be achieved by the end of the next decade with reasonable prospects of success based on the design, construction, and operation of a Demonstration Tokamak Hybrid Reactor (DTHR)[8]. The Tokamak Fusion Test Reactor (TFTR), under construction at Princeton, is scheduled to provide the first demonstration of D-T operation with a reactor-grade plasma in the early 1980's. The Westinghouse studies have shown that TFTR can serve as the "plasma prototype" for the DTHR and can lead to demonstration of the production of very significant amounts of fissile fuel - at least 100 kg per year in initial operation. A demonstration of this type is an essential step in adapting existing fission reactor technology to the blanket environment characteristics of a hybrid, thereby ensuring viability of the concept. The objectives of the DTHR are thus to couple a fusion neutron source based on TFTR with existing fission reactor technology in as simple and straightforward a manner as possible to demonstrate the technology of fissile fuel production by the later 1980's. The concept employed is a beam-driven tokamak of about 5-meter major radius and 1-meter minor radius surrounded by a partial blanket of fertile material which could be designed to produce significant quantities of either Pu-239 or U-233 fuel. The DTHR is designed to operate on the D-T fuel cycle to produce 1-2 MW/m^2 of fusion neutrons at the first wall. Resolution of most of the critical scientific and physics questions prerequisite for the DTHR should be provided in the fusion program during the next five years[9]. Supporting research efforts will be needed in certain key technologies, of course, to ensure that long-pulse, high duty cycle operation can be achieved and that blanket fuel elements can function properly under the pulsed operation environment of the hybrid. Resolution of remaining problem areas in these technologies appears to be a reasonable goal, provided judiciously conceived development programs are conducted on a timely basis. Finally, investment in the development of these technologies can provide the basis for improved hybrid performance as better plasma confinement conditions are achieved, and will ultimately supply the experience in reactor engineering needed for the realization of pure fusion power. However, these conclusions regarding the prospects for a near-term hybrid test facility such as the DTHR are based on a limited amount of engineering study to date. More intensive studies are needed over the next several years before deciding to embark on a major hybrid development effort such as the DTHR.

REFERENCES

[1] ELECTRIC POWER RESEARCH INSTITUTE, Research and Development Program for 1978–1982 Overview, EPRI Rep., Palo Alto, CA (1 Sep. 1977).

[2] ROSE, R.P., et al., Trans. Am. Nucl. Soc. **27** (1977) 337.

[3] Proc. US-USSR Symp. on Fusion-Fission Reactors, Livermore, 1976, CONF-760733 (UC-20) (1976).

[4] ENGLE, R.L., DEONIGI, D.E., Electric Power Research Institute Rep. ER-469, Project 268-1, Part A (1976).

[5] DEONIGI, D.E., ENGLE, R.L., Battelle Pacific Northwest Labs Rep. BNWL-2139 (UC-20) (1977).

[6] AUGENSTEIN, B., Rand Paper No. P-6047, presented at the 2nd DMFE Fusion-Fission Energy Review Meeting, Nov. 1977, to be published.

[7] SCHULTZ, K.R., et al., A U-233 Fusion-Fission Power System Without Reprocessing – A Preliminary Report, General Atomic Rep. GA-A14635 (1977).

[8] SU, S.F., WOODRUFF, G.L., McCORMICK, N.J., Nucl. Technol. **29** (1976) 392.

[9] WESTINGHOUSE ELECTRIC, March 1978 Status Report on the Preliminary Conceptual Design of a Demonstration Tokamak Hybrid Reactor (DTHR), Rep. WFPS-TME-086 (1978).

DISCUSSION

R.G. LOGAN: Can the support ratio be sufficient to offset the higher cost of a fusion hybrid breeder compared to a fast breeder?

R.P. ROSE: We first need a better assessment of how great the capital cost of the hybrid will really be. A credible answer will require more in-depth engineering effort on commercial hybrid designs. With what we know today, and in anticipation of learning curve effects to reduce costs for commercial deployment, it appears that the attainable LWR support ratios will be sufficient to allow fuel production from the hybrid on an economically competitive basis.

F.L. RIBE: I might add, with regard to Dr. Logan's question, that the hybrid must not consume too much of its own electricity. In other words, the hybrid recirculating power fraction must not be too large because of the cost of electricity. Economic studies done by Battelle Northwest, the Rand Corporation and the University of Washington indicate that this fraction must be less than 50%.

ACCELERATION OF MACROPARTICLES BY LASER LIGHT

M.D.J. BURGESS*, H. MOTZ+
Department of Engineering Science,
Oxford University, Oxford

I.J. SPALDING, A.C. WALKER
Culham Laboratory,
(Euratom/UKAEA Fusion Association),
Abingdon, Oxon.,
United Kingdom

Abstract

ACCELERATION OF MACROPARTICLES BY LASER LIGHT.

Previous experimental investigations of the laser-induced acceleration of small metallic particles have been extended to lower-Z (polyethylene and solid deuterium) targets, of potential interest for refuelling fusion reactors. The variation of particle velocity with incident beam energy, focal spot size, pulse length, wavelength and target material has been examined over a much wider range of physical conditions than has been published hitherto. In particular the multikilojoule CO_2 laser Trojan has been used to accelerate 500 μm $(CH_2)_n$ cubes to velocities of ~ 900 ms^{-1} and 300-μm-diameter D_2 cylinders containing $\sim 3.0 \times 10^{18}$ atoms to velocities of ~ 800 ms^{-1} (within a full cone angle of $\sim 60°$). As the pulse duration is lengthened from 50 ns to $\lesssim 1$ μs, more of the D_2 burns through, leaving small fragments having directed velocities $\gtrsim 10^4$ ms^{-1}. Target accelerations of order 10^{10} ms^{-2} are inferred from shadowgram and interferometric observations. The validity of scaling laws derived from analytic models of the laser-target interactions, and some implications for pellet refuelling of toroidal reactors, are also discussed.

1. INTRODUCTION

There is a continuing interest [1-3] in the acceleration of macroparticles by focused laser radiation [4-7] as a technique for realising high-velocity pellet re-fuelling of fusion-reactors. For typical toroidal magnetic-confinement reactor systems, it is estimated that velocities of 10^4 m/s and greater will be required [8] if one assumes pellet dimensions of order 1mm. Centrifugal accelerators [9], gas guns [10] and electrostatic techniques are currently being developed for experimental tests of the pellet-ablation theory. Acceleration by the rocket effect, obtained by directional ablation of material from a pellet under laser irradiation has

---

* Present address: National Research Council, Ottawa, Canada.
\+ Present address: Clarendon Laboratory, Oxford, UK.

already, it is claimed, produced velocities of 10^4 to 10^6 m/s [5,6] for sub-millimetre corundum particles and thin (10-100 μm) Al foils respectively. Previous investigations at Culham of the laser-induced acceleration of small Mo targets [1] have now been extended to lower $\bar{Z}$ targets of potential interest for re-fuelling applications, and the scaling laws have been examined in some detail. Although other authors [2,11] have recently examined theoretical implications of using laser-driven ablation pressure to accelerate pellets to hypervelocities ($> 10^4$ ms^{-1}), it is thought that the work presented here still represents the only controlled experimental study of the velocities which can be achieved as the incident laser beam energy, focal spot size, pulse length, wavelength and target materials are systematically varied.

2. THEORETICAL MODELS

The pressure which accelerates the pellet during irradiation has two components: thermal and ablative. For plane targets having dimensions exceeding the focal spot size

$$\frac{d}{dt}(Mv) = [n_e kT_e + n_i kT_i + \dot{M}(v-u)]\, a \qquad (1)$$

where M and v are the mass and velocity of the pellet at a particular time t; n_e, n_i and T_e, T_i are the electron and ion densities and temperatures; $\dot{M}$ is the mass ablation rate per unit area; u is the ablation velocity relative to the target surface; a is the illuminated area and k is Boltzmann's constant. (Here, for simplicity, we postulate that the ablating plasma has an area comparable to a, i.e. that transverse thermal conduction may be neglected). When $T_e = T_i$ and $n_e = \bar{Z}\, n_i$, it follows that

$$\frac{M dv}{dt} = n_i (\bar{Z} + 1)\, kT_e\, a + |\dot{M}u|\, a \qquad (2)$$

By solving the conservation equations and assuming inverse bremsstrahlung absorption, the dependence of $\dot{M}$, u, n_i and T_e on the experimental variables can be calculated using an adaptation of the self-regulating model with the assumption of high absorption; the plasma expansion is assumed to be one dimensional [11-13]. Hence we can deduce the total plasma pressure acting on the target:

$$P = \frac{M}{a}\frac{dv}{dt} = 1.2 \times 10^{-4} [\bar{Z}^3 (1+\bar{Z})^{3/2} \lambda^2 t]^{-\frac{1}{8}} A^{-7/2} \phi^{\frac{3}{4}} \text{ Newtons m}^{-2} \qquad (3)$$

where ϕ is the irradiance, λ the laser wavelength, A the atomic weight, and MKS units are used throughout. Integration permits the velocity to be determined after time t. One-temperature fluid models showing strong inverse bremsstrahlung absorption are most appropriate when $\bar{Z} \gg 1$, so that $[\bar{Z}^3 (1+\bar{Z})^{3/2}]^{-\frac{1}{8}}$ will here be simplified to $\bar{Z}_1^{-9/16}$. The mean irradiance $\phi = E/a\tau$, where E is the laser pulse energy and τ its duration. When the target is sufficiently thick that its mass is almost constant whilst accelerating, its terminal velocity can be written:

$$v_{1D} = 1.0 \times 10^{-4} M_o^{-1} \bar{Z}_1^{-9/16} A^{7/16} \lambda^{-1/4} a^{1/4} \tau^{1/8} E^{3/4} \text{ ms}^{-1} \qquad (4)$$

Alternatively, at some distance from the target the expansion may become quasi-spherical, leading to a more rapid decrease in density. Adopting a three-dimensional fluid model [14,15], the terminal velocity for small mass decrements is then [3]:

$$v_{3D} = 3.1 \times 10^{-4}\ M_o^{-1}\ Z_1^{-1/2}\ A^{7/18}\ \lambda^{-2/9}\ a^{1/6}\ \tau^{2/9}\ E^{7/9}\ ms^{-1} \qquad (5)$$

For low-Z targets at high irradiation intensities the assumptions of inverse bremsstrahlung absorption and a one-temperature fluid expansion become increasingly inappropriate. A one-dimensional flux-limiting convective model of energy transport and ablation [16] has therefore been modified to suit the present D_2 experiments. Here, we have postulated a two-temperature electron fluid - having the ratio of cold-electron to hot-electron densitites $n_c/n_h = 2$ discussed in reference [17]. Assuming (resonant) absorption with a coefficient α near the critical surface, balanced by electron heat transport of magnitude $\frac{1}{2}\xi n m_e v h^3$, it can be shown:

$$v_{FL} = \sim 3.3 \times 10^{-6}\ M_o^{-1}\ [1 + (2Z)^{-1}]\ (\alpha/\xi)^{2/3}\ \lambda^{-2/3}\ a^{1/3}\ \tau^{1/3}\ E^{2/3}\ ms^{-1} \qquad (6)$$

where ξ (the flux limiter) will hereafter be given the value 1/16, as in reference [17]. (Note that different computer simulations suggest a slightly lower value for ξ [18].) In equation (6) the ion temperature has, for simplicity, been equated to the cold-electron temperature; density profile modifications are assumed to be weak; and the numerical multiplier takes values of 3.3×10^{-6} or 3.7×10^{-6}, depending whether an isothermal or adiabatic sound velocity is adopted for the expanding plasma [11].

3. EXPERIMENTAL TECHNIQUE

Using a pulsed 5J (18 ns) ruby laser and a 2J (45 ns) TEA CO_2 laser, previous work reported the velocity scaling of metallic foils with laser wavelength, incident intensity (ϕ) and atomic weight [1]. Velocities were measured from shadowgraphs taken with a 20 ns (FWHM) ruby laser. Using the same technique the focal spot size and pulse-length dependence have been studied, using a 1-4J ruby laser of variable pulse duration and the energy scaling extended by three orders of magnitude, using the multikilojoule CO_2 TROJAN laser [16,19,20]. Although molybdenum targets proved convenient for these scaling measurements, polyethylene foils have also been used to provide tests of scaling at lower $\bar{Z}$ (and with more modest values of tensile strength). Finally, some preliminary experiments on deuterium pellet acceleration by TROJAN are reported.

The small ruby laser incorporated feed-back control [3], which allowed its pulse duration to be varied from 18 to ~ 300 ns. The high-energy TROJAN laser is an e-beam controlled device which gives an initial 50 ns pulse followed by a tail of approximately one eighth the power, adjustable in duration up to 2.5 μs. An F/22 optical system focuses this pulse to a spot with 50% of the energy within a 1 mm diameter. The stationary targets of Mo or $(CH_2)_n$ were suspended by silica or glass fibres of diameter $\lesssim 10$ μm. The deuterium targets were free-falling ~ 300 μm diameter cylinders, between 500 and 900 μm long. They were manufactured using a commercial, miniaturised, version of an IPP prototype [21] which drops them tumbling, but with low angular scatter, some 25 cm into the (stationary) focal zone of TROJAN.

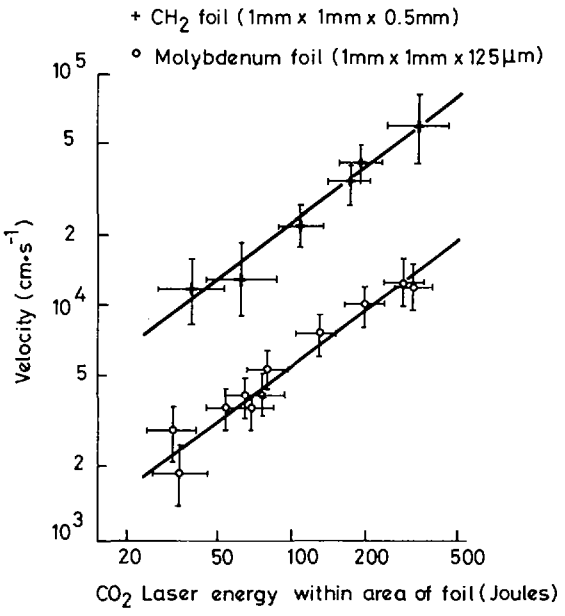


FIG.1. Dependence of velocity on CO_2 laser pulse energy for polyethylene and molybdenum foils. Lines drawn with slope of 7/9.

4. VELOCITY-SCALING MEASUREMENTS

The 1D and 3D expansion models predict energy scaling to the power 0.75 and 0.78 respectively. Measurements on Mo and $(CH_2)_n$ foils accelerated by the TROJAN laser are plotted in Fig.1, where it can be seen that the experimental points fit the (relative) energy scaling indicated. However, experimental errors preclude any distinction being made between the two models from the similar slopes predicted by equations (4) and (5). These Mo foil measurements have been combined with previous work at lower (0.1 - 2J) CO_2 laser energies [22], and are plotted in Fig. 2. A good absolute fit is obtained between the 1D expansion theory and the low-energy results, which were obtained with 0.75 x 0.75 x 0.025 mm foils irradiated by laser pulses of energy $\lesssim$ 2 J in a spot of 0.28 mm diameter. At higher energies 1 x 1 x 0.125mm targets were used; the parameter plotted, MV/a^4, thus facilitates intercomparison of the two sets of data. Here, a significant fraction of the incident laser energy is not initially intercepted by the foil, although later in the pulse absorption occurs in the ablating corona. In consequence conduction permits plasma blow-off at a wider range of solid angles around the target, contributing less to the net directional thrust and therefore giving a lower velocity than that predicted by equation (4). This interpretation has been confirmed by interferometric measurements of the ablating plasma. However, it is interesting to note that the relative scaling remains in good agreement.

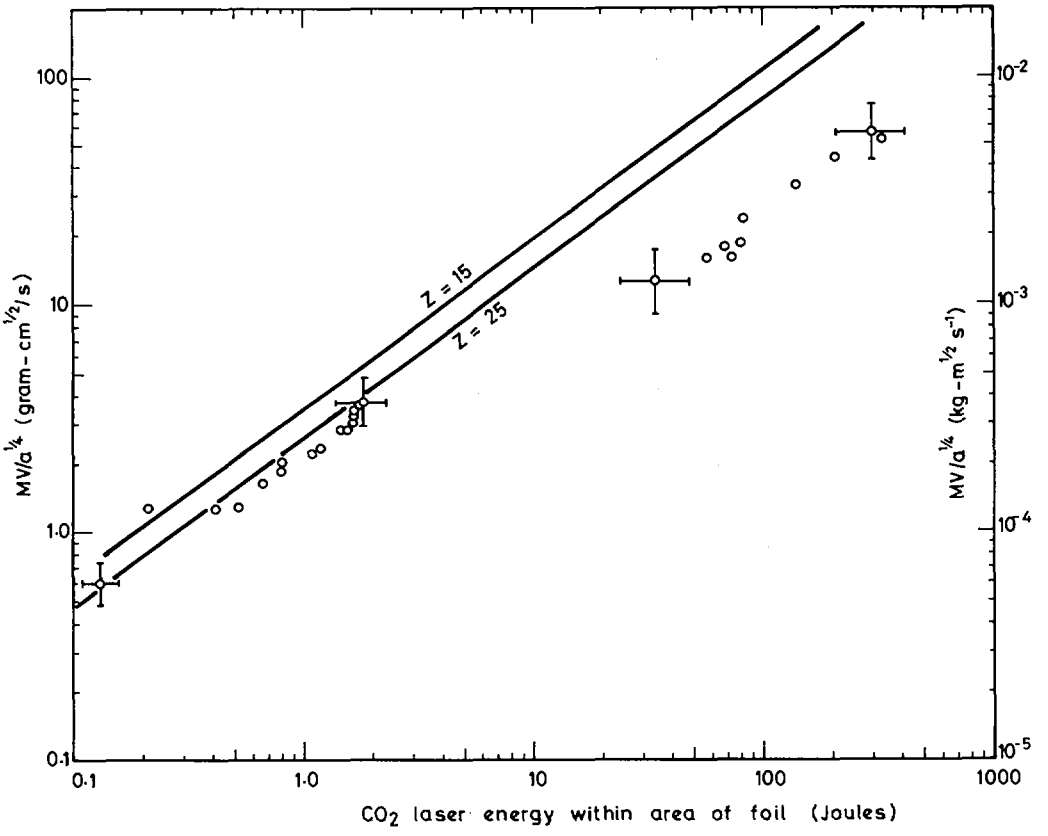


FIG.2. Comparison of the theoretical predictions of Eq.(4) for two Z values (continuous lines) with the experimental points obtained for CO_2 laser acceleration of molybdenum foils.

Fig. 3 illustrates the significant difference in velocity produced by different laser wavelengths (λ = 0.69 and 10.6 μm), at similar (0.1 - 5J) laser energies; identical Mo foil targets were used for this comparison. Allowing for the different spot sizes and pulse lengths (ruby: a = 2 x 10^{-7} m^2, τ = 18 ns; CO_2 : a = 6 x 10^{-8} m^2, τ = 45 ns), the experimental factor of 2.2 agrees with the wavelength scaling predicted by equations (4) or (5) to $\pm$ 15%. The weak dependence of velocity upon focal spot size, and upon target material, was tested using the 5J ruby laser (with focal areas varied systematically from 1.5 to 30 x 10^{-7} m^2); detailed results are discussed in [3]. Fig. 4 illustrates a slight (but definite) dependence of velocity on laser pulse duration observed when the TROJAN laser is used to irradiate 1 x 1 x 0.125 mm Mo foils. The 50 ns and 1.6 μs pulses were obtained by adjusting the duration of the electron-beam ionizer. A thirty-fold increase in irradiation-time produced a small increase in target velocity, at identical incident energies, consistent with the scaling of equation (4). A similar, but less conclusive, result was obtained by varying the 5J ruby laser pulse between 18 and 250 ns [3].

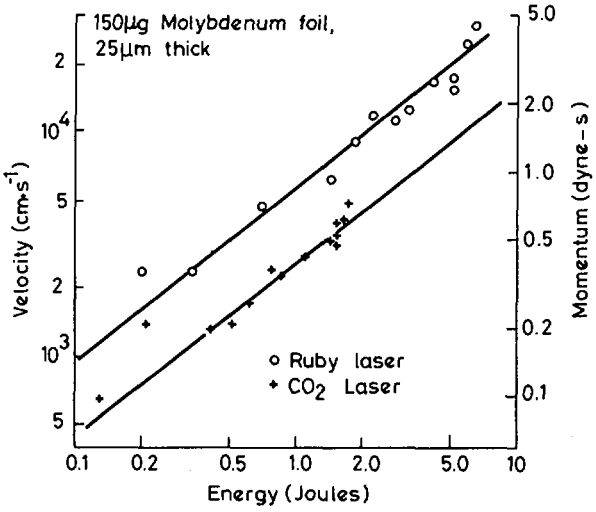


FIG. 3. Dependence of velocity on pulse energy for two laser wavelengths: ruby, 0.694 μm; and CO_2, 10.6 μm. Lines drawn with slope of 7/9.

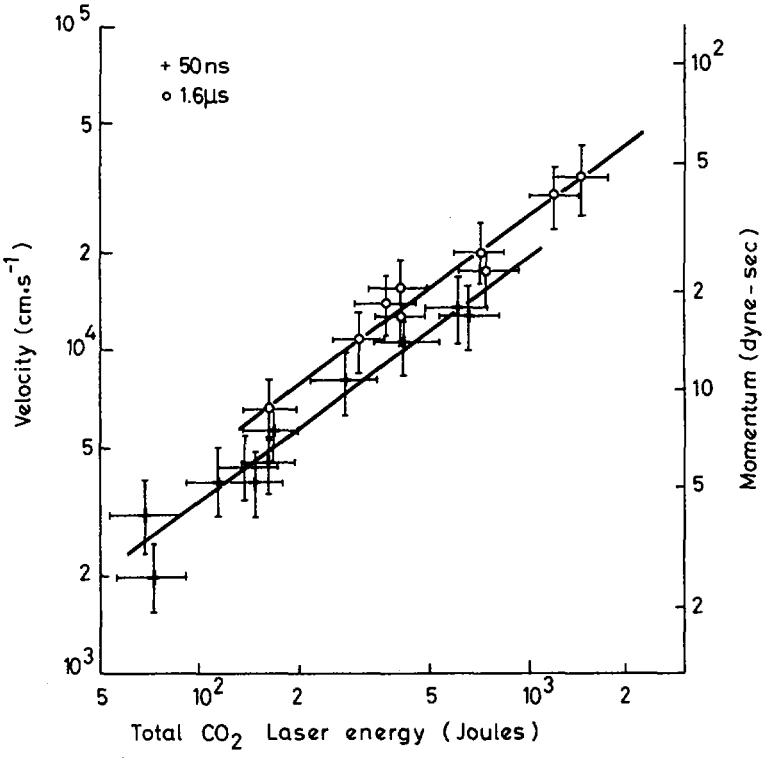


FIG. 4. Dependence of Mo-foil velocity on CO_2 laser energy for two pulse durations: 50 ns and 1.6 μs. Lines drawn with slope of 7/9.

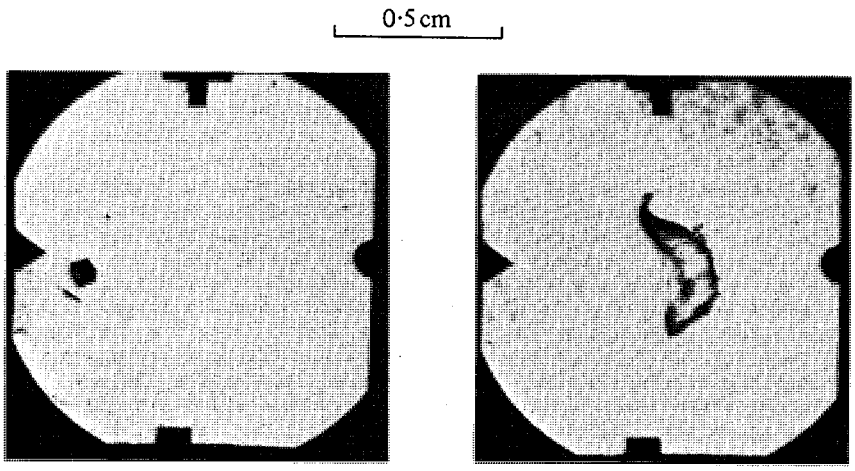


FIG.5. Left: shadowgraph of 0.5-mm polyethylene cube before irradiation. Right: shadowgraph of pellet 4.6 μs after start of irradiation by a 1.5-kJ (1.8-μs) CO_2 laser, incident from left.

5. PELLET FRAGMENTATION

Two factors contribute to the disintegration of pellets during acceleration. Firstly, shocks driven by the rapidly rising laser intensity can cause spallation of material from the far side of the target, and changes of state within the bulk of the pellet. Secondly, the longer-duration laser pulses can burn through (i.e. completely ablate) the target. Low-energy ruby and CO_2 lasers produced scarcely any observable fragmentation of Mo targets, thus simplifying the scaling discussed above. However, a long (1.6 μs) "TROJAN" pulse did cause fragmentation of a 50 μm Mo foil, whilst a short (50 ns) pulse of equal energy did not; clearly burn-through of the foil can contribute to the fragmentation observed. Polyethylene, with its weaker bond-strength, is obviously disrupted more readily [23]. Fig. 5 shows the result of accelerating a 0.5 mm cube of $(CH_2)_n$ to a velocity $\gtrsim$ 1000 ms^{-1} [20]; it can be seen that the pellet is expanding in all directions, due to internal heating. What prospect is there, then, for D_2 pellet re-fuelling of magnetically confined plasmas by laser techniques? When free-falling D_2 pellets were irradiated by a 0.5 kJ, 50 ns, "TROJAN" pulse (containing only ~ 100 J within the initial target area), bulk velocities of $\gtrsim$ 800 ms^{-1} were observed. However, pellet disintegration within a full cone angle of ~ 60° was apparent in the shadowgram, corresponding to transverse velocities approaching 400 ms^{-1}. Using longer pulses of ~ 1 kJ in 1 μs, individual fragments are accelerated to > 10^4 ms^{-1} but the mass of deuterium involved is only a small fraction of the initial pellet. At higher energies still, the pellet appears to burn through. These pellet velocities are ~ $\frac{1}{3}$ of the values predicted by eqn. (6): a discrepancy compatible with the interferometrically observed tendency of the corona to surround the pellet.

6. CONCLUSIONS

For high-Z targets such as Mo, the 1D model of equation (4) provides marginally better agreement with the scaling experiments. At higher intensities and with lower-Z materials, such as D_2, better absolute agreement is obtained with the two (electron) temperature model of equation (6), but present preliminary observations do not permit extensive scaling tests. The dominant parameter in determining the pellet velocity appears to be the absorbed laser energy: changes in target material, wavelength, focal diameter and pulse duration are of less importance. Presently achievable $(CH_2)_n$ or D_2 pellet velocities may already be of interest for (single-shot) Tokamak re-fuelling studies [24]; pellet fragmentation of these weakly bound materials is an important limiting factor on the maximum (directed) velocities attainable. However, the "TROJAN" system is at present primarily arranged to produce highly ionized laser-plasmas in CLEO Stellarator [16]. Weaker acceleration over longer flight-paths can be achieved by lengthening the laser pulse-duration and focal-length of the optics; this should permit larger pellets to be accelerated without exceeding the tensile strength of deuterium. Finally, reactor re-fuelling requirements neccessitate very long flight-paths ($\gtrsim$ 1 m) and/or radial confinement of the accelerating pellet. It is possible that an appropriate combination of cylindrical jacket and/or annular laser beam [25] would facilitate the technical development required.

ACKNOWLEDGEMENTS

I.J. Spalding and A.C. Walker wish to acknowledge the co-operation of Drs M. Salvat and W. Riedmüller in collaborative aspects of Euratom's D_2 pellet-source development, and of Dr. S. Kogoshi in helping to commission the Culham equipment.

REFERENCES

[1] BURGESS, M.D.J., MOTZ, H., RUMSBY, P.T., MICHAELIS, M.M., in Plasma Physics and Controlled Nuclear Fusion Research 1976 (Proc. 6th Int. Conf. Berchtesgaden, 1976) Vol.3, IAEA, Vienna (1977) 405.
[2] McCANN, T.E., DeGROOT, J.S., APS Bull. **22** (1977) 1205.
[3] BURGESS, M.D.J., D. Phil. Thesis, University of Oxford (1978).
[4] ASKAR'YAN, G.A., MOROZ, E.M., Sov. Phys.-JETP **16** (1963) 1638.
[5] ASKAR'YAN, G.A., RABINOVICH, M.S., SAVCHENKO, M.M., STEPANOV, V.K., STUDENOV, V.B., JETP Lett. **5** (1967) 208.
[6] BELOUSEV, V.N., et al., in Technology of Inertial Confinement Experiments (Proc. Advisory Group Mtg Dubna, 1976), IAEA Tech. Doc. No.200, IAEA, Vienna (1976) 241.
[7] WANIEK, R.W., JARMUZ, P.J., Appl. Phys. Lett. **12** (1968) 52.
[8] PARKS, P.B., TURNBULL, R.J., FOSTER, C.A., Nucl. Fusion **17** (1977) 539.
[9] CLARKE, J.F., Tokamak Reactors for Break-even (Proc. Conf. Erice-Trapani,1976), (1976) 283.
[10] DIMOCK, D., JENSEN, K., JENSEN, V.O., JØRGENSEN, L.W., PECSELI, H.L., SØRENSEN, H., OSTER, F., Risø Rep. No. 332 (1975).
[11] COOPER, R.S., Am. Inst. Aeron. Astron. J. **11** (1973) 831.

[12] CARUSO, A., GRATTON, R., Plasma Phys. **10** (1968) 867.
[13] KROKHIN, O.N., Physics of High Energy Density (Proc. Int. School of Physics, Enrico Fermi), Course XLVIII, Academic Press (1971) 278.
[14] NEMIHIROV, I.V., Appl. Math. Mech. **31** (1967) 320.
[15] PUELL, H., Z. Naturforsch. **25a** (1970) 1807.
[16] SPALDING, I.J., et al., in Plasma Physics and Controlled Nuclear Fusion Research 1976 (Proc. 6th Int. Conf. Berchtesgaden, 1976) Vol.2, IAEA, Vienna (1977) 589.
[17] MORSE, R.L., NIELSON, C.W., Phys. Fluids **16** (1973) 909.
[18] MANHEIMER, W.M., KLEIN, H.H., Phys. Fluids **18** (1975) 1299.
[19] WALKER, A.C., et al., in Controlled Fusion and Plasma Physics (Proc. 8th Europ. Conf. Prague, 1977) Vol.1 (1977) 54 (Culham Rep. CLM – P488).
[20] WALKER, A.C., STAMATAKIS, T.S., SPALDING, I.J., Culham Rep. CLM – P543 (1978), submitted to J. Phys. D.
[21] BAUMHACKER, H., BRINKSCHULTE, H., LANG, R.S., RIEDMÜLLER, W., SALVAT, M., Appl. Phys. Lett. **30** (1977) 461.
[22] RUMSBY, P.T., MICHAELIS, M.M., BURGESS, M., Opt. Commun. **15** (1975) 422.
[23] DONALDSON, T.P., KACHEN, G.I., SPALDING, I.J., J. Phys. D: Appl. Phys. **10** (1977) 129.
[24] FOSTER, C.A., et al.,Nucl. Fusion **17** (1977) 1067.
[25] SPALDING, I.J., UK Patent Ref. 11164, Wd. Cm. (1973).

APPLICATION OF BUNDLE DIVERTORS TO EXPERIMENTAL TOKAMAKS AND REACTORS AND SOME CONSEQUENCES OF COLLISIONLESS EXHAUST FLOW TO DIVERTOR TARGETS

P.J. HARBOUR, M.F.A. HARRISON,
A.D. SANDERSON, P.E. STOTT
Culham Laboratory,
(Euratom/UKAEA Fusion Association),
Abingdon, Oxon.,
United Kingdom

Abstract

APPLICATION OF BUNDLE DIVERTORS TO EXPERIMENTAL TOKAMAKS AND REACTORS AND SOME CONSEQUENCES OF COLLISIONLESS EXHAUST FLOW TO DIVERTOR TARGETS.

Two separate aspects of magnetic divertors in tokamak devices are discussed. The first part of the paper is concerned with the application of bundle divertors as a means of controlling the plasma exhaust and purity in experimental tokamaks and reactors. A brief review of the DITE experimental results is given and the extrapolation of the magnetic design to larger tokamaks and to reactors is discussed. The second part of the paper discusses some consequences of the collisionless flow of plasma into an idealized model divertor, which results in a high exhaust temperature and sheath potential.

1. INTRODUCTION

If a tokamak fusion reactor, fueled with deuterium and tritium, is to operate in a steady-state mode or for pulses lasting for several plasma containment times, some means must be found to:

(i) control impurities which would otherwise cool the plasma by radiation, making it more difficult to reach ignition;

(ii) exhaust the α-particles which together with the impurities would dilute the fuel;

(iii) reduce the power loading on the torus wall due to the fraction of the fusion power which is transferred to the plasma by the α-particles.

It has been proposed that these three essential roles can be achieved by means of a magnetic divertor, whereby field lines at the periphery of the containment region are arranged to channel the boundary layer plasma out of the torus into a separate divertor chamber where the plasma can be neutralized, the power can be dissipated on a large area of target, and any resulting gas and impurities can be pumped away.

In the first part of this paper we (A.D. Sanderson and P.E. Stott) briefly review the results of divertor experiments in DITE and discuss the extrapolation of the design of bundle divertors to larger tokamaks and reactors. In the second part of the paper we (P.J. Harbour and M.F.A. Harrison) consider some of the consequences of collisionless exhaust flow to the divertor target.

2. BUNDLE DIVERTOR EXPERIMENTS AND EXTRAPOLATION TO REACTORS

Two main types of divertor have been considered for tokamaks. One type is the poloidal-field divertor which has been demonstrated on DIVA and which will be further tested on the forthcoming PDX and ASDEX experiments. The theoretical advantage of this type of divertor is that it preserves the basic axisymmetry of the tokamak. The penalty is that the divertor coils link the toroidal field coils and must carry large currents. This presents severe technological problems in reactor design and maintenance.

The second type of divertor which is being considered for a tokamak is the bundle divertor [1,2]. In this configuration (Fig. 1) the divertor coils do not link any other coils and it has the attractive feature that the divertor coils and plasma exhaust system can be completely external to the main torus. In an experimental tokamak this simplifies the installation and preserves the option to use the full bore of the torus for non-divertor experiments. In a fusion reactor the bundle divertor coils could be more easily shielded from neutrons and removed for maintenance than the internal coils of a poloidal field divertor. The perturbation of the tokamak fields is necessarily non-axisymmetric, but experiments in DITE have so far shown that, at least in collisional plasmas, there are no deleterious effects. The following section summarises the experimental results which have been published previously [3,4,5,6].

2.1. Review of Divertor Experiments on DITE

The bundle divertor concept has been demonstrated experimentally on DITE at a toroidal field $B_T \approx 0.9$ T with a discharge current $I_p \approx 50$ kA

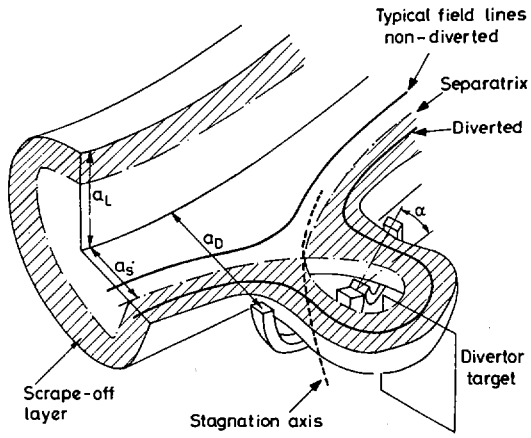


FIG.1. Schematic diagram of a bundle divertor indicating the coil angle α, and the minor radii: a_s of the magnetic limiter, a_L of the material limiter or torus wall, and a_D of the outer leg of the divertor coil.

corresponding to $q \approx 3$ at the magnetic limiter radius $a_s = 20$ cm. A relatively low density limit, $\bar{n}_e \lesssim 1.0 \times 10^{13}$ cm^{-3}, results from the low toroidal field. Typical values of the central plasma temperatures are $T_e(o) \simeq 300$ eV and $T_i(o) \simeq 100$ eV.

To investigate the effects of the divertor, comparison has been made between three situations; (i) diverted discharges with a magnetic limiter radius $a_s \simeq 20$ cm and a material (molybdenum) limiter radius $a_L \simeq 26$ cm; (ii) undiverted discharges with the material limiter at $a_L = 26$ cm; (iii) undiverted discharges with $a_L = 20$ cm. These experiments have clearly demonstrated that the bundle divertor exhausts both particles and energy, and reduces the influx of impurities into the plasma.

The plasma exhaust is clearly seen by direct measurement of particle fluxes into the divertor and results in a decaying density unless the discharge is refuelled by puffing hydrogen gas into the torus. The total power measured on the divertor plate corresponds to about 60% of the ohmic input. This is a dramatic change in the power balance. In undiverted discharges over half of the ohmic input is radiated, with a radiation power profile peaked on axis. The divertor reduces the radiated power by a factor of between 5 and 8.

A reduced influx of impurities at the plasma edge ($r \simeq 26$ cm) is observed spectroscopically and with a carbon collector probe [7]. The influx of oxygen is reduced to 60% compared to undiverted discharges and the molybdenum to 16% even with a molydbenum divertor plate, thus showing that backflow from the divertor is small. These results indicate a substantial reduction in the plasma-wall interaction. The mechanism for reduced impurity release is thought to be reduced arcing due to a cooling of the plasma boundary.

The impurity influx into the undiverted core of the discharge is further reduced by the divertor screening effect whereby impurities are ionised and swept into the divertor as they penetrate the boundary layer. The screening efficiency is estimated from the relative intensities of spectral lines at a_s and at the wall. Typically, for oxygen $\xi_s \simeq 50\%$ and for molybdenum $\xi_s \simeq 75\%$. These values are in reasonably good agreement with a simple model calculation [2].

2.2. Extrapolation of Bundle Divertors to Higher Magnetic Fields

Extrapolating the bundle divertor concept to higher values of the toroidal field B_T has stimulated a reappraisal of the design of the divertor coils. A simple extrapolation of the first DITE divertor (now designated Mk IB) from its working limit of $B_T = 1.5$ T to $B_T = 2.8$ T, which is the maximum field of DITE, would almost double the required divertor coil current and thus almost quadruple the power dissipated and the electromagnetic forces. Improvements in the magnetic design following the principles outlined below have resulted in a new divertor design (Mk II) which will operate at 2.8 T with almost the same coil current as the Mk IB coil requires at 1.5 T.

Consideration of several factors influences the design of bundle divertor coils. The basic physics parameters are the plasma exhaust efficiency, the thickness of the scrape-off layer and the perturbation of the toroidal field. Once these are specified, the diameter, angle and position of the coils can be varied to optimise the engineering parameters such as the coil current, current density, power dissipation and forces.

The thickness of the scrape-off layer between the magnetic limiter radius a_s and the wall or material limiter a_L is a very important parameter. The layer must be made sufficiently thick to provide adequate exhaust and impurity screening, but if it is made too thick the volume of contained

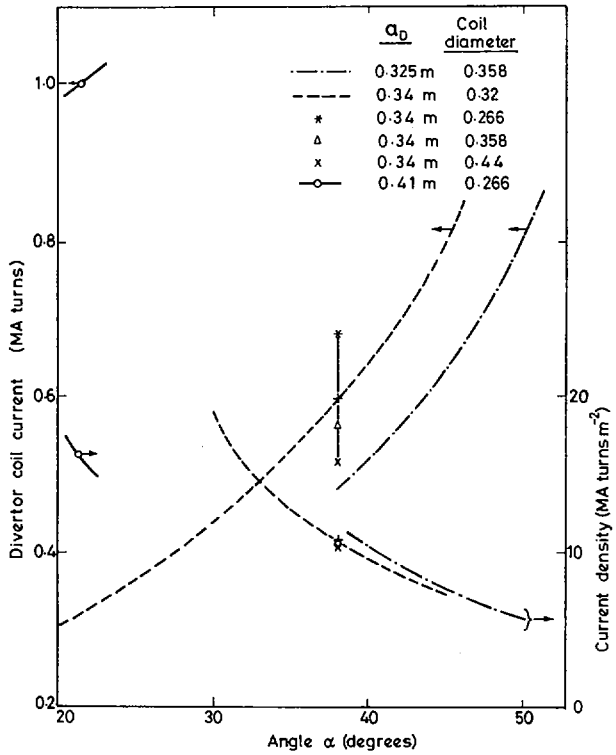


FIG.2. Divertor coil current and current density versus coil angle α for fixed values $a_s = 0.21$ *m and* $a_L = 0.27$ *m. The effects of varying the coil diameter* d *and the position of the outer leg* a_D *are also indicated.*

plasma will be reduced and there will be a serious increase in the current required for the divertor coils. It is important to make a realistic estimate of the scrape-off layer thickness but this is difficult as we do not have an adequate understanding of plasma diffusion in the scrape-off layer or even in the boundary layer of a non-divertor tokamak. This requires further theoretical and experimental study and so we have based the DITE Mk II divertor design on an empirical scrape-off layer width of 6 cm (i.e. a_s = 21 cm, a_L = 27 cm) similar to the width of 7 cm which seems to be satisfactory in the Mk I DITE divertor.

The first step in optimising the divertor coils is to position them as close as possible to the plasma boundary. The minimum distance is set by the thickness of the vacuum wall, and in a reactor by the neutron shield.

It is convenient to specify the divertor position by the minor radius of the outer leg of the coil which we denote by a_D. We will keep this distance and the coil diameter d fixed while we vary the coil angle α, allowing in effect the central leg of the coil to move in and out radially and the outer leg to slide around the outside of the torus wall. As the angle α is increased, Fig. 2 shows that the coil current needed to maintain a fixed width of scrape-off layer increases, but more slowly than the area A available for the coil, so that the net current density in the central limb of the coil decreases. The power dissipated in the coil which scales approximately as I^2/A and the electromagnetic stresses which scale approximately as B_T I/A are minimised for $\alpha \simeq 45^\circ$. Figure 2 also shows that the coil current is reduced substantially by reducing a_D, emphasising the desirability of positioning the coil as close as possible to the plasma boundary. The effect of increasing the coil diameter is also to reduce the required coil current, but at the expense of increasing the perturbation of the toroidal field. In the case of DITE the B_T coils limit the size of the divertor coils $d \leq 40$ cm, which results in $\Delta B_T/B_T \simeq 2.6\%$ at the centre of the discharge.

2.3. Extrapolation to Larger Tokamaks and to Reactors

One of the most important results of this work is the realisation that bundle divertors appear to be feasible for large tokamaks and even for fusion reactors. The extrapolation is mainly one of size rather than field strength and the space available for the divertor coils and their support structure is found to increase with size more rapidly than the total forces or power dissipation. Thus although the divertor coils in a large tokamak may be subjected to extremely large forces, the actual stresses in the coil and its support structure may be no worse than in a medium-sized tokamak such as DITE.

As an example we have carried out a very preliminary study of a large torus with $B_T = 3.5$ T, R = 2.48 m and $a_L = 0.9$ m, similar to TFTR. With a scrape-off layer width of 0.2 m, the toroidal field which must be diverted at the magnetic separatrix radius $a_s = 0.7$ m is 2.7 T and therefore no larger than in the DITE Mk II divertor. Coils with the parameters $\alpha = 45^\circ$, $a_D = 1.27$ m and d = 0.7 m would require a total divertor current of 3.2 MA turns and a net current density approximately one half that of the DITE divertor. On the basis of this preliminary design study a bundle divertor for TFTR seems feasible.

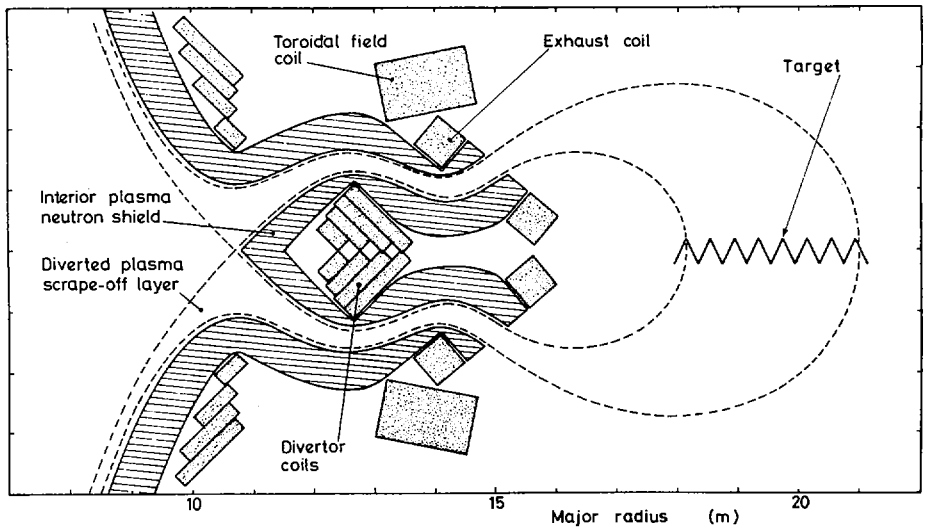


FIG.3. Section through a reactor-sized bundle divertor showing the expansion of the diverted flux outside the toroidal field coils by means of additional exhaust coils.

We have also carried out a preliminary magnetic design study of a bundle divertor based upon the Culham conceptual tokamak reactor Mk II [8]. In this case the separation of the divertor coils from the plasma boundary must be increased to accommodate a neutron shield. Recent studies indicate that a minimum shield thickness of 0.75 m will be required to ensure an adequate lifetime for electrical insulators in the coil. For water-cooled copper divertor coils the power consumption would be 92 MW which, although high in absolute terms, is less than 5% of the nominal electrical output (2000 MWe) of the reactor. The current density in the coil would be 1.5 kA cm^{-2}, sufficiently low to permit continuous operation. Figure 3 shows the arrangement of the divertor coils together with a supplementary pair of exhaust coils which allow the plasma to expand before it intercepts the target, as discussed in the following section.

The power consumption of a conventional set of divertor coils makes it desirable to consider using superconducting windings. The average magnetic field inside the divertor coils is about 5 T and the maximum value, at the inner edge of the coil, is close to 7 T. The average current density in the coil is 1.5 kA cm^{-2}. These values appear to be reasonable even in terms of present-day superconducting technology.

3. SOME CONSEQUENCES OF COLLISIONLESS EXHAUST FLOW TO THE DIVERTOR TARGET OF A FUSION REACTOR

A tokamak reactor, fuelled with a deuterium-tritium mixture and operating in a steady state, must be capable of accommodating the power associated with the formation of the 3.52-MeV α-particles. This power, some 800 MW for a 5000 MW (thermal) reactor, could be radiated to the first wall; alternatively it could be removed from the torus by particle transport into a divertor. Transport into the divertor could be under conditions of high plasma density with the objective of exhausting the α-particle power by conduction and radiation within the divertor. However, such transport implies a dense scrape-off plasma so that charge-exchange and impurity radiation losses to the first wall may be unavoidable. Further, the high thermal conduction rate along the magnetic field may require that the exhaust path be too long to be accommodated within a bundle divertor. An alternative is to operate in a lower-density regime so that, apart from the inevitable but small bremsstrahlung losses, the energy is exhausted by non-radiative transport of particles into the divertor. Under these conditions the energy must be removed from the divertor plasma before the particles can be exhausted, and one approach that has been studied in some detail (albeit in the poloidal divertor of UWMAK III [9]) is to allow the plasma to impact upon a target. Practical considerations of the material properties of the target limit its power loading, and so the magnetic fields in the divertor must allow the plasma to expand and cover a large area at the target. Consequently the plasma density is low and, for the present purposes, the exhaust plasma can be considered as collisionless within the divertor although it must originate in a much more dense region close to the separatrix where particle collisions can take place. It is the objective of this section of the paper to consider some of the consequences of such collisionless exhaust of particles and energy from a tokamak reactor.

3.1. Modelling of a Collisionless Exhaust

A simple one-dimensional model [10] has been developed and its principal aspects are illustrated in Figure 4. An electron-repelling plasma sheath must be formed in front of the divertor target in order that the loss rate of electrons and ions can be so balanced that the global loss of charge from the tokamak be zero. For a hot reactor plasma, both the electrons and ions that strike the target have sufficient energy to release appreciable numbers of secondary electrons [11]. These electrons are accelerated into the exhaust plasma by the action of the sheath potential. They

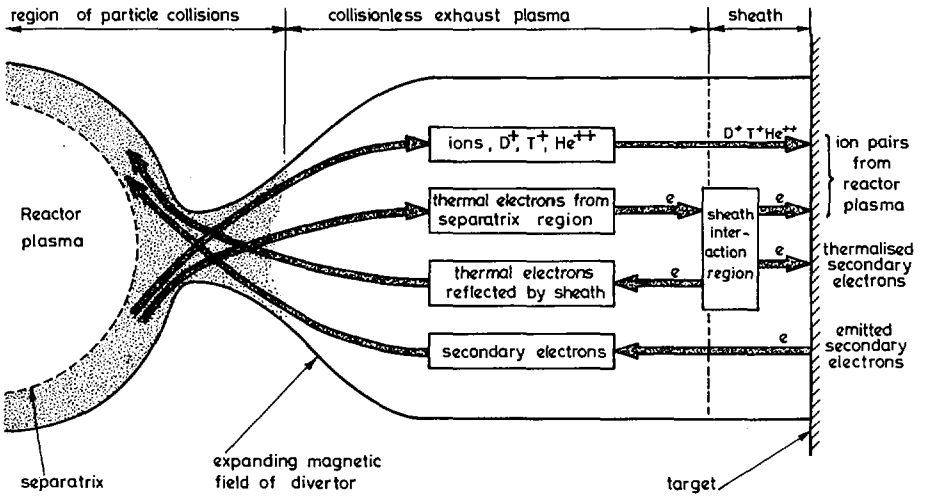


FIG.4. Idealized exhaust by collisionless flow to a divertor target.

can travel, guided by the magnetic field, back through the exhaust plasma and then interact with the dense plasma near to the separatrix where they thermalise before returning to the divertor. This increases the ability of the exhaust plasma to convect energy to the divertor target.

An analysis has been performed of the effect of secondary electrons on sheath potential and energy and particle transport through the sheath [12]. It is assumed that electric fields are zero except in the sheath and that all the particles striking the target are lost. Truncated Maxwellian distributions of electron and ion velocities are used to allow for these losses and in addition the ions are allowed to have a superimposed drift velocity. The secondary electrons are assumed to have a velocity corresponding to their acceleration within the sheath. The model assumes constant area and neglects the magnetic field because the field in the divertor is assumed to be uniform and normal to the target. Conditions for charge neutrality and current continuity lead to a relationship between sheath potential and secondary electron yield, both of which are then related to the energy, $\delta_t kT_e$, carried by each ion and its paired electron together with the associated secondary electrons. Solution of the Poisson equation shows that the maximum yield of secondary electrons is limited by space-charge saturation in the sheath. Corresponding to this maximum yield

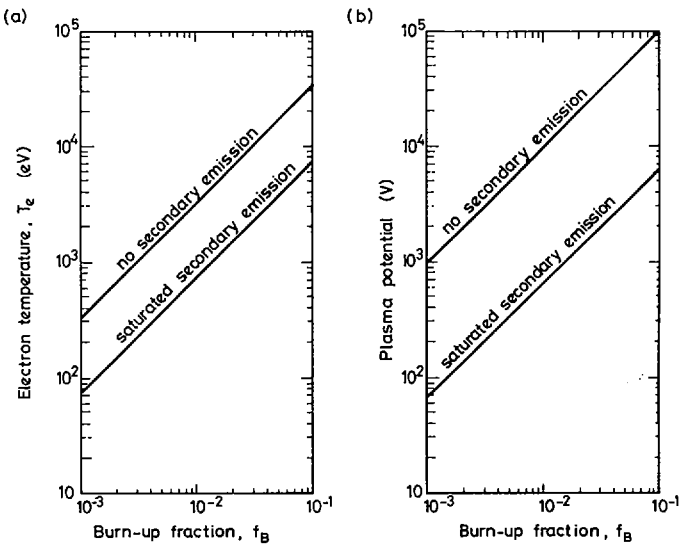


FIG.5. Electron temperature (a) and potential (b) of the exhaust plasma plotted versus burn-up fraction f_B. Two conditions are illustrated: no secondary electron emission ($\delta_t = 5.8$, $\delta_i = 0.5$, $\phi_w = 3.3$) and saturated electron emission ($\delta_t = 23$, $\delta_i = 0.53$ and $\phi_w = 0.865$).

is a lower bound in sheath potential and also an upper bound in the energy transport coefficient δ_t. The Bohm criterion provides a further constraint upon sheath conditions. The maximum value of δ_t is found to be about 23 and this is four times larger than in the case of no secondary emission.

3.2. Collisionless Exhaust Conditions for a Reactor

The power input to the divertor is governed by the α-particle power and so the temperature of the collisionless exhaust plasma depends upon how many particles can share in the energy (E_α = 3.52 MeV) of each α-particle. Sharing can take place with the secondary electrons and also with any unburnt D-T fuel whose burn-up fraction, f_B, can be defined as

$$f_B = \frac{\Phi_\alpha + \Phi_{\text{neutrons}}}{\Psi_D + \Psi_T} = \frac{2\Phi_\alpha}{\Psi_D + \Psi_T}$$

Here Ψ and Φ are respectively the fluxes of particles entering and leaving the reactor, and the subscripts are self-explanatory. Neglecting relatively small sources and sinks of energy, the electron temperature of the exhaust plasma can be expressed by

$$kT_e \approx E_\alpha f_B / 2\delta_t$$

This temperature is plotted in Fig. 5(a) as a function of f_B for two values of the energy transport coefficient, δ_t = 5.8 and 23, representative of zero and saturated secondary electron yield respectively. The target sheath potential is related to T_e and has been shown [10,12] to be about 3.3 kT_e/e for the case of no secondary electron field and 0.87 kT_e/e when secondary emission is space-charge limited. The variation of sheath potential with f_B is shown in Fig. 5(b) for these two cases. It is evident that even when the secondary emission is saturated and f_B = 0.05 the temperature of the exhaust plasma is about 4 keV and its sheath potential is about 3.5 kV. The temperature of the exhaust plasma must be less than the temperature at the separatrix and the average temperature of the reactor plasma within the separatrix is not likely to exceed 15 keV. Thus it is evident that the burn-up fraction for a reactor with a collisionless exhaust must not exceed a few per cent and indeed $f_B \approx 0.05$ could well be an upper limit. When practical levels of power density on the target are considered (1 to 10 MW m^{-2}) it is evident that the plasma density must be low (10^{14} to 10^{16} m^{-3}) and so the collisionless conditions implicit in the model are satisfied within the divertor [10]. However, the model does not allow for non-normal incidence of the magnetic field at the target nor for mirroring of secondary electrons by the magnetic field. The consequences are likely to be a reduction in the yield of secondary electrons and a lower probability of thermalisation in the separatrix region so that the exhaust temperature is raised and more stringent limits must then be imposed upon the burn-up fraction.

4. CONCLUSION

It has been argued [13,14] that a reactor divertor should operate in the unload mode in which the α-particle power is transported into the divertor rather than to the first wall. In such a divertor the plasma flow could be considered as collisionless [9] but the present idealised model shows that both the exhaust temperature and sheath potential are very high. As a result, target erosion and impurity production due to sputtering and unipolar arcing will be significant. Although secondary electrons can help reduce the exhaust temperature and potential, the only way to reduce the plasma potential of a collisionless divertor to below the unipolar arc threshold is by drastic reduction in burn-up fraction, i.e. $f_B \approx 10^{-4}$. If arcing is unavoidable, then the exhaust plasma will become collisional and the present model is no longer applicable.

Experiments in DITE have demonstrated that a bundle divertor controls the plasma exhaust and impurity influx in a tokamak. Magnetic design studies show that the concept can be extrapolated to larger tori and higher magnetic fields, and has sufficient reactor potential to justify a more detailed design study.

REFERENCES

[1] STOTT, P.E., WILSON, C.M., GIBSON, A., Nucl. Fusion **17** (1977) 481.
[2] STOTT, P.E., WILSON, C.M., GIBSON, A., Nucl. Fusion **18** (1978) 475.
[3] PAUL, J.W.M., et al., in Plasma Physics and Controlled Nuclear Fusion Research 1976 (Proc. 6th Int. Conf. Berchtesgaden, 1976) Vol. 2, IAEA, Vienna (1977) 269.
[4] STOTT, P.E., et al., Symp. Plasma-Wall Interactions, Jülich, 1976, Paper No. E3.
[5] FIELDING, S.J., et al., in Controlled Fusion and Plasma Physics (Proc. 8th Europ. Conf. Prague, 1977) Vol. 1 (1977) 36.
[6] STOTT, P.E., et al., to appear in J. Nucl. Mater.
[7] McCRACKEN, G.M., et al., in Controlled Fusion and Plasma Physics (Proc. 8th Europ. Conf. Prague, 1977) Vol. 1 (1977) 40.
[8] SANDERSON, A., STOTT, P.E., to appear in J. Nucl. Mater.
[9] CONN, R.W., et al., in Plasma Physics and Controlled Nuclear Fusion Research 1976 (Proc. 6th Int. Conf. Berchtesgaden, 1976) Vol. 3, IAEA, Vienna (1977) 203.
[10] HARBOUR, P.J., HARRISON, M.F.A., Nucl. Fusion **19** 6 (1979), in press.
[11] HARBOUR, P.J., HARRISON, M.F.A., 3rd Int. Conf. on Plasma Surface Interactions in Controlled Fusion Devices, Culham, 1978 (Culham Rep. CLM-P 528 (1978)).
[12] HARBOUR, P.J., The Effect of Secondary Electron Emission on a Plasma Sheath, Culham Rep. CLM-P 535 (1978), to be published.
[13] CARRUTHERS, R., in Controlled Fusion and Plasma Physics (Proc. 8th Europ. Conf. Prague, 1977) Vol. 2 (1977) 217.
[14] CONN, R.W., 3rd Int. Conf. on Plasma Surface Interactions in Controlled Fusion Devices, Culham, 1978.

DISCUSSION

ON PAPERS R-5-1 AND R-5-2

H.J. HOPMAN: I have a question concerning paper R-5-1. If the pellets are accelerated by ablation, the optimum load is $\approx 20\%$; thus 20% of the pellet material is injected into the plasma, but 80% reaches the plasma edge as ablated gas. How is one to deal with this enormous gas load in tokamak reactors?

H. MOTZ: Perhaps I could answer that question. The gas is accelerated backwards and need not reach the reactor at all, particularly if the end path is free flight.

G.A. EMMERT: In the bundle divertor design, is it possible to give a limiting value for the toroidal magnetic field and still keep the stresses acceptable?

P.E. STOTT: In our reactor design study, the toroidal field on axis is about 6 T. This does not appear to be a limiting value, but further detailed calculations of the coil structure and the stresses are required.

G.A. EMMERT: We have done similar calculations and find that we can reduce the electron temperature by choosing a re-fuelling profile peaked near the edge. But we are not able to get it low enough to change the conclusion that arcing is a real problem for the collector plate.

P.E. STOTT: Since we have considered a zero-dimensional reactor plasma, our conclusions do not depend on the re-fuelling profile; rather, they depend on the total re-fuelling rate and on the burn-up fraction. The burn-up fraction does depend on the re-fuelling profile, but, provided it is known, the exhaust temperature and plasma potential can be determined. We are particularly concerned to highlight the problem of arcing at the collector plate, so your comment is very much to the point.

J.P. GIRARD: What sort of toroidal ripple is introduced by the presence of the bundle divertor, and does this ripple influence significantly the confinement of high-energy ions and α-particles?

P.E. STOTT: In the DITE Mk I Bundle Divertor, the toroidal ripple at the centre of the confined plasma is about 1.5%. No deleterious effects have been observed experimentally, although so far we have not worked in the collisionless plasma regime where we might expect to see more marked effects. We are at present calculating the effect of this perturbation on the confinement of high-energy ions and α-particles, and these results will be published shortly.

H. CONRADS: How long can you maintain the divertor current compared to the plasma current in the case of water-cooled divertor coils?

P.E. STOTT: In the preliminary magnetic design study for a reactor-sized bundle divertor – see Ref.[8] – the current density in the divertor coil would be 1.5 $kA \cdot cm^{-2}$. This is sufficiently low to permit continuous operation.

SUMMARY SESSION

Chairman

R.J. BICKERTON
UK

SUMMARY ON MAGNETIC-CONFINEMENT EXPERIMENTS*

C.M. BRAAMS
FOM-Institute for Plasma Physics,
Jutphaas, Netherlands

Let me start with a quotation:

"It is now clear to all that our original beliefs that the doors into the desired region of ultra-high temperatures would open smoothly at the first powerful pressure exerted by the creative energy of physicists, have proved as unfounded as the sinner's hope of entering Paradise without passing through Purgatory. And yet there can be scarcely any doubt that the problem of controlled fusion will eventually be solved. We just do not know how long we shall have to remain in Purgatory. We shall have to leave it with an ideal vacuum technology, with thoroughly elaborated magnetic field configurations, with accurately prescribed geometry of the lines of force, and with programmed cycles for the electrical circuits, bearing in our hands the high-temperature plasma, stable and quiescent, pure as a concept in theoretical physics when it is still uncontaminated by contact with experimental fact."

The quotation is from the summary lecture presented by Lev Artsimovich at the 1961 IAEA Conference in Salzburg. Here then is our continuing Report from Purgatory, Issue number 7, Chapter 1, Magnetic Confinement Experiments.

TOKAMAKS

The largest body of experimental evidence, consisting of many interlocking contributions from different laboratories, is that concerning the tokamak. Also the most striking single result, passing the milestone marked "D-T ignition temperature", was achieved in such a device. It is true that very energetic ion populations have been produced before; it is also true that we are still some distance away from actual ignition conditions. The reason why, nevertheless, we attach so much weight to the results from the Princeton Large Tokamak is that we now have proof that one

* This summary talk was also published in Nucl. Fusion **19** 1 (1979) 125.

confinement method can satisfy both the temperature requirement and the requirements of plasma purity and isolation that are necessary for plasma energy breakeven in a beam-plasma system, or – if one wishes to call it so – for the scientific proof of the feasibility of deuterium-tritium fusion energy production. The $n\tau$ and purity requirements had previously been met in Alcator and subsequently in other machines; the latest Alcator figure (C-4) $n\tau = 3 \times 10^{13}$ cm$^{-3} \cdot$ s is well in the range of two-component operation. PLT has now demonstrated (C-3) that injection of neutral beams can bring the ion temperature up to the required value, and that, when moving far into the regime of long mean free path, one is not blocked by new anomalous ion energy loss mechanisms, such as trapped-ion instabilities. Since also the electron energy loss, though still anomalous, did not get worse – if anything, it got better – one must conclude that the prospects for reaching breakeven conditions in the next generation of large tokamaks, now under construction in different parts of the world, appear to be excellent.

Every owner of a tokamak worries about current disruptions and would like to understand and to control them. Many contributions have been offered at this Conference, but no unified picture has yet emerged. Most tokamak groups find that external disruptions are always preceded by m = 2 oscillations (e.g. A-5). A steepening of the current profile near the q = 2 resonant surface, causing instability of the m = 2 tearing mode, is held responsible. But in some cases, Princeton did not observe the m = 2 oscillations, and Fontenay sees also mainly m = 3, so there remains doubt about the universal validity of this description (A-1, A-6). And, for the cases where m = 2 is present, there is evidence from several experiments that coupling to m = 3, with n = 2, plays a role, but again, no single description appears to fit all disruptions. The influx of high-Z impurities from the wall and the limiter is one of the determining factors, presumably because they affect the temperature and current profiles; we shall return to these impurities in a moment.

Observations on several aspects of helical modes, associated island formation, anomalous transport, and minor disruptions are reported by the groups just mentioned, and by the Garching, Oak Ridge, Culham, T-II, Tuman, T-11, and Tokyo Tokyo teams (C-5, N-2, N-4, T-1, T-2). Plasma behaviour in Pulsator could be influenced by manipulation of the q = 1 resonant surface by means of an m = 1 helical winding, but selective application of this technique is difficult, because it also affects the q = 2 surface (T-4). Windings with m = 2 have, of course, been applied to the q = 2 surface quite successfully to either stimulate, or retard, the onset of the m = 2 mode, and the Kurchatov Institute has obtained good results with feed-back stabilization of this mode, which caused both the temperature and the density to go up (N-1).

We have already mentioned the effect of impurities on disruptions. They can change almost any characteristic of the discharge, and methods to clean up the plasma, therefore, receive much attention. The technique of discharge cleaning initiated at MIT has found widespread application, even in an alumina torus in

Los Alamos (E-1-1). In addition, gettering is found to be essential by several teams. Feeding neutral gas during the discharge, and using a carbon or steel limiter, rather than one of heavy metal, also contribute to lowering Z_{eff} (A-1 to A-3, A-6, N-4, C-4). Conditioning of the limiter is found to be very important in the Kurchatov Institute. Both ISX-A and TFR-600 appear to benefit from a distance of 6 cm between the plasma and the nearest part of the wall (N-4, A-6). Feedback is practised extensively for control of the position of the plasma column, particularly when the copper shell is abandoned. On the basis of a comparative study, the DITE team finds gettering effective against low-Z impurities, and gas inlet against high-Z; they offer the suppression of unipolar arcs as an explanation for the effect of gas inlet (A-3), where the DIVA team (T-3-1) with support from PLT hold ion sputtering responsible for high-Z contamination. DITE and DIVA, together with the T-12 team, report striking improvements in plasma purity and reduction of radiation losses with their bundle, single axisymmetric and double axisymmetric divertors, respectively (T-3-2). Only scattered evidence exists on the merits of a cold mantle between plasma and wall. Insufficient impurity control detracts from the value of experiments on heating and confinement when we do not know how the reported behaviour would change if the plasma were clean. We shall not find our way out of Purgatory before our vacuum techniques and our control of the discharge have improved to the point where Z is always one unless impurities are deliberately admitted, or helium is produced.

Be that as it may, we certainly shall not get rid of impurities entirely, and the questions: how rapidly do they penetrate and to what extent do they accumulate in the centre are of crucial importance for reactor design, in particular with regard to the performance required of the divertor, if any. Related to this is the question how fuel distributes itself through the plasma column, and what will be required of fuel injectors, if any. So what have we learned about particle transport?

The evidence is ambiguous. In the small Hybtok experiment at Nagoya, the impurity transport is found to be consistent with Pfirsch-Schlüter diffusion (T-2). In ISX-A, asymmetric hydrogen inlet drove neon out of the discharge as predicted by neoclassical theory (N-4). Concentration of impurities in the centre of the discharge, long ago predicted and feared, but so far never observed, was finally recorded in Pulsator when a quiescent regime was established at the high-density operating limit (A-5). (This reminds one that a certain measure of turbulence is not necessarily bad for tokamak reactor operation. But it is of great interest for our understanding of particle transport that conditions have now been found where classical behaviour appears to obtain.) Against these examples of classical behaviour, however, we have many more of anomalous penetration of impurities, like in PLT (A-1).

The rate at which hydrogen penetrates the plasma is also highly anomalous in tokamaks operated with pulsed gas inlet. The anomaly is not restricted to the edge region, where rapid re-circulation of the gas is driven by strong density

turbulence (C-4, N-4, N-5-2), and appears to be fairly well described in the case of DITE by a particle transport coefficient one fifth of the electron heat conduction, combined with the neoclassical pinch effect (F-2). One is tempted to speculate that all anomalous transport will cease in the high-density regime, but the experimental evidence is insufficient to prove the point. We have no complete picture of how various transport processes are related to various modes of instability.

This makes it difficult to establish scaling laws; although some fairly successful attempts have been made to relate existing experimental data, their predictive value is small because the underlying physics is unclear so that one does not know what will happen when new regions in parameter space are entered. Nevertheless, there is rather broad agreement that, if the q-profile is kept under control so as to restrict MHD activity, ion heat losses in the centre are neoclassical to within experimental error, although we must admit that at the frontier this error becomes large. There is also broad agreement that electron heat loss goes down with density, either proportionally, or nearly so. It is evident that, in the end, the resulting improvement in overall energy confinement runs up against the neoclassical limit, where ion heat conduction has replaced the electron channel as the dominant loss mechanism.

It is important for reactor economy that beta values are further increased. Figures of five to ten per cent have been mentioned in this connection for the average across the tube, but there is, of course, not a sharp threshold. Stable operation at low q is relevant and many groups report successful operation in the range of 2–2.5, and even below 2, when the plasma is very pure, as in DIVA (T-3-1). Peak beta values then arrive in the range of 2 to 3 per cent, or even 3 to 5 per cent in the case of T-11 (C-5). Alcator scaling of the confinement time continues to hold in DIVA, with an even higher numerical factor in front of $a^2 n q_a^{1/2}$.

There is ample evidence that cleaning and controlled gas inlet are important; T-II in Nagoya and Alcator employ the combined effect of gas injection and programmed current rise to reduce the plasma-wall interaction (N-2 C-4). Tosca in Culham shows no effect of a non-circular cross-section, either horizontally or vertically elongated on q or β (T-1-1). The Fontenay group have run into some difficulty with TFR-600, which might contain a warning against abandoning the copper shell, but, then, other tokamaks have good results without one (A-6).

Clearly then, tokamaks can operate at a β-value of several per cent. We must await further additional heating or pulsed high-β tokamak experiments before we can conclude whether or not a fundamental limitation has been reached.

We shall come back to the injection experiments, but for the moment, we conclude our report on tokamak confinement with some scattered remarks. There are several observations on super-Maxwellian tails of the electron energy distribution. An interesting observation from Garching introduces runaway-electron orbit islands that may exist in ergodized field-line regions (T-4). Stockholm established scaling laws for cold blankets (X-3). The new findings on rapid

recirculation of hydrogen in the plasma edge, if shown to be of general validity, would favour pellet re-fuelling which, as Oak Ridge has shown, costs less ionization energy (N-4). It was gratifying to learn that Doublet III passed engineering tests, and and that the new high-field tokamak in Frascati started to produce good physics (C-1, C-2). FT confirms Alcator scaling, including the a^2 dependence of τ. These machines will extend the available range of tokamak parameters in the next few years. Many of the results reported here could not have been obtained without new refined diagnostics and sophisticated data handling, which time, unfortunately, does not permit us to discuss. Finally, a review such as this one, concentrating on experimental evidence, fails to do full justice to the true character of plasma physics. Pieces of theory, cut to shape by experimental tests of their validity range, are cemented together by computational modelling. And so, stone by stone, a solid foundation is laid for the fusion technology of the future.

HEATING

Our next subject is heating. For tokamaks as well as for mirror machines, neutral injection is until now by far the most successful heating method and it is used in too many places to mention them all. The recent availability of significant additional heating has freed the tokamak of one of the constraints which used to tie the plasma parameters to the toroidal current, and has opened the way to scaling studies that were impossible before. The T-11 machine in the Kurchatov Institute is specifically devoted to injection experiments (C-5). With 350 kW of injected power, the ion temperature was more than doubled and it reached 400 eV. The plasma arrived in the low-collisionality domain with $\nu^* = 0.2$ without any detrimental effects. Low values of Z_{eff} and q made it possible to obtain this result. But the record was set by Princeton, where 2 MW yielded a fivefold increase of the ion temperature in PLT (C-3). The development of reliable powerful neutral-beam injectors, on which both the tokamak and the mirror machine now lean so heavily, is a truly remarkable achievement of technical physics.

Lower-hybrid heating comes next in the list of widely used additional heating methods. Typically, in medium-size tokamaks, the temperature goes up by 100 eV when a power of 100 kW is applied. The emission characteristics of the coupling system, mostly a set of properly phased open waveguides, or sometimes a special antenna, determine the parallel index of refraction of the wave, and this can be adjusted so as to favour either electron or ion heating (A-4, C-2, T-2). The most powerful heating was done in the Petula tokamak in Grenoble, where 1 MW was applied with a low refractive index. There appeared a 1–2 keV ion population, and the group is studying the non-linear mode conversion responsible

for the heating. There also resulted strong electron heating. This method shows promise of further development as a competitor to neutral injection, and we look forward to the tests in larger machines that are required before we can judge its potential reactor applications.

Transit-time magnetic pumping was investigated in the Petula tokamak at Grenoble (Q-1). The method has the advantage of requiring a relatively low frequency, but this is offset by poor absorption efficiency. With a 10-MW oscillator, 10 kW could be delivered to the ions, giving a temperature rise of the order of 30 per cent, when starting at some 200 eV. It is expected that the efficiency will improve when the method is applied in larger machines with higher temperatures.

Groups in Stuttgart, Kyoto, and in various US laboratories studied Alfvén and magnetosonic wave heating in thetapinches and stellarators (L-1, Q-3, Q-4). It was observed that an Alfvén and magnetosonic wave heating in thetapinches and stellarators (L-1, Q-3, Q-4). It was observed that an Alfvén wave converts to an ion-acoustic wave when it propagates into the essentially unmagnetized plasma of a high-beta theta pinch. In the Heliotron-D stellarator, the ion temperature was increased from 80 to 130 eV when an Alfvén shear wave was applied. Deliberately resonating a $\ell = 3$ heating winding with the $\ell = 3$ field winding of Proto-Cleo, Wisconsin demonstrated that the induced island formation causes losses proportional to the oscillating amplitude.

Relativistic electron beam heating is applied to multi-mirror devices in Novosibirsk (Y-2). The method gives good energy transfer: ten per cent of the beam power is dissipated per metre of length in a plasma of a few times 10^{14} cm^{-3}.

Turbulent heating with a pulsed toroidal current superimposed on the normal tokamak current gave rise to rapid deposition and thermalization of about one kJ in a small experiment in Jutphaas (Y-4-1). This result has only been exceeded so far by neutral injection in much larger machines. Comparable work was done in Tokyo and Osaka with toroidal and poloidal excitations, respectively (Y-4-2). Not all is clear about the heating processes and about the amount of wall contact provoked by the pulse. The paper from Jutphaas discusses application in larger experiments. The ultimate potential of this method cannot be judged, however, until repeated application of turbulent heating pulses is tested.

STELLARATORS

Is the stellarator a method of stabilizing a tokamak or is the tokamak a method of heating a stellarator? What is worse, an $m = 2$ winding or an $m = 2$ instability? What is more difficult to build into a reactor: a helical winding or a poloidal divertor? Whatever the answers to these questions may be, and whatever may have been thought about the virtues of axial symmetry, we know now that stellarators can confine a hot plasma. Soon, perhaps, laboratories will start tearing down their tokamaks and converting them into stellarators.

Wendelstein VIIA is the largest one and, followed by the Lebedev L2, it achieves the highest parameters (H-2, H-4). It was operated in the high-density regime by gas puffing, confinement went up with density in the intermediate density range, and the relevant parameter turned out to be V_d/V_{th}. Sufficient external rotational transform suppresses disruptions and depresses m = 2 tearing modes. Even a small amount of impurities can spoil the game, constricting the channel by radiation. Ion heat transport is neoclassical. The m = 2 mode couples to m = 1 when the amplitude grows. At large amplitude, it locks to the limiter without provoking a disruption as it would do in a tokamak under these conditions (H-3).

Much of this is also found in Cleo, whose outstanding contribution is, however, to be first with neutral injection (H-1). An increase in power by, at least, a factor of three will be necessary, though, to allow the toroidal current to be shut off altogether. But it is encouraging that the helical-field ripples present no problems with tangential injection. Strong density fluctuations are observed by recording distortions of micro-wave wavefronts, but the effect on transport is not yet established.

In Heliotron-D, significant electron heating was obtained with an Alfvén shear wave (L-1). The method works effectively when the electrons are not too cold to start with, but the machine allows sufficient Ohmic heating current density to overcome this difficulty. Sukhumi reports on feed-back stabilization of m = 2 and m = 3 modes (L-5).

MIRRORS

Mirror machines have a long standing as potential fusion reactors, although it was clear from the onset that the margin between optimal, that is classical, performance and failure would be small. This margin can be widened by the introduction of end-stoppering, for which we have a number of proposals. The ambipolar, or tandem mirror, field reversal, either by the plasma or by relativistic particle rings, and radio-frequency stoppering were discussed at this conference. Alternatively, one can contend with an energy multiplication factor, Q, around one, and use a fission blanket for energy multiplication or fissile fuel production, but this is beyond the scope of our review.

The great advances made with the 2XIIB experiment had been reported already at the IAEA Berchtesgaden Conference (1976) and elsewhere, so what we heard this week was not sensational (J-1). It was good, however, to hear that all goes well, including the preparations for the new tandem mirror experiment. The stabilizing current, driven by the hot plasma through the warm plasma stream, follows theoretical scaling predictions. The identification of the observed oscillations with the drift cyclotron loss-cone mode was further confirmed by frequency

and wavelength analysis. The electron temperature was raised to 140 eV. The field reversal factor went up to 0.9. The plasma radius was increased by geometrical re-adjustment of the injectors.

In the Kurchatov Institute, losses caused by cyclotron oscillations were found to be in the radial direction (S-2).

The radio-frequency plugging experiment at Nagoya, done in a spindle cusp, yielded an improved confinement time by a factor 5 (J-2). Simultaneously, the ion temperature went up from 15 to 60 eV, and if this is taken into account, the confinement with RF-fields on is really 20 times better than without. The results were obtained in a plasma with a density of 5×10^{13} cm^{-3}. An upgraded experiment has been constructed.

Relativistic electron or ion rings may be thought of as methods of stopping end losses on mirror machines or as toroidal devices in their own right. It is not possible to adhere to sharp distinctions in this connection. In Nagoya, the aim is to produce a stable Z-pinch or a reversed-field pinch (X-5). With an electron ring, a plasma with 100 eV ion temperature was confined and it rose to 300 eV upon major-radius compression. The ring lived for more than 1 ms. This interesting result may also relate to the spheromak reactor concept (X-1).

In other laboratories, the thinking is more in the direction of field-reversed mirrors and the like. Anyway, field-reversing rings with life-times of the order of a millisecond were also produced at Cornell, where the emphasis is on compressing and transporting these rings in a mirror system (S-4). In Irvine, the reversal is produced on a shorter time scale (S-5). The feasibility of ion ring reversal is investigated at Cornell and in the Naval Research Laboratory (S-4).

The idea of the tandem mirror was first launched two years ago at Berchtesgaden in papers from Novosibirsk and Livermore (J-1, J-3). And now, we have a paper from the University of Tsukuba which shows that in two years time a major experimental device, including tandem mirrors, neutral beam injection, RF plugging, relativistic electron beam heating and some diagnostics, was conceived, designed, constructed, and put into operation (J-5). Early results appear to confirm that the beams are trapped in the end mirrors, that heating the electrons with the REB raises the ambipolar potential as it should, and that the RF plugs do improve the confinement. We are looking forward to a further elaboration of these points in this interesting experiment and, of course, in the machines now under construction in Livermore, Novosibirsk and elsewhere.

It is hardly surprising that the concept of tandem mirrors, when looked at more closely, brings along some complications. The shape of the drift surfaces in the end mirrors, which for stability are thought of as baseball-coil fields, introduces like-particle diffusion analogous to neoclassical transport in toroidal fields. Such effects were studied in an electron model experiment in Novosibirsk (J-3). Theory describes a neoclassical, a resonant, and a stochastic regime, and the experiment so far has demonstrated the stochastic effect.

The Elmo Bumpy Torus combines in a clever way a toroidal minimum average B with a stabilized mirror. The plasma of some 10^{12} cm^{-3} density has an ion temperature up to 600 eV, and this was achieved with 30 kW at 10 GHz in the oscillators. Upgrading these to 300 kW at 28 GHz, as is planned, should lead to very interesting results.

HIGH BETA

There was a time when reports on high-beta experiments used to start with observations on the poor performance of tokamaks and stellarators, in particular with respect to β. Although this argument is becoming weaker, there is still a good case for studying high-beta plasmas, whether or not the method used to produce them has reactor potential by itself. The reversed-field pinch (RFP) has such potential, as we heard again during this meeting, and we shall start our comments on high-beta experiments with this scheme.

The case for RFP as a reactor rests on two arguments. First, it should be possible to reach ignition with Ohmic heating. Second, long-pulse operation should become possible if the stable configuration is continuously restored by self-reversal whenever it threatens to get lost by resistive field decay. Continued self-reversal has been demonstrated experimentally, and it is expected that this process will be not too violent for good confinement, as soon as the plasma conductivity increases as a consequence of a higher temperature.

New evidence in support of the underlying theoretical concept of the RFP as a minimum-energy state for given toroidal flux and current is provided by Eta-Beta in Padua (E-1-3), and HBTX in Culham (E-1-2), where the discharges stay close to the theoretical field-reversal parameter, whether they are programmed to do so or are left to self-reversal. The evidence is supported and further augmented by experiments in Tokyo, Nagoya, and Los Alamos (E-2, E-1-1).

But among the most interesting experimental data concerning the RFP are still those from ZETA and Alpha, in which self-reversal led to a quiescent regime at a far higher temperature than has since been achieved. ZETA was operational twenty years ago, and the quiescent regime was fully documented ten years ago at the IAEA Novosibirsk Conference (1968). It has taken far too long for theory to pick up the point, and it is taking far too long for experiment to give it an appropriate follow-up. We find it quite unsatisfactory that we cannot seem to do better than to produce radiation-limited discharges with a few tens of eV electron temperature, although it is, of course, encouraging to hear of peak beta values of 20 to 30 per cent. The process of self-reversal was studied in considerable detail in HBTX, and it was found to be caused by $m = 1$ kinks in strongly compressed pinches and by low-amplitude $m = 1$ modes in case of weak compression (E-1-2).

Belt pinches, screw pinches, and high-beta tokamaks are also studied in small-to-medium-scale devices in many laboratories. It is difficult to draw sharp dividing lines between these confinement schemes. Their importance is mainly that they yield information on the MHD-behaviour of high-beta plasmas in toroidal systems with different cross-sections, thus making it possible to test the validity of theoretical models relevant to the tokamak. These concepts deal with field configurations that are subject to relatively rapid decay, so that possible reactor operation has been envisaged as being in the short-pulse mode, which implies re-fuelling between pulses. But the penalty one has to pay for this in terms of circulating energy is difficult to offset by the higher beta, unless one can find a way to increase the pulse length and to re-fuel the plasma, as may be possible in the reversed-field pinch.

Contributions on these high-beta toroidal systems were presented by Columbia University, Maryland, Nagoya, Tokyo, the Kurchatov Institute, and Garching (U-1, E-2, U-4-1, U-2). The high-beta tokamak STP 2 at Nagoya demonstrates the importance of rapid implosion for the reduction of plasma-wall interaction. TPE-1a at the Electrotechnical Laboratory in Tokyo has a D-shaped cross-section and is used both to study the MHD-activity in unstable q-profiles and to make the profiles required for obtaining stable discharges. The belt pinch in Garching reaches an average beta of 0.6 and displays classical diffusion, but since the electron temperature is low, one cannot draw far-reaching conclusions from this observation. The experiment is being scaled up in order to reach higher temperatures. Torus I and II at Columbia University have rectangular cross-sections and are run in a high-beta tokamak mode. Average beta is 10%. Again in Torus I the temperature is radiation-limited; it is hoped that it will be higher in Torus II. The Thor experiment in Maryland is a tokamak starting as a toroidal theta pinch and it reaches ion temperatures up to 2 keV. Turbulent heating produces a two-component electron energy distribution with a bulk temperature of 200 eV. It should be interesting to see if this way to make a high-beta tokamak can be improved so as to lead to a more durable equilibrium; in the present experiment, this was lost on a time scale in the order of 10 μs.

The theta pinch is one of the oldest, and the simplest, way to produce a dense hot-ion plasma. If it were possible to circumvent the end losses, there could be little doubt that this would be the straight-forward way to demonstrate fusion scientifically. The pulsed nature of the process would be a disadvantage on the further, technological road, but we would worry about that later. It is for good reasons, therefore, that theta-pinch research is continuing to receive considerable attention, and the art has reached a high degree of sophistication under Los Alamos leadership (U-5). But also smaller laboratories can make significant contributions, as witnessed by a number of university laboratories and by the Nuclear Research Center in Tehran, a welcome newcomer in the fusion community (U-4-3, U-5).

In the field-reversal experiment of Los Alamos, a trapped-reversed field connects at the ends with the external field to produce a closed configuration

(S-1-1). Axial contraction then makes it a compact toroid. This "unstabilized" toroidal pinch with ion temperature in the 100 eV range has a surprisingly long life of 30 to 40 ms, determined by field decay. The improvement over a previous experiment which suffered a rotational m = 2 instability is ascribed to reduced plasma impurity. The experiment and the accompanying theory may throw new light on the old question why theta-pinch plasmas rotate.

End stoppering with solid plugs is reported also by Los Alamos, as well as by Tehran (U-5, U-4-3). A threefold improvement of the energy life-time was obtained with LiD plugs, whereas heavier materials gave little improvement because of high-Z losses. As a side benefit, one obtained stable rotation of the m = 1 wobble, which is the only dangerous MHD-mode in this device. Detailed studies of ablation, plasma flow, heat conduction, and of the wobble mode are presented by Los Alamos.

An entirely different high-beta system is Tormak, a toroidal bicusp configuration, in which rapid pulsing produces a hot ion, cold electron plasma with a relatively long ion confinement time (E-4).

Advanced high-voltage technology has made it possible to produce Z-pinches on a timescale of a fraction of a microsecond at Imperial College (E-3). The shock, which does not show the familiar bouncing at the axis, is well described by the so-called slug model, which accounts for accumulation of plasma in a zone of uniform pressure between shock and piston.

Investigations on plasma focus in five laboratories were presented jointly at this Conference (U-3). The main emphasis is on scaling laws for optimized devices and on what to do to optimize. Neutron yield proportional to the fourth power of the current, which should correspond to the square of the energy in the condensor bank, obtains up to 0.5 MJ, and should hold up to 1 MJ with further improvements. The highest yield so far is 10^{12} neutrons per shot for 0.5 MJ. Much has been learned about insulation, breakdown, and pinching, and about the neutron source: partly beam and partly plasma. The plasma focus is also an interesting X-ray flash and has promise as a pulsed electron, or ion beam, source.

Seventeen years is not long by divine standards.

We still have to stay in Purgatory for a while, before we can say, as Dante said at the end of his voyage through it: "Pure and ready to rise to the stars".

But, eventually, we will rise to the stars!

SUMMARY ON MAGNETIC-CONFINEMENT THEORY*

D.D. RYUTOV
Nuclear Physics Institute of the Siberian Section
of the USSR Academy of Sciences,
Novosibirsk, Union of Soviet Socialist Republics

Professor Rosenbluth, who gave the summary lecture on magnetic confinement theory at Berchtesgaden, said in the course of his talk: "I strongly suspect that by the time of the next IAEA meeting this summary will have to be given by a computer". Now, although I hope you believe that I am not in fact a computer, I have decided to include in my lecture a number of elements which a computer would certainly include if it were doing the job. I shall accordingly begin with a statistical analysis of the papers.

Altogether fifty-two papers on magnetic confinement theory were presented at this Conference, and they were divided by subject matter roughly in the manner shown in Table I.

These fifty-two papers include not just purely theoretical work but also a number of mixed experimental and theoretical papers (in which, however, theory is given an important place). The distribution of papers shown in Table I is a fairly unambiguous classification, for most of the papers are addressed to quite specific types of installation: toakamaks, stellarators, magnetic mirror machines and so on. The tokamaks clearly absorbed the lion's share of the theoreticians' efforts; if we include the papers on plasma heating in this category (since these do in fact largely concern tokamaks), then the fraction devoted to tokamaks will be about 70%. The remaining papers are divided up more or less equally among stellarators, toroidal pinches and open-mirror systems.

The fact that the theoretical papers are quite specific, as I mentioned, does not, of course, mean that plasma theory has lost any of its internal unity and integrity. The papers can also quite naturally be divided up in accordance with the more traditional branches of theory rather than with the type of machine they are devoted to. Table II shows this type of division.

I hope that I have now imitated computer activity long enough so that Professor Rosenbluth will feel satisfied that the prediction he made at Berchtesgaden has been fulfilled. Perhaps all the other theoreticians present will experience something of the same feeling: one more prediction of theory has proved in the final analysis to be correct (at least in part)!

---

* This summary talk was also published in Nucl. Fusion **19** 1 (1979) 125.

TABLE I. DIVISION OF PAPERS ON MAGNETIC CONFINEMENT THEORY BY SUBJECT MATTER

	Number of papers	Percentage of total
Tokamaks	31	59.6
Other toroidal systems	8	15.4
Open traps	5	9.6
Plasma heating	5	9.6
General topics	3	5.8
Total	52	100

TABLE II. DIVISION OF PAPERS ON MAGNETIC CONFINEMENT THEORY BY TRADITIONAL BRANCHES OF THEORY

	Number of papers	Percentage of total
MHD equilibria and stability	25	48.1
Microinstabilities	7	13.5
Linear and non-linear waves	6	11.5
Turbulence	3	5.8
Transport processes	11	21.1
Total	52	100

The breakdown of my presentation will follow Table I, since it is aimed not only at theoreticians – indeed not so much at the theoreticians as at the experimentalists, who are presumably not interested so much in plasma theory generally as in its concrete applications to their own machines. Furthermore, it seemed sensible to me to separate tokamak theory from everything else, because otherwise the papers devoted to the tokamak's younger brothers would simply get submerged in the sea of papers devoted to tokamaks.

TOKAMAKS

Here a great deal of progress has been made in the theory of MHD equilibria and linear MHD stability. This area of work has in fact been quite thoroughly covered. A combination of numerical and analytical methods now enables us to find axisymmetric plasma equilibria and to predict confidently how stable they will be for virtually any shape of chamber cross-section (an exception may be configurations with singularities of the internal-separatrix type).

A particularly strong impression was made on us by the development of ballooning mode theory (the papers of Taylor (P-1), Frieman (P-2) and Mercier (P-3-2)), which in many respects was stimulated by the familiar paper of Connor, Hastie and Taylor (Phys. Rev. Lett. **40** (1978) 396) in which, for purposes of investigating stability, the perturbation was written in the following form:

$$u(r, \varphi, \theta) = e^{-in\theta} \sum_{m} e^{-im\varphi} \int_{-\infty}^{+\infty} \hat{u}(r, \eta)\, e^{im\eta}\, d\eta \qquad (1)$$

where φ and θ are the poloidal and toroidal angles, respectively, r is the radial variable, n and m are integers and the variable η has infinite limits. In the work of Connor and co-workers which I have referred to,stability was studied in zeroth approximation with respect to 1/n. Now, in their present papers, Taylor (P-1) and Freeman (P-2) have put forward a method of deriving first-order corrections which should make it possible to determine both the eigenfrequency and the shape of the radial envelope. It turns out that the modes with maximum n are the most unstable ones.

In the work reported by Mercier, similar results are arrived at by a method different from that used by Taylor and Frieman. An advantage of Mercier's approach lies, it would seem, in the fact that it permits application to non-axisymmetric systems as well.

Very interesting, too, is the paper by Zakharov (P-3-1), which gives a physical interpretation of expression (1) such that the use of this expression ceases to be merely an adroit mathematical trick and takes on plausible qualitative meaning. Similar arguments in justification of expression (1) were advanced by Y.C. Lee (W-5).

Apart from the results already mentioned, Mercier and Zakharov affirm that in the case of equilibria with circular magnetic surfaces there is a region of stability against ballooning modes not only with small β but also with large β. This affirmation has numerous practical implications, and it would accordingly be useful to check its validity for the widest possible range of equilibria. A

similar result has been obtained by Coppi and co-workers for a tokamak with flux conservation (W-4(B)).

A large group of papers was devoted to numerical optimization of β in various types of tokamak. The optimum distribution of plasma parameters is determined by competition between two different effects: for stabilization of ballooning modes it is desirable to have a fairly broad distribution of current, whereas stabilization of the external modes requires current distributions which diminish towards the edges. Typical limiting values of beta are 7–10% on condition that the wall is located sufficiently close to the plasma boundary. These results, we might add, ought to be regarded as preliminary for the time being because in much of the work that has been done the stability conditions employed were not sufficiently complete. However, the present state of the art in MHD calculations justifies the hope that by the time of the next IAEA Conference a good deal of light will have been shed on this problem – and in particular that the question of the existence and possible role of a second island of stability against the ballooning mode will have been solved.

It goes without saying that we still have to be sure that a real tokamak can be put in a state corresponding to maximum β, and that this will be compatible with the transport equations, the distribution of heating sources and so on. Nevertheless, further work on detailed MHD optimization would seem to be useful.

In this context we should also like to point out that it does appear to be possible, in optimizing β, to accept some level of MHD activity in the internal regions of the plasma; this might not lead to a catastrophic growth of losses, yet at the same time would make possible a further increase in β. Some evidence that this is a real and interesting possibility is to be found in the paper by Sykes (K-5) who explained that in the TOSCA tokamak the maximum β was about 1.5 times the theoretical prediction. A similar conclusion can be reached on the basis of Mukhovatov's report (C-5) concerning experiments on the T-11. The gain in β can be quite considerable: the calculations presented by Dobrott (P-4) show that the acceptance of some MHD activity in the axial region can increase β by a factor of 1.5. We must, of course, be aware of the fact that the inclusion of unstable regions in a model is bound to make all the predictions based on it less reliable.

The paper by H.P. Furth on the spheromak (X-1) is exceptionally interesting. If the problems of MHD stability can be satisfactorily solved, a system of this kind could well provide a good basis for a thermonuclear reactor.

Five papers were devoted to tearing modes, and three of these (F-1-1 to F-1-3) which pursue similar lines of thought were summarized in the very clear and convincing presentation of J.D. Callen. The paper of the Oak Ridge group (F-1-1) gives us a general analysis of tearing modes in relation to tokamak dynamics. It presents a disruption model based on the assumption that a stochastic field region

appears during the development of modes with incommensurable m/n: as this region comes into contact with the limiter, the disruption takes place. Apparently, this model gives a good description of the whole disruption morphology.

An approach quite similar in spirit to this was used by Mirnov (F-1-2) in formulating a scaling law for tokamaks. In this paper Mirnov proposes essentially that we should insert in the expression for the plasma lifetime not the radius of the limiter but the radius of the $q = 2$ surface, since transport occurs very rapidly in the outer region.

Dnestrovskij and co-workers have given a numerical model of a discharge including current disruptions (F-1-3).

A completely different explanation of disruptions (different, that is, from the approach taken in the three papers summarized by Callen) was offered by DuBois and Samain (K-4). This is in essence a kind of turbulence model for tearing modes with a large m and n.

Coppi and Taroni, in their paper (F-4), point to the possibility of disruptions arising in the internal regions of a tokamak reactor as a result of plasma heating by alpha-particles.

Something that should be pointed out is that the role of the tearing instability has often not been taken into account in optimizing β in the MHD calculations we have referred to. On the other hand, there is reason to hope that it will prove possible to stabilize at least modes with small m by means of feedback. The linear theory of this method was described by Arsenin at the Prague conference last year. At this IAEA Conference, Arsenin and co-workers presented an experimental paper in which they described the actual observation that even a very simple feedback system can have a fairly strong influence on the tearing mode. That being so, it was especially interesting for us to hear the paper presented here by Monticello, White and Rosenbluth (K-3) pointing out that, for complete suppression of the instability, phase information must be taken into account, and proposing a realistic scheme which would satisfy that requirement.

Let us pass now from these more or less hydrodynamic problems to the theory of microinstabilities. In the last year a number of unexpected results have been obtained concerning the influence of shear on microinstabilities: it emerged that in the, as a rule, previously used slab model the plasma was stable at least for $k_\perp \rho_L < 1$. At this Conference, we have heard similar results reported by the Princeton group (W-2). With $k_\perp \rho_L < 1$ the instability re-appears only if allowance is made for toroidal effects the investigation of which normally requires the use of highly refined numerical methods. Examples of this are in fact given in the papers of Tang (W-2) and Ross (W-4 (A)).

In a number of papers the influence of finite β on plasma microinstabilities is investigated and the authors show that on the whole an increase in β leads to favourable results.

Let us go on to the theory of transport processes. The key question here is to what extent these processes are influenced by microturbulence. In most of the

experiments that have been conducted so far the ion thermal conductivity does not, over a broad range of conditions, differ too strongly from the neoclassical predictions. Accordingly, we may assume that turbulence, even when it is present, will not substantially alter the character of ion heat transport as a whole but will only change the effective collision frequency – in other words, we shall have a "pseudoclassical" situation. Since tokamaks have so far operated in the plateau region, it has been impossible to derive the collision frequency from experimental data. Now we have the hope of shedding further light on this problem after obtaining and evaluating experimental results from well within the collisionless region (from experiments on, say, PLT or T-11).

Certain characteristics of the derivation of turbulent transport coefficients in toroidal devices were discussed here in the paper by Engelmann (F-5).

For the sake of brevity, we shall not dwell here on the numerical calculations of transport processes. Let us just point out that this area of calculational plasma physics has made substantial progress in the last few years.

We shall now go on to a branch of study where the most unexpected things have happened since the last Conference; or, better still, we should say that at that time this branch of study simply did not exist. What I have in mind is the theory of electron heat conduction in braided magnetic fields. An analogous problem has been under discussion in astrophysics for many years in connection with efforts to assess the diffusion coefficient of cosmic rays. The problem is, however, quite new in its application to tokamaks. An important contribution towards the formulation of the problem was made by Stix; subsequently interesting results were obtained by Rosenbluth and Rechester; and now, at this Conference, we have heard the paper of Kadomtsev and Pogutse (O-1), which in a certain sense may be regarded as an exhaustive treatment of the subject – exhaustive in the sense that it indicates a method which allows the transverse electron thermal conductivity to be found for any correlation function of the magnetic field perturbations. The problem is solved in two stages. First the "diffusion coefficient" of the lines of force is found, and then the actual heat conductivity of the electrons. Highly refined methods, developed earlier in solid-state theory, are used for this purpose.

Naturally, if one wishes to apply these results to the calculation of any specific device, one must know the correlation properties of the magnetic field perturbations; and if these are not known, one is obliged to have recourse to more or less arbitrary assumptions. However, we do want to stress once more that the *initial* part of this problem – the finding of $\chi_\perp$ from known perturbation properties – is completely solved.

With that we should like to conclude the tokamak section of this summary talk and draw a few summary conclusions. On the whole, theory has not brought us any particularly unpleasant or unexpected news in this sphere. On the contrary, there appear to be grounds for optimism, for the following reasons:

(1) Optimized MHD calculations have shown that MHD-stable states are possible in tokamaks with β of around 10%.

(2) We have reason to hope that tearing modes can be suppressed by means of feedback systems; and

(3) Microinstabilities in plasmas reveal a tendency to damp as β increases.

The problem of electron heat conduction does, it is true, still cause us some concern.

OTHER TOROIDAL DEVICES

As far as non-axisymmetric systems are concerned, the main effort has been devoted to the development of three-dimensional codes yielding equilibrium configurations with high β (Garching group (L-2)). The limiting values of β are now in excess of a few percent. The tasks confronting workers in this field are rather complex, and a number of papers have contained results which, on occasion and to a certain degree, appear to contradict each other. In particular, there is a contradiction (perhaps only an apparent one) between paper L-3-2 and earlier papers on the stability of systems with $\ell = 3$. We can only associate ourselves with the opinion of Freidberg in this connection and express the hope that this contradiction will be resolved before the next IAEA Conference.

Lortz and Nührenberg use refined asymptotic methods for the investigation of the three-dimensional equilibria (H-5).

In toroidal pinch systems, the situation as regards MHD stability within the framework of ideal magnetohydrodynamics is entirely favourable (we have in mind reversed-field pinches here); what we require now perhaps is a more thorough and systematic study of resistive modes – in this connection we should refer to Mr. Bodin's presentation as rapporteur of the papers E-1-1 to E-1-3. Here, too, theory predicts the formation of magnetic islands and stochastic transport.

It seems that there have been no new difficulties in connection with the Elmo Bumpy Torus design (L-4).

As far as the Tormac concept is concerned, theory seems to have outdistanced experiment by a wide margin, and the accumulation of a broad base of experimental data will undoubtedly assist a more soundly based selection of theoretical models (E-4).

OPEN SYSTEMS

At the Berchtesgaden Conference we hear a report about the record results obtained on the 2XIIB device at Livermore, and at the same time Dimov and co-

workers proposed a method which was supposed to lead to a substantial reduction of plasma losses in the axial direction. All this awakened fresh interest in open systems, with a consequent intensification of theoretical work related to them.

In the theory of transport processes in open traps, we realized the important influence which magnetic field asymmetry has on transverse plasma losses owing to neoclassical-type effects. Something new, by comparison with toroidal systems, is the existence here of "resonant" and "stochastic" diffusion regimes which are found in long open traps. In these long devices, stochastic diffusion can arise not only as a result of axial asymmetry of the mirrors but also through accidental distortions of the magnetic field associated with imperfections in the windings of a long solenoid. The diffusion mechanism here is to some extent reminiscent of the effect produced by "braided" magnetic surfaces in tokamaks, but with the difference that it is the drift surfaces, not the magnetic surfaces which become "braided" in this case (we should note that allowance for the effect of drift may also be of interest in connection with the problem of anomalous heat conduction in tokamaks).

Although transverse transport puts quite severe limitations on the parameters attainable in traps of this type, it is not in fact a "lethal" effect. Much more dangerous are the instabilities associated with anisotropy of the distribution function in end mirror machines. The current status of theory in these matters has been set out very fully in the exceptionally clear paper of Baldwin (J-4). For the future, we should give more attention to the role played by radial and azimuthal inhomogeneity effects and the influence of stabilizing streams in the problem of the drift-cyclotron loss-cone (DCLC) instability.

Since the problem of anisotropic instabilities, in particular the DCLC mode, seems to be very serious in applications involving "traditional" open traps, it may be necessary to seek other solutions, e.g. to try traps with a length in excess of the free path length, for example.

Another possible solution might be systems employing field reversal, though this line of endeavour has a serious obstacle in the electron drag effect (Pearlstein's review on papers S-1-1 and S-1-2). We may nevertheless hope that this difficulty will be overcome in one way or another.

As we have seen from Krall's paper (S-3), the theory of drift microinstabilities does not seem to have revealed any particularly dangerous effects for open systems.

On the whole, then, we may say that the combined labours of experimentalists and theoreticians have already led to considerable progress in open systems; it seems that we may be confident, despite the problems that still persist, that this progress will continue.

PLASMA HEATING

For the sake of brevity, we shall restrict ourselves here to quoting the titles of the relevant papers presented at the Conference: Lower hybrid resonance cones

in tokamaks (G-1(A)); Stochastic ion heating by an electrostatic wave in a sheared magnetic field (G-1(B)); Ohmic pumping by means of externally driven tearing modes (G-2); Parametric instabilities induced by a low-frequency heating wave in a magnetically confined plasma (Q-2); Progress in heating of fusion plasmas with Alfvén waves and magnetoacoustic oscillations (Q-3); Excitation of fast magnetoacoustic waves in a plasma in large tokamaks (Q-4). In these papers useful results which directly correspond to the problems posed by experiment were obtained.

CONCLUSIONS

What can we conclude, then, about the status of magnetic confinement theory as a whole? Considerable progress has been made in MHD theory and in the theory of transport processes. Effective numerical methods have been developed for the investigation of microinstabilities in complex geometry. The techniques available to plasma theoreticians have expanded remarkably, and problems which seemed quite hopeless two years ago can now effectively be solved.

At the same time, the tendency towards an increasingly specific formulation of our problems is continuing; more and more, theoreticians are devoting themselves to the service of some particular experiment. This would seem to be only right and natural, since nowadays we are building ever larger and more expensive installations, and everyone naturally wants to find out as soon as possible how these facilities behave. At the same time, however, we should not forget that theory has its own problems, its own internal logic of development; and we theoreticians should not lose sight of the more general and traditional tasks before us. In this sense, I believe that the present Conference has given us reason for optimism. We have heard here a number of extremely fine papers, which have brought into the service of plasma physics some completely new methods and which will serve as a basis for many new investigations. Thanks to this type of work, plasma theory has recovered some of that artistic character which it used to have in the past, and which of late had seemed to be vanishing, as it were, beneath the weight of vast calculations. Thus I do not think that at the next Conference this paper will have to be given by a computer.

SUMMARY ON INERTIAL-CONFINEMENT FUSION*

K. NISHIKAWA
Faculty of Science, University of Hiroshima,
Hiroshima, Japan

Let me start with the Basov diagram showing the energy extraction scheme in inertial-confinement fusion (Fig.1). A driver of efficiency η delivers energy E to initiate a nuclear reaction yielding the energy κE with a gain factor κ. This energy is, with a generator efficiency of α, partly used to supply the driver energy E/η and partly to yield the electrical energy $(\alpha\kappa - \eta^{-1})E$. The remaining energy is converted into heat. The primary object of the present research work is to demonstrate "break-even", which is given by the condition $\kappa = 1$, but to this end sufficient fuel compression is required, typically 10–100 times the liquid density, with $\rho R \sim 0.5\ g \cdot cm^{-2}$, where ρ is the fuel density and R the radius of the compressed pellet. This number may be somewhat reduced for beam fusion, where a larger amount of energy is available than in the laser case. The driver requirements for the break-even are estimated to be an energy of 100 kJ and a power of 100 TW. The ultimate goal is, of course, to construct a large-scale commercial reactor. For a reactor of 10 GW operating at 10 pps, we need $(\alpha\kappa - \eta^{-1})E > 10^9$ J. It is estimated that a few MJ of driver energy yield are required.

Table I shows the present state of laser pellet compression research, where, for the purpose of comparison, some of the results at the time of the 6th International IAEA Conference (1976, Berchtesgaden) as well as those to be expected in the years 1980–1985 are also presented. From this table, we see that there is a considerable distance between the present status and the goal, but, at the same time, a clear progress has been made in the past two years. In fact, this is not the whole story; in addition to these explicit results, remarkable inexplicit progress has been made in the last two years, particularly in understanding laser-plasma coupling and the implosion process with the aid of various diagnostic developments.

We shall summarize the problems relevant to this progress by classifying them into three topics: I) driver technology, II) driver-plasma coupling, and III) implosion and target design.

---

* This summary talk was also published in Nucl. Fusion 19 1 (1979) 125.

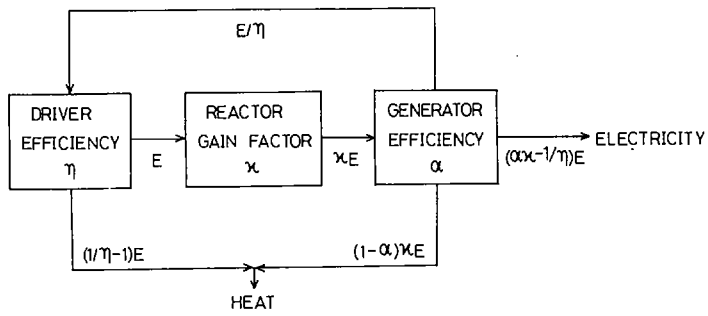


FIG.1. Basov diagram.

In driver technology, we should like to stress that we now have a multiple option for driver sources, steady progress has been made in increasing the output energy, the prospects for future high-power drivers have been improved, and pulse-shaping technology for high ablative compression is being developed. In driver-plasma coupling, we have now arrived at some basic understanding of laser-plasma coupling, at least, for short-pulse laser illumination, while for beam-plasma coupling the importance of basic studies in REB-plasma interaction is now recognized. Some high-quality theoretical and experimental work on non-linear phenomena has also been carried out. In implosion and target design, we should like to point out development of several new diagnostic techniques which allowed us to make reliable measurements of the gross behaviour of the implosion process; the results seem to show general agreement with those of computer analyses. A preliminary compression experiment using cryogenic and solid-layered targets has been performed and some sophisticated high-gain targets have been designed. Finally, we wish to mention some problems to be studied or discussed.

Naturally, we cannot cover all subjects relevant to inertial confinement fusion on an equal footing, but admittedly this summary is biased towards those subjects which are more or less familiar to the author. In particular, we shall restrict ourselves to pellet compression fusion. However, we want to point out that interesting theoretical and experimental work has been reported at this Conference, on ion implosion (V4), liner compression (E5) and laser and REB heating of long magnetically confined plasmas (U5, Y2).

I) DRIVER TECHNOLOGY

As mentioned before, we now have a multiple option for driver sources. In lasers, in addition to the Nd-glass laser, the use of the CO_2-laser seems very

TABLE I. PAST, PRESENT AND FUTURE STATES OF LASER PELLET COMPRESSION RESEARCH

Name of machine	Power (TW)	Pulse energy (kJ)	Neutron yield	Compression ρ (g · cm^{-3})	Comments
1976					
Argus (LLL)	4.5	2.2	2×10^9	0.5	Nd
TBS (LASL)	0.4	0.4	0	–	CO_2
KMS-0	0.4	0.1	2×10^9	2	Nd
Coquelicot (Limeil)	0.25	0.02	10^5	10^{-4}	Nd
Gekko II (Osaka)	0.6	0.2	10^5	0.2	Nd, D-D fuel
Lekko I (Osaka)	0.2	0.2	–	–	CO_2
1978					
SHIVA (LLL)	26	10	7.5×10^9 ($\sim 10^{12}$)	1 (100–200)	test run, Nd (expected in autumn)
TBS (LASL)	0.8	0.8	3×10^5	0.04	CO_2
Helios (LASL)	21	10.7	–	–	CO_2 just started
KMS-I	0.8	0.2	10^8	7	Nd, cryogenic and solid-layered target
Camelia (Limeil)	1	–	10^7	–	Nd preliminary
Gekko IV (Osaka)	4	2	10^7		Nd, D-D fuel
Lekko II (Osaka)	1	1	–	–	CO_2
1980–1985					
(expected) Nova (LLL)	300	500	5×10^{18}	200–300	Nd
Antares (LASL)	200	100	10^{17}	100	CO_2
KMS-II	4	1	10^{10}	30	$\lambda = 0.35\ \mu m$
Gekko-XII (Osaka)	20	20	10^{14}	10–100	Nd
Lekko X (Osaka)	10	10	$10^{13} - 10^{14}$	10–100	CO_2

promising, and there is some possibility of using other new lasers. The laser, as a driver source, has the advantage of yielding high power density with no technological problems for target illumination, but it is suffering from low driver efficiency and low total output energy. The increase of the output energy is the most important issue in the laser technology development. Three types of charged beams are being studied as driver sources: REB (relativistic electron beam), LIB (light-ion beam) and HIB (heavy-ion beam). Charged beams are suffering from low power density or low current and technological difficulties in target illumination, but have the advantage of yielding high total energy at high efficiency. Beam focus and transport in the reactor vessel for target illumination will be the key technological problem in beam fusion.

Let us discuss some further details of each of these driver sources. First, the Nd-glass laser is most advanced in laser technology, and a remarkable increase in the output energy has been achieved by reducing the non-linear refractive index and optimizing the optical cross-section, particularly with the use of phosphate (B4, D3, M4) and fluorophosphate (B1, M4) glasses. Furthermore, developments of various optical fabrication techniques and of the image-relaying technique now shows great promise for the construction of a 100-kJ, 100-TW glass laser system (B1) meeting the requirements for the break-even experiment. With a view to the construction of a 1-MJ laser, which is needed for a commercial reactor, further technological advancement, such as multipass regenerative amplifiers with proper switching technique and segmented disk amplifiers to suppress the parasitic oscillations due to optical feedback, is under consideration (B1, M4).

The CO_2-laser is advantageous in that it operates at high efficiency (2–10%) and high repetition rate (10–60 pps). Recent technological advancements, such as multiline double-band energy extraction, He-free operation, gas and solid saturable absorbers to suppress the parasitic oscillations, etc. (D1, M4) have enabled the construction of a 10-KJ, 20-TW laser system (D1). Another increase in the output energy, up to 100 KJ or 1 MJ, may be possible by further development of various optical elements. Moreover, substantial cost reduction will be possible if a multipass energy extraction scheme can be used. In addition, the previous concern on the feasibility of long-wavelength lasers for pellet compression is found to be less serious (D1).

In addition to these two lasers, some new lasers are being studied. For instance, an iodine laser of 1 TW and 500 J has been constructed as a cost-effective laser source (Garching). Raman compression of a KrF laser is being studied as a promising high-efficiency (3–6%), short-wavelength (0.27 μm) laser (B1). In this connection, we note that green-light (0.53 μm) illumination experiments using the second harmonics of the Nd-glass laser have been carried out, which showed high absorption and efficient momentum transfer to the target as compared with infra-red-light (1.06 μm) illumination (B2, D4).

Finally, the pulse-shaping technology needed for high ablative compression has been developed by assembling picosecond pulses, by using non-linear optical effects, etc., in connection with target design (B1, B3, D1, D3, D4, M4).

Let us now turn to the problem of charged-beam technology. There are two types of acceleration methods, the diode acceleration for the case of REB and LIB, and the use of linac or synchrotron for the case of HIB. The former method yields a relatively high current (several hundred kiloamperes per beam) with moderate energy per particle ($\sim$ 1 MeV), whereas the latter method yields high particle energy (10–20 GeV) with low current ($\sim$ 1 μA per beam). In either case, the achieved particle energy is almost sufficient for break-even demonstration, but the current is much lower than the level required (a total current of 10 MA for REB and LIB and 5 KA for HIB). In the case of REB and LIB, substantial success has been achieved in both beam transmission and diode acceleration by the magnetic insulation (B3, M1, M3), while for target illumination further studies are needed. A single e-beam has been transported over a distance of 1 m through a plasma channel produced by wire evaporation (M3), but focusing of LIB seems to require further technological studies. The accelerator technology for HIB can count on high-level experience in proton acceleration studies, but little effort has been made on heavy-ion beam acceleration at high currents. Here, the maintenance of beam quality from the ion sources seems to be the key technological problem. In addition, the space-charge limit for beam transport in vacuum and in the reactor vessel seems to require careful study (V3).

II) DRIVER-PLASMA COUPLING

At the time of the IAEA Berchtesgaden Conference (1976), the experimental data for laser-light absorption and reflection coefficients, when plotted against the laser power density I, were almost stochastically scattered, and a number of mysterious results for hot electrons, fast ions and the self-generated magnetic field had been reported. It is our feeling that, at this Conference, we have arrived at some basic understanding of laser-plasma coupling, at least in the case of short-pulse illumination. We shall start by listing the results on which, we think, the physicists working in this field more or less agree with each other:

1) It has been predicted theoretically and now verified by a number of experiments using interferometry that there exists a steep density gradient at the critical density, except for the case of very weak long-pulse illumination where the inverse bremsstrahlung absorption inhibits laser light penetration to the critical density. The gradient length is found to be of the order of the incident laser wavelength (D4, M4, V1, LLL).

2) As a result of density steepening, resonance absorption becomes the dominant absorption mechanism at high power density ($I\lambda^2 \geqslant 5 \times 10^{14}$ W$\cdot\mu$m$^2\cdot$cm^{-2}).

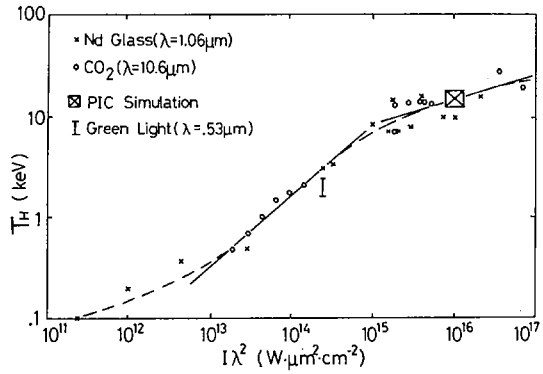


FIG.2. Hot-electron temperature versus $I\lambda^2$. Data other than for green light are taken from the LASL report, La-UR 77-2431, by R.B. Perkins.

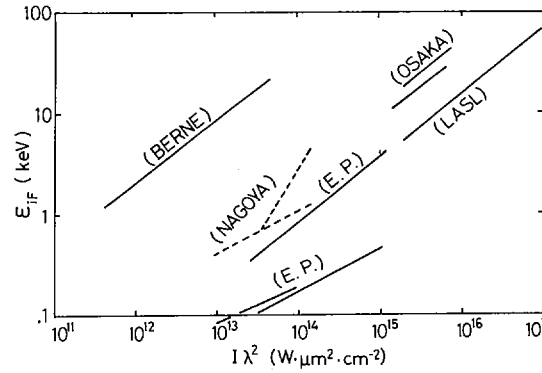


FIG.3. Fast-ion energy versus $I\lambda^2$. EP stands for Ecole polytechnique. Data other than those of Berne are supplied by M. Matoba, Institute of Laser Engineering, Osaka University.

This is verified by observing stronger absorption for the p-polarized wave than for the s-polarized one and by observing the angular dependence of the absorption which agrees qualitatively with the theoretical prediction (B1, D4, M4).

3) Absorption at low power density (2×10^{11} W·μm²·cm$^{-2} \leqslant I\lambda^2 \leqslant 3 \times 10^{13}$ W·μm²·cm^{-2}) is confirmed to be due to the inverse bremsstrahlung modified by the resonance absorption, using the Nd-glass laser illumination of a flat target (V1–1).

4) Parametric instabilities near the critical density are unimportant because of density steepening at high power densities, but at intermediate power densities (10^{13} W·μm²·cm$^{-2} < I\lambda^2 < 5 \times 10^{14}$ W·μm²·cm^{-2}) they may play a significant role (M4).

5) The hot electron temperature T_H is a universal function of $I\lambda^2 \sim I/n_c$ (n_c is the critical density) as shown in Fig.2 (D1, D4, M4, LLL). This implies that these hot electrons are produced by a localized resonance field near the critical density. The saturating tendency of T_H at large values of $I\lambda^2$ will be due to the profile steepening effect which limits the local field intensity. This fact implies that long-wavelength lasers, such as the CO_2-laser, do not produce extremely hot electrons which pre-heat the fuel and thereby suppress the compression efficiency.

6) In the power range of $I\lambda^2 \leqslant 10^{15}$ W · μm^2 · cm^{-2}, there exists a group of fast ions whose energy scales similar to T_H (Fig.3). These fast ions can be explained as being created by the isothermal expansion of the hot electrons from the critical surface. The result for $I\lambda^2 > 10^{15}$ W · μm^2 · cm^{-2} may also be explained by the same mechanism if we take into account the fact that the ambipolar potential energy becomes higher than T_H in this range of power densities, owing to the electron quivering motion due to the localized resonance field. However, observation of ultra-fast ions has also been carried out at low power densities (V1), which indicates the existence of an independent acceleration mechanism of ions.

7) Some indirect evidence of critical surface rippling is found, such as less polarization dependence and less angular dependence of absorption than is predicted by the flat-critical-surface theory (V1–1, LLL), and a side-peak observation in the reflection coefficient of the s-polarized wave (M4).

8) At high-power ($I\lambda^2 \geqslant 10^{14}$ W · μm^2 · cm^{-2}), short-pulse ($\leqslant 100$ pps) illumination, the absorption and reflection are nearly independent of $I\lambda^2$, though they depend on the illumination geometry. Previous results for low reflection at $I\lambda^2 > 10^{15}$ W · μm^2 · cm^{-2} have been corrected by a careful optical balance analysis (Garching).

9) Green-light illumination experiments at intermediate power densities show increase of absorption and substantial reduction of hot electrons and fast ions as compared to infra-red-light illumination at the same power density (B2, D4).

10) Stimulated Brillouin scattering (SBS) is important for targets with pre-formed plasmas (B3, D2, D4, M4, LLL). Previous results indicating the absence of SBS backscattering can be attributed to the suppression of the instability of density steepening produced by the short, intense laser light. The scattered signal due to the SBS shows an interesting temporal behaviour indicating the presence of non-linear effects (D2, D4, M4, LLL).

All these results seem to be explained theoretically by a consistent model where the profile modification due to the laser light ponderomotive force, a sharp temperature gradient due to local heating, etc., plays a crucial role. In verifying this model experimentally, various high-quality diagnostic techniques, such as a complete optical balance study (Garching), density measurements by

interferometry with a spatial resolution of down to 1 μm (Osaka), X-ray streak study with a time resolution of down to 2 ps (D3), and energy and Z/A analyses of fast ions by the Thomson parabola (B2, LASL, LLL), have been used.

In addition to these investigations, a number of very-high-quality theoretical and experimental studies have been made on the structure of the density profile (B2, M4), the implications of caviton formation (V1–1, V1–2, V2–1, V2–2, V2–3), the non-linear evolution and saturation mechanism of parametric instabilities (V2–1) and the associated a.c. resistivity, anomalous absorption, hot-electron formation, etc. (V2–1, LASL), effects of pre-pulse on X-ray emission, fast ions and magnetic field (B3, D4), the problem of reduced thermal conduction of electrons and its implications (B2, D3, D4), etc. Further studies on these problems seem to be very important.

Turning to the problem of the REB-plasma interaction, we note that some interesting experimental results have been reported. Whereas beam energy deposition at high-Z targets can be explained by classical collisional absorption with self-generated electric and magnetic field effects on the beam trajectory (M1, M3), energy deposition on low-Z targets, where collisions are less effective, is observed to be more efficient than on high-Z targets (M4). This indicates the importance of collective plasma effects on beam relaxation in low-Z targets, although further studies are needed to allow any definitive conclusion.

III) IMPLOSION AND TARGET DESIGN

We should first like to point out that the development of various new diagnostics has now allowed us to carry out reliable measurements of ion temperature T_i, compressed fuel density ρ, radius of compressed core R and implosion velocity V. These include the α-particle zone-plate imaging to locate the reaction region (B1, B4), the time-of-flight measurement of the reaction products to measure T_i (B1, B2, D5), X-ray shadowgraphy to measure ρR (B1, D5), X-ray streak studies to measure V (B1, B4, D3, D5, M4), and use of Ne- or A-filled fuel for spectroscopic analyses (B1, B4, D1, D5, M4), such as the Stark broadening of optically thin lines of Ne or A to measure ρ, the opacity broadening of optically thick lines to measure ρR, spatial distinction of the glass and the fill-gas region by the emission lines of different chemical compositions, the Doppler shift of Ne or A lines to determine V, etc. Combined use of different diagnostics allows us to make a cross check of the measured data which seems to demonstrate the overall consistency of the results (B4).

Computer calculations of the implosion dynamics have also been made extensively. The importance of including the ponderomotive-force effect (B1, B2, D1, D3, etc.), the non-LTE distribution of high-Z targets (B1), etc., has been recognized. The results of the code analyses seem to show general agreement with the observed data.

The results of the explosive-pusher-type compression studies show that $\rho \sim (0.1-2)\mathrm{g \cdot cm^{-3}}$ for the case of gas fuel and $\rho \sim (0.5-7)\mathrm{g \cdot cm^{-3}}$ for the case of cryogenic and solid-layered target (B2). A maximum neutron yield of 7.5×10^9 is obtained in the test run of SHIVA in LLL and a maximum yield of 10^{12} is expected for full operation to be taken up in the autumn.

In target studies, some experimental investigations have been made on the transition between explosive-pusher-type and ablative compression by changing pulse length, laser intensity, etc. (D3, Sandia). Some interesting stability analyses for the Rayleigh-Taylor instability have been reported. In particular, the possibility of dynamic stabilization of the ablation surface has been proposed by a computer analysis (B3), while an experimental evidence showing anomalous Al penetration into the core from the outer target surface as detected by X-ray spectroscopy has been reported (D5). I think that further studies on these problems are very important.

A sophisticated high-gain target design was made for laser, LIB and HIB fusion (B1), while in REB fusion it is necessary to pre-heat the central core to initiate the nuclear reaction (M1, M3), and an idea concerning magnetic thermo-insulation of pre-heated fuel was tested (M3).

IV) SOME PROBLEMS TO BE STUDIED OR DISCUSSED

We should like to conclude this summary by discussing some problems which, in our opinion, particularly need further investigation or discussion. We start by problems in the laser-fusion research. Most of the studies undertaken so far are on explosive-pusher-type compression, where a short, intense laser pulse heats almost the entire target isothermally. Because of fuel pre-heating, no high compression can be expected of this method. For high compression, ablative compression is needed, where a relatively low-intensity, long pulse heats only the surface of the target, keeping the rest of the fuel at low temperatures. Two important problems seem to need further extensive investigations: one is laser-plasma coupling by a relatively low-intensity ($\sim 10^{14}\ \mathrm{W \cdot cm^{-2}}$), long pulse ($\sim$ 10 ns) where SBS and other parametric instabilities may occur. In addition, the wavelength dependence of the absorption characteristics is to be investigated. The other problem is the Rayleigh-Taylor instability, which is important not only for achieving high compression, but also for avoiding substantial mixing of the fuel with the target materials since this can reduce the burn rate. Note that mixing may occur even as a result of high-wavenumber mode instabilities. We should also like to comment on the problem of the α-particle self-heating which is absolutely necessary for high-gain targets. Although some theoretical work has been reported on this problem (M4, V5), we think that much more elaborate work will be needed in close connection with the target design. Finally, certain types of scaling laws for the compressed density, neutron

yield, etc., as functions of laser wavelength, intensity, pulse length, filling-gas pressure, target parameters, etc., will in the future be helpful for the design of the target, for pulse-shaping and for the choice of the driver.

Concerning the charged-beam fusion, we do not feel to be in a position to comment on future problems, but we think that more basic studies are needed, particularly in REB-plasma interaction, focusing and space-charge effects on ion-beam transport.

In conclusion, we should like to state inertial-confinement fusion research has grown up to a certain level of maturity, particularly in laser-plasma coupling physics, space-time-resolved diagnostics and computer analyses. We imagine that this research work will run into some unexpected difficulties in the course of development. To overcome these difficulties, we think that international collaboration is of paramount importance; in addition, research based on overall system analyses including driver technology, driver-plasma coupling and target design should be encouraged. Finally, we point out that the classification policy followed in some countries may be a hindrance to timely progress of research in the near future by impeding useful and necessary international collaboration.

SUMMARY ON REACTOR SYSTEMS*

R.W. CONN
Nuclear Engineering Department,
University of Wisconsin,
Madison, United States of America

The Conference included papers on reactor systems and technology in two separate sessions which primarily dealt with two topics, reactor design and plasma engineering. One paper on parametric systems studies by Argonne National Laboratory (ANL) and McDonnell-Douglas Co. considered the effects of materials performance, tritium handling and Ohmic heating power supplies on the economics of tokamak reactors. A more comprehensive overview of recent work on reactor design can be found in the summary of the Second IAEA Technical Committee Meeting and Workshop on Fusion Reactor Design recently published in Nulear Fusion (Nucl. Fusion **18** (1978) 985).

The reactor systems papers presented at the Innsbruck Conference can be conveniently divided into four categories: tokamaks; magnetic confinement, non-tokamaks; inertial confinement; and special topics that include plasma engineering and alternate applications of fusion.

Tokamak studies in the last several years have covered both near-term and commercial reactor systems. At this Conference, only near-term tokamak reactor designs for ignition machines were discussed. Designs of the Oak Ridge National Laboratory and the General Atomic Company are for medium-field ($\sim 10-11$ T at the coil) and medium-size (major radius of $4-5$ m) ignition reactors. In contrast, Coppi and Taroni (F-4) presented a design for a very-high-field (26 T), compact (major radius 0.85 m) machine. Areas in which these designs differ to some degree point to the key issues for tokamak reactors. The ORNL design utilizes Nb_3Sn superconducting coils, the GA design employs NbTi superconducting coils, while the C/T design has high-field water-cooled copper magnets. All designs provide for auxiliary heating, neutral beams in the case of the ORNL and GA machines, adiabatic compression in the C/T design. The C/T design has a very high Ohmic-heating current density and will therefore achieve a higher temperature by Ohmic heating alone. Whether this is sufficient to achieve ignition without auxiliary heating ultimately depends on the plasma transport scaling laws. The ORNL design includes a compact poloidal divertor for impurity control while the GA and C/T designs have no divertor. Fuelling is by gas re-cycle in the GA and C/T approaches whereas pellet injection is considered in the ORNL

---

* This summary talk was also published in Nucl. Fusion **19** 1 (1979) 125.

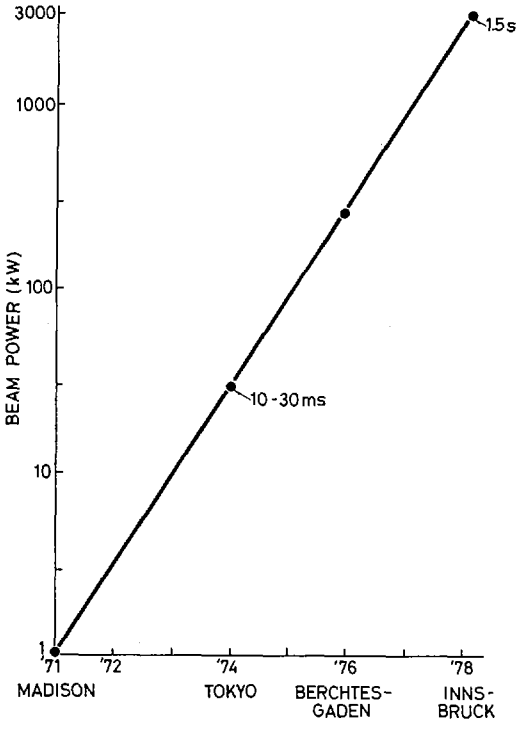


FIG. 1. Progress in neutral-beam-power development.

machine. Thus, the key plasma reactor physics issues are transport scaling, β-limits, the effects of plasma shaping, impurity control, plasma heating, plasma fuelling, thermal burn stability and control, and burn time limits.

Many of these topics were the subject of special topic papers at the Conference. Stott, Sanderson et al. (R-5-2) treated the design of a reactor with a bundle divertor and showed that, with proper optimization, the bundle divertor coils can be shielded and adequately supported. Harbour and Harrison (R-5-2) treated the problem where the plasma is collisionless in the scrape-off layer of a divertor and concluded that very high temperatures will result, leading to a sheath potential in excess of that required for unipolar arcing. Attempts to lower the edge temperature and the sheath potential may imply very low fractional burn-ups. This in turn could lead to a high tritium inventory in the exhaust and re-fuelling systems.

Advances in neutral-beam injector development have been remarkable in recent years as shown in Fig. 1. Pyle reported that full-scale tests have now been made of a 120-keV, 65-A source operated for 20 ms. Tests with a pulse length

of 500 ms are due shortly (I-5). Experiments on direct recovery of the unneutralized portion of the beam have given 85% recovery efficiency at low power but experiments at high power were less encouraging and more work is needed. Negative ion beams are being produced either by direct extraction from negative ion plasma sources or by double charge exchange of positive ions in caesium or other vapours. The goals of this programme are to demonstrate a 200-kV, 5-A (D^0) long-pulse system by 1980 and a 400-kV, 20-A (D^0) d.c. system by 1983.

Fuelling studies have been carried out on the ISX tokamak at ORNL using pellet injection with favourable results. It is found that the density can be increased by pellet fuelling much more rapidly than by gas puffing without inducing a disruption. Further, the power loss during the density rise is about half that found with gas puffing. In another study, Burgess et al. (R-5-1) have investigated laser-induced acceleration of low-Z targets (D_2, polyethylene, etc.) and have derived a scaling law indicating the feasibility of extrapolating this approach to a reactor. Work on large superconducting magnets, not reported at the Conference, complements the above efforts and indicates that the major technological issues presented by near-term tokamak ignition experiments are being addressed.

The advances in tokamak physics and the trend towards more substantial tokamak experiments make it important to have a sharper measure of the role of alternative concepts. Reactor studies are thus an important element in an overall evaluation of the more promising concepts that would be deserving of additional support.

Commercial-scale fusion reactor designs were presented at the meeting for the tandem mirror, the Elmo Bumpy Torus (EBT), and the reversed-field pinch (RFP). Scoping studies were reported on fast-imploding liners, the linear theta pinch, and the toroidal bicusp (Tormac). A study by Logan et al. from LLL (R-3) showed that a low-power-density tandem mirror with a Q of 10 is possible. Plug confinement is enhanced by the use of tritium in the plugs and auxiliary electron heating is used to lower the beam energy requirement. An interesting proposal is to inject beams into an outside field ripple of the plug plasma to raise the potential there to the same value as in the central cell. Plug ions then see only the central cell potential and the beam energy is reduced from previous designs to 600 kV. The plug magnetic field is 12 T, similar to that in the tokamak near-term reactor designs although the plug beta is taken as 1 and the central cell beta is 0.9. The potential advantages of the tandem mirror lie in its linear geometry, the de-coupling of the fusion core (central cell) from the high-technology zones (plugs), its potentially adequate plasma Q and the fact that the magnetic fields are steady-state.

The tandem mirror appears ideally suited for alternate applications such as a hybrid since the plug technology requirements are then quite modest. The

key issues for the tandem mirror are that one must yet demonstrate $n\tau$ enhancement and high central-cell beta, negative-ion neutral injectors, high plug magnetic fields (12 – 18 T), and end-loss direct convertors.

The EBT reactor presented by Uckan et al. from ORNL (I-3) has an overall length ($2\pi R$) about equal to the tandem mirror reactor but it has a much higher plasma Q. The potential advantages of EBT systems are that the plasma scaling depends only on the aspect ratio in the collisionless regime, the large aspect ratio improves accessibility, the plasma has high beta, and the system has a natural divertor for impurity control. The key issues are the demonstration of the confinement and scaling properties of the toroidal plasma, the demonstration of high-beta operation and impurity control, the demonstration that aspect ratio enhancement coils can reduce reactor size, and the development of high-power microwave heating sources ($\sim 3 - 6$ MW) at $\omega \sim 120$ GHz. Such microwave sources are being developed for the next proposed EBT experiment.

The reversed-field pinch (RFP) discussed by Hancox et al. from Culham (I-1) and Krakowski et al. from LASL (I-2) has the advantages of high beta, no auxiliary heating requirements, moderate energy storage requirements (< 10 GJ), and an aspect ratio that is unconstrained by the physics. It has been found by the Culham Group that the use of the copper field windings leads to excessive Ohmic heating losses and an unacceptably high re-circulating power fraction ($\sim 42\%$). The LASL Group finds a lower re-circulating power fraction ($\sim 21\%$) because their burn time is shorter. Nevertheless, both groups now consider large pulsed superconducting windings as most desirable. This technology will require extensive development since the pulse field is about $10\ \mathrm{T \cdot s^{-1}}$ but success is not out of the question. A key issue for the RFP will be the energy loss in setting up the field-reversed plasma state. In addition, a conducting shell near the plasma is required for stability. Both designs use a 2- to 2.5-cm copper shell operated at about 300°C which can absorb as much as 25% of the energy. The Cu-shell has a short field diffusion time constant compared with the desired pulse length in a reactor (in contrast to the situation in present experiments) so that, in the Culham design, additional feedback stabilization coils are located in the blanket.

The other alternate concepts, namely the fast-imploding liner (FLR), the linear theta pinch (LTPR) and the toroidal bicusp (Tormac) were examined by Krakowski et al.

For the FLR, a comprehensive physics model was developed and used to optimize the physics parameters with respect to reactor yield for small, cylindrical liners. The re-cycle of leads and liner material appears to be a crucial economic and technical issue. Plasma turbulence and plasma preparation remain physics uncertainties that could lead to a fatal flaw in the concept. The FLR has very high system power density and, aside from the economics of replaceable leads and liners, low costs may be possible.

For the LTPR, end loss remains the crucial, unresolved issue. Based on known physics, no solution could be identified and a significant new development

and/or change from classical physics must occur. The technology requirements and plant cost remain similar to those predicted for the most recent toroidal theta-pinch reactor designs (RTPR/1976) if the endplug "magic" gives axial confinement similar to that predicted for the re-entrant endplug.

For Tormac, point-plasma, steady-state reactor studies were made using a simple scaling, i.e. $\tau_E \sim \tau_{ii}(a/\rho_i)$. Reactor performance is not too sensitive to β as long as it exceeds $0.3 - 0.5$. Performance is very sensitive to the sheath thickness Δs which must be less than $(2-3)\rho_i$. Start-up and maintenance of the Tormac plasma/field configuration remains unresolved for a reactor, but work is still in progress.

Parametric studies on tokamak reactor systems were reported by ANL and McDonnell-Douglas Co. (I-4). In comparing the influence of radiation effects on reactor performance and economics, they find that alloys of vanadium may be superior to those of stainless steel if the down-time for replacement of blanket modules exceeds about 60 days. Otherwise, the higher costs of advanced alloys can offset superior performance in a radiation environment. Further, the study assumed that stainless steel would operate at 500°C and have a life-time of $3 - 5\ \mathrm{MW \cdot a \cdot m^{-2}}$. If the blanket region near the first wall is operated at a lower temperature (e.g. $350 - 400$°C), the life-time is estimated to be more like $15 - 20\ \mathrm{MW \cdot a \cdot m^{-2}}$ for Type 316 stainless steel. The outlet coolant temperature can still be maintained at 500°C. In this case, the advanced alloy would have even more difficulty competing economically.

An important point found in the study is that off-the-shelf motor generator sets can be used for tokamak reactor start-up if the current rise-time is extended beyond 5 s. This is similar to start-up scenarios used in early tokamak reactor studies (such as the Princeton Reference Design, PRD, and UWMAK-II and III) where the current rise time is about 10 s.

Reactor aspects of inertial confinement systems were only briefly discussed in papers on laser fusion by Emmett (B-1) and on e-beam fusion by Yonas (M-3). The LLL laser fusion concept uses segmented falling liquid lithium sheets of the order of 1 m thick to stop neutrons before they can reach the first structural wall. The system employs high gain ($G \sim 700 - 1000$) and a driver with $2 - 5\%$ electrical efficiency. The e-beam concept has an inherently high efficiency driver ($> 25\%$) but the target performance is assumed to lead to pellet gains that are less than about 50. With 1-3MJ on target, a high repetition rate is required to achieve moderate ($500 - 1000$ MW(e)) plant power output. In general, ICF systems have a high degree of accessibility while the moderate vacuum requirements permit design approaches not possible with magnetic confinement. Some key issues for ICF reactors include demonstrating a target gain of at least 50, developing high-energy drivers (> 1 MJ) with moderate efficiencies ($\gtrsim 5\%$), isolating the driver from the reactor cavity, fabricating targets at acceptable cost, and injecting and tracking targets. By comparison with magnetic confinement, the

detailed study of ICF reactor systems has only recently begun in earnest, and one can expect more definitive studies in the next two years.

Two alternate applications of fusion were described in papers by Rose et al. from the USA (R-4) and by Vasil'ev et al. from the USSR (R-1). Vasil'ev et al. have examined the potential of very-high-temperature tokamak fusion reactors for both electricity generation using an MHD power cycle ($T \sim 2000$ K) and for synthetic fuel production, specifically H_2. Such high-temperature blanket systems are found to be much more complex than more conventional designs and many unresolved issues remain. Such reactors are, therefore, not considered likely for near-term applications. The fission-fusion hybrid system was also analysed by Vasil'ev et al. At moderate values of neutron wall loading (~ 1 MW $\cdot$ m^{-2}) and blanket operating temperature ($\sim 350 - 400$°C), a tokamak with a "D"-shaped plasma and double-wall poloidal divertor produces 6650 MW(th), 2000 MW(e) net, and re-circulates 570 MW(e). The blanket is designed for plutonium production and the calculated value of the production rate is 4200 kg $\cdot$ a^{-1}. The potential for near-term application is considered to be high.

Rose et al. from the USA considered fission-fusion hybrid reactors which may be useful in several applications. These include hybrids used primarily to produce fissile fuel for fission reactors, hybrids to produce both electricity and fission fuel, and once-through fission fuel cycle hybrids used to produce electricity, synthetic fuels, or other non-fission related products. The context in which the hybrid is considered is defined by the desire to achieve proliferation-resistant fuel cycles, the potential shortfall of fissile fuel in the early 21st century, and the potential need for extra fissile fuel which would provide start-up fuel for fast-breeder reactors and which could be used to shorten the fuel-doubling time. The latter point is particularly important for breeder reactors based upon the Th-^{233}U fuel cycle.

One general conclusion is that an optimum Th-^{233}U system would employ a hybrid at an international nuclear centre (INC) where ^{238}U and re-cycled Pu could be used in the hybrid to enhance ^{233}U production. ^{233}U would then be processed into thermal reactor fuel and shipped to such reactors located outside the INC. For thermal reactors, ^{233}U is a superior fuel to Pu from the viewpoint of neutronic performance.

A re-fresh cycle in which high-temperature-reactor (HTR) coated-particle fuels are used in the hybrid and then directly transferred to the HTR without re-processing appears feasible and highly proliferation-resistant. However, fuel utilization is only modest without re-processing and is limited by fission product build-up.

The prospects for a near-term hybrid demonstration reactor based on a tokamak operated in the hot-ion mode ($Q \sim 6$) with physics assumptions expected to be tested in TFTR appear to be good. Such a reactor could be designed for operation around 1990 using fusion technology expected to be established in

the next five years. Fuel production initially is estimated to be 640 $kg \cdot a^{-1}$ of Pu or 420 $kg \cdot a^{-1}$ of ^{233}U in a device with a major radius of 5.2 m, a plasma radius of 1.2 m, a plasma elongation of 1.6, and an on-axis toroidal field of 55 kG. The neutral-beam-injected power is 150 MW, and 950 MW of fusion power is produced. In an upgraded mode, the ultimate fuel production performance of the reactor is estimated to be 3400 $kg \cdot a^{-1}$ of Pu or 2200 $kg \cdot a^{-1}$ of ^{233}U. In either case, this is sufficient to provide make-up fuel for nine light water reactors. This option, including tritium breeding in the blanket, thus appears to warrant further study.

CHAIRMEN OF SESSIONS

Session A	R.S. PEASE	UK
Session C	K.A. RAZUMOVA	USSR
Session N	S. MORI	Japan
Session T	H.P. FURTH	USA
Session F	B.B. KADOMTSEV	USSR
Session K	M.N. ROSENBLUTH	USA
Session O	B. LEHNERT	Sweden
Session P	D. PFIRSCH	FRG
Session W	P.E. VANDENPLAS	Belgium
Session E	H. DREICER	USA
Session U	R. TOSCHI	Italy
Session H	D. PALUMBO	CEC
Session L	R. WIENECKE	FRG
Session J	F. ENGELMANN	Netherlands
Session S	V.O. JENSEN	Denmark
Session G	F.F. CAP	Austria
Session Q	E.S. WEIBEL	Switzerland
Session Y	T. CONSOLI	France
Session B	C. YAMANAKA	Japan
Session D	M.V. BABYKIN	USSR
Session M	J.P. WATTEAU	France
Session V	C.M. STICKLEY	USA
Session X	C.N. WATSON-MUNRO	Australia
Session I	P.E. REBUT	CEC
Session R	J.F. CLARKE	USA
Summary Session	R.J. BICKERTON	UK

SECRETARIAT OF THE CONFERENCE

Scientific Secretaries:	J.A. PHILLIPS V.S. VLASENKOV	Division of Research and Laboratories, IAEA
Administrative Secretary:	Caroline DE MOL VAN OTTERLOO	Division of External Relations, IAEA
Editors:	J.W. WEIL Miriam LEWIS	Division of Publications, IAEA
Records Officer:	S.A. EDMINSTER	Division of Languages, IAEA

LIST OF PARTICIPANTS

ARGENTINA

Bruzzone, H.	Laboratorio de Física del Plasma, Facultad de Ciencias Exactas y Naturales, Ciudad Universitaria – Pabellón 1, 1428 Buenos Aires
Gratton, J.	Laboratorio de Física del Plasma, Facultad de Ciencias Exactas y Naturales, Ciudad Universitaria – Pabellón 1, 1428 Buenos Aires
Rodrigo, A.	Comisión Nacional de Energía Atómica, Avenida Libertador 8250, 1429 Buenos Aires

AUSTRALIA

Brennan, M.H.	School of Physical Sciences, Flinders University, Bedford Park, S.A. 5042
Butler, S.T.	Australian Atomic Energy Commission, Research Establishment, Lucas Heights, N.S.W. 2232
Hora, H.	Department of Theoretical Physics, University of New South Wales, P.O. Box 1, Kensington, N.S.W. 2033
Hugrass, W.N.	School of Physical Sciences, Flinders University, Bedford Park, S.A. 5042
Jessup, B.L.	Centre d'études nucléaires de Grenoble, DPh – PFC – SIG, F-38041 Grenoble Cedex, France
Jones, I.R.	School of Physical Sciences, Flinders University, Bedford Park, S.A. 5042

AUSTRALIA (cont.)

Storer, R.G.	School of Physical Sciences, Flinders University, Bedford Park, S.A. 5042
Watson-Munro, C.N.	Wills Plasma Physics Department, University of Sydney, N.S.W. 2006

AUSTRIA

Auer, G.	Institut für Theoretische Physik an der Universität Innsbruck, Sillgasse 8, A-6020 Innsbruck
Cap, F.	Institut für Theoretische Physik an der Universität Innsbruck, Sillgasse 8, A-6020 Innsbruck
Deutsch, R.	Institut für Theoretische Physik an der Universität Innsbruck, Innrain 52, A-6020 Innsbruck
Edenstrasser, J.W.	Institut für Theoretische Physik an der Universität Innsbruck, Sillgasse 8, A-6020 Innsbruck
Friedmann, H.	Institut für Radiumforschung und Kernphysik, Boltzmanngasse 3, A-1090 Vienna
Gilli, P.V.	Institut für Dampfkesselbau, Reaktortechnik und Wärmewirtschaft, Technische Universität Graz, Kopernikusgasse 24, A-8010 Graz
Kuhn, S.	Institut für Theoretische Physik an der Universität Innsbruck, Sillgasse 8, A-6020 Innsbruck

Leubner, M.
Institut für Theoretische Physik an der Universität Innsbruck,
Sillgasse 8,
A-6020 Innsbruck

Märk, E.
Institut für Theoretische Physik an der Universität Innsbruck,
Sillgasse 8,
A-6020 Innsbruck

Putz, F.
Österreichische Studiengesellschaft für Atomenergie GmbH,
Institut für Reaktorsicherheit,
Lenaugasse 10,
A-1080 Wien

Stössel, F.P.
Institut für Theoretische Physik and der Universität Innsbruck,
Innrain 52,
A-6020 Innsbruck

Zygelman, S.
Institut für Theoretische Physik an der Universität Innsbruck,
Sillgasse 8,
A-6020 Innsbruck

BELGIUM

Bhatnagar, V.
Laboratoire de physique des plasmas,
Association Euratom-Etat belge,
Ecole royale militaire,
avenue de la Renaissance 30,
B-1040 Brussels

Bosia, G.F.
Laboratoire de physique des plasmas,
Association Euratom-Etat belge,
Ecole royale militaire,
avenue de la Renaissance 30,
B-1040 Brussels

Collée, R.F.
Université de Liège,
rue A. Stevart 2,
B-4000 Liège

Messiaen, A.M.
Laboratoire de physique des plasmas,
Association Euratom-Etat belge,
Ecole royale militaire,
avenue de la Renaissance 30,
B-1040 Brussels

BELGIUM (cont.)

Prohoroff, S.
Département d'électricité générale et de physique des plasmas,
Université libre de Bruxelles,
avenue F.D. Roosevelt 50,
B-1050 Brussels

Vandenplas, P.E.
Laboratoire de physique des plasmas,
Association Euratom-Etat belge,
Ecole royale militaire,
avenue de la Renaissance 30,
B-1040 Brussels

Weynants, R.R.
Laboratoire de physique des plasmas,
Association Euratom-Etat belge,
Ecole royale militaire,
avenue de la Renaissance 30,
B-1040 Brussels

BRAZIL

Chian, A.C.-L.
Instituto de Fisica,
Universidade Federal Fluminense,
Valonguinho, Niteroi,
Rio de Janeiro

Nascimento, I.C.
Instituto de Fisica, Universidade de São Paulo,
C.P. 20516, São Paulo

Sakanaka, P.H.
Instituto de Fisica, Universidade Estadual de Campinas,
13100 Campinas, São Paulo

CANADA

Gregory, B.C.
INRS-Energie, Université du Québec,
C.P. 1020, Varennes, Quebec J0L 2P0

Hirose, A.
Department of Physics,
University of Saskatchewan,
Saskatoon, Saskatchewan S7N 0W0

Kekez, M.M.
Mechanical Engineering Division,
National Research Council of Canada,
Montreal Road, Ottawa, Ontario K1A 0R6

Offenberger, A.A.	Department of Electrical Engineering, University of Alberta, Edmonton, Alberta T6G 2E1
Pitt, L.	Department of Electrical Engineering, University of Alberta, Edmonton, Alberta T6G 2E1
Shubaly, M.R.	Atomic Energy of Canada Ltd., Chalk River Nuclear Laboratories, Chalk River, Ontario K0J 1J0
Van Andel, H.W.H.	Département de physique, Université de Montréal, C.P. 6128, Montreal, Quebec H3C 3J7

CZECHOSLOVAKIA

Schmiedberger, P.	Faculty of Science and Physical Engineering, Technical University of Prague, Brehova 7, 115 19 Prague 1

DENMARK

Chang, C.-T.	Risø National Laboratory, DK-4000 Roskilde
Jensen, V.O.	Risø National Laboratory, DK-4000 Roskilde
Nielsen, P.	Risø National Laboratory, DK-4000 Roskilde

FINLAND

Karttunen, S.J.	Technical Research Centre of Finland, Nuclear Engineering Laboratory, SF-02150 Espoo
Salomaa, R.E.	Technical Research Centre of Finland, Nuclear Engineering Laboratory, SF-02150 Espoo

FRANCE

Bamière, Christine G.	Secrétariat général de la défense nationale, 51 boulevard de Latour Maubourg, F-75700 Paris
Bernard, A.	Centre d'études de Limeil, B.P. 27, F-94190 Villeneuve-Saint-Georges
Bernard, M.G.	Centre d'études nucléaires de Grenoble, DPh – PFC – SIG, 85X, F-38041 Grenoble Cedex
Blum, J.	Laboratoire d'analyse numérique de Paris VI, 4 place Jussieu, F-75230 Paris
Canobbio, E.	Centre d'études nucléaires de Grenoble, DPh – PFC – SIG, 85X, F-38041 Grenoble Cedex
Consoli, T.	Centre d'études nucléaires de Grenoble, DPh – PFC – SIG, 85X, F-38041 Grenoble Cedex
Doucet, H.J.	Laboratoire de physique des milieux ionisés, Ecole polytechnique, F-91128 Palaiseau Cedex
Dubois, M.	Association Euratom-CEA sur la fusion, Centre d'études nucléaires de Fontenay-aux-Roses, DPh – PFC – SCP, B.P. 6, F-92260 Fontenay-aux-Roses
Fabre, E.	Laboratoire de physique des milieux ionisés, Ecole polytechnique, F-91128 Palaiseau Cedex
Fain, A.G.	Centre d'études de Limeil, B.P. 27, F-94190 Villeneuve-Saint-Georges
Girard, J.P.	Centre d'études de Fontenay-aux-Roses, DPh – PFC – SCP, B.P. 6, F-92260 Fontenay-aux-Roses

Holstein, P.A.	Centre d'études de Limeil, B.P. 27, F-94190 Villeneuve-Saint-Georges
Horowitz, J.J.	Institut de recherche fondamentale, Centre d'études nucléaires de Saclay, B.P. 2, F-91190 Gif-sur-Yvette
Jablon, C.J.	Laboratoire de physique des plasmas, Université Paris-Sud, F-91405 Orsay
Mercier, C.	Centre d'études nucléaires de Fontenay-aux-Roses, DPh – PFC – STGI, B.P. 6, F-92260 Fontenay-aux-Roses
Moreau, D.	Centre d'études nucléaires de Grenoble, DPh – PFC – SIG, 85X, F-38041 Grenoble Cedex
Rebut, P.H. (see also under CEC)	The JET Project, Culham Laboratory, Abingdon, Oxon., OX14 3DB
Renaud, C.M.	Centre d'études nucléaires de Fontenay-aux-Roses, DPh – PFC – SCP, B.P. 6, F-92260 Fontenay-aux-Roses
Tachon, J.	Centre d'études nucléaires de Fontenay-aux-Roses, DPh – PFC – SCP, B.P. 6, F-92260 Fontenay-aux-Roses
Tonon, G.	Centre d'études nucléaires de Grenoble, DPh – PFC – SIG, 85X, F-38041 Grenoble Cedex
Trocheris, M.	Centre d'études nucléaires de Fontenay-aux-Roses, DPh – PFC – DIR, B.P. 6, F-92260 Fontenay-aux-Roses
Watteau, J.P.	Centre d'études de Limeil, B.P. 27, F-94190 Villeneuve-Saint-Georges

GERMAN DEMOCRATIC REPUBLIC

Sauer, K.	Zentralinstitut für Elektronenphysik der Akademie der Wissenschaften der DDR, Mohrenstrasse, DDR-108 Berlin

GERMANY, FEDERAL REPUBLIC OF

Angert, N.K.	Gesellschaft für Schwerionenforschung mbH, Postfach 11 05 41, D-6100 Darmstadt
Becker, G.	Max-Planck-Institut für Plasmaphysik, D-8046 Garching
Behrisch, R.	Max-Planck-Institut für Plasmaphysik, D-8046 Garching
Bein, B.K.	Institut für Theoretische Physik, Ruhr-Universität Bochum, D-4630 Bochum
Bogen, P.	Institut für Plasmaphysik der Kernforschungsanlage Jülich, Postfach 1913, D-5170 Jülich 1
Borrass, K.	Max-Planck-Institut für Plasmaphysik, D-8046 Garching
Brinkschulte, H.W.	Max-Planck-Institut für Plasmaphysik, D-8046 Garching
Bruhns, H.	Institut für Angewandte Physik II, Universität Heidelberg, Albert-Ueberle-Strasse 3–5, D-6900 Heidelberg 1
Cavallo, A.	Max-Planck-Institut für Plasmaphysik, D-8046 Garching
Chodura, R.	Max-Planck-Institut für Plasmaphysik, D-8046 Garching
Conrads, J.	Institut für Plasmaphysik der Kernforschungsanlage Jülich, Postfach 1913, D-5170 Jülich

Daybelge, U.	Institut für Theoretische Physik, Ruhr-Universität Bochum, D-4630 Bochum
Decker, G.	Physikalisches Institut I, Universität Düsseldorf, Universitätsstrasse 1, D-4000 Düsseldorf 1
Dietz, J.K.	Institut für Plasmaphysik der Kernforschungs- anlage Jülich, Postfach 1913, D-5170 Jülich
Dippel, K.H.	Institut für Plasmaphysik der Kernforschungs- anlage Jülich, Postfach 1913, D-5170 Jülich
Düchs, D.F.	Max-Planck-Institut für Plasmaphysik, D-8046 Garching
Eberhagen, A.	Max-Planck-Institut für Plasmaphysik, D-8046 Garching
Elsässer, K.	Institut für Theoretische Physik, Ruhr-Universität Bochum, D-4630 Bochum
Engelhardt, W.	Max-Planck-Institut für Plasmaphysik, D-8046 Garching
Erckmann, V.	Institut für Plasmaforschung der Universität Stuttgart, Pfaffenwaldring 31, D-7000 Stuttgart 80
Fahrbach, H.-U.	Max-Planck-Institut für Plasmaphysik, D-8046 Garching
Faulkner, J.E.	Max-Planck-Institut für Plasmaphysik, D-8046 Garching
Feneberg, W.	Max-Planck-Institut für Plasmaphysik, D-8046 Garching
Fussmann, G.	Max-Planck-Institut für Plasmaphysik, D-8046 Garching

GERMANY, FEDERAL REPUBLIC OF (cont.)

Gehre, O.	Max-Planck-Institut für Plasmaphysik, D-8046 Garching
von Gierke, G.	Max-Planck-Institut für Plasmaphysik, D-8046 Garching
Glock, E.	Max-Planck-Institut für Plasmaphysik, D-8046 Garching
Gottardi, N.A.	Max-Planck-Institut für Plasmaphysik, D-8046 Garching
Grieger, G.	Max-Planck-Institut für Plasmaphysik, D-8046 Garching
Gruber, O.	Max-Planck-Institut für Plasmaphysik, D-8046 Garching
Haas, G.	Max-Planck-Institut für Plasmaphysik, D-8046 Garching
Hacker, H.	Max-Planck-Institut für Plasmaphysik, D-8046 Garching
Heinz, W.	Institut für Technische Physik, Kernforschungszentrum Karlsruhe, Postfach 3640, D-7500 Karlsruhe 1
Henkes, P.R.W.	Institut für Kernverfahrenstechnik, Kernforschungszentrum Karlsruhe, Postfach 3640, D-7500 Karlsruhe 1
Herold, H.	Institut für Plasmaforschung der Universität Stuttgart, Pfaffenwaldring 31, D-7000 Stuttgart 80
Herrnegger, F.	Max-Planck-Institut für Plasmaphysik, D-8046 Garching
Hintz, E.A.K.	Institut für Plasmaphysik der Kernforschungs- anlage Jülich, Postfach 1913, D-5170 Jülich

Hisam, E.	Institut für Plasmaforschung der Universität Stuttgart, Pfaffenwaldring 31, D-7000 Stuttgart 80
Hofmann, I.	Max-Planck-Institut für Plasmaphysik, D-8046 Garching
How, J.	Max-Planck-Institut für Plasmaphysik, D-8046 Garching
Hübenthal, K.	Bundesministerium für Forschung und Technologie, Postfach 20 07 06, D-5300 Bonn
Hübner, K.	Institut für Angewandte Physik II, Universität Heidelberg, Albert-Ueberle-Strasse 3–5, D-6900 Heidelberg 1
Jäckel, H.	Max-Planck-Institut für Plasmaphysik, D-8046 Garching
Jaenicke, R.	Max-Planck-Institut für Plasmaphysik, D-8046 Garching
Janzen, G.	Institut für Plasmaforschung der Universität Stuttgart, Pfaffenwaldring 31, D-7000 Stuttgart 80
Junker, J.	Max-Planck-Institut für Plasmaphysik, D-8046 Garching
Kaeppeler, H.J.	Institut für Plasmaforschung der Universität Stuttgart, Pfaffenwaldring 31, D-7000 Stuttgart 80
Karger, F.	Max-Planck-Institut für Plasmaphysik, D-8046 Garching
Keilhacker, M.	Max-Planck-Institut für Plasmaphysik, D-8046 Garching
Kerner, W.	Max-Planck-Institut für Plasmaphysik, D-8046 Garching

GERMANY, FEDERAL REPUBLIC OF (cont.)

Kever, H.	Institut für Plasmaphysik der Kernforschungsanlage Jülich, Postfach 1913, D-5170 Jülich
Klüber, O.	Max-Planck-Institut für Plasmaphysik, D-8046 Garching
Knobloch, A.F.	Max-Planck-Institut für Plasmaphysik, D-8046 Garching
Komarek, P.	Institut für Technische Physik, Kernforschungszentrum Karlsruhe, Postfach 3640, D-7500 Karlsruhe 1
Konle, W.	Institut für Plasmaforschung der Universität Stuttgart, Pfaffenwaldring 31, D-7000 Stuttgart 80
Köppendörfer, W.	Max-Planck-Institut für Plasmaphysik, D-8046 Garching
Krause, H.	Max-Planck-Institut für Plasmaphysik, D-8046 Garching
Kreutz, R.	Interatom, Friedrich-Ebert-Strasse, D-5060 Bergisch-Gladbach 1
Krompholz, H.	Institut für Angewandte Physik, Technische Hochschule Darmstadt, Schlossgartenstrasse 7, D-6100 Darmstadt
Kronast, B.	Institut für Experimentalphysik, Ruhr-Universität Bochum, Postfach 2148, D-4630 Bochum
Kull, H.	Projektgruppe für Laserforschung der Max-Planck-Gesellschaft, D-8046 Garching
Kunze, H.-J.	Institut für Experimentalphysik, Ruhr-Universität Bochum, Postfach 2148, D-4630 Bochum

Lackner, K.	Max-Planck-Institut für Plasmaphysik, D-8046 Garching
Lengyel, L.	Max-Planck-Institut für Plasmaphysik, D-8046 Garching
Lerch, G.G.	Leybold-Heraeus, Wilhelm-Rohn-Strasse, D-6450 Hanau
Leuterer, F.	Max-Planck-Institut für Plasmaphysik, D-8046 Garching
Lisitano, G.	Max-Planck-Institut für Plasmaphysik, D-8046 Garching
Maaswinkel, A.G.	Projektgruppe für Laserforschung der Max-Planck-Gesellschaft, D-8046 Garching
Marlier, S.	Max-Planck-Institut für Plasmaphysik, D-8046 Garching
Mayer, H.M.	Max-Planck-Institut für Plasmaphysik, D-8046 Garching
McKenney, A.M.	Max-Planck-Institut für Plasmaphysik, D-8046 Garching
Moser, F.	Institut für Plasmaforschung der Universität Stuttgart, Pfaffenwaldring 31, D-7000 Stuttgart 80
Müller, G.	Institut für Plasmaforschung der Universität Stuttgart, Pfaffenwaldring 31, D-7000 Stuttgart 80
Mulser, P.	Projektgruppe für Laserforschung der Max-Planck-Gesellschaft, D-8046 Garching
Murmann, H.-D.	Max-Planck-Institut für Plasmaphysik, D-8046 Garching
Nahrath, B.	Institut für Plasmaforschung der Universität Stuttgart, Pfaffenwaldring 31, D-7000 Stuttgart 80

GERMANY, FEDERAL REPUBLIC OF (cont.)

Nührenberg, J.	Max-Planck-Institut für Plasmaphysik, D-8046 Garching
Ohlendorf, W.	Max-Planck-Institut für Plasmaphysik, D-8046 Garching
Oppenländer, T.W.	Institut für Plasmaforschung der Universität Stuttgart, Pfaffenwaldring 31, D-7000 Stuttgart 80
Pacher, G.W.	Max-Planck-Institut für Plasmaphysik, D-8046 Garching
Pacher, H.D.	Max-Planck-Institut für Plasmaphysik, D-8046 Garching
Petsch, R.	Projektgruppe für Laserforschung der Max-Planck-Gesellschaft, D-8046 Garching
Pfirsch, D.	Max-Planck-Institut für Plasmaphysik, D-8046 Garching
Pross, G.	Physikalisches Institut I der Universität Düsseldorf, Universitätstrasse 1, D-4000 Düsseldorf
Raeder, J.	Max-Planck-Institut für Plasmaphysik, D-8046 Garching
Rapp, H.K.	Max-Planck-Institut für Plasmaphysik, D-8046 Garching
Rau, F.	Max-Planck-Institut für Plasmaphysik, D-8046 Garching
Rehker, S.-H.	Max-Planck-Institut für Plasmaphysik, D-8046 Garching
Renner, H.	Max-Planck-Institut für Plasmaphysik, D-8046 Garching
Repp, H.	Institut für Plasmaphysik der Kernforschungsanlage Jülich, Postfach 1913, D-5170 Jülich

Riedmüller, W.	Max-Planck-Institut für Plasmaphysik, D-8046 Garching
Ringler, H.	Max-Planck-Institut für Plasmaphysik, D-8046 Garching
Rogister, A.	Institut für Plasmaphysik der Kernforschungs-anlage Jülich, Postfach 1913, D-5170 Jülich
Rückle, B.	Institut für Plasmaforschung der Universität Stuttgart, Pfaffenwaldring 31, D-7000 Stuttgart 80
Rusch, D.	Institut für Neutronenphysik and Reaktortechnik, Kernforschungszentrum Karlsruhe, Postfach 3640, D-7500 Karlsruhe
Salat, A.	Max-Planck-Institut für Plasmaphysik, D-8046 Garching
Salge, J.G.H.	Institut für Hochspannungstechnik, Technische Universität Braunschweig, Postfach 3329, D-3300 Braunschweig
Sardei, F.	Max-Planck-Institut für Plasmaphysik, D-8046 Garching
Schaper, U.	Max-Planck-Institut für Plasmaphysik, D-8046 Garching
Schilling, P.	Institut für Plasmaforschung der Universität Stuttgart, Pfaffenwaldring 31, D-7000 Stuttgart 80
Schindler, H.A.	Siemens AG, Research Laboratory, Plasma Physics Department, Günther-Scharowsky-Strasse, D-8520 Erlangen
Schlüter, A.	Max-Planck-Institut für Plasmaphysik, D-8046 Garching

GERMANY, FEDERAL REPUBLIC OF (cont.)

Schlüter, J.	Institut für Plasmaphysik der Kernforschungsanlage Jülich, Postfach 1913, D-5170 Jülich
Schmidt, H.	Institut für Plasmaforschung der Universität Stuttgart, Pfaffenwaldring 31, D-7000 Stuttgart 80
Schmitter, K.H.	Max-Planck-Institut für Plasmaphysik, D-8046 Garching
Schneider, E.	Institut für Plasmaforschung der Universität Stuttgart, Pfaffenwaldring 31, D-7000 Stuttgart 80
Schneider, W.	Max-Planck-Institut für Plasmaphysik, D-8046 Garching
Schönbach, K.H.	Institut für Angewandte Physik, Technische Hochschule Darmstadt, Schlossgartenstrasse 7, D-6100 Darmstadt
Schüller, P.-G.	Institut für Plasmaforschung der Universität Stuttgart, Pfaffenwaldring 31, D-7000 Stuttgart 80
Schumacher, U.	Max-Planck-Institut für Plasmaphysik, D-8046 Garching
Spatschek, K.-H.	Fachbereich Physik, Universität Essen, D-4300 Essen
Speth, E.	Max-Planck-Institut für Plasmaphysik, D-8046 Garching
Spindler, G.	Projektgruppe für Laserforschung der Max-Planck-Gesellschaft, D-8046 Garching
Stäbler, A.	Max-Planck-Institut für Plasmaphysik, D-8046 Garching

Staudenmaier, G.J.	Max-Planck-Institut für Plasmaphysik, D-8046 Garching
Steinmetz, K.	Institut für Angewandte Physik II, Universität Heidelberg, Albert-Ueberle-Strasse 3–5, D-6900 Heidelberg 1
Steuer, K.-H.	Max-Planck-Institut für Plasmaphysik, D-8046 Garching
Tasso, H.	Max-Planck-Institut für Plasmaphysik, D-8046 Garching
Theenhaus, R.	Kernforschungsanlage Jülich, Postfach 1913, D-5170 Jülich
Thumm, M.	Institut für Plasmaforschung der Universität Stuttgart, Pfaffenwaldring 31, D-7000 Stuttgart 80
Tsakiris, G.D.	Projektgruppe für Laserforschung der Max-Planck-Gesellschaft, D-8046 Garching
Tweer, Ilse	Zentralstelle Dokumentation Elektrotechnik e.V. beim Verband Deutscher Elektrotechniker, D-6000 Offenbach
Ullrich, R.	Edelweisstrasse 39, D-8031 Puchheim
Waelbroek, F.G.	Institut für Plasmaphysik der Kernforschungsanlage Jülich, Postfach 1913, D-5170 Jülich
Wägli, P.	Deutsche Forschungs- und Versuchsanstalt für Luft- und Raumfahrt, Institut für Technische Physik, Pfaffenwaldring 38–40, D-7000 Stuttgart 80
Wagner, F.	Max-Planck-Institut für Plasmaphysik, D-8046 Garching
Weller, A.	Max-Planck-Institut für Plasmaphysik, D-8046 Garching

GERMANY, FEDERAL REPUBLIC OF (cont.)

Wienecke, R.	Max-Planck-Institut für Plasmaphysik, D-8046 Garching
Wilhelm, R.W.	Max-Planck-Institut für Plasmaphysik, D-8046 Garching
Wimmel, H.K.	Max-Planck-Institut für Plasmaphysik, D-8046 Garching
Wischgoll, B.	Physikalisches Institut I der Universität Düsseldorf, Universitätstrasse 1, D-4000 Düsseldorf
Witkowski, S.W.A.	Projektgruppe für Laserforschung der Max-Planck-Gesellschaft, D-8046 Garching
Wobig, H.	Max-Planck-Institut für Plasmaphysik, D-8046 Garching
Wolf, G.H.	Institut für Plasmaphysik der Kernforschungsanlage Jülich, Postfach 1913, D-5170 Jülich
Würsching, E.	Max-Planck-Institut für Plasmaphysik, D-8046 Garching
Yu, M.-Y.	Ruhr-Universität Bochum, D-4630 Bochum
Zankl, G.	Max-Planck-Institut für Plasmaphysik, D-8046 Garching
Zwicker, H.	Institut für Plasmaforschung der Universität Stuttgart, Pfaffenwaldring 31, D-7000 Stuttgart 80

HUNGARY

Hrehuss, G.	Central Research Institute for Physics of the Hungarian Academy of Sciences, P.O. Box 49, H-1525 Budapest

Szentpétery, I. — Central Research Institute for Physics of the Hungarian Academy of Sciences, P.O. Box 49, H-1525 Budapest

INDIA

Rohatgi, V.K. — Plasma Physics Section, Bhabha Atomic Research Centre, Trombay, Bombay 400 085

Sen, A. — Physical Research Laboratory, Navrangpura, Ahmedabad 380 009

IRAN

Azodi, H. — Nuclear Research Centre, Atomic Energy Organization of Iran, P.O. Box 3327, Tehran

Naraghi, M. — Nuclear Research Centre, Atomic Energy Organization of Iran, P.O. Box 3327, Tehran

Tahsiri, H. — Nuclear Research Centre, Atomic Energy Organization of Iran, P.O. Box 3327, Tehran

Torabi-Fard, A. — Nuclear Research Centre, Atomic Energy Organization of Iran, P.O. Box 3327, Tehran

IRELAND

McGuire, K.M. — Culham Laboratory, Abingdon, Oxon, OX14 3DB

ISRAEL

Avivi, P.	Plasma Physics Division, Racah Institute of Physics, Hebrew University, Jerusalem
Barak, G.	Hebrew University, Jerusalem
Braun, A.D.	Hebrew University, Jerusalem
Cuperman, S.	Department of Physics and Astronomy, Tel-Aviv University, Ramat Aviv
Eliezer, S.	Soreq Nuclear Research Centre, Yavne 70600
Sapir, M.	Nuclear Research Centre – Negev, P.O. Box 9001, Beer-Sheva
Shvarts, D.	Nuclear Research Centre – Negev, P.O. Box 9001, Beer-Sheva
Szichman, H.	Soreq Nuclear Research Centre, Yavne 70600
Zmora, H.	Soreq Nuclear Research Centre, Yavne 70600

ITALY

Brunelli, B.	Laboratorio Gas Ionizzati, Centro CNEN, C.P. 65, I-00044 Frascati (Rome)
D'Ambrogio, E.	Istituto di Meccanica dell'Università di Trieste, Piazzale Europa 1, I-34127 Trieste
Galanti, M.	Associazione Euratom-CNEN sulla Fusione, Centro CNEN, C.P. 65, I-00044 Frascati (Rome)

Luppi, R.
Laboratorio Gas Ionizzati, Centro CNEN,
C.P. 65,
I-00044 Frascati (Rome)

Nardi, V.
Istituto Elettrotecnico Nazionale Galileo Ferraris,
Corso M. D'Azeglio 42,
Turin

Ortolani, S.
Centro di Studio sui Gas Ionizzati,
Associazione Euratom-CNR,
Via Gradenigo 6/A,
I-35100 Padua

Pozzoli, R.
Laboratorio di Fisica del Plasma,
Associazione Euratom-CNR,
Via Bassini 15,
I-20132 Milan

Rager, J.-P.
(see also under CEC)
Laboratorio Gas Ionizzati, Centro CNEN,
C.P. 65,
I-00044 Frascati (Rome)

Samuelli, M.
Associazione Euratom-CNEN sulla Fusione,
Centre CNEN,
C.P. 65,
I-00044 Frascati (Rome)

Segre, S.
Laboratorio Gas Ionizzati, Centro CNEN,
C.P. 65,
I-00044 Frascati (Rome)

Sestero, A.
Laboratorio Gas Ionizzati, Centro CNEN,
C.P. 65,
I-00044 Frascati (Rome)

Taroni, A.
Centro di Calcolo-CNEN,
Via Mazzini 2,
I-40138 Bologna

Toschi, R.
Associazione Euratom-CNEN sulla Fusione,
Centro CNEN,
C.P. 65,
I-00044 Frascati (Rome)

JAPAN

Hayase, K.
Electrotechnical Laboratory, Tanashi,
5–4–1 Mukodai, Tanashi, Tokyo

JAPAN (cont.)

Hosogane, N.	Plasma Physics Laboratory, Faculty of Engineering, Osaka University, Yamada-kami, Suita, Osaka
Ido, S.	Department of Nuclear Engineering, Faculty of Engineering, University of Tokyo, 7–3–1 Hongo, Bunkyo-ku, 113 Tokyo
Iiyoshi, A.	Plasma Physics Laboratory, Kyoto University, Gokasho, Uji, 611 Kyoto
Inoue, K.	Energy Research Laboratory, Hitachi Ltd, 1168 Moriyama-cho, Hitachi-shi, Ibaraki-ken
Inoue, S.	Department of Physics, Faculty of Science, University of Tokyo, 7–3–1 Hongo, Bunkyo-ku, 113 Tokyo
Ishimura, T.	Plasma Physics Laboratory, Faculty of Engineering, Osaka University, Yamada-kami, Suita, Osaka
Itoh, K.	Department of Physics, Faculty of Science, University of Tokyo, 7–3–1 Hongo, Bunkyo-ku, 113 Tokyo
Itoh, S.	Institute of Plasma Physics, Nagoya University, Chikusa-ku, 464 Nagoya
Kawabe, T.	Institute of Physics, University of Tsukuba, Niihari-Gun, Ibaraki-ken 300–31
Kawakami, I.	Atomic Energy Institute, Nihon University, 1–8 Suruga-dai, Chiyoda-ku, 101 Tokyo
Kinoshita, M.	Energy and Environment Laboratory, Central Research Institute of Electric Power Industry, 2–11–1 Komae-shi, Setagaya-ku, 182 Tokyo

Konoshima, S.	Japan Atomic Energy Research Institute, Tokai-mura, Naka-gun, Ibaraki-ken
Kumazawa, R.	Institute of Plasma Physics, Nagoya University, Furo-cho, Chikusa-ku, 464 Nagoya
Maeda, H.	Japan Atomic Energy Research Institute, Tokai-mura, Naka-gun, Ibaraki-ken
Matsuura, K.	Institute of Plasma Physics, Nagoya University, Chikusa-ku, 464 Nagoya
Miyoshi, S.	Institute of Physics, University of Tsukuba, Niihari-gun, Ibaraki-ken
Mohri, A.	Institute of Plasma Physics, Nagoya University, Chikusa-ku, 464 Nagoya
Mori, S.	Japan Atomic Energy Research Institute, Tokai-mura, Naka-gun, Ibaraki-ken
Nakai, S.	Institute of Laser Engineering, Osaka University, Suita, 565 Osaka
Nishikawa, K.	Institute for Fusion Theory, Hiroshima University, 1–1–89 Higashi-senda-machi, 730 Hiroshima
Nogi, Y.	Department of Physics and Atomic Energy Research Institute, College of Science and Technology, Nihon University, 1–8, Kanda Surugadai, Chiyoda-ku, Tokyo
Okada, O.	Central Research Laboratory, Hitachi Ltd, Kokubunji, 185 Tokyo
Sato, K.N.	Institute of Plasma Physics, Nagoya University, Chikusa-ku, 464 Nagoya
Sato, T.	Institute of Plasma Physics, Nagoya University, Chikusa-ku, 464 Nagoya

JAPAN (cont.)

Sekiguchi, T.	Department of Electronics Engineering, University of Tokyo, Hongo, Bunkyo-ku, 113 Tokyo
Shiina, S.	Atomic Energy Research Institute, College of Science and Technology, Nihon University, Kanda-Surugadai, Chiyoda-ku, Tokyo
Sugai, H.	Department of Electrical Engineering, Nagoya University, Chikusa-ku, 464 Nagoya
Suzuki, Y.	Japan Atomic Energy Research Institute, Tokai-mura, Naka-gun, Ibaraki-ken
Takayama, K.	Institute of Plasma Physics, Nagoya University, Chikusa-ku, 464 Nagoya
Tamaru, T.	Electrotechnical Laboratory, Tanashi, 5–4–1 Mukodai, Tanashi-shi, Tokyo
Tanaka, Y.	Japan Atomic Energy Research Institute, Tokai-mura, Naka-gun, Ibaraki-ken
Terashima, Y.	Institute of Plasma Physics, Nagoya University, Chikusa-ku, 464 Nagoya
Toyama, H.	Department of Physics, Faculty of Science, University of Tokyo, Bunkyo-ku, 113 Tokyo
Uchida, T.	Department of Nuclear Engineering, Faculty of Engineering, University of Tokyo, 7–3–1 Hongo, Bunkyo-ku, 113 Tokyo
Ueno, I.	Department of Electrical Engineering, Faculty of Engineering, University of Tokyo, 7–3–1 Hongo, Bunkyo-ku, 113 Tokyo
Uo, K.	Plasma Physics Laboratory, Kyoto University, Gokasho, Uji, 611 Kyoto

Wakatani, M.	Plasma Physics Laboratory, Kyoto University, Gokasho, Uji, 611 Kyoto
Yamanaka, C.	Institute of Laser Engineering, Osaka University, Suita, 565 Osaka
Yatsu, K.	Institute of Physics, University of Tsukuba, Niihari-gun, Ibaraki-ken 300–31
Yoshikawa, M.	Japan Atomic Energy Research Institute, Tokai-mura, Naka-gun, Ibaraki-ken

MEXICO

Jiménez Domínguez, H.	Instituto Nacional de Energía Nuclear, Avenida Insurgentes Sur 1079, México 19, D.F.

NETHERLANDS

Barbian, E.P.	FOM-Instituut voor Plasmafysica, Rijnhuizen, P.O. Box 7, Nieuwegein (Jutphaas)
Bobeldijk, C.	FOM-Instituut voor Plasmafysica, Rijnhuizen, P.O. Box 7, Nieuwegein (Jutphaas)
Bornatici, M.	FOM-Instituut voor Plasmafysica, Rijnhuizen, P.O. Box 7, Nieuwegein (Jutphaas)
Braams, C.M.	FOM-Instituut voor Plasmafysica, Rijnhuizen, P.O. Box 7, Nieuwegein (Jutphaas)
De Kluiver, H.	FOM-Instituut voor Plasmafysica, Rijnhuizen, P.O. Box 7, Nieuwegein (Jutphaas)
Engelmann, F.	FOM-Instituut voor Plasmafysica, Rijnhuizen, P.O. Box 7, Nieuwegein (Jutphaas)
Hoekzema, F.	FOM-Instituut voor Plasmafysica, Rijnhuizen, P.O. Box 7, Nieuwegein (Jutphaas)

NETHERLANDS (cont.)

Hopman, H.J.	FOM-Instituut voor Atoom en Molecuul Fysica, Kruislaan 407, Amsterdam 1098
Janssen, P.A.	Eindhoven University of Technology, P.O. Box 513, Eindhoven
Jurgens, B.	FOM-Instituut voor Atoom en Molecuul Fysica, Kruislaan 407, Amsterdam 1098
Lister, G.G.	FOM-Instituut voor Plasmafysica, Rijnhuizen, P.O. Box 7, Nieuwegein (Jutphaas)
Lok, J.	FOM-Instituut voor Plasmafysica, Rijnhuizen, P.O. Box 7, Nieuwegein (Jutphaas)
Oepts, D.	FOM-Instituut voor Plasmafysica, Rijnhuizen, P.O. Box 7, Nieuwegein (Jutphaas)
Ornstein, L.T.M.	FOM-Instituut voor Plasmafysica, Rijnhuizen, P.O. Box 7, Nieuwegein (Jutphaas)
Piekaar, H.W.	FOM-Instituut voor Plasmafysica, Rijnhuizen, P.O. Box 7, Nieuwegein (Jutphaas)
Polman, R.W.	FOM-Instituut voor Plasmafysica, Rijnhuizen, P.O. Box 7, Nieuwegein (Jutphaas)
Rem, J.	FOM-Instituut voor Plasmafysica, Rijnhuizen, P.O. Box 7, Nieuwegein (Jutphaas)
Rietjens, L.H.T.	Eindhoven University of Technology, P.O. Box 513, Eindhoven
Schram, D.C.	Eindhoven University of Technology, P.O. Box 513, Eindhoven

Schüller, F.C.	FOM-Instituut voor Plasmafysica, Rijnhuizen, P.O. Box 7, Nieuwegein (Jutphaas)
Schuurman, W.	FOM-Instituut voor Plasmafysica, Rijnhuizen, P.O. Box 7, Nieuwegein (Jutphaas)

POLAND

Gryziński, M.W.	Institute of Nuclear Research, 05–400 Otwock-Świerk
Kowalski, S.	Institute of Plasma Physics and Laser Microfusion, P.O. Box 49, 00–908 Warsaw
Wołowski, J.	Institute of Plasma Physics and Laser Microfusion, P.O. Box 49, 00–908 Warsaw

ROMANIA

Mihailescu, I.	Romanian State Committee for Nuclear Energy, Laser Department, Central Institute of Physics, P.O. Box 5206, 7 Magurele-Bucharest

SPAIN

Cordero López, F.	Junta de Energía Nuclear, Avenida Complutense-22, Ciudad Universitaria, Madrid-3
Guasp Peréz, J.	Junta de Energía Nuclear, Avenida Complutense-22, Ciudad Universitaria, Madrid-3
Manero-Amoros, F.	Junta de Energía Nuclear, Avenida Complutense-22, Ciudad Universitaria, Madrid-3

SWEDEN

Bonnevier, B.
Department of Plasma Physics and Fusion Research,
Royal Institute of Technology,
S-100 44 Stockholm 77

Hellsten, T.A.K.
Department of Plasma Physics and Fusion Research,
Royal Institute of Technology,
S-100 44 Stockholm 70

Lehnert, B.
Department of Plasma Physics and Fusion Research,
Royal Institute of Technology,
S-100 44 Stockholm 70

Ohlsson, D.
Swedish Fusion Office,
c/o NE, P.O. Box 21048,
S-10031 Stockholm 21

Persson, H.
Swedish Defense Research Institute,
Section 376,
Box 416,
S-172 04 Sundbyberg

Tennfors, E.
Department of Plasma Physics and Fusion Research,
Royal Institute of Technology,
S-100 44 Stockholm 70

Wilhelmsson, H.
Institute for Electromagnetic Field Theory,
Chalmers University of Technology,
S-402 20 Göteborg

Wilner, B.
Division of Fusion Research,
Royal Institute of Technology,
S-100 44 Stockholm 70

SWITZERLAND

Balmer, J.E.
Institut für Angewandte Physik,
Universität Bern,
Sidlerstrasse 5,
CH-3012 Bern

Cheetham, A.D.
Centre de recherches en physique des plasmas,
21 avenue des Bains,
CH-1007 Lausanne

Donaldson, T.P.	Institut für Angewandte Physik, Universität Bern, Sidlerstrasse 5, CH-3012 Bern
Hofmann, F.	Centre de recherches en physique des plasmas, 21 avenue des Bains, CH-1007 Lausanne
Hollenstein, C.	Centre de recherches en physique des plasmas, 12 avenue des Bains, CH-1007 Lausanne
Kuse, D.	Brown, Boveri & Cie AG, Abt. Entwicklung und Fabrikation Elektronenröhren, CH-5401 Baden
Lädrach, P.	Institut für Angewandte Physik, Universität Bern, Sidlerstrasse 5, CH-3012 Bern
Lister, J.B.	Centre de recherches en physique des plasmas, 21 avenue des Bains, CH-1007 Lausanne
Pant, A.	Swiss Federal Institute for Reactor Research, CH-5303 Würenlingen
Troyon, F.	Centre de recherches en physique des plasmas, 21 avenue des Bains, CH-1007 Lausanne
Watterson, R.L.	Centre de recherches en physique des plasmas, 21 avenue des Bains, CH-1007 Lausanne
Weibel, E.S.	Centre de recherches en physique des plasmas, 21 avenue des Bains, CH-1007 Lausanne

TURKEY

Sinman, Ayten	Ankara Nuclear Research and Training Centre, Beşevler-Ankara
Sinman, S.	Electrical Engineering Department, Middle East Technical University, Ankara

UNION OF SOVIET SOCIALIST REPUBLICS

Andryukhina, Emma D.	Lebedev Institute of Physics, Academy of Sciences of the USSR, Leninskij Prospekt 53, Moscow V 312
Babykin, M.V.	Kurchatov Institute of Atomic Energy, P.O. Box 3402, Moscow 123182
Bogomolov, H.D.	Institute of Physical Problems, Academy of Sciences of the USSR, Moscow
Buchelnikova, Natalia S.	Institute of Nuclear Physics, Novosibirsk 90
Kadomtsev, B.B.	Kurchatov Institute of Atomic Energy, P.O. Box 3402, Moscow 123182
Kolesnichenko, Ya.I.	Institute for Nuclear Research, Academy of Sciences of the Ukrainian SSR, Kiev
Kornev, N.P.	Permanent Mission of the USSR to the IAEA, Wohllebengasse 4, A-1040 Vienna, Austria
Lagunov, V.M.	Institute of Nuclear Physics, Novosibirsk 90
Lominadze, D.G.	Astrophysical Observatory, Academy of Sciences of the Georgian SSR, Tbilisi
Mukhovatov, V.S.	Kurchatov Institute of Atomic Energy, P.O. Box 3402, Moscow 123182
Pataraya, A.D.	Astrophysical Observatory, Academy of Sciences of the Georgian SSR, Tbilisi
Rabinovich, M.S.	Lebedev Institute of Physics, Academy of Sciences of the USSR, Leninskij Prospekt 53, Moscow V 312

Razumova, Xenia A.	Kurchatov Institute of Atomic Energy, P.O. Box 3402, Moscow 123182
Ryutov, D.D.	Nuclear Physics Institute of the Siberian Section of the USSR Academy of Sciences, Prospekt Nauki 11, Novosibirsk 630090
Stepanov, K.N.	Physical-Technical Institute of the Ukrainian SSR Academy of Sciences, Kharkov 108
Tshakaya, D.D.	Institute of Physics, Academy of Sciences of the Georgian SSR, Tbilisi
Zatsepin, V.G.	Institute of Physical Problems, Academy of Sciences of the USSR, Moscow

UNITED KINGDOM

Bickerton, R.	UKAEA, Culham Laboratory, Abingdon, Oxon., OX14 3DB
Bodin, H.A.B.	UKAEA, Culham Laboratory, Abingdon, Oxon., OX14 3DB
Choi, P.	Blackett Laboratory, Imperial College, Prince Consort Road, London SW7 2AZ
Evans, R.G.	Science Research Council, Rutherford Laboratory, Chilton, Didcot, Oxon., OX11 0QX
Fieldhouse, P.	AWRE, Bldg. N56, Aldermaston, Reading, Berks., RG7 4PR
Folkierski, A.	Blackett Laboratory, Imperial College, Prince Consort Road, London SW7 2AZ
Haines, M.G.	Blackett Laboratory, Imperial College, Prince Consort Road, London SW7 2AZ

UNITED KINGDOM (cont.)

Hancox, R.	UKAEA, Culham Laboratory, Abingdon, Oxon., OX14 3DB
Harbour, P.J.	UKAEA, Culham Laboratory, Abingdon, Oxon., OX14 3DB
Hughes, M.H.	UKAEA, Culham Laboratory, Abingdon, Oxon., OX14 3DB
Hugill, J.	UKAEA, Culham Laboratory, Abingdon, Oxon., OX14 3DB
Irving, J.	Department of Natural Philosophy, University of Strathclyde, John Anderson Building, Glasgow G4 0NG
James, T.E.	UKAEA, Culham Laboratory, Abingdon, Oxon., OX14 3DB
Laing, E.W.	Department of Natural Philosophy, University of Glasgow, Glasgow G12 8QQ
Lees, D.J.	UKAEA, Culham Laboratory, Abingdon, Oxon., OX14 3DB
McCracken, G.M.	UKAEA, Culham Laboratory, Abingdon, Oxon., OX14 3DB
Motz, H.	Department of Engineering, Oxford University, Parks Road, Oxford
Peacock, N.J.	UKAEA, Culham Laboratory, Abingdon, Oxon., OX14 3DB
Pease, R.S.	UKAEA, Culham Laboratory, Abingdon, Oxon., OX14 3DB
Potter, D.E.	Blackett Laboratory, Imperial College, Prince Consort Road, London SW7 2AZ
Roberts, K.V.	UKAEA, Culham Laboratory, Abingdon, Oxon., OX14 3DB

Robinson, D.C.	UKAEA, Culham Laboratory, Abingdon, Oxon., OX14 3DB
Slade, P.D.	Blackett Laboratory, Imperial College, Prince Consort Road, London SW7 2AZ
Stott, P.E.	UKAEA, Culham Laboratory, Abingdon, Oxon., OX14 3DB
Sweetman, D.R.	UKAEA, Culham Laboratory, Abingdon, Oxon., OX14 3DB
Sykes, A.	UKAEA, Culham Laboratory, Abingdon, Oxon., OX14 3DB
Taylor, J.B.	UKAEA, Culham Laboratory, Abingdon, Oxon., OX14 3DB
Taylor, J.C.	Department of Natural Philosophy, University of Glasgow, Glasgow G12 8QQ
Taylor, Julie V.	Mathematics Department, University of Strathclyde, George Street, Glasgow G12 8QQ
Thompson, P.C.	Theoretical Physics Division, AWRE, Bldg. E3, Aldermaston, Reading, Berks., RG7 4PR
Webb, C.J.	Rutherford Laboratory, Chilton, Didcot, Oxon., OX11 0QX
Wooding, E.	Department of Physics, Royal Holloway College, Egham Hill, Egham, Surrey TW20 0EX

UNITED STATES OF AMERICA

Aamodt, R.E.	Science Applications Inc., 934, Pearl St., Boulder, CO 80302
Alexeff, I.	Electrical Engineering, Ferris Hall, University of Tennessee, Knoxville, TN 37916

UNITED STATES OF AMERICA (cont.)

Anderson, D.T.	Department of Electrical Engineering, University of Wisconsin, Madison, WI 53706
Baker, C.C.	Argonne National Laboratory, Fusion Power Program, 9700 South Cass Avenue, Argonne,IL 60439
Baker, D.A.	Los Alamos Scientific Laboratory, P.O. Box 1663, Los Alamos,NM 87545
Baldwin, D.E.	Lawrence Livermore Laboratory, University of California, P.O. Box 808, Livermore, CA 94550
Berk, H.L.	Lawrence Berkeley Laboratory, University of California, Berkeley, CA 94720
Bers, A.	Massachusetts Institute of Technology, Cambridge, MA 02139
Bodner, S.E.	Naval Research Laboratory, Washington, DC 20375
Bol, K.	Plasma Physics Laboratory, Princeton University, James Forrestal Campus, P.O. Box 451, Princeton, NJ 08540
Book, D.L.	Naval Research Laboratory, Washington, DC 20375
Boris, J.P.	Naval Research Laboratory, Washington, DC 20375
Boyd, D.	Department of Physics and Astronomy, University of Maryland, College Park, MD 20742
Braunschweig, E.D.	Office of Laser Fusion, US Department of Energy, Washington, DC 20545

Burke, R.J.	Argonne National Laboratory, 9700 South Cass Avenue, Argonne, IL 60439
Burns, E.J.T.	Sandia Laboratories, Albuquerque, NM 87115
Byrne, R.N.	Science Applications Inc., La Jolla, CA 92037
Callen, J.D.	Oak Ridge National Laboratory, Fusion Energy Division, P.O. Box Y, Oak Ridge, TN 37830
Chu, C.K.	Plasma Physics Laboratory, Columbia University, New York, NY 10027
Clarke, J.F.	US Department of Energy, G234, Washington, DC 20545
Coffey, T.	Naval Research Laboratory, Washington, DC 20375
Coffman, F.E.	US Department of Energy, Washington, DC 20545
Collins, S.S.	DARCOM STITEUR, C.W. Abrams Building, Room 740, Bremerstrasse, D-6000 Frankfurt, Federal Republic of Germany
Conn, R.W.	Nuclear Engineering Department, University of Wisconsin, 443 Engineering Research Building, 1500 Johnson Drive, Madison, WI 53706
Coppi, B.	Massachusetts Institute of Technology (26–201), Cambridge, MA 02139
Dandl, R.A.	Oak Ridge National Laboratory, P.O. Box Y, Oak Ridge, TN 37830
Dawson, J.M.	Department of Physics, University of California, Los Angeles, CA 90024

UNITED STATES OF AMERICA (cont.)

Decker, J.F.	US Department of Energy, Washington, DC 20545
Dobrott, D.	General Atomic Company, P.O. Box 81608, San Diego, CA 92138
Dory, R.A.	Oak Ridge National Laboratory, P.O. Box Y, Oak Ridge, TN 37830
Dreicer, H.	Los Alamos Scientific Laboratory, P.O. Box 1663, Los Alamos, NM 87545
Emmert, G.A.	Department of Nuclear Engineering, University of Wisconsin, Madison, WI 53706
Emmett, J.L.	Lawrence Livermore Laboratory, University of California, P.O. Box 808, Livermore, CA 94550
Fleischmann, H.H.	Department of Applied Physics, Cornell University, Ithaca, NY 14853
Fowler, T.K.	Lawrence Livermore Laboratory, University of California, P.O. Box 808, Livermore, CA 94550
Freeman, R.L.	General Atomic Company, P.O. Box 81608, San Diego, CA 92138
Freidberg, J.P.	Los Alamos Scientific Laboratory, P.O. Box 1663, Los Alamos, NM 87545
Frieman, E.A.	Plasma Physics Laboratory, Princeton University, James Forrestal Campus, P.O. Box 451, Princeton, NJ 08540

Furth, H.P.	Plasma Physics Laboratory, Princeton University, James Forrestal Campus, P.O. Box 451, Princeton, NJ 08540
Gilleland, J.R.	General Atomic Company, P.O. Box 81608, San Diego, CA 92138
Godlove, T.F.	Office of Laser Fusion – C404, US Department of Energy, Washington, DC 20545
Goldston, R.J.	Plasma Physics Laboratory, Princeton University, James Forrestal Campus, P.O. Box 451, Princeton, NJ 08540
Gondhalekar, A.	Massachusetts Institute of Technology, Cambridge, MA 02139
Gottlieb, M.B.	Plasma Physics Laboratory, Princeton University, James Forrestal Campus, P.O. Box 451, Princeton NJ 08540
Gross, R.A.	School of Engineering and Applied Sciences, Columbia University, 226 S.W. Mudd, New York, NY 10027
Guillory, J.U.	University of Maryland, College Park, MD 20742
Hamasaki, S.	Science Applications, Inc., 1200 Prospect St., La Jolla, CA 92037
Harris, J.H.	Department of Electrical and Computer Engineering, University of Wisconsin, 1425 Johnson Drive, Madison, WI 53706
Hasegawa, A.	Bell Laboratories, Murray Hill, NJ 07974

UNITED STATES OF AMERICA (cont.)

Horton, W.	Fusion Research Center and Physics Department, University of Texas, Austin, TX 78712
Huff, R.W.	Physics Department, University of California, Los Angeles, CA 90024
Huse, R.A. (see also under AIF)	Atomic Industrial Forum, 1747 Penn. Ave., Washington, DC 20000
Johnson, R.R.	KMS Fusion Inc., P.O. Box 1567, Ann Arbor, MI 48106
Kalman, G.J.	Department of Physics, Center for Energy Research, Boston College, Chestnut Hill, MA 02167
Kammash, T.	University of Michigan, P.O. Box 1567, Ann Arbor, MI 48106
Kane, J.H.	US Department of Energy, Washington, DC 20545
Kaw, P.K.	Plasma Physics Laboratory, Princeton University, James Forrestal Campus, P.O. Box 451, Princeton, NJ 08540
Killeen, J.	Lawrence Livermore Laboratory, University of California, P.O. Box 5509, Livermore, CA 94550
Kintner, E.E.	US Department of Energy, Washington, DC 20545
Klein, H.H.	Science Applications Inc., 1200 Prospect St., La Jolla, CA 92037

Kolb, C.A.	Maxwell Laboratories Inc., 8835 Balboa, San Diego, CA 92123
Koloc, P.M.	Prometheus II Ltd, P.O. Box 222, College Park, MD 20740
Krakowski, R.A.	Los Alamos Scientific Laboratory, P.O. Box 1663, Los Alamos, NM 87545
Krall, N.A.	Science Applications Inc., 1200 Prospect St., La Jolla, CA 92037
Kruer, W.L.	Lawrence Livermore Laboratory, University of California, P.O. Box 808, Livermore, CA 94550
Lee, Y.-C.	University of California, 405 Hilgard, Los Angeles, CA 90024
Linford, R.K.	Los Alamos Scientific Laboratory, P.O. Box 1663, Los Alamos, NM 87545
Liu, C. S.	University of Maryland, College Park, MD 20742
Logan, B.G.	Lawrence Livermore Laboratory, University of California, P.O. Box 808, Livermore, CA 94550
Mayer, F.J.	KMS Fusion Inc., 3941 Research Park Drive, Ann Arbor, MI 48106
McBride, J.B.	Science Applications Inc., 1200 Prospect St., La Jolla, CA 92037
McKenna, K.F.	Los Alamos Scientific Laboratory, P.O. Box 1663, Los Alamos, NM 87545
McNally, J.H.	Los Alamos Scientific Laboratory, P.O. Box 1663, Los Alamos, NM 87545

UNITED STATES OF AMERICA (cont.)

McNamara, B.	Lawrence Livermore Laboratory, University of California, P.O. Box 808, Livermore, CA 94550
Murakami, M.	Oak Ridge National Laboratory, P.O. Box Y, Oak Ridge, TN 37830
Navratil, G.A.	Columbia University, New York, NY 10027
Ohkawa, T.	General Atomic Company, P.O. Box 81608, San Diego, CA 92138
Overskei, D.	Massachusetts Institute of Technology, Cambridge, MA 02139
Papadopoulos, K.	Naval Research Laboratory, Washington, DC 20375
Parker, R.R.	Massachusetts Institute of Technology, Cambridge, MA 02139
Pearlstein, L.D.	Lawrence Livermore Laboratory, University of California, P.O. Box 808, Livermore, CA 94550
Perkins, R.B.	Los Alamos Scientific Laboratory, P.O. Box 1663, Los Alamos, NM 87545
Post, D.E., Jr.	Plasma Physics Laboratory, Princeton University, James Forrestal Campus, P.O. Box 451, Princeton, NJ 08540
Pyle, R.V.	Lawrence Berkeley Laboratory, University of California, Berkeley, CA 94720
Rasband, S.N.	Departments of Physics and Astronomy, Brigham Young University, Provo, UT 84057

Reardon, P.J.	Plasma Physics Laboratory, Princeton University, James Forrestal Campus, P.O. Box 451, Princeton, NJ 08540
Ribe, F.L.	Department of Nuclear Engineering, University of Washington, Seattle, WA 89115
Roberson, C.W.	Department of Physics, University of California, Irvine, CA 92717
Robson, A.E.	Naval Research Laboratory, Washington, DC 20375
Rose, R.P.	Fusion Power Systems Department, Westinghouse Electric Corporation, P.O. Box 10864, Pittsburgh, PA 15236
Rosenbluth, M.N.	Institute for Advanced Study, School of Natural Science, Princeton, NJ 08540
Ross, D.W.	Fusion Research Center, University of Texas, Austin, TX 78712
Rostoker, N.	Department of Physics, University of California, Irvine, CA 92717
Rutherford, P.H.	Plasma Physics Laboratory, Princeton University, James Forrestal Campus, P.O. Box 451, Princeton, NJ 08540
Sager, P.H., Jr.	General Atomic Company, P.O. Box 81608, San Diego, CA 92138
Sauthoff, N.	Plasma Physics Laboratory, Princeton University, James Forrestal Campus, P.O. Box 451, Princeton, NJ 08540

UNITED STATES OF AMERICA (cont.)

Scannell, E.P.	Reynolds Metals Co., Energy Conversion Division, P.O. Box 1200, Sheffield, AL 35660
Schwirzke, F.R.	Department of Physics, Naval Postgraduate School, Monterey, CA 93940
Segawa, D.K.	Hoya Optics USA Inc., Menlo Park, California
Shohet, J.L.	Department of Electrical and Computer Engineering, University of Wisconsin, Madison, WI 53706
Simonen, T.C.	Lawrence Livermore Laboratory, University of California, P.O. Box 808, Livermore, CA 94550
Smith, C.	University of Wisconsin, Madison, WI 53706
Stewart, L.	Exxon Nuclear Company, Plasma Physics Laboratory, Princeton University, James Forrestal Campus, P.O. Box 451, Princeton, NJ 08540
Stickley, C.M.	Office of Laser Fusion, US Department of Energy, Washington, DC 20545
Sudan, R.N.	Laboratory of Plasma Studies, Upson Hall, Cornell University, Ithaca, NY 14853
Surko, C.M.	Bell Laboratories, Room IC 352, Murray Hill, NJ 08836

Tang, W.M.
Plasma Physics Laboratory,
Princeton University,
James Forrestal Campus,
P.O. Box 451,
Princeton, NJ 08540

Tataronis, J.A.
Courant Institute of Mathematical Sciences,
New York University,
New York, NY 10012

Thorsos, E.
Laboratory for Laser Energetics,
University of Rochester,
Rochester, NY 14623

Turchi, P.J.
Naval Research Laboratory,
Washington, DC 20735

Uckan, Nermin A.
Oak Ridge National Laboratory,
Fusion Energy Division,
P.O. Box Y,
Oak Ridge, TN 37830

Uckan, T.
Oak Ridge National Laboratory,
Fusion Energy Division,
P.O. Box Y,
Oak Ridge, TN 37830

White, R.B.
Plasma Physics Laboratory,
Princeton University,
James Forrestal Campus,
P.O. Box 451,
Princeton, NJ 08540

Yonas, G.
Sandia Laboratories,
P.O. Box 5800,
Albuquerque, NM 87115

Yoshikawa, S.
Plasma Physics Laboratory,
Princeton University,
James Forrestal Campus,
P.O. Box 451,
Princeton, NJ 08540

VENEZUELA

Sanchez, A.
Departamento de Física,
Universidad Simon Bolivar,
Apartado 5354,
Caracas

YUGOSLAVIA

Miljanić, D.	Institut Rudjer Bošković, P.O. Box 1016, YU-41001 Zagreb
Vuković, S.	Institute of Physics, P.O. Box 57, YU-11001 Belgrade

ORGANIZATIONS

ATOMIC INDUSTRIAL FORUM (AIF)

Huse, R.A. (see also under USA)	Atomic Industrial Forum, 1747 Penn. Ave., Washington, DC 20000

COMMISSION OF THE EUROPEAN COMMUNITIES (CEC)

Brambilla, M.	Association Euratom/CEA, Centre d'études nucléaires de Grenoble, B.P. 85, F-38041 Grenoble, France
Finzi, V.	Commission des communautés européennes, rue de la Loi 200, B-1049 Brussels, Belgium
Gibson, A.	The JET Project, Culham Laboratory, Abingdon, Oxon., OX14 3DB, UK
Green, B.J.	The JET Project, Culham Laboratory, Abingdon, Oxon., OX14 3DB, UK
Maisonnier, C.J.	Commission des communautés européennes, rue de la Loi 200, B-1049 Brussels, Belgium
Palumbo, D.	Commission des communautés européennes, rue de la Loi 200, B-1049 Brussels, Belgium

Rager, J.-P.
(see also under Italy)
Laboratorio Gas Ionizzati,
Centro CNEN,
C.P. 65,
I-0044 Frascati (Rome), Italy

Rebut, P.H.
(see also under France)
The JET Project,
Culham Laboratory,
Abingdon, Oxon., OX14 3DB, UK

Sand, F.
Commission des communautés européennes,
rue de la Loi 200,
B-1049 Brussels, Belgium

INTERNATIONAL ATOMIC ENERGY AGENCY (IAEA)

Dee, J.B.
Division of Nuclear Power and Reactors, IAEA,
P.O. Box 590,
A-1011 Vienna

Seligman, H.
IAEA,
P.O. Box 590,
A-1011 Vienna

Twersky, Dorianna
Division of Scientific and Technical Information,
IAEA,
P.O. Box 590,
A-1011 Vienna

AUTHOR INDEX

Roman numerals are volume numbers.
Italic numerals refer to the first page of a paper by the author concerned.
Upright numerals denote comments and questions in discussions.

Aamodt, R.E.: II 481, *483*
Aase, D.T.: III *413*
Abdou, M.A.: III *357*
Adati, K.: II *401*
Adcock, S.J.: I *157*
Ainsworth, N.R.: I *745*
Aizawa, M.: II *609*
Akimune, H.: II *323*
Akulina, D.K.: II *287*
Alcock, M.W.: I *745*
Alexeff, I.: II 79; III 223
Amano, T.: I *269;* II *323*
Amiranoff, F.: III *75*
Anderson, D.V.: II *457*
Anderson, O.A.: III *369*
Andreev, N.E.: III *167, 187*
Andryukhina, Eh.D.: II *287,* 307
Anno, K.: I *377*
Aoki, T.: II *401*
Appelt, J.: III *225*
Arai, T.: I *377*
Aranchuk, L.E.: III *105*
Arimoto, H.: II *55*
Arkhangel'skij, Yu.I.: III *105*
Armstrong, C.M.: III *17*
Armstrong, W.T.: II *447*
Arsenin, V.V.: I *233*
Artemenkov, L.I.: I *233*
Arunasalam, V.: I *11, 167*
Arzhannikov, A.V.: II *623*
Ascoli-Bartoli, U.: I *149*
Atkinson, D.W.: II *251*
Avivi, P.: III 52, 154
Axon, K.B.: I *51*
Aydemir, A.: II *105*
Azechi, H.: III *135*
Azodi, H.: II *217*
Azumi, M.: I *377, 415*
Babykin, M.V.: III *105,* 122
Bagatin, M.: II *37*
Bagdasarov, A.A.: I *35*
Baity, F.W., Jr.: II *365*
Bajgarin, K.A.: III *105*
Bakaj, A.S.: III *285*
Baker, C.C.: III 132, *357,* 367, 368, 386
Baker, D.A.: II *3*
Baker, D.R.: I *157*
Baker, W.R.: III *369*
Baldwin, D.E.: II 410, *427,* 435, 443, *457*
Balmer, J.E.: III *157*
Bañuelos, A.: II *173*
Baranchikov, E.I.: III *105*
Baranowski, J.: III *225*
Barber, G.C.: III *369*
Bardet, R.: II *545*
Bardotti, G.: I *149*
Barnes, D.C.: II *345*
Barr, W.L.: III *369, 401*
Barth, C.J.: II *639*
Bartiromo, R.: I *149*
Bartov, A.V.: III *105*
Bartsch, R.R.: II *229*
Batchelor, D.B.: II *365;* III *343*
Bates, S.C.: I *269*

Battaglia, G.: I *149*
Baumgärtel, K.: III *187*
Baur, J.F.: I *157*
Baxter, G.A.: I *51*
Becker, G.: II 113, *115*, 122
Becraft, W.R.: III *369*
Bekiarian, A.: III *65*
Belikov, V.S.: I *561*
Benattar, R.: III *75*
Bender, D.J.: III *401*
Berezhetskij, M.S.: II *287*
Berezin, A.B.: II *205*
Berezovskij, E.L.: I *349*
Berger, D.P.: I *579*
Berger, R.L.: III *3*
Berk, H.L.: I 363, 687, 774, 786; II *81*, 247, 363
Berkner, K.H.: III *369*
Berlizov, A.B.: I *35*
Bernard, A.: II *159*
Bernard, L.C.: I *717*
Bernard, M.: II *545*, 556, 557
Betancourt, O.: II *355*
Bettis, E.S.: III *343*
Bielik, M.: III *225*
Birdsall, D.H.: III *369*
Bitter, M.: I *11*, *167*
Blanc, P.: I *97*
Blau, F.P.: I *157*
Blue, C.W.: III *369*
Blum, J.: I 470, *521*, 547
Bodin, H.A.B.: II *23*, 53, 227, 247, 363,467, 496
Bodner, S.E.: III *17*, 28, 63
Bol, K.: I *11*, 33, 64, *167*, 245, 386
Bonnedal, M.: II *535*
Bonnevier, B.: III *265*
Book, D.L.: II *93*
Boozer, A.H.: II *81*, *457*
Boris, J.P.: III *17*, 72
Bornatici, M.: I *507*
Bortnikov, A.V.: I *387*
Bostick, W.H.: II *143*
Boyd, D.: I *11*, *167*
Braams, C.M.: III *447*
Brackbill, J.U.: II *229*, *345*
Bradford, R.E.: I *745*
Bradley, J.E.: II *251*
Brambilla, M.: II *521*, 533, 581
Branum, D.R.: III *369*
Brau, K.: I *11*
Brejzman, B.N.: II *623*
Bretz, N.: I *11*, *167*
Brevnov, N.N.: I *387*
Briand, P.: I *65*
Bridwell, L.B.: I *297*
Briffod, G.: II *545*
Bristow, T.: III *29*
Brocken, H.J.B.M.: II *639*
Brogli, R.H.: III *413*
Brooks, J.: III *357*
Brooks, N.H.: I *157*
Brown, I.G.: II *81*
Bruhns, H.: II *135*
Brunelli, B.: I 823
Brusati, M.: I *149*
Bruzzone, H.: II *173*
Buchenauer, C.J.: II *3*
Buffa, A.: II *37*
Buratti, P.: I *149*
Burdakov, A.V.: II *623*
Buresi, E.: III *65*
Burgess, M.D.J.: III *421*
Burkhardt, L.C.: II *3*
Burmasov, A.S.: II *623*
Burnett, S.C.: III *413*
Burrell, C.F.: III *369*
Burrell, K.H.: I *269*; III *369*
Burt, J.: I *51*
Burton, R.L.: II *93*
Burtsev, V.A.: II *205*
Bush, C.E.: I *269*
Busnardo-Neto, J.: II *105*
Bussac, J.-P.: I *167*

Bussac, M.N.: III *249*
Buzankin, V.V.: I *287*
Byers, J.A.: II *457*
Byrne, R.N.: II *105*
Caarls, J.J.L.: II *639*
Caldas, I.L.: I *637*
Callen, J.D.: 267, *415*, 455, 456, 575, 623, 662, 761, 823; II 263, 264, 276
Callis, R.W.: I *157*
Campbell, P.M.: III *3*
Cannici, B.: II *265, 277*
Canobbio, E.: II *535*, 541, 542
Cantrell, E.L.: II *93*
Carlson, G.A.: III *401*
Carolan, P.G.: II *23*
Carpenter, K.H.: II *365*
Carreras, B.: I *415*
Castillo, R.: III *237*
Cattanei, G.: II *265, 277*
Catto, P.J.: I *415*
Cavallo, A.: II *265, 277*
Cayton, T.E.: II *345*
Cenacchi, G.: I *487*
Chan, C.F.: III *369*
Chan, V.S.: I *157*
Chance, M.S.: I *677*
Chang, C.T.: I *315*
Charatis, G.: III *3*
Charlton, L.A.: I *579*
Chen, H.H.: II *483;* III *181*
Chen, L.: I *763;* II *569*
Chen, Y.G.: II *105*
Cheng, C.Z.: I *763*
Cherkashin, M.Yu.: I *233*
Chernenko, A.S.: III *105*
Chernin, D.: II *483*
Chin-Fatt, C.: II *105*
Chirikov, B.V.: II *411*
Chodura, R.: II *335*
Choi, P.: II *69*
Chong, Y.P.: II *105*
Chu, C.K.: I 603; II *3, 105*, 122
Chu, M.S.: I *717*
Chudnovskij, A.N.: I *233*
Cima, G.: I *149*
Cissoko, G.: I *521*
Clark, R.G.: III *237*
Clark, W.H.M.: I *51*
Clauser, J.F.: II *385*
Clausing, R.E.: I *269*
Clément, M.: II *545*
Clemmer, R.: III *557*
Cobble, J.A.: II *365*
Coensgen, F.H.: II *389*
Cohen, B.I.: II *457*
Cohen, R.H.: II *427, 457*
Cohen, S.: I *11, 167*
Colchin, R.J.: I *269*
Colestock, P.: I *11, 167*
Collins, P.R.: I *745*
Commisso, R.J.: II *229*
Condit, W.C.: II *457*
Conn, R.W.: I 49; II 275; III 28, 275, 341, 367, 410
Connor, J.W.: I *667*
Conrads, H.: II 185; III 410, 443
Coonrod, J.: II *81*
Cooper, A.L.: II *93*
Cooper, W.S.: III *369*
Cooperstein, G.: III *17*
Coppi, B.: I 49, 145, 198, 363, 399, 470, *487*, 506, 591, 662, 715, 793; II 541
Cordey, J.G.: I *745*
Correll, D.L.: II *389*
Cortese, C.: II *143*
Coudeville, A.: III *65*
Crawford, E.A.: II *229*
Crume, E.C., Jr.: I *269*
Cummins, W.F.: II *389*
Dagazian, R.Y.: II *345*
Dagenhart, W.K.: III *369*
Dandl, R.A.: II *365*, 372; III *343*

Dangor, A.E.: II *69*
Danilkin, I.S.: II *287*
Dautray, R.: III *65*
Davidson, R.C.: II *483*
Davis, R.C.: III *369*
Davis, S.: I *11*, *167*
Dawson, J.M.: III *277*, 309
Daybelge, U.: I *549*, 559
De Angelis, A.: I *149*
De Angelis, R.: II *37*
Dearnaley, G.: I *297*
DeBoo, J.C.: I *269*
Decker, G.: II *135*, *666*
Decoste, R.: III *17*
DeGrassie, J.S.: I *157*
De Groot, B.: II *639*
Dei Cas, R.: I *521*
De Kluiver, H.: II 542, *639*, 661
Deleano, L.: II *365*
Delellis, R.: II *173*
Delettrez, J.: III *29*
Dellis, A.N.: II *251*
Delobeau, F.: III *65*
De Marco, F.: I *149*
De Mascureau, J.: II *159*
Demidov, B.A.: III *105*
Demirkhanov, R.A.: II *373*
Dennis, C.: III *357*
DeSilva, A.W.: II *105*
De Stigter, B.: II *639*
DeVore, K.R.: III *369*
Devoto, R.S.: III *401*
Dewar, R.L.: I *677*
Dexter, W.L.: III *401*
DiMarco, J.N.: II *3*
Dimock, D.: I *11*, *167*
D'Ippolito, D.: I *799*
Dnestrovskij, Yu.N.: I *35*, *287*, *443*
Dobrott, D.: I 591, 603, *717*, 732; II 661
Dodo, T.: I *365*
Doggett, J.N.: III *401*
Donaldson, T.P.: III *157*, 179
Donskaya, N.P.: II *303*
Dorst, D.: II *265*, *277*
Dory, R.A.: I *579*, 591
Downing, J.N.: II *3*
Downward, J.G.: III *3*
Drake, J.F.: I *799*
Drake, J.R.: III *265*
Drake, R.P.: II *389*
Dreicer, H.: II 372
Dreike, P.L.: II *497*
Drobot, A.: II *497*; III *17*
Dubois, M.: I *615*, 623, 663
Dûchs, D.F.: I *315*
Duffy, T.J.: III *369*
Dunlap, J.L.: I *269*
Dupas, L.: I *65*
Durvaux, M.: I *97*
D'yachenko, V.V.: I *113*
Dyer, G.R.: I *269*
Dylla, F.: I *11*, *167*
Eames, D.: I *11*
Eason, H.O.: II *365*
Edlington, T.: I *745*
Edmonds, P.H.: I *269*
Efthimion, P.: I *11*, *167*
Ehlers, K.W.: III *369*
Ehrhardt, J.: II *135*
Ehst, D.: III *357*
Ejima, S.: I *157*
Ekdahl, C.A.: II *229*
Elsner, A.: II *265*, *277*
Emerson, L.C.: I *269*
Emmert, G.A.: I 399, 484; III 443
Engelhardt, W.: I *123*, 133, 134, *401*
Engelmann, F.: I *507*, 519, 825
England, A.C.: I *269*
Enriques, L.: I *149*
Ensberg, E.S.: I *269*
Entenberg, A.: III *29*
Equipe TFR: I *135*
Esipchuk, Yu.V.: I *35*, *257*

Es'kov, A.G.: II *187*
Eubank, H.: I *11, 167*
Evans, K.: III *357*
Evans, R.G.: III *87*
Fabbro, R.: III *75*
Fabre, E.: III *75*, 85
Fanchenko, S.D.: III *105*
Fedyanin, O.I.: II *287*
Feinberg, B.: II *81*
Feneberg, W.: I *401*
Feugeas, J.: II *143*
Fielding, P.J.: I *625*
Fielding, S.J.: I *51, 303*
Filreis, J.: I *793*
Fink, J.F.: III *401*
Fisher, A.: II *509*
Fisher, R.K.: I *157*
Fleischmann, H.H.: II 363, 467, *497*, 508; III 320, 342
Fletcher, W.H.W.: I *745*
Folkierski, A.: II *69*
Fomel', B.M.: II *411*
Foote, J.H.: II *389, 427*
Ford, R.D.: II *93*
Foster, C.A.: I *269;* III *369*
Fowler, T.K.: II *457;* III *401*
Freeman, R.L.: I *157*, 165, 399, 824
Freese, K.B.: II *229*
Freidberg, J.P.: I 687, 732; II *229*, 263, 286, *345*, 363, 496
Freis, R.P.: II *457*
Friedman, A.: II *497*
Frieman, E.A.: I *677*, 686, 687, *763*
Fritts, M.J.: III *17*
Fujii, T.: I *85*
Fujisawa, N.: I *85*
Fujita, H.: III *135*
Fujita, J.: I *247;* III *135*
Fukagawa, T.: II *401, 609*
Fuller, G.M.: III *357*
Funahashi, A.: I *85, 377*
Fursa, A.D.: I *561*
Furth, H.P.: I 156, 455, 636, 732; II 307; III *249*, 264, 398
Fussmann, G.: I *123, 401*
Futch, A.H.: II *389*
Garabedian, P.: II *355*
Garban, C.: III *75*
Garçonnet, J.P.: II *159*
Gardner, J.H.: III *17*
Gardner, W.L.: III *369*
Gary, S.P.: II *229*, 495
Gasparotto, M.: I *149*
Gauthier, A.: II *545*
Gazit, Y.: III *29*
Gell, Y.: II *527*
Gentilini, A.: II *123*
Georgiou, G.: II *105*
Gerasimov, S.N.: I *387*
Gerber, K.A.: II *509*
Gernhardt, J.: I *401*
Gerwin, R.A.: II *93*
Gibson, A.: I 49, 363, 591, 732; III 332, 398
Gill, R.D.: I *51*
Gilleland, J.R.: I *157*
Girard, J.P.: I 33, 198, 256, 285, 363, 484; III 398, 443
Gladd, N.T.: II *81, 483*
Gladushchak, V.I.: I *349*
Glasser, A.H.: I *677*
Glock, E.: I *123, 401*
Glowienka, J.C.: II *365*
Godlove, T.F.: III *211*, 222, 223
Golant, V.E.: I *113*
Golden, J.: II *497*
Goldenbaum, G.C.: II *105, 509*
Goldfinger, R.C.: II *365*
Goldman, L.: III *29*
Goldsack, T.: III *87*
Goldstein, S.A.: III *17*
Goldston, R.J.: I *11*, 64, *167*, 198, 267, 285, 470, 471, 575
Golovato, S.N.: I *65*

Gomay, Y.: I *269*
Gondhalekar, A.: I *199*
Goodall, D.H.J.: I *51, 297*
Goodman, R.K.: II *389*
Gorbunov, E.P.: I *35*
Gordeev, A.V.: III *105*
Gormezano, C.: I *97*
Górski, E.: III *225*
Gottardi, N.: I *123*
Gourlan, C.: II *123*
Gowers, C.W.: II *23*
Grad, H.: II *345*
Graham, W.G.: III *369*
Granetz, R.: I *199*
Gratton, J.: II *173*
Gratton, R.: II *173*
Grebenshchikov, S.E.: II *287*
Grebogi, C.: III *181*
Green, B.: I 198, 546; II 557, 605; III 275, 398
Greene, J.M.: I *677*
Greenspan, M.: II *497*
Greenwald, M.: II *81*
Grégoire, M.: II *545*
Gregory, B.C.: II 410
Grelot, P.: I *65;* II *545*
Gribble, R.F.: II *229*
Grieger, G.: I 484; II *265, 277, 663*
Griem, H.R.: II *105*
Grimm, R.C.: I *471, 677*
Grisham, L.: I *167*
Grolli, M.: I *149*
Gross, R.A.: II *105,* 113
Grossman, M.: III *369*
Grossmann, W.: II *345, 569*
Grubb, D.P.: II *389*
Gruber, O.: II *115*
Gruber, R.: I *593*
Gryziński, M.: III *225*
Guest, G.E.: I *157*
Guillaneux, P.: III *65*
Guillory, J.U.: III 320
Gusev, V.K.: I *113*
Guss, W.C.: I *157*
Guzdar, P.N.: I *763*
Gvozdkov, Yu.V.: I *233*
Gwinn, D.: I *199*
Haas, F.A.: I *625*
Haas, G.: I *315*
Haberstich, A.: II *3*
Hacker, H.: II *265, 277*
Haegi, M.: I *149*
Hagenson, R.L.: III *333*
Hagiwara, S.: II *437*
Hall, L.S.: II *345, 427*
Hall, T.A.: III *87*
Hamada, S.: II *323*
Hamasaki, S.: II *93, 483*
Hamilton, G.W.: III *369, 401*
Hammer, D.A.: II *497, 509*
Hammer, J.: II *81*
Hanatani, K.: II *323*
Hancox, R.: III *323,* 331, 332
Harbour, P.J.: I 823, 824; III *431*
Hares, J.D.: III *87*
Harkness, S.: III *357*
Harrison, M.F.A.: III *431*
Harvey, R.W.: I *157*
Hasegawa, A.: II 541, 568, *569;* III 179, 309
Haselton, H.H.: III *369*
Hasselberg, G.: I *809, 815*
Haste, G.: II *545*
Haste, G.R.: II *365*
Hastie, R.J.: I *667*
Hatori, T.: II *401*
Hauer, A.: III *29*
Hawryluk, R.J.: I *11, 167, 471*
Hayase, K.: II *55*
Hazeltine, R.D.: I *787*
Heavy Ion Beam Group, ORNL: II *365*
Heckman, E.J.: I *157*
Hedrick, C.L.: II *365;* III *343*

Heinz, W.: III 28
Helton, F.J.: I *157, 717*
Henderson, T.M.: III *3*
Henins, I.: II *93*
Herold, H.: II *135*
Herring, J.S.: III *343*
Herrnegger, F.: II 344, *355*
Hess, R.A.: II *105*
Hess, W.: I *97*
Hesse, M.E.: II *365*
Hicks, H.R.: I *415*
Hidekuma, S.: II *401*
Hill, K.W.: I *11, 167, 269*
Hinnov, E.: I *11, 167*
Hinton, F.L.: I 787
Hirano, K.: II *55*
Hirano, Y.: II *55*
Hiratsuka, H.: I *377*
Hirayama, T.: I *85*
Hiroe, S.: II *365, 401*
Hirshman, S.P.: I *471*
Hobby, M.: I *51, 303*
Hoffman, A.L.: II *229*
Hogan, J.T.: I *579*
Hoida, H.W.: II *229*
Holmes, J.A.: I *415*
Holstein, P.A.: III 154
Holzhauer, E.: II *569*
Hooper, E.B., Jr.: III *369*
Hopkins, D.B.: III *369*
Hopman, H.J.: II 246, 518, 621; III 154, 443
Hora, H.: II 637; III 73, 179, 209, 222, 223 *237,* 245
Hordósy, G.: I *257*
Horodeński, A.: III *225*
Horton, W.: III 309
Hosea, J.: I *11,* 167
Hosogane, N.: II *649*
How, J.: II *265, 277*
Howe, H.C.: I *269*
Howell, R.B.: II *3*
Hrehuss, G.: I *257*
Hsieh, C.L.: I *157*
Hsieh, D.: I 471
Hsuan, H.: I *11, 167*
Huba, J.D.: II *483*
Hubbard, E.L.: I *157*
Hubbard, J.: II *509*
Hübner, K.: II *135*
Huff, R.W.: III *277*
Hughes, M.H.: I *303, 457*
Hugill, J.: I *51,* 64, *457,* 470
Hui, B.: II *93*
Hulse, R.A.: I *471*
Humphries, S., Jr.: II *497*
Hunt, A.L.: II *389*
Hutchinson, I.: I *199*
Ichimura, M.: II *401, 649*
Ichtchenko, G.: I *97*
Ido, S.: II *55*
Iioshi, A.: II *323*
Ikuta, K.: III *311*
Imai, T.: I *85*
Imasaki, K.: III *135*
Inoue, N.: II *649*
Inoue, S.: I 662, *777*
Ipatov, V.A.: I *349*
Ishii, K.: II *437*
Ishimura, T.: II *649*
Ishizuka, H.: II *437*
Isler, R.C.: I *269*
Itakura, A.: II *437*
Itoh, K.: I *777,* 786
Itoh, S.: I *247*
Ivanov, N.V.: I *233*
Ivanov, V.I.: I *113*
Iwahashi, A.: I *365*
Izawa, Y.: III *135*
Izvozchikov, A.B.: I *35, 287*
Jäckel, H.: II *265, 277*
Jackson, G.L.: I *157*
Jacobson, A.R.: II *3*
Jaeger, E.F.: II *365;* III *343*

Jaenicke, R.: II *265, 277,* 286
Jahns, G.L.: I *157*
Jahoda, F.C.: II *229*
Jakubowski, L.: III *225*
Janzen, G.: II *569*
Jarboe, T.R.: II *93*
Jardin, S.C.: I *677*
Jassby, D.L.: I *471*
Javel, P.: II *265, 277*
Jenkins, D.J.: II *93*
Jensen, R.V.: I *471*
Jensen, T.H.: I *157*
Jernigan, T.C.: I *269*
Jerzykiewicz, A.: III *225*
Jobes, F.: I *11*
Johnson, D.: I *11, 167*
Johnson, J.L.: I *677*
Johnson, P.C.: II *251*
Johnson, R.R.: III *3*
Jolas, A.: II *159*
Jones, E.M.: I *745*
Jones, I.R.: III 264
Jukes, J.D.: I *733*
Junker, J.: II *265, 277*
Kadomtsev, B.B.: I 197, *649,* 662, 663; III 386, 387
Kadota, K.: I *247*
Kaeppeler, H.J.: II *135*
Kahan, E.: II *69*
Kaiser, T.B.: II *427, 457*
Kakurin, A.M.: I *233*
Kalfsbeek, H.W.: II *639*
Kalinin, Yu.G.: III *105*
Kalmykov, S.G.: I *349*
Kamimura, T.: III *277*
Kane, E.L.: III *237*
Kaneko, H.: I *365*
Kapetanakos, C.A.: II *497*
Kardon, B.: I *257*
Karger, F.: I *123, 401*
Karr, H.J.: II *3*
Kasai, S.: I *85, 377*
Kato, Y.: III *135*
Kaufmann, M.: II *335*
Kaw, P.K.: I 121, 455, *763;* III 63
Kawabe, T.: II 399, 435, *437,* 637, 661, *669*
Kawada, Y.: I *365*
Kawahata, K.: I *247*
Kawakami, I.: II *55*
Kawakami, K.: I *85*
Kawakami, T.: I *377*
Kawamoto, T.: II *401*
Kawamura, Y.: III *135*
Kawasumi, Y.: I *247*
Kearney, D.W.: III *413*
Keilhacker, M.: I *315,* 330
Kelly, H.: II *173*
Kerner, W.: I *593*
Kesner, J.: II *427*
Ketterer, H.E.: I *269*
Key, M.H.: III *87*
Khimchenko, L.N.: I *387*
Khol'nov, Yu.V.: II *287*
Khudoleev, A.V.: I *349*
Kick, M.: II *265, 277*
Kies, W.: II *135*
Kikuchi, M.: II *649*
Kilkenny, J.D.: III *87*
Killeen, J.: I *471*
Kim, J.: III *369*
Kimura, H.: I *377*
King, P.W.: I *269*
Kinoshita, S.: II *323*
Kintner, E.E.: I *3*
Kirchesch, P.: II *135*
Kirov, A.G.: II *373*
Kishinevskij, M.E.: II *411*
Kislov, A.Ya.: I *35*
Kita, Y.: II *55*
Kitagawa, S.: II *55*
Klüber, O.: I *123*
Koba, Yu.V.: III *105*
Kojdan, V.S.: II *623*

Kolbasov, B.N.: III *379*
Kolesnichenko, Ya.I.: I *561*, 575
Kondo, K.: II *323*
Konoshima, S.: I *85*
Konyukhov, V.V.: II *623*
Kornev, B.I.: II *287*
Kornilov, V.A.: II *623*
Korolev, V.D.: III *105*
Kosarev, P.M.: II *469*
Kostomarov, D.P.: I *443*
Kovrov, P.E.: I *257*
Krakowski, R.A.: III 276, *333*, 341, 342, 368, 386, 410
Krall, N.A.: II *93*, *365*, *483*, 495, 496
Krause, H.: II *115*
Kreshchuk, A.P.: II *187*
Kribel, R.E.: II *497*
Kroegler, H.: II *123*
Kruer, W.: III 85
Kruglyakov, Eh.P.: II *623*
Kubasov, V.A.: II *205*
Kubota, Y.: III *311*
Kumagai, K.: I *85*, *377*
Kumazawa, R.: II *401*
Kunkel, W.B.: II *81*; III *369*
Kurbatov, D.K.: III *379*
Kuroda, T.: I *247*, *365*
Kurtmullaev, R.Kh.: II *187*
Kurzyna, J.: III *225*
Kusse, B.: I *199*
Kustom, R.: III *357*
Kuthy, A.: III *265*
Kuznetsov, N.V.: I *387*
Kuzushima, T.: I *365*
Lackner, K.: I *315*, 559, *593*, 715
Lädrach, P.: III *157*
Lallia, P.: I *97*
Lam, C.: III *369*
Langley, R.A.: I *269*
Langner, J.: III *225*
Lappa, D.: III *401*
Larionov, M.M.: I *113*
Larrabee, D.A.: II *497*
Larson, R.: III *369*
Lashkul, S.I.: I *349*
Laukhin, Ya.N.: II *187*
Lawrence, V.F.: III *237*
Lazar, N.H.: II *365*
Lazarus, E.: III *29*
Lebedev, A.D.: I *113*
Lebedev, S.V.: I *349*
Le Breton, J.P.: II *159*
Lee, C.: III *29*
Lee, D.K.: I *415*
Lee, J.D.: III *401*
Lee, R.: III *17*
Lee, W.W.: I *763*
Lee, Y.-C.: I 775, 792, *799*; II *483*
Lees, D.J.: II *251*, 263, 264
Legardeur, R.: I *65*
Lehmberg, R.H.: III *17*
Lehnert, B.: I 134, 636, 826; III *265*, 275, 276, 410
Lengyel, L.L.: I *315*; II 621
Leonard, B.R., Jr.: III *413*
Leonard, T.A.: III *3*
Leonov, V.M.: I *211*
Letzring, S.: III *29*
Leuterer, F.: II *265*, *277*
Levin, L.S.: I *113*
Levine, M.A.: II *81*
Lewis, C.L.S.: III *87*
Lewis, H.R.: II *229*
Lidsky, L.M.: III *343*
Lietzke, A.F.: I *157*
Liewer, P.C.: I *799*; II *3*, *93*, *105*
Likhtenshtejn, V.Kh.: II *469*
Lin, A.T.: I *799*
Lin, D.N.: III *105*
Linford, R.K.: II *447*
Lipin, B.M.: I *349*
Lipiński, B.: III *225*
Lisitano, G.: I *123*, 519, 613, 614, 623; II 533, 542

Little, E.M.: II *3*
Litunovskij, V.N.: II *205*
Liu, C.S.: I *799;* II *483;* III *181,* 209
Logan, B.G.: II *427,* 443, 637, *669;* III 356, *401,* 410, 411, 419
Lohr, J.: I *157, 211*
Lomas, P.J.: II *251*
Lominadze, Dzh.G.: II 481
Longinov, A.V.: II *583*
Loring, C.M.: III *369*
Lortz, D.: II *309*
Lotz, W.: II *335*
Lovelace, R.V.: II *497*
Lowenthal, D.D.: II *229*
Lozovskij, S.N.: II *373*
Lubin, M.: III *29*
Luckhardt, S.C.: II *497*
Lui, H.C.: II *105*
Lukash, V.E.: III *379*
Luk'yanov, S.Yu.: I *35*
Luk'yanov, V.N.: II *623*
Lunney, J.G.: III *87*
Luxon, J.L.: I *157*
Lynch, S.J.: I *415*
Lyon, J.F.: I *269*
Lysenko, S.E.: I *35, 443*
Lysyanskij, P.B.: II *411*
Lyublin, B.V.: II *205*
Maaswinkel, A.G.M.: III 85
Machalek, M.D.: II *3*
Maeda, H.: I *377,* 399
Maejima, Y.: II *55*
Maeno, M.: I *85*
Magne, R.: I *97*
Mahaffey, R.A.: II *497*
Mahajan, S.M.: I *787*
Mahdavi, M.A.: I *157*
Mahn, C.: II *265, 277*
Maisonnier, C.: II *123,* 185
Makishima, K.: I *365*
Maksimov, Yu.S.: I *35, 387*
Malesani, G.: II *37*
Malone, R.C.: II *93*
Malyutin, A.I.: II *187*
Manickam, J.: I *677*
Mankofsky, A.: II *497*
Mansfield, M.W.D.: I *303*
Marconero, R.: I *149*
Marcus, F.B.: I *157*
Mark, J.W.-K.: I *793*
Markin, A.I.: II *187*
Marlier, S.: II *265, 277*
Marmar, E.: I *199*
Maroni, V.: III *357*
Marsen, J.: II *105*
Marsh, S.J.: II *497*
Marshall, J.: II *93*
Marshall, T.C.: II *105*
Martin, G.: I *167*
Martone, M.: I *149*
Martyushov, Yu.S.: II *187*
Mascheroni, L.: II *93*
Massoletti, D.J.: III *369*
Mast, F.: II *115*
Masuzaki, M.: III *311*
Matoba, M.: III *135*
Matsuoka, K.: I *247*
Matsushita, H.: I *365*
Matsuura, K.: I *247,* 256
Mayer, F.J.: III *3*
Mayer, H.M.: I *123*
Maysenhölder, W.: II *135*
Mazzitelli, G.: I *149*
Mazzucato, E.: I *11, 149*
McAlees, D.G.: III *343*
McBride, J.B.: II *365, 483*
McCormick, N.J.: III *413*
McCoy, M.G.: I *471*
McCracken, G.M.: I *51, 297*
McCrory, R.: III *29*
McGuire, K.: I *335*
McKenna, K.F.: II *229,* 247
McKenney, A.: I *471*
McKenzie-Wilson, R.: III *369*

McLean, E.A.: III *17*
McNeill, D.H.: I *269*
Meade, D.M.: I *471*
Mechler, G.: II *135*
Medley, S.: I *11, 167*
Meisel, D.: I *123*
Mekler, K.I.: II *623*
Melin, G.: I *65;* II *389*
Melzacki, K.: III *225*
Menon, M.M.: III *369*
Mercier, C.: I *521, 701,* 715
Merezhkin, V.G.: I *211*
Merlino, R.L.: II *105*
Meservey, E.: I *11, 167*
Mihalczo, J.T.: I *269*
Mikhajlov, E.A.: I *287*
Mikkelsen, D.R.: I *471*
Milanese, M.: II *173*
Millar, W.: II *251*
Miller, G.: II *229*
Miller, R.D.C.: III *237*
Miller, R.L.: I *157;* III *333*
Milnes, K.A.: III *369*
Milora, S.L.: I *269;* III *369*
Mima, K.: III *135*
Mirin, A.A.: I *471;* III *401*
Mirnov, S.V.: I *433*
Mironov, B.N.: II *187*
Mitrovich, D.: III *3*
Miyahara, A.: I *247*
Miyamoto, K.: I *247*
Miyamoto, S.: III *135*
Miyoshi, S.: II *437,* 443
Mizhiritskij, V.I.: III *105*
Mizumoto, Y.: III *135*
Mizuuchi, T.: II *323*
Mochizuki, T.: III *135*
Moeller, C.P.: I *157*
Moffa, P.J.: III *17*
Mohri, A.: III *311,* 320
Moir, R.W.: III *369, 401*
Molotkov, L.I.: I *233*
Molvik, A.W.: II *389*
Moncur, N.K.: III *3*
Monticello, D.A.: I *605*
Montry, G.R.: III *3*
Moore, A.: III *87*
Moore, R.W.: I *717*
Moreau, D.: II *559,* 568
Morera, J.P.: I *521*
Morimoto, S.: II *323*
Moser, F.: II *569*
Moses, R.W.: II *93*; III *333*
Mosher, D.: III *17*
Mostrom, M.A.: II *81*
Motojima, O.: II *323*
Motz, H.: III 179, *421,* 443
Mucha, Z.: II *105*
Mukaiyama, T.: III *29*
Mukhovatov, V.S.: I *211,* 245
Müller, G.: II *265, 277, 569*
Mulser, P.: III 209, 245
Munro, J.K.: I *579*
Murakami, M.: I *269,* 284, 285, 330
Murdoch, J.: III *87*
Murmann, H.: I *123*
Murphy, D.P.: II *105*
Musinski, D.L.: III *3*
Mutoh, T.: II *323*
Myers, B.R.: II *81*
Nagami, M.: I *377*
Nagashima, A.: I *85, 377*
Nagashima, T.: I *85*
Nagata, A.: II *55*
Nagayama, Y.: I *365*
Nahrath, B.: II *135*
Naitou, H.: III *277*
Nakach, R.: II *527*
Nakai, S.: III *135*
Nakamura, K.: I *365*
Nakasuga, M.: II *323*
Namkung, W.: I *269*
Naraghi, M.: II *217,* 227
Nardi, V.: II *143,* 185; III 121, 122

Narihara, K.: III *311*
Navarro, A.P.: I *269*
Navratil, G.A.: II *105*
Nawrocki, Z.: III *225*
Nedoseev, S.L.: III *105*
Nedospasov, A.V.: III *379*
Neef, W.D., Jr.: III *401*
Nefedkina, L.B.: III *379*
Neidigh, R.V.: I *269*
Neilson, G.H.: I *269*
Nelson, D.B.: I *579;* III *343*
Nevins, W.M.: I *763*
Nexsen, W.E.: II *389*
Ng, A.: III *53*
Ng, P.H.: II *483*
Nguyen, T.K.: I *97*
Nicholas, D.J.: III *87*
Nicholson, B.: III *29*
Nicholson, D.R.: II *483*
Nicholson-Florence, M.F.: III *237*
Niland, R.A.: II *81*
Nishihara, K.: III *135*
Nishikawa, K.: I *777*
Nishimura, H.: III *135*
Nocentini, A.: I *507*
Noda, N.: I *247*
Nolen, R.L.: III *3*
Norimatsu, T.: III *135*
Notkin, G.E.: I *35*
Novak, M.M.: III *237*
Nowikowski, J.: III *225*
Nührenberg, J.: II *309,* 320
Nyushkov, A.V.: II *373*
Obayashi, H.: II *401*
Oberman, C.R.: I *763*
Obiki, T.: II *323*
Ochiai, I.: I *365*
Odajima, K.: I *377*
Offenberger, A.A.: III *53,* 63, 64
Ogawa, K.: II *55*
Ogawa, Y.: II *649*
Ogden, J.M.: I *471*
Ohasa, K.: I *377*
Ohi, S.: II *649*
Ohkawa, T.: I *157,* 663
Ohkubo, K.: I *247*
Ohlendorf, W.: II *265, 277*
Ohlsson, D.: III *265*
Ohtake, I.: II *323*
Ohtsuka, H.: I *377*
Oka, Y.: I *365*
Okabayashi, M.: I *471, 677;* III *249*
Okada, O.: I *365*
Okada, S.: II *401, 609*
Okamura, S.: II *401*
Okuda, H.: I *763*
Okuda, T.: I *365*
Oliphant, W.F.: III *17*
O'Neill, F.: III *87*
Oppenländer, T.: II *135, 666*
Orens, J.H.: III *17*
Orlov, M.M.: II *187*
Orlov, V.V.: III *379*
Ornstein, L.Th.M.: I 156, 825
Ortolani, S.: II *37*
Orzechowski, T.J.: III *369*
Ottinger, P.: III *17*
Overskei, D.: I 144, *199,* 455, 456
Owen, L.W.: II *365;* III *343*
Owren, H.M.: III *369*
Ozaki, A.: II *649*
Pacher, G.W.: I *97*
Pacher, H.D.: I *97*
Palumbo, D.: III 386
Panov, D.A.: II *469*
Pant, A.: III 331, 332
Papadopoulos, K.: I 165; III 64, 154
Pappas, D.: I *199*
Paré, V.K.: I *269*
Park, W.: II *3*
Parker, R.R.: I *199,* 209, 266
Parlange, F.: II *545*
Pasechnikov, A.M.: III *105*
Pasour, J.A.: II *497*

Pataraya, A.: II 533, 581
Paterson, J.A.: III *369*
Patou, C.: III *65*
Paul, J.W.M.: I *51*
Pautov, V.L.: I *349*
Payne, M.F.: I *745*
Peacock, N.J.: I *303*
Pearlstein, L.D.: II *427, 457,* 467
Pease, R.S.: I 134, 209, 575; II 185; III 368
Pegoraro, F.: I *507*
Peng, Y.-K.M.: I *579*
Pen'kina, V.S.: III *105*
Pereverzev, G.V.: I *35, 287, 443*
Pergament, V.I.: I *387*
Perkins, R.B.: III *41,* 52
Perry, B.: III *29*
Perry, R.T.: III *413*
Peter, W.: II *509*
Peterson, M.A.: III *401*
Petrasso, R.: I *199*
Petrov, V.G.: III *379*
Petsch, R.: III 179
Pfeiffer, W.W.: I *157*
Pickrell, M.: I *199*
Piekaar, H.W.: II *639*
Pieroni, L.: I *149*
Pietrzyk, Z.A.: II *229*
Pinet, D.: II *545*
Pistunovich, V.I.: III *379*
Pitt, L.: III *53*
Pittenger, L.C.: III *369*
Platts, D.A.: II *447*
Podyminogin, A.A.: II *623*
Pogutse, O.P.: I *649*
Ponte, S.: III *369*
Popovics, C.: III *75*
Poquerusse, A.: III *75*
Porrote, E.: II *545*
Post, D.E.: I 144, 284, *471,* 484, 485
Post, R.F.: II *457*
Potok, R.E.: III *343*
Potter, D.E.: II *69,* 79
Poulsen, P.: III *369*
Pouzo, J.: II *173*
Powell, B.A.: I *51*
Powers, L.V.: III *3*
Prater, R.: I *269*
Prelec, K.: III *369*
Prentice, R.: I *51*
Prior, W.: II *143*
Pritchett, P.L.: I *799*
Proshletsov, A.P.: II *187*
Pross, G.: II *135*
Pyle, R.V.: III *369*
Quimby, D.C.: II *229*
Quon, B.H.: II *365*
Rabinovich, M.S.: I 33, 64; II *303,* 307
Rager, J.P.: II *123, 666*
Rau, F.: II *265, 277*
Räuchle, E.: II *569*
Raven, A.: III *87*
Ravestein, A.: II *639*
Razdobarin, G.T.: I *113*
Ray, P.S.: III *237*
Razumova, K.A.: I *35,* 49, *257,* 266, 267
Reid, G.W.: I *51*
Reisse, J.M.: III *65*
Rej, D.J.: II *497*
Renaud, C.: I 144, 145, 198, 267, 455
Renner, H.: II *265,* 275, 276, *277*
Rensink, M.E.: I *471;* II *457;* III *401*
Rewoldt, G.: I *763*
Rey, G.: II *545*
Ribe, F.L.: II 363, 372; III 387, *413,* 419
Rice, J.: I *199*
Righetti, G.B.: I *149*
Ringler, H.: II *265, 277*
Riordan, J.C.: I *157*
Ripin, B.H.: III *17*
Rivière, A.C.: I *745*

Rizzo, J.: III *29*
Roberson, C.W.: II *509*, 518, 580
Roberts, K.V.: I 674; II 605; III 264
Roberts, M.: III *389*
Robertson, S.: II *509*
Robinson, D.C.: I *335*, 363; II *23*
Robouch, B.V.: II *123*
Robson, A.E.: II *93*, *509*
Rodríguez Trelles, F.: II *173*
Rogister, A.: I *809*, *815*, 821
Rognlien, T.D.: II *427*
Rogozin, A.I.: II *623*
Rose, R.P.: III 332, *413*, 419
Rosenbluth, M.N.: I *605*, 732, 762, 786; II *483*; III *249*
Ross, D.W.: I *787*, 792
Ross, I.N.: III *87*
Rossow, T.L.: III *369*
Rostoker, N.: II *509*
Rozhdestvenskij, V.V.: I *349*
Ruby, L.: III *369*
Ruchko, L.F.: II *373*
Rückle, B.: II *135*
Rudakov, L.I.: III *105*
Rumsby, P.T.: III *87*
Rutgers, W.R.: II *639*
Rutherford, P.H.: I *471*, *763*
Ryan, P.M.: III *369*
Ryutov, D.D.: I 715; II 399, *411*, 426, 435, *623*, 637, *669*; III 133
Sadowski, M.: III *225*
Saenz, G.: II *509*
Saffert, J.: II *265*, *277*
Sager, P.F., Jr.: III *389*, 398
Saito, H.: II *401*, *609*
Sakuma, K.: I *365*
Sakurai, K.: *247*, *365*
Saltmarsh, M.J.: I *269*
Salzmann, D.: III *53*
Samain, A.: I *615*
Samuelli, M.: I *149*
Sandel, F.: III *17*
Sanderson, A.D.: III *431*
Sandia Laboratories Particle Beam Fusion Group: III *125*
Sannikov, V.V.: I *211*
Santoro, R.T.: III *343*
Sapper, J.: II *265*, *277*
Sasaki, A.: II *323*
Sasaki, T.: III *135*
Sato, K.: I *247*; II *55*
Sato, K.N.: II 247, *401*, 609, 621
Sato, M.: I *247*, *323*
Sato, T.: II *401*, 410
Sauer, K.: III *187*
Sauerbrunn, A.: II *135*
Sauthoff, N.: I *11*, 133, *167*, 245, 505; II 286
Sawyer, G.A.: II *93*
Sbitnikova, I.S.: II *287*
Scaturro, L.: I *199*
Schaffer, M.J.: I *269*
Schechter, D.E.: III *369*
Schep, T.: I *507*
Schilling, G.: I *167*
Schilling, P.: II *135*
Schivell, J.: I *167*
Schlüter, A.: II *335*, 344
Schmidt, G.: I *11*, *167*
Schmidt, H.: II *135*
Schmidt, J.A.: I *471*
Schmitter, K.H.: III 331, 387
Schneider, E.: II *569*
Schneider, W.: II *345*
Schofield, A.E.: II *3*
Schreiber, R.: I *593*
Schüller, P.G.: II *569*
Schultz, K.R.: III *413*
Schuss, J.: I *199*
Schwenterly, S.W.: III *369*
Schwirzke, F.R.: I 663; II 426, 443, 621; III 367
Segall, S.B.: III *3*

Segre, S.E.: I *149*, 156
Seidl, F.G.P.: I *471*
Sekiguchi, T.: II *401*, *609*
Selden, A.C.: II *251*
Semenov, V.N.: II *187*
Sengoku, S.: I *377*
Serebrenyj, G.A.: I *113*
Sesnic, S.: I *123*, *401*
Sessler, A.: II *81*
Sethian, J.D.: II *509*
Sgro, A.G.: II *3*, *105*, *229*
Shakhatre, M.: II *135*
Shakhovets, K.G.: I *349*
Shanny, R.: II *93*
Sharp, L.E.: II *251*
Sharp, W.: II *81*
Shatalov, G.E.: III *379*
Shatford, P.A.: II *251*
Shaw, R.: II *81*
Shcheglov, D.A.: I *35*
Shchemelinin, S.G.: I *349*
Shcherbakov, A.G.: II *469*
Shcherbinin, O.N.: I *113*
Shea, J.H.: I *297*
Shepanski, J.R.: III *237*
Sherwood, A.R.: II *93*
Sherwood, E.G.: II *447*
Shibata, T.: I *377*
Shikanov, A.S.: III *167*
Shimada, M.: I *85*
Shimada, T.: II *55*
Shimomura, Y.: I *377*
Shinohara, S.: I *365*
Shirakata, H.: I *85*
Shohet, J.L.: II 307, 334, 556, *564*, 580, 581
Shoji, T.: I *85*, *377*
Shpigel', I.S.: II *287*
Shprits, I.D.: I *349*
Shukla, P.K.: III *201*
Shulte, S.C.: III *413*
Shul'zhenko, G.I.: II *411*
Shumaker, D.E.: I *471*
Shvindt, N.N.: I *233*
Sidorov, V.P.: II *373*
Siebert, L.D.: III *3*
Siemon, R.E.: II *229*
Sigel, R.: III *75*
Sigmar, D.J.: I *579*
Simms, R.J.: III *3*
Simonen, T.C.: II *389*, 399, 443
Simpkins, J.E.: I *269*
Singh, C.M.: I *65*
Sitt, B.: III *65*
Składnik-Sadowska, E.: III *225*
Skoryupin, V.A.: III *105*
Skovoroda, A.A.: II *469*
Skupsky, S.: III *29*
Slade, P.D.: II *69*
Slater, D.C.: III *3*
Slusher, R.E.: I *199*
Sluyters, Th.: III *369*
Smeulders, P.: II *265*, *277*
Smirnov, A.G.: II *205*
Smirnov, V.G.: II *205*
Smirnov, V.P.: III *105*
Smith, D.: III *357*
Smith, G.R.: II *457*
Smith, J.: I *415*
Smith, M.E.: III *369*
Smith, R.R.: III *369*
Sofield, C.J.: I *297*
Söldner, F.: I *97*
Soler, M.: I *415*
Solomon, D.E.: III *3*
Soroka, L.: II *81*
Sosunov, Yu.B.: II *187*
Soures, J.: III *29*
Spalding, I.J.: III *421*
Spatschek, K.H.: III *201*
Spector, D.N.: II *509*
Spong, D.A.: II *365*; III *343*
Stallard, B.W.: II *389*
Stamper, J.A.: III *17*

Stanisławski, J.: III *225*
Start, D.F.H.: I *745*
Stauffer, F.: I *11, 167*
Stearns, J.W.: III *369*
Steed, C.A.: I *745*
Steel, D.: III *29*
Steele, W.F.: III *369*
Steinmetz, K.: II *135*
Stenz, C.: III *75*
Sternleib, A.: III *17*
Stepanov, K.N.: II 386, *583,* 605
Stephanakis, S.J.: III *17*
Stewart, L.: I *167*
Stevens, D.C.: II *345*
Stevens, H.: III *357*
Stirling, W.L.: III *369*
Stodiek, W.: I *11, 167*
Stooksberry, R.: I *167*
Stott, P.E.: I *51;* III *431,* 443
Strachan, J.: I *11, 167*
Strangio, C.: I *149*
Strauss, H.R.: *787*
Strelkov, V.S.: I *35*
Strickler, D.J.: I *579*
Stupakov, G.V.: II *411*
Suckewer, S.: I *11, 167, 471*
Sudan, R.N.: II 79, *497;* III 133
Sudlitz, K.: III *225*
Sudo, S.: II *401*
Sugie, T.: I *85, 377*
Sugisaki, K.: II *55*
Sukachov, A.V.: II *373*
Sulton, A.L., Jr.: II *365*
Summers, D.D.R.: I *51*
Summers, H. P.: I *303*
Sunaoshi, H.: I *377*
Surko, C.M.: I *199,* 675; II 263, 533
Sutter, D.F.: III *211*
Suydam, B.R.: II *93*
Suzuki, N.: I *85*
Suzuki, U.: I *365*
Swain, D.W.: I *269*
Swannack, C.E.: II *93*
Sweetman, D.R.: I *745,* 761, 762; II 426, 467, 508
Sykes, A.: I 591, *593, 625,* 636, 686, 731; III 309
Szentpétery, I.: I *257*
Tachon, J.: I *411*
Tahsiri, H.: II *217*
Tait, G.: I *11, 167*
Takabe, H.: III *135*
Takahashi, H.: I *167*
Takahashi, K.: I *85, 377*
Takamura, S.: I *365*
Takayama, K.: II *401*
Takeuchi, H.: I *85, 377*
Talmadge, J.N.: II *569*
Tamano, T.: I *157*
Tamaru, T.: II *55*
Tanahasi, S.: I *247*
Tanaka, Y.: I *85, 365*
Tang, W.M.: I *763,* 774, 775, 821
Tange, T.: I *777*
Taquet, B.: II *545*
Tarasyan, K.N.: I *443*
Taroni, A.: I *487*
Tarter, C.B.: I *471*
Tarumov, E.Z.: III *105*
Tasso, H.: I *637*
Tataronis, J.A.: I *717;* II *569*
Taylor, J.B.: I 603, *667,* 675, 715; II 495
Tenney, F.: I *471*
Tennfors, E.: III *265*
Teofilo, V.L.: III *413*
Terashima, Y.: I *247*
Thomas, C.E.: III *3*
Thomas, K.S.: II *3*
Thomas, P.R.: II *251*
Thompson, P.C.: III 52
Thomson, J.J.: III *135*
Thorsos, E.: III *29*
Tikhonchuk, V.T.: III *167*

Tilinin, G.N.: I *211*
Timmers, T.: I *507*
Todd, A.M.M.: I *677;* III *249*
Todd, T.N.: I *745*
Toi, K.: I *247*
Tokor, M.Z.: III *379*
Tokunov, A.I.: I *113*
Tolliver, J.S.: II *365*
Tomita, Y.: III *311*
Toner, W.T.: III *87*
Tonon, G.: I *97*
Tooker, J.F.: I *157*
Torabi-Fard, A.: II *217*
Toyama, H.: I *365*
Tripathi, V.K.: III *181*
Troyon, F.: I *593,* 603
Trunk, M.: II *135*
Tsai, C.C.: III *369*
Tsang, K.T.: I *415*
Tshakaya, D.D.: III 209
Tsivinsky, A.I.: III *237*
Tsuji, S.: I *365*
Tsuji, Y.: I *365*
Tsurikov, V.A.: II *583*
Tsuzuki, T.: III *311*
Tuccillo, A.: I *149*
Turchi, P.J.: II *93;* III 264
Turkel, E.: II *345*
Turner, J.: I *297*
Turner, L.: II *229*; III *357*
Turner, M.F.: I *625*
Turner, W.C.: I *297*; II *389*
Tuszewski, M.: II *497*
Tutter, M.: II *265, 277*
Tzach, D.: II *509*
Uchida, T.: II *649*
Uckan, N.A.: I 330; III *343,* 356
Uckan, T.: II *365*; III *343*
Uehara, K.: I *85*
Uesugi, Y.: I *365*
Ulrickson, M.: I *11, 167*
Uo, K.: II 307, *323,* 334
UV Spectroscopy Group, ORNL: II *365*
Van Andel, H.W.H.: II *639*
Van Dam, J.W.: I *799*
Vandenplas, P.E.: I 675; II 557
Van der Laan, P.C.T.: II *3*
Van der Ven, H.W.: II *639*
Varljen, T.C.: III *413*
Vasil'ev, N.N.: III *379*
Vasin, N.L.: I *35*
Vaslow, D.F.: I *157*
Vedel, J.M.: III *65*
Vella, M.: II *81*
Vershkov, V.A.: I *287*
Vertiporokh, A.N.: I *35*
Vil'dzhyunas, M.I.: I *349*
Vinogradov, V.P.: I *35*
Vinogradova, N.D.: I *257*
Virmont, J.: III *75*
Vlasenkov, V.S.: I *211*
Vlases, G.C.: II *229;* III *413*
Vollmer, O.: II *265, 277*
Von Goeler, S.: I *11, 167*
Voronov, G.S.: II *287, 303*
Vyacheslavov, L.N.: II *623*
Waddell, B.V.: I *415*
Waelbroeck, F.G.: I 761
Wägli, P.: III *157*
Wagner, F.: I *123*
Wakatani, M.: II *55, 323*
Walker, A.C.: III *421*
Walters, C.R.: III *323*
Wang, T.S.: I *157*
Ward, J.M.: III *87*
Watanabe, T.: II *401*
Watari, T.: II *401*
Watson-Munro, C.N.: II 580
Watteau, J.P.: III *65,* 72, 73
Watts, H.L.: III *343*
Watts, M.R.C.: II *23*
Webb, S.J.: II *69*
Weber, P.G.: II *105*

Wegrowe, J.G.: I *97*
Weinfeld, M.: III *75*
Weisse, J.: II *545*
Weitzner, H.: I *717*
Weller, A.: II *265, 277*
Werkoff, F.: I *521*
Wesley, J.C.: I *157*
Wesson, J.A.: I *593*
West, J.: I *199*
Weynants, R.R.: II 605
Whealton, J.H.: III *369*
White, M.S.: III *87*
White, R.B.: I *605,* 613, 614, *763*
White, T.L.: II *365*
Whitson, J.C.: I *415*
Wilgen, J.B.: I *269*
Wilhelm, R.: II *115*
Williams, P.R.: III *87*
Wilner, B.: III *265*
Wing, W.R.: I *269*
Winske, D.: II *229*
Witkowski, S.W.A.: III 63
Wobig, H.: I 284, *643;* II *265, 277,* 320, 334
Wolf, G.H.: I 826
Wolfe, S.: I *199*
Wollman, S.: II *345*
Wong, S.K.: I *269*
Woodruff, G.L.: III *413*
Wootton, A.J.: I *51, 335*
Wright, R.E.: III *369*
Wu, C.C.: III *277*
Würsching, E.: II *265, 277*
Yaakobi, B.: III *29*
Yamada, M.: I *167*
Yamada, S.: II *55*
Yamagishi, K.: I *365*
Yamaguchi, S.: I *365*; II *55*
Yamamoto, S.: I *377*
Yamamoto, T.: I *85;* II *649*
Yamanaka, C.: III 52, *135,* 154
Yamanaka, T.: III *135*
Yamauchi, T.: I *85, 377*
Yamazaki, K.: II *649*
Yasuda, H.: II *609*
Yatsu, K.: II *437*
Yee, D.P.: III *369*
Yeh, H.T.: III *343*
Yokoyama, K.: I *377*
Yonas, G.: III *125,* 132, 133
Yoshida, K.: III *135*
Yoshikawa, M.: I 121
Yoshikawa, S.: I *365,* 399, 762, *777;* II 264
Yoshino, R.: II *401, 609*
Young, F.: III *17*
Yu, M.Y.: III *201*
Zahn, H.S.: III *357*
Zakharenkov, Yu.A.: III *167*
Zakharov, L.E.: I *689*
Zaveryaev, V.S.: I *35*
Zehrfeld, H.P.: I *401*
Zelenov, L.A.: II *205*
Zhil'tsov, V.A.: II *469*
Zhukov, A.P.: II *205*
Zhukovskij, V.G.: I *387*
Zippe, M.: II *277*
Zorev, N.N.: III *167*
Zurro, B.: I *269*
Zwicker, H.: II 53
Zymanski, S.: I *65*

The following conversion table is provided for the convenience of readers and to encourage the use of SI units.

FACTORS FOR CONVERTING SOME OT THE MORE COMMON UNITS TO INTERNATIONAL SYSTEM OF UNITS (SI) EQUIVALENTS

NOTES:

(1) SI base units are the metre (m), kilogram (kg), second (s), ampere (A), kelvin (K), candela (cd) and mole (mol).

(2) ▶ indicates SI derived units and those accepted for use with SI;
▷ indicates additional units accepted for use with SI for a limited time.
[*For further information see The International System of Units (SI), 1977 ed., published in English by HMSO, London, and National Bureau of Standards, Washington, DC, and International Standards ISO-1000 and the several parts of ISO-31 published by ISO, Geneva.*]

(3) The correct abbreviation for the unit in column 1 is given in column 2.

(4) ✻ indicates conversion factors given exactly; other factors are given rounded, mostly to 4 significant figures.
≡ indicates a definition of an SI derived unit: [ ] in column 3+4 enclose factors given for the sake of completeness.

Column 1 *Multiply data given in:*	Column 2	Column 3 *by:*	Column 4 *to obtain data in:*	
Radiation units				
▶ becquerel	1 Bq	(has dimensions of s^{-1})		
disintegrations per second (= dis/s)	1 s^{-1}	≡ 1.00×10^{0}	Bq	✻
▷ curie	1 Ci	= 3.70×10^{10}	Bq	✻
▷ roentgen	1 R	[= 2.58×10^{-4}	C/kg]	✻
▶ gray	1 Gy	[≡ 1.00×10^{0}	J/kg]	✻
▷ rad	1 rad	= 1.00×10^{-2}	Gy	✻
sievert *(radiation protection only)*	1 Sv	[= 1.00×10^{0}	J/kg]	✻
rem *(radiation protection only)*	1 rem	[= 1.00×10^{-2}	J/kg]	✻
Mass				
▶ unified atomic mass unit ($\frac{1}{12}$ of the mass of ^{12}C)	1 u	[= $1.660\,57 \times 10^{-27}$	kg, approx.]	
▶ tonne (= metric ton)	1 t	[= 1.00×10^{3}	kg]	✻
pound mass (avoirdupois)	1 lbm	= 4.536×10^{-1}	kg	
ounce mass (avoirdupois)	1 ozm	= 2.835×10^{1}	g	
ton (long) (= 2240 lbm)	1 ton	= 1.016×10^{3}	kg	
ton (short) (= 2000 lbm)	1 short ton	= 9.072×10^{2}	kg	
Length				
statute mile	1 mile	= 1.609×10^{0}	km	
nautical mile (international)	1 n mile	= 1.852×10^{0}	km	✻
yard	1 yd	= 9.144×10^{-1}	m	✻
foot	1 ft	= 3.048×10^{-1}	m	✻
inch	1 in	= 2.54×10^{1}	mm	✻
mil (= 10^{-3} in)	1 mil	= 2.54×10^{-2}	mm	✻
Area				
▷ hectare	1 ha	[= 1.00×10^{4}	m^2]	✻
▷ barn *(effective cross-section, nuclear physics)*	1 b	[= 1.00×10^{-28}	m^2]	✻
square mile, (statute mile)^2	1 $mile^2$	= 2.590×10^{0}	km^2	
acre	1 acre	= 4.047×10^{3}	m^2	
square yard	1 yd^2	= 8.361×10^{-1}	m^2	
square foot	1 ft^2	= 9.290×10^{-2}	m^2	
square inch	1 in^2	= 6.452×10^{2}	mm^2	
Volume				
▶ litre	1 l *or* 1 ltr	[= 1.00×10^{-3}	m^3]	✻
cubic yard	1 yd^3	= 7.646×10^{-1}	m^3	
cubic foot	1 ft^3	= 2.832×10^{-2}	m^3	
cubic inch	1 in^3	= 1.639×10^{4}	mm^3	
gallon (imperial)	1 gal (UK)	= 4.546×10^{-3}	m^3	
gallon (US liquid)	1 gal (US)	= 3.785×10^{-3}	m^3	
Velocity, acceleration				
foot per second (= fps)	1 ft/s	= 3.048×10^{-1}	m/s	✻
foot per minute	1 ft/min	= 5.08×10^{-3}	m/s	✻
mile per hour (= mph)	1 mile/h	= 4.470×10^{-1} = 1.609×10^{0}	m/s km/h	
▷ knot (international)	1 knot	= 1.852×10^{0}	km/h	✻
free fall, standard, g		= 9.807×10^{0}	m/s^2	
foot per second squared	1 ft/s^2	= 3.048×10^{-1}	m/s^2	✻

This table has been prepared by E.R.A. Beck for use by the Division of Publications of the IAEA. While every effort has been made to ensure accuracy, the Agency cannot be held responsible for errors arising from the use of this table.

Column 1 *Multiply data given in:*	Column 2	Column 3 *by:*	Column 4 *to obtain data in:*
Density, volumetric rate			
pound mass per cubic inch	1 lbm/in^3	= 2.768×10^4	kg/m^3
pound mass per cubic foot	1 lbm/ft^3	= 1.602×10^1	kg/m^3
cubic feet per second	1 ft^3/s	= 2.832×10^{-2}	m^3/s
cubic feet per minute	1 ft^3/min	= 4.719×10^{-4}	m^3/s
Force			
▶ newton	1 N	[≡ 1.00×10^0	$m \cdot kg \cdot s^{-2}$] *
dyne	1 dyn	= 1.00×10^{-5}	N *
kilogram force (= kilopond (kp))	1 kgf	= 9.807×10^0	N
poundal	1 pdl	= 1.383×10^{-1}	N
pound force (avoirdupois)	1 lbf	= 4.448×10^0	N
ounce force (avoirdupois)	1 ozf	= 2.780×10^{-1}	N
Pressure, stress			
▶ pascal	1 Pa	[≡ 1.00×10^0	N/m^2] *
▷ atmosphere[a], standard	1 atm	= $1.013\,25 \times 10^5$	Pa *
▷ bar	1 bar	= 1.00×10^5	Pa *
centimetres of mercury (0°C)	1 cmHg	= 1.333×10^3	Pa
dyne per square centimetre	1 dyn/cm^2	= 1.00×10^{-1}	Pa *
feet of water (4°C)	1 ftH_2O	= 2.989×10^3	Pa
inches of mercury (0°C)	1 inHg	= 3.386×10^3	Pa
inches of water (4°C)	1 inH_2O	= 2.491×10^2	Pa
kilogram force per square centimetre	1 kgf/cm^2	= 9.807×10^4	Pa
pound force per square foot	1 lbf/ft^2	= 4.788×10^1	Pa
pound force per square inch (= psi)[b]	1 lbf/in^2	= 6.895×10^3	Pa
torr (0°C) (= mmHg)	1 torr	= 1.333×10^2	Pa
Energy, work, quantity of heat			
▶ joule (≡ W·s)	1 J	[≡ 1.00×10^0	N·m] *
▶ electronvolt	1 eV	[= $1.602\,19 \times 10^{-19}$	J, approx.]
British thermal unit (International Table)	1 Btu	= 1.055×10^3	J
calorie (thermochemical)	1 cal	= 4.184×10^0	J *
calorie (International Table)	1 cal_{IT}	= 4.187×10^0	J
erg	1 erg	= 1.00×10^{-7}	J *
foot-pound force	1 ft·lbf	= 1.356×10^0	J
kilowatt-hour	1 kW·h	= 3.60×10^6	J *
kiloton explosive yield (PNE) (≡ 10^{12} g-cal)	1 kt yield	≃ 4.2×10^{12}	J
Power, radiant flux			
▶ watt	1 W	[≡ 1.00×10^0	J/s] *
British thermal unit (International Table) per second	1 Btu/s	= 1.055×10^3	W
calorie (International Table) per second	1 cal_{IT}/s	= 4.187×10^0	W
foot-pound force/second	1 ft·lbf/s	= 1.356×10^0	W
horsepower (electric)	1 hp	= 7.46×10^2	W *
horsepower (metric) (= ps)	1 ps	= 7.355×10^2	W
horsepower (550 ft·lbf/s)	1 hp	= 7.457×10^2	W
Temperature			
▶ temperature in degrees Celsius, t where T is the thermodynamic temperature in kelvin and T_0 is defined as 273.15 K	$t = T - T_0$		
degree Fahrenheit	$t_{°F} - 32$	× (5/9) gives	t *(in degrees Celsius)* *
degree Rankine	$T_{°R}$		T *(in kelvin)* *
degrees of temperature difference[c]	$\Delta T_{°R}$ (= $\Delta t_{°F}$)		ΔT (= Δt) *
Thermal conductivity[c]			
1 Btu·in/(ft²·s·°F) *(International Table Btu)*		= 5.192×10^2	$W \cdot m^{-1} \cdot K^{-1}$
1 Btu/(ft·s·°F) *(International Table Btu)*		= 6.231×10^3	$W \cdot m^{-1} \cdot K^{-1}$
1 $cal_{IT}/(cm \cdot s \cdot °C)$		= 4.187×10^2	$W \cdot m^{-1} \cdot K^{-1}$

[a] atm abs, ata: atmospheres absolute; atm (g), atü: atmospheres gauge.

[b] lbf/in^2 (g) (= psig): gauge pressure; lbf/in^2 abs (= psia): absolute pressure.

[c] The abbreviation for temperature difference, deg (= degK = degC), is no longer acceptable as an SI unit.

HOW TO ORDER IAEA PUBLICATIONS

An exclusive sales agent for IAEA publications, to whom all orders and inquiries should be addressed, has been appointed in the following country:

UNITED STATES OF AMERICA UNIPUB, 345 Park Avenue South, New York, NY 10010

In the following countries IAEA publications may be purchased from the sales agents or booksellers listed or through your major local booksellers. Payment can be made in local currency or with UNESCO coupons.

ARGENTINA	Comisión Nacional de Energía Atomica, Avenida del Libertador 8250, RA-1429 Buenos Aires
AUSTRALIA	Hunter Publications, 58 A Gipps Street, Collingwood, Victoria 3066
BELGIUM	Service du Courrier de l'UNESCO, 202, Avenue du Roi, B-1060 Brussels
CZECHOSLOVAKIA	S.N.T.L., Spálená 51, CS-113 02 Prague 1 Alfa, Publishers, Hurbanovo námestie 6, CS-893 31 Bratislava
FRANCE	Office International de Documentation et Librairie, 48, rue Gay-Lussac, F-75240 Paris Cedex 05
HUNGARY	Kultura, Hungarian Trading Company for Books and Newspapers, P.O. Box 149, H-1389 Budapest 62
INDIA	Oxford Book and Stationery Co., 17, Park Street, Calcutta-700 016 Oxford Book and Stationery Co., Scindia House, New Delhi-110 001
ISRAEL	Heiliger and Co., Ltd., Scientific and Medical Books, 3, Nathan Strauss Street, Jerusalem
ITALY	Libreria Scientifica, Dott. Lucio de Biasio "aeiou", Via Meravigli 16, I-20123 Milan
JAPAN	Maruzen Company, Ltd., P.O. Box 5050, 100-31 Tokyo International
NETHERLANDS	Martinus Nijhoff B.V., Booksellers, Lange Voorhout 9-11, P.O. Box 269, NL-2501 The Hague
PAKISTAN	Mirza Book Agency, 65, Shahrah Quaid-e-Azam, P.O. Box 729, Lahore 3
POLAND	Ars Polona-Ruch, Centrala Handlu Zagranicznego, Krakowskie Przedmiescie 7, PL-00-068 Warsaw
ROMANIA	Ilexim, P.O. Box 136-137, Bucarest
SOUTH AFRICA	Van Schaik's Bookstore (Pty) Ltd., Libri Building, Church Street, P.O. Box 724, Pretoria 0001
SPAIN	Diaz de Santos, Lagasca 95, Madrid-6 Diaz de Santos, Balmes 417, Barcelona-6
SWEDEN	AB C.E. Fritzes Kungl. Hovbokhandel, Fredsgatan 2, P.O. Box 16356, S-103 27 Stockholm
UNITED KINGDOM	Her Majesty's Stationery Office, P.O. Box 569, London SE 1 9NH
U.S.S.R.	Mezhdunarodnaya Kniga, Smolenskaya-Sennaya 32-34, Moscow G-200
YUGOSLAVIA	Jugoslovenska Knjiga, Terazije 27, P.O. Box 36, YU-11001 Belgrade

---

Orders from countries where sales agents have not yet been appointed and requests for information should be addressed directly to:



Division of Publications
International Atomic Energy Agency
Kärntner Ring 11, P.O. Box 590, A-1011 Vienna, Austria

79-6273

INTERNATIONAL
ATOMIC ENERGY AGENCY
VIENNA, 1979

SUBJECT GROUP: III
Physics/Plasma Physics, Fusion
PRICE: Austrian Schillings 800,–